

\*Original contains color  
plates. All DTIC reproductions  
will be in black and  
white\*

PL-TR-93-2031

AD-A266 064



DTIC  
ELECTE  
JUN 14 1993  
S C D

(2)

## ANALYSIS OF GEOPHYSICAL MEASUREMENTS AND SPACECRAFT INTERACTIONS

J. N. Bass  
N. A. Bonito  
P. L. Grady  
C. A. Hein  
M. J. Kendra  
D. S. Reynolds  
M. F. Tautz

K. H. Bhavnani  
K. H. Bounar  
J. M. Griffin  
C. E. Jordan  
W. J. McNeil  
A. Setayesh  
R. P. Vancour

Radex, Inc.  
Three Preston Court  
Bedford, MA 01730

January 29, 1993

Final Report  
June 1989 - January 1993

Approved for public release; distribution unlimited

93 6 14 09 6

93-13287



**PHILLIPS LABORATORY**  
**Directorate of Geophysics**  
**AIR FORCE MATERIEL COMMAND**  
**HANSCOM AIR FORCE BASE, MA 01731-3010**

"This technical report has been reviewed and is approved for publication"



EDWARD C. ROBINSON  
Contract Manager  
Data Analysis Division



ROBERT E. MCINERNEY, Director  
Data Analysis Division

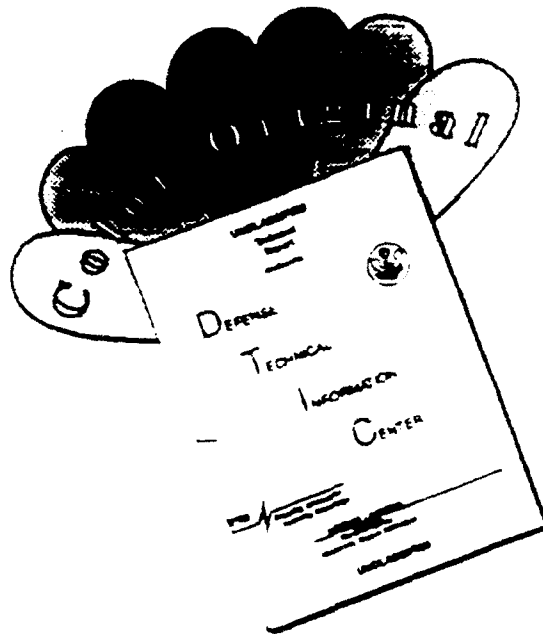
This report has been reviewed by the ESD Public Affairs Office (PA) and is releasable to the National Technical Information Service (NTIS).

Qualified requestors may obtain additional copies from the Defense Technical Information Center. All others should apply to the National Technical Information Service.

If your address has changed, or if you wish to be removed from the mailing list, or if the addressee is no longer employed by your organization, please notify GL/IMA, Hanscom AFB, MA 01731. This will assist us in maintaining a current mailing list.

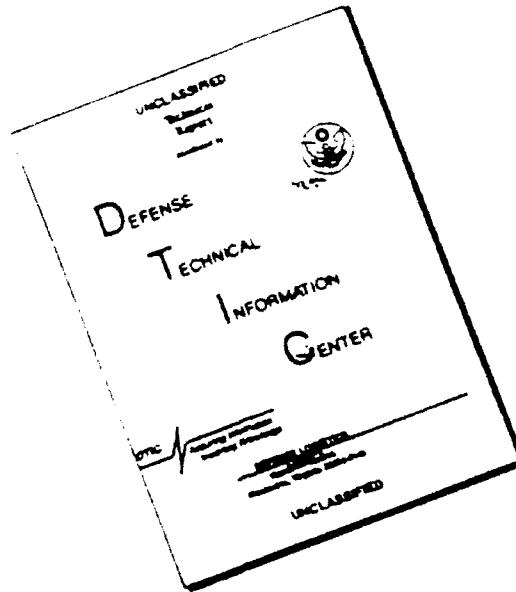
Do not return copies of this report unless contractual obligations or notices on a specific document requires that it be returned.

# DISCLAIMER NOTICE



THIS DOCUMENT IS BEST QUALITY AVAILABLE. THE COPY FURNISHED TO DTIC CONTAINED A SIGNIFICANT NUMBER OF COLOR PAGES WHICH DO NOT REPRODUCE LEGIBLY ON BLACK AND WHITE MICROFICHE.

# DISCLAIMER NOTICE



THIS DOCUMENT IS BEST QUALITY AVAILABLE. THE COPY FURNISHED TO DTIC CONTAINED A SIGNIFICANT NUMBER OF PAGES WHICH DO NOT REPRODUCE LEGIBLY.



REPORT DOCUMENTATION PAGE			Form Approved GMB No. 0704-0188
<small>Public reporting burden for this collection of information is estimated to average 1 hour per response, including the time for reviewing instructions, searching existing data sources, gathering and maintaining the data needed, and completing and reviewing the collection of information. Send comments regarding this burden estimate or any other aspect of this collection of information, including suggestions for reducing this burden, to Washington Headquarters Services, Directorate for Information Operations and Reports, 1215 Jefferson Davis Highway, Suite 1204, Arlington, VA 22202-4302, and to the Office of Management and Budget, Paperwork Reduction Project (0704-0188), Washington, DC 20503.</small>			
1. AGENCY USE ONLY (Leave blank)	2. REPORT DATE 29 January 1993	3. REPORT TYPE AND DATES COVERED Final Report (June 1989 - January 1993)	
4. TITLE AND SUBTITLE  Analysis of Geophysical Measurements and Spacecraft Interactions		5. FUNDING NUMBERS  PE 62101F PR 7659 TA 05 WU AB  Contract F19628-89-C-0068	
6. AUTHOR(S) J. N. Bass, K. H. Bhavnani, N. A. Bonito, K. H. Bounar, P. L. Grady, J. M. Griffin, C. A. Hein, C. E. Jordan, M. J. Kendra, W. J. McNeil, D. S. Reynolds, A. Setayesh, M. F. Tautz, R. P. Vancour			
7. PERFORMING ORGANIZATION NAME(S) AND ADDRESS(ES)  RADEX, Inc. Three Preston Court Bedford, MA 01730		8. PERFORMING ORGANIZATION REPORT NUMBER  RXR-93011	
9. SPONSORING/MONITORING AGENCY NAME(S) AND ADDRESS(ES)  Phillips Laboratory 29 Randolph Road Hanscom AFB, MA 01731-3010  Contract Manager: Edward C. Robinson/GPD		10. SPONSORING/MONITORING AGENCY REPORT NUMBER  PL-TR-93-2031	
11. SUPPLEMENTARY NOTES			
12a. DISTRIBUTION/AVAILABILITY STATEMENT Approved for Public Release Distribution Unlimited		12b. DISTRIBUTION CODE	
13. ABSTRACT (Maximum 200 words) Investigations were supported to analyze geophysical measurements with integrated applications of ephemerides, physics, and mathematics of the ionosphere and near space. Projects undertaken included analytical and computational simulation of spacecraft interactions processes associated with charging, contamination, liquid venting, and critical ionization velocity; data based and analytical investigations of trapped particles, dosage, magnetic fields and instrumentation for the CRRES experiment; data based studies of auroral electron and ion precipitation including neural network techniques, ionospheric scintillation and OTH backscatter, and atmospheric density and orbital decay. Systems were developed and applied for calibration and processing of the CRRES and APEX magnetometers, and for generation of satellite attitude and ephemeris. Techniques employed for applying coordinate systems, depicting vehicle and astronomical circumstances, and interactively presenting data in conventional and color formats are also described.			
14. SUBJECT TERMS Spacecraft charging, Contamination, CIV, Liquid venting, CRRES, Radiation belts, PROTEL, Dosimeter, Magnetic fields, Magnetometer calibration and processing, Auroral electron and ion precipitation, Scintillation, OTH backscatter, Atmospheric density, APEX, Attitude		15. NUMBER OF PAGES 286	
		16. PRICE CODE	
17. SECURITY CLASSIFICATION OF REPORT Unclassified	18. SECURITY CLASSIFICATION OF THIS PAGE Unclassified	19. SECURITY CLASSIFICATION OF ABSTRACT Unclassified	20. LIMITATION OF ABSTRACT  Unlimited

# TABLE OF CONTENTS

Section	Page
<b>1. INVESTIGATION OF SPACECRAFT INTERACTIONS</b>	<b>1</b>
<b>1.1 SPACECRAFT CHARGING</b>	<b>1</b>
1.1.1 Introduction	1
1.1.2 Analysis of the CHAWS experiment	1
1.1.3 Plasma Chamber Simulations with MACH	2
1.1.4 Wake-Shield Simulations with POLAR	5
<b>1.2 SPACECRAFT CONTAMINATION - SOCRATES</b>	<b>9</b>
1.2.1 Monte Carlo Simulation of Shuttle Contamination with SOCRATES	9
1.2.2 Research and Analysis using SOCRATES	10
<b>1.3 THREE DIMENSIONAL COLOR DISPLAY OF DATA</b>	<b>22</b>
<b>1.4 SPACECRAFT LIQUID VENTING MODELS</b>	<b>23</b>
1.4.1 Liquid Water Release into Space	23
1.4.2 Liquid Water Vent Modeling	24
1.4.2.1 One Dimensional Liquid Water Vent Modeling	24
1.4.2.2 Two Dimensional Liquid Water Vent Modeling	31
<b>1.5 INVESTIGATIONS OF THE CRITICAL IONIZATION VELOCITY IN SPACE</b>	<b>40</b>
1.5.1 Simulation of CIV in Various Species	40
1.5.1.1 Kinetic Processes	41
1.5.1.2 Neutral Species	42
1.5.1.3 The Simulations	42
1.5.1.4 Results	43
1.5.1.5 Conclusions	45
1.5.2 Amplification of CIV by Associative Ionization	45
1.5.2.1 Associative Ionization	46
1.5.2.2 AI Mistaken for CIV	46
1.5.2.3 Combined AI and CIV	47
1.5.2.4 Comparison with Other Processes	47
1.5.2.5 A Proposed Experiment	49
1.5.3 The Importance of Seed Ionization In CIV Space Experiments	49
1.5.3.1 Laboratory Conditions	50
1.5.3.2 Space Conditions	50
1.5.3.3 The Difficulty of CIV in Space	51
1.5.3.4 A CIV Yield Model	51
1.5.3.5 Reasons for a Delay	53
1.5.3.6 Conclusions	54
1.5.4 CIV in a Mixture	54
1.5.4.1 Energy Budget	55
1.5.4.2 Ionization Model	55
1.5.4.3 An Application	56
1.5.5 Amplification of CIV by a Pulsed Neutral Beam	58
1.5.5.1 Simulation	58
1.5.5.2 Conclusion	58

By _____	
Distribution / _____	
Availability Cod _____	
Dist	Avail and/or Special
A-1	

## Table of Contents (cont'd)

<u>Section</u>	<u>Page</u>
1.5.6 Altitude Effects on CIV Experiments in Space . . . . .	59
1.5.6.1 Electron Heating . . . . .	59
1.5.6.2 Energy Losses . . . . .	60
1.5.6.3 Charge Exchange . . . . .	60
1.5.7 Conclusion . . . . .	60
1.6 REFERENCES . . . . .	61
 <b>2. COMBINED RELEASE AND RADIATION EFFECTS SATELLITE (CRRES) . . . . .</b>	 <b>65</b>
2.1 CRRES INSTRUMENT MODELING . . . . .	65
2.1.1 PROTEL . . . . .	65
2.1.1.1 Introduction . . . . .	65
2.1.1.2 Description of the PROTEL Contamination Code . . . . .	66
2.1.1.3 Results . . . . .	68
2.1.2 CRRES Dosimeter Modeling . . . . .	74
2.2 RADIATION BELT MODELING STUDIES . . . . .	80
2.2.1 Adiabatic Invariants and Dipole-Equivalent Invariants . . . . .	80
2.2.1.1 Equivalent Parameters . . . . .	81
2.2.1.2 Software . . . . .	82
2.2.1.3 Computer Timing . . . . .	86
2.2.1.4 Properties of Invariants . . . . .	87
2.2.2 Dose Modeling and Analysis Support . . . . .	92
2.2.2.1 Dose Calculations . . . . .	92
2.2.2.2 Transformation from L, B/B <sub>0</sub> to Geographic Coordinates . . . . .	96
2.2.2.3 L, B, and B <sub>0</sub> for JSTAR Ephemeris . . . . .	100
2.2.2.4 Development of an Internal Field B <sub>0</sub> /B Model . . . . .	101
2.2.3 HEEF-Dosimeter-GOES Electron Measurement Intercomparison . . . . .	105
2.2.3.1 GOES-HEEF Comparison . . . . .	106
2.2.3.2 HEEF-Dosimeter Comparison . . . . .	112
2.2.3.3 Conclusions . . . . .	112
2.2.4 Dynamic Magnetic Field Models . . . . .	112
2.2.4.1 Models Published Before 1989 . . . . .	112
2.2.4.2 Models Published in 1989 or Later . . . . .	115
2.2.4.3 Preliminary Ring Current Study . . . . .	120
2.2.4.4 Existing Models . . . . .	123
2.2.5 Support of Related Research . . . . .	123
2.3 REFERENCES . . . . .	132

## Table of Contents (cont'd)

<u>Section</u>	<u>Page</u>
<b>3. IONOSPHERIC STUDIES</b> .....	134
3.1 IONOSPHERIC SCINTILLATION .....	134
3.1.1 SDS Software Processing System .....	134
3.1.2 Airborne Ionospheric Observation (AIO) .....	136
3.1.2.1 Intensity Only .....	140
3.1.2.2 Intensity and Phase .....	141
3.1.2.3 Comments .....	141
3.1.3 Wideband Scintillation Model (WBMOD) .....	142
3.2 GENERAL ELECTRIC OVER THE HORIZON (OTH) BACKSCATTER RADAR .....	146
3.2.1 OTH Tape Processing System .....	146
3.2.2 Amplitude Range Doppler Data Studies .....	149
3.2.3 OTH Backscatter Sounder Data Studies .....	157
3.2.4 Ionospheric Models and Ray Tracing .....	161
3.3 REFERENCES .....	167
<b>4. MAGNETOMETER DATA PROCESSING SYSTEMS</b> .....	169
4.1 CALIBRATION AND PROCESSING OF THE CRRES FLUXGATE MAGNETOMETER DATA .....	169
4.1.1 The Satellite and Instrument .....	169
4.1.2 Pre-Launch Activities .....	169
4.1.3 Calibration .....	170
4.1.3.1 The Spin Fit .....	171
4.1.3.2 Elevations .....	171
4.1.3.3 Gain Ratios .....	172
4.1.3.4 Offsets .....	172
4.1.3.5 Absolute Gains and Phase .....	172
4.1.4 Calculation of Assumed Quantities .....	173
4.1.4.1 Spin Axis Offset .....	173
4.1.4.2 Absolute Phase .....	173
4.1.4.3 Absolute Gain .....	174
4.1.5 Despinning .....	174
4.1.6 Data Products .....	174
4.2 DMSP MAGNETOMETER .....	176
4.3 REFERENCES .....	177
<b>5. ATMOSPHERIC DENSITY</b> .....	178
5.1 SEMIANNUAL AND EUV VARIATIONS .....	178
5.1.1 Introduction .....	178
5.1.2 Computational Procedures .....	179
5.1.3 Results .....	180
5.1.3.1 Semiannual Variation .....	180
5.1.3.2 EUV Variation .....	183

## Table of Contents (cont'd)

<u>Section</u>	<u>Page</u>
5.2 ANALYSIS OF VARIATIONS IN LIDAR DENSITY DATA .....	186
5.3 EVALUATION OF GRAM88 MODEL .....	194
5.4 DETERMINATION OF ATMOSPHERIC DENSITY FROM ORBITAL ELEMENT SETS .....	197
5.5 ORBITAL DECAY .....	203
5.6 REFERENCES .....	212
<b>6. AURORAL PARTICLE PRECIPITATION .....</b>	<b>214</b>
6.1 ELECTRON PRECIPITATION .....	214
6.1.1 Introduction .....	214
6.1.2 Electron Precipitation Data Base .....	214
6.1.3 Electron Precipitation Models .....	215
6.1.4 Integral Probability of Electron Flux Events .....	215
6.1.5 Persistence of Auroral Electron Flux Events .....	218
6.2 FUNCTIONAL REPRESENTATION OF PATTERNS OF AVERAGE AURORAL ION PRECIPITATION .....	226
6.2.1 Introduction .....	226
6.2.2 The Statistical Model .....	226
6.2.3 Fitting Procedures .....	226
6.2.4 Results .....	227
6.3 NEURAL NETWORKS .....	229
6.4 REFERENCES .....	231
<b>7. EPHEMERIS .....</b>	<b>233</b>
7.1 LOKANGL .....	233
7.1.1 STS53 Mission Support with Ephemeris and Graphics Software .....	233
7.1.2 Viewing Diagrams for Low Earth Satellites (Hussey Charts) .....	233
7.2 COORDINATE SYSTEMS AND TRANSFORMATIONS .....	236
7.2.1 Coordinate Systems for Space and Geophysical Applications .....	236
7.2.2 Reference Frames - FK4/FK5/J2000 .....	237
7.2.3 Quaternions .....	243
7.3 REFERENCES .....	245
<b>8. SOFTWARE SYSTEMS .....</b>	<b>247</b>
8.1 AITS AND IBSS SUNRISE AND SUNSET .....	247
8.2 SUATEK ENHANCEMENTS .....	249
8.2.1 SUAMENU Example I .....	249
8.2.2 SUAMENU Example II .....	251
8.3 ROCKET TRAJECTORY .....	254
8.4 PC TEKSIM .....	254

## Table of Contents (cont'd)

<u>Section</u>	<u>Page</u>
<b>8.5 PHIZYX</b> .....	255
8.5.1 Introduction .....	255
8.5.2 Development .....	256
8.5.3 Features .....	256
8.5.4 Concepts .....	257
8.5.5 PHIZYX Data Format .....	257
<b>8.6 MODELING OF THE CRRES ATTITUDE</b> .....	260
8.6.1 The CRRES Attitude Problem .....	260
8.6.2 The Model .....	261
8.6.2.1 Spin Axis Vector .....	261
8.6.2.2 Spin Rate .....	261
8.6.2.3 Eclipses .....	263
8.6.3 Results .....	263
<b>8.7 APEX ATTITUDE &amp; EPHEMERIS</b> .....	263
8.7.1 Ephemeris .....	263
8.7.2 Attitude .....	264
8.7.2.1 Magnetometer Calibration .....	264
8.7.2.2 Sunlit Attitude .....	264
8.7.2.3 Eclipse Attitude .....	266
<b>8.8 REFERENCES</b> .....	267

## LIST OF FIGURES

Figure	Page
1. Schematic of instability in electrostatic potential . . . . .	3
2. Trapped electron density . . . . .	3
3. Comparison of measured and MACH chamber potentials: (a) Chamber potentials measured with an emissive probe; (b) Chamber potentials from MACH simulation . . . . .	4
4. Particle orbits from MACH chamber simulation: (a) Forward trajectories for probe 1 cm behind the disk; (b) Forward trajectories for probe 3 cm behind the disk; (c) Forward trajectories for probe at 5 cm behind the disk . . . . .	5
5. Sequence of steps to generate the POLAR IV characteristics . . . . .	6
6. Schematic of the Wake-shield Model . . . . .	7
7. POLAR electrostatic potentials for -1 KV probe, tilt angle = 0 . . . . .	7
8. POLAR IV characteristics with tilt angle as parameter . . . . .	8
9. Total solution region averaged values for CO vibrational excitations in unsteady state condition . . . . .	13
10. Gray scale plots showing the co vibrational excitations at $4.6 \mu\text{m}$ from the mechanism $\text{O} + \text{CO}_2 \rightarrow \text{CO}^* + \text{O}_2$ . . . . .	14
11. Total solution region averaged values for $\text{OH}^*$ vibrational excitation . . . . .	15
12. Gray scale plots showing the OH vibrational excitations at $2.7 \mu\text{m}$ from the mechanism $\text{H} + \text{CO}_2 \rightarrow \text{OH}^* + \text{CO}$ . . . . .	16
13. Contour plots showing the $\text{CO}_2$ , CO, and OH vibrational excitations for the same scale . . . . .	18
14. Contour plots showing the $\text{CO}_2$ , CO, and OH reaction rates for the same scale . . . . .	19
15. SOCRATES simulation of shuttle PRCS ram burn . . . . .	25
16. Pitot-Pressure measured at the vapor expansion flow radial to the jet . . . . .	26
17. The effect of initial particle size on particle number density . . . . .	28
18. Particle size as a function of distance . . . . .	29
19. The effect of initial particle size on particle velocity . . . . .	30
20. Curves of plasma density as a function of time for the four gases studied at various beam velocities . . . . .	44
21. Demonstration of the effect of neutral density on CIV in barium. As density increases, the line excitation processes dominate over ionization . . . . .	44
22. The beam density arising from Associative Ionization for simple expansion models of the CRRES and CRIT II releases . . . . .	48
23. The infinite time yield of ions as a function of the delay time before ionization begins, $t_d$ . . . . .	53
24. Parametric domain for CIV in a 50% mixture of He and Ne . . . . .	57
25. Parametric domain for CIV in a 50% mixture of H and Ne . . . . .	57
26. Plasma density increase for one, two and three beams, all of the same total length . . . . .	59
27. PROTEL HEH cross section (not to scale) . . . . .	66
28. Response functions, channel 11, isotropic case . . . . .	71
29. Response functions, channel 12, isotropic case . . . . .	71
30. Response functions, channel 11, mirror plane distribution . . . . .	72
31. Response functions, channel 12, mirror plane distribution . . . . .	73
32. Path length distribution computed using the Monte Carlo method . . . . .	76

# List of Figures (cont'd)

Figure	Page
33. Overview of software for computation of adiabatic invariants and dipole equivalent invariants . . . . .	83
34. Dipole-equivalent L, as percent difference from the equatorial crossing distance . . . . .	88
35. McIlwain L, as percent difference from the equatorial crossing distance . . . . .	89
36. Dipole-equivalent pitch angle (difference from actual) . . . . .	90
37. Dipole-equivalent momentum (ratio to actual) . . . . .	91
38. Electron distribution function, before (line) and after (symbols) the 8/26/90 sudden storm commencement . . . . .	93
39. Flux predicted for the CRRES HEEF 2.0 to 2.5 MeV electron channel based on the NASA model AE8MAX, along with the measured data, before the March 1991 storm . . . . .	94
40. Flux predicted for the CRRES HEEF 2.0 to 2.5 MeV electron channel based on the NASA model AE8MAX, along with the measured data, after the March storm . . . . .	95
41. Dose calculated at the center of the LoLet Dome 1 electrons summed over 10 orbits at a time . . . . .	98
42. HEEF (L = 6.5) - GOES comparison . . . . .	107
43. GOES particle data 21-30 March 1991 . . . . .	108
44. HEEF > 2 MeV electrons L > 5 orbit 600, and GOES measurement at L = 7.2 . . . . .	109
45. CRRES dosimeter count rate ratio predicted to actual (symbols) and HEEF operating temperature (line) . . . . .	113
46. Same as Figure 45, except coverage limited to first 100 CRRES orbits . . . . .	114
47. Model comparison during a magnetically quiet period . . . . .	116
48. Model comparison during a substorm . . . . .	117
49. Sample of a preliminary comparison of these models to CRRES data . . . . .	118
50. The angle between the CRRES magnetometer measured field vectors and the model field vectors for part of 26 August 1990 . . . . .	119
51. SM local time, SM latitude, Kp, and $\Delta B$ for CRRES orbit 587, 23 March 1991 . . . . .	121
52. $\Delta B_{min}$ is shown for each of the 50 orbits spanning 21 March to 9 April 1991 . . . . .	122
53. $\Delta B_{min}$ binned by latitude and L-shell for Kp less than 2+ . . . . .	124
54. $\Delta B_{min}$ binned by latitude and L-shell for Kp between 3- and 5+ . . . . .	125
55. $\Delta B_{min}$ binned by latitude and L-shell for Kp greater than 6- . . . . .	126
56. Equatorial constant B contours for 40° pitch angle particles as determined from the Hilmer-Voigt model . . . . .	127
57. Pitch angle coverage for a detector facing along the +x axis in spacecraft coordinates for attitude configuration V at 0hrs LT . . . . .	128
58. Pitch angle coverage for a detector facing along the +y axis in spacecraft coordinates for attitude configuration V at 0hrs LT . . . . .	129
59. Latitude and local time coverage in SM coordinates of CRRES through 1276 orbits . . . . .	131
60. Complex scintillation signal received at Sondrestrom, Greenland, on December 5, 1988. In mode 3 of operation, three spaced receiving stations record data in three channels. The top and bottom panels show the in-phase and quadrature signals, respectively . . . . .	135
61. The detrended scintillation phase and the normalized scintillation intensity at Sondrestrom, Greenland, starting at 02:02 on December 6, 1988. The scintillation signal is from channel 2. In each panel, the top plot gives the intensity in decibels from -30 to +10 dB, and the bottom plot gives the phase in radians from -50 to +50 radians . . . . .	137



# List of Figures (cont'd)

Figure	Page
62. The scintillation intensity and phase spectra for two consecutive 164-second data blocks. On the upper right of each plot are provided the statistics of the scintillation signal describing the spectrum characteristics. The signal frequency varies from 0.01 to 25 Hz . . . . .	138
63. The three statistical parameters of the scintillation intensity and phase for a period of 4 hours are shown for all of the data processed from the evening of December 5, 1988 observations at Sondrestrom, Greenland . . . . .	139
64. The top panel shows the scintillation intensity over Andoya, Norway, during the AIO campaign on January 16, 1990. The period shown is from 02:45:37 to 02:48:17. The bottom panel shows the corresponding intensity spectra. On the upper right of each the spectral plot are provided the statistics of the scintillation intensity for an 82-second window. The signal frequency varies from 0.01 to 25 Hz . . . . .	143
65. The top panel shows the scintillation intensity for the same period as Figure 64. Here, the intensity spectra is actually the average of two 82-second spectra. The bottom panel shows the phase spectrum for the same period. On the upper right of each the spectral plot are provided the scintillation statistics . . . . .	144
66. OTH coverage areas . . . . .	151
67. Sample ARD data plot . . . . .	152
68. Time averaged ARD data . . . . .	152
69. Sample ground clutter amplitude plot . . . . .	154
70. Simulated equatorial backscatter doppler spectrum . . . . .	155
71. Ground clutter excision . . . . .	156
72. Equatorial clutter fit . . . . .	156
73. Sample backscatter ionogram . . . . .	158
74. Winter, 1991-92 ionogram data base . . . . .	159
75. Equatorial clutter scatter plot . . . . .	159
76. 1991-92 ECRS clutter . . . . .	160
77. FAIM contour . . . . .	162
78. Ray trace with ionospheric contour overlay . . . . .	163
79. Individual ray trace plot with overlays . . . . .	164
80. Synthesized backscatter ionogram . . . . .	166
81. VDH survey plot . . . . .	175
82(a). Semiannual variation of total mass density: measured (symbols), least squares fit (solid curve), and MSIS86 model (light curve) . . . . .	181
82(b). Semiannual variation of total mass density: measured (symbols), least squares fit (solid curve), and MSIS86 model (light curve) . . . . .	182
83. Response of total mass density to EUV variations: measured (symbols), least squares fit (solid curve), and MSIS86 model (dashed curve). The curves are with the last two terms of Eq. (89) removed . . . . .	185
84. The measured density (ratios to US76) for the 61 profiles, overlaid on a single page . . . . .	187
85. (and Figures 86 - 90) The ratios for the individual profiles, seen separately. Each curve is accompanied by a straight vertical line designating unity ratio. The tick mark to the immediately left corresponds to a ratio of -4, and the tick mark to the immediate right designates +6 . . . . .	187

# List of Figures (cont'd)

Figure	Page
86. Ratio for individual profile . . . . .	188
87. Ratio for individual profile . . . . .	188
88. Ratio for individual profile . . . . .	189
89. Ratio for individual profile . . . . .	189
90. Ratio for individual profile . . . . .	190
91. The measurement error standard deviation, computed as the square root of the mean of the square of the measurement errors given in the file . . . . .	190
92. The total standard deviation of the density data . . . . .	191
93. The mean density . . . . .	191
94. The mean density, with horizontal bars running between + and - the estimated real density variation . . . . .	192
95. The total and measurement error standard deviations . . . . .	192
96. The total standard deviation vs. the measurement error standard deviation . . . . .	193
97. The estimated mean square of the real density variation . . . . .	193
98. Comparisons of GRAMM88 with other models . . . . .	196
99. BSTAR values . . . . .	199
100. Densities at altitude at epoch obtained from BSTAR values . . . . .	200
101. MSIS86 density values . . . . .	201
102. BSTAR derived density values in semi-logarithmic scale . . . . .	202
103. The effect of inclination on orbit life . . . . .	205
104. Perigee and apogee decay histories of a slightly elliptical orbit (Case 2) . . . . .	206
105. Abrupt changes in satellite orbit as calculated by DECAY . . . . .	208
106. DECAY calculations after correction of Bessel function coefficient . . . . .	209
107. Reproduction of King-Hele's Figure 2.5 . . . . .	210
108. Mueller code results . . . . .	211
109. Polar contour plot of the percent probability of the electron event occurrence in geomagnetic coordinate system. The geomagnetic activity level (given $K_p$ ), and the characteristics of the event (given by $E_{ave}$ and $JE_{tot}$ ) are shown on the right. The percent probability values are given in linear scale . . . . .	216
110. Contour plot of the probability distribution of the average energy versus the energy flux in geomagnetic coordinate system. The geomagnetic location (given by MLT and CGL), and the geomagnetic activity level (given by $K_p$ ) are shown on the right. The percent probability values are given in logarithmic scale . . . . .	217
111. Integral probability of occurrence of auroral electron events defined by the parameter ranges shown on the right. The probability is given as a function of the reference latitude (CGL) and the differential latitude ( $\Delta CGL$ ) which takes positive values poleward of CGL, and negative values otherwise. The bottom panel shows the total count for this event as a function of geomagnetic location. The maximum probability for $JE_{tot} \geq 0.5kR$ is 9%, and occurs at $65^\circ$ CGL. By varying $\Delta CGL$ , an integral probability as high as 16.2% can be achieved . . . . .	219
112. Integral probability of occurrence of same auroral electron events as in Figure 111, except that $JE_{tot} \geq 160kR$ . The maximum probability drops to about 0.3%, and occurs at $67^\circ$ CGL. By varying $\Delta CGL$ , an integral probability of about 2.7% can be achieved . . . . .	220

# List of Figures (cont'd)

Figure	Page
113. Integral probability of occurrence of auroral electron events defined by the parameter ranges shown on the right of the plot. The maximum probability for a low $K_p$ ( $0_0$ to $1+$ ) of 0.7% occurs at $67^\circ$ CGL, and by varying $\Delta$ CGL, the maximum probability can be as much as 3.15% . . . . .	221
114. Integral probability of occurrence of auroral electron events as defined in Figure 113, but for a disturbed $K_p$ level ( $6-$ to $9_0$ ). The maximum probability drops to 0.75% at $61^\circ$ CGL, and by varying $\Delta$ CGL, a maximum probability of 1.5% can be achieved . . . . .	222
115. Integral probability of occurrence of auroral electron events as defined in Figure 113, but for a moderate $K_p$ level ( $2-$ to $3+$ ). The maximum probability drops of 8% occurs at $65^\circ$ CGL, and by varying $\Delta$ CGL, the maximum probability can be as much as 14.4% . . . . .	223
116. Superposed epochs of 4-day $K_p$ (dashed line) and auroral events per hemispheric pass (solid line) sampled at 1.2 hours. The auroral events are given by an energy flux greater than $2kR$ . The solid curve is a 3-point smoothing of the electron events shown in plus signs (+). There were 74 cases where the $K_p$ threshold of 4.0 is satisfied for at least 3.0 hours . . . . .	225
117. Sample contour plot of raw ion data (left) and model (right) for $K_p=3$ . . . . .	228
118. Sample set of plots . . . . .	234
119. Satellite viewing (Hussey) charts . . . . .	235
120. Typical SUAMENU plot . . . . .	250
121. Linear combination example . . . . .	253
122. Typical PHIZYX plot, where Z values were collected and averaged into bins defined by specific X and Y ranges . . . . .	258
123. Typical PHIZYX plot, where Z values were determined at reasonable intervals at specific X and Y values . . . . .	259
124. The angle between a model magnetic field and the field as measured by the fluxgate magnetometer. Attitude is modeled by the original CADP routine . . . . .	262
125. Same as Figure 124, but with the attitude model generated by the current attitude modeling software . . . . .	262
126. Typical pitch and yaw (sun directed) angles during sunlit operation . . . . .	265

## LIST OF TABLES

<u>Table</u>	<u>Page</u>
1. Molecular Parameters Used in the Calculations . . . . .	11
2. Rate Coefficients Used in SOCRATES, $k = A T^n \exp(-E_a/kT)$ . . . . .	11
3. Atmospheric Density and Temperature . . . . .	12
4. Parameters Used in the Simulations for a 5mm Nozzle Diameter . . . . .	17
5. Molecular Parameters Used in the Calculations . . . . .	20
6. Rate Coefficient Used in SOCRATES, $k = A T^n \exp(-E_a/kT)$ . . . . .	20
7. Parameters Used in the Simulations . . . . .	21
8. Parameters Used for the Figures . . . . .	31
9. Fraction of PROTEL HEH Counts Due to Contamination . . . . .	69
10. Fraction of PROTEL HEH Counts Due to Contamination Due to Protons with $E > 10090$ MeV . . . . .	69
11. Fraction of PROTEL HEH Counts Due to Contamination Due to Protons with $E > 200$ MeV . . . . .	70
12. Fraction of PROTEL HEH Counts Due to Contamination Mirror Plane Limit, Azimuth = 0 degrees . . . . .	70
13. Fraction of PROTEL HEH Counts Due to Contamination Mirror Plane Limit, Azimuth = 90 degrees . . . . .	70
14. Physical and Geometric Parameters of the CRRES Detectors . . . . .	74
15. Energy - Range Relation used in Computation: $R(E) = 0.0011824 E^{1.772518}$ ; $R(\text{cm})$ , $E(\text{MeV})$ - Computation based upon Dosimeter Isotropic Path Length Distribution . . . . .	78
16. Janni Energy - Range Relation Used in Computation - Computation based upon Dosimeter Path Length Distribution . . . . .	79
17. Dosimeter Count Comparison, Path Length Distribution vs. Infinite Slab . . . . .	80
18. HILET and LOLET Proton and Electron Energy Ranges . . . . .	96
19. Sample of Model Dose Tables Produced for the CRRES Spacerad Dosimeter . . . . .	97
20. Hourly Depth Dose Profiles for the Dosimeter LOLET and HILET Channels using AE8MAX and AP8MAC . . . . .	99
21. Ratios of Model $B_0$ to IGRF85 Computed $B_0$ for Selected Geographic Locations . . . . .	103
22. Ratios of Model $B_0$ to IGRF85 Computed $B_0$ for Selected Geographic Locations . . . . .	104
23. Proton and Electron Fluences . . . . .	130
24. OTH Record Formats Supported by READOTH . . . . .	146
25. Tape Audit File Generated by READOTH . . . . .	147
26. Typical READOTH Output Listings - CO Calls . . . . .	148
27. Typical READOTH Output Listings - RC Calls . . . . .	149
28. Summary of Selected ARD Data Header Parameters . . . . .	150
29. Description of Table 28 Columns . . . . .	150

# List of Tables (cont'd)

<u>Table</u>	<u>Page</u>
30. Corrections Applied to Measurements . . . . .	155
31. Observables and Assumed Quantities . . . . .	171
32. Neutral Atmospheric Density Data Base Characteristics . . . . .	178
33. Normalized Density - Semiannual Variation Least-Squares Fit Coefficients . . . . .	184
34. Model Usage . . . . .	194
35. Sample Test Case Results - Latitude = 40° . . . . .	195
36. Sample Test Case Results - Latitude = 60° . . . . .	195
37. Orbital Decay Models Summary . . . . .	204
38. M50 to J2000 Rotation Matrix Calculated from the Astronomical Almanac . . . . .	240
39. Leiske's M50 to J2000 Rotation Matrix . . . . .	240
40. Studies of M50 to J2000 Rotation Matrix Over Time . . . . .	240
41. CSTC Supplied State Vectors, Epoch 22 March 1993 at 14:15:29.13 . . . . .	242
42. Rotation Matrix, J2000 to TOD FK5 Using PRECS2 and NUTAT2 . . . . .	242
43. Rotation Matrix, M50 to TOD FK4 Using PRECESS and NUTATE . . . . .	242
44. Rotation Matrix, FK4 to FK5 at 14:15:29.13 on 22 MAR 93 Using Equation 102 . . . . .	242
45. Rotation Matrix, FK4 to FK5 at 0h on 1 JAN 84 Using Equation 102 . . . . .	242
46. Results of First Modification . . . . .	247
47. Results of Second Modification . . . . .	248
48. Results with Propagation Errors Removed . . . . .	248

## **ACKNOWLEDGEMENTS**

The work described in this report required the involvement and guidance of numerous individuals at PL, and their interest and encouragement is gratefully acknowledged.

Ed Robinson of the Data Analysis Division both initiated and coordinated the activities as Contract Monitor. His continuing contributions are deeply appreciated.

Various investigators were involved throughout the projects, and provided essential support and the opportunity for some challenging studies in their fields:

Al Griffin, Bob McNerney, and Bob Raistrick

Data Analysis Division;

Sue Gussenhoven, Dave Hardy, and Gary Mullen

Space Particle Environment Branch;

David Cooke, Shu Lai, Ed Murad, and Charles Pike

Spacecraft Interactions Branch;

Howard Singer

Space Plasmas and Fields Branch;

Santimay Basu, Jurgen Buchau, and Frank Marcos

Ionospheric Effects Branch.

This report has been compiled and prepared by Susan Cline.

## LIST OF ACRONYMS

AFGWC	Air Force Global Weather Central
AIO	Airborne Ionospheric Observation
AITS	AFGL Interactive Targeting System
AMOS	Air Force Maui Optical Station
APEX	Advanced Photovoltaic and Electronic Experiment satellite (P90-1)
ARD	Amplitude Range Doppler
CADP	CRRES Attitude Determination Program
CGL	Corrected Geomagnetic Latitude
CHAWS	Charge Analysis and Wake Studies
CIT	Coherent Integration Time
CIV	Critical Ionization Velocity
CNR	Clutter to noise ratio
CO	Communications processor
CRUX/CREDO	Cosmic Ray Upset Experiment/Cosmic Ray Environment and Dosimeter Experiment
CSCS	Coordinate Systems Conversion Software
CSTC	Consolidated Space Test Center
DCAT	Data Collection and Analysis Team
DL	Dip Latitude
DMA	Defense Mapping Agency
DMSP	Defense Meteorological Satellite Program
ECF	Earth Centered Fixed reference frame
ECI	Earth Centered Inertial
ECRS	East Coast Radar System
EISCAT	European Incoherent Scatter
EUV	Extreme Ultraviolet
FAIM	Fully Analytic Ionospheric Model
FERRO	Ferroelectric Memory Experiment
GCD	Ground Clutter Doppler
GE	General Electric
GF	Simple Geometric Factor
GFE	Effective Geometric Factor
GI	Geometrical Ion
GOES	Geosynchronous Operational Environmental Satellite
HEH	High Energy Head
HS	Hoyng-Stevens
IBSS	Infrared Background Signature Survey (experiment)
IONCAP	Ionospheric Communication Analysis and Prediction Program
IRMA	IRis MANipulator
JPL	Jet Propulsion Laboratory
LEH	Low Energy Head
LEO	Low Earth orbit
MACH	Mesothermal Auroral Charging Code

# List of Acronyms (Cont'd)

MEB	Midnight Equatorward Boundary
MLT	Magnetic Local Time
NASCAP	NASA Charging Analyzer Program
OTH	Over-the-Horizon
PASP-Plus	Photovoltaic Array Space Power Plus Diagnostics experiment
PATH	Postflight Attitude and Trajectory History tape (NASA)
PE	Processing Element
PIM	Parameterized Ionospheric Model
PL	Phillips Laboratory
POLAR	Potential of Large Objects in the Auroral Region
PRCS	Primary Reaction Control System
PRISM	Parameterized Real-time Ionospheric Specification Model
PROTEL	Proton Telescope
RC	Radar Control and Environmental Assessment (RC) processor
RMS	Root-Mean-Square
RPA	Retarding Potential Analyzer
SOCRATES	Spacecraft/Orbiter Contamination Representation Accounting for Transiently Emitted Species
SSC	Storm Sudden Commencement
SSM	fluxgate magnetometer
UT	Universal Time
VRCS	Vernier Reaction Control System
VSTS	Velocity Space Topology Search
WCRS	West Coast Radar System
WRF	primary Waveform Repetition Frequency





# 1. INVESTIGATION OF SPACECRAFT INTERACTIONS

## 1.1 SPACECRAFT CHARGING

### 1.1.1 Introduction

Charge can accumulate on the surfaces of a spacecraft in the plasma environment of Earth orbit when the vehicle encounters energetic electrons from a geomagnetic substorm or when the spacecraft is actively biased. The potential differences that occur due to the surface charge can interfere with the spacecraft mission by disturbing instrument measurements, increasing surface erosion, or initiating discharges. The reliable estimation of the charging effects on present and future space vehicles has been a concern of the Air Force and NASA for several years, and subject to considerable R&D activity. PL has placed strong emphasis on accurate modeling of charging phenomena, and has contracted for the production of two sophisticated models, first NASCAP and then POLAR, both written by S-Cubed. The NASCAP program represents an attempt to simulate spacecraft charging at geosynchronous orbits in three dimensions. NASCAP is still being maintained and used, but PL is now focusing on POLAR and other supportive models such as MACH.

The Potential of Large Objects in the Auroral Region (POLAR) code [Lilley, *et al.*, 1989] extends the NASCAP analysis to lower Earth orbit and near polar orbits, where the higher density plasmas require the consideration and treatment of more complicated processes. For example, the ion current must be determined by particle tracking, instead of from an orbit limited approximation. The numerical algorithms must solve, in a mutually consistent way, the Poisson-Vlasov system of non-linear coupled equations. POLAR can input complicated vehicle geometries, variable surface materials with complex electrical connections, and flexible specifications of the ambient plasma, enabling an accurate representation of real spacecraft and environment to be configured.

The Mesothermal Auroral Charging (MACH) code [Tautz and Cooke, 1988] was written to validate the physical and numerical methods of POLAR. It solves the same Poisson-Vlasov equations as POLAR, but under different conditions. The main difference is that no assumption about the sheath edge is made; the sheath and wake are determined by self-consistent Poisson-Vlasov iteration. Thus, MACH is closer to first principles than POLAR. However, the geometry of MACH is restricted to two dimensions (axially symmetric), precluding detailed application to real spacecraft. We have used MACH to verify the POLAR code for simplified geometries and to treat some problems not currently addressable by POLAR [Bass, *et al.*, 1989].

### 1.1.2 Analysis of the CHAWS experiment

We have studied the CHAWS experiment by means of the two computer codes POLAR and MACH. This experiment is described below, along with the work that has been done on this problem.

The Charge Analysis and Wake Studies (CHAWS) experiment will investigate the charging behavior of a probe in the wake of another larger body in low Earth orbit. The shuttle based experiment will measure the current-voltage characteristic of a Langmuir probe attached to the wake side of a front shielding disk, which will be oriented through a sequence of tilt angles with respect to the shuttle direction of motion. Retarding potential analyzer (RPA) sensors will be mounted on the ram and wake sides of the deployed wake-shield device to measure the density, temperature, and directionality of the ions. In an associated vacuum chamber experiment, an ion thruster is used to produce a flowing plasma

into which a disk is inserted to provide a shielded wake. A smaller probe is mounted on an XY table and placed in the disk's wake, and the IV characteristic of the probe is measured as a function of position. An RPA sensor is used to measure the ion beam structure, and chamber potentials are measured with an emissive probe. A major objective of the CHAWS experiment is to investigate the extent to which the physics of wake formation and current collection, as determined by the chamber experiment, can be scaled to space.

The POLAR code is specific to the space environment. It can accept chamber plasma parameters but cannot account for other important differences between chamber and space conditions. These include wall effects, ion beam divergence, and electron trapping. MACH, on the other hand, can simulate both chamber and space conditions, with an approach that differs significantly from POLAR. Thus, we use MACH to model the chamber experiment and space cases with axial symmetry and to bridge the gap between chamber and space, and to verify the full 3D wake-shield simulations done with POLAR.

### 1.1.3 Plasma Chamber Simulations with MACH

The MACH program was originally designed for the investigation of spacecraft charging problems and was subsequently modified to also handle chamber simulations. This entailed changing the outer grid boundary conditions to represent absorbing chamber walls and modeling the ion thruster beam. The MACH program solves Poisson's equation by successive relaxation with a charge stabilization algorithm, similar to that used in POLAR. MACH obtains ion density by inside-out tracking of time reversed orbits, using the Velocity Space Topology Search (VSTS) method. VSTS is an algorithm that we have invented for efficiently selecting the time reversed orbits needed to adequately resolve the distribution function while carrying out the three dimensional velocity space quadrature to accumulate the inside-out particle density. In order to achieve good agreement with the measured chamber potentials, it was found necessary to add a trapped electron model [Tautz, 1991] to treat electron collisional effects and to suppress unstable solutions due to unphysical build up of space charge. This model is described briefly below.

The nature of the numerical instability that is encountered in the chamber simulations is illustrated schematically in Figure 1. The ion beam enters the chamber from the ion thruster at the throat, and creates a region of positive charge. This positive charge attracts electrons from the neutralizing source located near the throat entrance, causing the electron density to decrease (for strictly one-dimensional motion, the density would fall off inversely as the square root of the local potential). On the other hand, the ions are repelled by the positive charge and tend to build up density at the turning point. These two effects serve to produce a region of increasing net positive charge which does not stabilize until a wall of positive potential builds up to the beam energy of the ions. At this point, the potential would shut off the ions, but this is an unphysical build up of charge because it neglects the effects of collisions, which are not normally accounted for in MACH, which is a Vlasov code (all particle orbits are collisionless and have positive total energy). To remedy this situation, we have added coding that allows for electrons to scatter into the potential well created by the ion space charge. The electrons are assumed to thermalize, with temperature equal to that of the untrapped ions. The numerical effect of the algorithm is as follows: whenever the local potential goes positive, that region receives a flood of negative charge due to electrons scattered into the well. This quenches any unphysical build up of positive potential. The functional dependence of the trapped electron density, normalized to one at infinity, is shown in Figure 2. The independent variable is the local potential energy divided by  $kT$ . It is apparent that the density increases very quickly for potential energies above 1  $kT$ , so that the quenching is rapid above this point. On iteration between Poisson and density calculations, the well depth adjusts so that a self-consistent solution

is obtained. The model contains one free parameter which is the normalization constant for the trapped electron density. This free parameter can be adjusted to improve the agreement with the measured potentials. The method requires the calculation of numerical quadratures, but no particle tracking, so that it is very fast compared to the inside-out method used for the ion density.

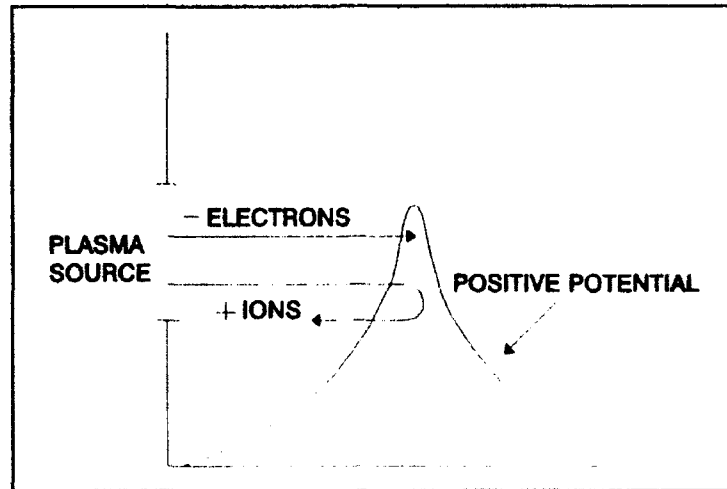


Figure 1. Schematic of instability in electrostatic potential.

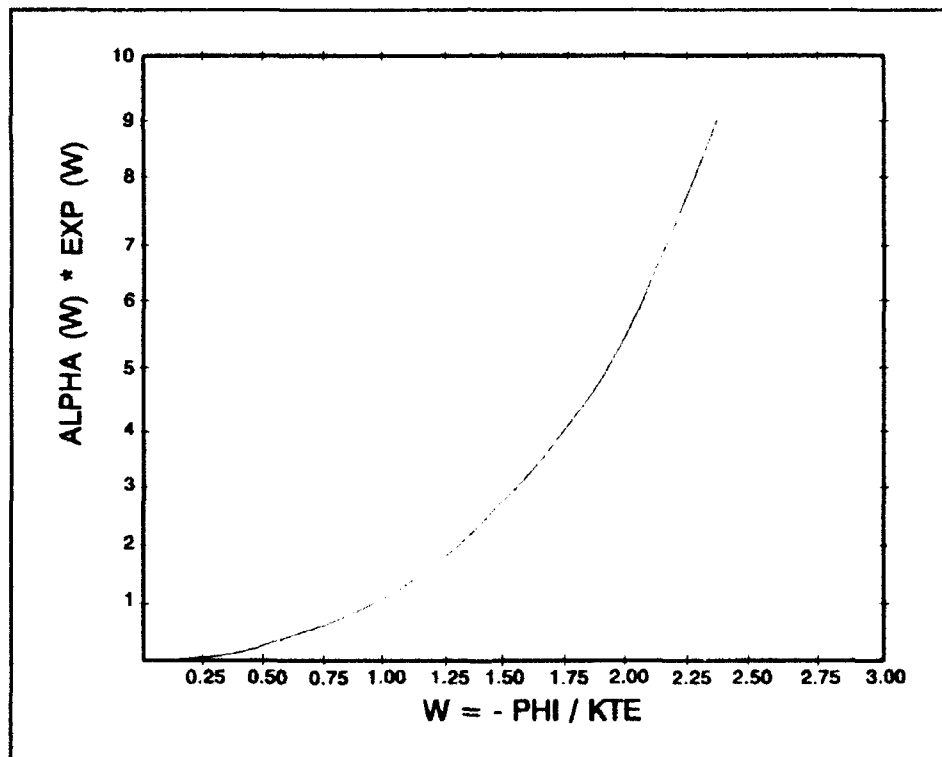


Figure 2. Trapped electron density.

We have used MACH, supplemented by this trapped electron model, to simulate the CHAWS chamber measurements [Chan, *et al.*, 1990] for cases where there is axial symmetry (the probe is restricted to lie on the chamber center line). Figure 3 shows a comparison of the potentials, measured with an emissive probe, and the MACH simulation results, for a -5 KV probe. We can see that the shape of the sheath region is approximately the same for the measured and simulation potentials. The high (negative) potentials surrounding the probe decline rapidly at the wake edge. Furthermore, MACH finds positive potentials of a few kT outside the sheath region, in agreement with the measurements.

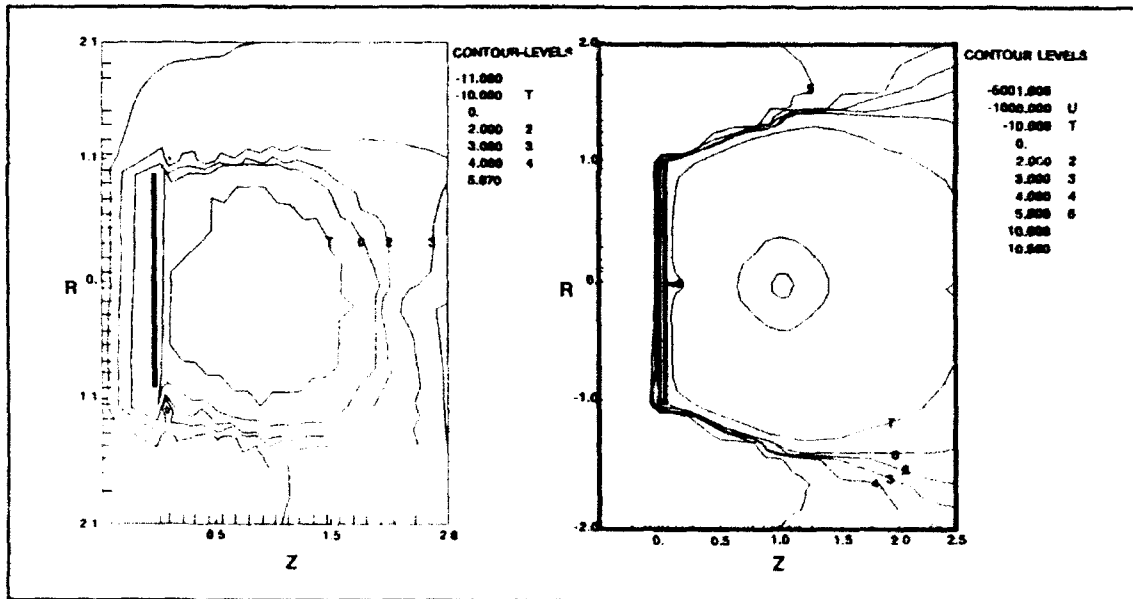
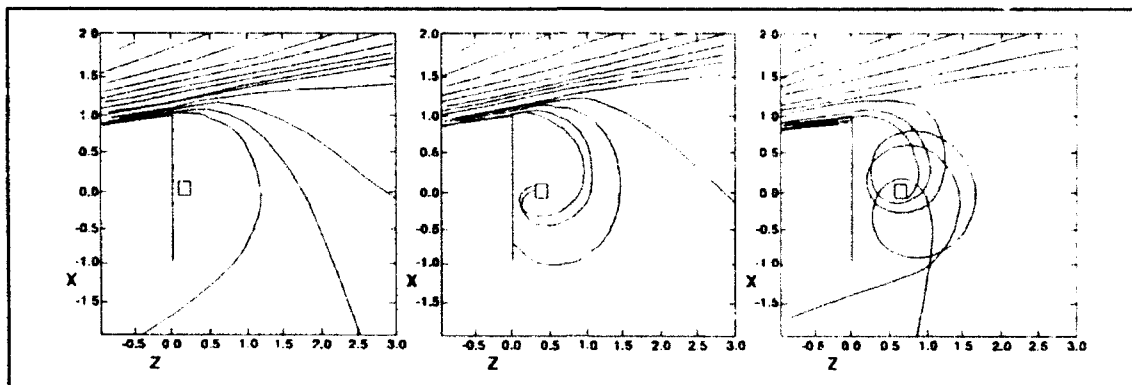


Figure 3. Comparison of measured and MACH chamber potentials: (left) Chamber potentials measured with an emissive probe; (right) Chamber potentials from MACH simulation.

The chamber measurements show a sharp threshold for ion current collection, and this threshold voltage goes through a minimum as the probe is moved downstream along the symmetry axis. We have understood this phenomena with MACH by means of an analysis of forward particle orbits. We have calculated the orbits of forward tracks at the beam energy through the electric field obtained by MACH for probes at different distances (1, 3, and 5 cm) behind the front disk, as depicted in Figure 4. Figure 4(a) shows that for the probe very close to the disk, practically no orbits connect to the probe, due to the strong angular momentum barrier. On the other hand, Figure 4(c) shows that orbits tend to circle around the probe when it is sufficiently far downstream from the disk. This is because the potentials around the probe are approximately given by Laplace's equation in the shielded region behind the disk where the ion density is close to zero, and the electrons are excluded by the strong probe field. Thus, the particles follow approximately Kepler orbits around the probe. However, as shown in the middle Figure 4(b), this situation changes when the probe is moved towards the front disk. In this case, the sharp drop in potential between the probe and the front grounded disk produces a strong electric field which diverts particles, which would otherwise travel between the disk and probe, into the probe. Thus, we see that, for the middle position of the probe from the disk, it is relatively easy to collect current, and this provides an explanation for the minimum that is seen in the measured threshold voltage. Another feature that is seen in the chamber measurements, is that the distribution of current over the probe surface

is non-uniform. This effect is again explainable by using orbit analysis. For example, in the middle Figure 4(b) we see that orbits that circle the probe tend to impact on the near side (to the disk). As the probe is moved downstream, more trajectories tend to hit on the far side of the probe, as indicated in Figure 4(c).



**Figure 4.** Particle orbits from MACH chamber simulation: (left) Forward trajectories for probe 1 cm behind the disk; (middle) Forward trajectories for probe 3 cm behind the disk; (right) Forward trajectories for probe at 5 cm behind the disk.

There is one free parameter in the MACH calculation, and the degree of faithfulness of the chamber model can contribute significant uncertainties. However, it is evident that the MACH code solutions capture the main features of the chamber measurements.

#### 1.1.4 Wake-Shield Simulations with POLAR

The POLAR code determines potentials by a finite element conjugate gradient method, with a charge stabilization algorithm which ensures quasi-neutrality in weak field regions and stable solutions of Poisson's equation in regions where the grid spacing is much greater than the Debye length. POLAR solves for ion and electron densities by a combination of heuristic methods. When a species is repelled, its density is taken to be Boltzmann, which is valid for an isotropic Maxwellian source and no excluded particle orbits. Attracted particle species densities are calculated by forward particle tracking from a sharp edged sheath boundary (assumed to be an equipotential surface at  $\sim kT$ ) which divides space into an exterior presheath and an interior sheath region. The density in the presheath region is approximated by a geometrical ion (GI) algorithm with an electric field correction. The fluxes to the sheath elements are found analytically, assuming a flowing Maxwellian distribution and orbit-limited theory. These fluxes are assigned to outside-in trajectories and followed until they escape the sheath or impinge on an object surface element. Sheath density is obtained by accumulating the charge deposited by the tracks as they pass through each volume cell.

The conventional version of POLAR (call it POLAR 1) employs a uniform grid space and it is not possible to efficiently model the wake-shield experiment, because the code cannot adequately resolve the probe in the near wake region (there is a 30:1 size ratio between the front disk and the probe). For this reason, we have used instead a variant of POLAR (version 2) which has a multi-grid capability that allows a set of uniform grids to be nested. By using a POLAR 2 configuration with a fine grid surrounding the probe and a course grid elsewhere, we were able to achieve the required resolution for

this problem. However, POLAR 2 is an unfinished version of POLAR and numerous modifications were needed in order to produce reliable solutions. For example, POLAR 2 does not calculate the GI densities needed in the presheath region. To overcome this limitation, we wrote a set of auxiliary programs which enable one to read the POLAR 1 continue files and extract data and to then insert this data into the POLAR 2 continue files. In this way, we were able to first do a POLAR 1 run (with the same course gridding as for POLAR 2) to calculate the GI, and then to transfer them into the POLAR 2 course grid space.

Figure 5 illustrates the complete sequence of steps that were needed to generate the runs for calculating the IV characteristics. First, the POLAR 1 runs were done to build the course grid models for the disk and probe. Then, the PATCHV module was used to combine these into a nested POLAR 2 computational grid. Next, the POLAR 1 GI were calculated and then inserted into POLAR 2, using the PATCHG module. POLAR 2 was then executed to produce the IV characteristic at this tilt angle. To vary the tilt angle, the GI densities had to be recalculated, and the procedure repeated. UNIX scripts were set up to automate most of the above steps.

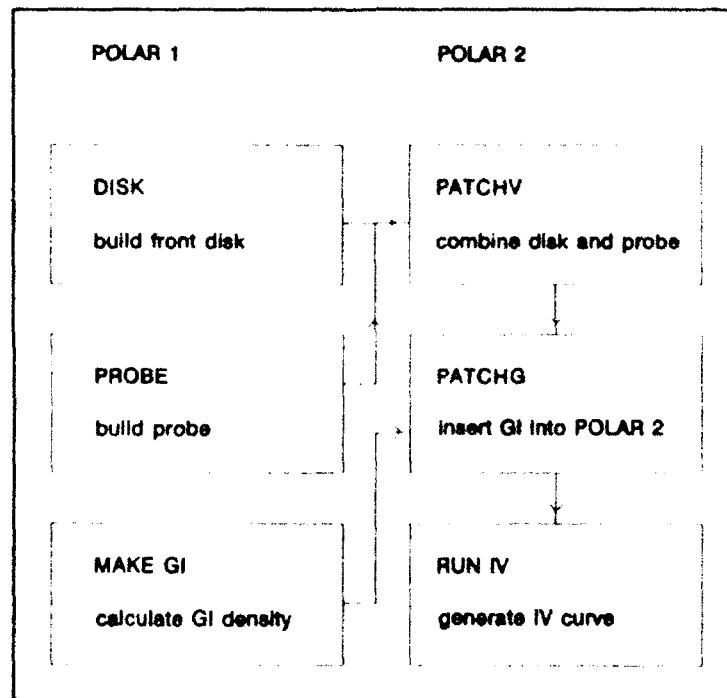


Figure 5. Sequence of steps to generate the POLAR IV characteristics.

To do a parameter study [Tautz, 1992] of the wake-shield experiment IV characteristics, we set the plasma environment to typical ambient values for a shuttle orbit. The probe voltage was varied from -1 KV to -9 KV in 2KV increments, and the tilt angle of the front shielding disk was varied from -40 to +40 degree in steps of 20 degrees. Figure 6 shows the model of the front disk and probe and defines the sign of the tilt angle. The disk was taken to be a octagor. (nine grid units wide, 1 unit thick) and the probe was constructed from three cubes mounted vertically and positioned on the back face of the octagon. A backing panel was added to the base of the probe to facilitate the join of the probe to the disk. Figure 7 shows the potentials obtained for the POLAR wake-shield simulation for the case of a

-1 KV probe. In the figure, the shielding disk is viewed from the side with the charged probe located on the negative x side of center. The inner box surrounding the probe outlines the extent of the high resolution nested grid. The small crosses denote the sheath edge contour from which particle trajectories are launched inwards towards the probe to calculate density and current.

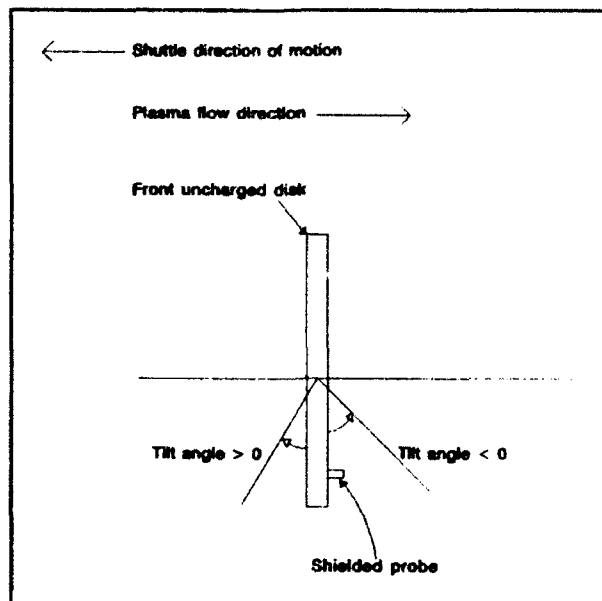


Figure 6. Schematic of the Wake-shield Model.

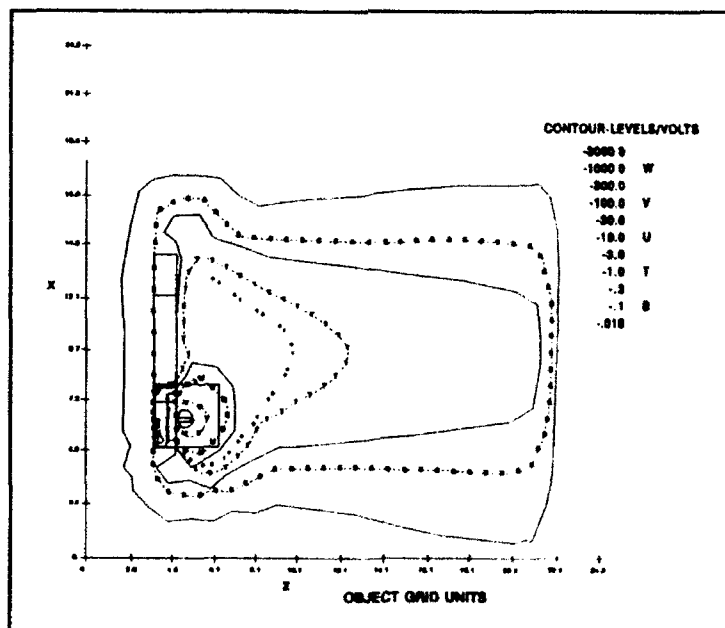


Figure 7. POLAR electrostatic potentials for -1 KV probe, tilt angle = 0.



The IV curves obtained by POLAR 2 are shown in Figure 8. There are two main features observed in the solutions:

- 1) The highest current tends to occur when the disk is rotated towards the ram direction (positive tilt angles) and the current is estimated to be less than 2 ma for this voltage range.
- 2) While the current tends to decrease as the disk is tilted towards the wake, there is an interesting inversion of this behavior at the largest back angle (-40 degrees).

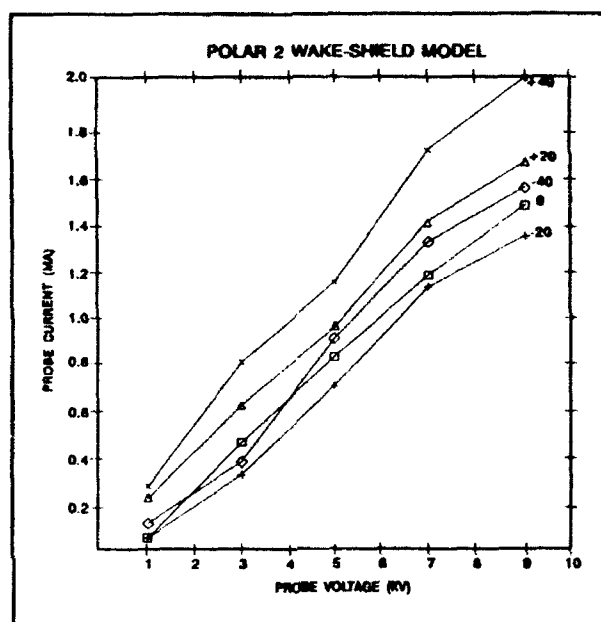


Figure 8. POLAR IV characteristics with tilt angle as parameter.

The stronger current found at positive tilt angles is due to the increased exposure of the probe and sheath to the ram flux. We have understood the above inversion effect by inspecting ion trajectories in the wake. It was found that for large enough negative tilt, the electric fields in the sheath can extend over to the far side of the disk and collect ions. The inversion is due to ions that cross over from the far side of the disk and impact on the probe, giving an increase in current.

The POLAR model of the probe by three vertically stacked cubes has thirteen exposed surface elements, allowing one to estimate the distribution of current over the probe. It was found that more current tends to fall on the side of the probe that faces away from the near edge of the disk, than on the side facing the near edge. This indicates that trajectories tend to orbit around to the far side of the probe, rather than fall directly into it. This effect can be verified by inspecting POLAR trajectory plots.

The above POLAR 2 simulations have been used to give design estimates of the expected currents in the wake-shield experiment.

## 1.2 SPACECRAFT CONTAMINATION - SOCRATES

### 1.2.1 Monte Carlo Simulation of Shuttle Contamination with SOCRATES

To conduct a meaningful experimental investigation in space, an understanding of the local environment prior to the experiment is required. The primary source for conducting experiments are on board or near by the spacecraft and satellites. A comprehensive model that describes the flow fields and contaminant fields surrounding the shuttle orbiter is therefore necessary for designing and performing experiments. Development of procedures for minimizing the contamination is crucial for conducting these experiments which are to fly on the shuttle. A comprehensive three-dimensional Monte Carlo code, Spacecraft/Orbiter Contamination Representation Accounting for Transiently Emitted Species (SOCRATES), has been developed by Spectral Sciences to account for contamination on spacecraft [Elgin and Sundberg, 1988]. It can calculate densities and reactions rates, as well as radiative emission rates for the flows generated by the interaction of a spacecraft's thruster exhaust with the atmosphere. The SOCRATES code is based on the direct simulation Monte Carlo technique which provides a powerful tool for the simulation of real gas flows [Bird, 1976]. The direct simulation Monte Carlo method has been revised and extended significantly to account for the energy dependent collision cross sections and a statistical model for internal energy effects. The method can briefly be described here. The solution region, a physical space, is a network of cells of different sizes. Initially, a discrete number of molecules are stored in the computer. These molecules are stored based on their velocity components, position coordinates, and other necessary information. The molecular motion and intermolecular collisions in the simulated region advance, and are modified with time, in a two stage process. In the first stage, the molecules advance along their trajectories according to their velocity components and the time increment. In this stage, some of the molecules may leave the solution domain and some will be introduced to the problem at hand according to the boundary conditions of the problem. In the second stage, a typical set of collisions will be simulated among the molecules in each cell with appropriate time increment. The repetition of these two stages over the small time interval will uncouple the molecular motion and intermolecular collisions. In SOCRATES simulations, periodically, the solution is sampled by accumulating statistical sums of number densities, velocities, and other basic properties. The solution is run repeatedly until statistical deviations are reduced to a desired limit, and the physically meaningful output quantities are computed from the statistical sums. The number of molecules represented is typically many thousands at a time, which is much smaller than the number of molecules occurring virtually in real flows. Hence, the construction of a dynamically similar flow to be simulated in the computer is an essential feature of the method.

The inner solution capabilities will be added to SOCRATES in the near future by Spectral Sciences. The separation into an inner and outer solution is necessitated by the physical and computational realities of the interaction between contaminant molecules and the surrounding atmosphere. In order to describe the scattering of contaminant molecules, the solution region must extend several mean free paths from the source of the contamination, which is typically tens of kilometers, and at the same time, in order to describe the detailed interaction between the flow field and the specific geometry of the vehicle in question, cells must be smaller than characteristic length scales of the spacecraft. The two requirements make it computationally feasible to have two distinct solutions, which are referred to as the inner and outer solutions.

### 1.2.2 Research and Analysis using SOCRATES

We have installed and maintained the SOCRATES code and its auxiliary programs on the Silicon Graphics workstations IRIS 4D/210S and IRIS INDIGO XS24 at the Spacecraft Interactions Branch. The code is also installed on the CONVEX mainframe computer. We have been using the SOCRATES code to simulate the interaction between the ambient atmosphere and shuttle engines, such as the Primary Reaction Control System (PRCS) and Vernier Reaction Control System (VRCS), at low orbit. The simulations provided important information, such as a) Scattering, where the densities of all species resulting from multiple scattering can be determined for each case; b) Collisional Transfer of Kinetic to Vibrational Energy (T-V Collisions) - it is important for absorbing the high collisions energy between the ambient O atoms and the exhaust plumes molecules; and c) Reactive Collisions - the possibility that reactions which do not proceed at room temperature due to large activation energies might become important in low Earth orbit because of the orbital velocity [Elgin, *et al.*, 1990]. PL scientists, Spectral Sciences and Radex personnel have used these simulations for a wide variety of analyses, from comparison with current experimental data to predicting the outcome of future experiments [Murad, *et al.*, 1990; Vierek, *et al.*, 1990; Elgin, *et al.*, 1991; Murad, *et al.*, 1991; and Broadfoot, *et al.*, 1991]. Some of these projects are briefly described here.

The ground-based video photography observations at the Air Force Maui Optical Station (AMOS) showed emissions extending nearly 4 km from the firings of Space Shuttle Primary Reaction Control System (PRCS) engines. One of the possible sources of this kind of radiation was the vibrationally excited OH which is formed by the reaction of H<sub>2</sub>O molecules in the exhaust and fast ambient O atoms. In Murad, *et al.* [1990], the OH emission was examined and simulated with the SOCRATES code.

In Elgin, *et al.* [1990], a model/data comparison was investigated for some visible data taken by AMOS of an 870 lb shuttle PRCS firings at an altitude of about 320 km. The data were obtained for three angles of attacks: 0°, 90°, and 180°. The modeling efforts were mainly on simulating the overall character of the plumes in the three orientations, and trying to understand the 6300 Å data feature. This feature is attributed to the atomic oxygen red line emission from the transition between the O(<sup>1</sup>D) excited state and the O(<sup>3</sup>P) ground state (O(<sup>1</sup>D) → O(<sup>3</sup>P)). The unsteady SOCRATES simulations were compared to the observations, and it was concluded that translation to electronic excitation is the dominant cause of the 6300 Å emission, with charge exchange playing a lesser role.

The SOCRATES code has also been used to simulate the interaction of CO<sub>2</sub> with atomic O and H in the upper atmosphere [Setayesh, 1991; Lai, *et al.* 1991; and Lai, *et al.* 1992]. These studies are parametric and provide predictive results for the ARGOS experiment which is proposed to be accomplished in the near future. The simulation of the CO<sub>2</sub> release into the upper atmosphere, using the SOCRATES code, can be summarized into two distinct investigations (cases) which will be discussed here.

In the first case Setayesh [1991], the SOCRATES contamination-interaction code has been used to predict the reactions of CO<sub>2</sub> with atomic oxygen and hydrogen for altitudes from 500 to 800 km. The reactions of CO<sub>2</sub> with atomic oxygen and hydrogen are:





The asterisk denotes vibrational excitation. The reaction of  $CO_2$  with atomic oxygen is endothermic by 0.33 electron volts and at orbital velocity, at  $180^\circ$  collision angle, it has excess energy of 4 electron volts. The simulation for the reaction  $CO_2$  and O for altitudes from 500 to 800 km is presented in two cases of unsteady and steady state conditions. However, for the reaction  $CO_2$  and H, only the steady state condition has been considered.

A nozzle with a small diameter is assumed to be the source of the  $CO_2$  gas released into space from a spacecraft in the ram direction. The diameter of the nozzle and mass flow rate of the  $CO_2$  remain constant. It is assumed that the gas release will last approximately 10 seconds. The temperature of the  $CO_2$  gas at the time of release is assumed to be about  $50^\circ C$ . The solution region for an unsteady case (only reaction 1 is considered) is taken to be a cubic space  $15.6 \text{ km}^3$  in volume ( $2.5 \times 2.5 \times 2.5 \text{ km}^3$ ) consisting of 6480 unevenly spaced cells, with 8 molecules in each cell. The solution domain in a steady state case (for both reactions) is taken to be a cubic space  $29.25 \text{ km}^3$  in volume ( $3.25 \times 3.0 \times 3.0 \text{ km}^3$ ) consisting of 8400 unevenly spaced cells. In each cell, there are 6 molecules for each species.

Tables 1-4 represent the parameters used for the simulation. Figure 9 shows plots of total intensity as a function of time. Figures 10 and 12 show panels of gray scale plots for the radiation intensity of CO and OH vibrational excitation in steady state conditions for different altitudes. Table 1 shows the reference collision cross-section, reference relative collision velocity, and number of internal degrees of freedom for the species. Table 2 shows the values used in Arrhenius Rate Coefficients for the different reactions.

**TABLE 1. Molecular Parameters Used in the Calculations**

Species	$\sigma_{ref}, \text{cm}^{-2}$	$v_{ref}, \text{cm/s}$	$v_i$
O	$1.75 \times 10^{-15}$	$2.49 \times 10^5$	0.00
CO	$3.46 \times 10^{-15}$	$2.09 \times 10^5$	2.00
$O_2$	$3.17 \times 10^{-15}$	$1.98 \times 10^5$	3.60
$CO_2$	$4.33 \times 10^{-15}$	$1.71 \times 10^5$	3.58
H	$1.03 \times 10^{-15}$	$1.09 \times 10^6$	0.00
OH	$1.77 \times 10^{-15}$	$8.00 \times 10^5$	2.00

**TABLE 2. Rate Coefficients Used in SOCRATES,  $k = A T^n \exp(-E_a/kT)$**

Reaction	A	n	$E_a$ (kcal/mole)	$\Delta H$ (kcal/mole)
$O_{fast} + CO_2 \rightarrow CO^* + O_2$	$2.0 \times 10^{-11}$	0.0	14.3	14.3
$H_{fast} + CO_2 \rightarrow CO + OH^*$	$2.5 \times 10^{-10}$	0.0	13.3	13.3

Table 3 shows the results of the MSIS-86 model simulation for atmospheric density and temperature for altitudes of 500 to 800 km. The code was run for some typical condition in late 1993 (the proposed date for the experiment).

**TABLE 3. Atmospheric Density and Temperature**

Altitude (km)	Number density (cm <sup>-3</sup> )	Temperature (°K)
500	2.735 x 10 <sup>7</sup>	1002.2
600	8.437 x 10 <sup>6</sup>	1002.3
700	3.652 x 10 <sup>6</sup>	1002.3
800	2.080 x 10 <sup>6</sup>	1002.3

It should be mentioned here that the unsteady simulation for CO<sub>2</sub> with O is considered to be up to 0.5 sec. However, it required 7.26 sec for both emissions from Reactions 1 and 2 to reach a steady state condition. The total emission values for Figure 10 are at the wavelength of 4.6 μm and in terms of Watts/Steradian.

Table 4 lists the other parameters that have been used in SOCRATES to simulate CO<sub>2</sub> released from a 5 mm diameter nozzle with a mass flow rate of 100 g/s. Figure 9 shows the total averaged emission from the mechanism of  $O + CO_2 \rightarrow CO^* + O_2$  (Reaction 1) for an unsteady state condition in the time range of 0.175 to 0.475 sec. The amounts of emission at altitudes of 700 and 800 km are close to each other in Figure 9. However, at altitudes of 500 and 600 km, the emission is almost an order of 100 and 10 higher, respectively, when compared to the reaction emission for the 700 or 800 km altitudes. Figure 10 shows a panel of gray scale plots for the radiation intensity of Reaction 1 at different altitudes, from 10<sup>-8</sup> to 10<sup>-12</sup> watts/cm<sup>2</sup>/sr. The figure shows that there is a sharp decrease in radiation from CO<sup>\*</sup> in going from 500 km to 800 km altitude. Figure 11 shows the total emission from the mechanism of  $H + CO_2 \rightarrow OH^* + CO$  (Reaction 2) for steady state conditions. As can be seen from the figure, the amount of reaction emission for 800 km is much more intense than the reaction emission for the 600 and 700 km altitudes. This is due to the increased H atom density at 800 km, compared with that at 600 or 700 km. This is shown in Figure 12, where the radiation at 2.7 μm (OH fundamental frequency) is plotted for altitudes of 500 to 800 km.

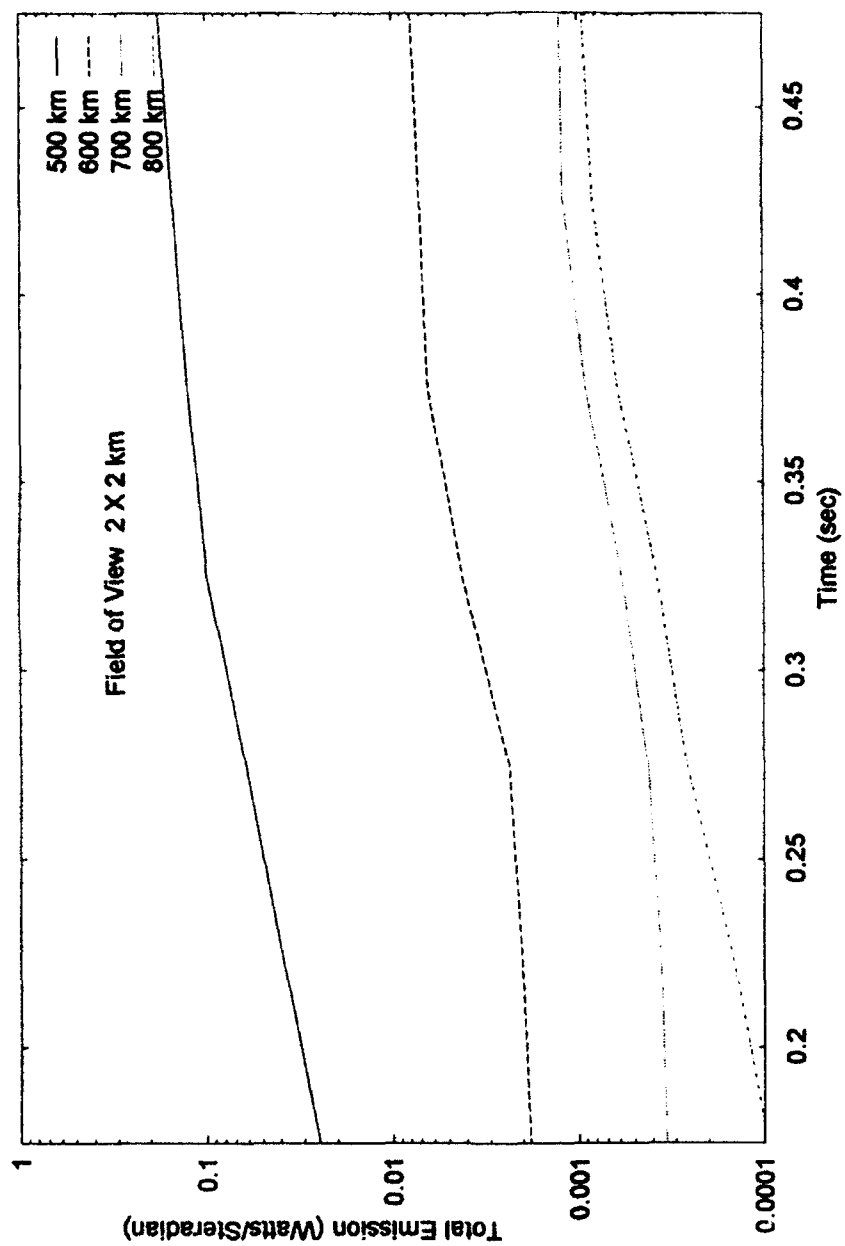


Figure 9. Total solution region values for CO vibrational excitations in unsteady state condition.

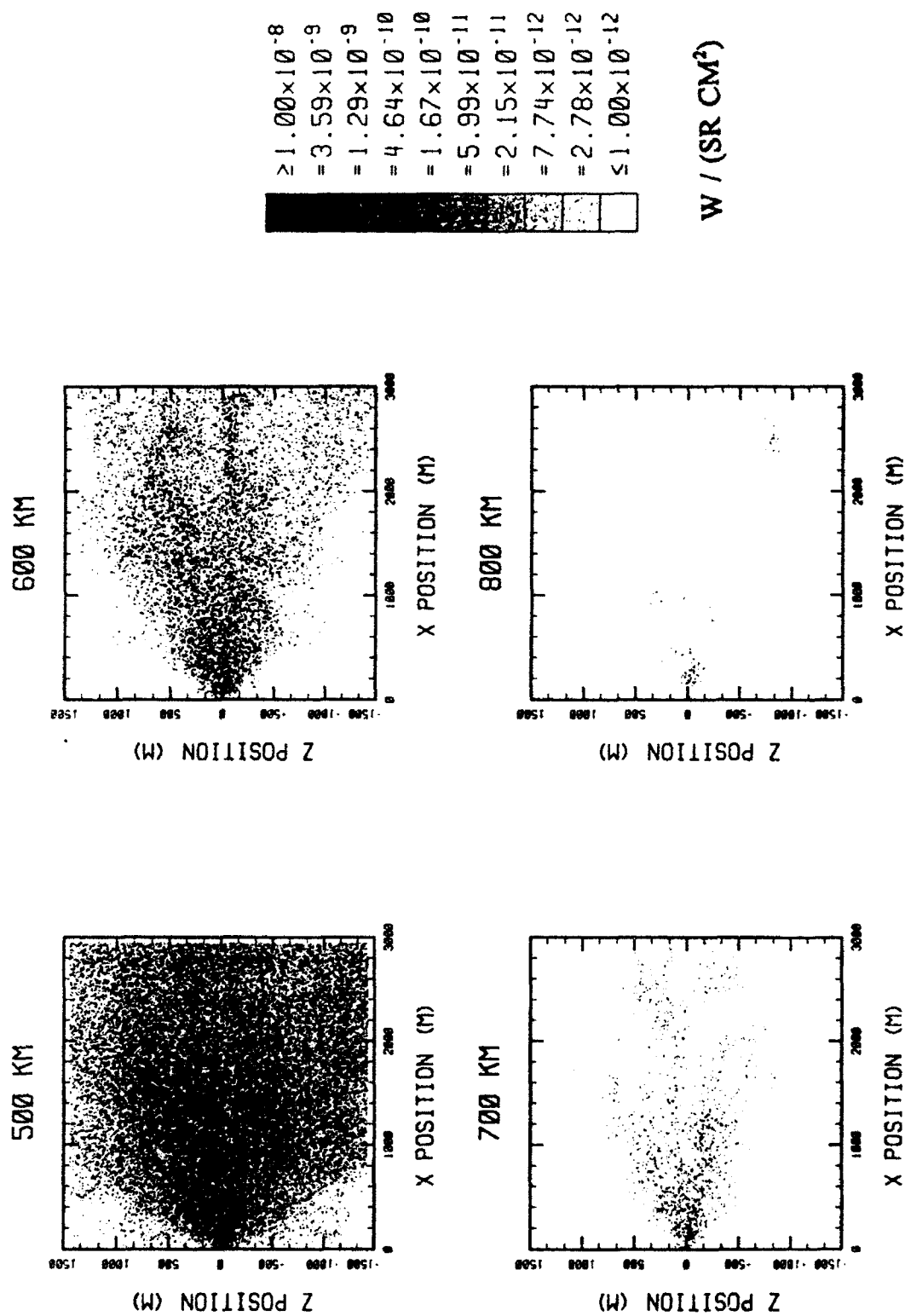


Figure 10. Gray scale plots showing the CO vibrational excitations at 4.6  $\mu$ m from the mechanism  $O + CO_2 \rightarrow CO^* + O_2$ .

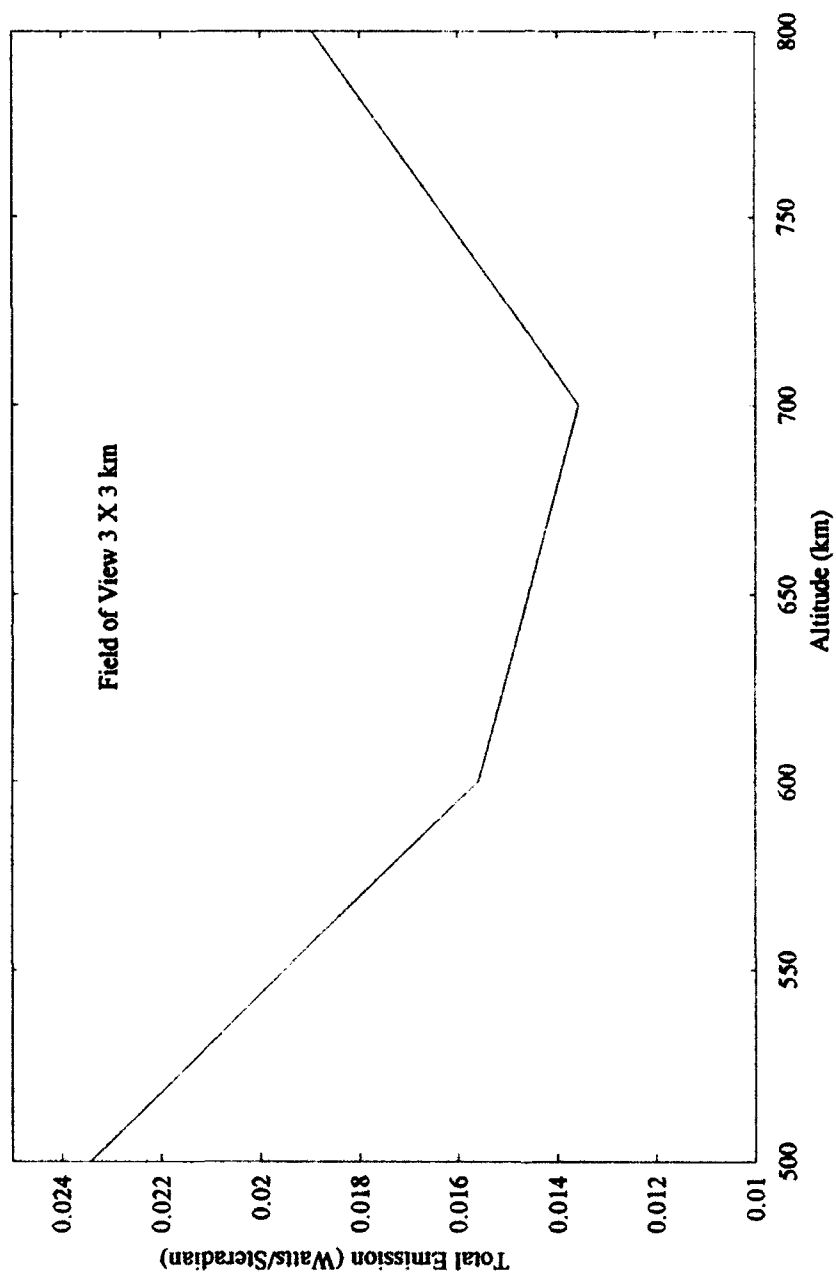


Figure 11. Total solution region values for OH<sup>+</sup> vibrational excitation.



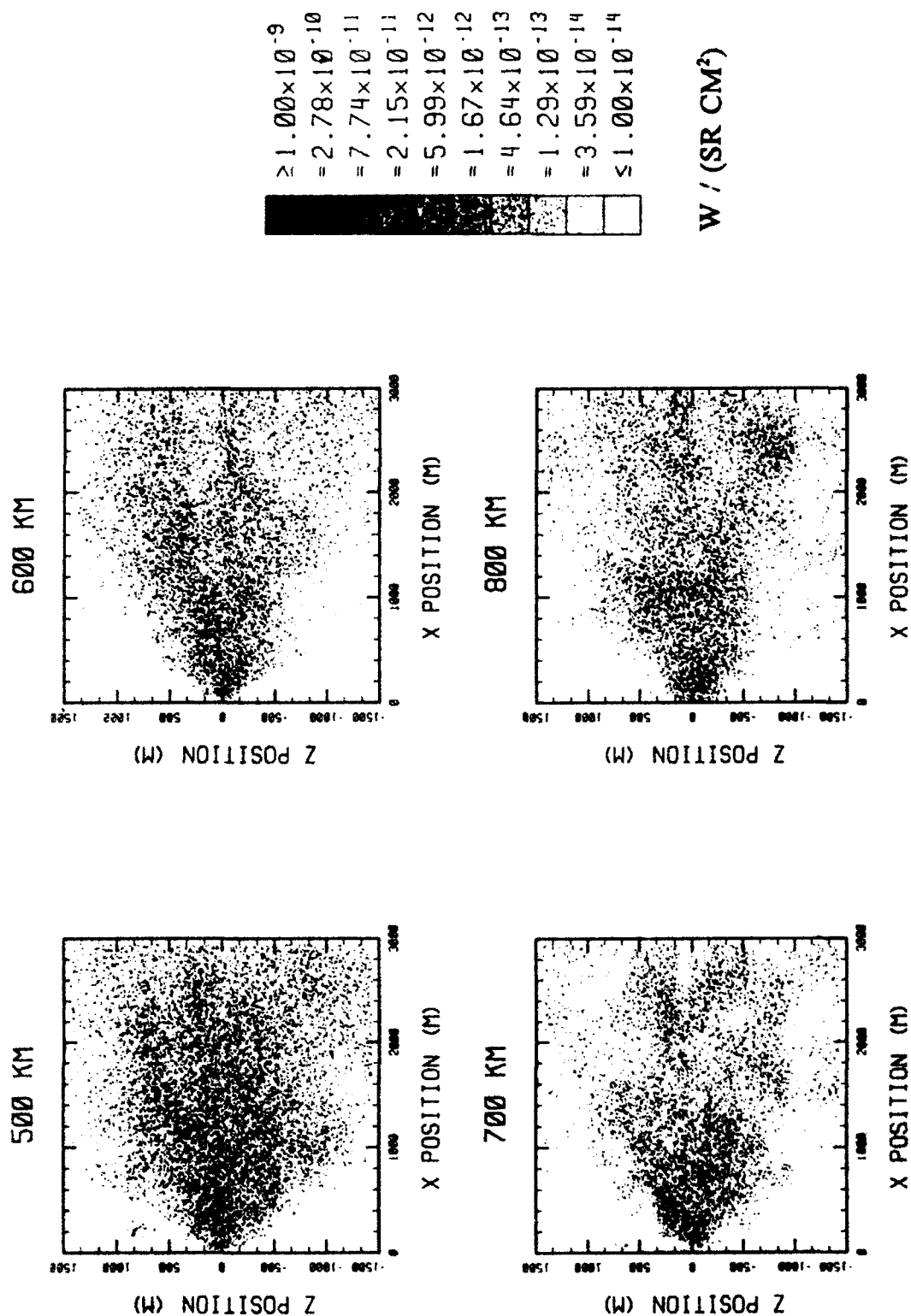
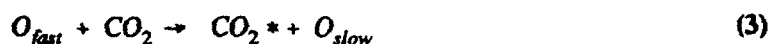


Figure 12. Gray scale plots showing the OH vibrational excitations at 2.7  $\mu$ m from the mechanism  $H + CO_2 \rightarrow OH^* + CO$ .

**TABLE 4. Parameters Used in the Simulations for a 5mm  
Nozzle Diameter**

Mass Flow	100.0 g/s
Exit Plane Area	$2.0 \times 10^{-1} \text{ cm}^2$
Ratio of Specific Heat	1.30
Exit Mach Number	3.53
Exit Nozzle Half Angle	8.00 degrees
Exit Plane Density	0.005092 g/cm <sup>3</sup>
Exit Plane Number Density	$6.969 \times 10^{19} \text{ molecules/cm}^3$
Exit Plane Velocity	1.0 km/s
Exit Plane Speed of Sound	$2.833 \times 10^4 \text{ cm/s}$
Exit Plane Temperature	326.7°K
Exit Plane Pressure	$3.143 \times 10^6 \text{ dynes/cm}^2$
Stagnation Temperature	937.3°K
Stagnation Pressure	$3.027 \times 10^8 \text{ dynes/cm}^2$
Thrust	23.86 lb
Velocity of Spacecraft	7.4 km/s

In the second investigation [Lai, *et al.*, 1992], we considered the CO<sub>2</sub> simulations using the SOCRATES code, as much as 30 km into space in two specific directions. In addition to reactions (1) and (2) in the previous case, the following reaction is also added to the investigation of CO<sub>2</sub> :



Reaction (3) represents the collisional transfer of kinetic energy to vibrational energy.

The ARGOS satellite is expected to be in a circular orbit at an altitude of approximately 800 km with an orbital velocity of 7.4 km/s. The CO<sub>2</sub> release experiment will be one of many experiments to be conducted onboard the satellite [Lai, *et al.*, 1992]. Two conditions for the release will be considered here: one in the ram direction and the other in the wake direction. It is also assumed that the gas release will last approximately 1.0 second (from a fraction of a second to several seconds has been proposed for the actual experiment). The temperature of the CO<sub>2</sub> gas at the time of release is assumed to be about 50°C. The solution domain in the steady state (for both reactions) is taken to be a cubic space 28,800 km<sup>3</sup> in volume (32 by 30 by 30 km<sup>3</sup>) consisting of 8400 unevenly spaced cells. In each cell there are 3 to 20 molecules (depending on the density of the species and cell location) for each species.

The simulation for the reaction of CO<sub>2</sub> with O and H for an altitude of 800 km is presented in panels of tables and plots for two cases of ram and wake directions. Tables 5-7 represent the parameters used for the simulation. Figures 13 and 14 show panels of contour plots of radiation intensity and reaction rates for CO<sub>2</sub>, CO, and OH, respectively, in the ram and wake directions.

Table 5 shows the reference collision cross-section  $\sigma_{ref}$ , reference relative collision velocity  $v_{ref}$ , number of internal degrees of freedom  $v_i$ , and heat formation for the species.



**Figure 13.** Contour plots showing the  $\text{CO}_2$ ,  $\text{CO}$ , and  $\text{OH}$  vibrational excitations for the same scale.

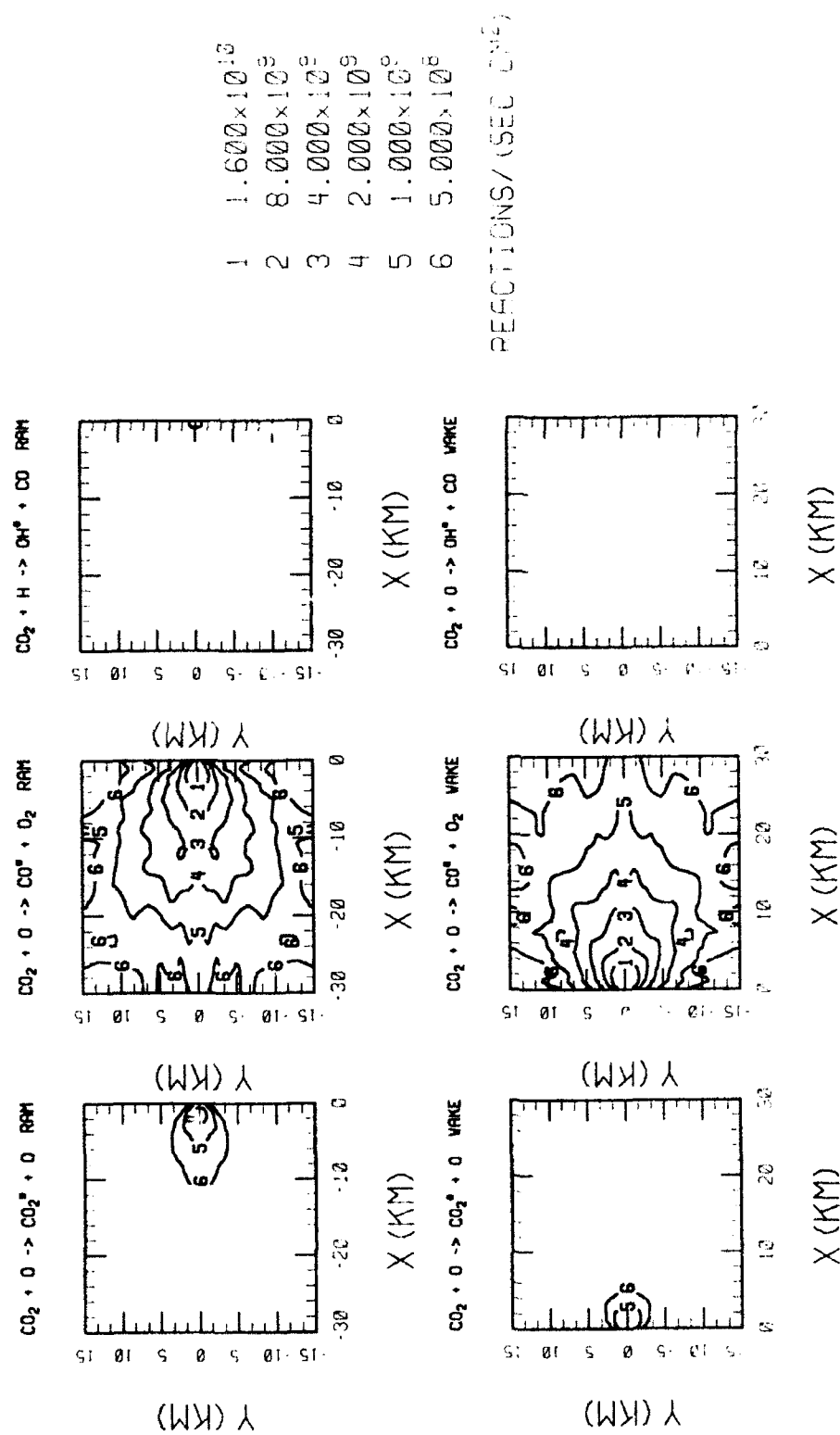


Figure 14. Contour plots showing the  $\text{CO}_2$ ,  $\text{CO}$ , and  $\text{OH}$  reaction rates for the same scale.

**TABLE 5. Molecular Parameters Used in the Calculations**

Species	$\sigma_{ref}$ cm <sup>2</sup>	$v_{ref}$ cm/s	$v_i$	Heat of Formation kcal/mole
CO <sub>2</sub>	$4.33 \times 10^{-15}$	$1.71 \times 10^5$	3.58	-94.10
O	$1.75 \times 10^{-15}$	$2.49 \times 10^5$	0.00	59.60
H	$1.03 \times 10^{-15}$	$1.09 \times 10^6$	0.00	52.0
CO <sub>2</sub> (4.3)	$4.33 \times 10^{-15}$	$1.71 \times 10^5$	3.58	-87.39
CO(4.7)	$3.46 \times 10^{-15}$	$2.09 \times 10^5$	2.00	-20.29
O <sub>2</sub>	$3.17 \times 10^{-15}$	$1.98 \times 10^5$	3.60	0.0
OH(2.7)	$1.77 \times 10^{-15}$	$8.00 \times 10^5$	2.00	9.4

Table 6 shows the values used in Arrhenius Rate Coefficients for the different reactions, where A, n, and k are constant parameters, T is temperature, and E<sub>a</sub> is the activation energy.

**TABLE 6. Rate Coefficient Used in SOCRATES,  $k = A T^n \exp(-E_a/kT)$** 

Reaction	A	n	E <sub>a</sub> (kcal/mole)
O <sub>fast</sub> + CO <sub>2</sub> → CO <sub>2</sub> (v) + O <sub>slow</sub>	$3.9 \times 10^{-20}$	1.8	6.71
O <sub>fast</sub> + CO <sub>2</sub> → CO(v) + O <sub>2</sub>	$5.6 \times 10^{-11}$	0.0	14.21
H <sub>fast</sub> + CO <sub>2</sub> → CO + OH(v)	$2.5 \times 10^{-10}$	0.0	26.43

Table 7 lists the other parameters that have been used in SOCRATES to simulate CO<sub>2</sub> released from a 5 mm diameter nozzle with a mass flow rate of 144 g/s.

**TABLE 7. Parameters Used in the Simulations**

Atmospheric Temperature	1002.3°K
Atmospheric Number density	$2.047 \times 10^6 \text{ cm}^{-3}$
Altitude	800 km
Mass Flow	144.0 g/s
Exit Plane Area	$2.5 \times 10^{-1} \text{ cm}^2$
Ratio of Specific Heat	1.30
Exit Mach Number	1.40
Exit Nozzle Half Angle	22.5 degrees
Exit Plane Density	$1.789 \times 10^{-2} \text{ g/cm}^3$
Exit Plane Number Density	$2.448 \times 10^{20} \text{ molecules/cm}^3$
Exit Plane Velocity	410.0 m/s
Exit Plane Speed of Sound	$2.929 \times 10^4 \text{ cm/s}$
Exit Plane Temperature	350.0°K
Exit Plane Pressure	$1.18 \times 10^7 \text{ dynes/cm}^2$
Stagnation Temperature	451.9°K
Stagnation Pressure	$3.607 \times 10^7 \text{ dynes/cm}^2$
Thrust	18.5 lb
Velocity of Spacecraft	7.4 km/s

Figure 13 shows the emission at  $4.3 \mu\text{m}$  from vibrational excitation of  $\text{CO}_2$  produced by collisional energy between O atoms and released  $\text{CO}_2$  molecules. The figure also shows the emission from the reactive collisions between  $\text{CO}_2$  and O and H atoms, respectively. The  $\text{CO}^*$  emission at  $4.7 \mu\text{m}$ , is a much higher rate of emission with respect to  $\text{CO}_2^*$ , and even more to  $\text{OH}^*$ . This is because the radiative lifetime of  $\text{CO}^*$  is of the order of  $\mu\text{s}$  compared with  $\text{CO}_2^*$ , whose radiative lifetime is of the order of ms. The rate coefficients given in Table 6 were used to calculate the contours in Figure 13.

Figure 14 shows the reaction rate per sec per  $\text{cm}^2$  for reactions 1, 2 and 3. As expected, the intensity of the reactions are similar to those of the emissions in Figure 13, respectively. The contour plots shown in the figures are in the two directions of ram and wake, where in the ram direction the flow has a relatively larger initial upstream velocity component, and this contributes to higher energy collisions; hence, higher levels of emission are produced.

### 1.3 THREE DIMENSIONAL COLOR DISPLAY OF DATA

We have developed a plotting program called IRIS MANipulater (IRMA) for three dimensional color display of data on IRIS workstations. Such a program is indispensable, not only for presentation of simulation results, but also for monitoring and diagnosing voluminous 3D distributions which are difficult to comprehend using only 2D projections. IRMA has been used extensively for display and analysis of simulation results from the MACH, POLAR, and SOCRATES codes.

The IRMA program was originally installed on an IRIS 3030 workstation and has been subsequently converted to run on an IRIS INDIGO mini-computer. IRMA consists of an approximately equal mixture of FORTRAN and C coding. It utilizes the multiple windowing capabilities of the IRIS workstations to manage up to a dozen windows which display viewports, information lists, text ports, and clipping plane configurations. The program is driven interactively by pop-up menus which are under mouse control. Practically all of the IRIS graphics viewing options are available to the user by means of a slider bar interface which enables one to set the graphics function arguments. The keyboard is queued into the program and provides an alternate way to enter commands and numbers. There are an extensive set of help files describing each graphics function and its arguments.

In order to organize the many graphics options in IRMA, the code is divided into modules. There are currently five modules for viewing and transforming objects, for creating objects and images, and for format control. We list below some of the features and capabilities of the IRMA modules:

- can read and plot polygon objects
- can read and plot trajectories
- can read and plot 2D image planes (compatible with IRAF program)
- can read scalar functions  $f(x,y,z)$  of data defined on a discrete  $x,y,z$  grid
- can create a dot pattern representing the grid nodes at  $(x,y,z)$
- can create contour level surfaces for  $f(x,y,z)$  using polygonal elements
- can strip the above contour surfaces along coordinate lines for emphasis
- can create planar slices through  $f(x,y,z)$  and color code them
- can create speckle plots representing the local magnitude of  $f(x,y,z)$
- can set up an arbitrary observer viewpoint with arbitrary object orientation
- can save parameter files specifying the current graphics state for easy restoration and continuation at a later date
- has special window modes for viewing the clipping planes, for comparing objects side by side and a display mode suitable for hard copy output

- can do a screen dump to an image file which can be later pasted to the screen and manipulated with the window manager
- has a flexible color legend and a choice of several color and grey maps
- has text ports for on-line insertion of captions and labeling of units and a text editor for modifying captions
- has data scanning capabilities for inspecting data at each node
- has a multi-grid option allowing for nested grid data
- has a zbuffer toggle for shadowing of hidden surfaces

The IRMA program accepts input files in ASCII, binary, and MSIO formats. It can also read the SOCRATES binary restart (.RST) files interactively, to give quick access to the SOCRATES data base for inspecting particle densities and reaction rates.

An important feature which was added to IRMA for SOCRATES analysis is an option to calculate integrated column densities. This option allows one to interactively calculate, for an arbitrary viewpoint and perspective, the radiance corresponding to input node data obtained from SOCRATES specifying the emission rate, thus providing a direct link to measured quantities. A sequence of image files representing the radiance of the shuttle plume can be written with IRMA to create a movie depicting the time dependence of the simulation. Selected frames from a sequence of images representing the case of a shuttle PRCS engine ram burn are shown in Figure 15. In the simulation, the shuttle is located at the origin and the thruster fires in the negative x direction for a three second duration. It can be seen that the intensity builds up until the three second point, and then diminishes as the gases disperse.

## 1.4 SPACECRAFT LIQUID VENTING MODELS

### 1.4.1 Liquid Water Release into Space

One of the components of the low Earth orbit environment is the presence of sub-micron to millimeter diameter particles resulting in part from the routine space shuttle liquid releases, such as waste management (including water) and fuel cell by-products. The liquid water venting in low Earth orbit can have significant physical and optical contamination effects on spacecraft, as well as applications in studying the use of liquid streams in space operations. The water venting can also have applications in studying the interaction of the vehicle with ionospheric plasma, transport of outgas, and energy balance of cometary material [Kofsky, *et al.*, 1992].

The study of water venting by the space shuttle orbiter has recently been performed, using both shuttle-based and ground-based cameras. This was an effort to monitor the stream and shuttle environment during venting, and to study the lifetime of the cloud. These studies have shown that the particulate cloud, which is formed by the water release, consists of both millimeter sized (large) and sub micron sized (small) diameter particles. The large particles result from the macroscopic breakup of the stream and subsequent freezing and shattering processes. The small particles result, in part, from the recondensation of overexpanded water vapor in the high pressure region near the stream origin. Other



sources for the small particles include the formation of satellite droplets at the point of stream breakup and the production of small particles during large particle shattering events. The relative importance of these latter processes to the total small-particle population is unknown at the present time [Gardner, et al., 1992]. The temperature history of the particles has also not been measured, although a qualitative understanding of this history exists, and an approximate calculation of the temperature as a function of time has been reported [Kofsky, et al., 1992].

#### 1.4.2 Liquid Water Vent Modeling

The need to model and predict the transient processes by which water released into vacuum of space evolves into a rapidly expanding multiphase mixture of evaporating liquid droplets, solid particulates, and vapor, arises from the virtual lack of tools and methods to model, simulate, and interpret these processes. The capability to accurately calculate the vent clouds is, therefore, a basic requirement for the analysis, evaluation, and interpretation of data related to water-release events. We have been developing mathematical models and computer codes to describe and analyze the water venting into space objectives. In parallel, we have also contributed to the analysis of water dump experiments [Kofsky, et al., 1992; Gardner, et al., 1992; Vierek, et al., 1990; Pike, et al., 1990; and Rall, et al., 1992].

##### 1.4.2.1 One Dimensional Liquid Water Vent Modeling

A mathematical model was developed by modifying and extending an existing model, in which the liquid and vapor phases of vented liquid are simultaneously present [Glenn, 1969]. Some of the equations were modified to enhance the model by incorporating the behavior of the particles after freezing, and heat radiation from the particles. The equations describing this model were the one-dimensional continuity, momentum, and energy equations for the vapor and particles. The analysis was governed by a sixth-order, non-linear, two-point boundary value problem. The governing equations used in this model are fully described in Setayesh [1990].

The data similar to those of recent shuttle orbiter water dumps into space have been used to give some indication of water flow characteristics into a vacuum environment. Comparison with our investigation showed a good agreement with a limited number of experimental and computational studies of liquid released into a vacuum [Setayesh, 1990]. For example, Figure 16 investigates the changes in vapor pressure as a function of radial distance  $R$ , based on Eq. (4). This equation relates the radial distance  $R$  to the Mach number and the specific heat ratio of vapor. The  $r_o$  is the fictitious sonic radius defined by Fuchs and Legge [1979]. Since the vapor flow is supersonic, the vapor pressure is calculated based on the Rayleigh-Pitot formula Eq. (5), where  $P_o$  is defined as a critical pressure at sonic  $r_o$ , which is considered by Fuchs and Legge [1979]. In this figure, the experimental measurement of Fuchs and Legge [1979] is compared with the calculated results of the present work. As can be seen from Figure 16, the curves start at some distance from the source, the distance that the vapor needs to travel to reach supersonic speed.

$$\frac{R}{r_o} = \frac{1}{M} \left[ \frac{2 + (\gamma - 1)M^2}{\gamma + 1} \right]^{\frac{(\gamma + 1)}{2(\gamma - 1)}} \quad (4)$$

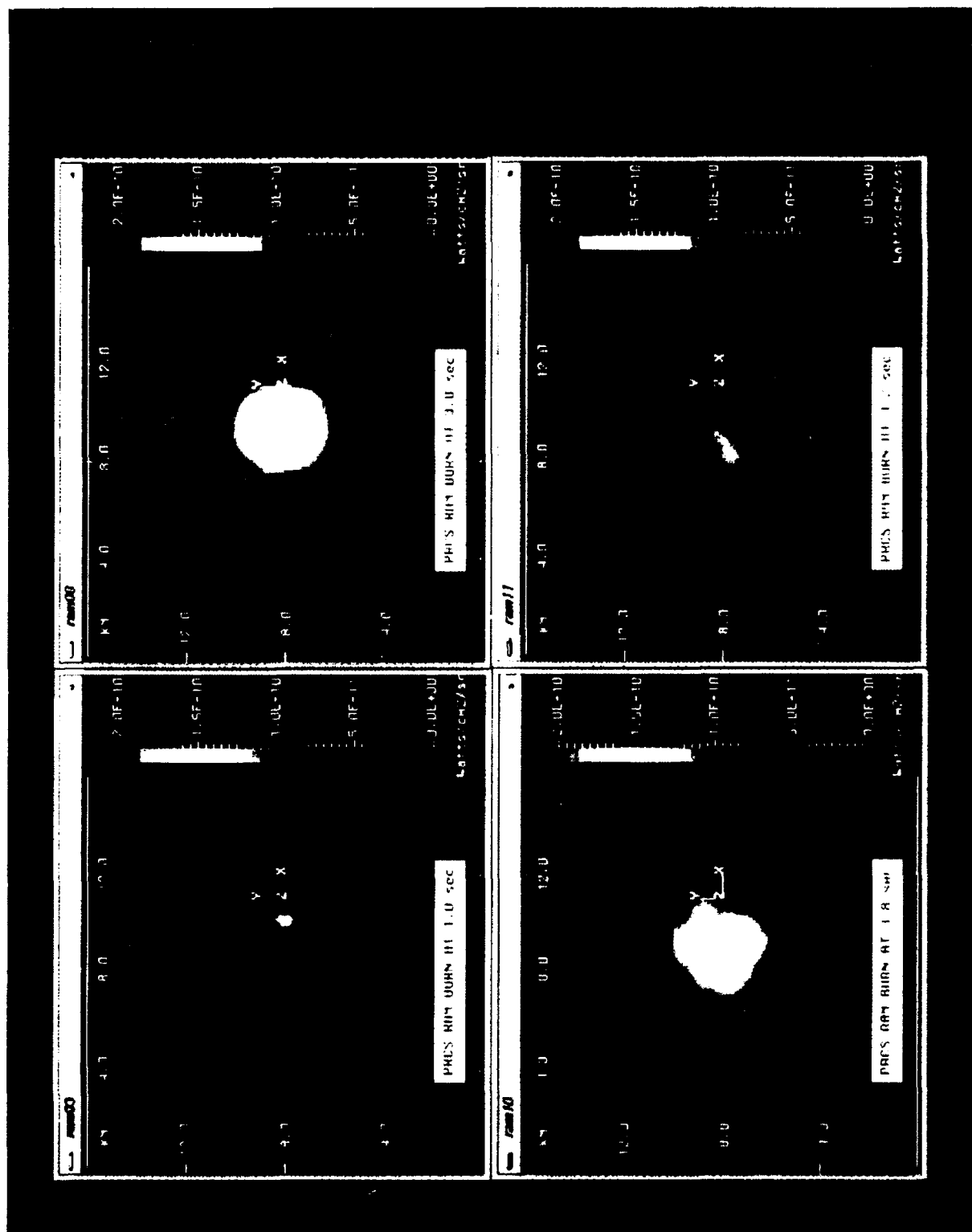


Figure 15. SOCRATES simulation of shuttle PRCs ram burn.

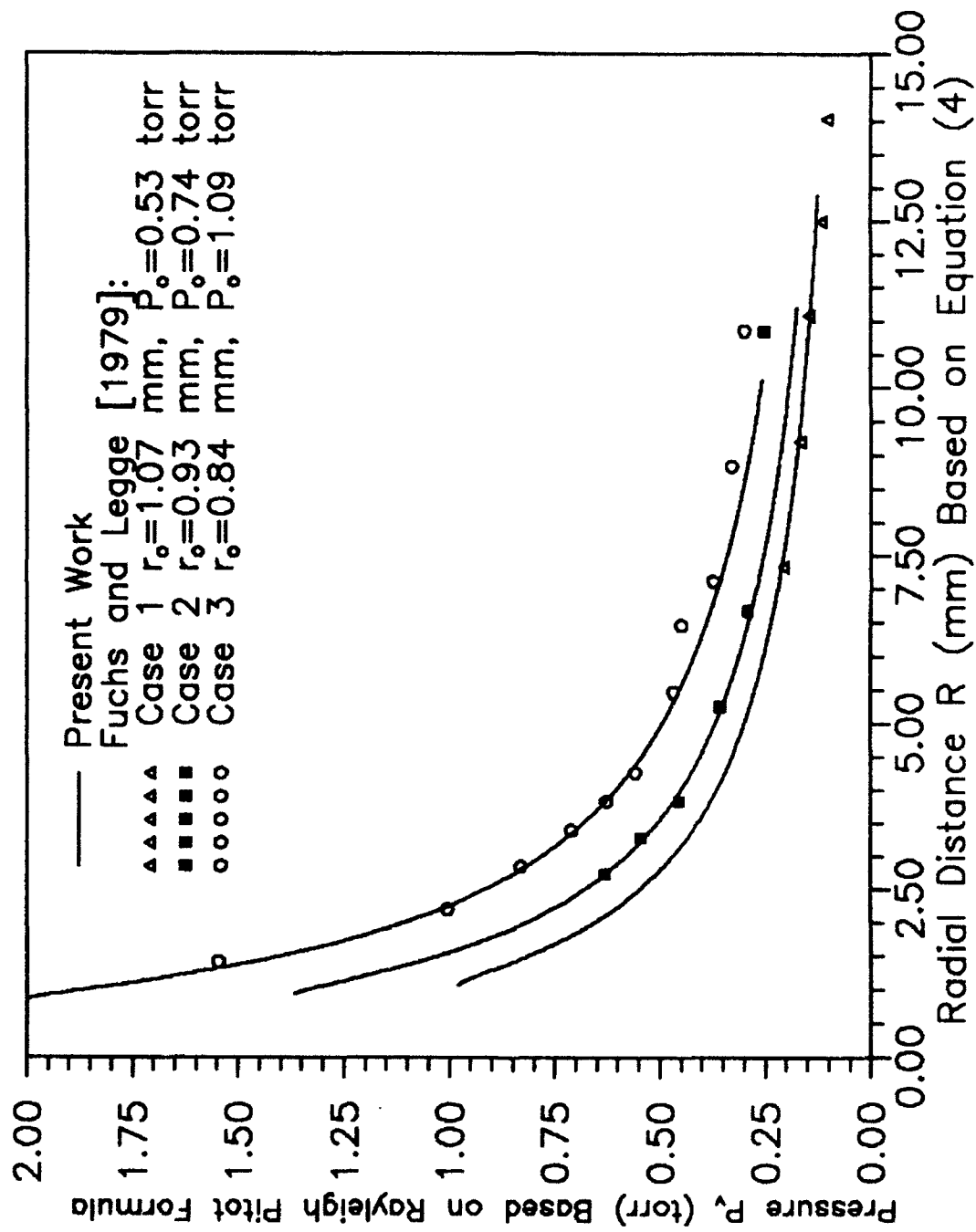


Figure 16. Pitot-Pressure measured at the vapor expansion flow radial to the jet.

$$\frac{P_v}{P_o} = \left\{ \left( \frac{\gamma+1}{2} \right)^{\frac{\gamma}{(\gamma-1)}} \left( \frac{(\gamma+1)M^2}{2+(\gamma-1)M^2} \right)^{\frac{\gamma}{(\gamma-1)}} \right. \\ \left. \left( \frac{2\gamma M^2 - (\gamma-1)}{\gamma+1} \right)^{-\frac{1}{(\gamma-1)}} \right\} \quad (5)$$

Figure 17 shows particle number density variations for 7.5, 25, and 250  $\mu\text{m}$  as a function of radial distance  $r$ . Figure 17 also shows a representation of the experimental measurements of *Curry, et al.* [1985] for a 0.13  $\mu\text{m}$  diameter particle. As can be seen from Figure 17, the trend of the particle number density calculations of the present work is consistent with the experimental work of *Curry, et al.* [1985].

Figure 18 shows the evaporation rate of the particles as a function of distance from the source. The particles with a smaller radius tend to evaporate faster. Figure 19 shows how particle velocity changes as a function of distance from the source. For the large particles, the velocity changes very little from its initial velocity of 15 m/s. However, for smaller particles, the velocity changes very rapidly near the source and becomes almost constant far from the source. This phenomenon can be explained by the forces that influence particle speeds. The vapor velocity increases very rapidly after ejection from the source. This has been illustrated in *Setayesh* [1990], in which, less than one half millimeter from the source, the vapor velocity reaches sonic speed. Therefore, this sharp increase in vapor velocity can affect the velocity of the particles, especially the smaller ones. This situation can be seen in Figure 19, where the 7.5  $\mu\text{m}$  particle velocity increases from 15 m/s to as much as 60 m/s. In contrast, the 250  $\mu\text{m}$  particle velocity increases very slightly (from 15 m/s to about 16 m/s). *Glenn* [1969] explained another factor, which is worth mentioning here. In Figure 18, it is clear that near the source, the evaporation rate for the smaller particles is much faster than for the larger ones. Therefore, it is possible that the local back pressure, which is created by evaporation, and as earlier discussed, vapor drag, could increase the velocity of the smaller particles.

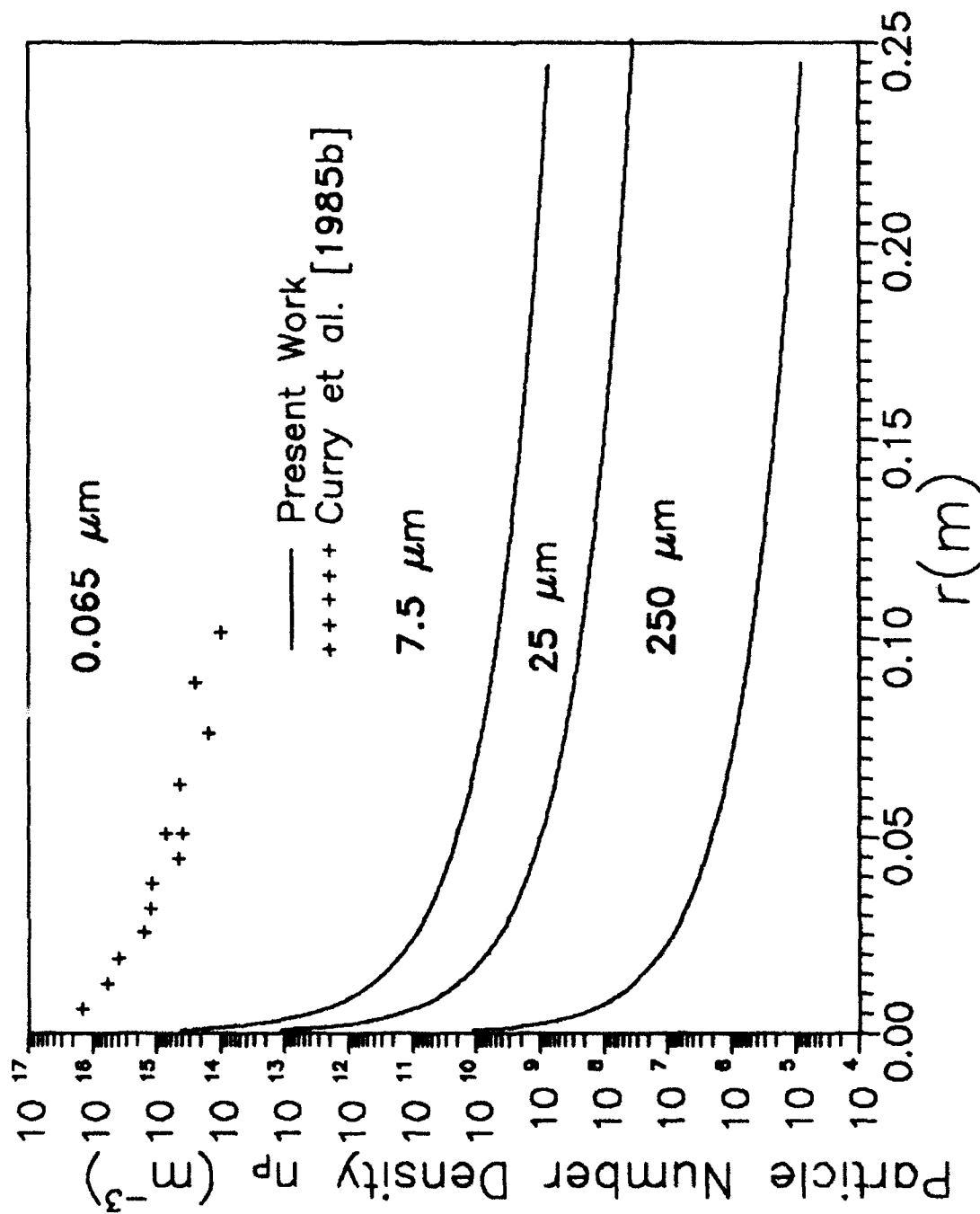


Figure 17. The effect of initial particle size on particle number density.

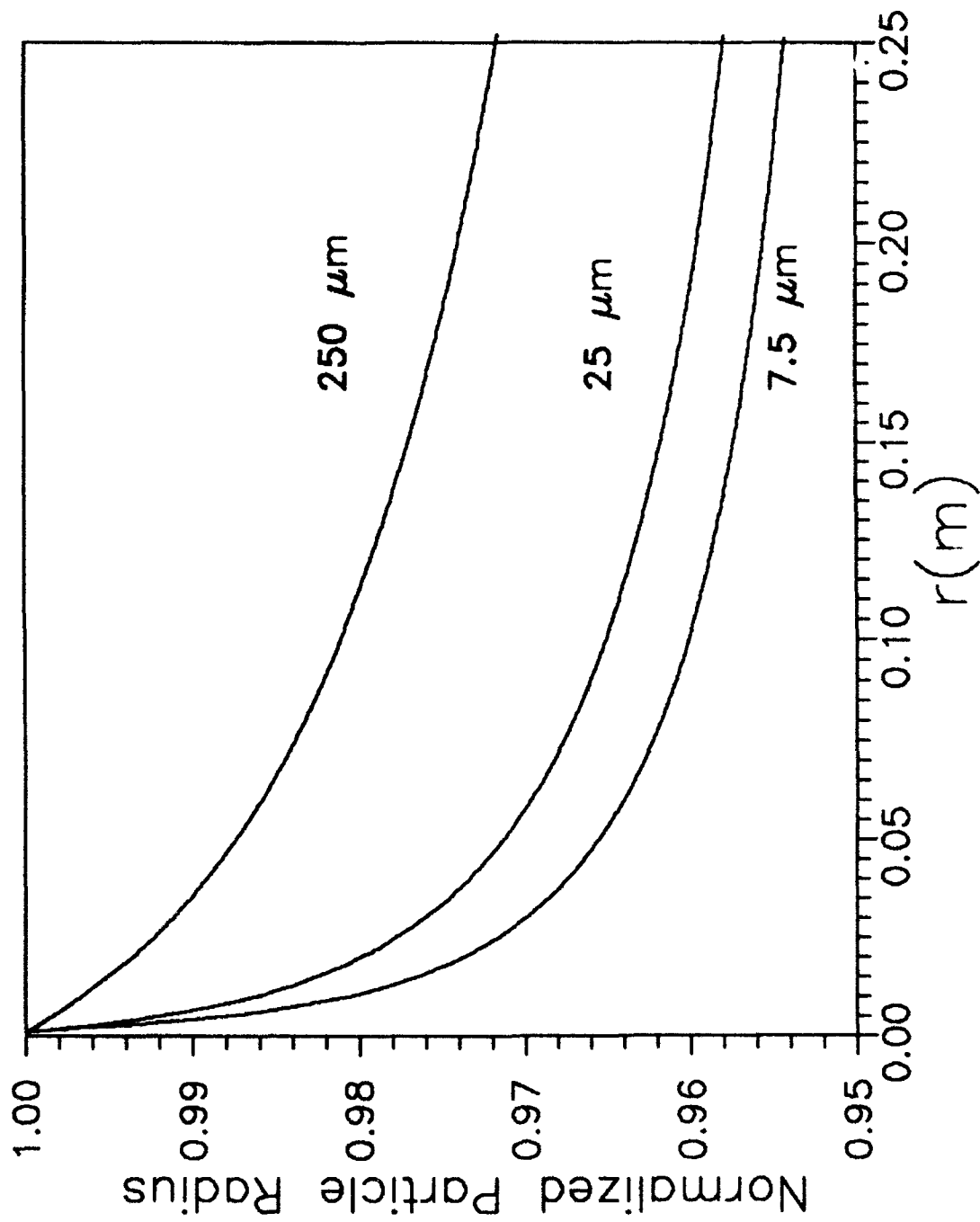


Figure 18. Particle size as a function of distance.

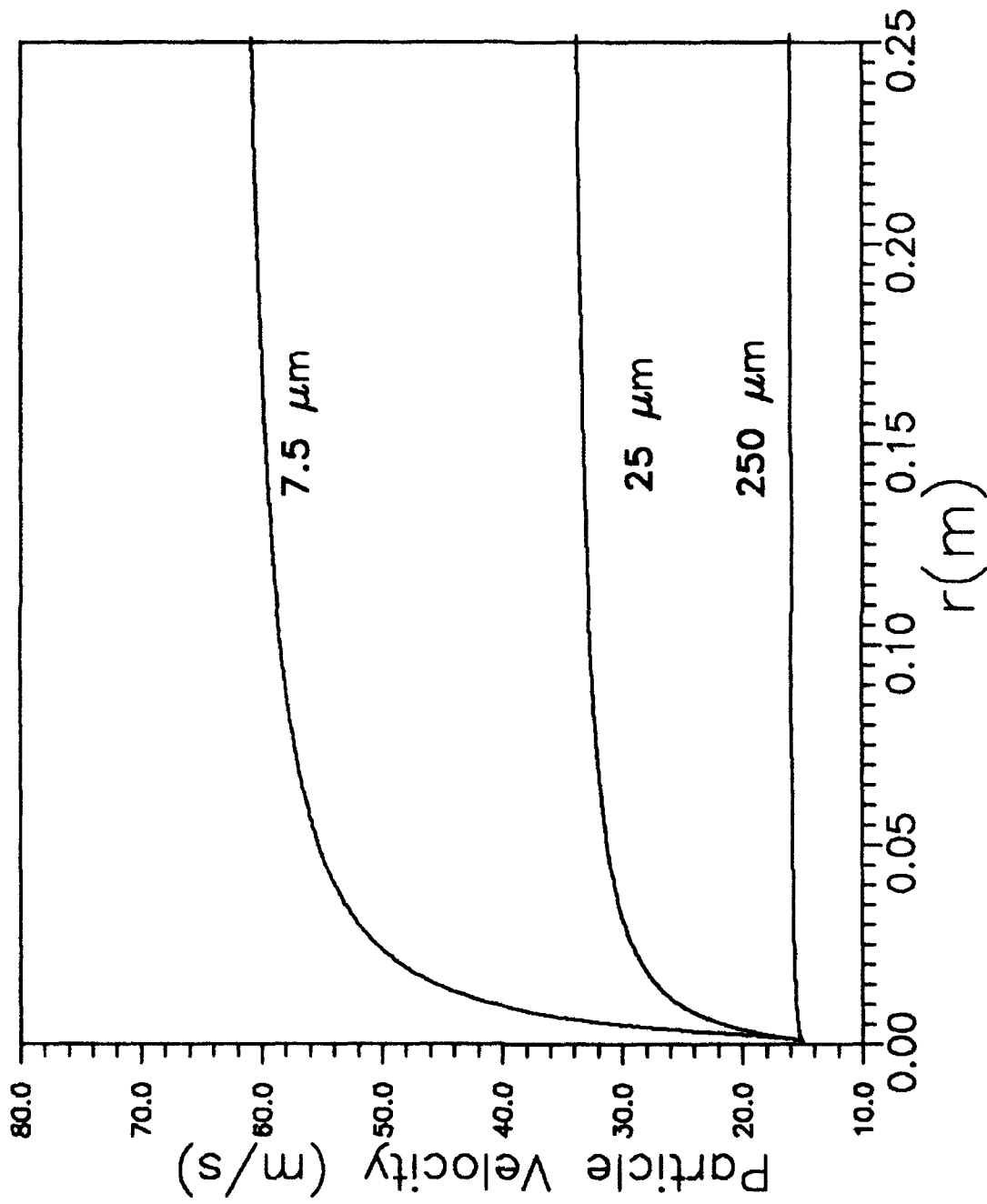


Figure 19. The effect of initial particle size on particle velocity.

**TABLE 8. Parameters Used for the Figures**

Parameter	Figure 16	Figures 17-19
Initial Temperature (°K)	300.15	343.15
Initial Velocity (m/s)	12	15
Initial Source Radius (m)	$1.0 \times 10^{-4}$	$7 \times 10^{-4}$
Initial Particle Radius ( $\mu\text{m}$ )	5	7.5, 25, or 250
Initial Vapor Pressure ( $\text{N/m}^2$ )	$4.0 \times 10^3$	$3.119 \times 10^4$
Initial Vapor Density ( $\text{kg/m}^3$ )	0.025	0.19833
Initial Volume Fraction	0.74	0.74
Evaporation Coefficient	0.05	0.05
Drag Coefficient	0.9	0.9
Particle Nusselt Number	2.73	2.73
Vapor Thermal Conductivity ( $\text{W/m } ^\circ\text{K}$ )	0.24403	0.024403
Vapor Specific Heat ( $\text{J/kg } ^\circ\text{K}$ )	1863.172	1863.172
Heat of Evaporation ( $\text{J/kg}$ )	$2.334 \times 10^6$	$2.334 \times 10^6$
Heat of Fusion ( $\text{J/kg}$ )	$3.341 \times 10^5$	$3.41 \times 10^5$
Particle Density ( $\text{kg/m}^3$ )	977.7	987.1
Gas Constant for Water ( $\text{J/kg } ^\circ\text{K}$ )	461.94	461.94
Stefan-Boltzman Constant ( $\text{W/m}^2 \text{ } ^\circ\text{K}^4$ )	--	$5.669 \times 10^{-8}$
Emissivity of Particle	--	0.9

#### 1.4.2.2 Two Dimensional Liquid Water Vent Modeling

The previous model could follow the evolution of only a single particle at a time for a short distance (less than a meter). The code was also limited to a stationary source of release into vacuum. Therefore, a comprehensive model that describes the water release into the vacuum of space was the next logical objective. The new model, unlike the previous model, should also incorporate steady and transient approaches to the long-time evolution of water dumps in the upper-atmospheric environment. We have been working on a comprehensive mathematical model and a numerical computer code which are suitable for simulating the flow of the constituents in a vent cloud, which consists of mixed phases of water vapor and particulate liquid and solid. We have included a full coupling of the dynamic and thermodynamic processes governing water dump and vent cloud. The development of present mathematical modeling was inspired by the work of *Lezius and Thomas* [1989] in fuel vent modeling. We have completed two important tasks in order to meet the stated objectives: (a) formulation of a complete set of gasdynamic equations of motion for a compressible, generally unsteady, mixed-phase flow with phase change; and (b) development of a set of transport models that describes the full dynamic, thermodynamic, and other energetic coupling between the phases. In the process of developing a model, the MACSYMA software capability (on the PL-VAX system) was employed to generate, symbolically, the eigenvalues and eigenvectors of many matrices which have been used in the problem. The liquid water vent modeling currently has the following specific features, which have been incorporated into the code:

1. The particle size distribution has been approximated by an arbitrary number of particle groups, each characterized by an average particle size determined by the code.



2. A temperature dependent vapor pressure equation and an arbitrarily adjustable sticking coefficient are used to describe the evaporation rate of liquid and solid water particles.
3. Mass transfer, aerodynamic, and thermodynamic processes between the gas, liquid, and solid phases are fully coupled.
4. A set of model equations are used to describe the drag coefficient for drag exerted on particulates by the vapor and by the upper atmosphere. The model smoothly includes the continuum through the transitional to the free molecular flow regime [Henderson, 1976]. Both vapor and atmospheric drag determine the particle motion of vent clouds released into the upper atmosphere, where the atmospheric drag causes spatially axisymmetric distortion of the particle cloud.
5. The particle heat transfer modeling includes evaporative cooling and radiation heat exchange with space, Earth, and the sun.
6. Particle-size changes, due to evaporation, are tracked by an additional equation in which is described the rate of particle changes, as a function of time and distance [Pai, 1977].

The numerical solution of the problem proceeds in two parts. In the first part, the expanding cloud of water vapor and particles is simulated simultaneously in the spherical configuration. In this region, the inflow boundary is subsonic and the outer boundary is slightly supersonic. This part of the problem can be described as the near-field region, where the motion of particles and vapor are generally coupled with each other. In the second part, numerical computation starts from the outer boundary of the near field region and proceeds in the forward direction. This region can be described as the far-field region of the problem, where vapor flow is supersonic and is independent of the particles' motion. The computer model, which is roughly 12000 lines of pure computational code, is currently being tested for boundary conditions for the transonic core region. In this region, the appropriate boundary conditions are needed for the outer boundary of the nearfield region, as well as for the inner boundary of the farfield region of the problem. The equations that describe the vapor transport model are the full two-dimensional and asymmetric (including viscous terms for the near field region) Navier-Stokes equations in general curvilinear coordinates [Hoffmann, 1989].

The mathematical model equations for this problem have been non-dimensionalized, and are written in the form of strong conservation laws. The equations have been transformed from the physical plane to the computational plane. The particle-cloud governing equations for each particle size group  $p$ , can be written in the following conservative vector form

$$\frac{\partial \bar{Q}_p}{\partial t} + \frac{\partial \bar{E}_p}{\partial \xi} + \frac{\partial \bar{F}_p}{\partial \eta} = \bar{S}_p^{int} + \bar{S}_p^{ext} + \bar{S}_p^{sp} \quad (6)$$

Where

$$\begin{aligned}
\bar{Q}_p &= \frac{1}{J} Q_p \\
\bar{E}_p &= \frac{1}{J} ( \xi_x E_p + \xi_y F_p ) \\
\bar{F}_p &= \frac{1}{J} ( \eta_x E_p + \eta_y F_p ) \\
\bar{S}_p^{int} &= \frac{1}{J} S_p^{int} \\
\bar{S}_p^{ext} &= \frac{1}{J} S_p^{ext} \\
\bar{S}_p &= \frac{1}{J} S_p
\end{aligned} \tag{7}$$

in which  $Q_p$ ,  $E_p$ , and  $F_p$  represent the conserved mass, momentum, and energy per unit of volume and  $S_p^{int}$  and  $S_p^{ext}$  are internal and external sources.

$$Q_p = \begin{bmatrix} \rho_p \\ \rho_p u_p \\ \rho_p v_p \\ \rho_p E_{t,p} \\ \bar{r}_p \end{bmatrix} \tag{8}$$

$$E_p = \begin{bmatrix} \rho_p u_p \\ \rho_p u_p^2 \\ \rho_p u_p v_p \\ \rho_p E_{t,p} u_p \\ \bar{r}_p u_p \end{bmatrix} \tag{9}$$

$$F_p = \begin{bmatrix} \rho_p v_p \\ \rho_p v_p u_p \\ \rho_p v_p^2 \\ \rho_p E_{t,p} v_p \\ \bar{r}_p v_p \end{bmatrix} \tag{10}$$

## Modeling of Transport Phenomena

### Internal Sources

$$S_p^{int} = S_{pv} + S_{pd} + S_{ph} \quad (11)$$

### External Sources

$$S_p^{ext} = S_{pr} + S_{am} \quad (12)$$

### Evaporative Mass Transfer

$$S_{pv} = w_{pv} \rho_p \left[ \begin{array}{c} 1 \\ u_p \\ v_p \\ E_{i_p} + \Delta h_v \\ \frac{\bar{r}_p}{3 \rho_p} \end{array} \right] \quad (13)$$

The evaporative mass-transfer rate is given by:

$$w_{pv} = -3 c \frac{[P_v(T_p) - P]}{\rho_c \bar{r}_p \sqrt{2 \pi R T_p}} \quad (14)$$

The equation state can be expressed as:

$$p = \rho R T \quad (15)$$

The vapor pressure over ice particles for the temperature range of -100° C to 0° C is given by:

$$P_v (T_p) = e^A \quad (16)$$

Where

$$A = C_1 T_p + C_2 + C_3 T_p + C_4 T_p^2 + C_5 T_p^3 + C_6 T_p^4 + C_7 \ln(T_p) \quad (17)$$

The vapor pressure over liquid particles for the temperature range of 0° C to 200° C is given by:

$$P_v(T_p) = e^B \quad (18)$$

Where

$$B = C_8 T_p + C_9 + C_{10} T_p + C_{11} T_p^2 + C_{12} T_p^3 + C_{13} \ln(T_p) \quad (19)$$

$C_1$  through  $C_{13}$  are some constant parameters. In Eqs. (14)-(19),  $T_p$  is in ° K and  $P(T_p)$  is in Pascals.

Aerodynamic Drag

$$S_{pd} = \phi_p \begin{bmatrix} 0 \\ u - u_p \\ v - v_p \\ u_p (u - u_p) + v_p (v - v_p) \\ 0 \end{bmatrix} \quad (20)$$

Where

$$\phi_p = \frac{3 \rho \rho_p C_D}{8 \rho_c r_p} [(u - u_p)^2 + (v - v_p)^2]^{\frac{1}{2}} \quad (21)$$

$C_D$  is the drag coefficient.

Heat transfer exchanges between the liquid/ice and the vapor phases per unit volume are given by:

$$S_{ph} = \begin{bmatrix} 0 \\ 0 \\ 0 \\ \dot{q}_p \\ 0 \end{bmatrix} \quad (22)$$

Where

$$\dot{q}_p = 4 Pr^{-2/3} \phi_p c_p (T_v - T_p) \quad (23)$$

The source for the radiation-transfer effects of sunshine, Earthshine, and radiative cooling per unit volume is defined as:

$$S_{pr} = \begin{bmatrix} 0 \\ 0 \\ 0 \\ \dot{q}_{pr} \\ 0 \end{bmatrix} \quad (24)$$

Where

$$\begin{aligned} \dot{q}_{pr} = & \frac{3 \rho_p}{4 \rho_c r_p} [\alpha_E H_E + \\ & \alpha_S H_S - 4 \epsilon \sigma (T_p^A - T_\infty^A)] \end{aligned} \quad (25)$$

External Atmospheric Drag

$$S_{atm} = \phi_{pa} \begin{bmatrix} 0 \\ u_\infty - u_p \\ v_\infty - v_p \\ u_p (u_\infty - u_p) + \\ v_p (v_\infty - v_p) \\ 0 \end{bmatrix} \quad (26)$$

Where

$$\phi_{p_{\infty}} = \frac{3 \rho_{\infty} \rho_p C_D}{8 \rho_c r_p} [(u_{\infty} - u_p)^2 + (v_{\infty} - v_p)^2]^{\frac{1}{2}} \quad (27)$$

The Equation Related to Change of the Radius of the Particles

$$S_{rp} = \begin{bmatrix} 0 \\ 0 \\ 0 \\ 0 \\ \bar{r}_p \left( \xi_x \frac{\partial u_p}{\partial \xi} + \xi_y \frac{\partial v_p}{\partial \xi} \right) + \\ \bar{r}_p \left( \eta_x \frac{\partial u_p}{\partial \eta} + \eta_y \frac{\partial v_p}{\partial \eta} \right) \end{bmatrix} \quad (28)$$

For Vapor

$$\frac{\partial \bar{Q}}{\partial t} + \frac{\partial \bar{E}}{\partial \xi} + \frac{\partial \bar{F}}{\partial \eta} - \frac{\partial \bar{E}_v}{\partial \xi} - \frac{\partial \bar{F}_v}{\partial \eta} = \bar{S}_g^{int} \quad (29)$$

Where

$$\begin{aligned} \bar{Q} &= \frac{1}{J} Q \\ \bar{E} &= \frac{1}{J} ( \xi_x E + \xi_y F ) \\ \bar{F} &= \frac{1}{J} ( \eta_x E + \eta_y F ) \\ \bar{E}_v &= \frac{1}{J} ( \xi_x E_v + \xi_y F_v ) \\ \bar{F}_v &= \frac{1}{J} ( \eta_x E_v + \eta_y F_v ) \\ \bar{S}_g^{int} &= \frac{1}{J} S_g^{int} \end{aligned} \quad (30)$$

in which Q, E, and F represent the conserved mass, momentum, and energy per unit of volume,  $E_v$  and  $F_v$  are the viscous terms in the Navier-Stokes equations, and  $S_g^{int}$  is the vapor internal source.

$$S_g^{int} = \sum_{p=1}^n S_p^{int} \quad (31)$$

$$Q = \begin{bmatrix} \rho \\ \rho u \\ \rho v \\ \rho E_t \end{bmatrix} \quad (32)$$

$$E = \begin{bmatrix} \rho u \\ \rho u^2 + P \\ \rho u v \\ (\rho E_t + P) u \end{bmatrix} \quad (33)$$

$$F = \begin{bmatrix} \rho v \\ \rho v u \\ \rho v^2 + P \\ (\rho E_t + P) v \end{bmatrix} \quad (34)$$

$$E_v = \begin{bmatrix} 0 \\ \tau_{xx} \\ \tau_{xy} \\ u \tau_{xx} + v \tau_{xy} - q_x \end{bmatrix} \quad (35)$$

$$F_v = \begin{bmatrix} 0 \\ \tau_{yx} \\ \tau_{yy} \\ u \tau_{yx} + v \tau_{yy} - q_y \end{bmatrix} \quad (36)$$

The Jacobian matrices are defined as

$$\xi_x = J y_\eta \quad (37)$$

$$\xi_y = -J x_\eta \quad (38)$$

$$\eta_x = -J y_\xi \quad (39)$$

$$\eta_y = J x_\xi \quad (40)$$

Where

$$J = \frac{1}{x_\xi y_\eta - y_\xi x_\eta} \quad (41)$$

In the present treatment, the problem investigates the state of the liquid water after stream breakup in space, where the flow can be characterized by a two phase mixture of vapor and nearly spherical particles. After the initial water breakup, the newly created water droplets separate from the water vapor in a short period of time as a result of rapid rarefaction of vapor in a vacuum. The effects of the rapid rarefaction of the expanding water vapor are coupled to initial particle acceleration by the particle-size-dependent drag model for continuum, transitional, and free molecular flow. The boundaries for these three types of flow are defined in terms of Knudsen numbers.

The solution of the problem is based on an implicit three point time differencing scheme, with an implicit approximate factorization finite difference algorithm [Beam and Warming, 1978]. The nonlinear terms have been locally linearized with respect to time, and the approximate factorization of the two-dimensional implicit operators are used to produce locally one-dimensional operators in both the vapor and the particle equations. The second order central finite difference operators have been used for space differencing in the vapor equations, and upwind operators are used to represent the space differencing in the particle equations. The starting point of the model is a small diameter nozzle which releases a liquid water stream at a specified velocity and temperature into space. The analysis begins by assuming some initial size distribution of liquid droplets mixed with water vapor. The governing equations of the vapor, the Navier-Stokes equations, and the transport equations of the particles, are coupled for an initial acceleration period. After this period, which is within a short distance from the source of the water release, the equations for vapor and particles become uncoupled from each other.



## 1.5 INVESTIGATIONS OF THE CRITICAL IONIZATION VELOCITY IN SPACE

The concept of a critical ionization velocity (CIV) was first introduced by *Alfvén* [1954] as a component of his theory for the formation of the solar system. As a neutral gas moves through a magnetized plasma, a rapid ionization of the neutrals takes place if the kinetic energy of the neutrals relative to the plasma exceeds the ionization potential of the neutrals. This defines the critical velocity

$$V_c = (2e\Phi_i/M)^{1/2} \quad (42)$$

where  $e\Phi$  is the ionization potential and  $M$  is the mass of the neutral. If the neutrals travel above this velocity, the CIV interaction is expected to take place. The concept was used to explain why the composition of the inner planets differs from that of the outer planets. The idea was that as neutral gas fell toward the Sun, each species present in the gas was preferentially ionized according to its critical velocity and, after ionization, was trapped at that radial distance by the Sun's magnetic field.

Recent attempts to explain the underlying mechanisms for ionization in CIV recognize it to be a process dependent on several steps. Some mechanism, such as charge exchange between the fast neutrals and cold plasma ions or photoionization, creates energetic ions. The relative motion between these ions and the plasma electrons creates an unstable situation which gives rise to the growth of plasma waves. These waves serve to remove energy from the ions and transfer it to the electrons. Since the occurrence of CIV seems to be dependent on the presence of a magnetic field in the direction perpendicular to the neutral velocity, instabilities such as the modified two stream or the lower hybrid instability have been suggested as potentially important in this energy transfer. The result of this energy transfer is an energetic population of electrons, capable of ionizing some of the neutrals. This creates additional ions moving at the neutral velocity. These ions feed energy into the unstable waves, heating more electrons. The exponential increase in plasma density is a consequence of this transfer cycle.

Although several laboratory experiments have confirmed the existence of the CIV interaction, the many attempts at inducing a CIV discharge in space have led to controversial and inconclusive results. Most space experiments result in only a small fraction of the neutrals becoming ionized. It would seem, then, that space and laboratory experimental conditions are sufficiently different to yield entirely different experimental results. Since there would be important consequences if CIV were to take place in space, it is important to understand exactly why it appears difficult to achieve a positive result. In pursuit of this, we have constructed several models to examine the underlying mechanisms of space CIV. These studies include (1) the microscopic simulation of energy balance in a CIV discharge, (2) the examination of the amplification of CIV by associative ionization, (3) the importance of seed ionization in initiating the discharge, (4) CIV in a mixture of different gases, (5) the CIV behavior of a pulsed neutral beam, and (6) the altitude effects in CIV. The overall purpose of these studies is to gain an understanding of the microscopic mechanisms of importance of CIV in space.

### 1.5.1 Simulation of CIV in Various Species

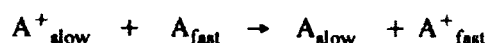
The end result of the CIV process must depend heavily on the precise nature of the flow of energy from ions to electrons and back to ions again. Since the flow is dominated by plasma instabilities, a useful approach to the problem utilizes the method of plasma simulation, first popularized by *Birdsall and Langdon* [1985]. This technique represents plasma ions and electrons by finite particles, following the development of instabilities through solution of the kinetic equations of motion and the field equations. In pioneering work, *Machida and Goertz* [1986] included chemical kinetic processes in a simulation of

this type, demonstrating for the first time that the cyclic CIV process could be induced in simulation. These authors modeled the cross sections for various processes based on a hypothetical species. However, it has been suggested [Lai, *et al.*, 1989] that the variations in reaction rates between species could potentially be important in the outcome of the discharge. For this reason, we undertook a comparative simulation of a CIV discharge modeling reaction rates from data for four potential CIV gases [McNeil, *et al.*, 1989].

We chose the gases: helium, neon, xenon and barium for this study. Barium is the typical choice for space CIV experiments, since both neutral and ionized barium are excited by sunlight in the visible spectrum. Xenon is perhaps the second most popular choice because its critical velocity can be obtained at orbital velocities. Helium and neon were included because they are often the choice for laboratory experiments. Thus comparisons drawn from the simulation might yield some information on the reason for differing laboratory and space CIV results. The chemical processes of ground state ionization, charge exchange, excitation and ionization of metastable states, excitation of allowed states, and elastic collisions were included.

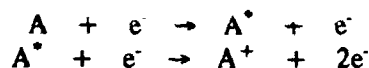
#### 1.5.1.1 Kinetic Processes

In order for a CIV discharge to be sustained, it must be that the energy gained by the creation of a fast ion through electron impact ionization at least equals that spent in performing the ionization. This is the basis of Eq. (40). When this "energy budget" is tight, an avalanche discharge may not occur in the absence of some secondary energy input mechanism. To sustain CIV, any available energy source, such as charge exchange between beam ions and beam neutrals can act to recharge the beam ions after they have given up some of their energy to the electrons.

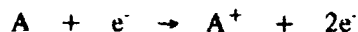


in fact, symmetric charge exchange may be taking place to a large extent in the early stages of a space CIV beam, which would explain the observed fact that ions seem to trail along for several ion gyro radii before actually becoming trapped along the field lines.

Metastable states provide a mechanism for pooling energy by allowing electrons with energy less than the ionization potential of a given species to participate in the ionization process.



The efficiency of this depends on the rate of excitation and the radiative life time of  $A^*$  and on the electron density. Because of this, only relatively long lived excited states (*i.e.*, metastables) contribute substantially. The efficiency also depends on the relative rate of this two-step process to the rate of direct ionization



leading to the result that the metastable state is only very important at the critical velocity threshold, as predicted by Lai, *et al.* [1988].

The excitation of neutrals to allowed states followed by spontaneous emission is an energy loss mechanism. The energy lost to this "line excitation" can be compared to that lost to ionization of the neutrals through examination of the quantity

$$\Phi = \frac{\int dE f_e(E) \Phi_{ex} \sigma_{ex}(E)}{\int dE f_e(E) \Phi_i \sigma_i(E)} \quad (43)$$

as Eq. (41) shows, this loss depends on the electron distribution function  $f_e$ , as well as on the cross sections for excitation and ionization,  $\sigma_{ex}$  and  $\sigma_i$ , and the thresholds for excitation and ionization  $\Phi_{ex}$  and  $\Phi_i$ . As such, the calculation of energy loss to line excitation becomes a complex problem, which is addressable only in a self-consistent simulation of energy input and transfer, such as the one performed here. One purpose of these simulations was to investigate the impact of the relative magnitudes of rates of these processes on the end result for the various species.

#### 1.5.1.2 Neutral Species

Of the four species modeled in the simulation, barium is remarkable in that it has an extremely large line excitation cross section. The value is almost four times that of its ionization cross section at higher energies. One might then suspect that a greater energy loss might obtain for the CIV process in barium, and that this might increase the threshold for CIV over that of the other gases. Also, for Xenon, we find a relatively large ionization cross section relative to that of symmetric charge exchange. When charge exchange is an important energy input mechanism, as it should be near threshold, this could lead to a comparatively lower overall ionization rate.

#### 1.5.1.3 The Simulations

These simulations are performed in one-and-three-halves-dimensions, using a simulation code following that of the basic ES1 algorithm [Birdsall and Langdon, 1985]. An electric field is allowed in the x direction and a magnetic field is imposed in the x-z plane at an angle  $\Theta$  to the z-axis. The velocity of each electron is therefore three-dimensional. Acceleration of the electrons occurs only in the x-direction, while cyclotron motion is modeled by the half-acceleration, rotation, half-acceleration algorithm in which the velocities are advanced one-half time step in response to the electric field, rotated by the appropriate fraction of the gyro period, then accelerated again through the remainder of the timestep. Following Machida and Goertz [1986], we perform our simulation at a constant ratio of  $kV_b/\omega_{pe}$  so that the instability growth rate is near its maximum [McNeil, et al., 1989]. With this choice, the ratio of beam to critical velocity is introduced by a parameter  $\zeta = V_b/V_*$ . This approach allows for the "beam velocity" to be varied without changing the growth rate of the instability.

In order to follow the motion of electrons as well as ions within a reasonable time, we assign an artificial mass ratio of 100 in the calculation of collective interactions. However, the actual mass ratios are employed in the calculation of ratio of symmetric charge exchange to electron/neutral processes. The energy dependent cross sections for the four species and the six processes are multiplied by the electron velocity  $v$  to include the flux and are normalized in energy to the corresponding ratio of  $V_e/V_*$  using the artificial mass ratio. They are further normalized in magnitude by a reference rate, chosen to be the rate of ionization of an electron at 1.5 times the critical velocity in a neon beam.

The kinetic processes are included as follows. A random number is generated  $0 < \alpha < 1$  and a collision is executed if

$$1 - e^{-p_0 p_i(v_i) \Delta t} > \alpha \quad (44)$$

where  $p_0$  is a chosen reference rate that depends linearly on the neutral density and  $p_i$  is the reaction rate for the  $i$ -th process, evaluated at the electron velocity  $v_i$ .  $\Delta t$  is the chosen time step, which is normalized to the initial electron plasma frequency  $\omega_{pe}$ . For symmetric charge exchange, a positive result is modeled by giving the ion involved the beam velocity. For ground state and metastable ionization, a new ion/electron pair is created with the ion moving at the beam velocity and the old electron is de-energized appropriately by the ionization potential. For line excitation, the electron is also de-energized but no new electron/ion pair is created. For elastic collisions, the direction of the electron velocity is reversed.

#### 1.5.1.4 Results

A main result of this simulation was the ability to compare ionization rates and thresholds for CIV in the four gases studied. Figure 20 shows the growth in plasma density at various values of  $\zeta$  for the various gases. Although it is quite difficult to determine a precise threshold for sustained ionization from these data, it is apparent that there is a rather abrupt increase in the rate of ionization with increasing  $\zeta$ . This one might well label as a threshold. It is also apparent that this value is quite different for different gases. For neon and helium we observe substantial ionization near the value of  $V_*$  predicted by Eq. (40). For xenon and especially for barium, we observe almost no ionization within the  $200\omega_{pe}^{-1}$  allowed in these runs for  $V_b$  near the Alfvén value. For barium, in fact, there is little ionization before  $V_b$  reaches almost twice  $V_*$ . This has important consequences for space CIV experiments using barium releases, in which velocities of typically twice the barium critical velocity are generally the highest obtained.

In the attempt to explain the differences in apparent CIV threshold between various species, we focused on the individual kinetic processes contributing to energy loss and gain. We found that the contribution of metastables to enhanced CIV was a transitory effect which increased the ionization rate only at the beginning of the discharge. This is reasonable since the effect is actually energy neutral in that it takes as much energy to excite a metastable and to ionize it as it does to ionize a ground state atom. Therefore, if the rate of ionization depends on the rate of energy flow, the overall rate would not be enhanced. In the case of charge exchange, the enhancement is crucial for observing CIV at  $\zeta$  values near unity, where the overall energy budget is probably negative. At higher  $\zeta$  values, however, symmetric charge exchange does little to enhance CIV since the process of ground state ionization is already energy positive.

Like charge exchange, line excitation can affect both the threshold for CIV and the effective rate of plasma increase. The method of interaction is fundamentally different, however. Unlike charge exchange, line excitation competes directly with ground state ionization for superheated electrons. In order to better explain these results, we introduced the concept of an excitation window. The energy range in the window starts from the excitation threshold  $\Phi_{ex}$  and continues to the ionization threshold  $\Phi_i$ . Electrons in this energy range experience line excitation but not ionization since  $\Phi_i$  has yet to be reached. All electrons reaching  $\Phi_i$  must pass through the window and if the rate of line excitation is sufficiently high, the window can remove all electrons before they reach  $\Phi_i$ , thus effectively shutting off ionization. We demonstrated this effect in simulation through variation of the parameter  $p_0$ , which is proportional to the neutral density and thus to the rate of line excitation as well. Figure 21 shows the effective ionization rate as a function of  $p_0$ . At sufficiently high values of  $p_0$ , ionization is completely shut off.

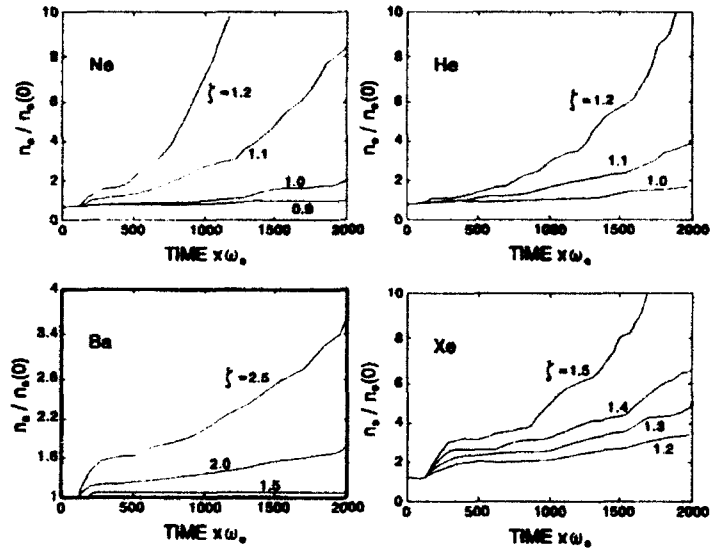


**Figure 20.** Curves of plasma density as a function of time for the four gases studied at various beam velocities.

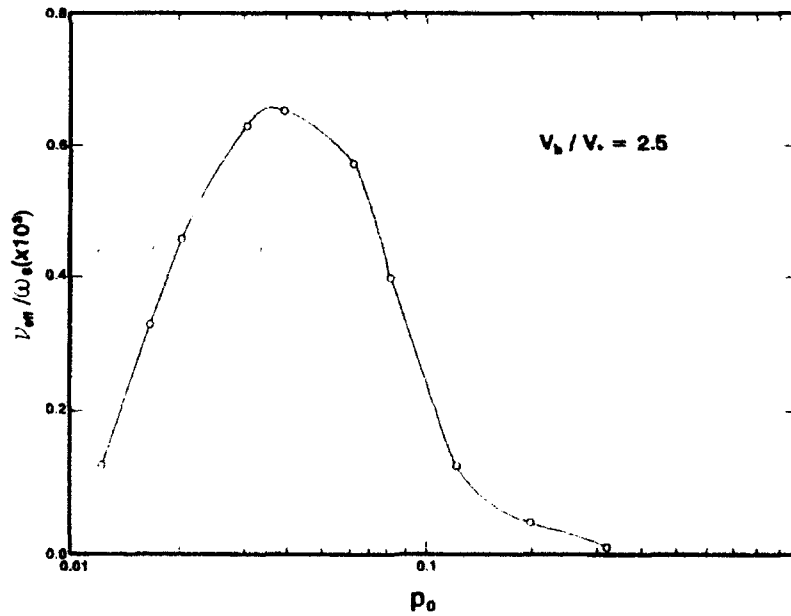


**Figure 21.** Demonstration of the effect of neutral density on CIV in barium. As density increases, the line excitation processes dominate over ionization.

We believe that this may be a major factor in the observed low rates of ionization in space CIV experiments, especially for barium where the line excitation cross section is rather large.

#### 1.5.1.5 Conclusions

Although the basic features of these results agree in several respects with earlier simulations, it appears that the use of cross sections representative of actual neutral species is essential in the correct prediction of thresholds and ionization rates. Line excitation appears to be an important energy loss mechanism in that it raises the threshold velocity and lowers the effective ionization rate for a CIV discharge. Of the four species studied, the inhibition is particularly large for barium and is also quite significant for xenon. We believe that these are significant results in view of the negative or indefinite results obtained so far using barium beams for attempts to prove CIV in space. It appears that a barium CIV discharge would be strongly quenched near the Alfvén critical velocity. It also appears that barium would exhibit a strong neutral density dependence while the other gases studied would not at realistic densities. We conclude that low ionization potential alone may not be the sufficient criterion for choosing beam species in attempts to demonstrate space CIV. Instead, one has to include among the considerations the magnitude of loss properties such as line excitation presented by various candidate species.

#### 1.5.2 Amplification of CIV by Associative Ionization

The conditions under which the laboratory and space CIV experiments are conducted are of necessity quite different: (1) neutral densities and magnetic field strengths are much higher in laboratory experiments; (2) laboratory conditions are controlled while space conditions vary depending on local time and geomagnetic activity; and (3) in typical space experiments a fast barium beam is injected into the ionosphere just below the Sun terminator, while in the laboratory experiments a plasma consisting of light ions is injected into a stationary target gas.

A complication in space experiments arises from alternate kinetic processes that may be mistaken for CIV. First, charge exchange between barium beam atoms and ambient oxygen ions can generate barium ions.



This reaction is exothermic by 8.4 eV and would be expected to have a large cross section over a wide range of collision energies. *Swenson, et al.* [1991] report that the cross section is as large as  $1(-14) \text{ cm}^2$ . A second process, stripping ionization, can also yield barium ions



The threshold for this reaction is 5.2 eV in the center of mass frame or about 49.8 eV (8.4 km/s) for a moving barium atom and stationary oxygen. This velocity is obtained for a substantial fraction of the neutrals in typical space CIV experiments.

We have investigated a third possibility [*Lai, et al.*, 1992], that of associative ionization (AI), considering both the possibilities that AI may be mistaken for CIV and that AI can amplify the CIV process by the generation of electrons and beam ions. By comparison, we find that AI may be more important than charge exchange and stripping ionization.

### 1.5.2.1 Associative Ionization

In an associative ionization reaction, a new chemical bond is formed with an increase in charge carrier. For barium, AI can proceed as



The threshold for this reaction is given by the dissociation energy of BaO minus the ionization potential of BaO. This is approximately 0.68 eV in the center of mass frame. In the laboratory frame, it is about 6.5 eV or 3 km/s for a moving barium. The majority of barium atoms exceed this velocity in typical releases.

Although the cross section for associative ionization of barium and oxygen has not been measured, measurements of similar systems yield cross sections on the order of  $\sigma_{\text{AI}} = 1(-15) \text{ cm}^2$ . Although this is probably a reasonable estimate, we also carry out the calculations in this model using a low estimate of  $\sigma_{\text{AI}} = 1(-17) \text{ cm}^2$ . Using a typical barium atom velocity of 6 km/s, one finds a rate constant of  $k_{\text{AI}} = 6(-10) \text{ cm}^3/\text{s}$  for the high cross section and  $k_{\text{AI}} = 6(-12) \text{ cm}^3/\text{s}$  for the low cross section. In a typical CIV experiment, the neutral density  $n_b$  of the barium jet is initially higher than the ambient atmospheric density  $n_a$ . As the jet expands, the beam density drops. However, the rate of creation of charges through AI,

$$\frac{dN^+}{dt} = k[\text{O}] \quad (45)$$

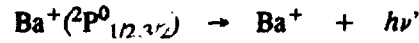
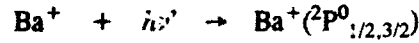
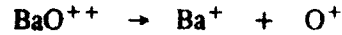
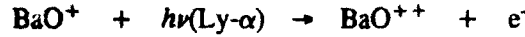
remains constant. This rate is reported for the CRIT II release at about 0.1% per second. At the 450 km altitude of CRIT II, the atomic oxygen density is about  $5(7) \text{ cm}^{-3}$ , which gives a rate between 3%/sec and 0.03%/sec for the two extremes of the cross section respectively. These values bracket the observed rate. This indicates that AI is predicted to proceed at levels comparable to that of the total ionization in the CRIT II experiment.

### 1.5.2.2 AI Mistaken for CIV

The  $\text{BaO}^+$  formed can travel along magnetic field lines into sunlight, where it will absorb solar radiation. Since the solar spectrum consists of radiation concentrated around 10.2 eV (the Lyman- $\alpha$ ), it is possible for  $\text{BaO}^+$  to be transformed into  $\text{Ba}^+$  through absorption of solar radiation by either of two schemes:



or



Both these scenarios are energetically feasible in sunlight.

### 1.5.2.3 Combined AI and CIV

The electrons from AI are, of course, indistinguishable from those generated by CIV. The newly formed ion  $\text{BaO}^+$  can also be a source of energy for the newly forming ion beam. Following a barium jet explosion, the initial beam ion density due to thermal ionization is higher than that of the ambient plasma. As the beam propagates, its transverse expansion reduces its ion density until it drops below the ambient density. As a rough approximation one can assume that about 0.05% of the atoms are ionized in the detonation and that the beam expands at 1.5 km/sec. This gives equal density beam and ambients at about 1 km distance from the release.

The maximum growth rate  $\gamma_{\text{max}}$  of the modified two stream instability is roughly proportional to the ratio of beam to ambient density. Thus, when the beam density falls below the ambient density, the intensity of the modified two stream interaction is reduced. AI can act to increase the spacial extent of ion production through CIV by keeping  $n_b \geq n_a$  for greater distances. In Figure 22, we present results for a simple spherical expansion representing the CRIT II and CRRES releases. The shaded portions of the curves show the beam density resulting from AI derived through a simple kinetic model

$$\begin{aligned} \frac{dN_{\text{Ba}}}{dt} &= -k_{\text{AI}}[\text{O}]N_{\text{Ba}} \\ \frac{dN_{\text{Ba}^+}}{dt} &= k_{\text{AI}}[\text{O}]N_{\text{Ba}} - 2N_{\text{BaO}^+}/\tau_g \end{aligned} \quad (46)$$

where  $\tau_g$  is the ion gyro time. The results show that AI is capable of maintaining a beam density greater than the ambient density for several tens of kilometers from the release point.

It is interesting that this result suggests that the crossover point is pushed farther along the beam as a result of AI. This may result in longer distances for electron energization and could explain the observed result that significant ionization takes place at large distances, far larger than would be expected from consideration of contact times of the beam.

### 1.5.2.4 Comparison with Other Processes

Other mechanisms may also generate ion beams traveling in the same direction as the CIV generated beam. Three such mechanisms are (1) charge exchange, (2) stripping, and (3) reflected  $\text{O}^+$  beams. The ions generated as a result of charge exchange can help sustain CIV in much the same way as was discussed above. However, the generation rate of this mechanism is expected to be lower than that of



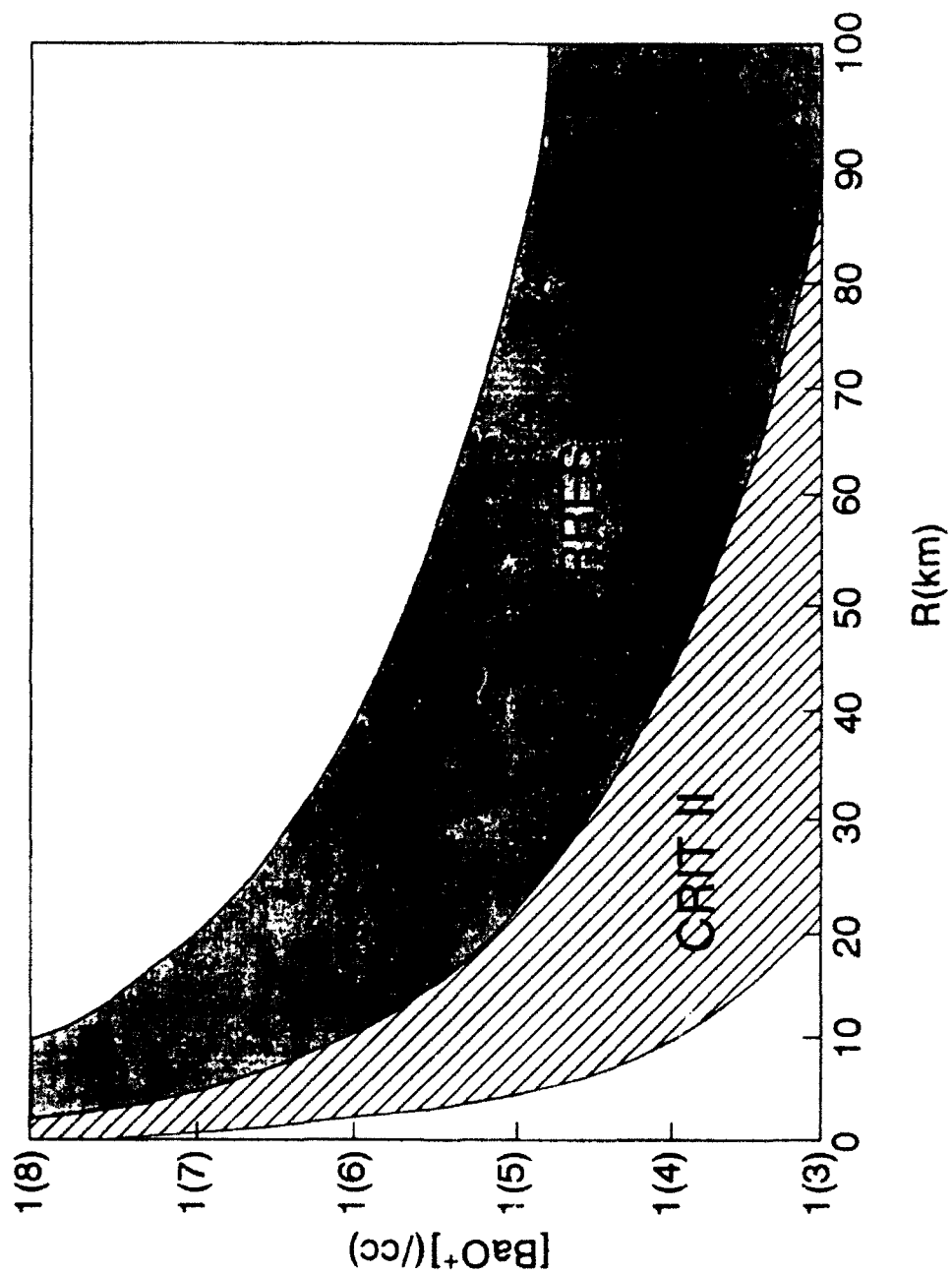


**Figure 22.** The beam density arising from Associative Ionization for simple expansion models of the CRRES and CRIT II releases.

the associative ionization mainly because the density of ambient  $O^+$ , which is necessary for charge exchange, is orders of magnitude lower than that of neutral  $O$  which is necessary for AI. Despite a potentially large cross section, the rate of ion beam production via charge exchange is always limited by the ambient plasma density. Taking the CRIT II experiment for example, one finds that for a charge exchange cross section of 1(-15)  $cm^3$  AI comes out ahead by a factor of between 10 and 10,000, reflecting the range of AI cross sections considered in this model.

In stripping ionization, the high mass ratio between barium and oxygen makes  $Ba^+$  beam formation likely. This additional beam ion kinetic energy can enhance CIV in a manner similar to that discussed above. Stripping ionization provides more electrons than charge exchange, although both provide ion beams. Using the estimated stripping cross section of 9(-18)  $cm^2$  one finds that AI can be comparable to stripping using the large cross section and will out perform stripping by a factor of 100 with the small cross section. Finally, we consider the reflected  $O^+$  beam, created through elastic collisions between  $O^+$  and  $Ba$ . Reflected  $O^+$  ions in the forward direction are also beamlike. The oxygen ions could potentially have energies comparable to the barium neutrals and could perhaps energize electrons. However, their reflected velocities would be substantially higher than those of the barium neutrals and any barium ions. Thus, the time spent in the neutral beam would be limited. It has been observed, however, that a small precursor of increased plasma density and wave structures precedes the neutrals. This is perhaps attributable to these scattered oxygen ions. This is a topic that warrants further investigation.

#### 1.5.2.5 A Proposed Experiment

It is possible to design an experiment that takes advantage of the assistance that AI provides in propagating CIV but yet where product ions will not be mistaken for CIV itself. In such an experiment, one would release a mixture of a species that can undergo AI and one which cannot. By performing an independent experiment with the latter of these alone, one could test the degree of enhancement provided by AI. A good candidate for AI is samarium. The cross section for the reaction



has been measured to be around 2(-16)  $cm^2$ . To estimate the ionization from AI in such an experiment, we return to the spherical expansion model, assuming an explosion similar to the CRIT II release. Substituting the new cross section shows a beam density of 3(5)  $cm^{-3}$  two seconds after release and a density of 5(4)  $cm^{-3}$  five seconds after release.

This suggests an AI-assisted experiment in which samarium AI is used to assist CIV in xenon. A neutral samarium beam would be ejected and an AI generated  $SmO^+$  beam would be formed. The electrons energized by the ion beam would serve to assist the onset and maintain energy input into the CIV process in the Xenon.

#### 1.5.3 The Importance of Seed Ionization In CIV Space Experiments

A remarkable aspect of Alfvén's critical ionization velocity (CIV) is the ease with which it can be induced in the laboratory and the apparent difficulty in demonstrating the effect in space. We have compared laboratory and space CIV experiments; focusing on one potentially important difference; the creation of an initial ion beam [Lai, et al. 1992b]. In the laboratory, the magnetic field is at rest along with the neutral gas while the plasma is forced across it. In space, on the other hand, both ambient plasma and magnetic field are at rest while the neutral gas moves relative to the two. Plasma instability cannot occur

until the neutral beam has obtained an ionized component. In space, the neutral cloud expands rapidly and the ultimate yield of ions depends strongly on the time it takes to develop an ion beam capable of producing super-thermal electrons. Photoionization, charge exchange, associative ionization and stripping are possible mechanisms for seeding of the neutral cloud. However, because these produce ions yet are not CIV related, their presence confounds the experiment. One wonders whether the presence of CIV-like symptoms; electron heating and lower hybrid waves, indicates that the CIV process is indeed active. In this work, we suggest that the CIV interaction may be delayed in space experiments and that this delay, coupled with the rapid expansion of the neutral cloud, may explain the observed low yields.

#### 1.5.3.1 Laboratory Conditions

The first laboratory experiment to test CIV used the homopolar device. In this device, a neutral gas and a plasma fill the space between two concentric cylinders. In the experiment, crossed electric and magnetic fields drive the plasma around the space between two cylinders through the neutral gas, which remains at rest. Alfvén described the homopolar experiment as follows: "When the fed-in energy increased gradually, the degree of ionization jumped suddenly from 0.1% to 100% in a time scale of a few  $\mu\text{s}$ ".

Following this epoch experiment, many laboratory experiments using the homopolar device or the coaxial plasma gun have been conducted to test CIV. In a coaxial gun, the magnetic field is parallel to the tube axis near the plasma source and perpendicular to the axis in the interaction region. In the experiment, a neutral gas is injected into the region, again at rest, and a puff of plasma is injected with an initial velocity well above  $V_{*}$ . As the plasma puff traverses the neutral gas, rapid ionization occurs. After passage through the gas, the plasma slows down to a final velocity  $V_f$ . Interestingly,  $V_f$  is near but above  $V_{*}$ .

Significantly, in both these arrangements, there exists from the outset a dense plasma which is moving relative to the neutral gas *and* the magnetic field. Also significantly, laboratory experiments universally fail at high neutral density. This effect has been attributed in part to inelastic collisions of superheated electrons with the neutrals.

#### 1.5.3.2 Space Conditions

In space experiments, a neutral gas is injected into the ambient plasma. Of the many such dedicated experiments, only three reported positive results. The three are Porcupine, CRIT II, and CRRES. The rest, including King Crab, Bubble Machine I, Bubble Machine II, Star of Lima, Star of Condor, George Orwell, CRIT I, and the ten rocket releases of Hallinan, all failed to obtain positive results. In addition, the early rocket releases of barium gas (not dedicated to tests of CIV) in the 1970s also failed to yield any evidence of CIV. The ionization yields in the three positive experiments are low (at 20%, 2%, and 1% approximately). Furthermore, it is questionable whether all of the ions observed were CIV generated. It has been pointed out that charge exchange, stripping ionization, and associative ionization may have occurred under the conditions of the three experiments. These non-CIV processes may be easily mistaken as CIV. Thus, it remains to be explained why the yield in space CIV experiments is uniformly low.

### 1.5.3.3 The Difficulty of CIV in Space

There may be several reasons why CIV acts so efficiently in the laboratory but leads to low yields in space. We focus here on one possible explanation, that initial conditions are not appropriate for the CIV interaction at the outset of the experiment and that, later, the rapid expansion of the neutral cloud leads to yields that are necessarily low. In a homopolar device or a plasma gun, the plasma is established prior to contact with neutrals. In the pure energized plasma, instability and hot electrons are produced, also before neutral contact. Thus, it is not too surprising that rapid ionization takes place. In space, on the other hand, there coexists a dense neutral cloud, an ambient, stationary plasma of considerable density and a tenuous beam made up of seed ions created from the neutrals. In this case, the dispersion of the modified two stream instability becomes

$$\frac{\omega_e^2}{(\Omega_e^2 - \omega^2)} - \frac{\omega_p^2(Ba)}{(\omega - \mathbf{k} \cdot \mathbf{V})^2} - \frac{\omega_p^2(O)}{\omega^2} = 1 \quad (47)$$

where  $\omega_e$  and  $\Omega_e$  are the electron plasma and gyrofrequencies and  $\omega_p(Ba)$  and  $\omega_p(O)$  are the plasma frequencies for the Barium beam and Oxygen background respectively.

The nature and extent of the wave heating of the electrons depends strongly on the relative density of beam and ambient ions. Also, when the neutral beam is very dense, electron/neutral elastic collisions can thwart the electron heating altogether. To be considered as well is the energy drain arising from electron excitation of the neutrals, which is preclusive to the CIV discharge when the excitation time is smaller than the heating time. This effect is especially severe for Barium, the element used for the vast majority of space CIV experiments.

We propose that these factors, and perhaps others, create a situation in which the neutrals are not properly seeded in the early portion of space experiments. Improper seeding would result from any process which restricts the free and efficient flow of ion kinetic energy to the creation of superthermal electrons. These restrictions can be thought of as creating a delay time  $t_d$  between the release of the gas and the initiation of the cyclic energy transfer process that is the CIV discharge. We show next that if  $t_d$  is too long, a simple model of the expansion predicts that the ultimate yield will be low.

### 1.5.3.4 A CIV Yield Model

We assume that the CIV discharge has been delayed by  $t_d$ . We can express the number of electrons  $e_i$  created by ionization through simple kinetics.

$$\frac{de_i}{dt} = k\alpha \frac{N - (e_s + e_i)}{V} (e_s + e_i) \Theta(t - t_d) \quad (48)$$

where  $e_s$  is the number of electrons created through seeding,  $N$  the number of neutrals of the beam,  $k = \langle v\sigma \rangle$  the reaction rate constant with  $v$  the electron velocity and  $\sigma$  the ionization cross section,  $\alpha$  the fraction of electrons energetic enough to ionize,  $V$  the volume of the neutral cloud,  $t$  is the time from release, and  $\Theta$  the Heavyside function. For spherical expansion, which approximates many of the releases quite well,  $V$  can be modeled as

$$V = \frac{4}{3} \pi v_r^3 t^3 \quad (49)$$

where  $v_r$  is the radial expansion velocity. If we neglect the contribution of seeding after  $t_d$ , we can divide by  $N$  on both sides, giving yield  $Y$  as a function of time

$$\frac{dY}{dt} = \left[ \frac{3Nk\alpha}{4\pi v_r^3} \right] \frac{(1-Y)Y}{t^3} \Theta(t-t_d) \quad (50)$$

where we have defined the yield  $Y$  as

$$Y = \frac{e_s + e_i}{N} \quad (51)$$

Solving the differential Eq. (48), one obtains

$$Y(t) = \left[ 1 + \left[ \frac{1}{Y_0} - 1 \right] \exp \left( -\frac{\beta}{2} \left[ \frac{1}{t_d^2} - \frac{1}{t^2} \right] \right) \right]^{-1} \quad (52)$$

for  $t \geq t_d$  and where  $\beta$  is a constant.

$$\beta = \frac{3Nk\alpha}{4\pi v_r^3} \quad (53)$$

If we assume that the seeding mechanism does not substantially deplete the initial number of barium atoms, and if we further assume that the process is linear, we find that before the discharge begins

$$\frac{dY}{dt} = \nu_s \quad (54)$$

where  $\nu_s$  is the seeding rate. This means that

$$Y_0 = \nu_s t_d \quad (55)$$

At  $t = \infty$ , the yield  $Y$  from the experiment becomes

$$Y = \left[ 1 + \left( \frac{1}{v_s t_d} - 1 \right) \exp \left( - \frac{3 N k \alpha}{8 \pi v_r^3 t_d^2} \right) \right]^{-1} \quad (56)$$

It is remarkable that the yield in Eq. (54) depends crucially on the delay time  $t_d$  and on the expansion velocity  $v_r$ . Figure 23 shows the yield as a function of delay time for typical releases. This result has an important implication. If electron impact ionization is not initiated soon enough in space barium injection experiments, the ultimate yield will be compromised, even if the experiment last a very long time and if the energy transfer efficiency is 100%.

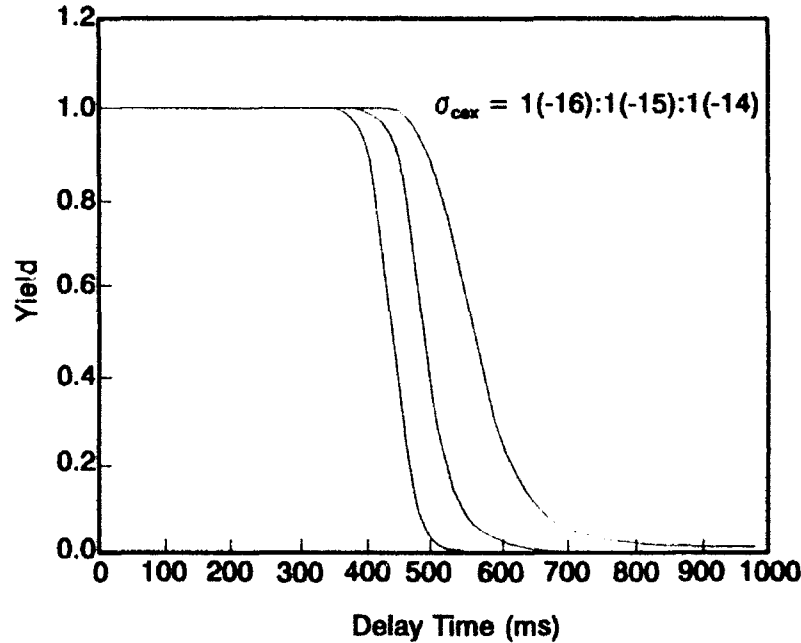


Figure 23. The infinite time yield of ions as a function of the delay time before ionization begins,  $t_d$ .

#### 1.5.3.5 Reasons for a Delay

In this model, we treated the delay time  $t_d$  as an absolute prohibition to electron impact ionization and we assumed that the boundary between no CIV ionization and CIV ionization was sharp. Although the boundary may not in fact be a step function, there are factors which prohibit the energy cycle from taking place early in the expansion of the cloud. Townsend's criterion requires that the beam transit time  $\tau_T$  across a magnetic field line exceeds the electron heating time  $\tau_H$ . Physically, this limits the energy cycle because electrons are essentially tied to field lines and cannot ionize if the neutral cloud passes them by before they are heated. This requires  $t_d$  to equal or exceed the critical transit time  $\tau_T$ . In space experiments, the heating time is probably a few tens of milli-seconds. According to the expansion model above,  $\tau_T$  would exceed  $\tau_H$  after one or a few milli-seconds at most. The Townsend criterion, then, is not a severely limiting factor to high yield.

For an expanding beam starting from a singularity, the neutral density  $N$  is extremely high initially. This has two effects. First, line excitation will prohibit electron impact ionization if the time for excitation of an allowed state of Barium  $\tau_{ex}$  is shorter than the heating time  $\tau_H$ . Barium has an unusually large excitation cross section of something around  $2(-15) \text{ cm}^2$  and, using the expansion model above, we find that  $\tau_{ex}$  is shorter than 1 ms up to about 400 ms into the release and does not equal  $\tau_H$  until about 1 second. Line excitation, then, appears to be a good candidate for the creation of a large  $t_d$ . High neutral density also leads to electron/neutral elastic scattering. It has been suggested that these collisions effectively suppress the modified two stream instability until such time as the elastic collision time  $\tau_{el}$  equals the lower hybrid time  $\omega_{LH}^{-1}$ . Evaluating this condition with the model above and an elastic collision cross section of  $3(-15) \text{ cm}^2$  results in a  $t_d$  value of about 500 ms, so that elastic collisions appear as a good candidate as well.

The above factors together impose restrictions on the experiment which can be imagined to result in a sharp boundary between no ionization and ionization at  $t_d$ . In addition, there is another factor due to the finite beam width  $L_{\parallel}$ . When  $L_{\parallel}$  is much less than the lower hybrid wavelength  $\lambda$ , the growth rate is reduced. In laboratory CIV experiment, this is not a problem because  $L_{\parallel} > \lambda$ . But, in space CIV experiments,  $\lambda$  is of the order of km;  $\lambda$  exceeds  $L_{\parallel}$  by a factor of 10 in the first 100 ms. This factor does not have any sharp transition time at all.

#### 1.5.3.6 Conclusions

The present state of CIV research presents a puzzle. On the one hand, CIV is induced readily in the laboratory with rapid and complete ionization. On the other hand, most CIV space experiments produced low yields. We have offered one explanation to the puzzle. In the laboratory, a plasma beam is readily available. In space CIV experiments, the ambient plasma is not beam like. It takes a delay time  $t_d$  for the neutral beam to form an ion beam and to initiate electron impact ionization. The yield obtained in a simple model shows strong dependence on the delay time  $t_d$  and the expansion velocity  $v_r$ . If  $t_d$  is too long, the yield drops off dramatically. The result is even more remarkable when one considers that the model includes no loss mechanisms for electrons and ions. The loss of electron energy to line excitation, for example, could make the critical  $t_d$  even lower.

Considering the many complications in the performance and diagnosis of space CIV experiments, it seems that it would take a shrewd experimenter to design a release destined to produce a 100% yield. Minimization of the cloud expansion, however, appears to be an important consideration.

#### 1.5.4 CIV in a Mixture

Single or multiple critical ionization velocities may exist in a mixture of species. By using a simple plateau tail model of hot electrons, we have examined the critical ionization in a simple model of multiple species of neutral gases [Lai, *et al.*, 1990]. We have found that the existence of single or multiple CIV thresholds depends on the neutral-plasma relative velocity and the extent of the hot tail. The values of these velocities are not those of individual species but are governed by an energy budget equation. Some species may serve as mere spectators while others undergo sustained ionization. Parametric domains delineate the various behaviors.

Axnäs [1978] reported experimental results showing that there was a single critical velocity in a mixture. He suggested the empirical formula

$$\alpha M_1 V_{*,1}^2 + (1-\alpha) M_2 V_{*,2}^2 = \alpha e \Phi_1 + (1-\alpha) e \Phi_2 \quad (57)$$

where  $\alpha$  is the fractional ionization of species 1. These results raise two questions. In a mixture of neutrals, each with a different critical velocity, why should there be only one critical velocity? Also, is it possible for some species to undergo CIV while other species act as spectators? In addition to the laboratory experiments, mixtures have been used in CIV experiments in space. It is important then to understand the variation of the critical ionization velocity in mixtures. Recently, the space shuttle exhaust has been considered as a possible domain of CIV.

The transfer of energy from ions to electrons, central to the CIV process, results in a heated electron population that resembles a tail. This has been predicted theoretically and also observed in computer simulation. We apply in this study a simple model in which there are two to several species of neutrals and in which the electrons are represented by a plateau tail distribution with a sharp energy cutoff. The aim is to gain physical insights as to the interplay between plasma and molecular processes in a mixture. As an application of this analysis, we will consider the space shuttle exhaust components to see whether CIV would be predicted.

#### 1.5.4.1 Energy Budget

For a model study, we consider two neutral species, A and B, with a single velocity  $U$  traveling together with ions across a magnetic field. Plasma instability and electron heating by waves are assumed to occur. When ionization occurs, some energy  $e\Phi$  is spent by a hot electron and some kinetic energy  $\frac{1}{2}MU^2$  is generated in the form of fast ions. The ion kinetic energy will be assumed to be transferred completely to the electrons. If the CIV cycle is to go on, the energy input must be positive. Said another way, each ionization must release energy to the plasma as opposed to draining it. We can express the energy transferred per ionization as

$$\Delta E = \frac{\nu_A [M_A U^2 - 2e\Phi_A] + \nu_B [M_B U^2 - 2e\Phi_B]}{2(\nu_A + \nu_B)} \quad (58)$$

where  $\nu_i$  is the ionization rate of species  $i$ . A velocity is sub-critical if it results in a negative  $\Delta E$ .

There are three possible scenarios for a mixture. (a) A and B have subcritical velocities. Both terms of  $\Delta E$  are negative and thus both species are subcritical. CIV does not take place. (b) A and B both have supercritical velocities. Both terms in  $\Delta E$  are positive and thus there is sufficient energy for CIV in both species. (c) One species has a supercritical velocity and one has a subcritical velocity. In this case, one species becomes the energy source and the other the energy sink. The source has to be larger than the sink in order for CIV to take place.

#### 1.5.4.2 Ionization Model

An approximate model for the electron distribution function is a plateau shape from a minimum energy of  $V_1$  to a maximum energy represented by a maximum velocity  $V_2$ . Since the value of  $V_2$  is somewhat speculative, we allow it to be a variable parameter in these simulations. For simplicity we assume that  $V_1$  is zero. This gives for the ionization rate



$$\nu_i = N_i \int_0^{V_2} dV V f(V) \sigma_i(V) \quad (59)$$

where  $N_i$  and  $\sigma_i$  are the neutral density and ionization cross section of species  $i$ . For a given mixture, then, the values of  $\nu_i$  are first calculated at a chosen value of  $V_2$  then the  $\Delta E$  equation is evaluated to find whether or not CIV is possible.

Using this simple model, we have calculated the domains in  $V_2$  and  $U$  space for several combinations of species. For helium and neon, shown in Figure 24, the lighter species, He, has the higher ionization energy. There are values of  $U$  and  $V_2$  for which only the higher mass species, Ne, is ionized yet for which there is a positive energy budget; there are no such values for helium. This indicates that it is possible to achieve one-component CIV (neon only) in this mixture.

In a different case, for a mixture of hydrogen and neon shown in Figure 25, the lighter species (H) has the lower ionization energy, the negative aspect of hydrogen in the energy budget does not allow for the ionization of either hydrogen or neon until the critical ionization velocity of the heavier species (Ne) is reached. These results indicate that in a mixture of species it may be possible for some species to act as spectators without contributing to the energy cycle of a discharge in other species. However, in certain circumstances, when ionization of one species with low ionization potential is energy inefficient, ionization of all species may be suppressed as governed by the energy budget. This has particular importance in the potential for CIV in space, where several neutral species may be present.

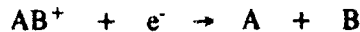
#### 1.5.4.3 An Application

Interest in the occurrence of CIV in space has been heightened by the implication of CIV in spacecraft contamination and space plumes [Lai, *et al.*, 1989]. By space plume, we mean the exhaust of spacecraft traveling at orbital velocity, an example being the space shuttle combustion engines. We have considered the five most abundant species in the shuttle exhaust;  $H_2O$ ,  $N_2$ ,  $H_2$ ,  $CO$  and  $CO_2$ . The generalized energy budget equation for several species is

$$\Delta E = \sum \nu_i [(1/2)M_i U^2 - e\Phi_i] / \sum \nu_i \geq 0 \quad (60)$$

Evaluation of this equation for the present case suggests that the critical velocity for the shuttle exhaust is somewhere around 11.6 km/s, which is substantially higher than of the single components with the lowest individual critical velocities;  $N_2$  (10.4 km/s) and  $CO_2$  (9.7 km/s).

We also consider the possibility that molecular dissociative recombination (MDR),



can take place after ionization. MDR is an unusually fast process in all these molecular ions. Should this take place, an identical analysis indicates that once the molecular ions have been transformed into atoms, the critical velocity of the mixture jumps to around 13.5 km/s. This suggests that if the shuttle exhaust velocity exceeds 11.6 km/s but is less than 13.5 km/s, CIV could occur transiently but would be quenched by MDR.

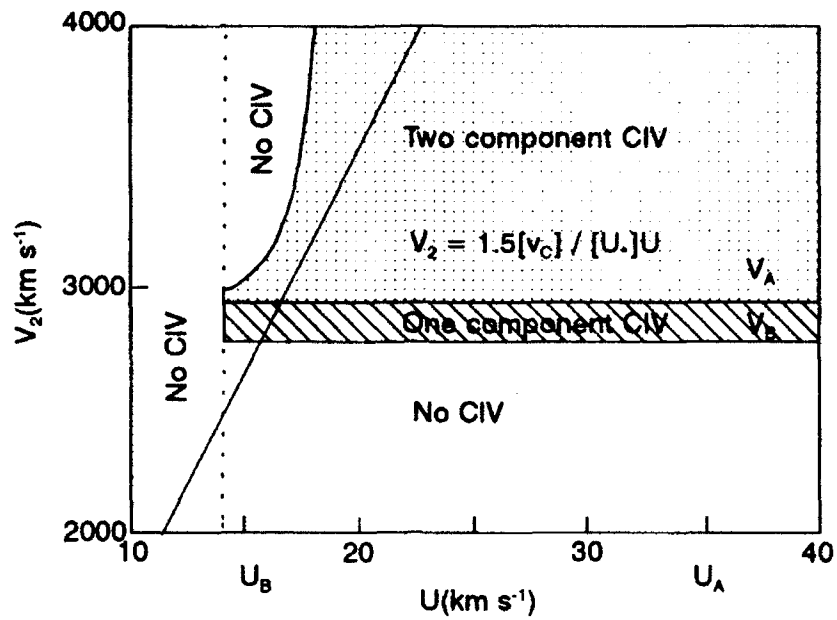


Figure 24. Parametric domain for CIV in a 50% mixture of He and Ne.

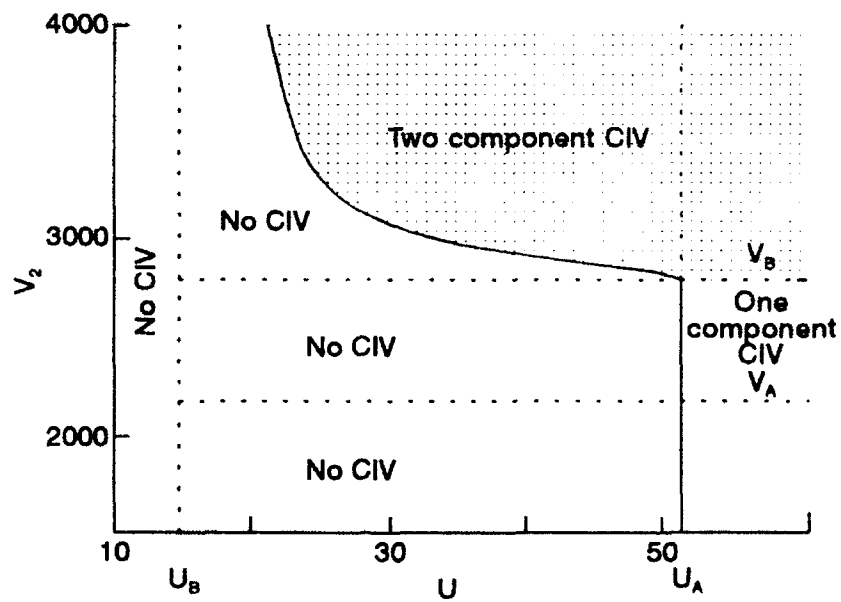


Figure 25. Parametric domain for CIV in a 50% mixture of H and Ne.

### 1.5.5 Amplification of CIV by a Pulsed Neutral Beam

In the quest to achieve CIV in space experiments, it seems essential to explore physical mechanisms which can be used to reinforce the positive conditions for discharge in such a way that beam-plasma interaction will lead to ionization. We have performed a study to investigate the influence of injecting a pulse of neutrals into a magnetized plasma, followed at a time later by the injection of another pulse [Lai, *et al.*, 1990b]. The time between pulses and the pulse length than may be used to advantage to build up the high energy tail to a larger amplitude and to higher energies than can be achieved by steady state injection.

In space experiments, the density of neutrals falls rapidly after release. When the neutral density is too low, Townsend's criterion, which states that a hot electron must spend at least the mean ionization time within the neutral beam, will not be satisfied. Thus, if CIV is to occur, it must occur before the pulse has traveled far from the explosion point. On the other hand, the pulse duration is also shortest near the explosion point. The electrons are pulled to some extent along with the neutrals through polarization drift, but due to their short gyroradius are accelerated mainly along magnetic field lines. This means that the heating time is limited by the interaction time between the neutrals and a given field line. This leads one to suspect that the finite nature of the pulse could affect the outcome of the experiment. By pulsing the neutrals, one might overcome this limitation.

#### 1.5.5.1 Simulation

The basis of our method for investigation is the plasma simulation technique described earlier. In this modification, a neutral beam of width  $\delta$  moves into the left-hand side of the box at velocity  $V_0$ . The neutrals interact with the cold ions through charge exchange, creating  $\text{secc}$  ions moving along with the beam. The relative motion between ions and electrons creates unstable waves which energize the electrons. If the electrons become hot enough, they can ionize additional neutrals. However, these processes take place only if the electrons and ions are within the bounds of the finite neutral beam. We have considered three cases, a single beam of width  $\delta$ , two beams of width  $\delta/2$  separated by a gap of  $\delta/2$ , and three beams of width  $\delta/3$  separated by gaps of  $\delta/3$ . Figure 26 shows the resulting increase in plasma density and shows that pulsing the neutrals can indeed increase the contact time and thus the rate of ionization.

#### 1.5.5.2 Conclusion

Results indicated that pulsed beams present a higher probability of achieving CIV than a single moving cloud such as one ejected from a shaped charge explosion, when the heating time for electrons is near the contact time of a pulse. Because ions slow down as they transfer energy to electrons, the effect is to create an ion cloud substantially larger than the initial pulse, allowing for increased heating and ionization of neutrals in subsequent pulses. These results apply to the high density, low contact time regime near the release point, where CIV is expected to take place if it does at all.

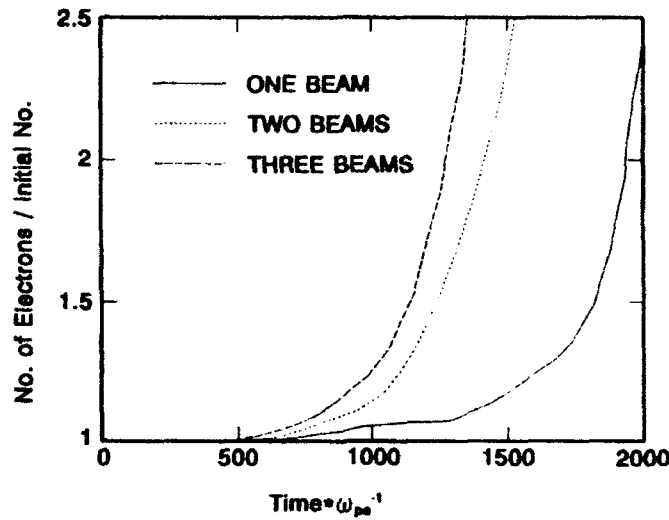


**Figure 26.** Plasma density increase for one, two, and three beams, all of the same total length.

#### 1.5.6 Altitude Effects on CIV Experiments in Space

The efficiency with which critical ionization velocity can be induced in space is affected by the altitude of the experiment. At around 500 km, higher plasma density enhances plasma lower hybrid waves, momentum coupling efficiency and charge exchange which is needed for seed ionization. At higher altitudes where atomic hydrogen and helium become the dominant ambient neutral species, the conditions for CIV discharge may improve considerably because less energy is lost to atmospheric ionization, even though the ambient density is reduced. We have examined several aspects of the altitude effects from a theoretical point of view [Lai, *et al.*, 1991] in an attempt to ascertain the benefits of specific altitudes in obtaining the optimum conditions for CIV.

##### 1.5.6.1 Electron Heating

The speed with which the ambient electrons is heated is particularly important in fast pulses of neutrals which are in contact with the magnetic field for only a short time. In such experiments the beam plasma density  $n_b$  is due to thermal ionization and is typically a few times the ambient plasma in the early stage of the beam. The electron heating time can be calculated through quasi-linear theory and is given by [Papadopoulos, 1984]

$$\tau_H = (n_b/n_a)\omega_{LH}^{-1} \quad (61)$$

where  $n_b$  is the total electron density,  $n_a$  is the ambient electron density and  $\omega_{LH}$  is the lower hybrid frequency. The beam plasma density is thus most likely to be intense in the daytime ionosphere at altitudes near 300 km where  $n_a$  obtains values sufficiently high to equal  $n_b$  near the release point.

### 1.5.6.2 Energy Losses

The maintenance of positive energy flow is critical to a CIV discharge. A major drain on the energy balance in the process is the loss of electron energy to the excitation of allowed states of the neutrals in the beam and in the ambient atmosphere. At altitudes less than 500 km, the dominant neutral species is O, while at 800 km, H and He become dominant. The transition altitude depends on the solar cycle, season and time of day. To investigate the effect of excitation as a function of distance along the release barium. Using data from the U.S. Standard Atmosphere, we model the relative densities of the atmospheric components. We assume an electron distribution that is flat up to 50 eV. Then the relative energy loss from a particular component, including barium, is given by

$$\epsilon_j = \int_0^{50\text{eV}} \sigma_j(E) E^{1/2} dE \quad (62)$$

The density of barium is given as a function of radial distance from a simple spherical expansion model

$$[Ba] = 3 N_{Ba} / 4 \pi r^3 \quad (63)$$

where  $r = v_e t$  is the expansion velocity. Comparisons show that at high activity the energy loss at 300 km is nearly 90% at a distance of 1 km from the release point, while at 800 km, the loss is less than 10% at the same distance. This shows that a high altitude release may be far more likely to succeed than one at a low altitude.

### 1.5.6.3 Charge Exchange

Charge exchange between fast beam neutrals and ambient ions results in a net gain in ion kinetic energy and provides valuable seed ions for initial beam-plasma interaction. Thus, higher ambient plasma density helps in fostering CIV in its early phases. In the ionosphere, plasma density peaks at about 300 km, with  $O^+$  being the dominant ion below a transition altitude of 500 km. Above that  $H^+$  is dominant. To illustrate the altitude effects, we have considered the creation of charges in an NO beam. The results show that at an altitude of 800 km, the rate of creation of beam ions through charge exchange is only about 15% that of the rate at 300 km.

### 1.5.7 Conclusion

Through examination and modeling of various aspects of the chemical and plasma processes that take place in a CIV experiment, we have gained considerable knowledge of the factors that may limit or enhance the probability of ionization. The major task ahead is to quantify these factors into a simple, self-consistent model that can be used to predict the ultimate yield of a CIV experiment. Such a model is precisely what is needed at present to shed light on the mystery of CIV in space. The model would, at the very least, need to incorporate microscopic aspects of energy flow and macroscopic aspects of beam and ambient density effects in a convincing manner. We believe that such a model is currently possible.

## 1.6 REFERENCES

- Alfvén, H., *On the Origin of the Solar System*, Oxford University Press, New York, 1954.
- Axnäs, I., Experimental investigation of the critical ionization velocity in gas mixtures, *Astrophys. Space Sci.*, **55**, 139, 1978.
- Bass, J. N., K. H. Bnavnani, N. A. Bonito, K. Bounar, C. A. Hein, C. J. Jordan, W. J. McNeil, M. M. Pratt, D. S. Reynolds, F. R. Roberts, C. J. Roth, D. A. Sannerud, M. F. Tautz, R. P. Vancour, "Integrated Analytical Evaluation and Optimization of Model Parameters Against Preprocessed Measurement Data", GL-TR-89-0163, 1989, ADA215518.
- Beam, R. M. and R. F. Warming, "An Implicit Factored Scheme for the Compressible Navier-Stokes Equations", *AIAA Journal*, Vol. 16, No. 4, 1978.
- Bird, G. A., *Molecular Gas Dynamics*, Clarendon Press, Oxford, 1976.
- Birdsall, C. K. and B. G. Langdon, *Plasma Physics via Computer Simulation*, McGraw-Hill, New York, 1985.
- Broadfoot, A. L., E. Anderson, P. Sherard, J. W. Chamberlain, L.S. Bernstein, J. B. Elgin, D. J. Knecht, C. P. Pike, I. L. Kofsky, D. L. Rall, C. A. Trowbridge, E. Murad, A. Setayesh, A. T. Stair, Jr., and R. A. Viereck, "Optical Emission Excited in Reaction of Space Shuttle Engine Exhaust with the Ambient Atmosphere", Spring Meeting, Baltimore, MD, May 28-31, 1991.
- Chan, C., M. A. Morgan, J. Browning, M. F. Tautz, D. L. Cooke, and C. L. Enloe, "Experimental and Computational Simulations of Spacecraft Wake Charging", Proceedings of 1989 Spacecraft Charging Tech. Conf., Naval Postgrad School, Monterey, CA, July 1990.
- Curry, B. P., R. J. Bryson, B. L. Seibner, and E. L. Kiech, "Additional Results from an Experiment on Venting an H<sub>2</sub>O Jet into Vacuum", Technical Report AEDC-TR-85-3, June 1985.
- Elgin, J. B. and R. L. Sundberg, "Model Description for the SOCRATES Contamination Code", Technical Report, AFGL-TR-88-0303, Spectral Sciences, Inc., Burlington, MA 01803, 1988, ADA205181.
- Elgin, J. B., D. C. Cooke, M. F. Tautz, and E. Murad, "Modeling of Atmospherically Induced Gas Phase Optical Contamination From Orbiting Spacecraft", *Journal of Geophysical Research*, Vol. 95, No. A8, Pages 12197-12208, 1990.
- Elgin, J. B., I. S. Bernstein, I. K. Kofsky, D. L. Rall, R. Viereck, D. Knecht, E. Murad, C. P. Pike, A. Setayesh, A. L. Broadfoot, "A Comparison of Shuttle Engine Firings in Space to Code Predictions", Proceedings of JANNAF Exhaust Plume Technology Meeting, U. S. Army Missile Command, Redstone Arsenal, AL, May 14-19, 1991.
- Fuchs, H. and H. Legge, "Flow of a Water Jet into Vacuum", *Acta Astronautica*, Vol. 6, 1979, pp. 1213-1226.

- Gardner, J. A., D. L. Rall, I. L. Kofsky, A. Setayesh, and E. Murad, "Liquid Dispersal Study: A proposed Space Shuttle Liquid Release Experiment", Presented at AIAA 30<sup>th</sup> Aerospace Sciences Meeting and Exhibit, Paper No. AIAA 92-0793, Reno, Nevada, January 6-9, 1992.
- Glenn, L. A., "Stationary Radial Source Flow of Liquid Particles into Vacuum", AIAA Journal, Vol. 7, No. 3, March 1969, pp. 468-482.
- Henderson, C. B., "Drag Coefficients of Spheres in Continuum and Rarefied Flows", AIAA Journal, Vol. 14, No. 6, June 1976, pp. 707-708.
- Hoffmann, K. A., *Computational Fluid Dynamics For Engineers*, Engineering Education System, 1989.
- Kofsky, I. L., D. L. Rall, C. A. Trowbridge, E. Murad, C. P. Pike, D. J. Knecht, R. A. Viereck, A. Berk, M. E. Gersh, J. B. Elgin, A. T. Stair, Jr., and A. Setayesh, "Proceedings of Space Environment Analysis Workshop", European Space Agency, ESTEC, Noordwijk, Netherlands 9-12, October, 1990.
- Kofsky, I. L., M. A. Maris, N. H. Tran, D. L. Rall, E. Murad, C. P. Pike, D. J. Knecht, R. A. Viereck, A. T. Stair, and A. Setayesh, "Phenomenology of a Water Venting in Low Earth Orbit", *Astronautica Acta*, vol 26, No.5, pp. 325-347, 1992.
- Lai, S. T., E. Murad and W. J. McNeil, "The Role of Metastable States in Critical Ionization Velocity Discharges", *J. Geophys. Res.*, **93**, 5871, 1988.
- Lai, S. T., E. Murad and W. J. McNeil, "An Overview of Atomic and Molecular Processes in Critical Velocity Ionization", *IEEE Trans. Plasma Sci.*, **17**, 124, 1989.
- Lai, S. T., E. Murad and W. J. McNeil, "Critical Ionization Velocity in a Mixture of Species", *Planet. Space Sci.*, **38**, 1011, 1990.
- Lai, S. T., W. J. McNeil and E. Murad, "Amplification of Critical Velocity Ionization by a Pulsed Neutral Beam", *Geophys. Res. Lett.*, **17**, 737, 1990.
- Lai, S. T., E. Murad and W. J. McNeil, "Effects of Altitude on Critical Ionization Velocity Experiments in Space", *Planet. Space Sci.*, **39**, 1707, 1991.
- Lai, S. T., E. Murad, C. P. Pike, W. J. McNeil, and A. Setayesh, "A Proposed Gas Release Experiment on the P91-1 Satellite", AGU Fall Meeting, San Francisco, CA, December 5-9, 1991.
- Lai, S. T., E. Murad and W. J. McNeil, Amplification of critical velocity ionization by associative ionization, *J. Geophys. Res.*, **97**, 4099, 1992.
- Lai, S. T., E. Murad and W. J. McNeil, The importance of seed ionization in CIV space experiments, *Proceedings of the 1992 Cambridge Workshop in Geoplasma Physics*, T. S. Chang, ed., Scientific Publishers, Inc., Cambridge, Massachusetts, 1992.

- Lai, S. T., E. Murad, C. P. Pike, W. J. McNeil, and A. Setayesh, "A Feasibility Study on the Xenon and Carbon Dioxide Gas Release Experiments on the ARGOS Satellite, COSPAR, The World Space Conference, Washington, DC, Aug 28-Sept 1, 1992 (Invited Paper); *Advances in Space Research*, accepted for publication, 1993.
- Lezius, D. K. and P. D. Thomas, "Fuel Vent Modeling", Technical Report, AL-TR-89-023, Lockheed Missiles & Space Company, Inc., Palo Alto, CA 94304, 1989.
- Lilley, J. L., D. Cooke, G. Jongeward, and I. Katz, "POLAR User's Manual", GL-TR-89-0307, 1989, ADA232103.
- Machida, S. and C. K. Goertz, A simulation study of the critical ionization velocity process, *J. Geophys. Res.*, **91**, 11,495, 1988.
- McNeil, W. J., S. T. Lai and E. Murad, Interplay between collective and collisional processes in critical velocity ionization, *J. Geophys. Res.*, **95**, 10,345, 1990.
- Murad, E., D. J. Knecht, R. A. Viereck, C. P. Pike, I. L. Kofsky, C. A. Trowbridge, D. L. A. Rall, G. Ashley, L. Twist, J. B. Elgin, A. Setayesh, A. T. Stair, Jr., and J. E. Blaha, "Visible Light Emission Excited by Interaction of Space Shuttle Exhaust with the Atmosphere", *Geophysical Research Letters*, Vol. 17, No. 12, Pages 2205-2208, November 1990.
- Murad, E., D. J. Knecht, R. A. Viereck, C. P. Pike, I. L. Kofsky, C. A. Trowbridge, D. L. A. Rall, G. Ashley, L. Twist, J. B. Elgin, A. Setayesh, A. T. Stair, Jr., and J. E. Blaha, "Effect of Orientation on the Collision of Space Shuttle Exhaust with the Atmosphere", *Proceedings Short Wavelength Phenomenology and Applications*, Johns Hopkins University, Laurel, MD, May 1991.
- Pai, S-I., *Two-Phase Flows*, Friedr Vieweg & Sohn Verlagsgesellschaft (Vieweg Tracts in Pure and Applied Physics), 1977.
- Papadopoulos, K., On the shuttle glow (the plasma alternative), *Radio Sci.*, **19**, 571, 1984.
- Pike, C. P., R. Viereck, D. J. Knecht, E. Murad, J. B. Elgin, I. L. Kofsky, D. L. Rall, A. Setayesh, and A. T. Stair, Jr., "Release of Liquid water From the Space Shuttle", AGU Fall Meeting, San Francisco, CA, December, 1990.
- Rall, D. L. A., I. L. Kofsky, C. A. Trowbridge, R. A. Viereck, E. Murad, C. P. Pike, D. J. Knecht, A. T. Stair, Jr., and A. Setayesh, "Optical Properties of water Released in low earth orbit", SPIE 1754-14 1992, International Symposium on Optical Applied Science and Engineering, Optical System Contamination: Effects, Measurement, Control III Conference, San Diego CA, July 1992.
- Setayesh, A., "One-Dimensional Analysis of a Radial Source Flow of Water Particles into a Vacuum", Geophysics Laboratory, Hanscom AFB, GL-TR-90-0246, August, 1990, ADA230729.
- Setayesh, A., "A Parametric Study of the Release of CO<sub>2</sub> in Space", Phillips Laboratory, AFSC, Hanscom AFB, PL-TR-91-2052, January, 1991, ADA236271.



- Swenson, G. R., S. B. Mende, R. E. Meyerott, and R. L. Rairden, Charge exchange contamination of CRIT II barium CIV experiment, *Geophys. Res. Lett.*, **18**, 401, 1991.
- Tautz, M. F. and D. Cooke, "Preliminary Documentation for the MACH code.", GL-TR-88-0035, 1988, ADA198956.
- Tautz, M. F., "A Trapped Electron Model for Application to the MACH Code", PL-TR-91-2106, April 1991, ADA238188.
- Tautz, M. F. and D. Cooke, "IRMA: A Program for Three Dimensional Color Display of Data", Technical Report in publication, 1993.
- Tautz, M. F., "POLAR 2 Model of the Wake-Shield Experiment", PL-TR-92-2343, December 1992.
- Viereck, R. A., E. Murad, C. P. Pike, I. L. Kofsky, C. A. Trowbridge, D. L. Rall, E. D. J. Knecht, A. Setayesh, A. Berk, and J. B. Elgin, "Photometric Analysis of Space Shuttle Water Venting", Proceedings of Space Operations Application Research, Albuquerque, New Mexico, June 1990.
- Viereck, R., D. J. Knecht, D. Cooke, E. Murad, C. P. Pike, J. B. Elgin, I. L. Kofsky, D. L. Rall, A. Setayesh, and A. T. Stair, Jr., "Collision of Space Shuttle Exhaust with the Atmosphere: The effect of Orientation", AGU Fall Meeting, San Francisco, CA, December, 1990.

## 2.0 COMBINED RELEASE AND RADIATION EFFECTS SATELLITE (CRRES)

### 2.1 CRRES INSTRUMENT MODELING

#### 2.1.1 PROTEL

##### 2.1.1.1 Introduction

The Proton Telescope (PROTEL) is one of several CRRES instruments used to measure proton energy and flux. Instruments of different types were used to obtain data over a wide energy range, and to provide redundancy where there is an overlap. PROTEL collected proton flux data in the 1 to 100 MeV energy range in the radiation belts. It consisted of two detector instruments, the Low Energy Head (LEH) (1 - 10 MeV) and the High Energy Head (HEH) (6 - 100 MeV) and a dedicated processor which processes the raw data, and at 1 second intervals, hands off the reduced data to the satellite's telemetry system. The reduced data consists of counts in 24 energy channels (8 for LEH, 16 for HEH) spaced logarithmically in the 1 - 100 MeV energy interval, together with environmental data and raw counts for each of the solid state particle detectors.

The PROTEL instrument operates in a hostile environment, where it was subjected to a high density flux of electrons, protons, and, to a lesser extent, heavier ions, particularly while passing through the radiation (Van Allen) belts. In addition to using passive shielding techniques and magnetic deflection of electrons, both the LEH and HEH use a technique which is sometimes called "active" shielding. Each head has an array of disk shaped silicon particle detectors, many of which have a second (ring shaped) active detection region. The energy deposited by a charged particle in each of the solid state detector's active regions is measured by pulse height analysis, and the on-board processor uses coincidence and anti-coincidence in the detector array (detection logic) to reduce false counts by excluding counts which result from protons entering outside the nominal acceptance cone, which enter from the rear, or do not deposit the correct energies corresponding to the proton energy channels.

In order to compare PROTEL data with data obtained from other CRRES instruments, it was necessary to model its behavior. In the radiation belts, it was expected that the LEH would be swamped by the high flux environment. In an earlier report [Redus, *et al.*, 1990], it was suggested that the HEH will have problems resulting from the penetration of high energy protons (above 100 MeV) from certain angles outside the entrance cone. These protons will produce false counts (contamination) in the data. The effect of contamination on observed counts strongly depends upon the energy spectrum and the angular distribution of the high energy protons.

The PROTEL Contamination Code, a software package which models the contamination problem for the HEH, was developed by Radex. The results provided here indicate that for certain "hard" proton spectra, particularly in the range between 100 and 350 MeV, the PROTEL HEH will be subjected to a high level of "contamination". The results obtained from this study (response functions) have been used to compare PROTEL data with data obtained from the CRRES dosimeters, and corrections obtained from the PROTEL modeling described here for the isotropic case have been successfully applied to the CRRES dosimeter data and to data obtained from other satellite instruments [Violet, 1992].

A detailed description of the PROTEL instrument is provided in a recent report [Lynch, *et al.*, 1989]. The PROTEL HEH detector contains six solid state detectors, D1-D6. D1-D5 each contain two detection

areas, a central disk, and a ring surrounding the disk. D6 has only a circular disk. Pulse height circuitry, coincidence and anti-coincidence circuitry and logic are used to classify detection events in the several particle detectors. A detection event is recorded in one of the energy channels only if it meets the energy deposit requirements of the detectors associated with the energy channel and the requirements of the coincidence/anticoincidence logic. The ring detectors and D6 are used in connection with the anti-coincidence logic. The anti-coincidence logic is used to reduce or eliminate counts due to protons which enter through the back or enter the detector from directions outside the nominal acceptance cone.

The geometry of the HEH is provided in Figure 27. The materials used for the passive shielding and in the construction of the HEH are indicated by shading.

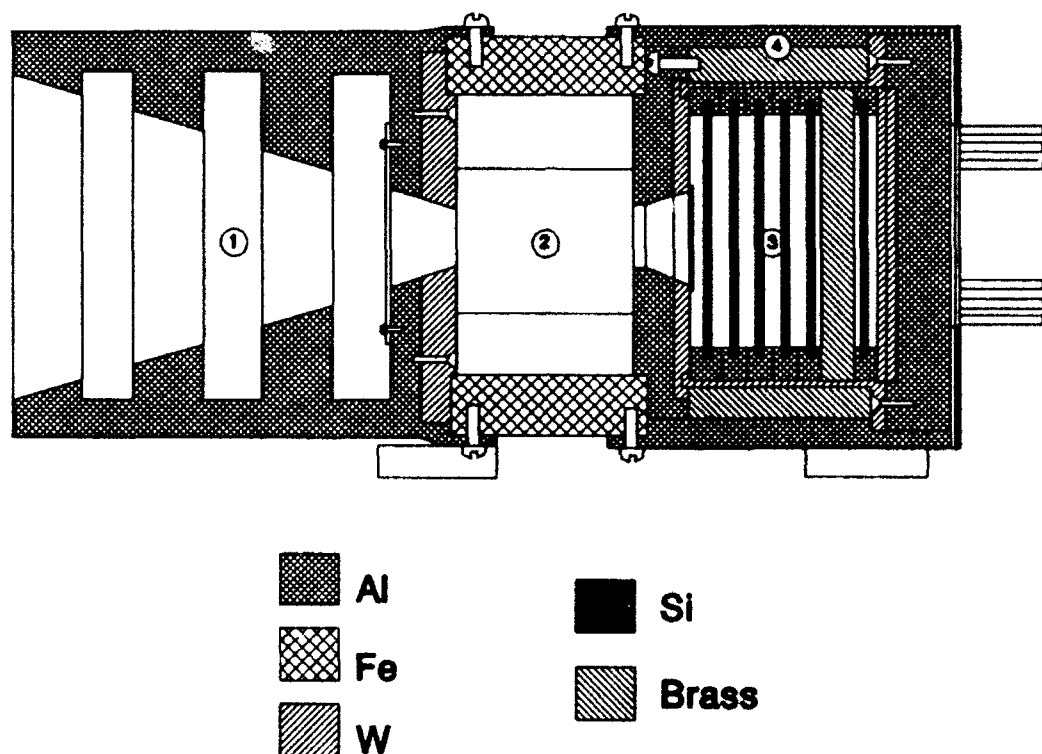


Figure 27. PROTEL HEH cross section (not to scale). (1) is the haffle, which defines the nominal entry cone. (2) is the electron magnetic deflection housing. (3) is the detector housing. (4) is the shielding for the detector array.

#### 2.1.1.2 Description of the PROTEL Contamination Code

The assumptions made in developing the PROTEL contamination code are as follows:

The primary effect is due to protons which penetrate the PROTEL housing/shielding and are decelerated in the direction of motion while interacting with the electrons in the material through which they pass. The protons are assumed to travel in straight lines until they either are stopped by or penetrate the material they are passing through. This is a relatively good assumption for high energy protons.

However, important effects are neglected, such as Coulomb scattering with the nuclei, inelastic scattering off of the nuclei, including "STARS" – nuclear reactions which produce protons, neutrons, and/or gamma rays.

Under this assumption, the computation of contamination effects proceeds as follows:

(1) A simplified mathematical description of the mass/geometry of the HEH was developed using the original blueprints. From the latter, measurements were made of the different materials used in the construction of the HEH and their locations. The materials used were aluminum, iron, brass, and tungsten. In addition, a magnet was used to deflect high energy electrons. The magnet was made of samarium and cobalt. From the blueprint diagrams of the magnet, it was not possible to determine the location of the actual boundary between the iron magnet holder and the magnet pieces. Partly for this reason, and partly to simplify the computations, it was decided to treat the entire magnet as iron.

(2) A ray tracing algorithm was developed which would determine the number of layers, compute the thickness of each layer, and identify the materials which a ray pointing in an arbitrary direction (starting from an arbitrary point within the detector volume) would encounter. Except for the case in which the path intersects the ridges on the inside surface of the PROTEL HEH baffle, the computed thicknesses are accurate to approximately 0.1 mm, which is better than the estimated 0.5 mm accuracy to which the dimensions of the various components of the PROTEL housing/shielding can be measured from the blueprints. Using the Janni energy-range relations and the Janni tables [Janni, 1982] a fast algorithm was developed which would, given a proton input spectrum, compute the spectrum resulting from passage through the materials associated with a given point and direction.

As a test of the methodology, calibration tests of the PROTEL HEH performed at the Harvard University cyclotron were successfully modeled using an early version of the PROTEL Contamination Code [Hein, 1990].

(3) A Monte Carlo code was used to model the behavior of the High Energy Head. For each Monte Carlo trial, a point on the surface of the first detector was randomly selected. Then, a direction (unit vector) was randomly selected (based upon the proton pitch angle distribution - isotropic, mirror plane, or  $\sin^N \alpha$ ). For each such point and direction, the ray-tracing routine was used to compute the thickness of each of the material "layers" through which a proton passes in the body and shielding of PROTEL in its path to each reference point on the first detector.

(4) The ray-tracing algorithm has a high computation overhead. For this reason, and the fact that the contamination computation will be repeated for various input spectrum and values of input parameters, it was necessary to generate a file containing the ray trace output data for each of the Monte Carlo "trials". The number  $N$  of "trials" required was determined by comparing runs performed with different "seeds";  $N = 20,000$  points was chosen over a solid angle defined by a 60 degree half-angle. For larger half angles, the fraction of protons which would strike more than one detector was small. The file contains the following information for each of the 20,000 reference points and reference directions:

- (a) The location of the reference point on the first detector.
- (b) The unit vector describing the direction of the ray.

- (c) The number of "layers" of material the ray passes through
- (d) For each layer, a matter flag which indicates what material the ray passes through (aluminum, iron, brass, tungsten, etc.)
- (e) The thickness of each layer.

(5) Because a variety of input spectra would be studied, the *response function* which describes the instrument's response to a flat energy spectrum as a function of energy was computed. For incident energies in the range of 5-105 MeV, the response function was computed at energy intervals of 0.1 MeV; from 105-400 MeV at 1 MeV intervals. The direction and thickness information in the file described above is used to compute the energy loss in each of the material layers using the Janni energy/range relation for each of the materials. For each trial in which the particle actually reaches the first detector, a determination is made, as to which detectors the ray passes through; then the path length through the detector is calculated, and the detector coincidence logic is used to determine the channel into which the corresponding "count" is to be recorded. For each of the incident energies, the fraction of counts detected are compared to the total number of trials.

(6) The tabulated response function is then used to compute the actual number of predicted counts for an arbitrary energy spectrum.

#### 2.1.1.3 Results

Tables 9-11 give the fraction of PROTEL HEH counts due to contamination for proton energy spectra of the form  $E^q$ , where  $E$  is in MeV and  $q$  varies in 0.5 steps from 0 to -6 for an isotropic distribution. Table 9 gives the contamination due to protons of all energies. Tables 10 and 11 give the fraction of the PROTEL HEH counts due to contamination from protons above 100 and 200 MeV, respectively. Tables 12 and 13 provide the data which corresponds to the first data set of Table 9 for the mirror plane case, for an orientation of the mirror plane of 0 and 90 degrees with respect to the direction of the maximum obstruction of the electron deflection magnet.

The tables are obtained from integrating the product of the computed response function with the indicated power law spectrum over the total energy range for Tables 9, 12, and 13, and over the ranges  $E > 100$  MeV and  $E > 200$  MeV for Tables 10 and 11. The differences in the entries in Tables 9 and 10 reflect the contamination contribution for the range  $0 < E < 100$ ; similarly for Tables 9 and 11 ( $0 < E < 200$ ) and Tables 10 and 11 ( $100 < E < 200$ ).

Response functions for some of the HEH channels are provided in graphical form in Figures 28 and 29 for the isotropic case, and Figures 30 and 31 for the two mirror plane orientations. For the latter, the two response functions are provided in each graph. The non-contamination response of each detector is represented by a "spike" in the  $0 < E < 100$  MeV range, with the spike "width" being the actual channel width. The bulk of the contamination occurs in the  $E > 100$  range, as is evident in the graphs.

The response function for the isotropic case was used to cross calibrate PROTEL data with data obtained from the CRRES dosimeters and other instruments. The data, associated with solar proton events, covered 20 orbits in March and June of 1991. The data was collected at high altitudes and was known to be near-isotropic; the energy spectra appeared to be relatively flat and stable over periods of several hours. This study [Violet, 1992] also compared the same PROTEL data with data obtained from the GEOS satellite. In this study, the PROTEL data was fitted to a power law spectrum of the form  $(J(10$

Mev)/J(E))<sup>N</sup>. The response function was used to compute corrected values of J(10) and N. The latter were compared, with good agreement to similar fits of data obtained from the CRRES dosimeter and the GEOS detectors. The corrections were found to be substantial, and increase for power law spectra as N approaches 0.

**TABLE 9.** Fraction of PROTEL HEH Counts Due to Contamination

Isotropic Distribution  
POWER LAW SPECTRUM E\*\*q

CHAN	q = 0	-.5	-1.0	-1.5	-2.0	-2.5	-3.0	-3.5	-4.0	-4.5	-5.0	-5.5	-6.0
1	.9928	.9606	.8153	.4671	.1882	.0950	.0687	.0581	.0513	.0460	.0416	.0377	.0343
2	.9833	.9210	.7056	.3537	.1421	.0739	.0526	.0433	.0373	.0327	.0289	.0255	.0227
3	.9659	.8616	.6045	.3344	.2086	.1660	.1491	.1396	.1326	.1268	.1217	.1171	.1129
4	.9642	.8607	.5986	.2906	.1293	.0729	.0526	.0430	.0371	.0326	.0290	.0260	.0234
5	.9768	.9152	.7416	.4557	.2313	.1313	.0943	.0791	.0712	.0662	.0626	.0599	.0579
6	.9736	.9119	.7556	.5167	.3267	.2338	.1949	.1767	.1660	.1584	.1522	.1468	.1421
7	.9721	.9103	.7543	.5002	.2746	.1539	.1018	.0786	.0663	.0583	.0523	.0475	.0434
8	.9817	.9459	.8535	.6673	.4246	.2340	.1314	.0839	.0613	.0489	.0412	.0356	.0314
9	.9762	.9370	.8474	.6868	.4882	.3256	.2274	.1753	.1472	.1304	.1190	.1104	.1034
10	.9828	.9573	.8993	.7846	.6071	.4114	.2582	.1643	.1125	.0837	.0666	.0553	.0471
11	.9739	.9406	.8733	.7573	.5996	.4388	.3129	.2303	.1800	.1492	.1292	.1153	.1048
12	.9835	.9643	.9255	.8537	.7379	.5855	.4283	.2995	.2101	.1532	.1175	.0944	.0786
13	.9770	.9543	.9127	.8430	.7403	.6128	.4818	.3689	.2837	.2241	.1835	.1554	.1353
14	.9852	.9717	.9473	.9052	.8381	.7423	.6240	.5000	.3888	.3008	.2366	.1914	.1596
15	.9872	.9770	.9594	.9299	.8830	.8137	.7207	.6102	.4952	.3897	.3028	.2362	.1874
16	.9884	.9807	.9682	.9485	.9182	.8735	.8113	.7306	.6346	.5310	.4297	.3391	.2636

**TABLE 10.** Fraction of PROTEL HEH Counts Due to Contamination

Due to Protons with E > 100 MeV

Isotropic Distribution  
POWER LAW SPECTRUM E\*\*q

CHAN	q = 0	-.5	-1.0	-1.5	-2.0	-2.5	-3.0	-3.5	-4.0	-4.5	-5.0	-5.5	-6.0
1	.9893	.9503	.7849	.4031	.1104	.0224	.0042	.0008	.0001	.0000	.0000	.0000	.0000
2	.9765	.9039	.6655	.2909	.0775	.0169	.0035	.0007	.0002	.0000	.0000	.0000	.0000
3	.9458	.8088	.4919	.1783	.0462	.0107	.0025	.0006	.0001	.0000	.0000	.0000	.0000
4	.9494	.8282	.5395	.2178	.0617	.0153	.0037	.0009	.0002	.0001	.0000	.0000	.0000
5	.9650	.8887	.6867	.3699	.1348	.0396	.0109	.0029	.0008	.0002	.0001	.0000	.0000
6	.9546	.8674	.6615	.3638	.1426	.0462	.0140	.0042	.0013	.0004	.0001	.0000	.0000
7	.9570	.8794	.6960	.4132	.1769	.0615	.0197	.0062	.0019	.0006	.0002	.0001	.0000
8	.9718	.9265	.8169	.6072	.3463	.1532	.0582	.0207	.0073	.0025	.0009	.0003	.0001
9	.9595	.9041	.7859	.5855	.3513	.1721	.0742	.0302	.0121	.0048	.0020	.0008	.0003
10	.9727	.9388	.8662	.7299	.5286	.3171	.1615	.0742	.0325	.0140	.0060	.0026	.0011
11	.9563	.9087	.8184	.6707	.4800	.2961	.1620	.0823	.0404	.0197	.0096	.0047	.0023
12	.9735	.9470	.8962	.8064	.6676	.4925	.3202	.1870	.1017	.0533	.0275	.0142	.0073
13	.9626	.9300	.8730	.7814	.6518	.4972	.3454	.2217	.1347	.0794	.0462	.0268	.0157
14	.9770	.9581	.9249	.8695	.7840	.6657	.5242	.3810	.2580	.1659	.1034	.0635	.0389
15	.9823	.9691	.9467	.9101	.8531	.7706	.6621	.5360	.4079	.2939	.2032	.1370	.0913
16	.9884	.9806	.9682	.9485	.9182	.8735	.8112	.7304	.6344	.5308	.4295	.3387	.2631

**TABLE 11. Fraction of PROTEL HEH Counts Due to Contamination**  
 Due to Protons with  $E > 200$  MeV  
 Isotropic Distribution  
 POWER LAW SPECTRUM  $E^{**q}$

CHAN	q = 0	- .5	-1.0	-1.5	-2.0	-2.5	-3.0	-3.5	-4.0	-4.5	-5.0	-5.5	-6.0
1	.3742	.3256	.2417	.1105	.0267	.0047	.0008	.0001	.0000	.0000	.0000	.0000	.0000
2	.3436	.2897	.1931	.0759	.0181	.0035	.0006	.0001	.0000	.0000	.0000	.0000	.0000
3	.4039	.3141	.1724	.0559	.0129	.0026	.0005	.0001	.0000	.0000	.0000	.0000	.0000
4	.4096	.3271	.1938	.0706	.0179	.0040	.0008	.0002	.0000	.0000	.0000	.0000	.0000
5	.4049	.3421	.2412	.1178	.0386	.0102	.0025	.0006	.0001	.0000	.0000	.0000	.0000
6	.4076	.3382	.2339	.1158	.0405	.0116	.0031	.0008	.0002	.0001	.0000	.0000	.0000
7	.4225	.3561	.2569	.1381	.0531	.0165	.0047	.0013	.0003	.0001	.0000	.0000	.0000
8	.4673	.4155	.3400	.2332	.1221	.0492	.0169	.0054	.0017	.0005	.0002	.0000	.0000
9	.4590	.3980	.3163	.2139	.1156	.0506	.0193	.0069	.0024	.0008	.0003	.0001	.0000
10	.5276	.4797	.4152	.3266	.2196	.1215	.0566	.0236	.0093	.0036	.0014	.0005	.0002
11	.5568	.4910	.4070	.3043	.1967	.1085	.0525	.0233	.0099	.0041	.0017	.0007	.0003
12	.7133	.6662	.6023	.5148	.4023	.2781	.1680	.0903	.0448	.0211	.0097	.0044	.0020
13	.7408	.6830	.6075	.5111	.3972	.2794	.1771	.1025	.0555	.0287	.0145	.0072	.0036
14	.8093	.7683	.7144	.6432	.5515	.4418	.3253	.2189	.1356	.0788	.0438	.0237	.0125
15	.8470	.8136	.7703	.7138	.6409	.5504	.4458	.3369	.2366	.1553	.0965	.0576	.0334
16	.9013	.8766	.8447	.8033	.7499	.6826	.6006	.5063	.4060	.3085	.2224	.1531	.1014

**TABLE 12. Fraction of PROTEL HEH Counts Due to Contamination**  
 Mirror Plane Limit, Azimuth = 0 degrees  
 POWER LAW SPECTRUM  $E^{**q}$

CHAN	q = 0	- .5	-1.0	-1.5	-2.0	-2.5	-3.0	-3.5	-4.0	-4.5	-5.0	-5.5	-6.0
1	.9867	.9245	.6768	.2874	.1022	.0560	.0436	.0382	.0345	.0316	.0290	.0268	.0247
2	.9608	.8377	.5352	.2252	.0872	.0446	.0308	.0248	.0213	.0187	.0166	.0148	.0133
3	.8197	.5192	.2596	.1544	.1196	.1057	.0980	.0928	.0887	.0853	.0823	.0796	.0772
4	.8146	.5089	.2194	.0897	.0458	.0296	.0219	.0174	.0143	.0121	.0104	.0091	.0080
5	.9201	.7522	.4642	.2273	.1186	.0784	.0627	.0554	.0513	.0488	.0472	.0462	.0457
6	.8602	.6428	.3864	.2287	.1605	.1315	.1170	.1082	.1019	.0969	.0929	.0895	.0864
7	.8407	.6098	.3433	.1765	.1016	.0689	.0525	.0427	.0360	.0310	.0271	.0239	.0213
8	.9108	.7695	.5369	.3098	.1710	.1044	.0733	.0571	.0475	.0410	.0363	.0328	.0301
9	.8697	.7089	.4962	.3184	.2120	.1561	.1258	.1075	.0950	.0857	.0782	.0721	.0668
10	.8986	.7751	.5865	.3897	.2456	.1608	.1141	.0873	.0705	.0588	.0500	.0431	.0374
11	.8696	.7394	.5655	.3990	.2781	.2029	.1579	.1299	.1112	.0977	.0872	.0789	.0719
12	.9030	.8057	.6589	.4897	.3417	.2368	.1704	.1293	.1030	.0851	.0721	.0621	.0542
13	.8904	.7981	.6692	.5256	.3973	.3005	.2341	.1897	.1596	.1382	.1223	.1099	.0999
14	.9153	.8453	.7410	.6107	.4771	.3628	.2769	.2168	.1756	.1469	.1261	.1105	.0983
15	.9239	.8668	.7814	.6696	.5445	.4252	.3260	.2508	.1966	.1582	.1306	.1104	.0951
16	.9288	.8841	.8190	.7321	.6278	.5167	.4113	.3207	.2482	.1929	.1517	.1211	.0982

**TABLE 13. Fraction of PROTEL HEH Counts Due to Contamination**  
 Mirror Plane Limit, Azimuth = 90 degrees  
 POWER LAW SPECTRUM  $E^{**q}$

CHAN	q = 0	- .5	-1.0	-1.5	-2.0	-2.5	-3.0	-3.5	-4.0	-4.5	-5.0	-5.5	-6.0
1	.9879	.9311	.6980	.3099	.1144	.0635	.0489	.0420	.0374	.0336	.0305	.0278	.0254
2	.9647	.8519	.5629	.2481	.1008	.0537	.0376	.0303	.0257	.0222	.0194	.0171	.0151
3	.8290	.5357	.2747	.1665	.1298	.1144	.1054	.0990	.0938	.0895	.0857	.0823	.0792
4	.8300	.5357	.2426	.1069	.0599	.0419	.0328	.0270	.0228	.0195	.0168	.0146	.0127
5	.9246	.7632	.4806	.2432	.1327	.0912	.0745	.0662	.0612	.0577	.0552	.0534	.0522
6	.8640	.6519	.3994	.2423	.1735	.1439	.1287	.1192	.1122	.1066	.1018	.0977	.0940
7	.8563	.6385	.3729	.1993	.1199	.0852	.0678	.0574	.0500	.0444	.0399	.0361	.0328
8	.9172	.7832	.5545	.3218	.1756	.1052	.0727	.0563	.0469	.0406	.0362	.0330	.0305
9	.8807	.7291	.5208	.3395	.2282	.1693	.1375	.1186	.1059	.0965	.0890	.0829	.0776
10	.9069	.7906	.6065	.4059	.2536	.1625	.1124	.0840	.0666	.0548	.0461	.0394	.0341
11	.8806	.7573	.5866	.4168	.2900	.2100	.1620	.1324	.1129	.0999	.0884	.0800	.0731
12	.9118	.8212	.6804	.5121	.3594	.2485	.1772	.1329	.1046	.0855	.0717	.0613	.0531
13	.8981	.8103	.6849	.5412	.4094	.3080	.2374	.1900	.1578	.1350	.1181	.1051	.0947
14	.9228	.8578	.7589	.6320	.4980	.3803	.2901	.2261	.1819	.1511	.1288	.1121	.0990
15	.9314	.8791	.7995	.6928	.5703	.4503	.3481	.2692	.2117	.1705	.1409	.1190	.1023
16	.9357	.8947	.8341	.7518	.6510	.5410	.4343	.3407	.2648	.2064	.1625	.1298	.1052

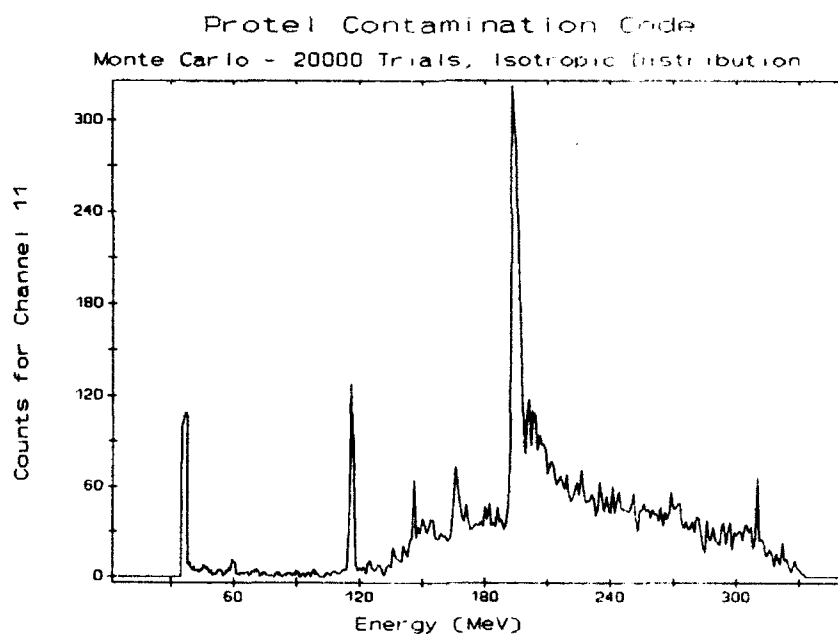


**Figure 28.** Response functions, channel 11, isotropic case.

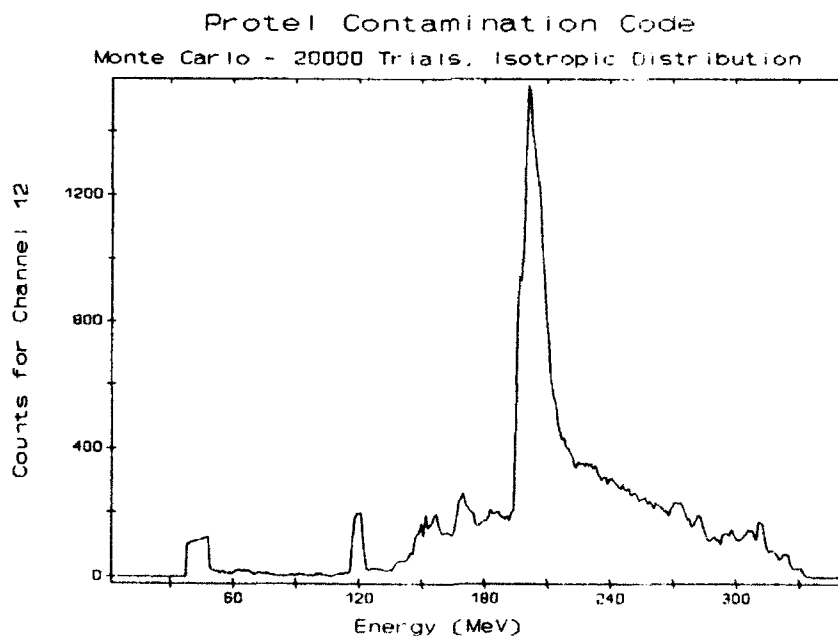
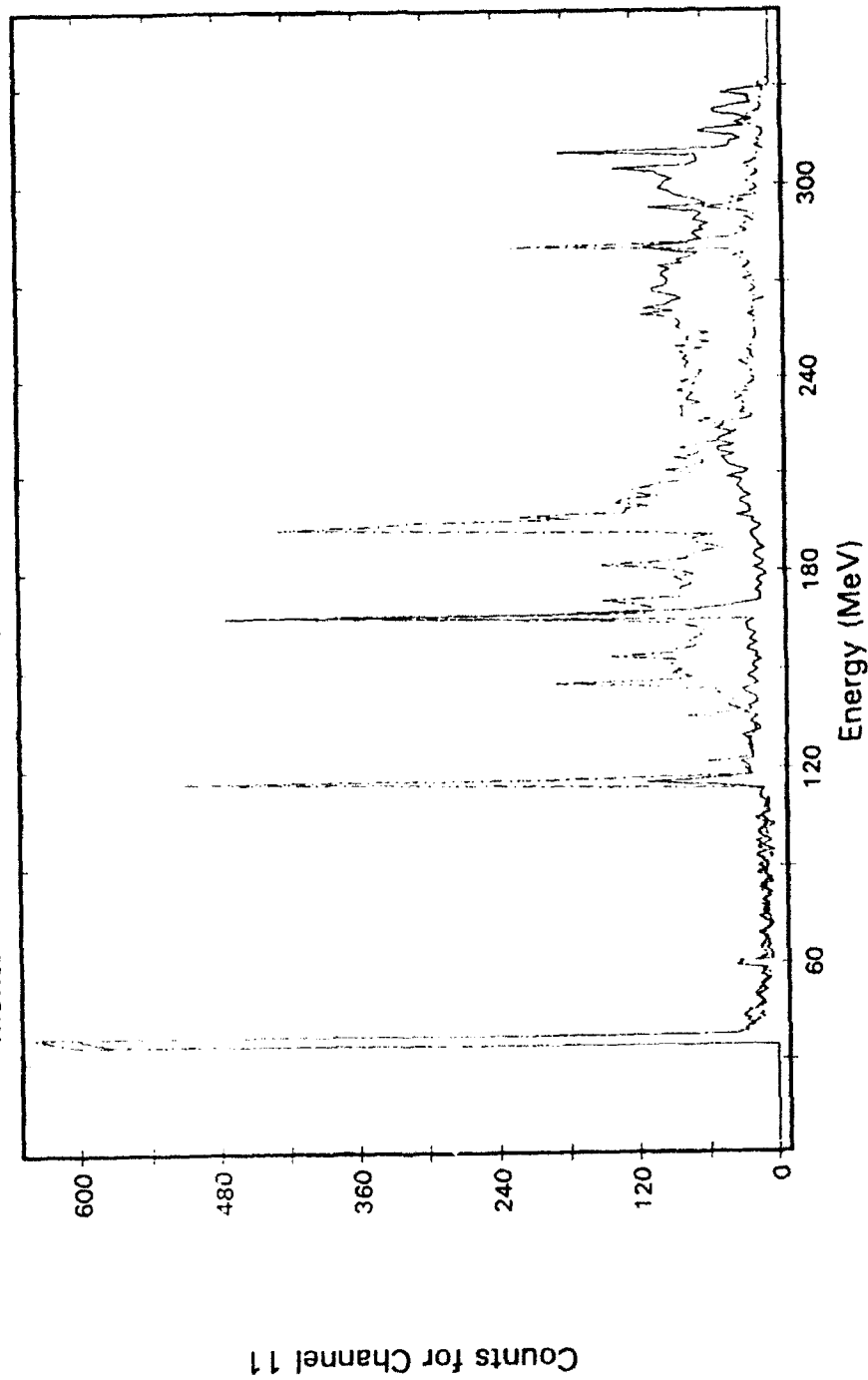


**Figure 29.** Response functions, channel 12, isotropic case.

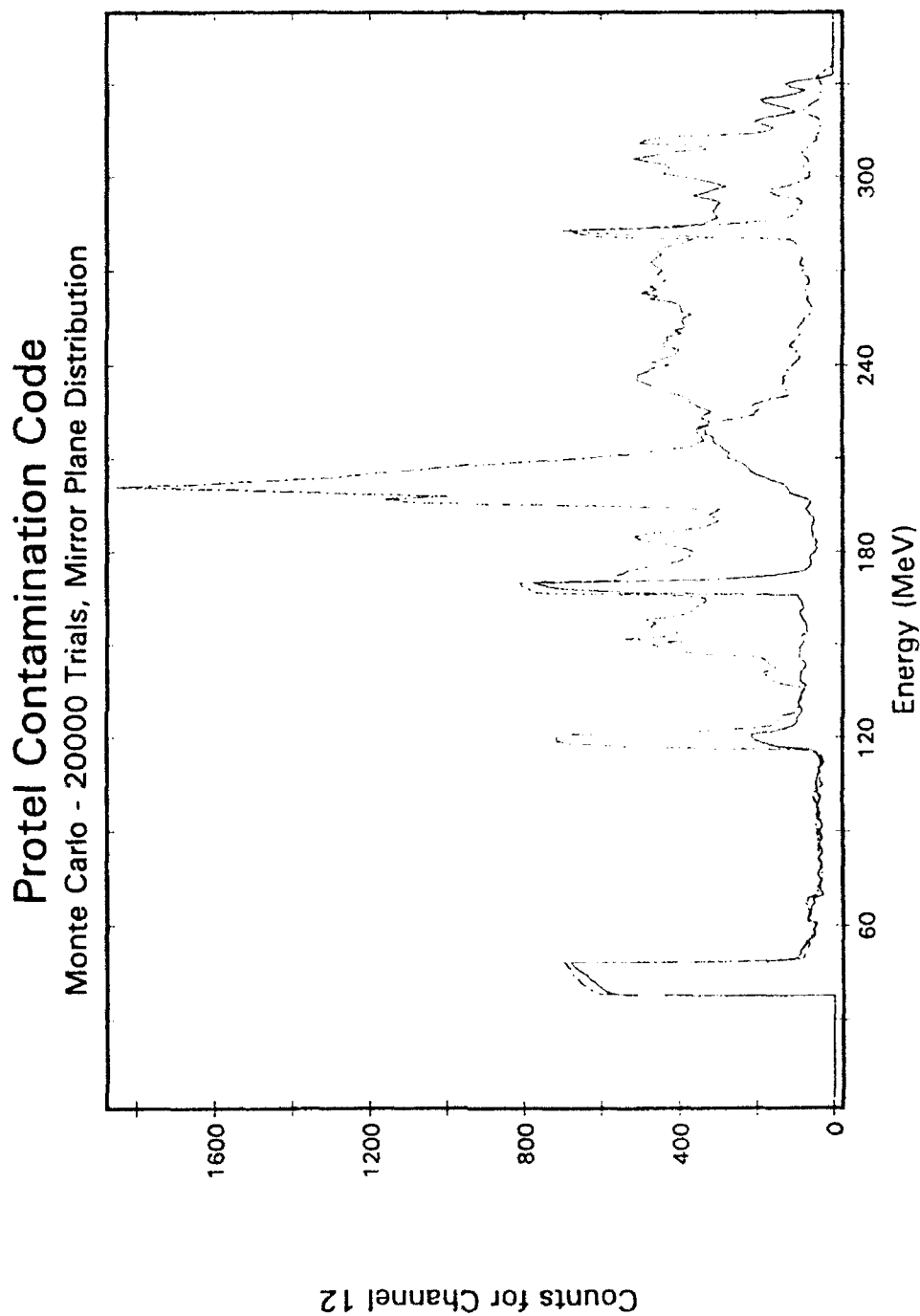


# Protel Contamination Code Monte Carlo - 20000 Trials, Mirror Plane Distribution



DATE RUN: 9/22/82

Figure 30. Response functions, channel 11, mirror plane distribution.



DATE RUN 3/22/82

**Figure 31.** Response functions, channel 12, mirror plane distribution.

### 2.1.2 CRRES Dosimeter Modeling

The design of the CRRES dosimeters is based on the Space Radiation Dosimeters successfully used on the DMSP 7 satellite [Gussenhoven, *et al.*, 1986]. Modifications of the original DMSP design were required because of the different operational environment and the orbit of the CRRES satellite; in particular, the CRRES orbit passes through the radiation belts, subjecting the CRRES dosimeter to much higher count and dose rates than those encountered by the 800 km altitude circular orbit of DMSP.

A description of the CRRES dosimeters may be found in Morel, *et al.* [1989]. An overall description of the CRRES Satellite and Experiments can be found in Gussenhoven, *et al.* [1987]. The CRRES dosimeters are a set of four disk shaped silicon particle detectors, each of which is mounted on a platform at the center of a hemispheric aluminum shell. The thickness of the hemispherical shell is chosen to set the lower energy limits of charged particles which will arrive at the detector. The physical and geometrical parameters of the detectors are presented in Table 14.

**TABLE 14.** Physical and Geometric Parameters of the CRRES detectors

Detector #	Detector Area [cm <sup>2</sup> ]	Detector Thickness [microns]	Ratio: thickness/radius D/R	Thickness of Al. Hemisphere [gm/cm <sup>2</sup> ]	Minimum Proton Energy Required to Penetrate Aluminum Hemisphere [MeV]
1	0.00815	403	0.79123	0.55	20
2	0.051	434	0.34063	1.55	35
3	0.051	399	0.31326	3.05	51
4	1.000	406	0.07196	5.91	75

The objective of the modeling effort was to develop a software model of the CRRES dosimeter to compute proton counts and dose for proton energy spectra, in particular, for the following proton angular distributions: isotropic, mirror plane, and  $\sin^N \alpha$  pitch angle distributions. The modeling of PROTEL and the CRRES dosimeter was performed in order to cross-calibrate the two instruments. The silicon detectors measure the energy loss of a charged particle passing through their active regions. For simplicity in computation, only the active portion of the detectors is modeled. The modeling assumes that the protons penetrate the detectors, travel in a straight line, and undergo deceleration in the direction of motion (and energy loss) due to the interaction of the protons with the electrons in the detector. Energy losses in silicon were computed both using the Janni energy-range relations [Janni, 1982] and power law fits to the Janni data. For each detector, there are two count and dose channels, LOLET, and HILET. The LOLET channels are sensitive to electrons, and respond to energy losses less than 1 MeV. The proton contribution to the LOLET channels is expected to be small compared that produced by high energy electrons which penetrate the aluminum hemisphere.

In previous studies, the infinite slab approximation was used to compute proton counts, dose and geometric factors. The infinite slab approximation is best suited to the case in which the thickness of the detector is small compared to its other dimensions. The loss of accuracy with thickness results from edge effects, that is, due to particles which enter the top and exit through the edge of the detector or enter the side and leave the side of the detector. The ratio of the thickness of the silicon detector to its linear

dimensions for detector 1 is small compared to the detectors used with DMSP, or the other CRRES dosimeter detectors. The validity of the infinite slab assumption does not appear to hold for detector 1.

The methodology that we used was to compute the path length distributions for the above proton angular distributions for the CRRES dosimeters, and apply them to compute the usual flux and dosage integrals, geometric factors and response functions.

The path length distribution may be considered to be either a histogram of possible path lengths, or the probability that a particle passing through the material object in a straight line will have a given path length. The path length distribution depends upon the geometry of the detector and on the particle angular distribution. The application of the path length distribution approach to electrons is unsuitable, because it is doubtful that a substantial fraction of electrons will travel in straight lines while passing through the detector.

A Monte Carlo approach was used to compute the path length distributions. Only the simplest case, an isotropic distribution, will be described here.

To facilitate the Monte Carlo computation, it was necessary to break the calculation into two parts, corresponding to the case (Case 1) in which a proton strikes the top surface, and leaves either through the bottom of the detector or through the side of the detector, and the case (Case 2) in which a proton enters the detector through the side and leaves either through the bottom or through the side of the detector. A geometric argument is then needed to combine the results of the two cases.

For Case 1, a Monte Carlo "trial" consists of the following steps: Select a random point (position vector)  $(x, y, D)$  on the top surface. Then select the velocity direction (unit vector)  $\mathbf{u} = (\cos \psi \sin \beta, \sin \psi \sin \beta, -\cos \beta)$  of the particle as follows: Select  $\mu^2 = \cos^2 \beta$  from a uniform distribution in the interval  $[0, 1]$ , where  $\beta$  is the angle between the normal to the surface and the direction of incidence (see Section 2.1). Compute  $\cos \beta$  and  $\sin \beta$ . Select the direction of the projection of the velocity vector onto the plane of the disk  $\psi$  from a uniform distribution in the interval  $[0, 2\pi]$ , and compute  $\mathbf{u}$ . We then use a trial value  $q = D/\cos \beta$ , and test whether  $(x + q \cos \psi \sin \beta)^2 + (y + q \sin \psi \sin \beta)^2 \leq R^2$ . If so, increment the appropriate top-bottom bin counter for  $q$  by 1. If not, solve the quadratic equation  $(x + q \cos \psi \sin \beta)^2 + (y + q \sin \psi \sin \beta)^2 = R^2$  for  $q$ , and increment the appropriate top-side bin counter for  $q$  by 1.

For Case 2, the coordinate system is the same as that used for Case 1, but the spherical coordinate system polar axis is the  $x$  axis,  $\theta$  is the polar angle, and  $\phi$  is the azimuth angle, measured from the  $y$  axis towards the  $-z$  axis.

A Monte Carlo "trial" consists of the following steps: For an arbitrary point on the circumference of the disk, randomly select a height  $h$  above the bottom surface from a uniform distribution in the interval  $[0, D]$ . For reasons of symmetry, the position vector of that point may be chosen to be  $(-R, 0, h)$ . The velocity direction (unit vector)  $\mathbf{u} = (\cos \theta, \cos \phi \sin \theta, -\sin \theta \sin \phi)$  of the particle is selected as follows: Select  $\cos^2 \theta$  from a uniform distribution between  $[0, 1]$ . Select  $\phi$  from a uniform distribution in the interval  $[0, \pi]$  and compute  $\mathbf{u}$ . For the trial value  $q = h/(\sin \theta \sin \phi)$  test whether  $(-R + q \cos \theta)^2 + (q \cos \phi \sin \theta)^2 \leq R^2$ . If so, increment the appropriate side-bottom bin counter for  $q$  by 1. If not, select the trial value  $q = 2R \cos \theta / (\cos^2 \theta + \sin^2 \theta \cos^2 \phi)$ . If  $0 < q \sin \theta \sin \phi \leq h$  increment the appropriate side-side bin counter for  $q$  by 1.

To combine the Case 1 and Case 2 Monte Carlo results into a single path length distribution, it is necessary to provide suitable geometric and physical reasoning which justifies the assumptions underlying the computation. First it is necessary to normalize both distributions. It is then necessary to determine the relative path length contributions entering from the top and from the side. For the Case 1 computation, the number of particles striking the top of the detector is proportional to the surface area,  $\pi R^2$ . The Case 2 computation was based upon the contribution due to particles striking the detector along a vertical line on the boundary. The number of particles striking the detector from the side is proportional to  $2 \pi D R$ . Of the latter, only one half of the particles are moving downward, the detector is screened from the upward moving particles by the shielding provided by the satellite and instrument housing. The normalized total contribution is the weighted sum of the two contributions, and is given by:

$$f(q) = (T(q) + D S(q))/(1 + D)$$

where T, S are the normalized Case 1 and Case 2 path length distributions.

Figure 32 shows the path length distribution computed using the Monte Carlo method described above for CRRES dosimeter detector 1 together with the corresponding truncated infinite slab path length distribution (smooth curve). Note that the minimum path length for the infinite slab distribution is equal to the thickness of the detector. The path length distribution "spike" at  $2 R$  is due to particles entering and exiting the side of the detector. The same normalization was used for the path length and infinite slab distributions.

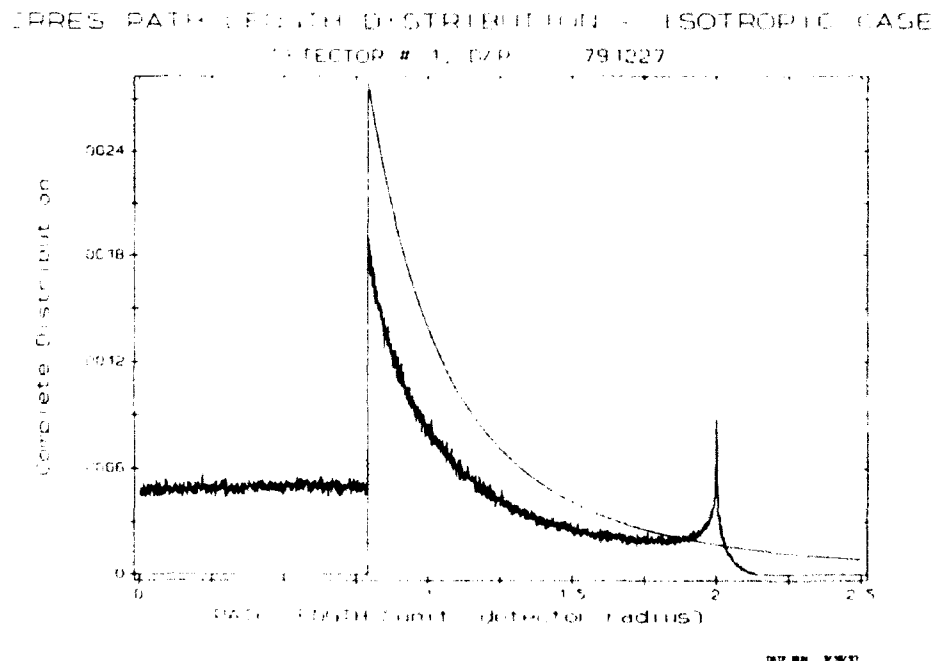


Figure 32. Path length distribution computed using the Monte Carlo method.

The computations for the mirror plane and  $\sin^N \alpha$  path length distributions were performed in a similar manner, using the appropriate angular distribution functions. These distributions are angle dependent, depending on the angle made by the detector and the magnetic field direction. Path length computations were performed at 5 degree intervals from 0 to 90 degrees for the mirror plane distribution, and at 5 degree intervals for  $N = 6, 8, 10$  and  $12$  for the  $\sin^N \alpha$  distributions. Typically, 100,000 trials were performed for each path length computation, using 2,500 "bins".

The computation of the response functions proceeds as follows: For each energy incident on the external dome, the corresponding energy arriving at the detector surface is computed using the Janni energy range relations for aluminum. Then, for each path length, the corresponding energy loss in silicon is computed; depending on the energy loss, the appropriate LOLET or HILET count channel is incremented by the value of the path length distribution function. For dose, the corresponding dose counter (as discretized by the Dosimeter's on-board processor) is incremented using the dose count (corresponding to the energy loss) multiplied by the value of the path length distribution. The resulting functions of energy for the LOLET and HILET channels are the count and dose response functions. The geometric factors are obtained by integrating over a particular proton energy spectrum. Tables 15 and 16 are tables of geometric factors for power law spectra; Table 15 uses the power law fit to the Janni tables for Silicon, and Table 16 uses the actual Janni tables. Both use the computed path length distribution for the isotropic case.

Table 17 provides a comparison of the proton counts for both the infinite slab approximation and the computed Dosimeter Path Length distribution for a sample proton energy spectrum.

TABLE 15. Energy - Range Relation used in Computation:  $R(E)=0.0011824 E^{*1.772518}$ ;  $R(\text{cm})$ ,  $E(\text{MeV})$  - Computation based upon Dosimeter Isotropic Path Length Distribution

N	CRRES Proton Flux Omnidirectional				Geometric Factors (cm <sup>2</sup> MeV) for Power Law Spectra J(E) ~ E <sub>N</sub>			
	HILET CHANNEL	HILET CHANNEL	HILET CHANNEL	HILET CHANNEL	LOLET CHANNEL	LOLET CHANNEL	LOLET CHANNEL	LOLET CHANNEL
1	1.175965	1.727819	1.401911	45.014470	4.487404	29.883640	29.294280	599.396600
2	1.165422	1.527662	1.215200	37.054920	3.364276	22.138560	21.646670	438.289600
3	1.155783	1.353948	1.055166	30.608450	2.539197	16.486190	16.070560	321.645000
4	1.146955	1.202734	.917698	25.364610	1.930194	12.344400	11.989450	236.931700
5	1.138858	1.070733	.799368	21.081410	1.478404	9.296537	8.990480	175.210100
6	1.131420	.955185	.697310	17.569320	1.141428	7.043482	6.777420	130.087900
7	1.124576	.853773	.609122	14.679160	.888646	5.369970	5.137056	96.984920
8	1.118270	.764544	.532782	12.292840	.697867	4.120666	3.915555	72.611020
9	1.112451	.685846	.466585	10.316380	.552960	3.183091	3.001564	54.596340
10	1.107073	.616276	.409090	8.674726	.442154	2.475578	2.314246	41.229900
11	1.102095	.554639	.359078	7.307454	.356829	1.938603	1.794719	31.272760
12	1.097482	.499917	.315510	6.165958	.290649	1.528644	1.399940	23.824830
13	1.093201	.451238	.277504	5.210768	.238934	1.213746	1.098337	18.230680
14	1.089222	.407851	.244307	4.409802	.198211	.970360	.866652	14.011070
15	1.085519	.369110	.215273	3.736860	.165896	.781049	.687692	10.814730
16	1.082068	.334460	.189851	3.170459	.140050	.632862	.548689	8.383138
17	1.078848	.303416	.167567	2.692949	.119217	.516116	.440124	6.525395
18	1.075841	.275559	.148011	2.289750	.102292	.423554	.354865	5.100049
19	1.073027	.250526	.130833	1.948827	.088436	.349698	.287546	4.001815
20	1.070392	.227997	.115730	1.660170	.077007	.290399	.234108	3.152112
22	1.065601	.189374	.090730	1.207808	.059560	.203563	.157275	1.977150
24	1.061369	.157851	.071303	.881331	.047178	.145581	.107406	1.257157
26	1.057614	.132002	.056159	.644805	.038158	.105999	.074435	.809347
28	1.054268	.110715	.044322	.472865	.031429	.078421	.052264	.526945
30	1.051273	.093116	.035045	.347504	.026300	.058847	.037124	.346572
35	1.045034	.061056	.019626	.162163	.017833	.030240	.016471	.126253
40	1.040154	.040569	.011090	.076388	.012883	.016490	.007669	.048035
45	1.036260	.027259	.006314	.036258	.009755	.009411	.003705	.018897
50	1.033095	.018491	.003619	.017320	.007658	.005566	.001843	.007633
60	1.028292	.008712	.001208	.004014	.005104	.002110	.000487	.001323
70	1.024844	.004208	.000411	.000945	.003662	.000863	.000137	.000243
80	1.022260	.002073	.000142	.000226	.002763	.000373	.000041	.000047
90	1.020257	.001037	.000049	.000054	.002162	.000167	.000013	.000009
100	1.018663	.000525	.000017	.000013	.001739	.000077	.000004	.000002

N	CRRES PROTON DOSE OMNIDIRECTIONAL				GEOMETRIC FACTORS (cm <sup>2</sup> MeV) for Power Law Spectra J(E) ~ E <sub>N</sub>			
	HILET CHANNEL	HILET CHANNEL	HILET CHANNEL	HILET CHANNEL	LOLET CHANNEL	LOLET CHANNEL	LOLET CHANNEL	LOLET CHANNEL
1	1.823316	4.514067	7.095098	15.057370	1.750899	13.225910	13.466020	161.239700
2	1.766865	4.066819	6.238049	12.544100	1.370369	10.130020	10.275370	120.671200
3	1.676009	3.671121	5.491841	10.481720	1.081687	7.807648	7.884712	90.700910
4	1.610230	3.320073	4.840966	8.782570	.861234	6.056236	6.084561	68.473220
5	1.549065	3.007829	4.272264	7.377483	.691726	4.728158	4.722136	51.921380
6	1.492099	2.729411	3.774550	6.211551	.560466	3.715373	3.685591	39.545390
7	1.438963	2.480574	3.338300	5.240990	.458081	2.938538	2.892794	30.252790
8	1.389321	2.257679	2.955365	4.430695	.377625	2.339151	2.283145	23.245690
9	1.342876	2.057601	2.618773	3.752364	.313925	1.873905	1.811805	17.939270
10	1.299358	1.877656	2.322537	3.183089	.263110	1.510592	1.445408	13.903450
11	1.258523	1.715504	2.061497	2.704246	.222267	1.225159	1.159051	10.820740
12	1.220154	1.569129	1.831216	2.300609	.189192	.999555	.934056	8.455955
13	1.184052	1.436775	1.627845	1.959724	.162210	.820171	.756339	6.634181
14	1.150037	1.316909	1.448058	1.671303	.140039	.676695	.615244	5.224876
15	1.117948	1.208190	1.288968	1.426878	.121693	.561276	.502660	4.130160
16	1.087636	1.109440	1.148065	1.219425	.106408	.467901	.412387	3.276399
17	1.058969	1.019627	1.023163	1.043104	.093590	.391944	.339663	2.607959
18	1.031824	.937837	.912356	.893049	.082771	.329828	.280810	2.082631
19	1.006090	.863265	.813977	.765196	.073586	.278771	.232977	1.668263
20	.981667	.795196	.726569	.656138	.065741	.236594	.193937	1.340269
22	.936388	.676101	.579717	.483430	.053189	.172404	.135636	.872195
24	.895339	.576270	.463345	.357058	.043746	.127418	.095929	.573299
26	.857974	.492285	.370914	.264293	.036509	.095375	.068525	.380221
28	.823833	.421401	.297349	.196006	.030870	.072214	.049386	.254193
30	.792525	.361397	.238687	.145614	.026407	.055247	.035875	.171156
35	.724584	.247932	.138497	.069717	.018669	.029418	.016620	.065387
40	.668364	.171584	.080864	.033635	.013887	.016420	.007973	.025762
45	.621065	.119608	.047460	.016328	.010750	.009521	.003933	.010399
50	.580696	.083884	.027978	.007966	.008587	.005697	.001986	.004281
60	.515342	.041870	.009829	.001920	.005880	.002195	.000535	.000760
70	.464593	.021223	.003493	.000469	.004308	.000910	.000153	.000142
80	.423938	.010886	.001253	.000115	.003306	.000398	.000046	.000027
90	.390572	.005636	.000453	.000029	.002625	.000180	.000014	.000005
100	.362658	.002940	.000165	.000007	.002139	.000084	.000004	.000001

**TABLE 16. Janni Energy - Range Relation Used in Computation - Computation based upon Dosimeter Path Length Distribution**

CRRES PROTON FLUX OMNIDIRECTIONAL GEOMETRIC FACTORS (cm <sup>2</sup> MeV) for Power Law Spectra J(E) = E <sub>N</sub>									
HILET CHANNEL				LOLET CHANNEL					
N	1	2	3	4	1	2	3	4	
.1	.175153	1.826273	1.492964	52.879600	4.884083	31.284520	30.747070	602.468400	
.2	.164678	1.600520	1.282461	42.701660	3.649133	23.133590	22.674630	440.355600	
.3	.155104	1.407825	1.104835	34.668180	2.745231	17.196590	16.800810	323.038500	
.4	.146339	1.242522	.954354	28.287120	2.080513	12.854770	12.510590	237.875500	
.5	.138301	1.100055	.826386	23.187720	1.589207	9.665914	9.364436	175.853500	
.6	.130919	.976730	.717190	19.088970	1.224088	7.313128	7.047437	130.530800	
.7	.124129	.869540	.623711	15.776510	.951170	5.568813	5.333450	97.294010	
.8	.117872	.776019	.543452	13.085750	.745901	4.268975	4.059573	72.830520	
.9	.112099	.694136	.474353	10.889510	.590496	3.295140	3.108163	54.755870	
1.0	.106764	.622205	.414710	9.088990	.472026	2.561423	2.393961	41.348830	
1.1	.101826	.558821	.363111	7.606799	.381057	2.005367	1.855001	31.363850	
1.2	.097250	.502811	.318374	6.382062	.310676	1.581383	1.446076	23.896640	
1.3	.093002	.453186	.279507	5.366561	.255796	1.256066	1.134088	18.288780	
1.4	.089054	.409108	.245679	4.521853	.212660	1.004847	.894709	14.059240	
1.5	.085379	.369866	.216186	3.817201	.178477	.809573	.709993	10.855430	
1.6	.081955	.334855	.190431	3.227820	.151164	.656779	.566636	8.418033	
1.7	.078759	.303556	.167908	2.733655	.129159	.536424	.454739	6.555671	
1.8	.075773	.275523	.148183	2.318421	.111285	.440990	.366900	5.126487	
1.9	.072979	.250368	.130887	1.968805	.096648	.364815	.297556	4.025030	
2.0	.070362	.227762	.115703	1.673894	.084564	.303616	.242510	3.172561	
2.2	.065602	.189065	.090616	1.213845	.064087	.213875	.163333	1.993053	
2.4	.061307	.157532	.071160	.883524	.052926	.153791	.111883	1.269509	
2.6	.057663	.131705	.056017	.645157	.043294	.112632	.077803	.818898	
2.8	.054334	.110454	.044194	.472411	.036070	.083835	.054831	.534291	
3.0	.051355	.092893	.034935	.346763	.030530	.063300	.039099	.352189	
3.5	.045141	.060917	.019558	.161507	.021289	.033033	.017523	.129071	
4.0	.040276	.040487	.011052	.076003	.015797	.018282	.008242	.049420	
4.5	.036391	.027212	.006294	.036058	.012273	.010580	.004021	.019570	
5.0	.033231	.018465	.003608	.017222	.009874	.006339	.002019	.007957	
6.0	.028432	.008704	.001205	.003992	.006897	.002459	.000543	.001397	
7.0	.024984	.004206	.000410	.000941	.005172	.001027	.000156	.000261	
8.0	.022399	.002072	.000141	.000225	.004073	.000451	.000047	.000051	
9.0	.020395	.001037	.000049	.000054	.003322	.000206	.000015	.000010	
10.0	.018799	.000525	.000017	.000013	.002783	.000096	.000005	.000002	

CRRES PROTON DOSE OMNIDIRECTIONAL GEOMETRIC FACTORS (cm <sup>2</sup> MeV) for Power Law Spectra J(E) = E <sub>N</sub>									
HILET CHANNEL				LOLET CHANNEL					
N	1	2	3	4	1	2	3	4	
.1	1.812747	4.636534	7.322987	17.223840	2.130049	16.214030	16.631670	192.859700	
.2	1.736932	4.156893	6.405598	14.104590	1.642228	12.255710	12.524360	143.069700	
.3	1.666669	3.737091	5.614662	11.607640	1.277361	9.323138	9.485706	106.593700	
.4	1.601443	3.368107	4.930633	9.596238	1.002697	7.139285	7.226717	79.769680	
.5	1.540793	3.042526	4.337356	7.966408	.794527	5.504204	5.538850	59.966060	
.6	1.484305	2.754210	3.821471	6.638445	.635624	4.273068	4.271091	45.285800	
.7	1.431610	2.498033	3.371792	5.550852	.513422	3.340618	3.313690	34.357800	
.8	1.382375	2.269720	2.978954	4.655879	.418715	2.630092	2.586628	26.187970	
.9	1.336304	2.065656	2.631092	3.916179	.344732	2.085275	2.031343	20.053350	
1.0	1.293130	1.882786	2.331526	3.302363	.286471	1.664857	1.604792	15.426470	
1.1	1.252612	1.718513	2.068616	2.791130	.240212	1.338319	1.275222	11.921060	
1.2	1.214533	1.570613	1.835538	2.363935	.203180	1.083039	1.019092	9.253299	
1.3	1.178697	1.437176	1.630168	2.005859	.173291	.882163	.818880	7.213882	
1.4	1.144926	1.316554	1.448974	1.704904	.148973	.723059	.661476	5.647811	
1.5	1.113059	1.207321	1.288909	1.451326	.129029	.596229	.537028	4.439885	
1.6	1.082951	1.108236	1.147351	1.237183	.112546	.494486	.438092	3.504129	
1.7	1.054471	1.018218	1.022022	1.055972	.098823	.412361	.359015	2.776116	
1.8	1.027495	.936321	.910959	.902345	.087313	.345672	.295484	2.207366	
1.9	1.001918	.861706	.812442	.771879	.077595	.291202	.244185	1.761241	
2.0	.977635	.793643	.724981	.660916	.069335	.246462	.202566	1.409925	
2.2	.932606	.674647	.578181	.485807	.056193	.178852	.140882	.911935	
2.4	.891763	.574972	.461969	.358174	.046363	.131838	.099231	.596502	
2.6	.854571	.491157	.369734	.264759	.038858	.098546	.070678	.394103	
2.8	.820574	.420440	.296361	.196148	.033021	.074580	.050838	.262707	
3.0	.789387	.360587	.237876	.145604	.028408	.057071	.036885	.176507	
3.5	.721670	.247415	.138021	.069625	.020405	.030470	.017074	.067236	
4.0	.665599	.171257	.080594	.033571	.015444	.017080	.008200	.026478	
4.5	.618401	.119400	.047308	.016292	.012173	.009954	.004054	.010698	
5.0	.578107	.083749	.027893	.007949	.009906	.005988	.002052	.004412	
6.0	.512858	.041810	.009802	.001916	.007043	.002332	.000557	.000787	
7.0	.462191	.021194	.003484	.000468	.005359	.000977	.000160	.000148	
8.0	.421614	.010871	.001250	.000115	.004273	.000431	.000048	.000029	
9.0	.388326	.005628	.000452	.000029	.003524	.000197	.000015	.000006	
10.0	.360492	.002935	.000164	.000007	.002983	.000093	.000005	.000001	



**TABLE 17. Dosimeter Count Comparison  
Path Length Distribution vs. Infinite Slab**

Energy Spectrum: $J(E) = 2.805402 (E/20)^{-2.02324}$				
DETECTOR	DOSIMETER COUNTS		INFINITE SLAB COUNTS	
	LOLET	HILET	LOLET	HILET
1	0.294389	0.466421	0.084265	0.710090
2	0.572721	1.002929	0.240510	1.377596
3	0.326724	0.385265	0.192270	0.540020
4	1.725260	3.877467	1.649000	4.044243

## 2.2 RADIATION BELT MODELING STUDIES

### 2.2.1 Adiabatic Invariants and Dipole-Equivalent Invariants

To facilitate the study of radiation belt dynamics, *Schulz [1991]* (Spring AGU Meeting) has recommended organizing the CRRES radiation belt particle data in terms of the adiabatic invariants. These are defined as action integrals pertaining, respectively, to the basic three approximately separable periodic components of the motion of magnetospherically trapped particles: the spiraling motion of the particle about a guiding center, the motion of the guiding center along field lines, and the longitudinal drift motion of the guiding center around Earth. In the absence of an electric field component parallel to the magnetic field, the first invariant reduces to a very simple expression:

$$\mu = p_{\perp}^2 / (2mB), \quad (64)$$

where  $p_{\perp}$  is the perpendicular momentum,  $p \sin \alpha$ , at a location traversed by the particle,  $\alpha$  is the particle's pitch angle when it is at that location,  $B$  is the magnetic field magnitude there, and  $m$  is the particle's mass. In the absence of a force component parallel to the magnetic field, the total momentum  $p$  is constant along a field line. Therefore,  $B_m = B/\sin^2 \alpha$  is constant, and the particle mirrors at points where its pitch angle is  $90^\circ$ , and the magnetic field magnitude is  $B_m$ .

The second adiabatic invariant is given by

$$J = 2pI_m, \quad (65)$$

where,

$$I_m = \int \sqrt{(1 - B(s)/B_m)} ds \quad (66)$$

with the integral taken along the field line between the particle's mirror points.  $B(s)$  is the magnetic field magnitude at a point  $s$  on the field line.

In these expressions, and in what follows, the subscript  $m$  is used to designate a mirror point quantity. Thus,  $B_m$  is the magnetic field at the mirror point of a particle, as opposed to the point of observation.  $I$ , without the subscript, can be considered a function of position if  $B_m$  is replaced by  $B$  at the position in question and the integral is taken between that position and its conjugate point. The subscript emphasizes the dependence of these quantities on the mirror points rather than the position of observation. The mirror point, in turn, is a function of the point of observation and the pitch angle.

The third adiabatic invariant is given by

$$\Phi = \oint \mathbf{B} \cdot d\mathbf{a}, \quad (67)$$

where the integral is over any surface enclosed by the drift orbit.

Note that, if the magnetic field is static, the particle momentum is fixed and the parameters  $I_m$  and  $B_m$  serve equally as well as the adiabatic invariants for parameterizing the particle trajectories, since they are then functions of  $\mu$  and  $J$  and are, therefore, themselves invariant. Thus,  $I_m$  and  $B_m$  specify the set of mirror points through which the particle passes in its orbit, and therefore, completely specify the orbit. In this case, the third invariant, the flux enclosed by the drift orbit, is not an independent parameter. However, its place as a constant of the motion may be taken by the particle's energy. The constancy of these parameters disappears in time-varying fields in which the resulting induction electric field does work on the particles, thus, changing their energies and momenta.  $I_m$  and  $B_m$  must correspondingly be adjusted to conserve  $\mu$  and  $J$ .

McIlwain [1961] has defined a shell parameter  $L_m$  as a function of  $I_m$  and  $B_m$ . This parameter is, therefore, adiabatically conserved if  $I_m$  and  $B_m$  are. In a dipole field,  $I_m$  is the equatorial crossing distance of the shell of field lines through which the particle passes. Therefore, at a given location, all particles have the same  $L_m$  value regardless of pitch angle. Since this relationship remains approximately valid in Earth's internal field,  $L_m$  has a distinct advantage over  $I_m$  for organizing the inner belts. As a function of position,  $L$  is constant along a dipole field line and approximately constant along field lines of Earth's internal field.

#### 2.2.1.1 Equivalent Parameters

A problem with the adiabatic invariants is the difficulty in working with them due to lack of familiarity. We are more accustomed to energy spectra, radial distributions, and pitch angle distributions. Thus, we are motivated to define a set of equivalent invariants - the energy,  $L_m$ , and equatorial pitch angle that particles with a given set of adiabatic invariants would attain if the magnetic field changed adiabatically to a specified reference field. In the past, the Mead model has been used as the reference field [Bass, *et al.*, 1989]. A simpler choice would be a dipole field. Roederer [1970] proposed such a set of parameters, which we call dipole-equivalent invariants. First, we have, for the dipole-equivalent  $L_{md}$ :

$$L_{md} = -2\pi M/\Phi, \quad (68)$$

where  $M$  is the dipole moment of the chosen dipole reference field. A review of Roederer [1970] and Schulz and Lanzerotti [1974] leads to the conclusion that this is the  $L$  parameter used by them in diffusion equations, rather than McIlwain's parameter. Unlike the latter,  $L_{md}$  is a function of the third adiabatic invariant, and, therefore, would not change under adiabatic variations of the magnetic field.

Furthermore, this  $L_{md}$  is actually independent of a particle's mirror points in a symmetric non-dipole field. Thus, any dependence on mirror points reflects shell-splitting in an asymmetric field.

To obtain the dipole-equivalent equatorial pitch angle,  $\alpha_d$ , we note the following [Roederer, 1970]:

$$I_m^2 B_m = \text{constant} \quad (69)$$

which follows from Eqs. (64) and (65), and constancy of  $J$  and  $\mu$ . After substituting known dipole expressions for  $B_{md}$  and  $I_{md}$ , as functions  $L_{md}$  and  $\alpha_d$ , we solve for  $\alpha_d$ . Finally, constancy of the first adiabatic invariant supplies the ratio  $p_d/p$ , where  $p_d$  is the dipole-equivalent momentum, and  $p$  is the observed momentum. From this ratio, we may obtain the dipole-equivalent energy  $E_d$  for any observed energy.

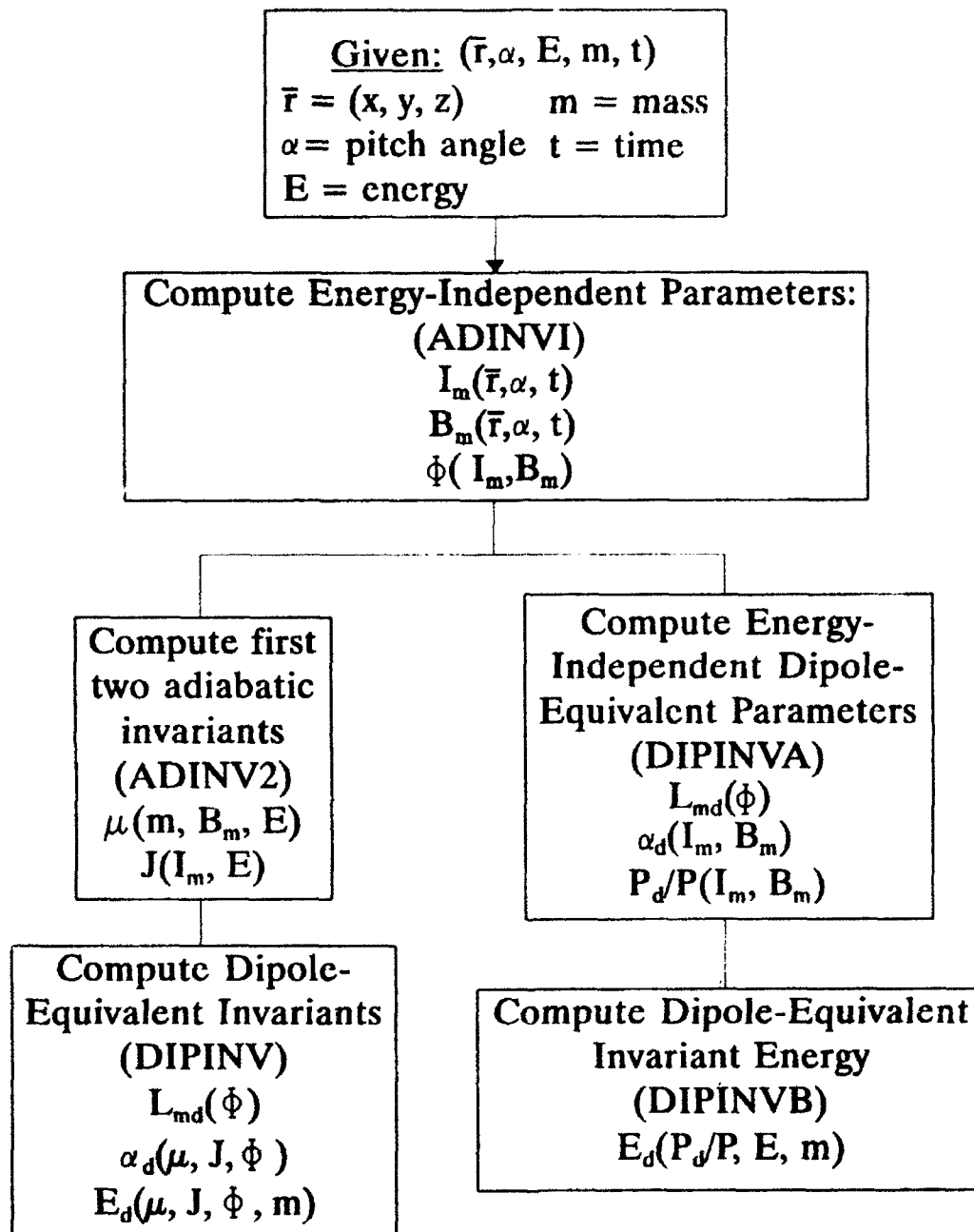
#### 2.2.1.2 Software

Figure 33 summarizes software that has been developed to compute the adiabatic invariants and dipole-equivalent invariants. As indicated in the top block, we are given the particle position, pitch angle, energy, mass, and the time. The first step is to compute the set of *energy-independent parameters* for specified positions and pitch angles in a given field model. These are the quantities  $B_m$ ,  $I_m$ ,  $L_m$ , and  $\Phi$ . Subroutine ADINVI performs this function (in this and all subsequent blocks, CAPS enclosed by parentheses indicate subroutine names). This is the most CP-time-intensive step of the process, and will be described in more detail below. The remainder of the procedure has two alternatives. If one desires the adiabatic invariants, it is prudent to take the left-hand branch, in which the first two adiabatic invariants,  $\mu$  and  $J$ , are obtained by direct application of Eqs. (64) and (65) (subroutine ADINV2). The dipole-equivalent invariants are then obtained, as described above, using subroutine DIPINV. The right-hand branch may be followed if one needs only the dipole-equivalent invariants, but is computing them for several energies and/or masses. Then it is noted that the first two of these,  $L_{md}$  and  $\alpha_d$ , are independent of mass and energy, thus, needing to be determined only once at a given location, time, and pitch angle. Along with these, a third mass/energy independent parameter, the ratio  $p/p_d$ , is also determined. These are collectively called *energy-independent dipole-equivalent parameters*. Finally, the dipole-equivalent energy can be determined for each mass and energy (subroutine DIPINVB).

The computation of the energy-independent parameters (subroutine ADINVI) requires three stages:

1. Trace the magnetic field line through the position of interest and compute the magnetic field value at that specified location.
2. For each pitch angle, determine the mirror point magnetic field value  $B_m$  and the mirror point integral  $I_m$ .
3. For each pitch angle, compute the third invariant  $\Phi$ .

Stage 3 requires the determination of the drift shell, defined by the set of field lines containing the mirror points of the requisite  $I_m$  and  $B_m$ . The magnetic equatorial crossing distances of the drift shell are determined at each of 25 equally spaced local times between 0 and 12 hours. That portion of the shell between 12 and 24 hours is determined from the portion between 0 and 12 hours by dawn-dusk symmetry. The required field line crossing the equator, at a given local time, is found by iterative search (subroutine LBSRCH). The initial guess for the crossing distance is the value of  $L_m$ , McIlwain's function of  $B_m$  and  $I_m$ . Then the value of  $L$  at the point  $B=B_m$  along this field line is found. If this value is within  $10^{-4} R_E$  of the required  $L_m$ , then the search is terminated. Otherwise, the difference is used to



**Figure 33.** Overview of software for computation of adiabatic invariants and dipole equivalent invariants.

correct the equatorial crossing distance and the process repeated until the crossing distance is determined to within specified accuracy ( $10^{-4} R_E$ ). Generally this takes 3-5 iterations.

Given the set of equatorial crossing distances defining the drift shell, the third invariant is computed by (subroutine INVAR3), using code provided by Lockheed, Inc. [Nightingale, *et al.*, 1986]. This code computes the third invariant in 3 different ways:

1. Compute directly the magnetic flux crossing that portion of the equatorial surface bounded by the drift shell. In this approach, the region of the equatorial surface near the origin is replaced by a hemisphere to avoid the singularity in the magnetic field at the origin.
2. Compute the flux crossing that portion of a hemispherical surface of specified radius enclosed by the drift shell.
3. Compute the line integral of the vector potential along the intersection of the drift shell with a hemispherical surface of specified radius.

For a divergence-free magnetic field, these approaches give the same result. However, since the latter two methods require the additional field line tracing to the specified surface, only the first method has been used here.

The magnetic field computation, field line tracing, and determination of the McIlwain L parameter are performed by the BFLDSM software package. Program OPTRACE [Bhavnani, *et al.*, 1987] has the capability to compute L for a specified point. This value relates to the second adiabatic invariant only for particles which mirror at this point, that is, particles whose pitch angles are  $90^\circ$  at this point. The second adiabatic invariant for a non- $90^\circ$  pitch angle particle is related instead to the L value at the points where that particle mirrors.

To perform the calculation requires the following steps:

1. Trace the field line through the initial point to the mirror points appropriate to the smallest pitch angle;
2. for each pitch angle compute the invariant integral  $I_m$ , Eq. (66), for these points, and then  $L_m$  from McIlwain's or Hilton's approximation.

Subroutine BFLDSM, a modification of the OPTRACE package, contains the option to save a traced field line in a common memory area. For each point along the line, the Cartesian coordinates, altitude, and magnetic field magnitude are saved. The inputs to the routine are:

1. Date and GMT
2. Positional coordinates

The output is the traced field line just described, stored northern-most points first. Step 2 can be performed by subroutine LB, part of the BFLDSM package. It takes as its input, a traced field line, as just described, and  $B_m$ , the B value at the mirror point. The output is the desired  $L_m$  value.

The BFLSDM package must be linked with the OPTRACE package, and with object modules named IGRF85 and BXYZMU, respectively, for the desired internal and external field models. These would be used instead of the default modules in the OPTRACE package.

Incidentally the BFLDSM package contains modules also for the following:

1. Writing saved field lines to disk for subsequent display using field line plot packages;
2. Finding the location and value of the minimum magnetic field magnitude;
3. Finding the equatorial crossing;
4. Finding the low altitude footprints.

There are two conditions under which the software fails to define a drift shell, and therefore fails to compute the invariants:

- a. The mirror point lies below Earth's surface.
- b. The drift shell intersects the magnetopause.

The first of these conditions is due to the failure of our tracing routine to go below the surface. This will happen for low pitch angles at low L. The second condition occurs because the tracing routine refuses to cross the magnetopause, as specified by David Stern's parabolic model. This happens for particles mirroring near the equator at high L ( $> 7$ ). This condition can be satisfied for CRRES in a quiet magnetosphere, since the highest L values occur when the vehicle is off the equator. However, it may prove convenient to include such cases for purposes of construction of rectangular interpolation tables. Therefore, this restriction may be removed.

A new problem occurs when one approaches the noon magnetopause: the field line may have two minima. In this case, the drift orbits of equatorially mirroring particles split, with some particles drifting through one of the noon minima, while others drift through the other noon minimum. If the magnetosphere is symmetric about the equator, the two minima lie equally distant from the equator, where there exists a local maximum, instead of a minimum, as is normally the case. The adiabatic invariants should be independent of which minimum a particle takes. However, if the magnetosphere is not symmetric about the equator, as would be the case for non-zero dipole tilt, the two minima could be unequal, resulting in multiple definition of the third adiabatic invariants for particles in a given drift orbit on the night side.

Two software packages have been developed to find L on field lines that have multiple minima, and therefore possible multiple pairs of mirror points for a given value of B. MULTMIN uses sophisticated techniques of BRENT [Press, *et al.*, 1986] to pinpoint the minima and mirror points. The other package, LIBMULT, uses the same techniques as LB, fitting B to a quadratic polynomial through three points near the location (mirror point or minimum) that is sought. These routines have not been fully tested, nor integrated into the BFLDSM package at this time.

### 2.2.1.3 Computer Timing

For an IGRF + quiet Hilmer-Voigt field, the software has been timed at ~3 seconds per pitch angle per field line on the VAX 9000. If we do this calculation for each point on the ephemeris file (~250 per orbit), for 19 pitch angles, this comes to ~15000 seconds per orbit. Examining the Hilmer code, I have found 3 places where time could be saved:

- a. Computation of the magnetopause shielding of tail currents: Hilmer is shielding only the dipole, but was making calls to a routine which actually computes the shielding terms for Voigt's tail field model [Voigt, 1981], and then multiplies them by zero in this specific application. I am now skipping the computation of these terms, which contain Bessel functions.
- b. Computation of the IMF, which is used in the general Voigt magnetopause model to incorporate partial transmission (i.e. merging) into the magnetosphere, but is not needed in the special case of the Hilmer-Voigt model, which assumes zero penetration of the IMF into the magnetosphere: this computation is now skipped.
- c. Hilmer's tail model: the tail is divided into 16 flat segments to simulate its curvature from the dipole equatorial plane near Earth to a plane parallel to the GSM equator at large distances from Earth. I have been experimenting with just 4 segments.

Modifications (a) and (b) have been verified not to change the resulting computed model field. Together, they reduce the computation time by 20%. Modification (c) reduces the time further by 40%, but must be examined further, in light of the changes in results.

Of course, we could try using another model. The Olson-Pfitzer static model, for example, is ~10 times faster, but fails the zero divergence requirement. This results in an ~10% difference between the magnetic flux intercepting the polar cap within a given shell (using Lockheed's code), and the flux intercepting the equator within the same shell. Thus, there would be a 10% uncertainty in the third invariant. I suspect that the Olson-Pfitzer dynamic model would have a similar problem. The Tsyganenko models don't have this problem, but we have considered them to be unsatisfactory in the near-Earth portion of the CRRES orbit, due to their poor ring current formulation.

Two speed improvements have been made recently in BFLDSM. The first of these results in replacing the internal field subroutine with that of Pfitzer [1991], which truncates the internal field, i.e. omitting insignificant higher order terms. The larger the radial distance, the more terms can be omitted. This has produced a nearly three-fold average speed improvement over the CRRES range from low altitude to near geosynchronous altitude. The other improvement results from the use of quadratic interpolation of  $B$  near the mirror points.  $B$  is needed at the midpoint of the segment from the mirror point to the closest stored point with  $B$  less than  $B_m$ , in order to perform the numerical integration in the computation of  $I_m$ , Eq. (66), over this segment. Previously,  $B$  was found here by numerically tracing the field line from the nearest stored point. The tracing method requires 10 additional computations of the field per pitch angle (5 for each mirror point) and therefore could consume a significant fraction of the total computation when several pitch angles are considered. The doubling of speed quoted here is for eight pitch angles.

#### 2.2.1.4 Properties of Invariants

In an attempt to get a feel for the dipole-equivalent parameters, I have been conducting studies of their properties vs. equatorial distance, equatorial pitch angle, and local time. I have, at midnight, noon, and dawn local times, computed the energy-independent dipole-equivalent parameters for the quiet Hilmer-Voigt + dipole field, for 25 equatorial distances, at selected pitch angles. According to my definition above, these differ from the dipole-equivalent invariants, by substitution of the energy-independent momentum ratio for the energy. Chiefly the following were examined:

- a. How do the dipole-equivalent parameters compare with the corresponding observed parameters?
- b. How does the dipole-equivalent  $L$  vary with pitch angle; how variable is it compared to the McIlwain  $L$ ?

Figure 34 shows the dipole-equivalent  $L$ , as a percent difference from the equatorial distance  $r$ , for midnight and noon local times. We see that the percent difference becomes steadily increasingly negative as  $r$  increases, except for large  $r$  at midnight. In an azimuthally symmetric field, there should be no shell spitting; particles found on a given field line at one longitude will remain together at all other longitudes. Therefore, the third invariant, and hence the dipole-equivalent  $L$ , should be independent of pitch angle. The observed variation with pitch angle therefore reflects the asymmetry, which we expect to grow with distance. Except at the largest distances, the variation of the dipole-equivalent  $L$  with pitch angle is generally much smaller than the relative difference between  $L$  and  $r$ . The trends are similar for the three local times, except that the variation with pitch angle is smaller at dawn, while the trend vs pitch angle is reversed at noon from what it is at midnight; the smallest magnitude difference occurs for the lowest pitch angles at noon, and for the highest pitch angles at midnight.

Figure 35 shows the McIlwain  $L$  percent difference from equatorial crossing distance, for the same cases as shown in Figure 34. In contrast to the dipole-equivalent, the McIlwain  $L$  variations with pitch angle are larger than its variations with distance. The McIlwain  $L$  exhibits, at small  $r$ , a pitch angle dependence which is due to the non-dipole character of the field. At these distances the equatorial field is weaker than the dipole, causing  $L$  to be larger for high pitch angles than for low pitch angles. The dipole-equivalent  $L$ , by comparison, depends negligibly on pitch angle at the smaller distances, because the field is approximately independent of local time. At large distances, shell splitting influences both  $L$  parameters similarly:  $L$  increases with increasing pitch angle at midnight, but decreases at noon. The noon dependence at large distances is the reverse of the dependence at smaller distances, producing the crossover in the bottom panel.

Figure 36 shows the difference between the equatorial dipole-equivalent pitch angle and the actual equatorial pitch angle. Although the difference is less than  $10^\circ$ , the variation is not monotonic with pitch angle, depends more on local time than the dipole-equivalent  $L$ , and is quite complex.

Figure 37 shows the ratio of dipole equivalent momentum to the actual momentum. For non-relativistic particles, the corresponding energy ratio is the square of the momentum ratio. The variations with  $r$  and pitch angle are nearly independent of local time. For all three local times, the maximum ratio is  $\sim 1.3$ , indicating, for non-relativistic particles, that the maximum % difference between dipole-equivalent and actual energies is  $\sim 70\%$ .



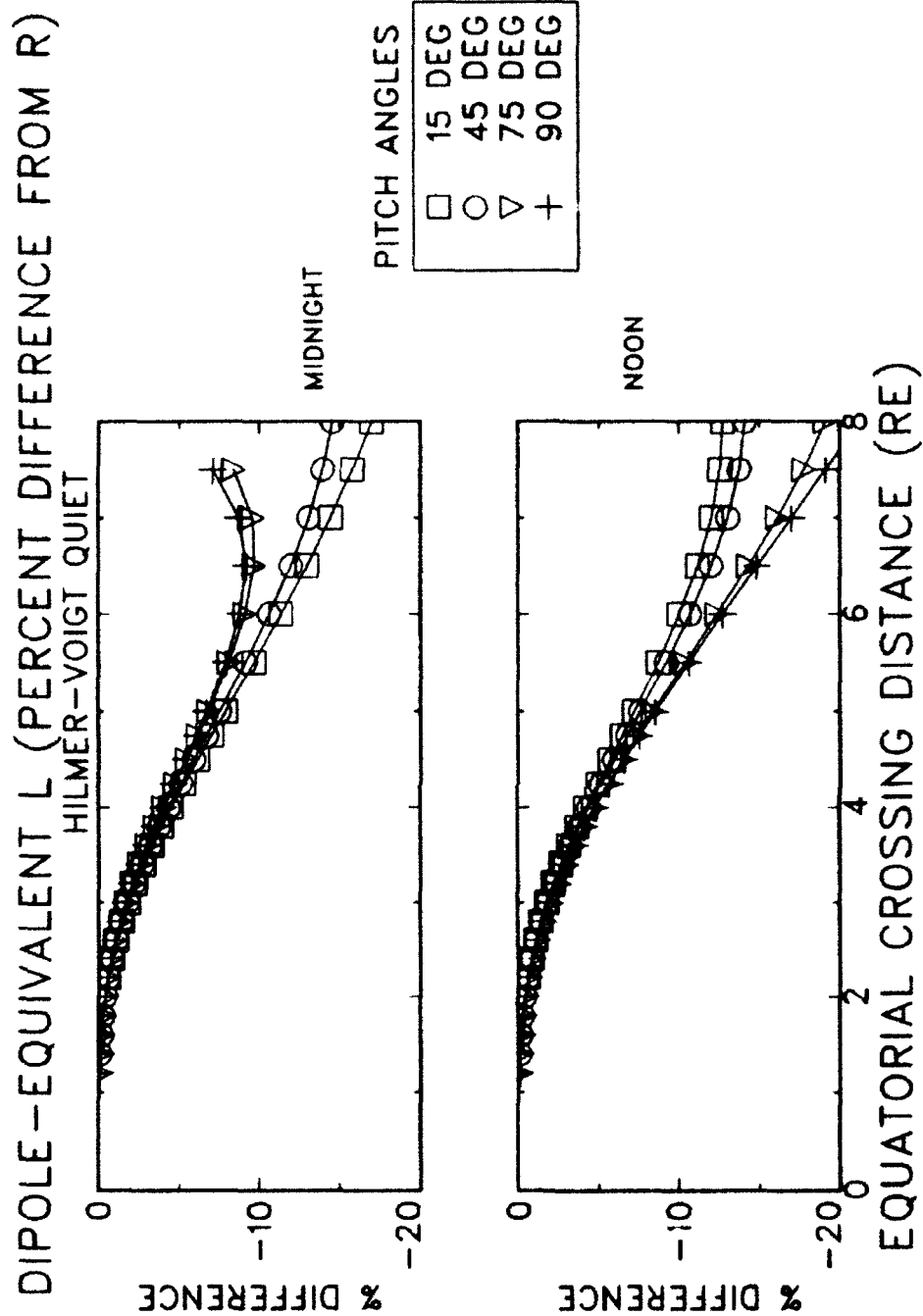


Figure 34. Dipole-equivalent L, as percent difference from the equatorial crossing distance.

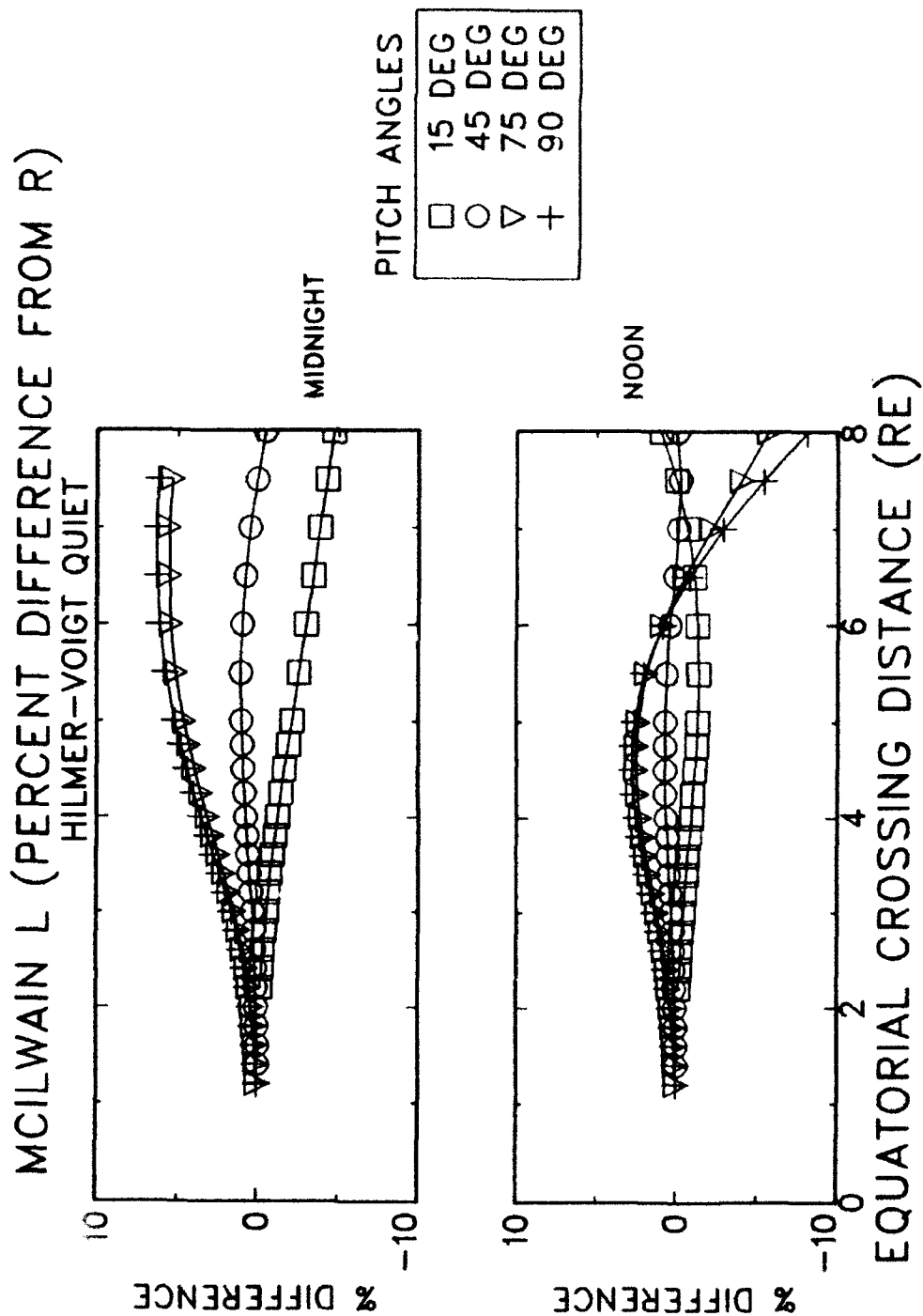
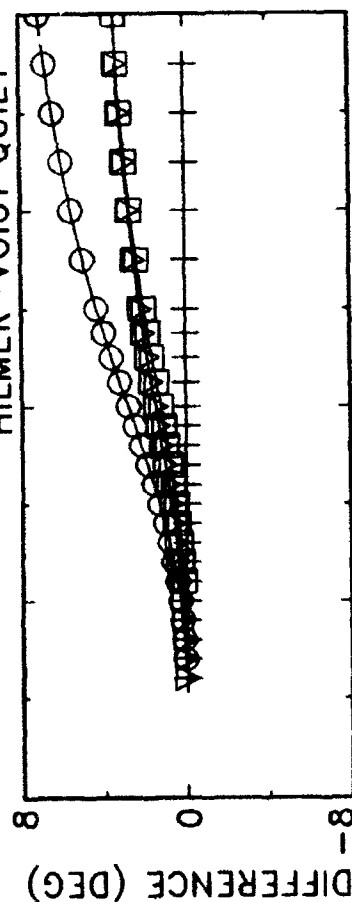


Figure 35. McIlwain L, as percent difference from the equatorial crossing distance.

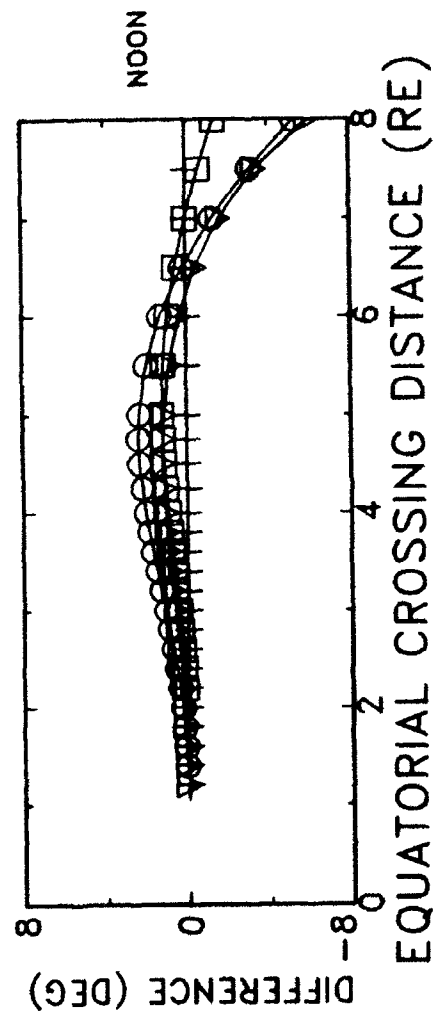
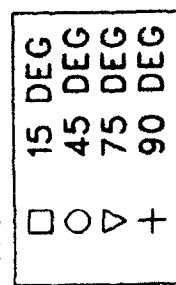
# DIPOLE-EQUIVALENT PITCH ANGLE (DIFF. FROM ACTUAL)

HILMER-VOIGT QUIET



MIDNIGHT

PITCH ANGLES



NOON

EQUATORIAL CROSSING DISTANCE (RE)

Figure 36. Dipole-equivalent pitch angle (difference from actual).

# DIPOLE-EQUIVALENT MOMENTUM (RATIO TO ACTUAL)

HILMER-VOIGT QUIET

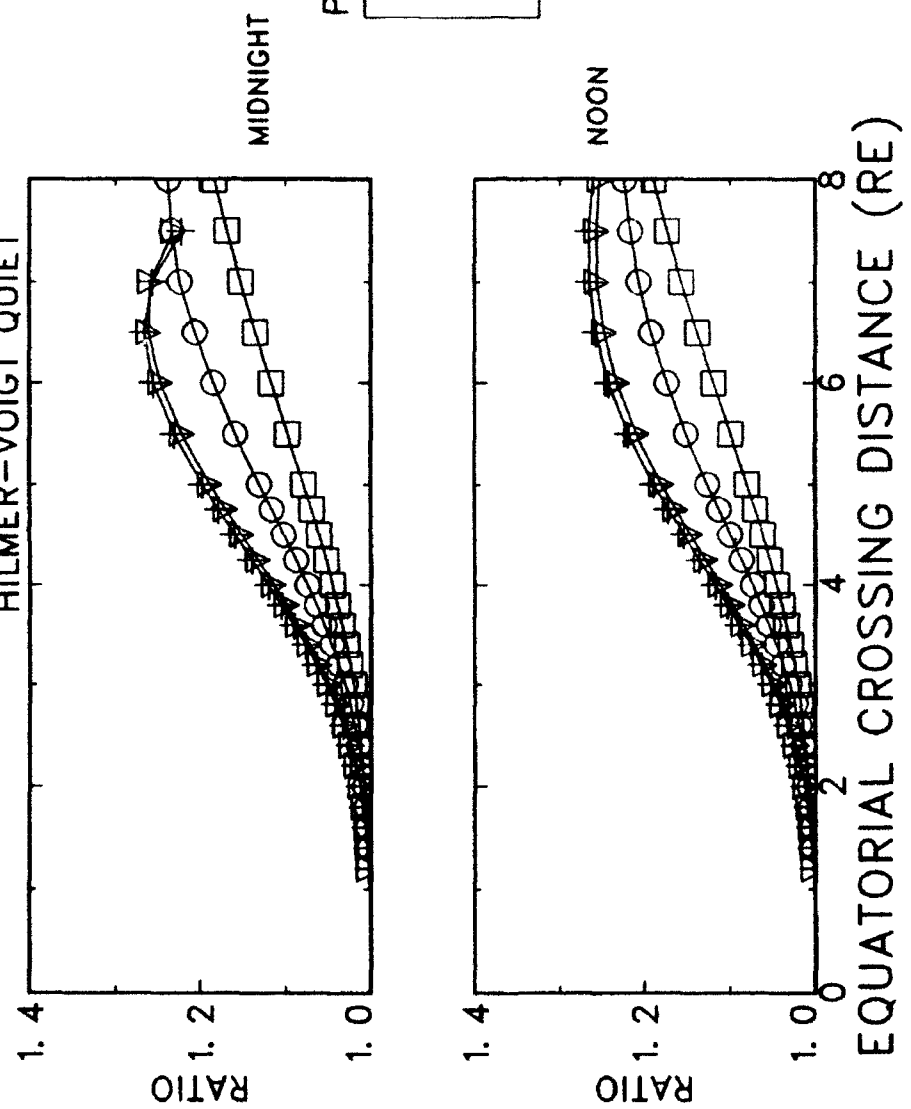


Figure 37. Dipole-equivalent momentum (ratio to actual).

On 26 August 1990, a magnetic storm commenced while CRRES was near apogee in its orbit 76. Measurements of 1-10 MeV electrons by the HEEF instrument on CRRES in the near synchronous region during this orbit were sorted into bins in the dipole-equivalent invariant space. The measurements were originally sorted into bins in the McIlwain L-observed pitch angle space, where the McIlwain L was computed from the Olson-Pfizer static magnetic field model. The resulting data base contains, for each energy channel, averaged measured fluxes for 5 degree pitch angle bins within  $1/20 R_E$  L bins. The center time and satellite coordinates of each L bin were saved. From these, the dipole-equivalent adiabatic invariants have been computed for each bin with L greater than  $5 R_E$ , using the Hilmer-Voigt model tailored for this period [Jordan, *et al.*, 1992]. Thus, each bin could be resorted into L-pitch angle bins in the dipole-equivalent space. The averaged fluxes in the original data base were fit to power law spectra in order to obtain the fluxes at a given set of dipole-equivalent energies. The data before and after the storm sudden commencement (SSC) were sorted separately. These are compared in Figure 38 as a function of the dipole equivalent L for electrons at fixed dipole equivalent energy (2.25 MeV) and equatorial pitch angle (45 degrees). If the adiabatic invariants were conserved, these two data sets would agree. Two dropouts after the SSC are evidence of dynamic nonadiabatic variations. Because of the off-equatorial location of CRRES, data at higher equatorial pitch angles were not sufficiently available after the SSC. Note also that the dipole-equivalent L for this period (4.2-5.7  $R_E$ ) is generally lower than the McIlwain L (5-6.7  $R_E$ ), consistent with what is seen in Figures 34 and 35.

## 2.2.2 Dose Modeling and Analysis Support

### 2.2.2.1 Dose Calculations

Before the CRRES launch, there was interest in simulating the data and creating mock data files for several of the instruments (Figures 39 and 40), including the SpaceRAD Dosimeter. In order to do this, we slightly modified the Yates and Rothwell dose code presently in use here at PL. The code takes a given orbit, computes the fluence from the NASA trapped radiation models, and then calculates the dose deposited at the center of an aluminum sphere. For the dosimeter, we specified the "aluminum sphere" radius to be the thickness of the dome surrounding the detector; the fluence and dose experienced by each detector were calculated only for specific electron and proton energy ranges expected to contribute to the HILET or LOLET dose for that detector. These parameters are given in Table 18. Some prelaunch files were produced. Following the launch, we began to produce the model doses per orbit based on orbital parameters from the ephemeris files. In addition, we kept a cumulative total of each of the HILET and LOLET channels (Table 19). Additionally, we produced plots of 10-orbit sums of Dose (Figure 41). These Tables and plots were regularly updated as new ephemeris files became available.

In addition to this work, dose was calculated for two special cases. The dose/day over one week of the DMSP F7 orbit was calculated for both solar minimum and maximum conditions. Secondly, dose tables were generated (Table 20) for the CRRES SpaceRad dosimeter vs. L and  $B/B_0$ . Since the Yates-Rothwell code computes dose per orbit, a driver program wrote a bogus orbit file with L and  $B/B_0$  set constant. The orbit file contains 5 points, spaced at 15 minute intervals, resulting in a one hour "orbit".

# ELECTRON DISTRIBUTION FUNCTION

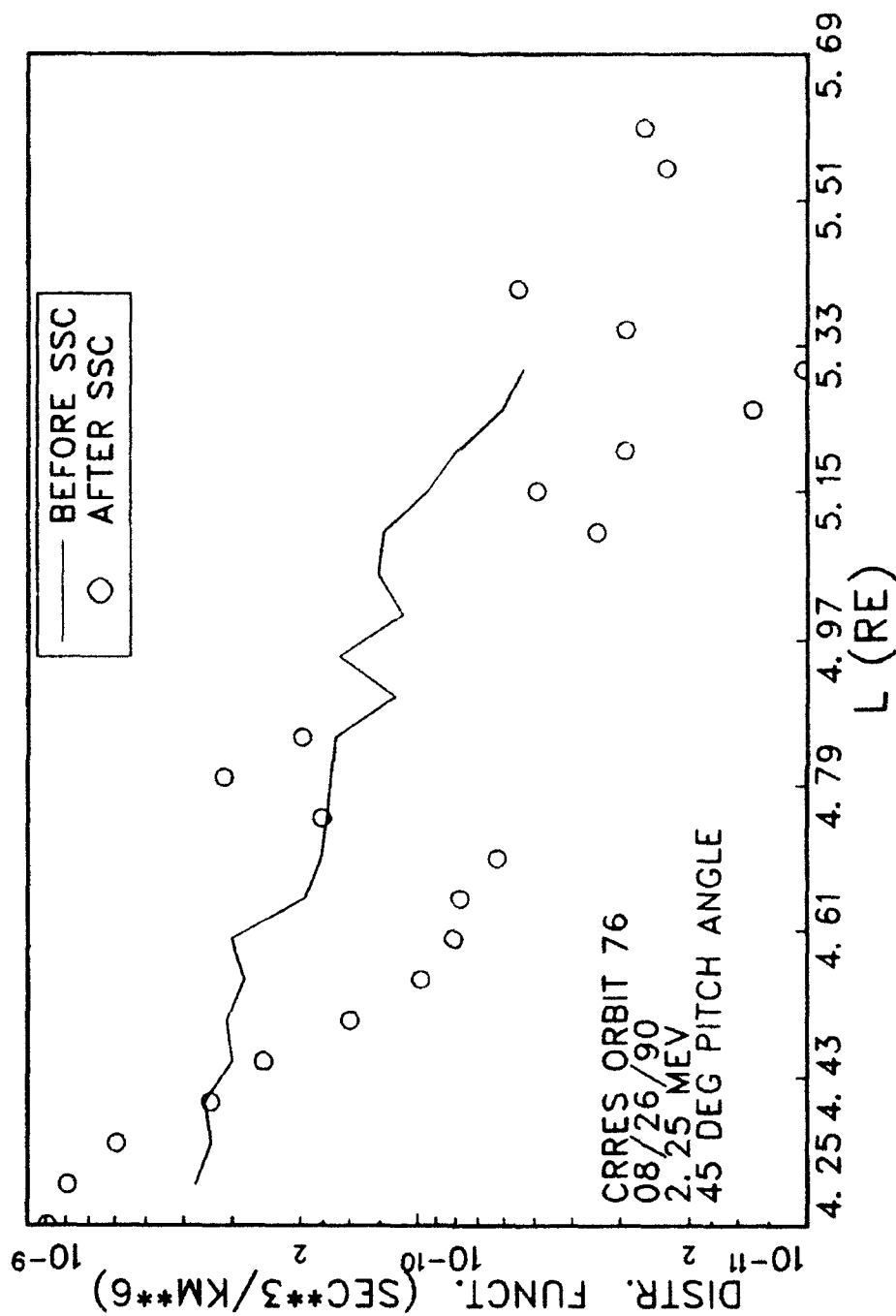


Figure 38. Electron distribution function, before (line) and after (symbols) the 8/26/90 sudden storm commencement.

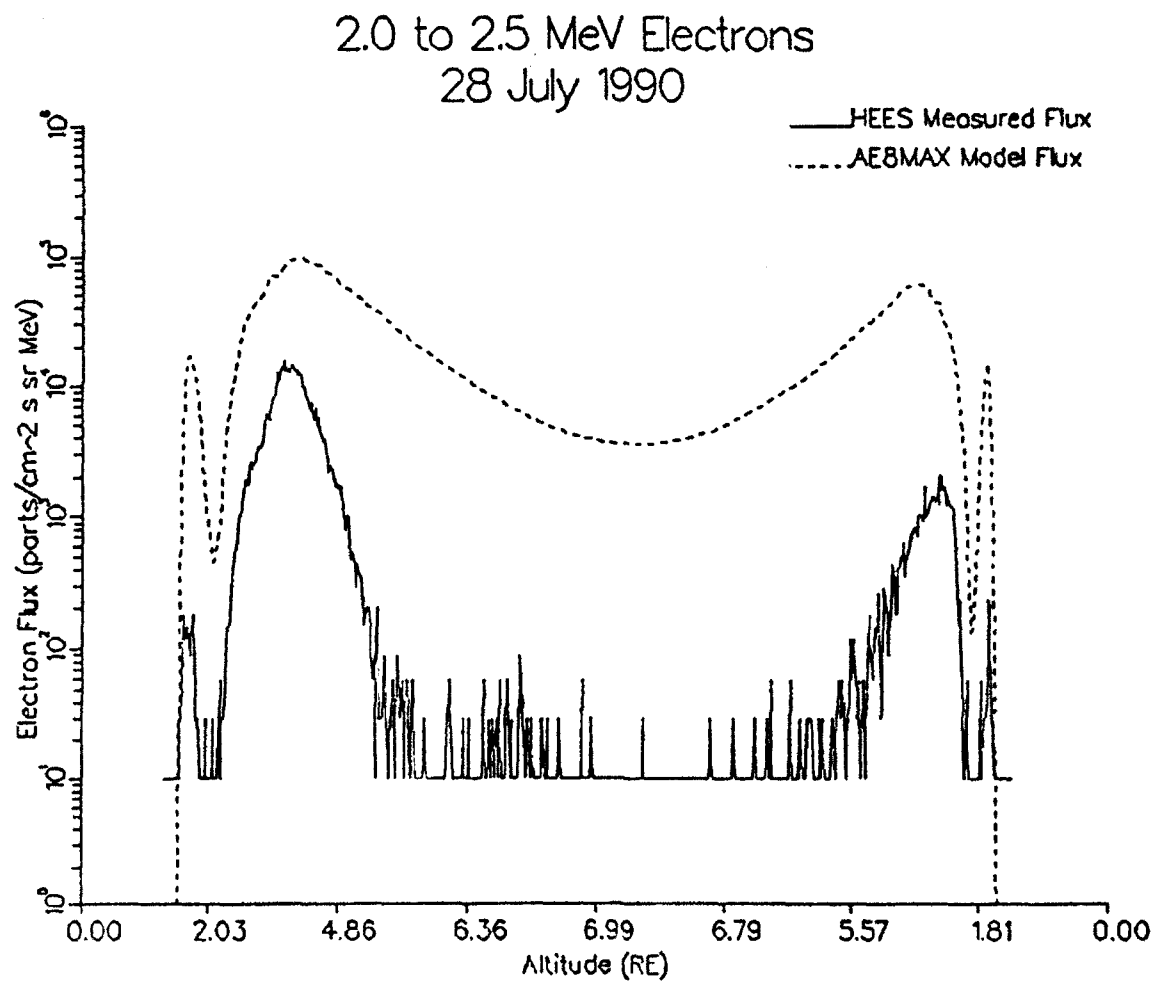
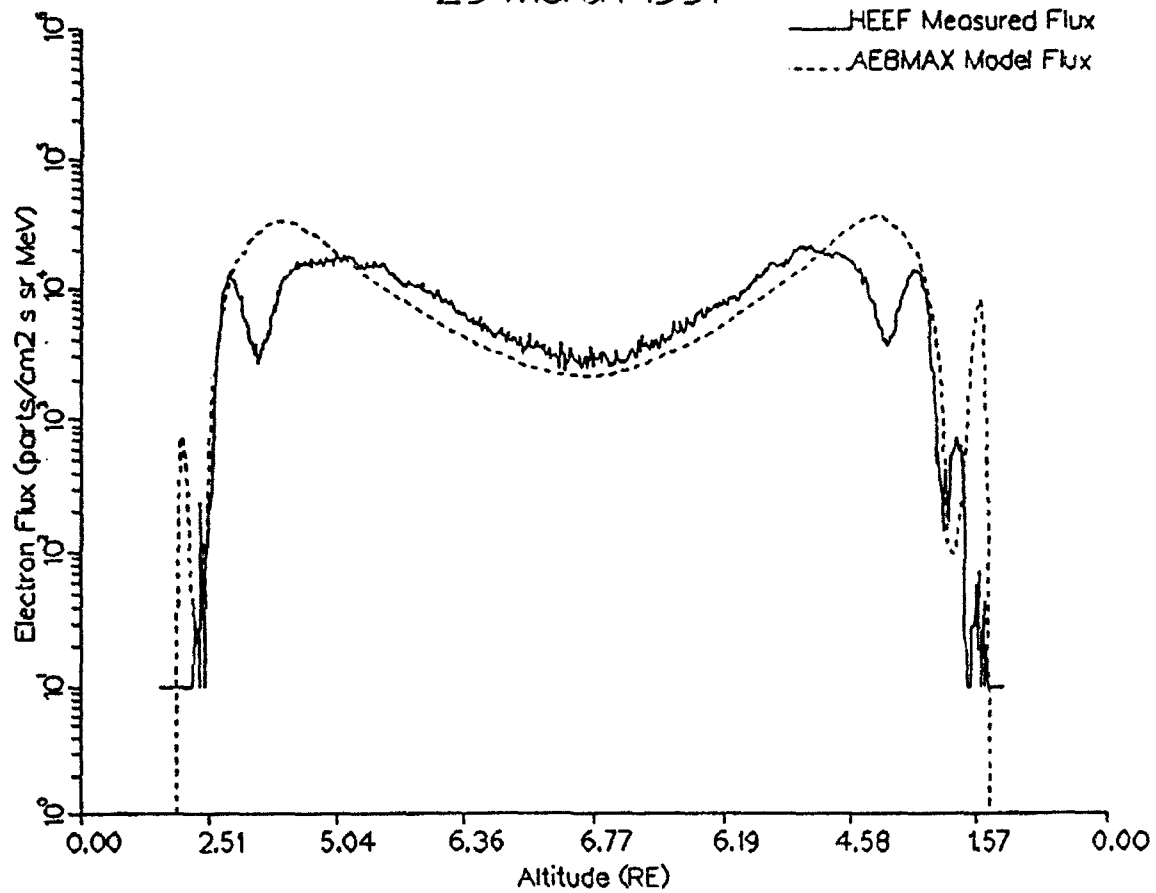


Figure 39. Flux predicted for the CRRES HEEF 2.0 to 2.5 MeV electron channel based on the NASA model AE8MAX, along with the measured data, before the March 1991 storm.

# 2.0 TO 2.5 MeV ELECTRONS 29 March 1991



**Figure 40.** Flux predicted for the CRRES HEEF 2.0 to 2.5 MeV electron channel based on the NASA model AE8MAX, along with the measured data, after the March storm.



**TABLE 18. HILET and LOLET Proton and Electron Energy Ranges**

Det. #	Dome Thickness (g/cm <sup>2</sup> )	LOLET		HILET
		Electrons	Protons	Protons
1	0.55	1.0-11.25	130-625	20-130.0
2	1.55	2.5-11.25	135-625	35-134.5
3	3.05	5.0-11.25	140-625	51-140.5
4	5.91		155-625	75-140.5

#### 2.2.2.2 Transformation from L, B/B<sub>0</sub> to Geographic Coordinates

Although radiation belt properties are normally organized by L and B/B<sub>0</sub>, it is necessary, for practical engineering applications, to display these on a geographic grid. Therefore, software was developed for mapping L and B/B<sub>0</sub> to geographic coordinates. Tables were generated, for specified longitudes, depicting geographic latitude and radial distance as functions of L and B/B<sub>0</sub>. These tables were generated for L values in the range 1.1 to 7.0 R<sub>E</sub>, in steps of 0.05 R<sub>E</sub>, and the following values of B/B<sub>0</sub>:

1.0	1.004	1.02	1.046	1.085	1.14	1.2
1.3	1.4	1.52	1.69	1.88	2.1	2.4
2.73	3.13	3.67	4.35	5.02	6.1	7.41

For each point on the grid, locations were computed in both the northern and southern magnetic hemispheres.

Program DRVTBL performs the transformation by an iterative procedure in which, for an estimated geographic position (radius and latitude), L, B/B<sub>0</sub>, and their partial derivatives with respect to radius and latitude, are computed. If the computed L and B/B<sub>0</sub> are sufficiently close to the desired values, the procedure is terminated. Otherwise, corrections to the estimated radius and latitude are computed by solution of the simultaneous linear equations constructed from the residuals (differences between the computed and desired L and B/B<sub>0</sub>) and the partials. The process is then repeated with the new estimates, until, through further iteration, the computed L and B/B<sub>0</sub> are sufficiently close to the desired values. The "sufficiently close" condition for L is 0.005 R<sub>E</sub>, while the condition for B/B<sub>0</sub> is as follows:

$B/B_0 < 1.14$	0.00005
$1.14 \leq B/B_0 < 1.4$	0.0005
$1.4 \leq B/B_0 < 7.41$	0.005
$B/B_0 \geq 7.41$	0.006

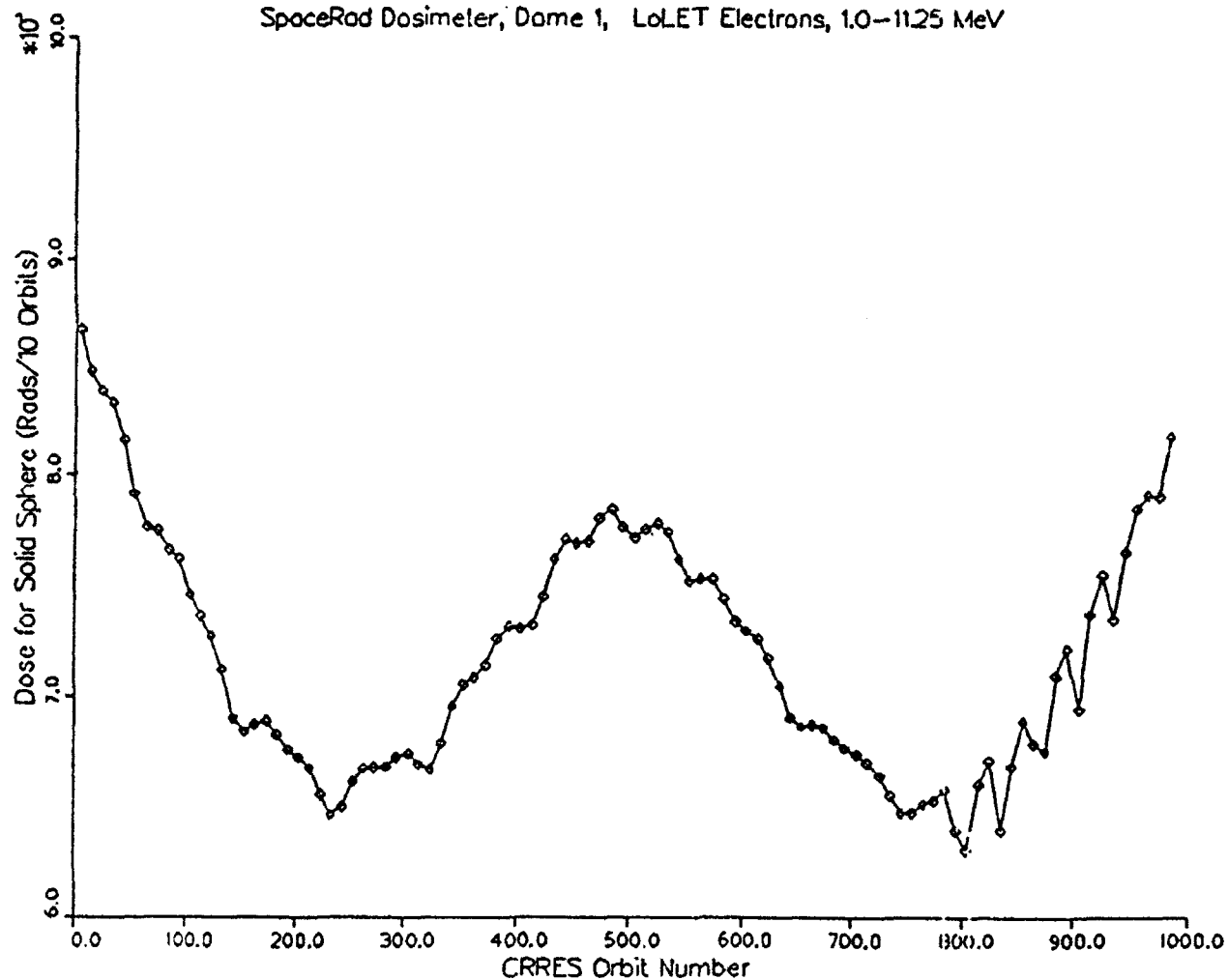
The initial guess is made by applying a dipole model, for which B/B<sub>0</sub> is known analytically as a function of magnetic colatitude and L is a known analytic function of radius and magnetic colatitude. The magnetic colatitude is found by Newton-Raphson iteration of the dipole expression for B/B<sub>0</sub>, starting with an initial guess of 45° if looking for the northern solution, or 135° if looking for the southern solution. Once the magnetic colatitude  $\theta$  is found, the radius is computed straightforwardly from

TABLE 19. Sample of Model Dose Tables Produced for the CRRES SpaceRad Dosimeter

Electron and proton fluences and dose for each of the HILET and LOLET channels along with cumulative dose through all orbits are given.

DEPTH DOSE PROFILES FOR THE DOSIMETER LOLET AND HILET CHANNELS USING AERMAX AND AP8MAC							
Orbit N/number	Omni/Directional Fluence (p/cm <sup>2</sup> /cm <sup>2</sup> )	Energy Range (MeV)	Al Dome Thickness (gm/cm <sup>2</sup> )	Dose for		Cumulative Dose	
				Solid Sphere (Rads)	LoLet Dose		
0	5.250E+10	1.0- 11.25	.55	9.592E+02	9.596E+02	9.596E+02	
0	5.967E+06	130.0-625.00	.55	3.506E-01			
0	2.870E+09	2.5- 11.25	1.55	2.579E+01	2.611E+01	2.611E+01	
0	5.625E+06	135.0-625.00	1.55	3.174E-01			
0	8.377E+06	5.0- 11.25	3.05	6.769E-03	3.077E-01	3.077E-01	
0	5.303E+06	140.0-625.00	3.05	3.009E-01			
0	4.447E+06	155.0-625.00	5.91	2.341E-01	2.431E-01	2.431E-01	
0	5.584E+07	20.0-130.00	.55	1.770E+01		1.770E+01	
0	2.510E+07	35.0-134.50	1.55	4.517E+00		4.517E+00	
0	1.685E+07	51.0-140.50	3.05	2.301E+00		2.301E+00	
0	1.199E+07	75.0-155.50	5.91	1.463E+00		1.463E+00	
1	3.866E+10	1.0- 11.25	.55	7.059E+02	7.064E+02	1.666E+03	
1	9.021E+06	130.0-625.00	.55	5.279E-01			
1	2.115E+09	2.5- 11.25	1.55	1.907E+01	1.955E+01	4.566E+01	
1	8.515E+06	135.0-625.00	1.55	4.798E-01			
1	6.197E+06	5.0- 11.25	3.05	5.017E-03	4.626E-01	7.703E-01	
1	8.038E+06	140.0-625.00	3.05	4.576E-01			
1	5.767E+06	155.0-625.00	5.91	3.698E-01	3.698E-01	6.129E-01	
1	3.011E+07	20.0-130.00	.55	2.471E+01		2.471E+01	
1	3.656E+07	35.0-134.50	1.55	6.414E+00		6.414E+01	
1	2.474E+07	51.0-140.50	3.05	3.343E+00		1.093E+01	
1	1.780E+07	75.0-155.50	5.91	2.081E+00		3.343E+00	
2	5.435E+10	1.0- 11.25	.55	9.960E+02	9.962E+02	3.544E+00	
2	2.694E+06	130.0-625.00	.55	1.591E-01		2.662E+03	
2	3.029E+09	2.5- 11.25	1.55	2.742E+01	2.757E+01	7.322E+01	
2	2.526E+06	135.0-625.00	1.55	1.476E-01			
2	9.205E+06	5.0- 11.25	3.05	7.434E-03	1.441E-01	9.144E-01	
2	2.369E+06	140.0-625.00	3.05	1.367E-01			
2	1.957E+06	155.0-625.00	5.91	1.103E-01	1.103E-01	7.232E-01	
2	2.799E+07	20.0-130.00	.55	8.759E+00		5.117E+01	
2	1.254E+07	35.0-134.50	1.55	2.305E+00		2.305E+01	
2	8.324E+06	51.0-140.50	3.05	1.132E+00		1.324E+01	
2	5.740E+06	75.0-155.50	5.91	6.955E-01		6.776E+00	
3	4.969E+10	1.0- 11.25	.55	9.072E+02	9.076E+02	4.239E+00	
3	6.861E+06	130.0-625.00	.55	3.983E-01			
3	2.702E+09	2.5- 11.25	1.55	2.434E+01	2.471E+01	3.570E+03	
3	6.472E+06	135.0-625.00	1.55	3.684E-01		9.793E+01	
3	7.917E+06	5.0- 11.25	3.05	6.399E-03	3.555E-01	1.270E+00	
3	6.105E+06	140.0-625.00	3.05	3.491E-01			
3	5.130E+06	155.0-625.00	5.91	2.817E-01	2.817E-01	1.005E+00	
3	5.662E+07	20.0-130.00	.55	1.726E+01		6.843E+01	
3	2.746E+07	35.0-134.50	1.55	5.022E+00		1.826E+01	
3	1.892E+07	51.0-140.50	3.05	2.671E+00		9.447E+00	
3	1.360E+07	75.0-155.50	5.91	1.585E+00		5.824E+00	

NASA Model Dose Summed Over 10 Orbits  
 SpaceRad Dosimeter, Dome 1, LoLET Electrons, 1.0-1125 MeV



**Figure 41.** Dose calculated at the center of the LoLet Dome 1 electrons summed over 10 orbits at a time.

**TABLE 20.** Hourly Depth Dose Profiles for the Dosimeter LOLET and HILET Channels using AE8MAX and AP8MAC

L-shell	B/B <sub>0</sub>	Omnidirectional Fluence (parts/cmsq)		Energy Range (MeV)	Al Dome Thickness (gm/cmsq)	Dose for Solid Sphere (Rads)
1.15	1.0000	1.175E+05	e	1.0- 11.25	0.55	2.592E-03
1.15	1.0000	2.549E+04	e	2.5- 11.25	1.55	3.222E-04
1.15	1.0000	1.297E+05	p	20.0-130.00	0.55	2.315E-02
1.15	1.0000	1.060E+05	p	35.0-134.50	1.55	1.781E-02
1.15	1.0000	8.133E+04	p	51.0-140.50	3.05	1.163E-02
1.15	1.0000	5.402E+04	p	75.0-155.50	5.91	6.259E-03
1.15	1.0040	1.104E+05	e	1.0- 11.25	0.55	2.436E-03
1.15	1.0040	2.396E+04	e	2.5- 11.25	1.55	3.028E-04
1.15	1.0040	1.086E+05	p	20.0-130.00	0.55	1.946E-02
1.15	1.0040	8.879E+04	p	35.0-134.50	1.55	1.491E-02
1.15	1.0040	6.812E+04	p	51.0-140.50	3.05	9.975E-03
1.15	1.0040	4.525E+04	p	75.0-155.50	5.91	5.767E-03
1.15	1.0200	8.401E+04	e	1.0- 11.25	0.55	1.853E-03
1.15	1.0200	1.824E+04	e	2.5- 11.25	1.55	2.307E-04
1.15	1.0200	5.213E+04	p	20.0-130.00	0.55	9.412E-03
1.15	1.0200	4.261E+04	p	35.0-134.50	1.55	6.862E-03
1.15	1.0200	3.269E+04	p	51.0-140.50	3.05	4.960E-03
1.15	1.0200	2.171E+04	p	75.0-155.50	5.91	2.712E-03
1.15	1.0460	2.827E+04	e	1.0- 11.25	0.55	5.795E-04
1.15	1.0460	2.269E+04	e	2.5- 11.25	1.55	8.909E-08
1.15	1.0460	8.958E+03	p	20.0-100.00	0.55	1.672E-03
1.15	1.0460	7.321E+03	p	35.0-100.00	1.55	1.299E-03
1.15	1.0460	5.620E+03	p	51.0-100.00	3.05	9.065E-04
1.15	1.0850	2.737E+04	e	1.0- 11.25	0.55	2.371E-08
1.20	1.0000	4.128E+06	e	1.0- 11.25	0.55	7.395E-02
1.20	1.0000	4.028E+06	p	130.0-625.00	0.55	2.148E-01
1.20	1.0000	1.855E+05	e	2.5- 11.25	1.55	1.196E-03
1.20	1.0000	3.890E+06	p	135.0-625.00	1.55	2.100E-01
1.20	1.0000	3.757E+06	p	140.0-625.00	3.05	1.968E-01
1.20	1.0000	3.384E+06	p	155.0-625.00	5.91	1.744E-01
1.20	1.0000	8.423E+06	p	20.0-130.00	0.55	1.121E+00
1.20	1.0000	7.523E+06	p	35.0-134.50	1.55	9.106E-01
1.20	1.0000	6.790E+06	p	51.0-140.50	3.05	7.829E-01
1.20	1.0000	5.825E+06	p	75.0-155.50	5.91	5.947E-01
1.20	1.0040	3.879E+06	e	1.0- 11.25	0.55	6.949E-02
1.20	1.0040	3.843E+06	p	130.0-625.00	0.55	2.016E-01
1.20	1.0040	1.743E+05	e	2.5- 11.25	1.55	1.124E-03
1.20	1.0040	3.712E+06	p	135.0-625.00	1.55	1.955E-01
1.20	1.0040	3.585E+06	p	140.0-625.00	3.05	1.855E-01
1.20	1.0040	3.229E+06	p	155.0-625.00	5.91	1.613E-01
1.20	1.0040	8.011E+06	p	20.0-130.00	0.55	1.105E+00
1.20	1.0040	7.155E+06	p	35.0-134.50	1.55	8.531E-01
1.20	1.0040	6.469E+06	p	51.0-140.50	3.05	7.397E-01
1.20	1.0040	5.553E+06	p	75.0-155.50	5.91	5.579E-01

$$r=L/\sin\theta^2$$

The geographic latitude is obtained by Newton-Raphson iteration of the transformation from geographic to magnetic colatitude at the specified geographic longitude, beginning with an initial guess that the geographic colatitude is equal to the magnetic colatitude.

Some problems were encountered, which led to errors in early versions of the tables:

There were problems near the magnetic equator, where the partial derivatives of  $L$  and  $B/B_0$  are very small and sometimes even 0. These occur for the small  $B/B_0$  cases, 1.0 or 1.004. Computed corrections to the estimated geographic coordinates were either infinite or abnormally large, and the process terminated, or ran astray. For the case in which the partials are zero, the current procedure is to add  $0.1^\circ$  to the latitude and leave the radius unchanged. In the case of very large corrections, detected if the corrected latitude exceeds  $65^\circ$  (north or south), we add only  $1^\circ$ , in the appropriate direction, and reduce the radius correction proportionally. These adjustments prevent the procedure from getting out of control, thus improving convergence.

Another problem, specifically for  $B/B_0=1.004$ , was convergence to the wrong hemisphere, which could occur due to the closeness of the northern and southern hemisphere solutions. To combat this, a comparison of the latitude of the current estimated point with the latitude of its conjugate is employed. If the current estimate is north of its conjugate, and we are looking for the southern hemisphere solution, then we know that we are in the wrong hemisphere; similarly, for the case in which we wish the northern hemisphere solution, and our current estimate is south of its conjugate. In these cases the search procedure is restarted with the latitude of the conjugate replacing the latitude of the current location.

A third problem has occurred for at least one case, at high  $B/B_0$ , where the search converged to a latitude greater than  $90^\circ$ , equivalent to a location  $180^\circ$  away in east longitude. At first, this was thought to be due to a large correction in latitude, so that it could be controlled by limiting the latitude correction as in the above cases. However, this failed to solve the problem, which was subsequently attributed to conjugate points being below the surface, causing detection of false minima in the magnetic field below the surface. Therefore, any time a minimum is found below the surface, the iterative procedure is given up without a solution.

#### 2.2.2.3 $L$ , $B$ , and $B_0$ for JSTAR Ephemeris

The data coverage of CRRES is limited to  $B/B_0$  less than about 10. To extend this to higher values, one can use data provided by polar orbiting DMSP satellites. These provide coverage for  $B/B_0$  up to 500 in the CRRES  $L$  range. To facilitate use of this data,  $L$ ,  $B$ , and  $B_0$  values were required for the DMSP JSTAR ephemeris files.

Since explicit computation of  $L$  and  $B_0$  requires computationally expensive field line tracing, it was decided to use available tabular or analytic methods, where possible. For  $L$ , this means the table lookup method developed by Kluge and Lenhart [1972]. Joseph Cain [private communication, 1987] has provided code implementing this method, with tables appropriate to 1990. However, the tables were generated using McIlwain's standard dipole moment,  $M=0.311653 \text{ G-R}_E^3$ . To extract  $L$  to the current dipole moment, the invariant integral  $I$  was determined from  $L$ ,  $B$ , and  $M$ , using the accurate analytic

formula provided by *McIlwain* [1966]; then,  $L$  was re-computed from  $I$ ,  $B$ , and the current dipole moment  $M'$  by the simple analytic approximation of *Hilton* [1971]. For  $B/B_0$ , an analytic model, described below, was developed and employed.

Both fast methods are valid for an internal field only. Therefore, at high  $L$  values, when the external field becomes significant, explicit field line tracing was required. Karl Pfitzer's subroutine [*Pfitzer*, 1991], was used for this purpose, since it gains efficiency by truncation of the internal magnetic field to exclude negligible terms. Comparison testing of the explicit and fast methods indicated that fast methods were sufficiently accurate for DMSP magnetic latitudes less than  $50^\circ$ . However, at lower latitudes, it was desired to eliminate points for which the conjugate was below Earth's surface. This was found to occur in the northern geographic hemisphere between  $90^\circ\text{E}$  and  $90^\circ\text{W}$  longitude. Therefore, in this region, the explicit field line tracing was used to detect those points whose conjugates were below the surface.

Program READEPHJB1 was developed to perform these calculations, driving various software modules implementing the methods mentioned above.  $L$ ,  $B$ , and  $B_0$  values were computed only for magnetic latitudes less than  $65^\circ$ , since higher latitudes were generally outside the  $L$  range of CRRES.

#### 2.2.2.4 Development of an Internal Field $B_0/B$ Model

The magnetic coordinates  $L$ -shell and  $B/B_0$  are regularly used to describe proton and electron particle distributions in near space. In an exact sense, this involves extensive line tracing calculations at every point of interest, to determine the conjugate or mirroring point, the invariant integral, and the location and value of  $B_0$ , the magnetic field minimum. At higher latitudes and at distances greater than a few Earth radii, the line tracing inevitably progresses through the external magnetic field which is subject to temporal, solar wind, and geomagnetic storm driven variations. As long as the steady internal field predominates, the effects of the varying external field on the results of line tracing are negligible, and the mapping from geographical/geocentric space to  $L$ -shell and  $B/B_0$  remains unique. Thus, up to mid-latitudes and a few Earth radii, or when zero external field values of  $L$ -shell and  $B/B_0$  are acceptable in specifying particle distributions, an analytical or tabular look-up model is warranted, in order to avoid repeated line tracing calculations at every geographic location. J. Cain has developed such an  $L$ -shell model which is quite accurate and is now regularly used at PL. In the present work, we have explored and similarly developed a fast  $B/B_0$  model that, given zero external field, generally provides an accuracy well in excess of 1%.

The model was obtained using the IGRF85 magnetic field propagated to 1/1/1990, and extensive line traces were first conducted to calculate  $B_0$  over a global grid. Since conversion between geocentric/geographic coordinates and geomagnetic coordinates is a straightforward procedure, the data were generated in eccentric dipole geomagnetic coordinates, that is, in coordinates that proved to be relatively optimal for analytical fitting with spherical harmonics. The vector dipole moment turns out to be 1853.0, -5374.4, 29760.9 nT, and the displacement from the geocenter is -398.25, 267.25, 187.06 km. Data were generated at 1.05, 1.1, 1.2, 1.5, 2, 3, 5, and 8 Emr (Emr = 6371.2 Km), from  $-80^\circ$  to  $80^\circ$  geomagnetic latitude in  $5^\circ$  steps, and  $0^\circ$  to  $350^\circ$  geomagnetic longitude in  $10^\circ$  steps. Whenever the geographical altitude happens to be negative, such as at 1.05 Emr near the equator at some longitudes, the data is discarded. In fact, since Fourier fitting is required next, the complete data set for all longitudes at that geomagnetic radial distance and latitude is ignored. The subsequent development has entailed a number of considerations that have progressively optimized the representation.

The line traces provide  $B_0$ , and a sign is appended to each  $B_0$  depending on whether the starting point itself is North or South of where  $B_0$  happens to be. A transformation is next invoked to obtain the equivalent dipole latitude  $\lambda$ , using the known dipole relationship:

$$B_0/B = \cos^6 \lambda / [1 + 3 \sin^2 \lambda]^{1/2}$$

Finally, the transformation  $\Lambda = \sin \lambda / (\text{Emr})^2$  is made to create the modeling data base consisting of GMLAT, GMLON, Emr and  $\Lambda$ . The advantage of this formulation is that the spherical harmonic representation for a pure dipole is given by unity, with no additional terms. The model coefficients thus represent the departures from the tilted eccentric dipole field due to the actual terrestrial field.

Conventional spherical harmonic fitting using 11th and higher order terms was first attempted, and gave reasonable results. However, testing for DMSP type orbits showed that a *different* data set, that concentrated on the low Earth radii alone, provided superior results, and that different analytical models would be required. This was undesirable, so further testing was conducted, which has led to a *single* model suitable for CRRES and DMSP type orbits. Initially, a special 10th order non-Legendre analytical fit is employed for each Fourier coefficient. The Fourier expansion coefficients  $C_j$  recover the bulk of the equivalent dipole latitude characteristics as follows:

$$C_j = \sum [ B_{1i} + B_{2i} \cos(B_{4i} \lambda - B_{3i}) ] / (\text{Emr})^{B_{5i}}$$

It may be of interest to observe that in this formulation the  $B_{5i}$  power law was empirically found to approximate the spherical harmonic case, except for the constant and first harmonic. The remaining coefficient residuals are then re-fit with a conventional 6th order spherical harmonic expansion. The final resulting model routine BOBM90 returns the ratio  $B_0/B$  for any specified geocentric radial distance, latitude, and longitude. Tables 21 and 22 give the ratio of *model* to *calculated*  $B_0$  for various geocentric altitudes, latitudes, and longitudes. Since these locations are not related in any way to the geomagnetic grid which was used for the data base and the original fitting, the results present a relatively random test sample. As was done for the tables, if  $B_0$  rather than  $B_0/B$  is required, the user must supply the field magnitude  $B$  at the specified location.

Although Earth's field is gradually diminishing with time, it is tacitly assumed that  $B_0/B$  will remain relatively constant over many decades. Some simple tests with earlier field models, or IGRF85 propagated to other epochs, should resolve this issue of accuracy. Our initial product provides an internal field dominated  $B_0/B$  model, even with extremely low nano-Tesla  $B_0$  values thence obtainable with reasonable fidelity. Additional rapid models can be developed for epochs greatly removed from 1990, and external field effects may be included by determining different sets of coefficients for different seasons and universal times.

**TABLE 21. Ratios of Model  $B_0$  to IGRF85 Computed  $B_0$  for Selected Geographic Locations**  
The IGRF85 Computed values of  $B_0$  are included for reference

400 KM		Longitude (E)										
LAT/ $B_0$	0	30	60	90	120	150	180	210	240	270	300	330
60. $B_0$	1.032 537	1.022 755	1.009 867	1.046 975	1.021 1138	.984 1236	.952 949	.999 430	.968 112	.954 33	1.036 58	.945 231
45. $B_0$	1.000 4474	1.001 5021	1.018 5298	1.022 5977	1.007 6651	.978 6992	.964 5623	.976 3352	1.012 1541	1.004 729	1.002 991	1.014 2634
30. $B_0$	.988 15329	.996 15785	1.009 16099	1.002 18401	.995 19024	.992 18367	.994 14880	.991 10842	1.008 7260	1.008 4395	.990 4925	1.005 10752
15. $B_0$	1.002 25596	.999 26944	1.002 27939	1.000 31363	.997 31091	.998 28313	.999 24579	.998 21012	1.003 17543	1.004 12717	1.000 12178	.999 20947
0. $B_0$	.995 22903	1.003 24978	1.000 27914	.999 30119	1.002 30165	1.003 27821	1.001 27785	1.000 26983	1.002 25246	.999 21497	1.001 19006	1.000 22892
-15. $B_0$	1.001 13191	1.006 13712	1.002 16032	1.006 16304	1.000 16748	.998 17008	1.000 20060	1.003 22502	.996 23474	1.001 23220	1.000 20676	.999 17337
-30. $B_0$	1.005 6224	.987 5427	1.013 5567	1.027 4793	1.005 4742	.981 5703	.990 8404	1.000 11778	1.001 14680	1.003 16996	1.000 16017	1.005 10532
-45. $B_0$	.993 2652	.986 1767	1.005 1211	1.026 660	1.006 515	.980 809	.995 1805	1.002 3636	1.011 6009	.996 8488	1.006 8556	1.005 5177
-60. $B_0$	1.001 897	1.038 426	.995 149	.968 28	.932 8	.966 23	1.000 146	1.006 574	1.003 1442	1.002 2530	1.022 2770	1.004 1799

2000 KM		Longitude (E)										
LAT/ $B_0$	0	30	60	90	120	150	180	210	240	270	300	330
60. $B_0$	.982 262	.984 412	.976 521	.979 617	.991 695	1.014 680	1.034 483	1.055 217	.981 62	.955 20	1.038 30	.948 106
45. $B_0$	.995 2122	.986 2631	.988 2958	.989 3378	.999 3714	1.008 3691	1.017 2905	1.014 1727	.990 807	.978 412	1.041 513	1.028 1198
30. $B_0$	1.002 7044	.997 7803	.994 8412	.992 9508	.998 9988	1.005 9614	1.009 7975	1.003 5776	.995 3727	.990 2359	1.022 2581	1.032 4821
15. $B_0$	1.005 12088	1.003 12960	.998 13946	.998 15460	.999 15696	1.001 14759	1.003 13167	1.001 11205	.996 8989	.993 6664	1.013 6538	1.016 9771
0. $B_0$	.996 12083	.996 12785	1.000 14004	1.001 14922	1.001 14978	1.000 14369	1.000 14375	1.000 14129	.999 13166	.995 11271	1.004 10388	1.002 11827
-15. $B_0$	.992 8070	.987 7979	.994 8549	.996 8467	1.000 8427	1.003 8735	1.002 10182	1.000 11723	1.000 12558	1.001 12403	1.000 11362	.998 9890
-30. $B_0$	.999 4124	.988 3439	.985 3164	.979 2662	1.000 2518	1.011 2988	1.006 4335	.999 6212	.997 7988	1.004 9183	1.008 8675	1.009 6258
-45. $B_0$	1.027 1674	1.023 1061	.973 676	.932 386	.991 303	1.038 451	1.020 965	.993 1957	.985 3273	.998 4458	1.025 4420	1.033 2960
-60. $B_0$	1.096 472	1.136 209	1.025 69	.889 15	.919 6	1.069 16	1.027 85	.974 315	.959 760	.989 1243	1.035 1325	1.060 913



**TABLE 22. Ratios of Model  $B_0$  to IGRF85 Computed  $B_0$  for Selected Geographic Locations**  
The IGRF85 Computed values of  $B_0$  are included for reference

10000 KM LAT/ $B_0$	Longitude (E)											
	0	30	60	90	120	150	180	210	240	270	300	330
60. $B_0$	.997 27	.962 55	.942 85	.948 109	.977 116	1.018 99	1.051 63	1.057 27	1.006 9	.963 3	1.059 3	1.037 10
45. $B_0$	1.014 218	.978 329	.962 428	.968 507	.991 539	1.020 495	1.038 370	1.030 218	.978 107	.959 61	1.043 65	1.055 119
30. $B_0$	1.018 738	.993 940	.981 1106	.985 1242	.997 1303	1.011 1240	1.019 1039	1.011 750	.981 482	.973 334	1.023 343	1.043 504
15. $B_0$	1.011 1390	1.001 1577	.995 1733	.997 1860	.999 1909	1.002 1868	1.005 1727	1.003 1471	.989 1153	.985 915	1.010 908	1.023 1130
0. $B_0$	1.000 1664	.999 1706	1.001 1751	1.000 1774	1.000 1779	1.000 1803	.999 1855	1.000 1847	.997 1715	.994 1534	1.002 1486	1.005 1588
-15. $B_0$	.995 1357	.994 1231	.992 1143	.987 1062	.999 1033	1.010 1109	1.006 1306	.999 1541	1.000 1686	1.001 1694	1.000 1630	.998 1520
-30. $B_0$	1.006 770	.998 589	.975 459	.955 368	.994 340	1.033 402	1.022 576	.996 839	.991 1100	.998 1246	1.005 1209	1.008 1011
-45. $B_0$	1.040 291	1.025 174	.961 99	.897 59	.980 50	1.073 71	1.042 141	.985 277	.968 452	.984 580	1.012 577	1.031 448
-60. $B_0$	1.104 63	1.111 26	1.007 8	.836 2	.911 1	1.126 4	1.052 15	.955 46	.927 101	.959 149	1.013 155	1.061 114

50000 KM LAT/ $B_0$	Longitude (E)											
	0	30	60	90	120	150	180	210	240	270	300	330
60. $B_0$	1.002 1	.939 1	.946 2	.972 3	.984 3	.994 3	.994 2	1.016 1	1.052 1	1.011 1	1.155 1	1.159 1
45. $B_0$	1.020 4	.974 8	.968 11	.984 13	.994 14	1.002 12	1.004 9	1.017 5	1.002 3	.994 2	1.048 1	1.077 2
30. $B_0$	1.017 16	.989 22	.983 27	.993 30	.998 31	1.002 29	1.003 24	1.009 17	.996 12	.994 9	1.021 8	1.042 11
15. $B_0$	1.010 32	.997 38	.995 42	.999 43	1.000 44	1.000 43	1.000 40	1.004 35	.997 28	.997 23	1.010 23	1.022 27
0. $B_0$	1.001 43	1.000 43	1.003 42	.999 41	1.000 40	1.001 42	1.001 44	1.000 44	1.000 42	1.000 39	1.003 38	1.006 40
-15. $B_0$	.995 37	1.002 33	1.004 28	.991 25	.998 24	1.007 27	1.006 32	.997 38	.999 41	.999 42	.999 42	.996 41
-30. $B_0$	.995 22	1.004 16	1.003 12	.975 9	.993 8	1.018 10	1.014 15	.993 21	.992 27	.993 30	.997 30	.993 27
-45. $B_0$	.996 8	1.010 5	1.011 3	.947 2	.980 1	1.040 2	1.024 4	.985 7	.978 11	.981 14	.994 14	.993 12
-60. $B_0$	.989 2	1.016 1	1.057 1	.908 1	.926 1	1.096 1	1.022 1	.966 1	.951 2	.961 3	.988 3	.991 3

### 2.2.3 HEEF-Dosimeter-GOES Electron Measurement Intercomparison

Inconsistencies have been found in the electron fluxes measured by different instruments on CRRES, and in the fluxes measured by the HEEF instrument on CRRES and the E1 instrument on GOES-7. In an extensive cross calibration of MEA and HEEF, Don Brautigam [*private communication*, 1991] found serious discrepancies between the two instruments in the region of energy overlap. This was also reported at the last CRRES Science Team Meeting (12-13 Nov., 1991) along with similar discrepancies between HEEF and the Lockheed instrument SEP. We found over an order of magnitude disagreement between the  $> 2$  MeV electron measurements made by HEEF and GOES-7 during an enhancement on 28-29 March, 1991, 4-5 days after the SSC of a major storm. In all of these cases the HEEF results are lower than the instrument with which it is being compared. While proton contamination of the instrument with the higher readings (i.e., MEA or SEP) may be the cause, we do not believe this to be the case for the GOES-7 instrument, as we will discuss below. Although CRRES and GOES-7 were at different locations in space, it appears, as will be demonstrated below, that this does not account for their disagreement.

Since initial HEEF calibration constants supplied to us were based on measurements made at room temperature, while typical operating temperature during the last 10 months of flight was  $-10^{\circ}$  C, Panametrics supplied us with a new set of calibrations [*Dichter and Hanser*, 1991], which also account for a temporary increase in the photomultiplier voltage which occurred between orbits 276 and 355. Application of these updated cals did not reduce the HEEF-GOES discrepancy. Since the temperature variation in the new cals reflects only the dependence of the photomultiplier tube gain, Panametrics has undertaken a search for other temperature effects, using the backup instrument which they have retained on the ground. As a result, a new set of cals is expected shortly. Using the updated cals mentioned above, we performed a comparison between the HEEF and Dosimeter data, obtaining the ratio of the predicted Dosimeter counting rates, as obtained from HEEF spectra, to the actual Dosimeter count rate. We found significant correlation with temperature.

It was suggested at the November, 1991, Science Team Meeting that a contributing cause of the cross-calibration discrepancies may be oversimplification in the extraction of fluxes from the raw counting rates. In the simplest approach, we assume that the count rate of a particular channel is the product of a geometric factor and the differential flux at some energy in the channel's response window (either the centroid or the energy of peak response). The geometric factor is derived from the calibration data assuming a flat spectrum. It was suggested that a more elaborate approach, described by *Hoyng and Stevens* [1974] be employed. Their formulation models response of an instrument channel to a spectrum of arbitrary shape, accounting for overlap in the energy response windows of different channels. We have developed an application of this method to the HEEF data for the post-March storm electron event mentioned above, but have found insignificant change in the results.

In the following, we will describe the HEEF-GOES and HEEF-Dosimeter comparisons we have made, including the application of the Hoyng-Stevens formulation in the former. Finally, we conclude that there is an unmodeled temperature effect on HEEF's response, which may be resolved by the upcoming cals.

### 2.2.3.1 GOES-HEEF Comparison

Figure 42 shows a comparison of directionally (spin-averaged) integrated electron flux above 2 MeV, derived from HEEF measurements at  $L=6.5$ , with that given by the GOES-7 E1 channel for the same period, days 80-89, 1991. The HEEF results were derived by three different methods to be described shortly. Gaps in the HEEF display occur when the counts are zero in all but the lowest energy channels, precluding reliable determination of the spectral shape by these methods.

There are two enhancements seen in the fluxes, one on days 82 and 83, which was not seen by HEEF, and a second beginning on day 87, seen by both instruments. Figure 43, which compares the GOES electron and proton channels over the same period, indicates that the proton channels also responded to the first enhancement, but not to the second. These results suggest that the first enhancement (days 82 and 83) is primarily due to protons, which contaminated the GOES electron channel, but not HEEF, due to the latter's triple coincidence counting requirement, designed to discriminate between electrons and protons. The second event, days 87-89, is recorded by both HEEF and the GOES electron channel, but not by the GOES proton channels, leading to the conclusion that, unlike the first event, this must be an electron event. The remaining discussion focusses on this event, during which GOES measured consistently 1-2 orders of magnitude higher flux than HEEF.

It has been suggested that the GOES-HEEF differences might be due to difference in location. However, it is clear that the GOES data, which covers all local time, exhibits little or no local time variation, relative to the difference between its steady level and that of HEEF. It is also possible that the flux is consistently greater at the GOES orbit simply because it is always outside the CRRES orbit. In Figure 44, a HEEF radial profile during CRRES orbit 600 is shown, when CRRES and GOES are within 3 hrs local time of each other. What we see is the falloff from the outer belt peak, i.e., a negative slope, whereas a positive slope would be desired to explain a higher flux at the GOES orbit. Plotted in the upper right-hand corner of this figure is the GOES L-shell (7.2) and flux value during this pass. The GOES-measured flux is an order of magnitude above the outer belt peak measured by HEEF. To explain such a difference in terms of radial position, one would have to assume that GOES was embedded in a different electron population, whose inner boundary lay between CRRES and GOES during the entire day 87-89 period. During the orbit 600 pass, GOES was at  $8.7^\circ\text{N}$  magnetic latitude, while CRRES varied from  $0$  to  $10^\circ\text{S}$  magnetic latitude. Thus, difference in latitude cannot explain the difference in the measured fluxes, unless there was a significant north-south hemispheric asymmetry in the population being observed. For these reasons, it is unlikely that we can explain the CRRES-GOES difference in terms of position.

The HEEF results were derived by three different methods: Hoyng-Stevens (indicated as HS in Figure 42), effective geometric factor (GFE), and simple geometric factor (GF). In the simplest of these, the simple geometric factor method, we assume a spectral-shape-independent geometric factor for each channel, such that the differential flux at the center energy  $E_{cn}$  of that channel's window is given as

$$J(E_{cn}) = C_n / GF_n \quad (70)$$

where  $n$  is the channel number,  $C_n$  is the count rate, corrected for dead time, of channel  $n$ , and  $GF_n$  is its geometric factor. The count rates were 5 minute averages over passes centered at  $L=6.5$ , one pass each for ascending and descending legs of each orbit.

# HEEF-GOES COMPARISON (> 2 MEV ELECTRONS) INTEGRAL FLUX (PART/CM\*\*2/SR/SEC)

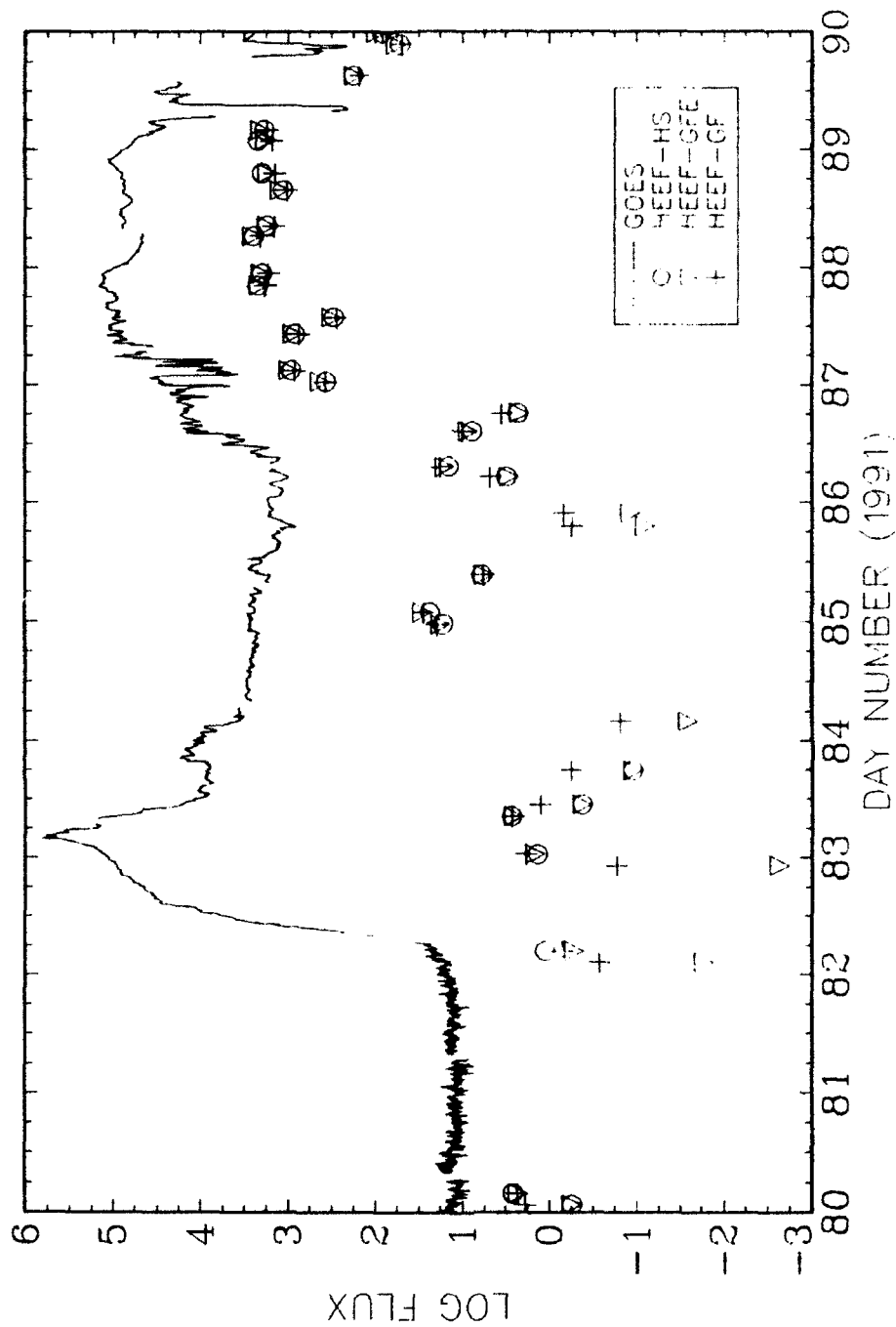


Figure 42. HEEF (L = 6.5) - GOES comparison.

# GOES PARTICLE DATA : E1 (ELECTRONS) AND P1-P7 (PROTONS)

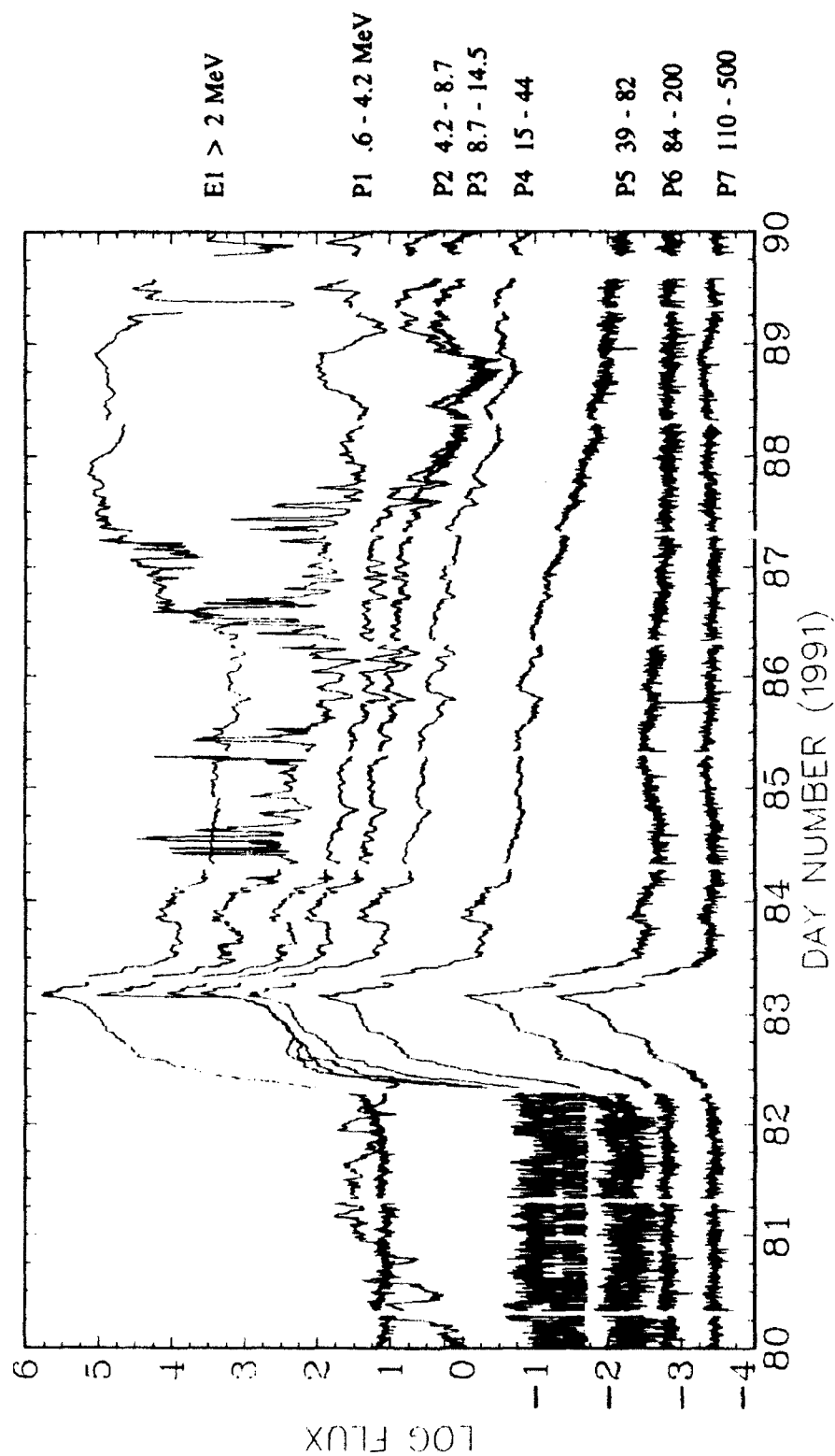


Figure 43. GOES particle data 21 - 30 March 1991.

HEEF > 2 MEV ELECTRONS ORBIT 600  
INTEGRAL FLUX (PART/CM\*\*2/SR/SEC)

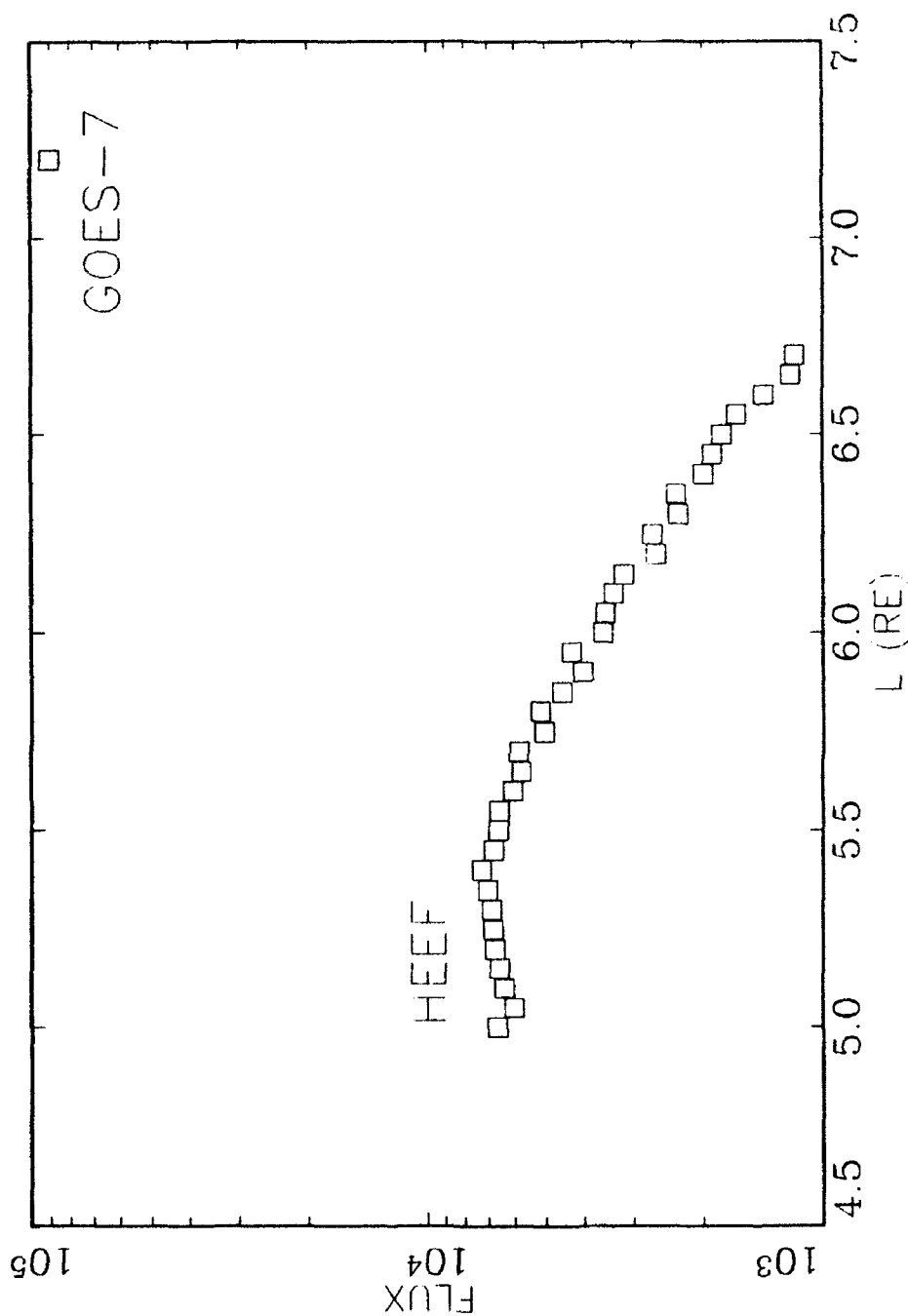


Figure 44. HEEF > 2 MeV electrons L > 5 orbit 600, and GOES measurement at L = 7.2.

The energy windows and geometric factors were derived as specified by *Dichter and Hanser* [1991], given the temperature and high voltage step, with the exception that the threshold energies were calculated by

$$E(L_n, HV_{step}, T) - L = \frac{E_0(L_n) - L}{G(HV_{step}, T)} \quad (71)$$

where  $L_n$  designates the channel (LL-L10),  $T$  is the temperature,  $E_0$  is the nominal threshold, and  $L$  is the energy loss in the two SSD detectors, estimated to be 0.56 MeV. This equation was used instead of Eq. 4.11 of *Dichter and Hanser* [1991], which neglects the energy loss in the solid state detectors, through which an electron passes before depositing the rest of its energy in the crystal. Since the response of the crystal (and subsequently the PMT) is proportional to the electron's energy at the crystal, not at the entrance to the instrument, it seems to me that the gain correction should be applied to that residual energy, rather than to the total energy of the electron before it entered the instrument. The thresholds thus computed define the boundaries of the channel energy windows, so that the upper boundary of channel  $n$ 's window is the lower boundary (threshold) for channel  $n+1$ . The center energy  $E_{cn}$  is the midpoint energy between the threshold of channel  $n$  and the threshold of channel  $n+1$ .

A corresponding correction was made in the definition of  $E'$  in Eq. 4.12, i.e.:

$$E' = G(E-L) + L \quad (72)$$

The resulting differential fluxes, at the assigned center energies, were fit to a power spectrum, which was integrated analytically to obtain the integral flux for comparison with GOES.

In the effective geometric factor approach, we allow for a spectral-shape-dependent response for each channel:

$$C_n = \int F_n(E) f(E) dE = \left[ \int F_n(E) \frac{f(E)}{f(E_{cn})} dE \right] f(E_{cn}) = GF_n' f(E_{cn}) \quad (73)$$

where  $GF_n'$  is the "effective" geometric factor for channel  $n$ ,  $f(E)$  is the differential electron spectrum, and  $F_n$  is the geometric factor of channel  $n$  for electrons of energy  $E$ :

$$F_n(E) = GF(E) R_n(E') \quad (74)$$

where  $GF(E)$  is the HEEF total effective geometric factor defined by *Dichter and Hanser* [1991], Eq. 4.5, computed by the fit polynomial given in Table 4.2 of that reference, and  $R_n(E')$  is the channel response function, specified by Eq. 4.7 and Table 4.3 of the same reference, evaluated at the energy  $E'$  given by Eq. (72) of this report.

The centroid energy  $E_{cn}$  is defined by

$$E_{cn} = \frac{\int F_n(E) E f(E) dE}{\int F_n(E) f(E) dE} \quad (75)$$

Here we have an "effective geometric factor" and centroid energy dependent on the spectral shape. We assume the spectrum to be a power law,  $\alpha E^{-\gamma}$ , with an initial guess  $\gamma=0$  (for a flat spectrum). Then for each iteration, given an estimate of the power law exponent, we compute the effective geometric factors, centroid energies, and differential fluxes at the centroid energies, which we fit to a power spectrum, obtaining a revised exponent. This process is repeated until sufficient convergence in the exponent is achieved, usually after  $\sim 5$  iterations. As with the simple geometric factor method, the final power law spectrum is integrated to obtain integral flux above the specified threshold, 2 MeV.

In the Hoyng-Stevens method, account is taken of the overlap in energy windows, as well as the steepness of the spectrum. A matrix equation relates the channel responses to the spectrum:

$$C = Ax \quad (76)$$

where  $C$  is the column matrix of count rates,  $x$  is a column matrix of integrated fluxes within selected energy intervals, and  $A$  is a rectangular matrix whose elements are given by

$$A_{ij} = \int_j dE [f(E)/x_j] F_i(E) \quad (77)$$

where  $f(E)$  is the differential spectrum,  $F_i(E)$  is the geometric factor of channel  $i$ , defined in Eq. (74), the integral is over the  $j$ th energy interval, and  $x_j$  is the integrated spectrum over the  $j$ th energy interval. The intervals discussed here are not the channel energy windows discussed earlier, but rather a set of intervals which may be chosen arbitrarily to cover the entire energy range of the problem. Any number of intervals may be selected up to the number of channels. If there are fewer intervals than channels, a least-squares approach may be used to solve the equations, although Hoyng-Stevens introduces other methods more suitable for very large matrix equations. We selected the number of intervals to be 10, the same as the number of channels, so we have a  $10 \times 10$  set of equations to be solved. The boundaries of the intervals are the same as channel thresholds, except that the lowest interval boundary was set to 1 MeV (since HEEF doesn't respond to lower energy) and the upper boundary of the highest interval was set to infinity. The matrix  $A$  depends on the spectral shape. Beginning with an initial guess of zero for the power law exponent, we compute  $A$  and solve for the interval fluxes. These are combined to form a set of integrated fluxes above the thresholds. These can be fit to a power law, since for a differential spectrum  $\alpha E^{-\gamma}$ , with  $\gamma$  greater than 1, the integrated flux above a threshold  $E_1$  is  $[\alpha/(\gamma-1)]E_1^{(1-\gamma)}$ . The resulting updated exponent is fed back into the matrix  $A$ , and the process iterated until sufficient convergence in the exponent is obtained.



We see in Figure 42 that, when HEEF levels were above noise (including the period of electron enhancement observed by both HEEF and GOES), there was very little difference between the results obtained by the three methods.

#### 2.2.3.2 HEEF-Dosimeter Comparison

To compare the HEEF and Dosimeter results, we obtained a "predicted" count rate for a given Dosimeter dome by integrating, with respect to energy, the product of the HEEF-obtained power-law-fit spectrum with the energy-dependent geometric factor for that dome. The HEEF spectrum was obtained by the simple geometric factor method described above. The energy-dependent geometric factor for each Dosimeter dome was taken to be the analytic expression given by Eq. 4.5 and Table 4.1 of the Panametrics Dosimeter calibration report. Figure 45 shows the ratio of the "predicted" to actual count rates for Dome 1, for selected orbits at  $L=5$ , averaged over  $0.05 R_E$  bins. Also shown, is the operating HEEF temperature (solid line) for those orbits plotted. Points for which the energy deposition per count in the Dosimeter was less than 200 keV were excluded, as these were assumed to be dominated by Bremsstrahlung. One can see a rough correlation between the predicted/actual count ratio and the temperature, indicating that there may be an unaccounted-for temperature dependence in the HEEF response. The correlation is more convincing in Figure 46, where we have taken the first 100 orbits, during which there was substantial temperature variation.

#### 2.2.3.3 Conclusions

There exists a serious discrepancy between the HEEF and GOES-7 electron measurements during an interesting period following the March, 1991, storm. Review of the two data sets indicates that the cause is probably neither the difference in locations of the two vehicles, nor the method of extraction of the electron spectra from the HEEF raw counts. A comparison of the HEEF and the Dosimeter data indicates a variation of relative response which correlates with temperature. Since most of the HEEF preflight calibration measurements were taken at room temperature, while the operating temperature during much of the flight was significantly lower, it is conceivable that the preflight cals do not accurately reflect the HEEF response properties during the flight. Panametrics personnel, recognizing this possibility, have performed measurements of the backup HEEF instrument at the lower temperatures actually encountered during the flight. The resulting updated calibration curves may remove the discrepancies found thus far.

#### 2.2.4 Dynamic Magnetic Field Models

##### 2.2.4.1 Models Published Before 1989

A pre-launch study of six existing magnetospheric magnetic field models was conducted. These are models of the external field, that is, the field due to the magnetospheric currents external to Earth. These models are the Olson-Pfitzer tilt dependent model, the Olson-Pfitzer dynamic model, the Mead-Fairfield model, the Tsyganenko-Usmanov model, the Tsyganenko 87 model, and the Stern parabolic magnetopause/stretched magnetosphere model. The Olson-Pfitzer tilt-dependent model is for quiet magnetosphere, and is valid only within  $15 R_E$  of Earth. The Olson-Pfitzer dynamic model encompasses disturbed, as well as quiet conditions, is valid to  $60 R_E$ , but only for zero tilt. It is driven by the magnetic index DST and the solar wind dynamic pressure. Neither model is rigorously divergence free. The Mead-Fairfield, Tsyganenko-Usmanov, and Tsyganenko 87 models are all functions of the magnetic index  $K_p$  and the dipole tilt. They are divergence free. However, the ring current model in the

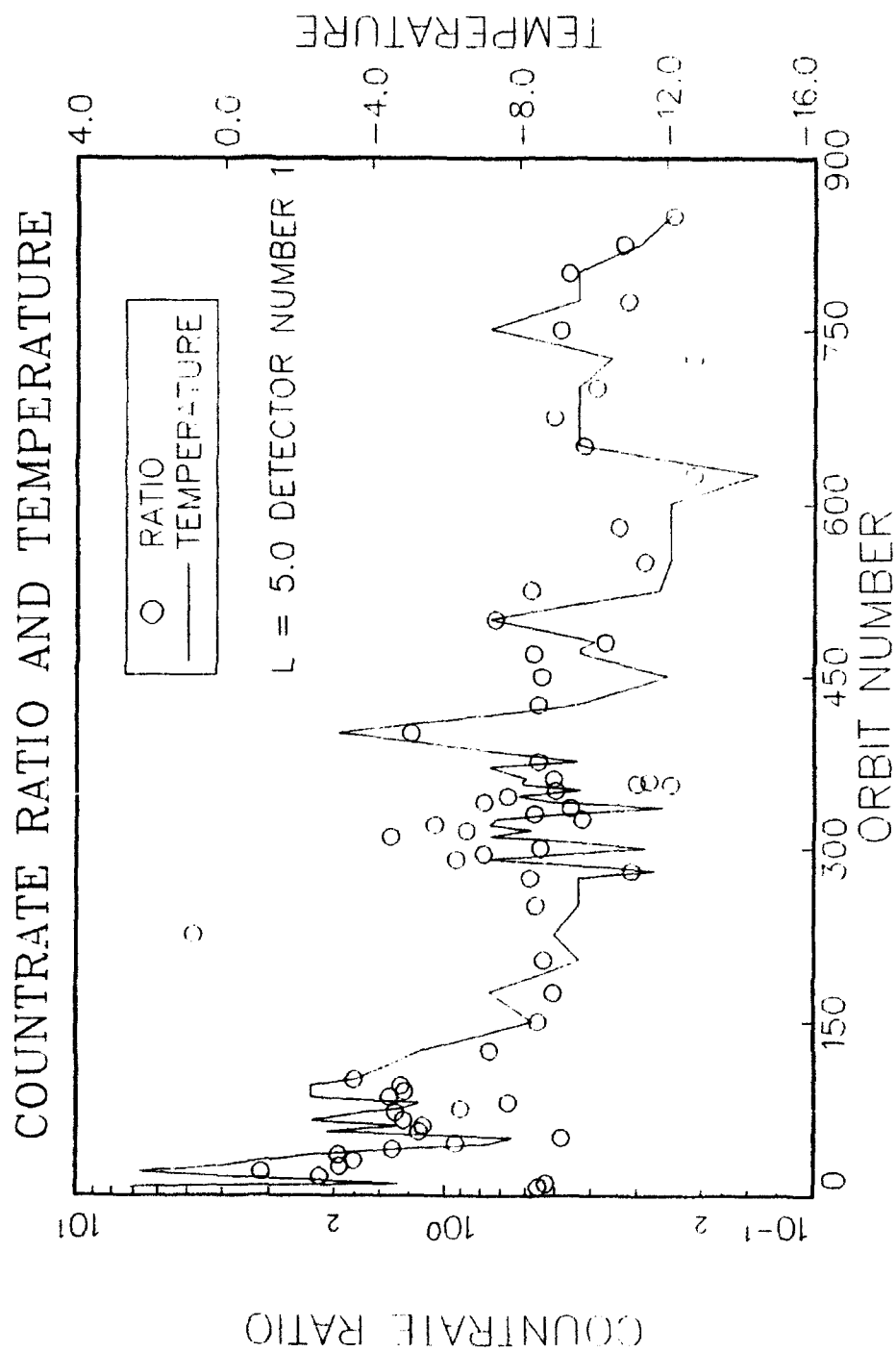


Figure 45. CRRES dosimeter count rate ratio predicted to actual (symbols) and HEEF operating temperature (line).

# COUNT RATE RATIO AND TEMPERATURE

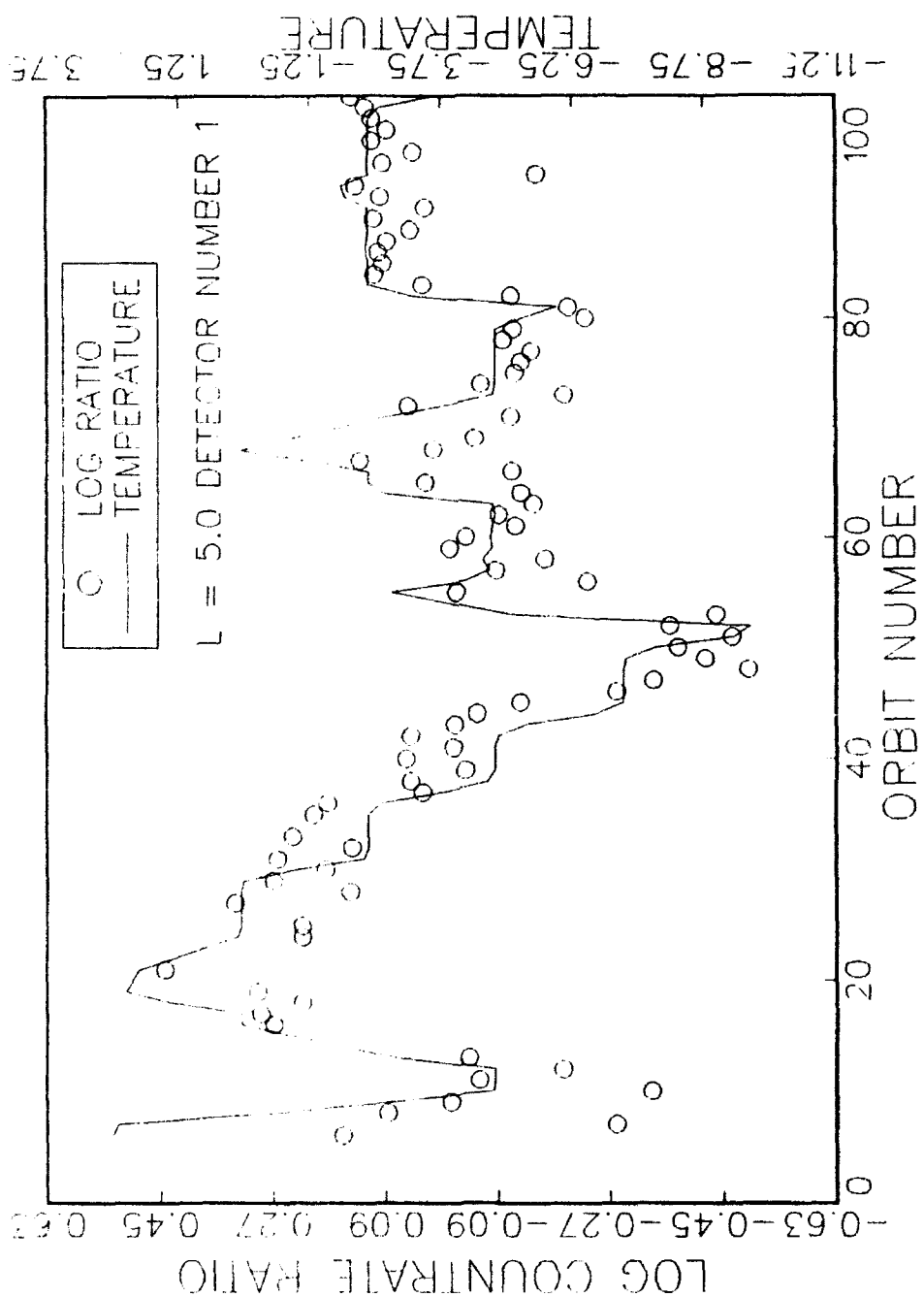


Figure 46. Same as Figure 45, except coverage limited to first 100 CRRES orbits.

Tsyganenko-Usmanov and Tsyganenko models lack a well-known feature, that the current reverses direction, from westward at higher altitudes, to eastward at low altitudes. The Stern model has an explicit magnetopause, parabolic shaped. It is a function of the standoff distance. The cross-tail field is modeled as a stretched dipole field. The ring current is of the Tsyganenko form, and therefore has the same deficiency. Unlike the other five models, the Stern model has not been fit to extensive data sets.

Since this study was performed before the CRRES launch, we compared model predictions with measurements by the SCATHA magnetometer. For these comparisons, the internal field, that due to Earth's core, was represented by the Barraclough 1975 model. For a magnetically quiet period (Figure 47), all the models agree reasonably well with the data, except the Stern model, which is not surprising, since that model was not fit extensively to data. For the others the main trend in  $\Delta B$ , the measured minus model difference, is a small overall increase from the beginning to the end of the 24-hour period shown. This increase is related to a small increase in the solar wind dynamic pressure observed during this period, slightly compressing the magnetosphere. Not surprisingly, the Olson-Pfizer dynamic model, which explicitly models such compressions, exhibits the smallest trend in  $\Delta B$ . For the Stern model, the other model which includes compression, the  $\Delta B$  overall increase (beginning to end) is also small, but this trend is overwhelmed by the large variations during the course of the day. During a substorm on the following day (Figure 48), the models deviate sometimes substantially from the measurements. The Olson-Pfizer dynamic model is marginally better than the others initially, but that may be due to its use of hourly indices, while the others depend on the 3-hourly  $K_p$  index.

#### 2.2.4.2 Models Published in 1989 or Later

##### *Tsyganenko 1989 Model*

After an initial study of the available external magnetospheric magnetic field models, we found two new models which had not been covered: Tsyganenko 1989 and Hilmer-Voigt. Thus, a subsequent study was performed to better evaluate these models along with the Olson-Pfizer Dynamic (1988) model. In fact, two similar studies were performed. The first was a comparison to SCATHA data (20 and 21 April, 1979), and the second was a comparison to CRRES data (26 August, 1990). Tsyganenko 1989 started with an axisymmetric, infinitely thin current disk for the tail current. He transformed the disk to allow for hinging (where the tail current bends away from the dipole equatorial plane in the near Earth region to become parallel to the plasma sheet in the GSM x-y plane). Also, the disk was modified to allow for transverse bending in the y-direction. Factors were added to drop off smoothly as the magnetopause was approached. The ring current is represented by the second derivative of the axisymmetric, infinitely thin current disk to better confine its contribution to the field. Only westward current was represented. There is no magnetopause. There is no inner edge to the current sheet. No data was included inside of four  $R_E$ . Thus, this model is not really intended for use in the inner magnetosphere. Finally, the data was binned by  $K_p$  and fit accordingly. Thus, this is an average model of the field within each  $K_p$  bin. As such, we found it to be in relatively good agreement with the data. It is not suited for looking at dynamic changes in the data, such as the compression of the field as the solar wind pressure increases and the magnetopause moves in, nor can it resolve fine scale activity ( $K_p$  is only available as three hour averages). However, as an average model, it did reasonably well in comparison to both our quiet time and early storm time data (Figures 49 and 50). It's fast and very easy to use.

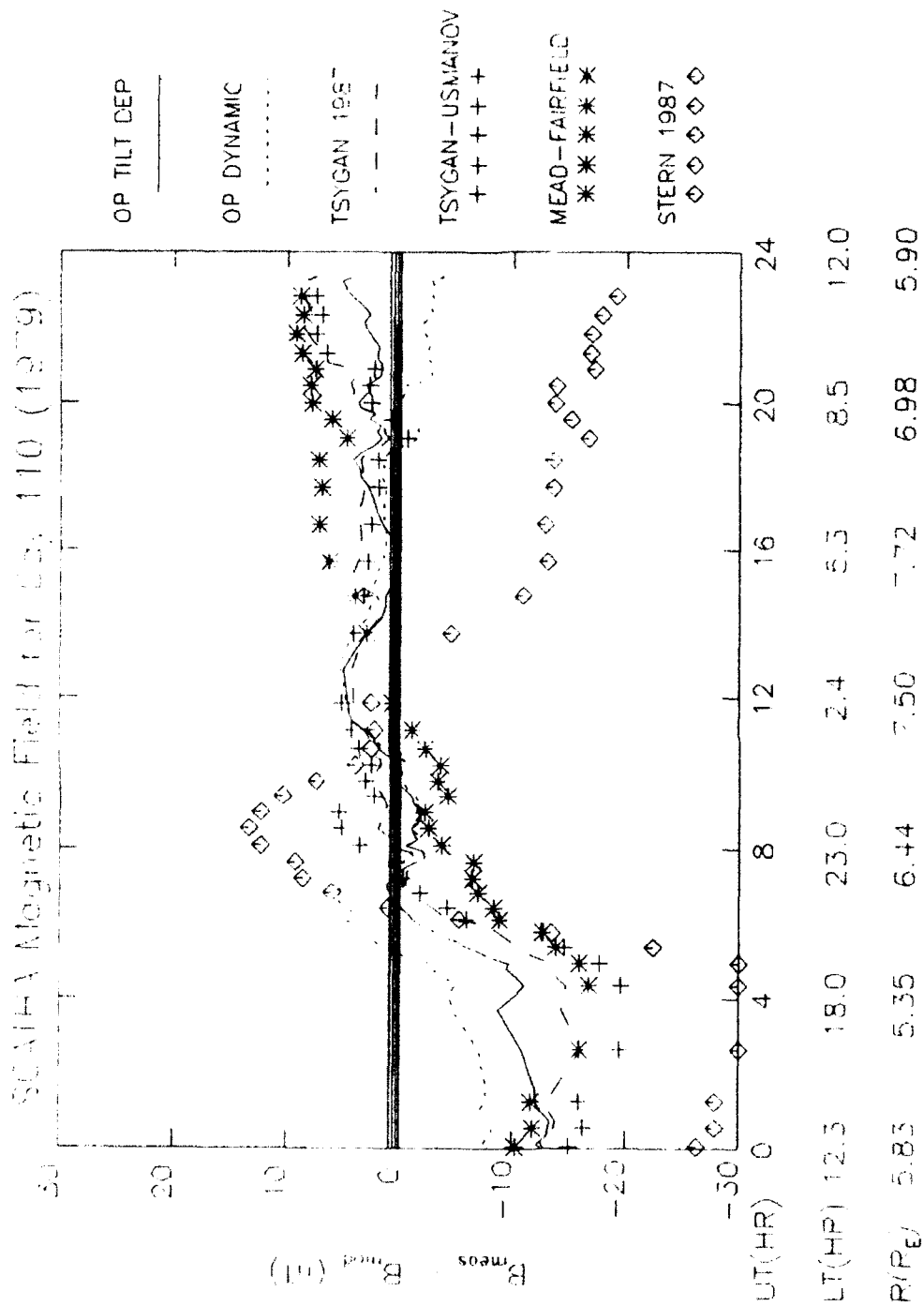


Figure 47. Model comparison during a magnetically quiet period.

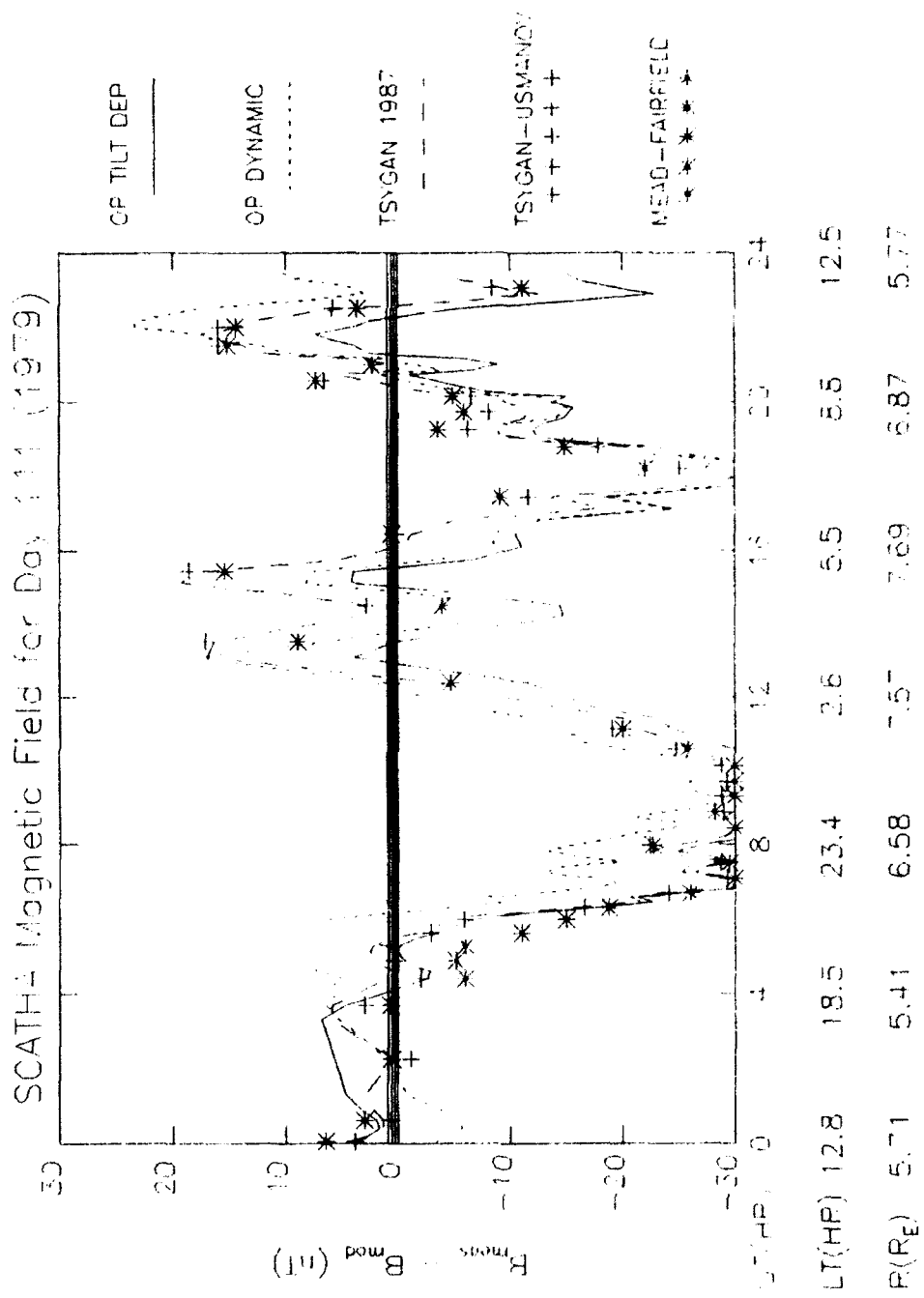


Figure 48. Model comparison during a substorm.

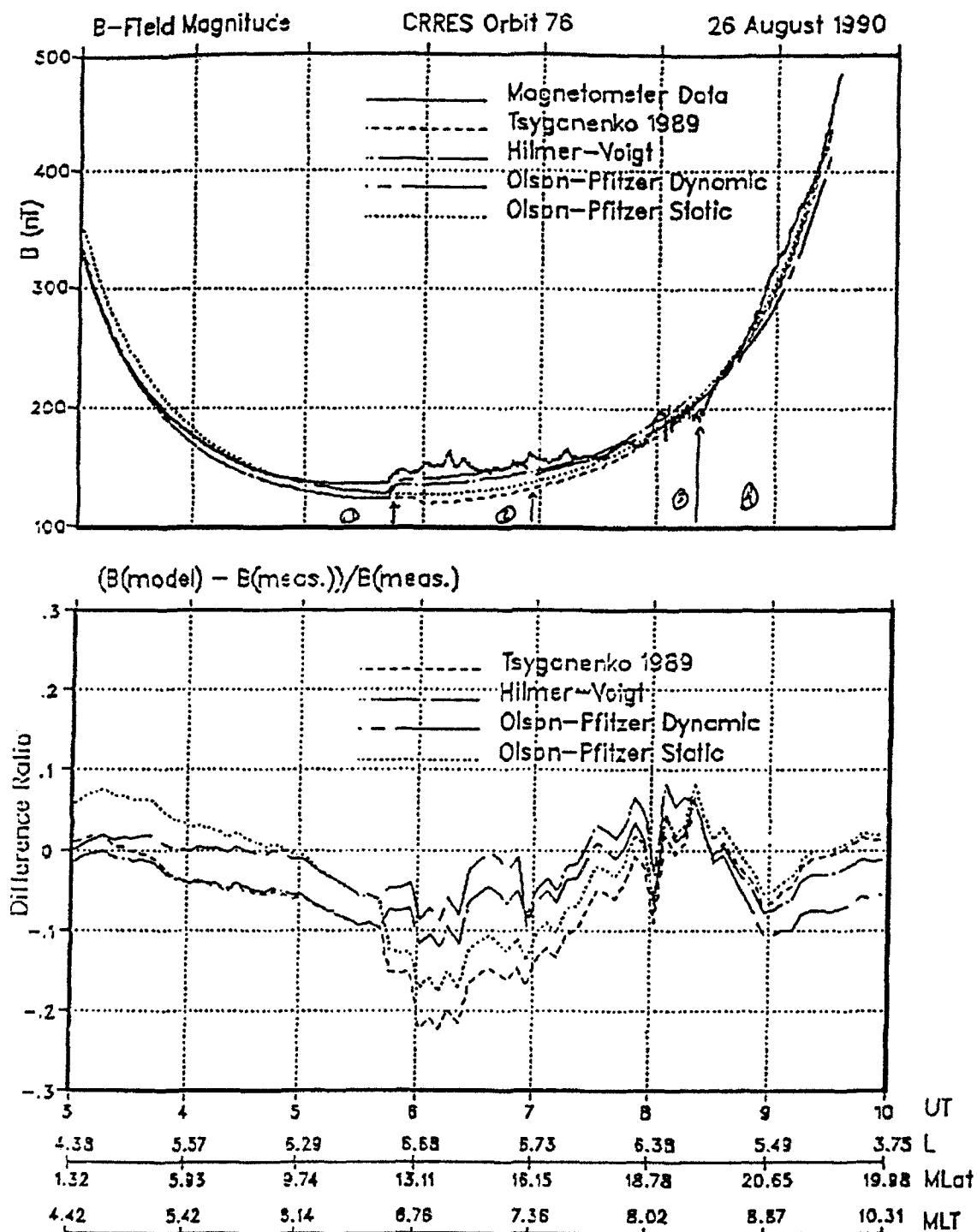


Figure 49. Sample of a preliminary comparison of these models to CRRES data.

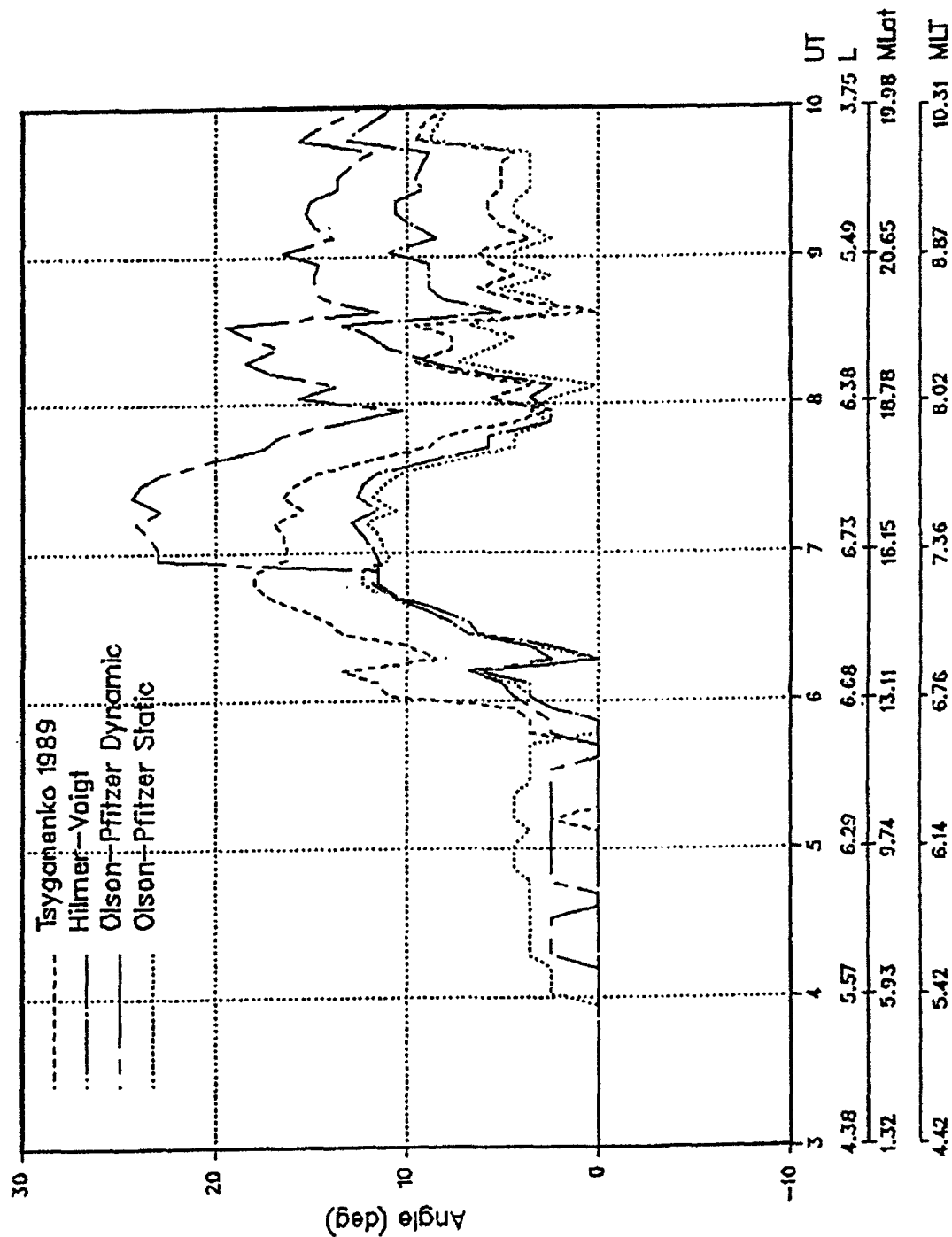


Figure 50. The angle between the CRRES magnetometer measured field vectors and the model field vectors for part of 26 August 1990.



### *Hilmer-Voigt Model*

Hilmer-Voigt is driven by four physical input parameters: dipole tilt, stand-off distance of the magnetopause, activity index Dst, and the midnight equatorward boundary of the diffuse aurora. Considering all of the models that we have looked at, this is the most flexible. The magnetopause is represented by Voigt's 1981 shielded vacuum dipole model, with a fixed shape of a hemisphere attached to a cylinder. The ring current is represented by a vector potential similar to that used by Tsyganenko 1987, but Hilmer's expression includes eastward travelling current. The tail current is based on a method used by Tsyganenko and Usmanov which uses magnetic filaments extending infinitely in  $y$ . The filaments are grouped in segments. Transverse bending and hinging are included. The stand-off distance determines the strength of the magnetopause currents, Dst controls the ring current, and the midnight equatorward boundary maps to the inner edge of the tail current sheet.

Therefore, this model is the most flexible in rendering the dynamic changes of the magnetosphere. However, it is also the slowest and most difficult to use. The four input parameters are used to find intermediate parameters which are actually required to run the model. Until very recently, this input parameter selection code was not available, so one had to contact Hilmer to get the necessary parameters to run his code for a given configuration of the field. We now have a preliminary release of this intermediate code to work with and test. Nonetheless, this model agreed best with the data overall (Figures 49 and 50). It is not really suitable for heavy data processing, but is very useful for modeling dynamic change on a fairly small scale.

#### 2.2.4.3 Preliminary Ring Current Study

External magnetospheric magnetic field models are typically comprised of explicit contributions from three main current systems: magnetopause, ring, and tail (field-aligned currents may be implicit, but as yet are not represented explicitly). In some of these models, Sugiura's  $\Delta B$  contours (1972) are used to determine the shape, size, and strength of the ring current. These contours cut-off at  $2.5 R_E$  and are only given for  $K_p=0,1$ . The CRRES magnetometer is well suited to extend these contours to lower  $L$  values and to determine contours for various activity levels. Thus, an initial study was conducted to map the ring current in activity during the 50 orbits spanning 21 March to 9 April, 1991.  $K_p$  was used as the activity index, since Dst was not yet available for that time period.

We averaged the CRRES magnetometer data into 1 minute intervals (the original data is sampled 16 times per second), calculated the internal field contribution (IGRF 1985) at these intervals, and subtracted the internal contribution from the measured total field ( $\Delta B$ ). We then looked for the maximum depression from the internal field ( $\Delta B_{\min}$ ). Binning the data into three  $K_p$  bins, we looked for changes in the magnitude and position of  $\Delta B_{\min}$  due to different activity levels. In this initial study, no attempt was made to remove the magnetopause and tail currents. This should be done to fully isolate the ring current. Plots were made of each of the 50 orbits showing  $\Delta B$ ,  $K_p$ , SM Latitude, and SM Local Time. In Figure 51, one sees a quiet to moderately active orbit ( $K_p \leq 3$ ), which suddenly becomes very active ( $K_p = 9$ ) due to the storm sudden commencement, as CRRES is descending. In Figure 52, the magnitude and position of  $\Delta B_{\min}$  is shown.  $\Delta B_{\min}$  moves inward and becomes enhanced with increased activity. For  $K_p \leq 2+$ ,  $\Delta B_{\min}$  is greater than -100 nT and is found mostly between 3 and  $5 R_E$ . For  $3- \leq K_p \leq 5+$ ,  $\Delta B_{\min} > -200$  nT and is also found between 3 and  $5 R_E$ . For  $K_p \geq 6-$ ,  $\Delta B_{\min} > -300$  nT and is now found from  $2.5$  to  $4.0 R_E$ .

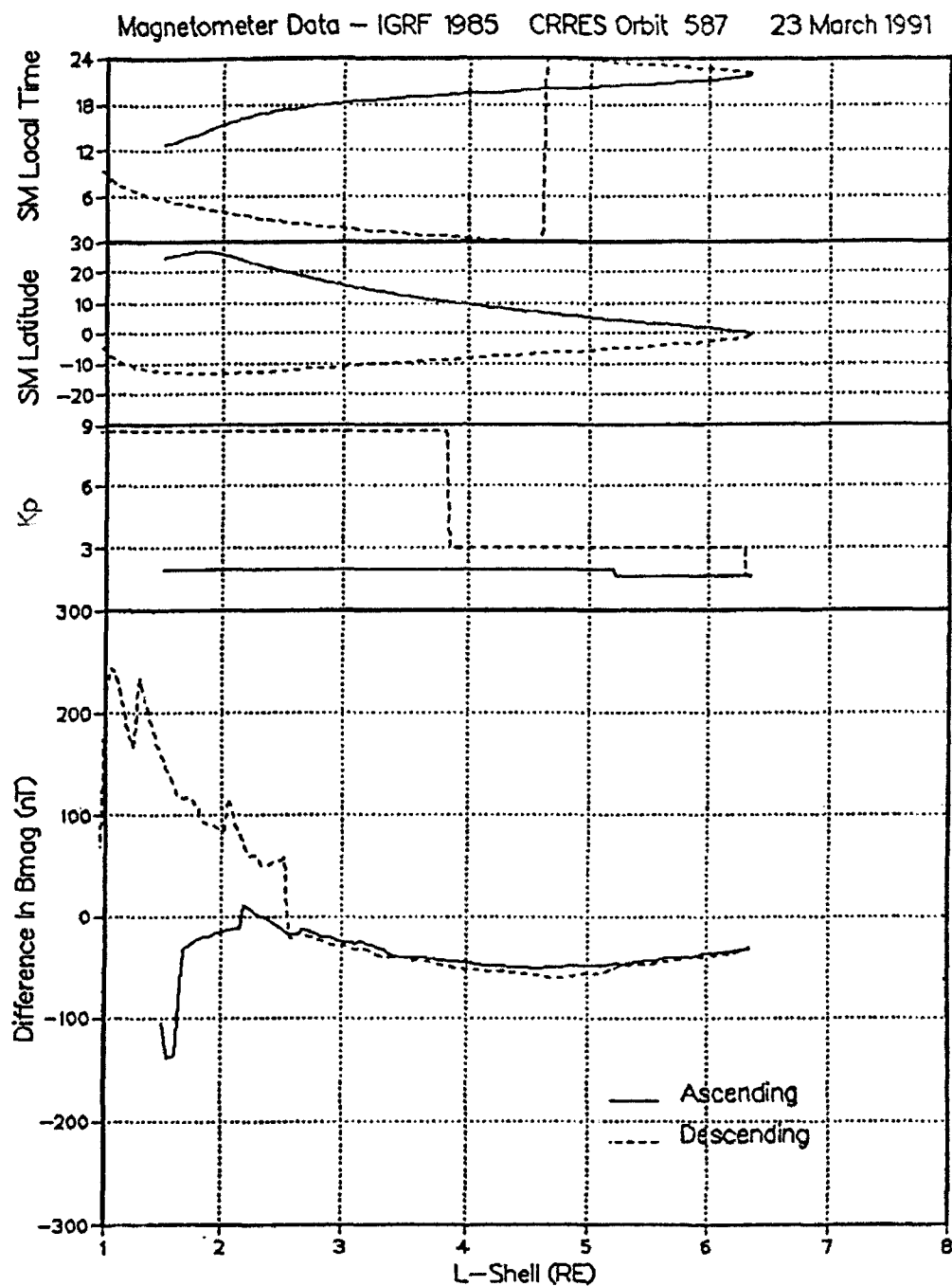


**Figure 51.** SM local time, SM latitude, Kp, and  $\Delta B$  for CRRES orbit 587, 23 March 1991. The solid line shows the ascending part of the orbit. The dashed line shows the descending part of the orbit.

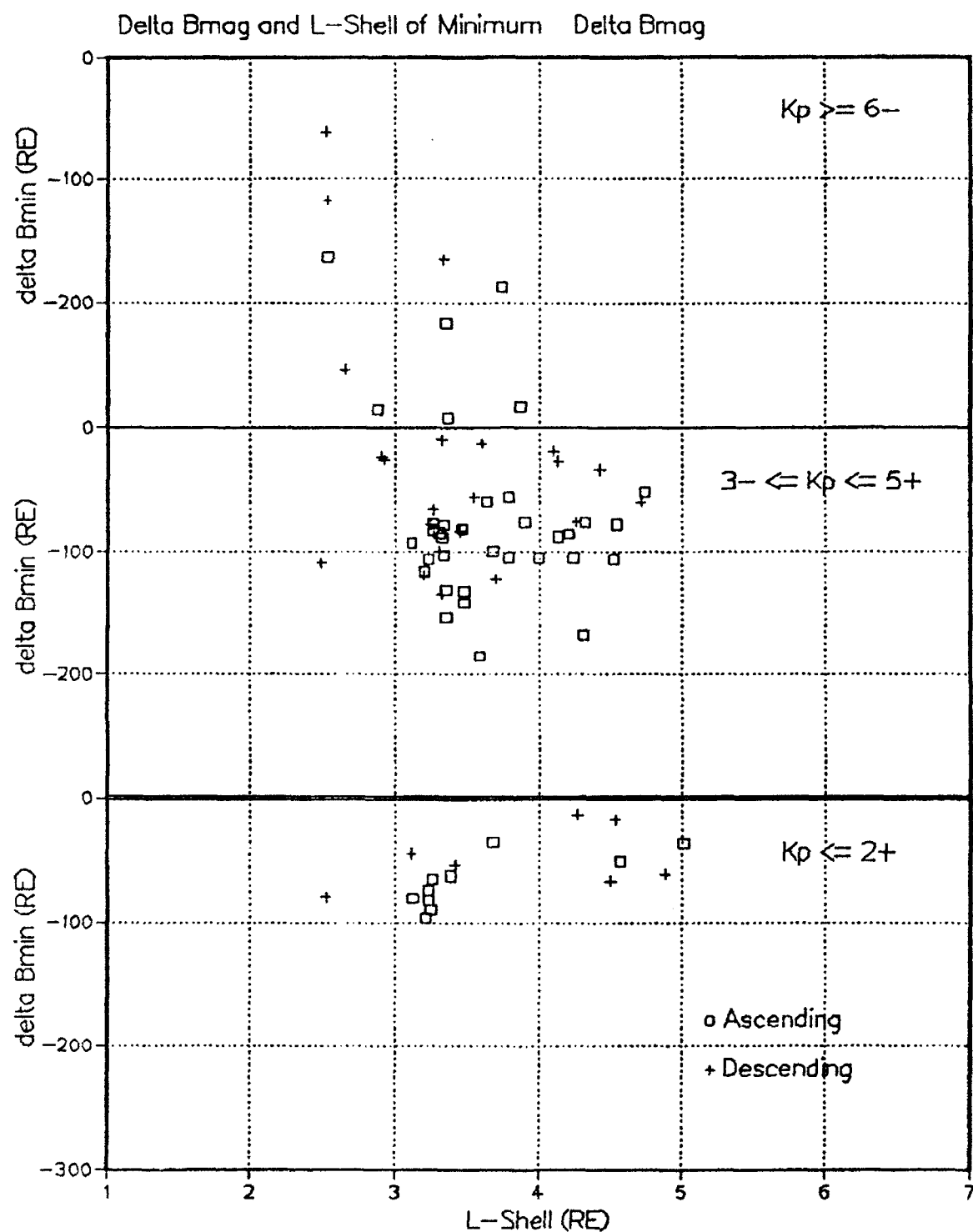


**Figure 52.**  $\Delta B_{\min}$  is shown for each of the 50 orbits spanning 21 March to 9 April 1991. These minima are grouped according to  $K_p$ .

In the color contour plots, the one-minute average  $\Delta B$  values are binned according to  $K_p$ , L-shell, and latitude. The white bins are empty. Figure 53 shows the quietest conditions with the magnetic field depressed to -100 nT from L values ranging from 2 to 5.5, and between latitudes of  $\pm 15^\circ$ . The positive field enhancements on the edges are outside of the ring current. Figure 54, moderately active, shows the field becoming more depressed, down to -150 nT, broadening in latitude, between  $\pm 20^\circ$ , and moving to lower L values. Note that we cannot determine the symmetry of the positive field enhancements because of the limited latitude coverage at higher L-shells. Figure 55, very disturbed conditions, shows a greatly enhanced field depression, to -300 nT, and further broadening in latitude and toward lower L-shells. However, the extent of the depression does not increase beyond 5.5  $R_E$ . Note that the statistics for this higher  $K_p$  range are limited, so one is cautioned not to generalize too broadly here.

This preliminary study has shown that  $\Delta B_{\min}$  moves to lower L values and becomes enhanced with increased activity. The contours also indicate that as activity increases,  $\Delta B$  strengthens, broadens latitudinally, and extends towards lower L-shells with no extension to higher L-shells observed.

#### 2.2.4.4 Existing Models

##### *Constant B Equatorial Contours*

In an effort to get a better handle on how to label, as well as model, the trapped particles, we needed to develop a better understanding of the correlation between particles at high latitude and low altitude with those at the equator. To this end, we made three sets of maps of constant equatorial B contours for  $90^\circ$ ,  $40^\circ$ , and  $10^\circ$ , respectively. Several different external field models were used with the IGRF 1980 internal field model, namely, Tsyganenko 1989, Hilmer-Voigt, Olson-Pfizer Tilt-Dependent, Mead Asymmetric, and Mead Symmetric. In addition, IGRF 1980 alone and the dipole were used for the SCATHA Day 110 (20 April, 1979) scenario. Plots were produced of the B contours for each of the models (Figure 56) and for the B contours for a given model with the dipole B contours superposed.

##### *Polar Cap Equatorial Projections*

In addition to the equatorial constant B contours discussed above, there was also interest in mapping particles which mirror at 840 km and 100 km back to the equator, and determining their constant B contours as well. The software was setup to do this (only slight modifications to the software were required from the previous work), however, no plots were ever generated. Due to other more pressing pre-launch work, this study was set aside.

#### 2.2.5 Support of Related Research

In addition to the more self-contained studies mentioned above, there has been a great deal of support work done to assist others in their research. In preparation for a shuttle mission with a Spartan spacecraft, a pitch angle study was done to find the optimum placement of two ESA detectors to obtain the best pitch angle coverage. These detectors are narrow fans covering  $140^\circ$ . Thus, we looked at the observed pitch angles at five steps along the fan (every  $35^\circ$ ). A range of pitch angles was then plotted for the detector facing +X, +Y, and -Y in the spacecraft axes, for two different types of orbital attitudes (V and W), each sampled at four local times (0h, 6h, 12h, and 18h). See Figures 57 and 58.

For studies dealing with the comparison of the CRRES data to the NASA trapped radiation belt flux models, many tables of flux (directly from the models) and dose (propagating fluences from these models

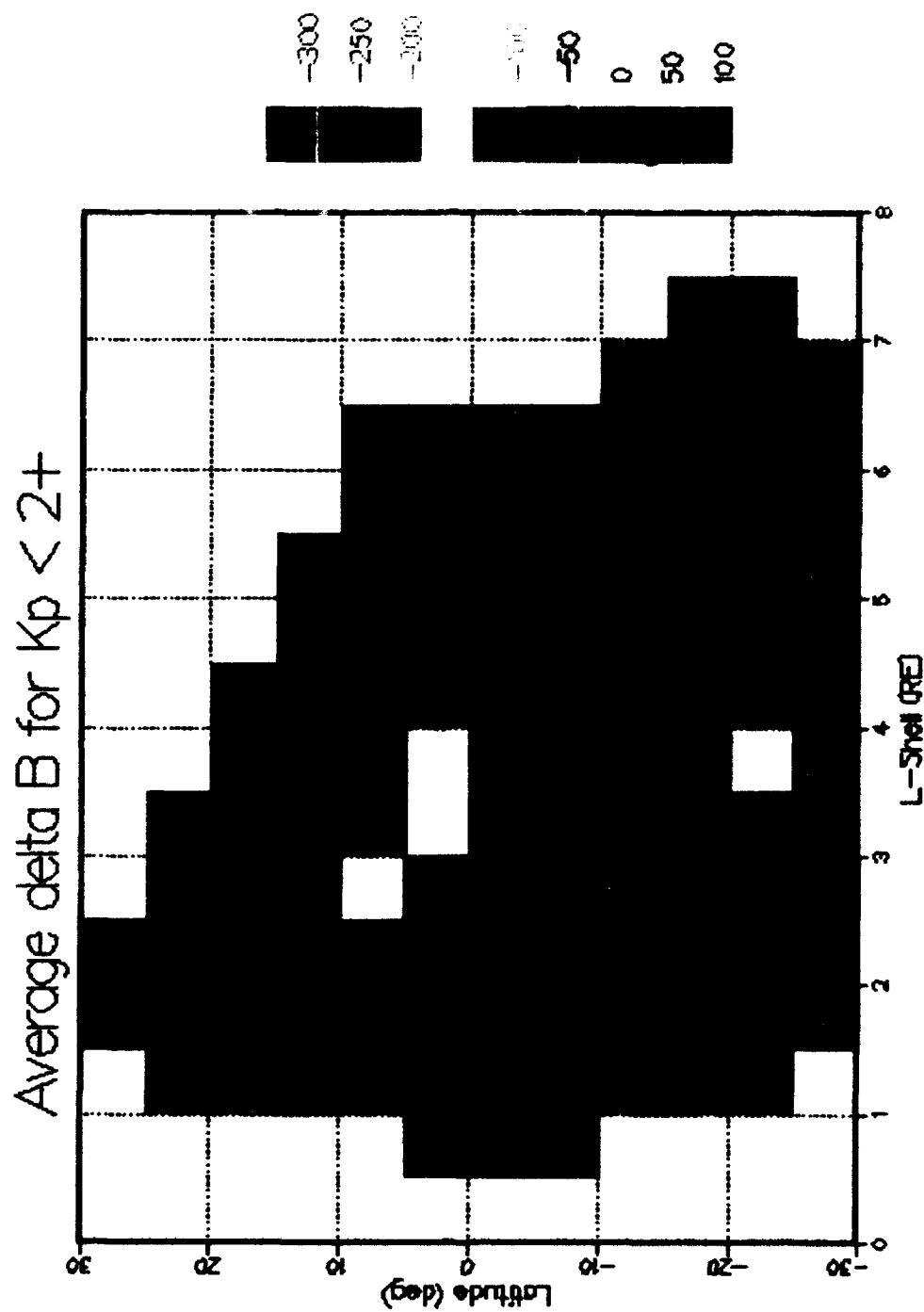


Figure 53.  $\Delta B_{min}$  binned by latitude and L-shell for  $K_p$  less than  $2+$ . The maximum depression of the field is  $-100$  nT.

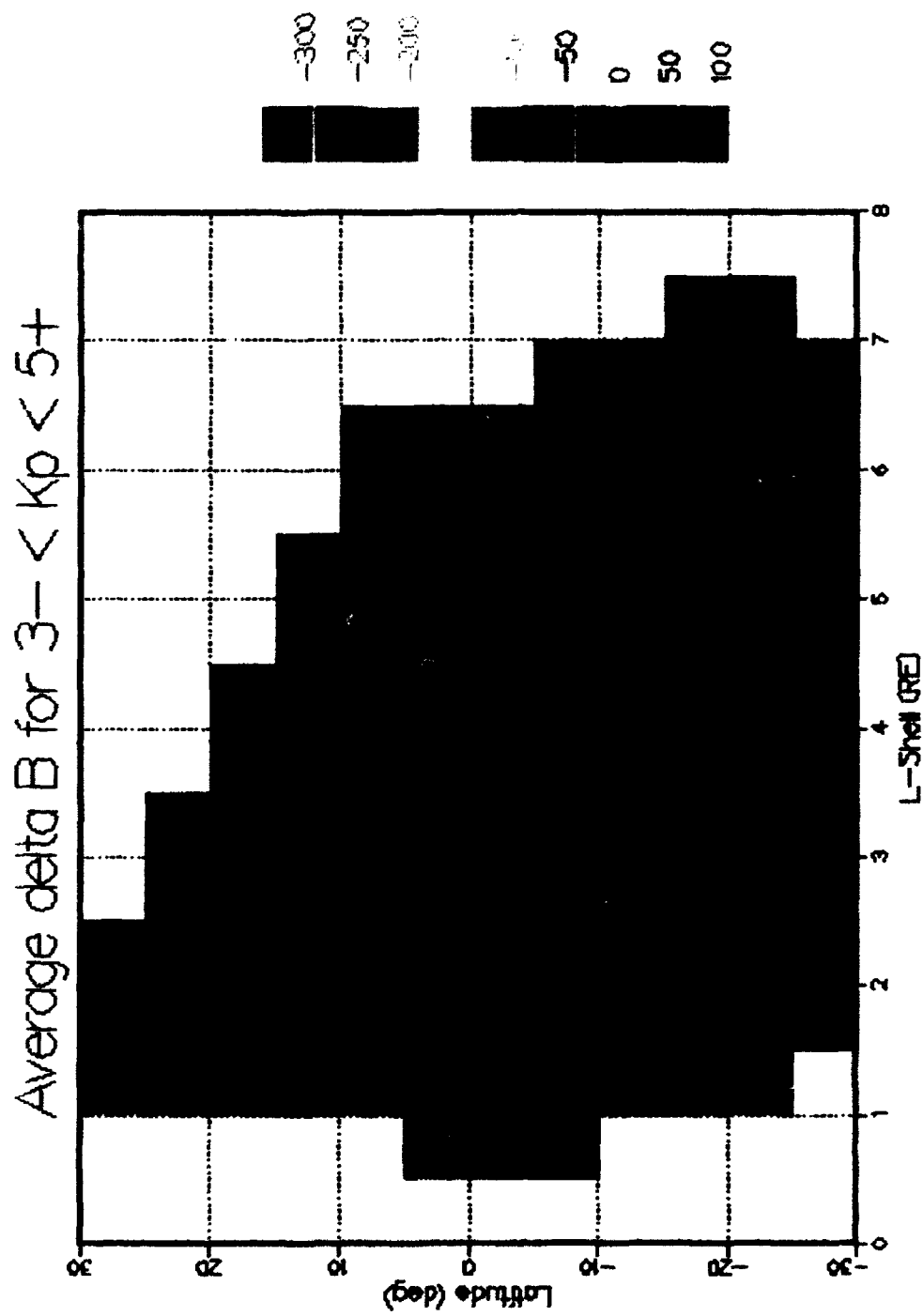


Figure 54.  $\Delta B_{\min}$  binned by latitude and L-shell for Kp between 3- and 5+. The maximum depression of the field is  $-150\text{nT}$ .

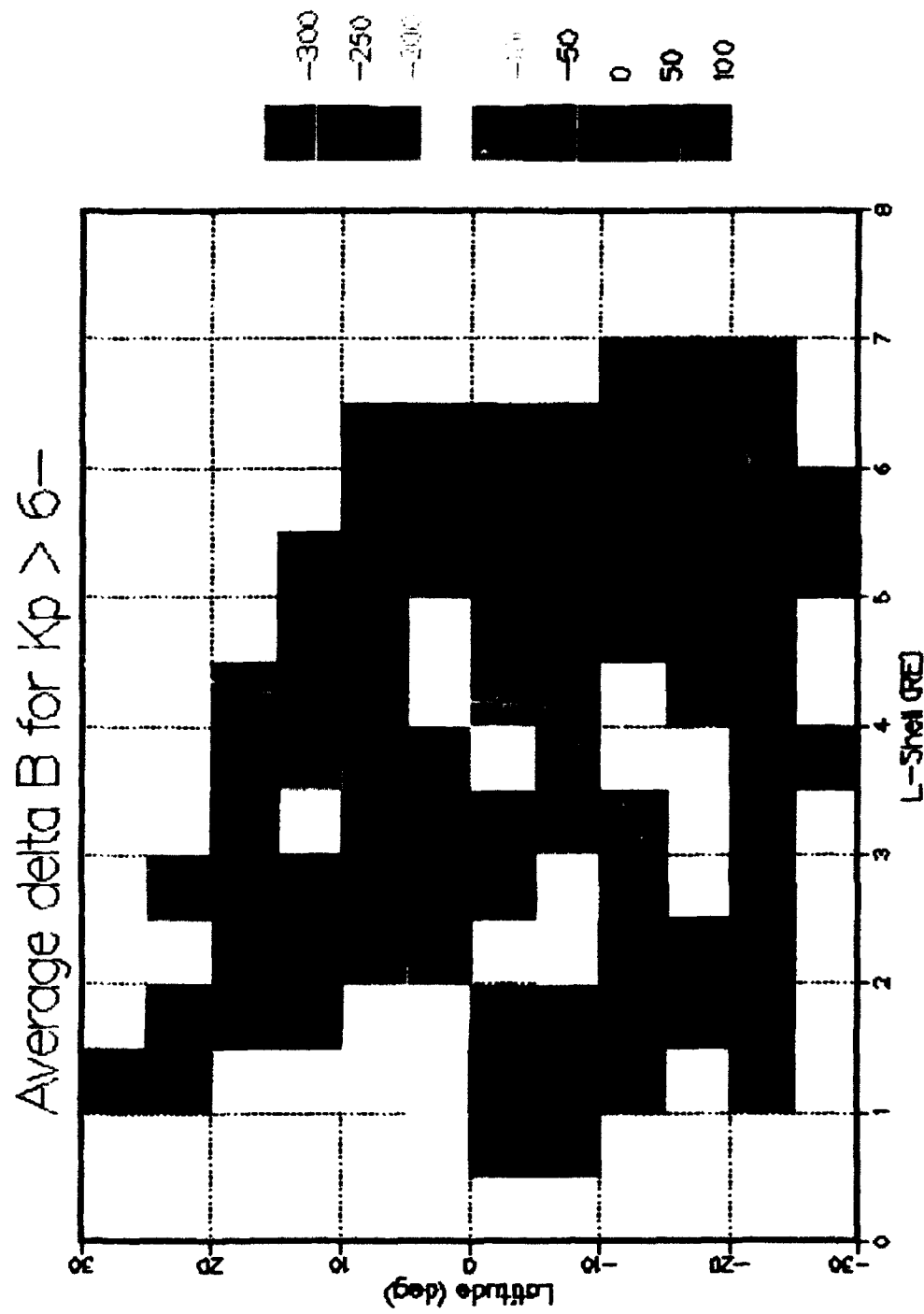
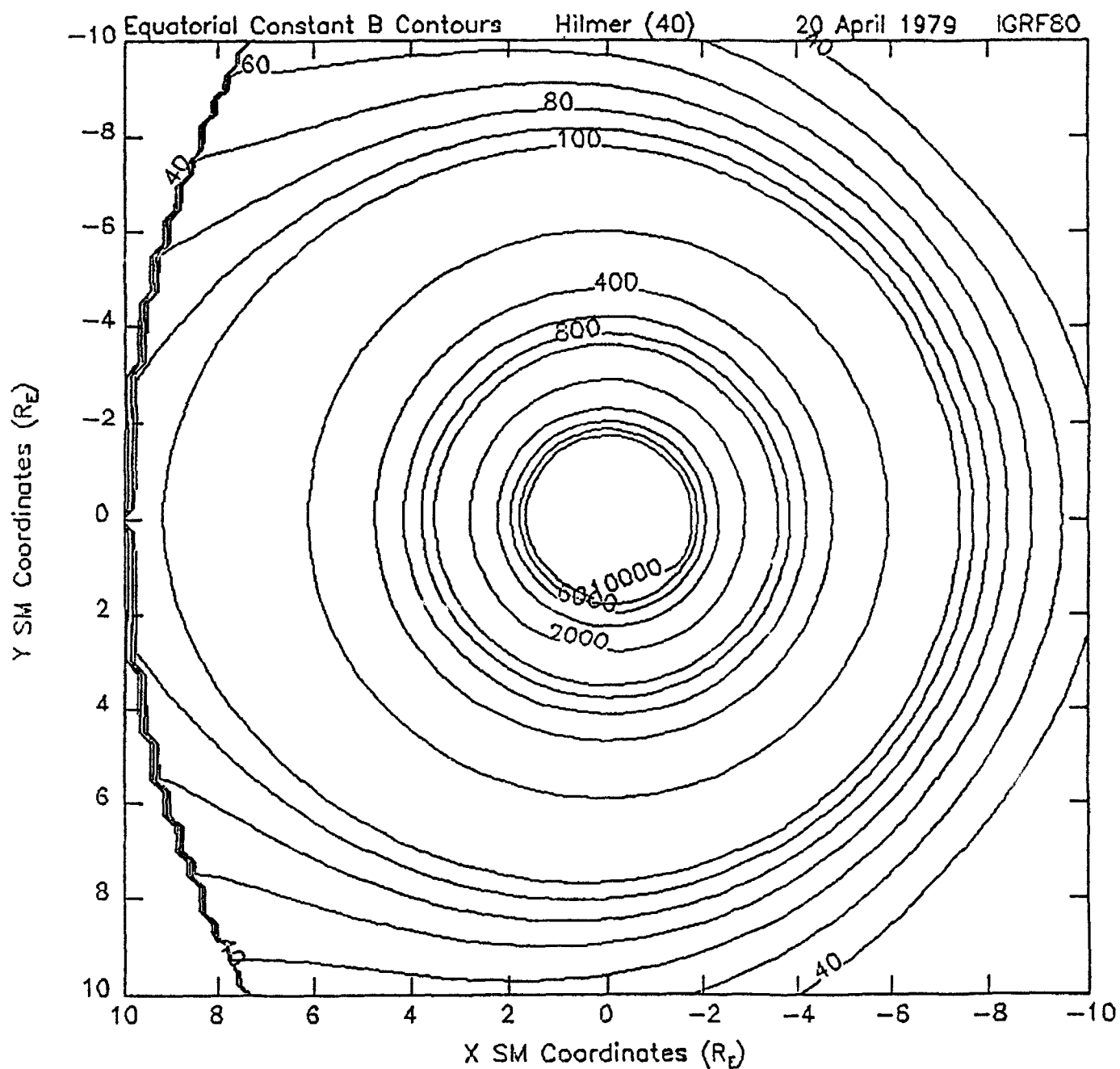


Figure 55.  $\Delta B_{\min}$  binned by latitude and L-shell for  $K_p$  greater than 6-. The maximum depression of the field is -300nT.



**Figure 56.** Equatorial constant B contours for  $40^\circ$  pitch angle particles as determined from the Hilmer-Voigt model. The jagged edge is where the model is cut off due to the magnetopause.



Pitch Angle vs. Time for Orbit SPZ00 Attitude V      Detector Facing +X

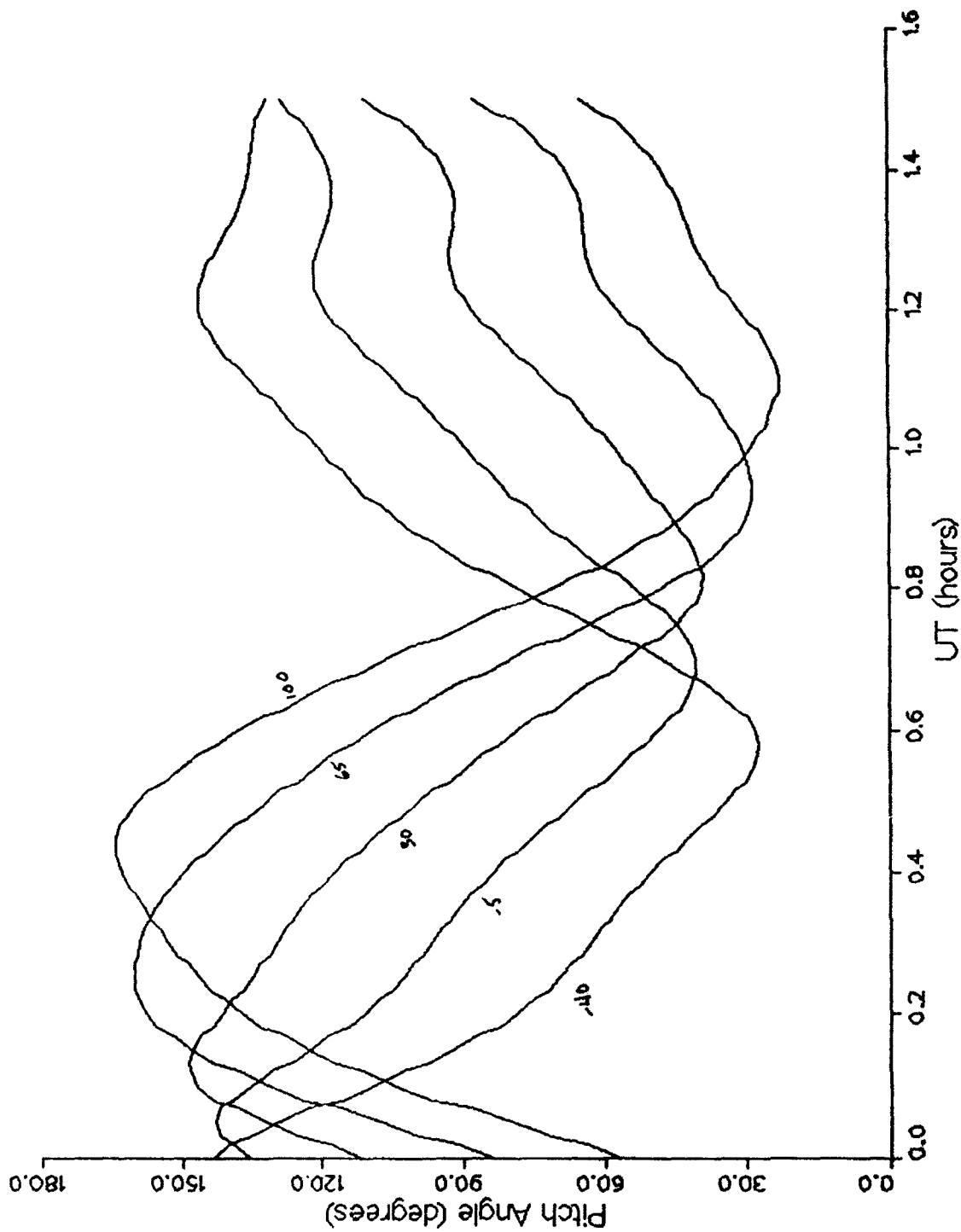


Figure 57. Pitch angle coverage for a detector facing along the +x axis in spacecraft coordinates for attitude configuration V at 0hrs L.T.

Pitch Angle vs. Time for Orbit SPZ00 Attitude V Detector Facing -Y

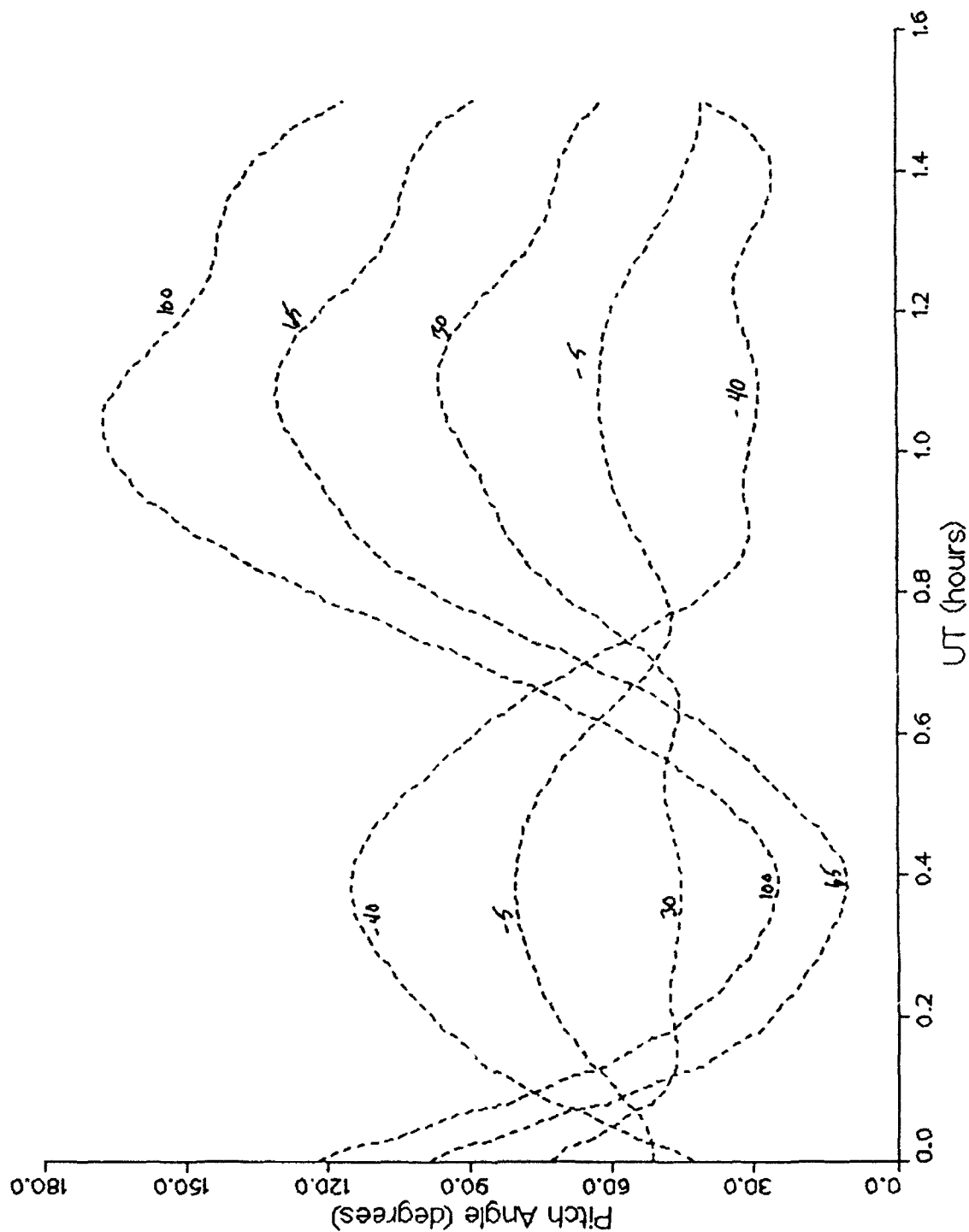


Figure 58. Pitch angle coverage for a detector facing along the +y axis in spacecraft coordinates for attitude configuration V at 0hrs LT.

through the Yates-Rothwell code) have been produced: omnidirectional differential fluxes for HEEF, PROTEL, and MEES channels simulated for various orbits using the NASA AE-8 and AP-8 models; tables of omnidirectional flux for HEEF and PROTEL channels at .05  $R_E$  steps in L-shell and for various  $B/B_0$  values; differential flux tables of the equatorial pitch angle distribution for HEEF and PROTEL channels at .05  $R_E$  steps in L-shell and  $5^\circ$  intervals in pitch angle; proton and electron fluences for the first year of CRRES for comparison to the environment used by those running the Tiger codes (Table 23); tables of one second fluences (NASA solar maximum models) and subsequently dose/s (Yates-Rothwell code) for  $B/B_0$  and L bins corresponding to those used in the CRRES dose models; dwell times in those same  $B/B_0$  and L bins for various orbits in order to determine the predicted NASA model dose vs. the CRRES model dose over the course of a satellite's lifetime; tables of dose/s at the equator using the NASA solar minimum models for the SpaceRad dosimeter channels for comparison to similar tables using the solar maximum models; listings of the energy, L, and  $B/B_0$ , grid points used in the NASA models; one second fluences from AE8MAX and AP8MAC for  $> 2.5$  MeV electrons and  $> 35$  MeV protons; and a routine to find the radius and latitude for a given longitude for the  $B/B_0$  and L grid points used in the CRRES dose models.

**TABLE 23. Proton and Electron Fluences**

365 Day Proton Fluence (protons cm <sup>-2</sup> ) for 10 Integral Energy Channels (10, 15, 20, 30, 50, 60, 80, 100, 200, 400 MeV)				
3.53E+11	1.37E+11	5.89E+10	3.00E+10	1.75E+10
1.51E+10	1.14E+10	8.62E+09	2.63E+09	3.73E+08
365 Day Electron Fluence (electrons cm <sup>-2</sup> ) for 10 Integral Energy Channels (.04, .25, .50, 1.0, 2.0, 3.0, 4.0, 5.0, 6.0, 7.0 MeV)				
2.10E+15	4.95E+14	1.41E+14	3.37E+13	4.78E+12
7.22E+11	8.45E+11	5.47E+09	2.70E+08	3.52E+07

Work performed to support other research also included: pre- and post-shock field line tracing in the noon/midnight and dawn/dusk meridians with various models for the 26 August, 1990 event; last dawn field line before magnetopause prior to the sudden storm commencement on 26 August, 1990, traced to its footprint and back again after the shock, to show how much the line shifted in longitude, as well as radius; field line traces at  $30^\circ$  longitude steps to look at the differences between the north and south 100 km intercepts at four L values; footprints of field lines observed by CRRES using various magnetic field models; plots of CRRES orbits through more than one thousand orbits to show the latitude and local time covered over the course of the lifetime of the mission (Figure 59); plots of measured and NASA model flux for HEEF, MEES, and PROTEL during various orbits; simulations of pitch angle dependent HEEF flux for low and high latitude orbits using the measured field to determine the pitch angle; and pressure densities through the noon/midnight meridian for four shock configurations using the Olson-Pfizer Dynamic and Stern models.

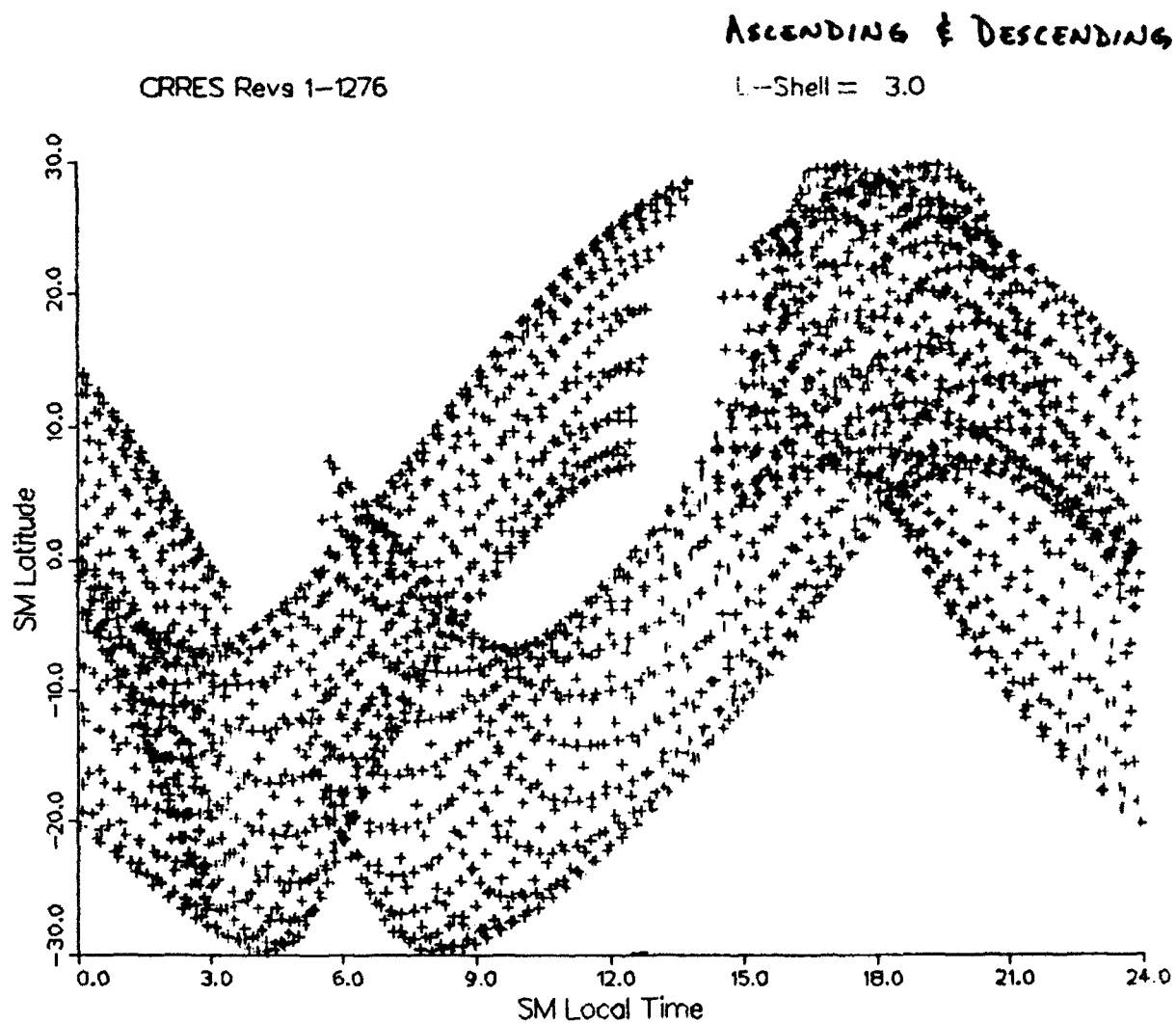


Figure 59. Latitude and local time coverage in SM coordinates of CRRES through 1276 orbits.

## 2.3 REFERENCES

- Bhavnani, K. H., N. A. Bonito, W. J. McNeil, "CRRES Data Processing Ephemeris File Generation System Product Development Specification", *RXR87041*, 49 pp., Radex, Inc., Bedford, MA 01730, 1987.
- Dichter, B. K., and F. A. Hanser, "Development and Use of Data Analysis Procedures for the CRRES Payloads AFGL-701-2/Dosimeter and AFGL-701-4/Fluxmeter and Application of the Data Analysis Results to Improve the Static and Dynamic Models of the Earth's Radiation Belts", *Scientific Report No. 3, PL-TR-91-2186*, Panametrics, Inc., Waltham, MA, 1991, ADA241399.
- Gussenhoven, M. S., E. G. Mullen, R. C. Filz, F. A. Hanser, K. A. Lynch, "Space Radiation Dosimeter SSJ\* for the Block 5D/Flight 7 DMSP Satellite: Calibration and Data Presentation", *AFGL-TR-86-0065*, 1986, ADA172178.
- Gussenhoven, M. S., E. G. Mullen, R. C. Sagalyn, (Editors), "CRRES/SPACERAD Experiment Descriptions", *AFGL-TR-85-0017*, 1987, ADA160504.
- Hein, C., *Private Communication*, February 1990.
- Hilton, H. H., "L Parameter, A New Approximation", *J. Geophys. Res.*, 76, 6952-6954, 1972.
- Hoyng, P., and G. A. Stevens, "On the Formation and Unfolding of Pulse Height Distributions", *Astrophys. and Space Sci.*, 27, 307-321, 1974.
- Janni, J., "Proton Range Energy Tables, 1 KeV - 10 GeV" in: *Atomic Data and Nuclear Data Tables*, Volume 27, 147-529, Academic Press, New York, 1982.
- Jordan, C. E., J. N. Bass, M. S. Gussenhoven, H. J. Singer, and H. V. Hilmer, "Comparison of Magnetospheric Magnetic Field Models with CRRES Observations During the August 26, 1990, Storm", *J. Geophys. Res.*, 97(A11), 16907-16920, 1992.
- Kluge, G., and K. G. Lenhart, "Numerical Fits for the Geomagnetic Shell Parameter", *Comp. Phys. Comm.*, 3, 31-35, 1972.
- Lynch, K., E. Boughan, D. Fisch, D. Hardy, K. Riehl, "PROTEL: Design, Fabrication, Calibration, Testing and Satellite Integration of a Proton Telescope", *AFGL-TR-89-0045*, Environmental Papers, # 337, 1989, ADA214564.
- McIlwain, C. E., "Coordinates for Mapping the Distribution of Magnetically Trapped Particles", *J. Geophys. Res.*, 66, 3681-3691, 1961.
- McIlwain, C. E., "Magnetic Coordinates", 45-61 in *Radiation Trapped in the Earth's Magnetic Field*, B. McCormac, editor, D. Reidel, Dordrecht, Netherlands, 1966.

- Morel, P. R., et. al., "Fabricate, Calibrate and Test a Dosimeter for Integration into the CRRES Satellite", GL-TR-89-0152, April 1989, ADA213812.
- Nightingale, R. W., T. T. Chiu, G. T. Davidson, W. E. Francis, M. A. Rinaldi, R. M. Robinson, and R. R. Vondrak, "A space Radiation Test Model Study", *AFGL-TR-86-0064*, 49 pp., Lockheed Palo Alto Space Research Laboratories, Palo Alto, CA, 1986, ADA169412.
- Press, W. H., B. P. Flannery, S. A. Teukolsky, and W. T. Vetterling, *Numerical Recipes The Art of Scientific Computing*, 818 pp., Cambridge University Press, Cambridge/New York/New Rochelle/Melbourne/Sydney, 1986.
- Pfitzer, K. A., "Improved Models of the Inner and Outer Radiation Belts", *Interim Technical Report, #DI-MISC-8071/T (102)*, 77 pp., McDonnell Douglas Space Systems Company, Advanced Product Development and Technology, Huntington Beach, CA, 1991.
- Redus, R., R. Filz, W. Swider, M. Violet, "Protel Analysis Report", 1990 (draft).
- Roederer, J. G., *Dynamics of Geomagnetically Trapped Radiation*, 163 pp., Springer-Verlag, Berlin/Heidelberg/New York, 1970.
- Schulz, M., and L. J. Lanzerotti, *Particle Diffusion in the Radiation Belts*, 215 pp., Springer-Verlag, Berlin/Heidelberg/New York, 1974.
- Schulz, M., "Opportunities for Radiation Belt Modeling: Empirical and Theoretical", *Spring Meeting 1991 Program and Abstracts, EOS Suppl.*, 232, 1991.
- Violet, M. D., K. Lynch, R. Redus, K. Riehl, E. Boughan, C. Hein, "The Proton Telescope (PROTEL) on the CRRES Spacecraft", to be published (1993).
- Violet, M., *Private Communication*, 1992.
- Voigt, G-H, "A Mathematical Magnetospheric Field Model with Independent Physical Parameters", *Planet. Space Sci.*, 29, 1-20, 1981.

### 3. IONOSPHERIC STUDIES

#### 3.1 IONOSPHERIC SCINTILLATION

Radio waves in VHF/UHF frequency bands are transmitted from quasi-geosynchronous Air Force satellites. As the radiowaves propagate through the ionosphere irregularity structures, an interference signal, which is due to refraction and reflection of these signals, is added to the transmitted signal. The interference to the communication system actually bears important information on the structure of the ionospheric medium. By analyzing the interference signal, much can be learned about the physics of the ionospheric layer.

Extensive software capabilities have been developed at PL to unpack the raw scintillation measurements, extract the scintillation phase and intensity signals, and analyze the scintillation observations. The objective is to infer ionospheric properties from ground and aircraft based measurements. We have been involved in all phases of the software development in both the PC and mainframe platforms, and some of the software implementation and upgrades are described below.

##### 3.1.1 SDS Software Processing System

An SDS software system known as SDSII has been developed to process scintillation signals that are the result of the diffraction of radio signals by the ionosphere [Bounar and Basu, 1989]. The VHF/UHF signals are transmitted by beacons onboard satellites, and are collected at ground stations in the northern and equatorial regions.

The scintillation data are digitally recorded as complex pairs at a rate of 50 samples per second. There are two recording modes, namely mode 1 and mode 3. The scintillation data are stored in records of 20 seconds in mode 3 operation, or in records of 60 seconds in mode 1 operation. In mode 3 operation, three spaced receivers at a ground site collect the radio signal, whereas in mode 1 operation, only one receiver is available.

The raw data format for a single record consists of complex data pairs, which are stored in the first 6000 16-bit words, and relevant information on the data, which is stored in an additional 20 words. This information includes the date and the time at the start of the record, the sampling rate, the carrier frequency, the station identification, and the mode of operation.

The in-phase and quadrature components represent the complex signal pairs. In mode 3 operation, there are 3 channels of data, each spanning 20 seconds. The in-phase and quadrature components, which again represent the complex signal pairs, are interleaved for the three channels. Figure 60 shows a 180-second window of the complex signal received at Sondrestrom, Greenland, starting at about 0100 hrs on December 6, 1988.

The scintillation data pairs (in-phase and quadrature signals) are first unpacked, then transformed into the scintillation intensity and phase. To avoid the effect of the modulo  $2\pi$  in the phase, a scheme was developed to reconstruct the total scintillation phase. This scheme is based on the fact that the complex signal is a chirp signal (a signal with a very wide frequency bandwidth). The complex signal is modulated at a frequency that changes linearly between each carrier frequency update, occurring regularly at 168-second intervals. Since the modulation frequency is the slope of the total phase signal, then the

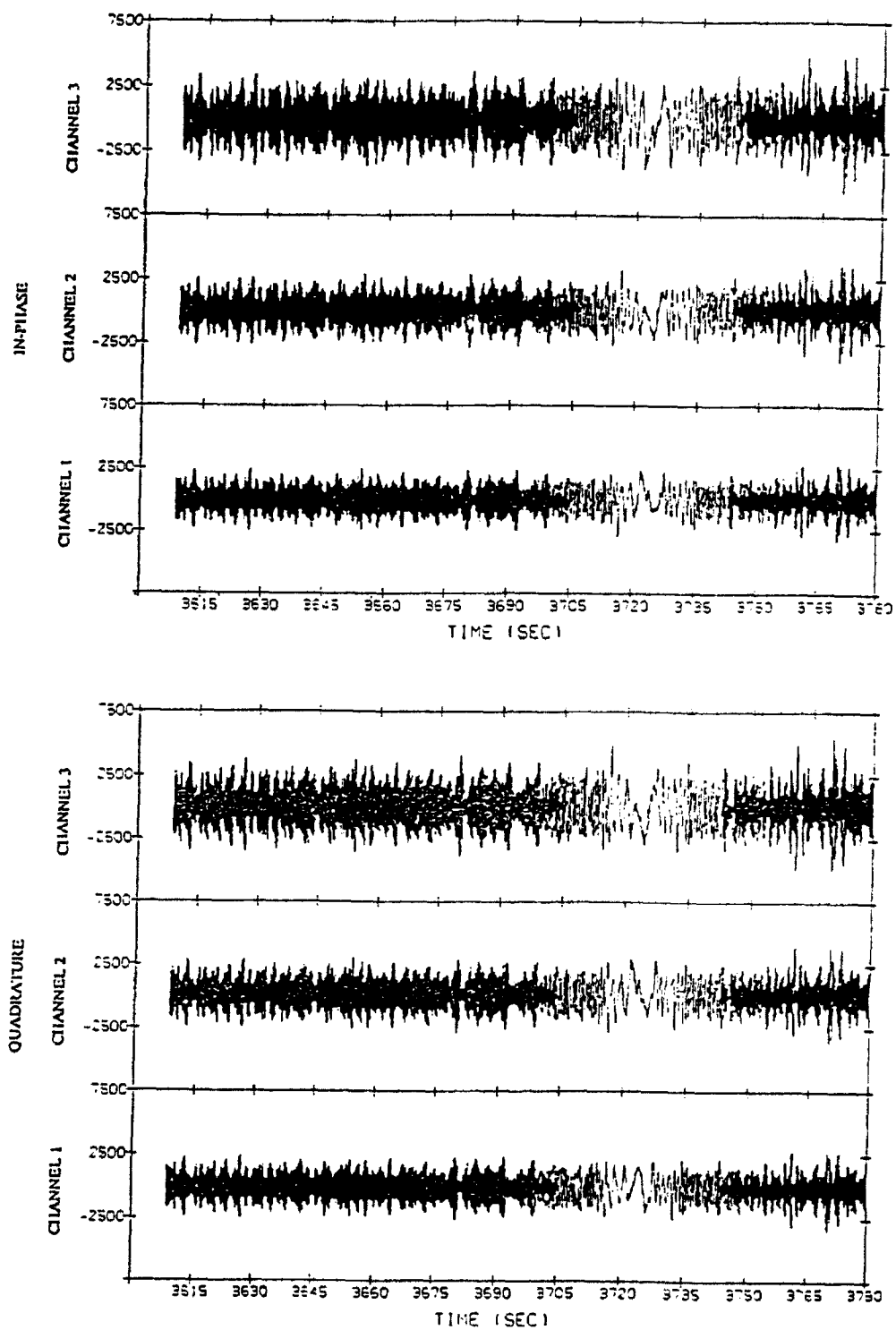


**Figure 60.** Complex scintillation signal received at Sondrestrom, Greenland, on December 5, 1988. In mode 3 of operation, three spaced receiving stations record data in three channels. The top and bottom panels show the in-phase and quadrature signals, respectively.



phase is a quadratic curve within every 168-second data block. The total phase makes it easy to detect the frequency updates of the transmitter aboard the satellite. The carrier frequency change leads to a breakpoint in the quadratic phase curve.

Out of each 168-second phase data block, 164 seconds of phase data can be extracted. The beginning and end of each block are avoided because they are near the frequency updates. The 164-second blocks are divided up into two equal 82-second blocks. Each of the 82-second blocks is then fitted to a quadratic curve, which represents the phase of the modulated radio wave. The difference between the total phase and the fitted curve yields the scintillation phase, which is the desired signal. At this processing stage, the intensity is normalized by removing the intensity envelope. Figure 61 shows the result of extracting the scintillation phase and normalizing the scintillation intensity. The processed data covers the universal time from 0205 to 0225 hrs on December 6, 1988. The intensity is given in decibels and the phase in radians with a wraparound of 50 radians.

The next processing stage includes the spectral analysis of the scintillation intensity and phase signals. The spectra of the intensity and phase are computed using the FFT algorithm. Before the Fourier transformation, windowing is applied to both intensity and phase data. One of the window functions suitable for the scintillation data is the Blackman-Harris window. The intensity or phase spectrum is based on the 164-second data blocks. 4096 samples are used, corresponding to 82-second intervals. Two spectra are obtained within each 164-second block. These individual spectra are then used to obtain the averaged spectrum. An option is available to generate two 82-second spectra instead of the averaged spectrum. Figure 62 shows two consecutive phase and intensity spectra corresponding to 164-second blocks of data.

At this stage, the statistical parameters are computed from the time series or the spectral data. The parameters computed from the time series include the S4 index, the phase root-mean-square  $\sigma_\phi$ , the intensity zero-crossing rate, the decorrelation time  $\tau$ , and the intensity fade depth. These parameters have been defined in several articles [Basu, *et al.*, 1981, 1982]. From the spectra, the statistical parameters that are computed include the intensity and phase slopes, and the spectral strengths at 1.0 Hz. All of these statistical parameters are accumulated over time, and three of these ionospheric parameters, namely S4,  $\sigma_\phi$  and  $\tau$ , are generally plotted over a four-hour window. Figure 63 shows these three parameters in the evening starting on December 5, 1988.

The SDSII software is operational at PL, and the processing has been successfully carried out on VHF/UHF radio observations from several high latitude receiving stations, namely: (1) Sondrestrom, Greenland (66.9°N, 50.8°W), (2) Goose Bay, Labrador (53.3°N, 60.3°W), (3) Thule, Greenland (76.5°N, 68.7°W), (4) Tromsø, Norway (69.7°N, 18.9°E), and (5) Malvik, Norway (65°N, 40°E).

### 3.1.2 Airborne Ionospheric Observation (AIO)

The AFGL Airborne Ionospheric Observation (AIO) campaign was coordinated with other missions to measure large-scale structures and dynamics of the polar cap F layer auroras and to investigate processes which generate small scale (< 1 km) ionospheric irregularities within the auroras [Weber, *et al.*, 1989]. The generation, transport, and decay of sub-kilometer ionospheric irregularities are important from a practical point of view, since they produce phase and amplitude scintillation on satellite-to-ground communications links. These fluctuations provide a measure of the strength of the ionospheric irregularities over a range of scale sizes, from 10 km to hundreds of meters (phase scintillation), and from 1 km to tens of meters (amplitude scintillation).

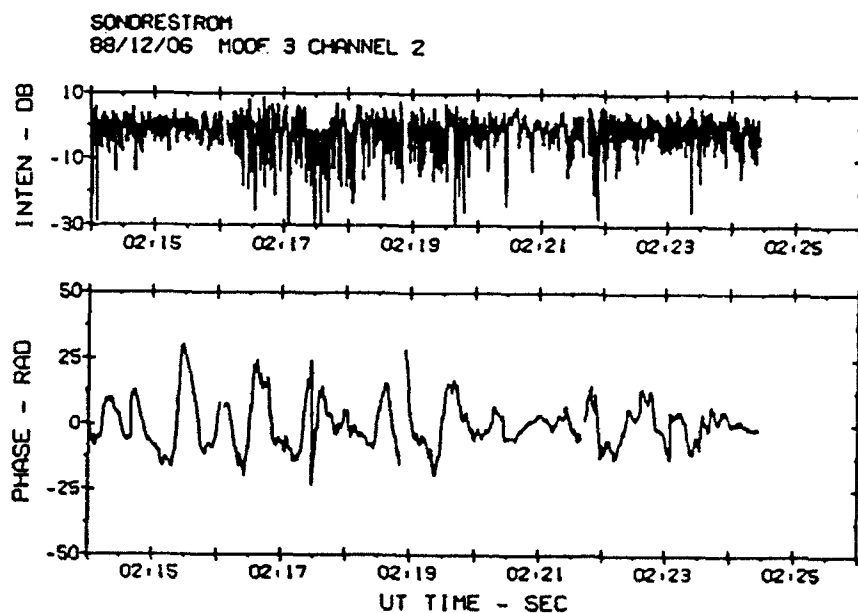
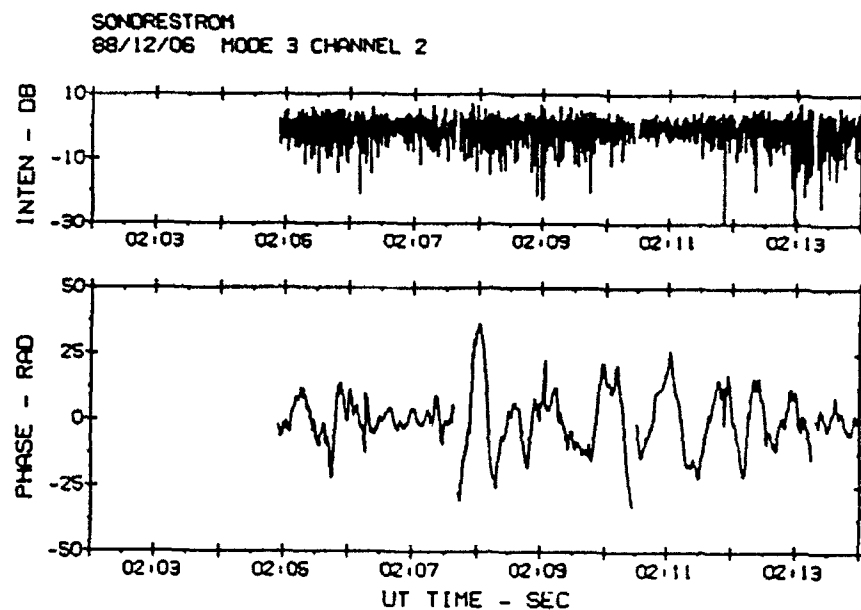


**Figure 61.** The detrended scintillation phase and the normalized scintillation intensity at Sondrestrom, Greenland, starting at 02:02 on December 6, 1988. The scintillation signal is from channel 2. In each panel, the top plot gives the intensity in decibels from -30 to +10 dB, and the bottom plot gives the phase in radians from -50 to +50 radians.

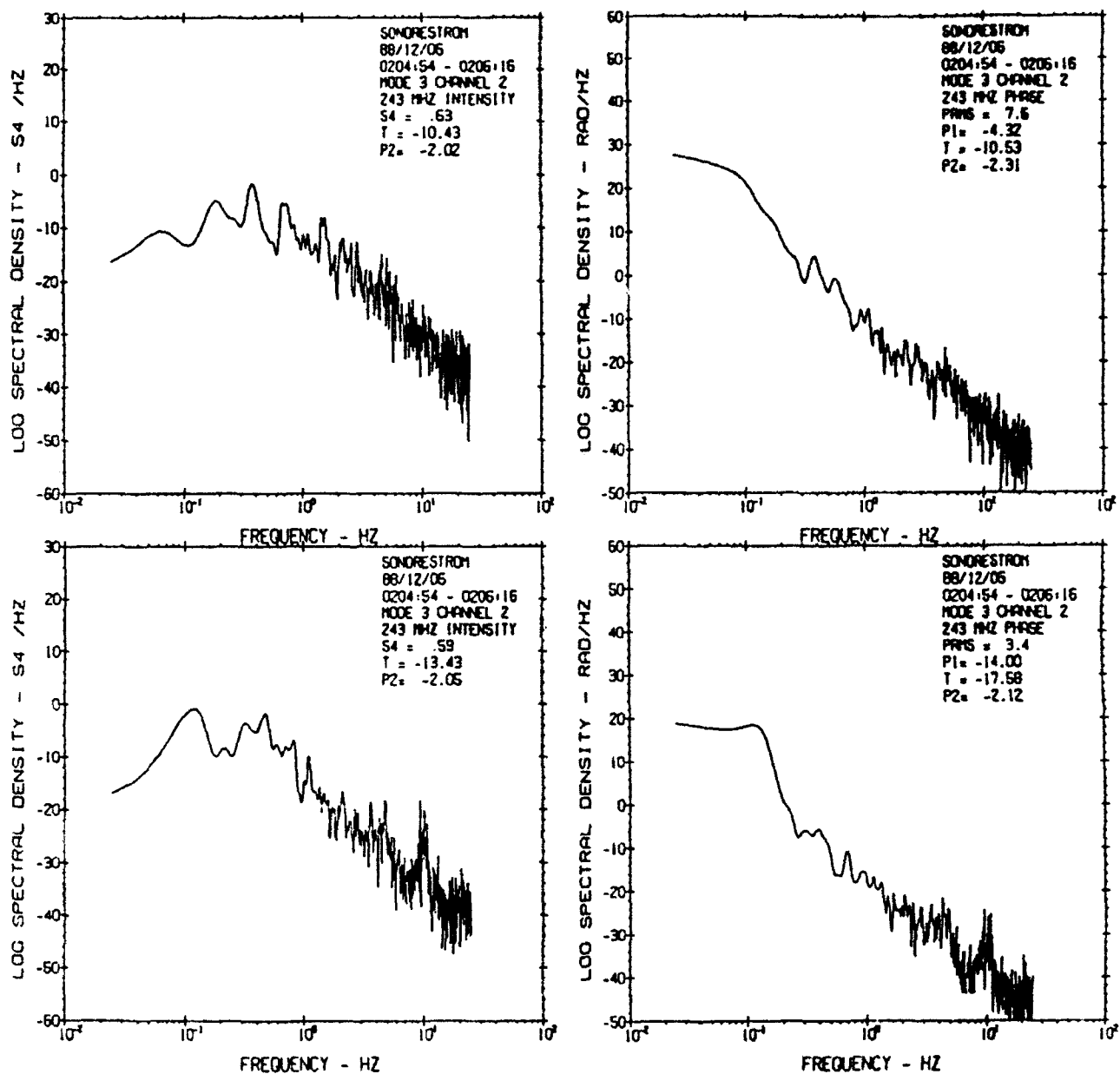
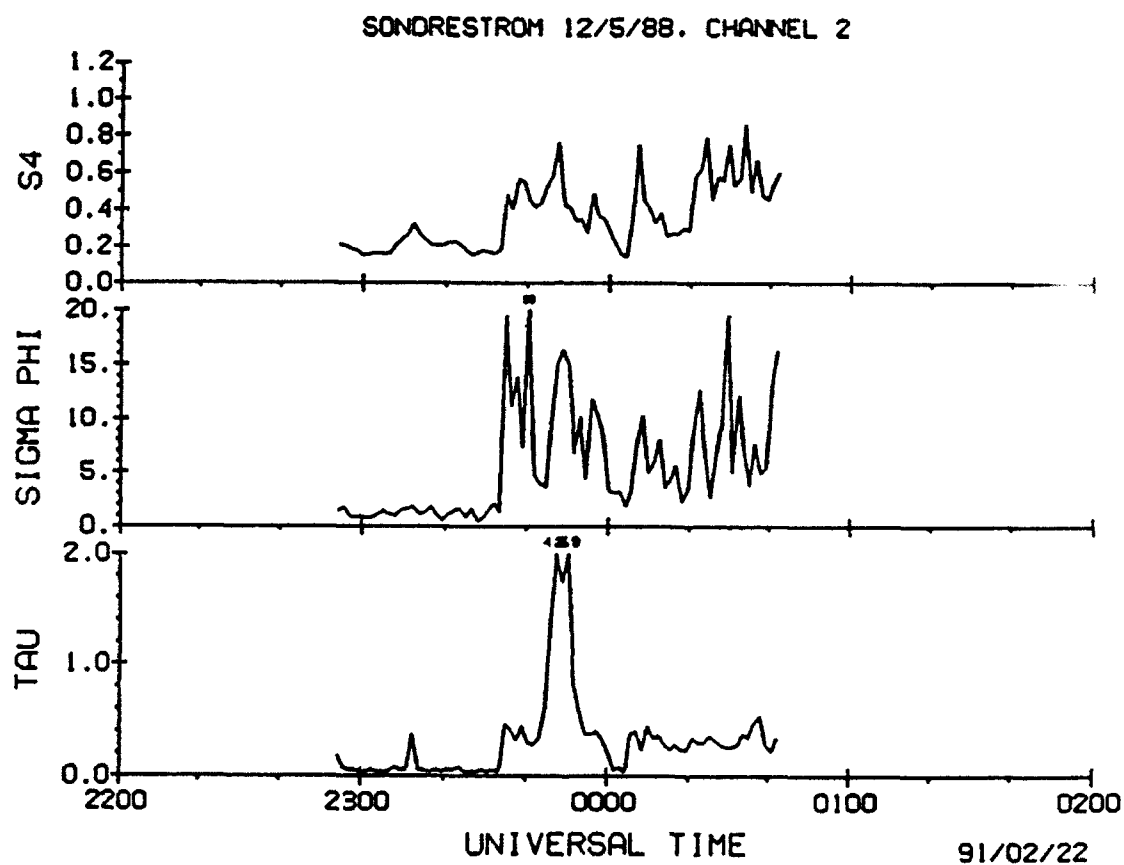


Figure 62. The scintillation intensity and phase spectra for two consecutive 164-second data blocks. On the upper right of each plot are provided the statistics of the scintillation signal describing the spectrum characteristics. The signal frequency varies from 0.01 to 25 Hz.



**Figure 63.** The three statistical parameters of the scintillation intensity and phase for a period of 4 hours are shown for all of the data processed from the evening of December 5, 1988 observations at Sondrestrom, Greenland.

The AIO experiment consisted of the aircraft flying multiple legs north-south along the European Incoherent Scatter (EISCAT) radar magnetic meridian every 30 minutes, covering the range  $\pm 2^\circ$  with respect to Andoya, Sweden. The AIO performed radio, optical, and scintillation measurements. The VHF/UHF amplitude and phase scintillation measurements were transmitted from a high-latitude polar beacon satellite. Continuous measurements were made using the high altitude polar beacon at 244 MHz. The satellite was quasi-stationary during the course of the measurements, and the motion of the subionospheric intercept point was due almost entirely to north-south motion of the aircraft. During the AIO experiment, the DMSP F9 satellite measured the latitude profile of precipitating electrons along the EISCAT radar meridian.

We developed a processing software of the AIO scintillation measurements, using the same processing approach as the one used in the ground measurement processing software. The processing can be done for the scintillation intensity only, or for both the scintillation intensity and phase. In the second case, not all of the recorded data are processed, since the extraction of the scintillation phase requires continuous data segments of a least 82 seconds.

#### 3.1.2.1 Intensity Only

We will briefly describe the steps involved in the processing of the AIO scintillation data.

In step 1, the unpacking of the field data is done. The data has a different format than that of the ground measurements, so the unpacking programs that were available had to be modified to properly unpack the raw data.

In step 2, the scintillation intensity is first corrected by removing the bias in the complex data. This interference, or leakage signal, tends to add side-lobes in the intensity spectrum. Its presence may yield erroneous estimates of the slope and strength obtained from the spectrum. The complex signal is then converted to the intensity signal, which is normalized. The time series are used to compute the zero-crossing rate, the fading depth, and the S4 index. The normalized time series is plotted in 160-second periods.

In step 3, the spectral estimate is then computed. A tapering window, named the Blackman-Tukey window, is first applied to the time series. The resulting time series is then Fourier transformed, and the power spectrum is obtained. From the spectrum, we obtain the spectral strength and slope. The two frequency-breakpoints are saved. The intensity spectrum is then smoothed, and the resulting power spectrum plotted. Two spectra are computed using two 82-second intensity data. Since the processing is done for 160-second data blocks, there is a 4-second data overlap.

In step 4, the normalized intensity data is also used to compute the correlation coefficients by Fourier transforming this data twice. The decorrelation time is then computed for when the correlation crosses the 0.5 threshold value.

In the final step, all of the statistics obtained from the time series and the spectrum are saved into a listing file for further analysis.

### 3.1.2.2 Intensity and Phase

In processing the scintillation intensity and phase, data blocking becomes critical to properly detrend the scintillation phase. The processing steps are described below.

In step 1, the unpacking of the raw data is done using the same program as was described in step 1 above.

In step 2, the phase scintillation is scanned to locate the frequency updates. These updates are to occur every 168 seconds. Only 160 seconds of data out of 168-second blocks are extracted. The data near the frequency updates are rejected. The scintillation phase is then detrended by filtering out the fitted second order polynomial, which was fitted to the total phase data. Subsequently, the scintillation intensity and phase are corrected by removing the bias in the complex signal. The leakage, or interference signal, tends to add side-lobes in the spectra. Its presence may yield erroneous estimates of the slope and strength, which are obtained from the spectra. The complex signal is then converted to the intensity and phase signal. The intensity signal is normalized. The intensity time series is used to compute the zero-crossing rate, the fading depth, and the S4 index. The phase time series is used to compute the phase standard deviation. The intensity and phase time series are then plotted.

In step 3, we compute the spectral estimates. We first perform an end-matching of the phase signal, then both the intensity and the phase time series are tapered by the Blackman-Tukey window. The resulting time series are then Fourier transformed, and the power spectra are obtained. From the intensity spectrum, we obtain the intensity spectral strength and slope. From the phase spectrum, we obtain the spectral strength at 1.0 Hz, and two spectral slopes for two different transition bands. The spectra are then smoothed, and the results are plotted. Two spectra are computed using two 82-second intensity data. Since the processing is done for 160-second data blocks, there is a 4-second data overlap.

In step 4, the normalized intensity data is also used to compute the correlation coefficients by Fourier transforming this data twice. The decorrelation time is then computed for when the correlation crosses the 0.5 threshold value.

In the final step, all of the statistics obtained from the time series and the spectra are saved into a listing file for further analysis.

### 3.1.2.3 Comments

Gaps in the raw data occurred from low signal levels (below 60 db from the mean intensity) that may be caused by the aircraft turns. As the aircraft turns, repeated tries to retune the signal may be necessary, and thus affect the quality of the data recorded. During these two days of measurements, there were quite a few gaps in the data. The gaps tend to complicate the extraction of the ionospheric phase signal. In order to obtain useful ionospheric phase data, the pattern of retunes must be located. The data blocks between two consecutive retunes are approximately 168 seconds long. Gaps in the segmented data will occur when the repeatable phase pattern cannot be locked up. The phase pattern detection is faulted by any discontinuity in the data, which occurs during retunes or an aircraft turn. Therefore, to detrend the scintillation phase from the data, more labor-intensive techniques must be used. Such techniques have not yet been tried.

The AIO scintillation data processed were from January 16 and 17, 1990. Figure 64 shows a 160-second window of the scintillation intensity from 2:45:37 to 2:48:17 and the corresponding spectral densities. The procedure to obtain these plots was described in Section 3.1.2.1 above. Each intensity spectrum represents 82-seconds of data. Using the procedure described in Section 3.1.2.2 yields the scintillation intensity and phase shown for a 160-second data block in Figure 65. We must note that the scintillation signal presents stronger fluctuations than is generally observed from ground observations. This may be due to the aircraft motion. The processing of the scintillation signals to obtain the scintillation statistics did not match those of ground-based measurements. We next summarize some of these statistics.

When the S4 index is high, the decorrelation time must be short, indicating the low correlation in the intensity samples. The decorrelation time from the AIO measurements tends to be as high as 6 to 8 seconds when the S4 index is high or near saturation.

The RMS phase values recorded by the AIO mission tend to be higher than those obtained on the ground. These values can be 10 to 20 radians higher. This is seen in the phase spectra where, most of the time, the energy is concentrated in the low-frequency band ( $< 0.1$  Hz). At times, there can be an important spectral enhancement in the frequency range of 0.1 to 1.0 Hz, resulting in erroneous calculations of the spectral slope and strength.

When S4 index is low ( $\leq 0.2$ ), the phase RMS value must be low (about 1.0 radians), as seen in ground measurements. For AIO measurements, the phase RMS values tend to be about 12.0 radians for low S4 index.

### 3.1.3 Wideband Scintillation Model (WBMOD)

A model of scintillation, called WBMOD, has been modeled using scintillation data and weak scintillation theory [Fremouw and Lasinger, 1981; Fremouw and Rino, 1978]. The model provides the phase and amplitude scintillation for certain input parameters, which include radio frequency of transmitted signal, geographic locations of transmitter and receiver, local solar time at penetration point, the sunspot number, and the Kp index. Two internal models may be used for the calculation of the irregularity drift velocity and the outer scale parameter.

WBMOD calculates the scintillation spectral strength, the power law index, and the two commonly used scintillation indices  $\sigma_\phi$  and  $S_4$ . To calculate these parameters, one must obtain certain parameters describing the ionospheric irregularities [Jursa, 1985], namely, the height of the ionospheric layer (which is fixed at 350 km), the vector drift velocity  $V_d$  of the irregularities, an outer scale  $\alpha$ , the shape and depth parameters characterizing the three-dimensional configurations of the irregularities, and the height integrated strength of turbulence  $C_s L$ . Note that the velocity drift and the outer scale parameters can be obtained from models within WBMOD program.

WBMOD has been calibrated quantitatively initially against Wideband data from a station in Poker Flat, Alaska, in the northern auroral zone. WBMOD has been modified to model ionospheric scintillation in the equatorial and mid-latitude regions. We have recently compared the scintillation parameters obtained from the model with those from actual ground-based observations in high latitude regions, such as Thule and Sondrestrom, Greenland. The results are summarized next.

We tested the WBMOD program for two ground sites in high latitudes, namely, Thule (76.5°N, 68.7°W) and Sondrestrom (66.9°N, 50.8°W) in Greenland, and compared the scintillation statistics to those

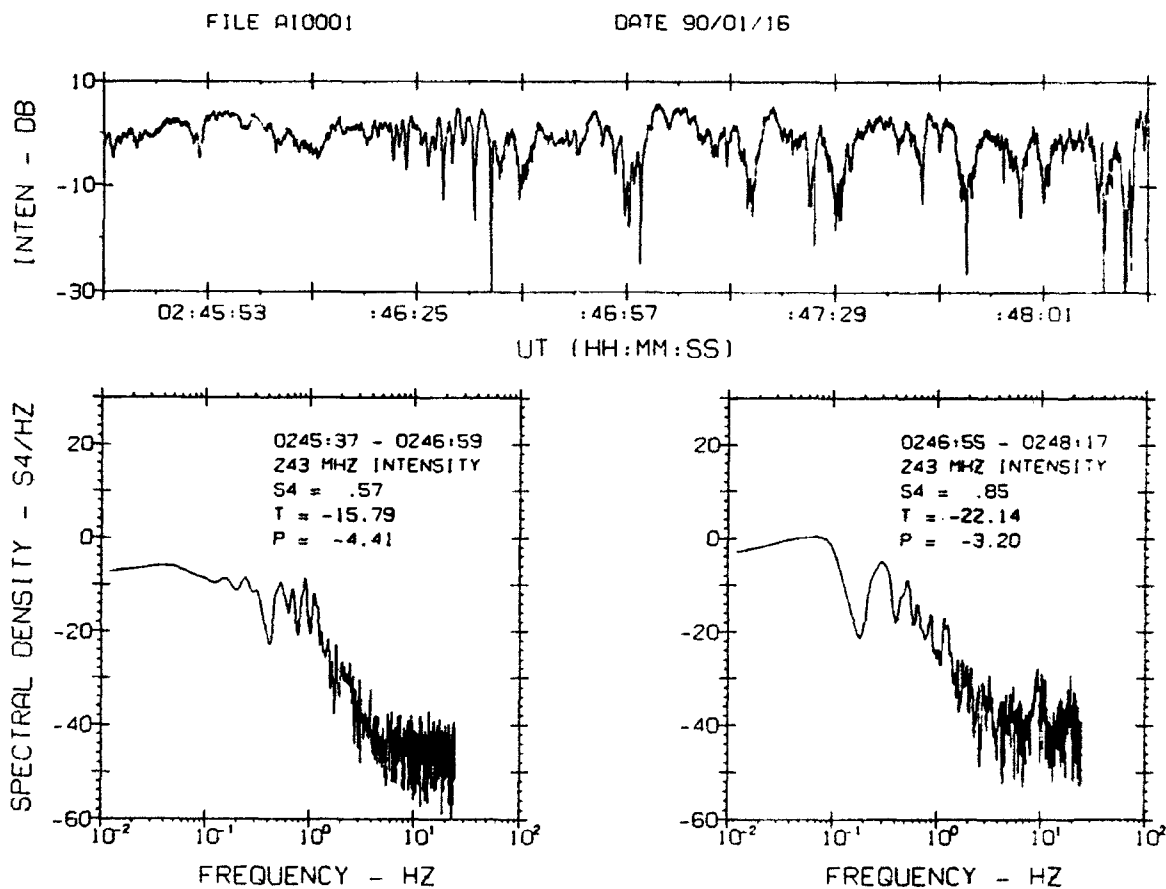


**Figure 64.** The top panel shows the scintillation intensity over Andoya, Norway, during the AIO campaign on January 16, 1990. The period shown is from 02:45:37 to 02:48:17. The bottom panel shows the corresponding intensity spectra. On the upper right of each the spectral plot are provided the statistics of the scintillation intensity for an 82-second window. The signal frequency varies from 0.01 to 25 Hz.



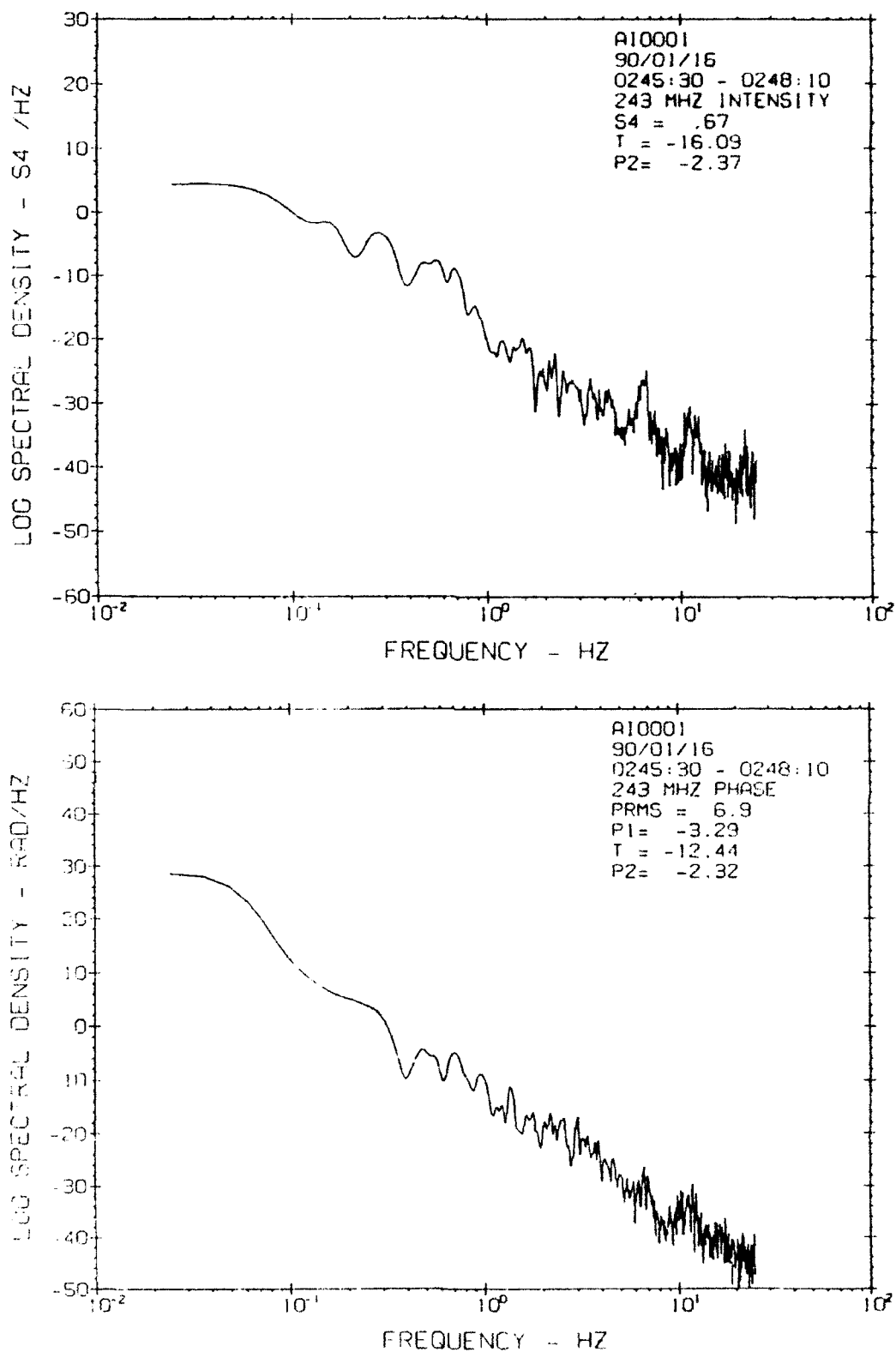


**Figure 65.** The top panel shows the scintillation intensity for the same period as Figure 64. Here, the intensity spectra is actually the average of two 82-second spectra. The bottom panel shows the phase spectrum for the same period. On the upper right of each the spectral plot are provided the scintillation statistics.

obtained from actual observations. The option used to run WBMOD is to increment the receiving station local solar time at 1.5 hours over a full day. We have used the monthly ground observation statistics, which are available for low and high geomagnetic activity in 6-hour UT intervals. These intervals are 2100-0300 UT, 0300-0900 UT, 0900-1500 UT, and 1500-2100 UT. We chose one month from each of the four seasons in 1990: March for spring, June for summer, September for fall, and December for winter. We ran the WBMOD program in three different days for each month, at the beginning, middle, and end of the month. The statistics for each of these days in 1.5-hour increments were then averaged. Besides the day number, the inputs to the model in a given month did not change. We have used the monthly averaged geomagnetic index Kp and the monthly smoothed sunspot number SSN. We must note that WBMOD appears to be very sensitive to these two parameters. For the Thule station, the model yielded the same statistics for all three days for any given hour. For the Sondrestrom station, there was a slight variation in the phase RMS value, but no variation in the S4 values for any given hour. The model statistical results are generally higher than the observations statistics.

We also studied how the model results are affected when other parameters are varied. We again selected the high latitude stations Thule and Sondrestrom, Greenland. The transmitter location was fixed. The variation of the solar activity, while other input parameters were fixed, resulted in a linear relationship between SSN and the S<sub>4</sub> or  $\sigma_{\phi}$  indices. The variation of the magnetic activity, while other input parameters were fixed, resulted in a linear relationship between Kp and the  $\sigma_{\phi}$  index, but no variation (or negligible variation for low Kp in Sondrestrom) for S<sub>4</sub>. There was surprisingly no variation in the scintillation statistics when the day number was varied.

### 3.2 GENERAL ELECTRIC OVER THE HORIZON (OTH) BACKSCATTER RADAR

#### 3.2.1 OTH Tape Processing System

Recent work has focused on the reduction and analysis of data from June, 1991 Equatorial Spread Clutter Campaign. In support of these efforts, the programs TAPEDISK and READOTH have been developed to process tapes received from the East Coast and West Coast Radar Systems (ECRS and WCRS). TAPEDISK is essentially a tape dump program, which creates a file for each record type on a tape. READOTH is then used to unpack each of the recognized data blocks, generating tables and data files for plotting.

The OTH record formats currently under study are generated by the Communications (CO) and Radar Control and Environmental Assessment (RC) processors. Table 24 briefly describes the record formats currently supported by the READOTH program [BDM Corporation, 1989]. In addition, incorporation of code to handle RC113 blocks (backscatter ionograms) is planned.

**TABLE 24. OTH Record Formats Supported by READOTH**

CO28	Geophysical Event Record Data
CO29	AFGWC Geomagnetic Data
CO30	Effective Sunspot Number WSN Message
CO31	Sea State Data
CO32	IONOS Record Data
CO33	IONHTS Record Data
CO35	AFGWC Auroral Oval Boundary Message
RC36	Coordinate Registration Tables Update Message
RC81	Sector Execution Message
RC94	NCNR for EA Support Sectors
RC95	NCNR for Barrier/Interrogate Sectors
RC97/98	Amplitude Range Doppler (ARD) Buffers

Table 25 shows a portion of the detailed tape audit file generated by READOTH. The following parameters are listed for each data block on the tape: the message identifier, or "call number" (ID); message length (in bytes); date and time; record number; and the current number of records received of the given type.

**TABLE 25. Tape Audit File Generated by READOTH**

ID	LENG	DATE	TIME	REC #	MESG #
25	1479	17-JUN-1991	22:46:21.82	66	59
22	1546	17-JUN-1991	22:46:21.82	67	1
25	1479	17-JUN-1991	22:46:22.24	68	60
108	64070	17-JUN-1991	22:46:50.59	69	1
109	10035	17-JUN-1991	22:46:50.60	70	1
81	63	17-JUN-1991	22:46:50.61	71	1
101	62400	17-JUN-1991	22:46:52.26	72	1
102	31802	17-JUN-1991	22:46:52.38	73	1
100	58832	17-JUN-1991	22:46:52.45	74	1
81	63	17-JUN-1991	22:46:52.69	75	2

Some typical READOTH output listings are shown in Tables 26 (CO calls) and 27 (RC calls). These calls and their parameters are described fully in the Data Collection and Analysis Team (DCAT) Data Reduction Product Portfolio [BDM Corporation, 1989]. RC94 and RC95 listings are rather lengthy, so samples have not been included; a detailed discussion of RC97/98 data is given in the following section.

TABLE 26. Typical READOTH Output Listings - CO Calls

C028

DATE	HOUR	MIN	GEO PHY EVNT	SOLAR GEOP	INTEN	ST DATE	ST HOUR	ST MIN	END DATE	END HOUR	END MINUTE
19	00	51	MNR MAG STORM		030//	18	21	00	19	00	00
19	04	45	MNR MAG STORM		032//	19	04	30	//	//	//
19	06	13	MNR MAG STORM		030//	19	04	30	19	06	00
20	02	36	X-RAY EVENT		M1///	20	02	32	//	//	//
20	02	38	X-RAY EVENT		M1///	20	02	32	20	02	37
20	05	05	X-RAY EVENT		M1///	20	05	04	//	//	//
20	05	07	X-RAY EVENT		M2///	20	05	04	//	//	//
20	05	17	X-RAY EVENT		M2///	20	05	04	20	05	17

C029

DATE	HOUR	MINUTE	24 HR. AP	3 HR. AP	3 HR. KP	REPORTING STATION	GAMMAS	INDEX
17	22	30	042	091	065	072712	0362	0007
17	22	30	042	091	065	071816	9999	9999
17	22	30	042	091	065	072469	9999	9999
17	22	30	042	091	065	025602	0572	0005
17	22	30	042	091	065	003655	0209	0006
17	22	30	042	091	065	004205	1102	0009
18	00	00	045	078	064	072712	0190	0006
18	00	00	045	078	064	071816	0750	0007

C030

DATE	HOUR	MIN	SUNSPOT NUM	FLX DATE	SNG FLUX	90 DAY MEAN
18	18	00	//133	169	173	203

C032

MESSAGE TIME	LOCATION	BLOCK	STATION	DATE	TIME	FOF2	F2	FOF1	F1	FOE	FE	FOES	M3000	FREQ	IONOS
17-JUN-1991 22:07:41.89	PAEI	70	265	7	22:00	043	//	//	//	036	11	//	34	39	0
17-JUN-1991 22:36:55.36	PAEI	70	265	6	22:30	//	//	//	//	033	12	033	//	29	1
17-JUN-1991 23:02:40.75	CYAR	71	807	2	23:00	079	34	026	17	019	15	021	27	15	6
17-JUN-1991 23:06:53.43	PAEI	70	265	6	23:00	045	//	//	//	033	12	033	34	20	0
17-JUN-1991 23:46:05.05	PAEI	70	265	16	23:30	048	18	//	//	036	11	//	35	37	0
17-JUN-1991 23:51:54.81	CYAR	71	807	81	22:30	071	//	//	//	023	13	023	24	16	0
17-JUN-1991 23:54:29.72	CYAR	71	807	114	22:00	068	//	041	18	024	11	024	24	15	0
18-JUN-1991 01:58:49.40	CYAR	71	807	88	00:30	042	31	//	//	015	13	018	29	11	0

C033

LOCATION	BLOCK	STATION	DATE	TIME	ZERO TRACE	VIRTUAL	GLS
	NUMBR	NUMBER			FREQUENCY	HEIGHT	
CYAR	71	807	06/17/1991	22:00	015	10	
CYAR	71	807	06/17/1991	22:00	016	10	
CYAR	71	807	06/17/1991	22:00	017	11	
CYAR	71	807	06/17/1991	22:00	018	11	
CYAR	71	807	06/17/1991	22:00	019	12	
CYAR	71	807	06/17/1991	22:00	020	12	
CYAR	71	807	06/17/1991	22:00	021	13	
CYAR	71	807	06/17/1991	22:00	022	14	

C035

FORECAST	OBSERVATION					
DATE AND TIME	DATE AND TIME	LAT	N-S	LONG	E-W	Q VALUE
168 23:46	168 21:29	57.54	N	000.00	W	+10.7
* 168 23:46	168 21:29	57.22	N	005.00	W	
* 168 23:46	168 21:29	56.98	N	010.00	W	
* 168 23:46	168 21:29	56.70	N	015.00	W	
* 168 23:46	168 21:29	56.36	N	020.00	W	
* 168 23:46	168 21:29	55.84	N	025.00	W	
* 168 23:46	168 21:29	55.17	N	030.00	W	
* 168 23:46	168 21:29	54.35	N	035.00	W	

TABLE 27. Typical READOTH Output Listings - RC Calls

RC36

	VAX DATE AND TIME		SEG	SEC	TYPE	SEC_AZ	OP_FREQ	PROP MOD	CHNGCNT	GR_ST	NUM_MLTM	
2	VIR_HT	VIR_HT	VIR_HT	VIR_HT	VIR_HT	VIR_HT	VIR_HT	VIR_HT	VIR_HT			
3	SL_RNG	SL_RNG	SL_RNG	SL_RNG	SL_RNG	SL_RNG	SL_RNG	SL_RNG	SL_RNG			
4	GR_RNG	GR_RNG	GR_RNG	GR_RNG	GR_RNG	GR_RNG	GR_RNG	GR_RNG	GR_RNG			
17-JUN-1991	22:46:53.90		1	1	BAR	163.8	20.918		F	0	1000	1
2	315	315	315	315	315	315	315	315	315			
3	1100.0	1200.0	1300.0	1400.0	1500.0	1600.0	1700.0	1800.0				
4	980.4	1083.0	1184.9	1286.2	1387.2	1487.9	1588.4	1688.7				
17-JUN-1991	22:46:55.11		1	2	BAR	171.3	20.918		F	0	1000	1
2	315	315	315	315	315	315	315	315	315			
3	1100.0	1200.0	1300.0	1400.0	1500.0	1600.0	1700.0	1800.0				
4	977.1	1079.6	1181.5	1282.8	1383.9	1484.5	1584.9	1685.2				
17-JUN-1991	22:46:57.46		1	3	BAR	178.8	20.918		F	0	1000	1
2	315	315	315	315	315	315	315	315	315			
3	1100.0	1200.0	1300.0	1400.0	1500.0	1600.0	1700.0	1800.0				
4	974.4	1077.0	1178.8	1280.2	1381.2	1481.8	1582.2	1682.5				

RC81

VAX TOD	SEG	SEC	TYPE	UP	FREQ	SEC_AZ	GR ST	RX	BMSPC	PRI	WBW	RFTT	ON	TX ANT	UPD	CAUS
17-JUN-1991 22:46:50.60	1	1	BAR		20.92	163.75	1000		0		8		F	3		
17-JUN-1991 22:46:50.60	1	2	BAR		20.92	171.25	1000		0		8		F	3		A
17-JUN-1991 22:46:50.60	1	3	BAR		20.92	178.75	1000		0		8		F	3		A
17-JUN-1991 22:46:50.60	1	4	BAR		20.92	186.25	1000		0		8		T	3		A
17-JUN-1991 22:46:50.60	1	5	BAR		20.92	193.75	1000		0		8		F	3		A
17-JUN-1991 22:46:50.60	1	6	BAR		20.92	201.25	1000		0		8		F	3		A
17-JUN-1991 22:46:50.60	1	7	BAR		20.92	208.75	1000		0		8		F	3		A
17-JUN-1991 22:46:50.60	1	8	BAR		20.92	216.25	1000		0		8		F	3		A

### 3.2.2 Amplitude Range Doppler Data Studies

The Amplitude Range Doppler (ARD) data contained in calls RC97 and RC98 is of particular interest for PL studies. These blocks contain backscatter doppler spectra, from which much information about equatorial ionospheric clutter may be derived.

The ARD data blocks consist of a header followed by the actual radar return values (gain), arranged by Doppler cell order. Table 28 shows a summary of selected ARD data header parameters; a brief description of each column is given in Table 29 [BDM Corporation, 1989]. The sample listing was generated from a tape containing approximately one hour of data. Output is separated by sector and segment; here, data is shown only for segment 1, sector 1. Updated header information is printed only when a change is detected in one of the following parameters:

- Operating frequency
- Waveform repetition frequency
- Slant range
- Primary coherent integration time
- Transmitter status (on/off), determined from EFFRPR: 50 dB indicates transmitter off, while 0 or 3 dB indicates transmitter on.

These parameters must be monitored separately for each type of beam, to avoid comparing data obtained from different operating modes. Note also that these listings include only the first of the three beams in each sector, since the parameters are the same for all three beams.

TABLE 28. Summary of Selected ARD Data Header Parameters

R E C	DATA TIME	W T S E										S W E			S S		
		D Y S C P		B		P		P		L F F		N P F		M A M		F F B	
		D E G R T		W		C		W		T A R		R		U D I		L D O	
		I I I T		I		I		F		S		C		R		Q B F S G	
		A D D D B D		D		T		C		R D R O P F		S C T R A Z		R S C		R	
10	21-JUN-1991 04:13:12.28	0	B	1	1	0	2.5	2.1333	30.0	18.60900	163.75	1112	24	3.00	57.22	33.70	50 123 1
415	21-JUN-1991 04:19:35.42	0	B	1	1	0	2.9	2.1333	30.0	15.85700	163.75	1112	25	3.00	57.22	33.70	50 121 1
919	21-JUN-1991 04:23:38.50	0	B	1	1	0	2.9	2.1333	30.0	16.07500	163.75	1112	26	3.00	57.22	33.70	42 71 1
1957	21-JUN-1991 04:30:01.49	0	B	1	1	0	2.9	2.1333	30.0	15.68600	163.75	1112	27	3.00	57.22	33.70	39 39 1
4834	21-JUN-1991 04:48:56.63	0	B	1	1	0	2.9	2.1333	30.0	15.73500	163.75	1112	28	3.00	57.22	33.70	42 81 1
64	21-JUN-1991 04:13:30.70	0	I	1	1	0	2.5	2.1333	15.0	18.60900	163.75	1114	20	3.00	57.22	31.10	49 95 1
430	21-JUN-1991 04:19:41.00	0	I	1	1	0	2.9	2.1333	15.0	15.85700	163.75	1114	21	3.00	57.22	31.10	53 128 1
964	21-JUN-1991 04:23:55.41	0	I	1	1	0	2.8	2.1333	15.0	16.07500	163.75	1114	22	3.00	57.22	31.10	47 85 1
1999	21-JUN-1991 04:30:12.00	0	I	1	1	0	2.9	2.1333	15.0	15.68600	163.75	1114	23	3.00	57.22	31.10	44 69 1
4804	21-JUN-1991 04:48:42.30	0	I	1	1	0	2.9	2.1333	15.0	15.73500	163.75	1114	24	3.00	57.22	31.10	51 77 1
499	21-JUN-1991 04:20:33.42	0	S	B	1	1	0	2.9	2.1333	30.0	15.85700	163.75	1112	0	50.00	57.22	33.70 52 47 1
514	21-JUN-1991 04:21:06.65	0	S	B	1	1	0	2.9	1.6000	20.0	15.85700	163.75	862	0	3.00	57.22	30.30 50 124 1
2323	21-JUN-1991 04:32:14.79	0	S	B	1	1	0	2.9	2.1333	30.0	15.68600	163.75	1112	0	50.00	57.22	33.70 52 49 1
2419	21-JUN-1991 04:32:51.76	0	S	B	1	1	0	2.9	1.6000	20.0	15.68600	163.75	862	0	3.00	57.22	30.30 51 124 1
4303	21-JUN-1991 04:44:28.83	0	S	B	1	1	0	2.9	2.1333	30.0	15.68600	163.75	1112	0	50.00	57.22	33.70 52 52 1
4390	21-JUN-1991 04:45:03.75	0	S	B	1	1	0	2.9	1.6000	20.0	15.68600	163.75	862	0	3.00	57.22	30.30 54 132 1
307	21-JUN-1991 04:17:50.80	0	S	I	1	1	0	2.5	2.1333	15.0	18.60900	163.75	1114	0	50.00	57.22	31.10 55 38 1
361	21-JUN-1991 04:18:23.33	0	S	I	1	1	0	2.5	1.6000	20.0	18.60900	163.75	864	0	3.00	57.22	30.30 51 119 1
1831	21-JUN-1991 04:29:13.21	0	S	I	1	1	0	2.8	2.1333	15.0	16.07500	163.75	1114	0	50.00	57.22	31.10 56 62 1
1915	21-JUN-1991 04:29:43.20	0	S	I	1	1	0	2.9	1.6000	20.0	16.07500	163.75	864	0	3.00	57.22	30.30 48 107 1
3808	21-JUN-1991 04:41:24.02	0	S	I	1	1	0	2.9	2.1333	15.0	15.68600	163.75	1114	0	50.00	57.22	31.10 50 31 1
3889	21-JUN-1991 04:41:56.92	0	S	I	1	1	0	2.9	1.6000	20.0	15.68600	163.75	864	0	3.00	57.22	30.30 51 126 1

TABLE 29. Description of Table 28 Columns

REC	The record number within the file.
DATE/TIME	Date and universal time of the sounding.
WDBDTA	The type of wideband data in the wideband message transmission.
TYPEID	The beam type: Barrier (B), Interrogate (I), Support Barrier (SB), or Support Interrogate (SI).
SEGID/SCTRID	Segment and sector identifiers.
EPMTTB	The EPM test mode.
BMWID	The receive bandwidth.
PRCIT	Primary coherent integration time (CIT).
PWRFC	Primary waveform repetition frequency (WRF).
RDROPF	The operating frequency of the radar (in MHz).
SCTRAZ	The azimuth at the center of the sector.
SLNTRS	Slant range start (measured along the ionospheric refraction path).
WFPARC	Waveform parameter change count.
EFFRPR	Effective Radiated Power Reduction.
QBFSG	Beamformer Signal Gain.
QSPSG	SP Signal Gain.
SFMUL,SFADD	Scale factors for ARD and CW data interpretation.
BMID	The beam identifier (1, 2, or 3).

When studying the ARD data, the areas of radar coverage are of primary importance. Figure 66 shows the coverage provided by the barrier sectors over a span of approximately eight minutes from the same data set summarized in Table 28. The location of the WCRS is indicated by the star, and segment areas are shown over a range of 500 NM to 2500 NM. As the name implies, the barrier sectors provide continuous coverage throughout the operating segments. Note that segment three was inactive during this time period, as indicated by the absence of a barrier.

Three beams are operated concurrently in each sector, with a beam width of  $2.5^\circ$ . Figure 67 shows ARD data for the three beams in segment 1, sector 1, plotted over a common slant range. Some of the most important radar system parameters are displayed along the top. Note that this plot covers a range of only 128 NM. Four plots would be required to show the entire 512 NM range extent.

An averaging process has been developed to smooth the data and to reduce the number of plots. Bins are defined containing five range cells, or individual pulses. These cells are then "range folded", and treated as if they occur over a common range. In addition, the three beams within each sector are combined, so that each bin contains a total of fifteen range cells. Data are sorted at each Doppler line (the discrete points) within the bin, and the median values are used to produce one composite range cell. Time averaging has also been implemented, and has typically been performed using five minute windows. The time averaged data in Figure 68 displays much smoother features than the raw data in Figure 67. Preliminary comparisons of averaged and unaveraged data have indicated that significant features of the data are generally retained by this averaging scheme.

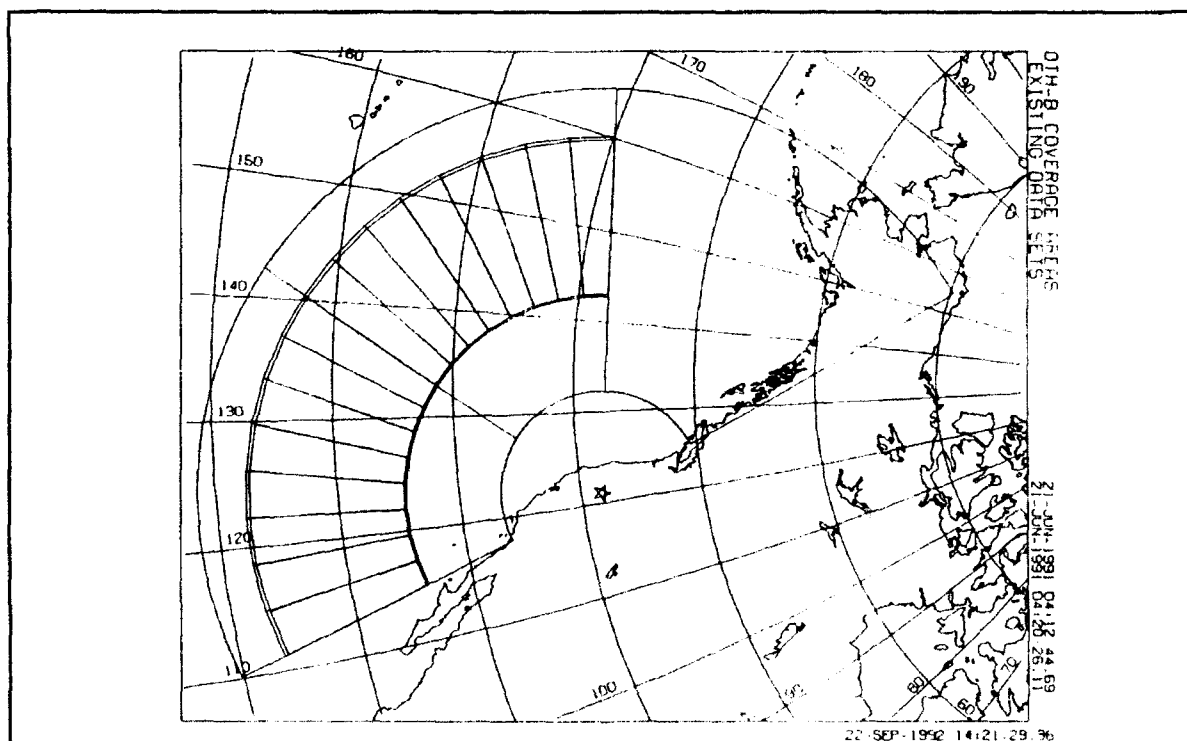


Figure 66. OTH coverage areas.



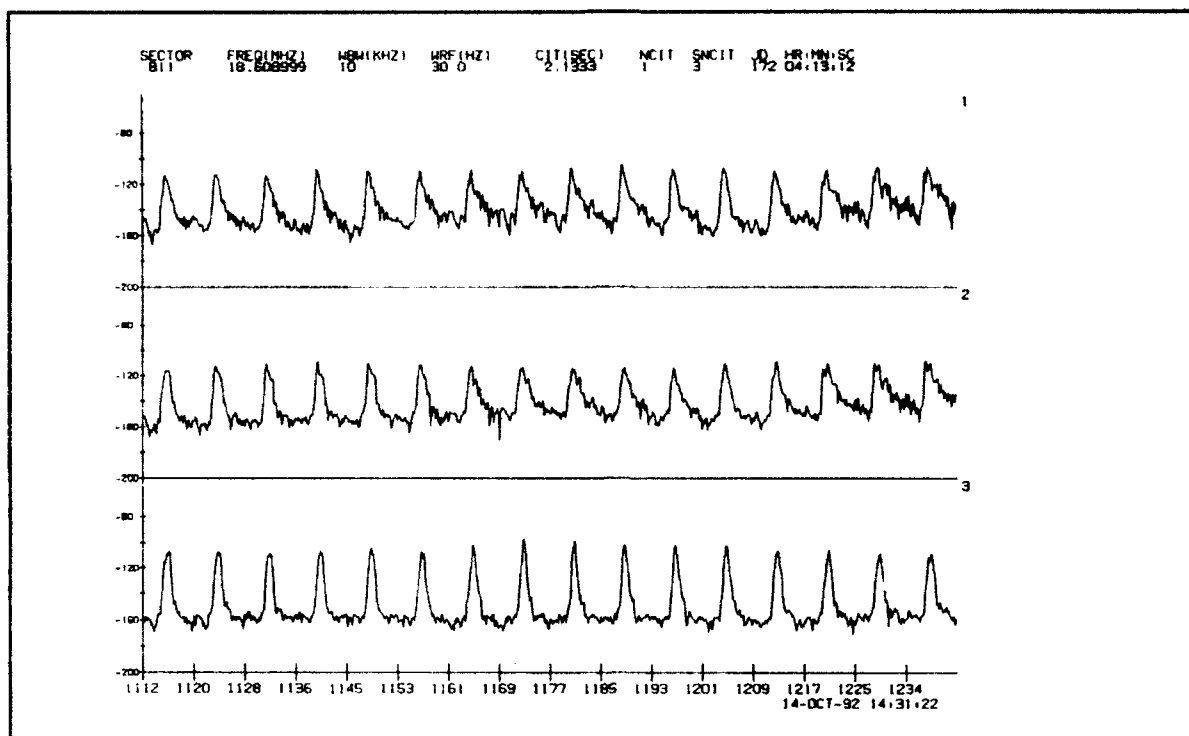


Figure 67. Sample ARD data plot.

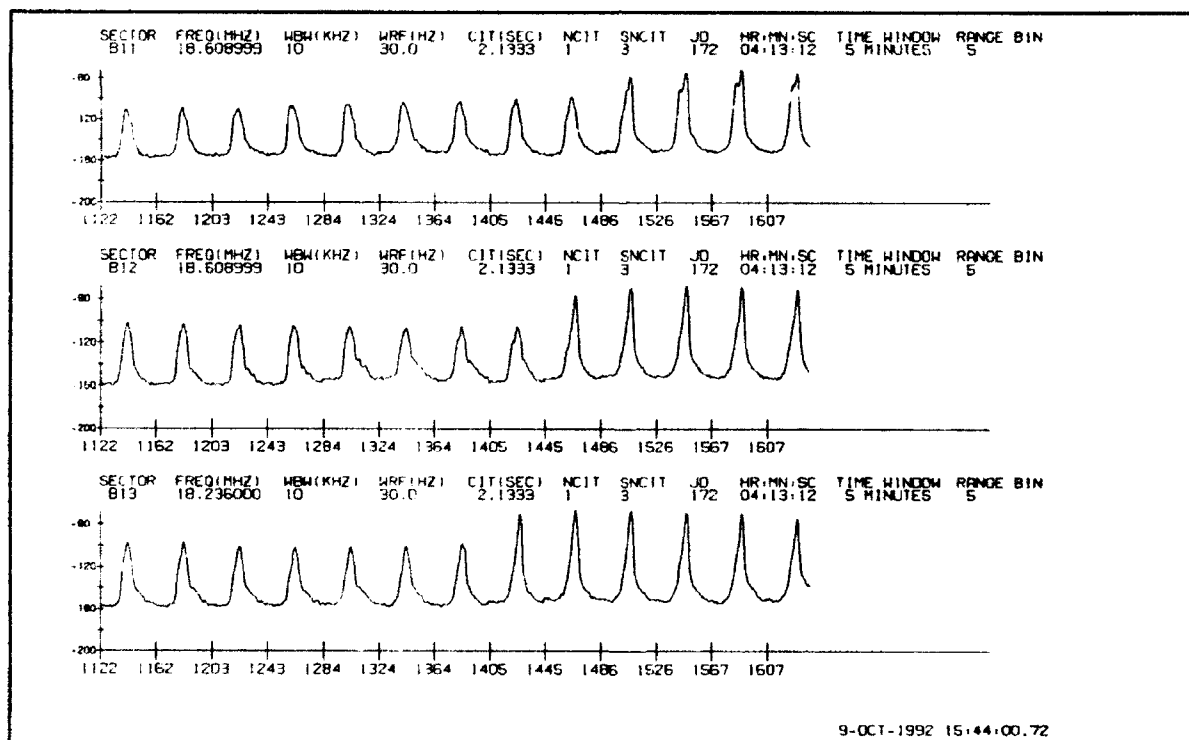


Figure 68. Time averaged ARD data.

Some characteristics of the ARD data that are of interest for PL studies are defined as follows [Providakes, 1992]:

- Ground clutter amplitude - the peak value (near 0 Hz Doppler) within an individual range cell.
- Ground clutter Doppler (GCD) - the velocity ( $V_r$ ) associated with the ground clutter amplitude, calculated from

$$V_r = \frac{cf_D}{2f_o}$$

where  $f_D$  is the Doppler frequency at the peak, ranging from  $WRF/2$  to  $-WRF/2$  within a range cell;  $f_o$  is the operating frequency.

- Median noise level - the median of the first four points and the last three points from a range cell.
- Clutter to noise ratio (CNR) - the difference between the ground clutter amplitude and the median noise level (or any other defined measure of Doppler clutter level).
- Excess noise level - the difference between the median noise level and the transmitter off noise level. This is the component of the noise that occurs due to radar system operation.

Ground clutter amplitude values from time averaged data are displayed for all active sectors in Figure 69. Numbers outside the segment boundaries indicate all operating frequencies in use during the five minute window.

The clutter/noise components from a typical Doppler spectrum of one range cell are depicted in Figure 70 [Sales, 1992]. In order to isolate the ionospheric (equatorial) clutter, the contribution of the ground clutter must first be removed from the data. This is done by excising all points with Doppler velocities (GCD) less than a predetermined value; the number of points to discard on either side of the peak is then calculated from

$$\frac{NDC * 2V_{EX} * f_o}{WRF * c}$$

where  $NDC$  is the number of Doppler bins per range cell,  $V_{EX}$  is the excision velocity,  $f_o$  is the operating frequency, and  $c$  is the speed of light. Various excision velocity threshold values have been tested to find the best compromise between removing the ground clutter and retaining the characteristics of the ionospheric clutter. Figure 71 shows results obtained using an excision velocity threshold of 40 m/s.

Two straight line fits are then made to the excised data (one on each side of the peak) to determine the approximate clutter spectrum shape in the excised region. The steeper of the two slopes is used to approximate the ground clutter on both sides of the peak. Thus, the ground clutter estimate will tend to be conservative. These approximations are extended outside the excised region, so that outlying points may be "corrected" to remove the estimated ground clutter contribution. Table 30 indicates the corrections applied to the measurements. "Difference" is found by subtracting the value given by the

GROUND CLUTTER AMPLITUDE  
5 RANGE CELL BINS  
5 MINUTE TIME AVERAGING

21-JUN-1991 04:13:12.28

9-OCT-1992 15:40:28.77

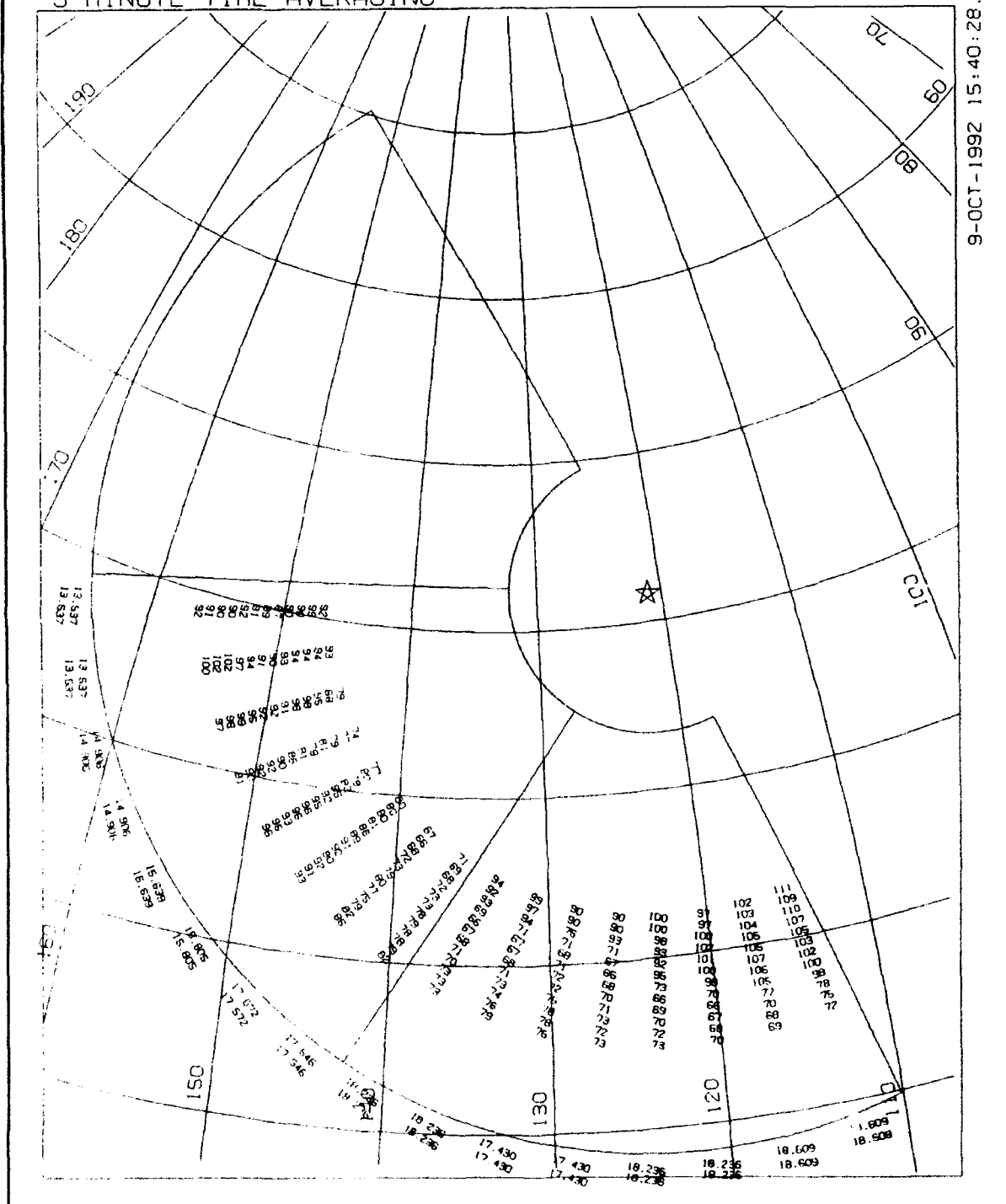
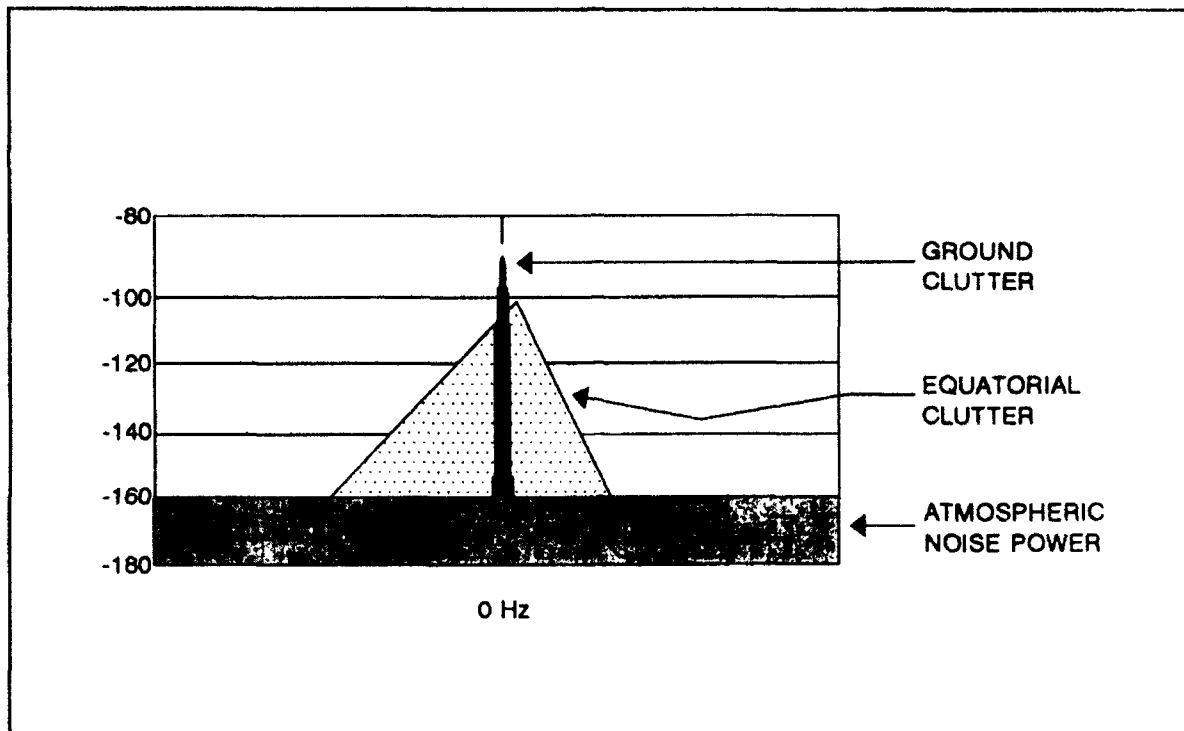


Figure 69. Sample ground clutter amplitude plot.



**Figure 70.** Simulated equatorial backscatter doppler spectrum.

straight line fit from the measured value. In most cases, only a few points on each side of the peak are altered by this approach.

The range cell is then scanned to remove data within a specified tolerance of the noise level (generally 6 dB). Finally, two straight line fits are made to the remaining points (one fit on each side of the original peak) to model the ionospheric clutter. Figure 72 shows a typical ionospheric clutter approximation generated using an excision velocity of 30 m/s.

**TABLE 30.** Corrections Applied to Measurements

Difference	Correction
$\leq 0$	None
1	7
2	4
3	3
4 or 5	2
6 - 9	1
$\geq 10$	0

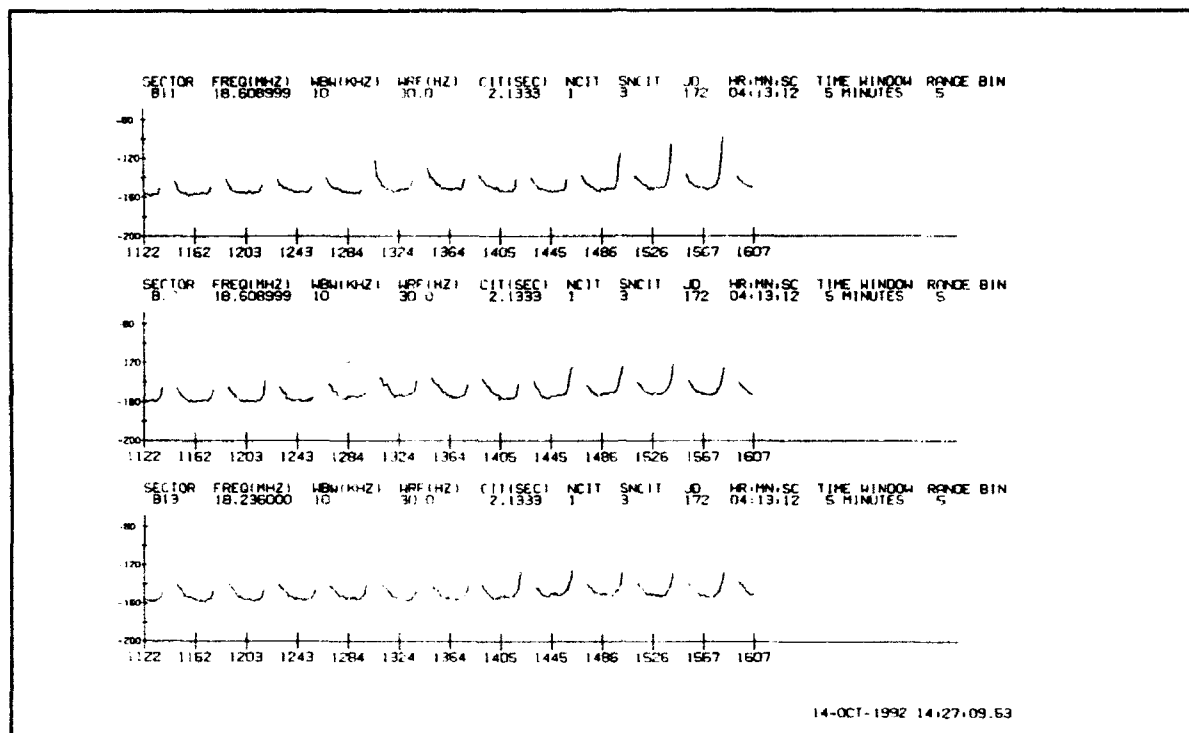


Figure 71. Ground Clutter Excision

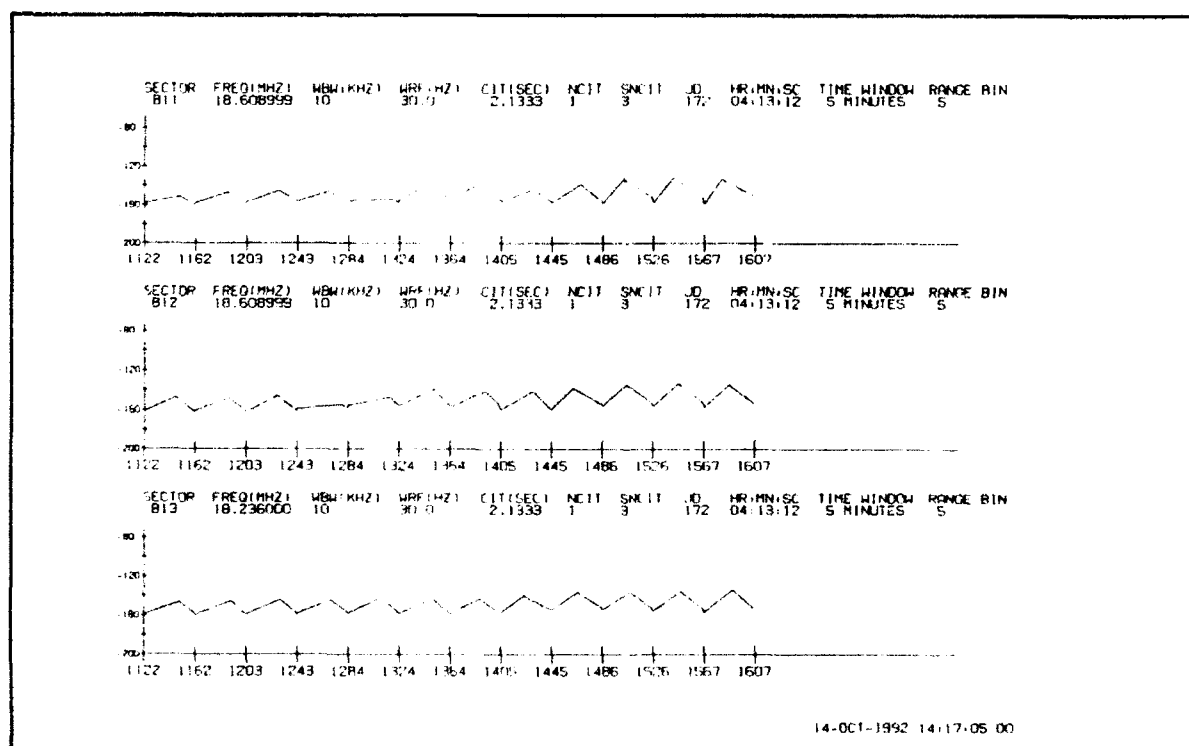


Figure 72. Equatorial Clutter Fit

### 3.2.3 OTH Backscatter Sounder Data Studies

The OTH system operates against the background of the equatorial ionosphere, which is subject to large disturbances at night. The performance of the radar is affected by range folded spread clutter from this region. The backscatter sounder of the ECRS provides a means of studying the source regions of the spread clutter [Buchau, *et al.*, 1992].

A backscatter/clutter data base has been assembled from long-range (8000 NM) backscatter ionograms made by the OTH-B sites. Most of this data has been collected from the ECRS, although a small sample of backscatter soundings was obtained from the WCRS over a two week period of operation during June, 1991, just before the facility was mothballed. The sample backscatter ionogram shown in Figure 73 (day 293, 1991) shows the typical backscatter signatures observed during Doppler spread clutter conditions, namely strong backscatter traces at almost constant ranges over large frequency bands. The analysis of this backscatter ionogram resulted in two entries in the ECRS data base: one clutter band from 4650 to 4800 NM, extending from 17.5 to 28 MHz; the second from 4800 to 6500 NM, and from 15 to 17.5 MHz. This ionogram clearly shows the slant leading edges of the first two "hops" (ground reference points) as dark regions covering the full frequency extent. The leading edge of the third hop is also visible, although it is much less clearly defined.

An overview of the available data base from the ECRS for Winter, 1992 is presented in Figure 74. The backscatter ionograms are indicated by dots, plotted on a grid of UT versus day number. Positions 1 through 6 correspond to soundings in segments 1, 2, and 3, for each of the two days displayed between the vertical lines. As the figure indicates, the sounder is typically operated in eight hour shifts, which are staggered to obtain coverage at various times of day.

The clutter data from the entire 1991-92 ECRS sounding data base is depicted in Figure 75. The time and range extent of the individual observations are displayed on a grid of dip angle vs. local time. This presentation suggests distinct concentrations due to contributions from the southern anomaly, the equatorial region, and the northern anomaly. The histograms along the bottom of the plot indicate the time dependence of the observations. "Count" shows the number of events in fifteen minute bins, while "Pct" indicates the frequency of clutter detection within these bins. Likewise, the histogram on the right shows count information for 2.5° dip angle bins. A percentage histogram is not necessary here, because the ionogram occurrences are distributed fairly uniformly relative to dip angle. These presentations have also been made using color to distinguish between the three segments of the radar system.

Figure 76 shows the 1991-92 clutter plotted in geographic coordinates, on a Mercator projection. As indicated at the lower left, clutter observations with range extents less than 200 NM are not shown. ECRS segment boundaries are marked with heavy lines, with range marks indicated by crosses every 1000 Km. Sectors for which at least one ionogram exists in the data base are shaded at short range. Complete sector-by-sector ionogram statistics are tabulated along the top of the plot. Dip latitude contours are shown for 0°, ±20°, and ±40°, where dip latitude (DL) is calculated from dip by

$$DL = \arctan\left(\frac{\tan(DIP)}{2}\right)$$

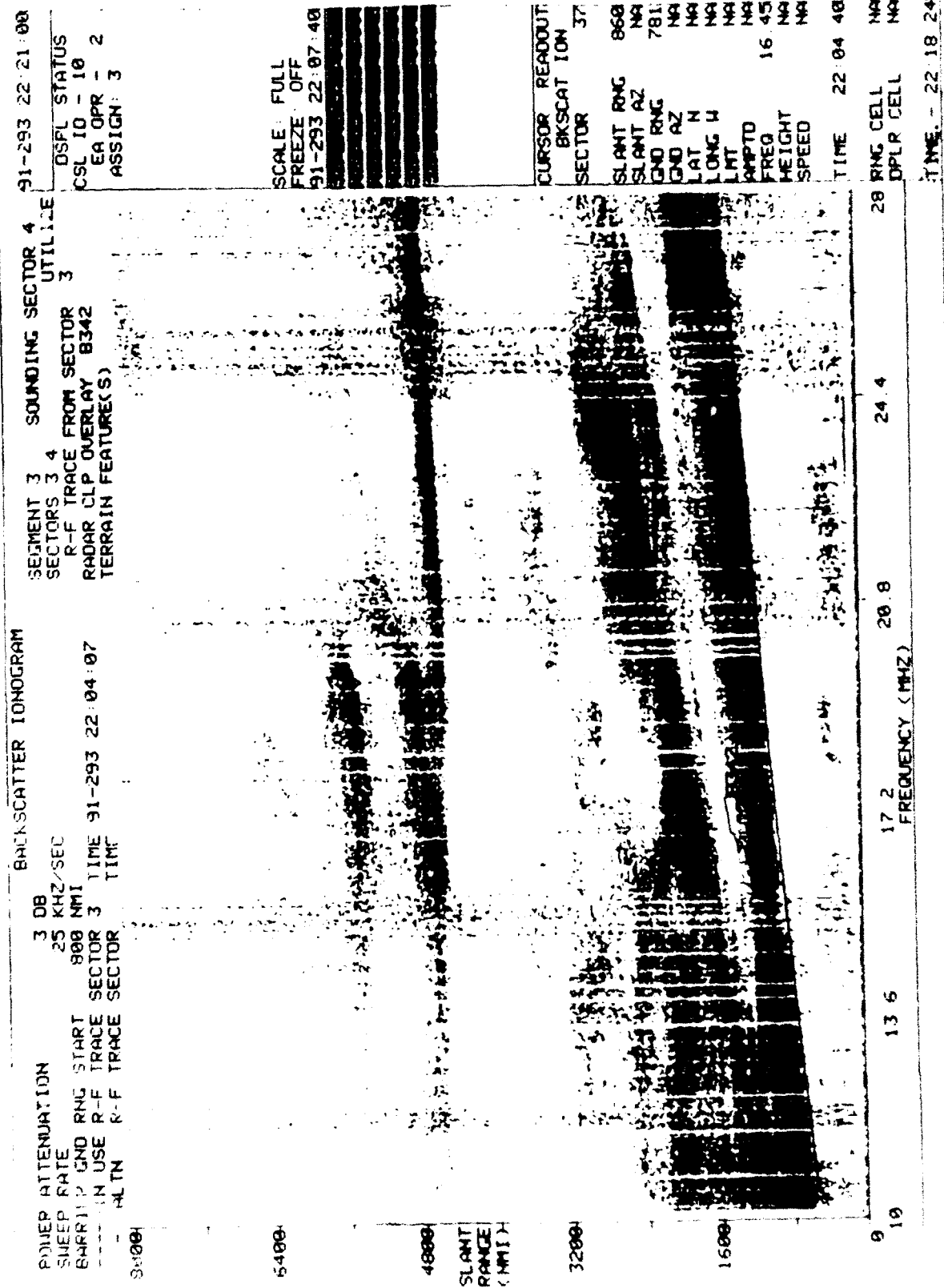


Figure 73. Sample backscatter ionogram.

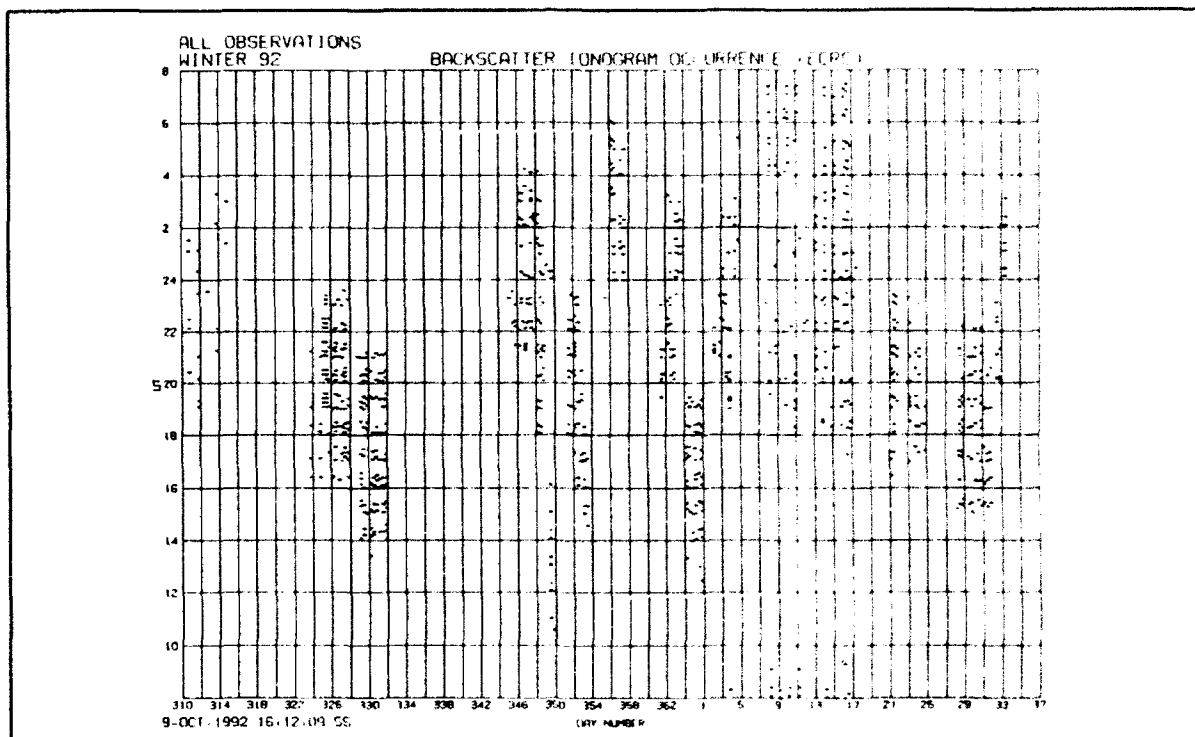


Figure 74. Winter, 1991-92 ionogram database.

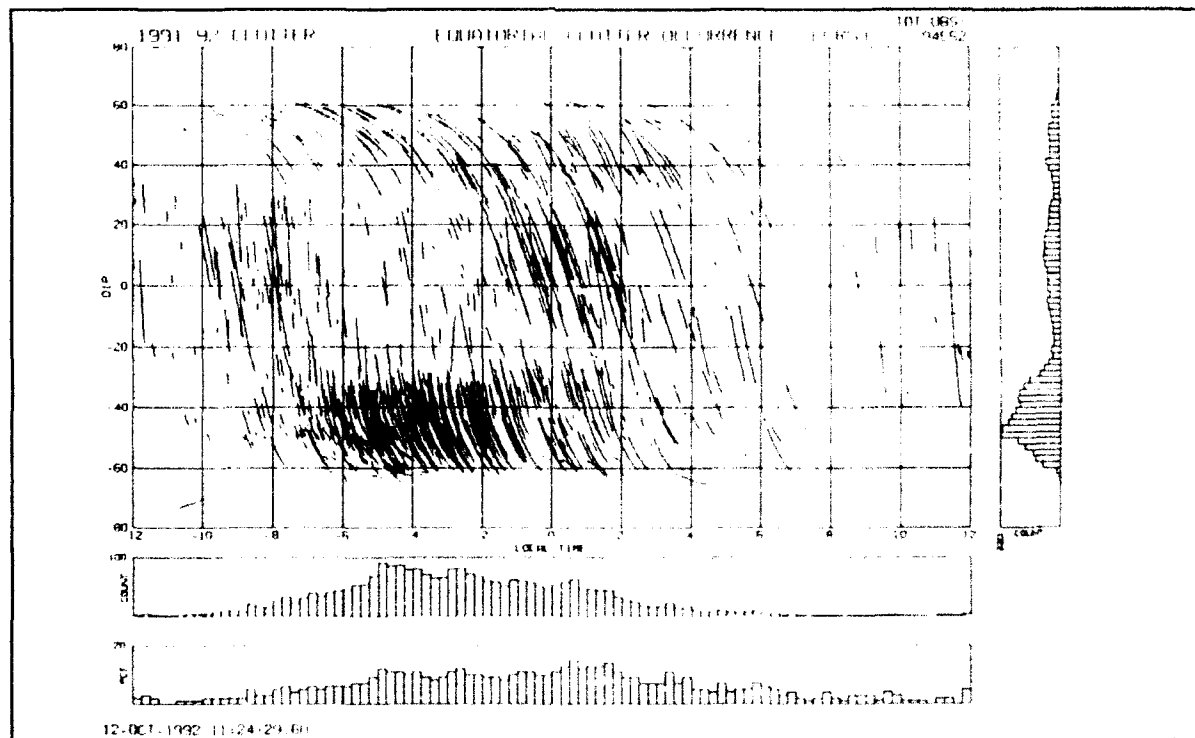


Figure 75. Equatorial clutter scatter plot.



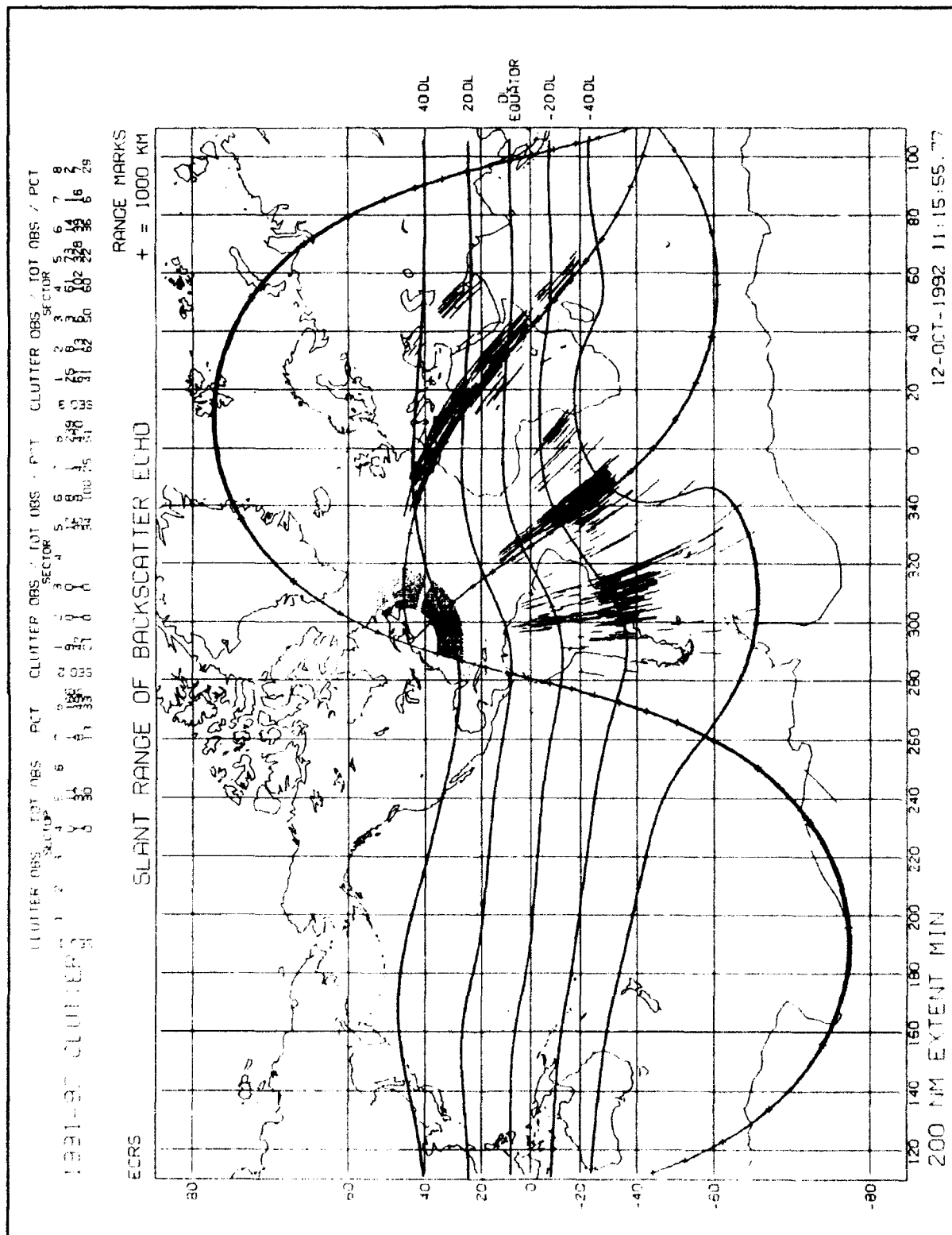


Figure 76. 1991-92 ECRS clutter.

Note that the ground clutter is concentrated within the  $-40^\circ$  dip latitude contour. This is true even in segment 3, where the  $-40^\circ$  dip latitude contour occurs at longer ranges due to the South Atlantic Magnetic Anomaly.

### 3.2.4 Ionospheric Models and Ray Tracing

The Jones-Stephenson three-dimensional, non-isotropic ray tracing program [Jones, *et al.*, 1975] has been used extensively to evaluate the propagation of OTH rays. Studying OTH ray propagation in conjunction with ionospheric contours provides a better understanding of the backscatter sounder clutter data.

The Jones-Stephenson program traces the path of radio waves through the ionosphere, given the transmitter location, and the wave frequency and direction. The original form of the program assumed a uniform ionosphere. Recently, the software has been modified to accept electron density profiles from any of the following ionospheric models:

- Ionospheric Communication Analysis and Prediction Program (IONCAP) - includes modeling of the auroral oval and the mid-latitude F-layer trough.
- General Electric (GE) Ionospheric Model - IONCAP extended to allow updating by real-time data.
- Fully Analytic Ionospheric Model (FAIM) - improves over IONCAP in the equatorial region [Anderson, *et al.*, 1989].
- Parameterized Ionospheric Model (PIM) - this is the base ionospheric model on which PRISM (Parameterized Real-time Ionospheric Specification Model) operates [Whartenby, 1992]; PRISM includes updating by real-time data.

The distribution version of the FAIM model generates a density profile at a particular location over an altitude range of 90 Km to 1000 Km, at 10 Km intervals. Since output is normally provided hourly in local time, an interpolation scheme has been added to allow output to be generated for any arbitrary universal time. A number of contour plots have been produced along great circle paths originating from the ECRS site. A sample is shown in Figure 77. Note that no data is available for approximately the first 1000 Km of range, since FAIM is only valid for latitudes between  $-40^\circ$  and  $40^\circ$ . This causes the contour lines to close artificially approaching the data limits. Similar behavior is seen in the region near 90 Km altitude.

Software has been developed to display results obtained from the Jones-Stephenson program, along with corresponding ionospheric contours. These plots show the propagation of OTH signals as they reflect off the ionosphere and extend the system's surveillance around Earth's curvature. Figure 78 shows a typical ray trace originating from Omaha, with an ionospheric contour overlay generated by the GE model. Omaha is shown in the center of the plot, with 6000 Km ranges displayed to the north and the south. The arched plot frame corresponds to the curvature of Earth's surface. Rays are shown with a variety of initial elevation angles; note that several of the highest elevation rays penetrate through the ionosphere without reflecting.

An individual ray trace plot for the ECRS is shown in Figure 79, along with three overlays. Since only one azimuth is shown in this example, the station appears at the left edge of the plot frame. The overlays provide the following information:

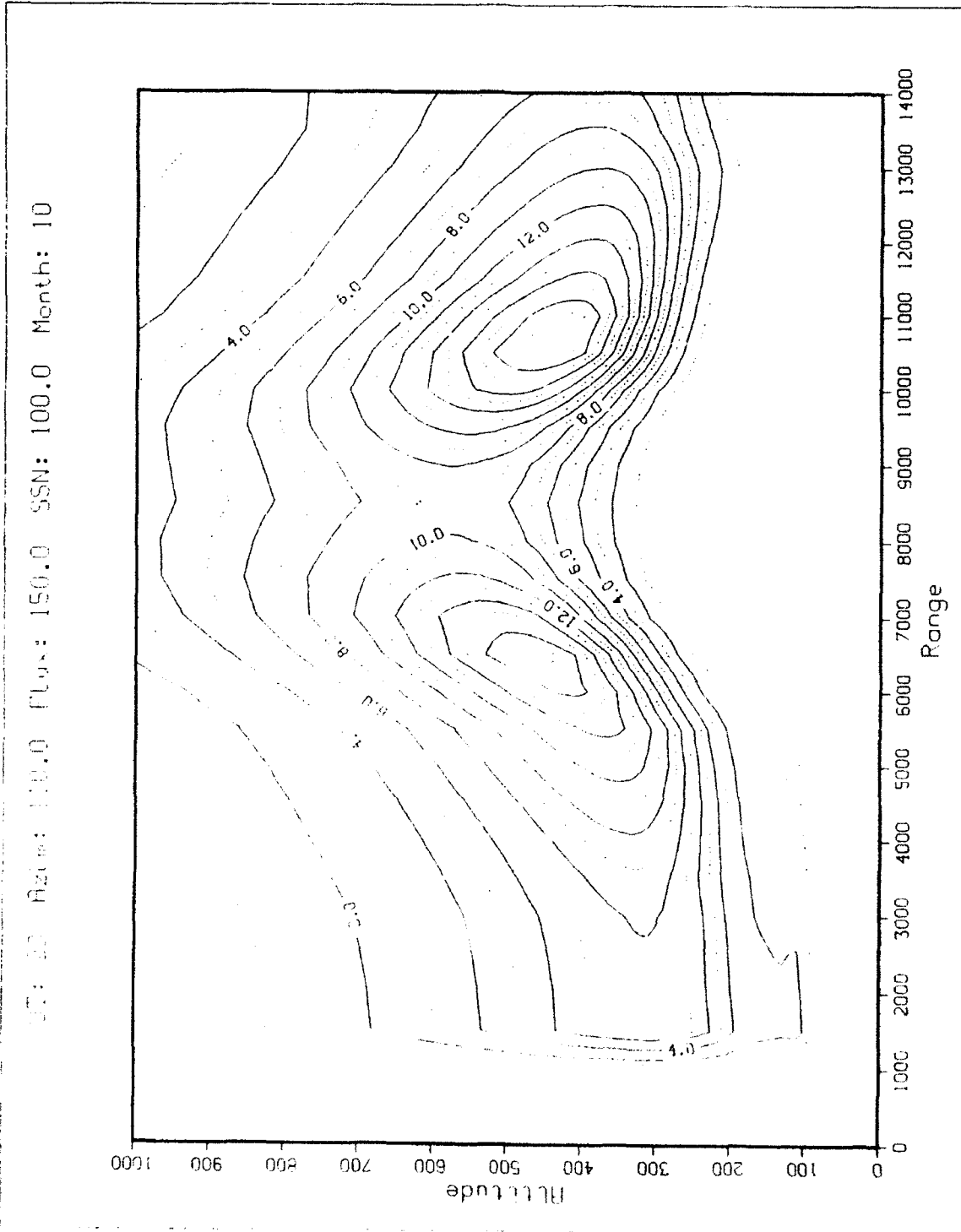
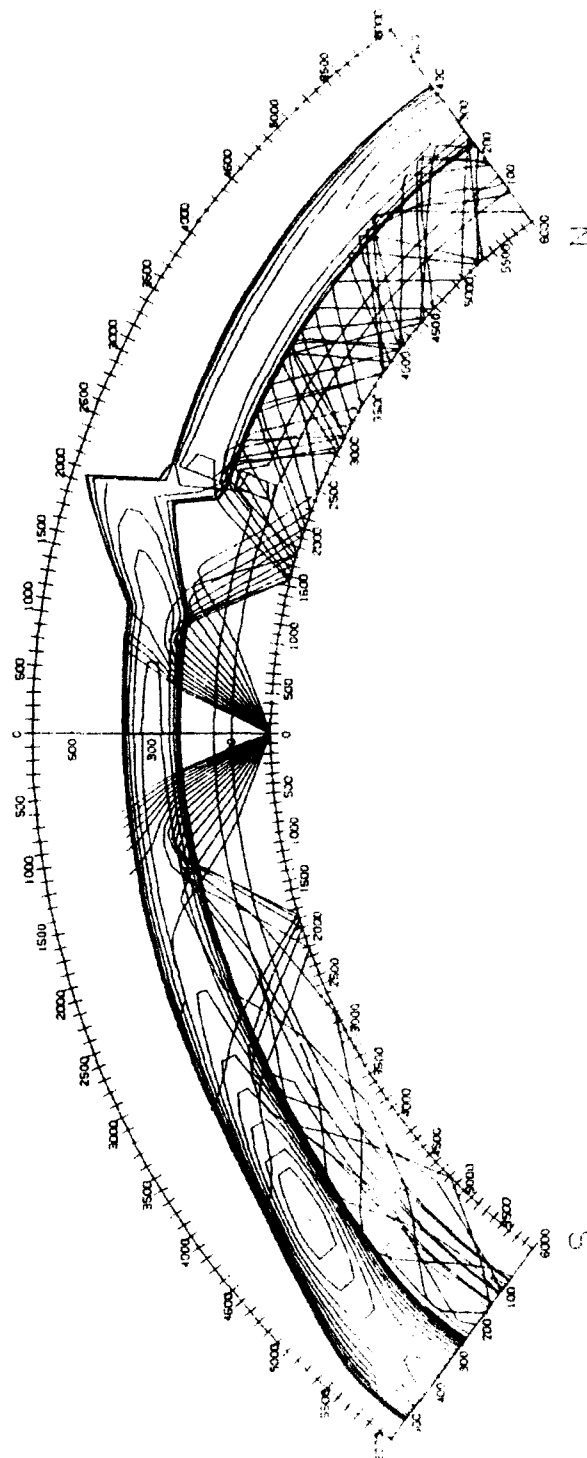


Figure 77. FAIM contour.

FILES :: OMA2214 : OMAH112  
 ORIGIN :: 40.00 265.00  
 DATE :: 12/15/1991 TIME :: 01:00 UT  
 FREQUENCY :: 14.0  
 SSN :: 100.0  
 KP :: 3.0  
 Q :: 3.0  
 MAXIMUM FOF2 :: 13.0 : 6.4  
 MAXIMUM FOF1 :: 3.1  
 MAXIMUM FOF :: 2.1 : 3.2  
 START ELEVATION ANGLE :: 3.0  
 STEP :: 2



**Figure 78.** Ray trace with ionospheric contour overlay.

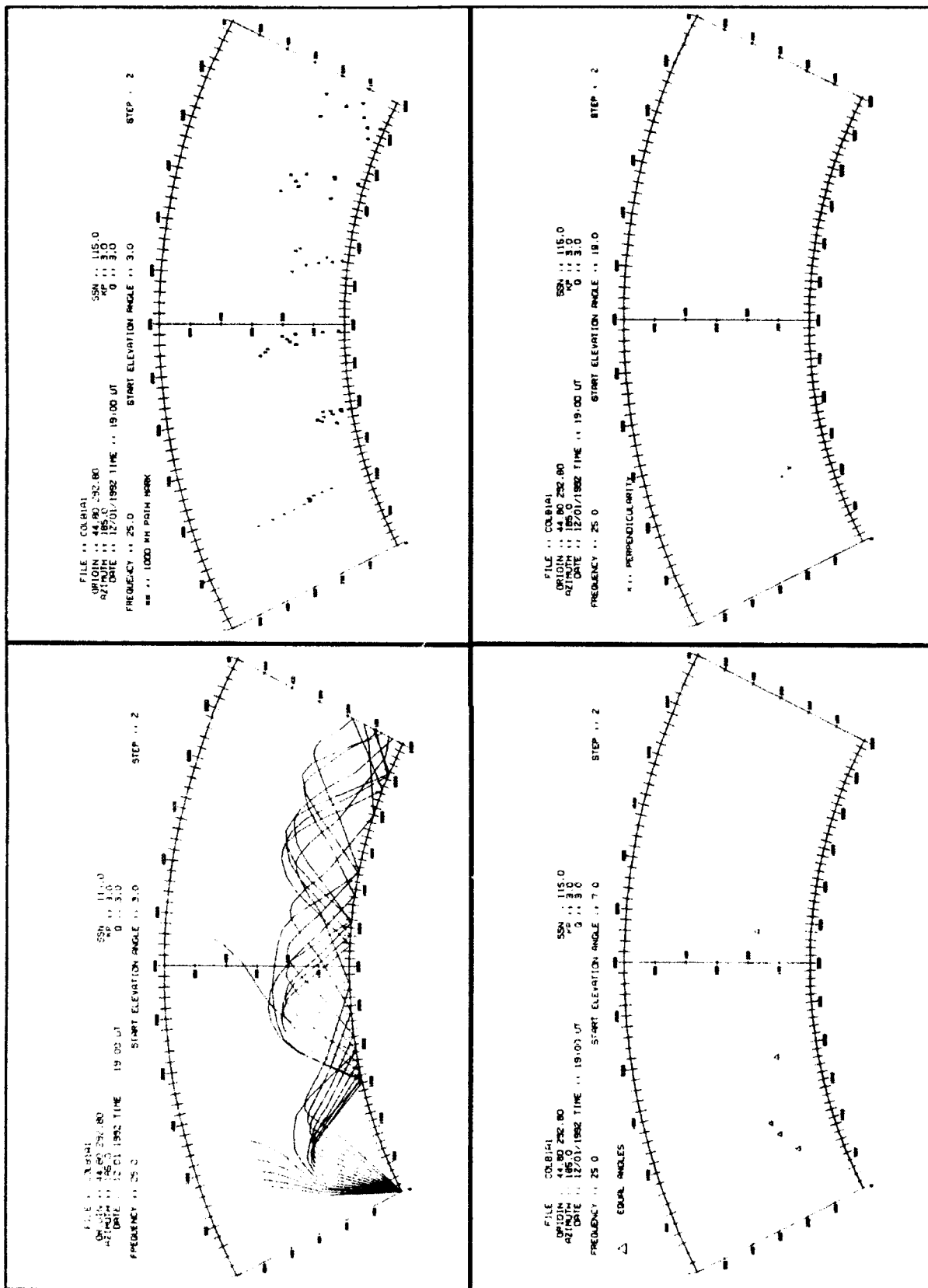


Figure 79. Individual ray trace plot with overlays.

- (upper right) 1000 Km marks - slant ranges (group paths) in multiples of 1000 kilometers. Slant range is the distance from the station, as measured along the path of the ray.
- (lower left) Equal angles - indicates points where two intersecting rays make equal angles with Earth's magnetic field. In this situation, the magnetic field may serve as a "mirror", allowing energy to be transferred from one ray to the other.
- (lower right) Perpendicularity - shows locations where a ray is perpendicular to Earth's magnetic field. The ray may be reflected back, or it may continue on in a greatly weakened state. The panel shows, that for a south looking radar, perpendicularity with the magnetic field (and therefore with field aligned electron densities) is achieved only on the first hop, and never near the equator.

A technique to generate synthetic backscatter ionograms by raytracing in a model ionosphere was developed in the 1960's [Croft, 1972]. These simulated ionograms may be produced by plotting the ground reference points from the ray tracing on a grid of frequency versus range. Typically, ray trace data has been generated using 2° elevation steps and 1 MHz frequency steps. In the example in Figure 80, the first three hops are plotted and indicated by rectangles, ovals, and triangles. The leading edges of the first two hops are sharply delineated while the third hop is less clear, as in typical ionograms. Of particular significance, is the region at 7000 Km, from 14 MHz to 28 MHz. This constant range ground clutter trace is similar to the backscatter clutter traces observed during spread Doppler conditions in large range backscatter ionograms (see example in Figure 75). In previous analysis, structures of this type have been treated as clutter when scanning the backscatter ionograms. However, the reproduction of this feature from ray trace data suggests that the ionogram interpretation needs to be reevaluated.

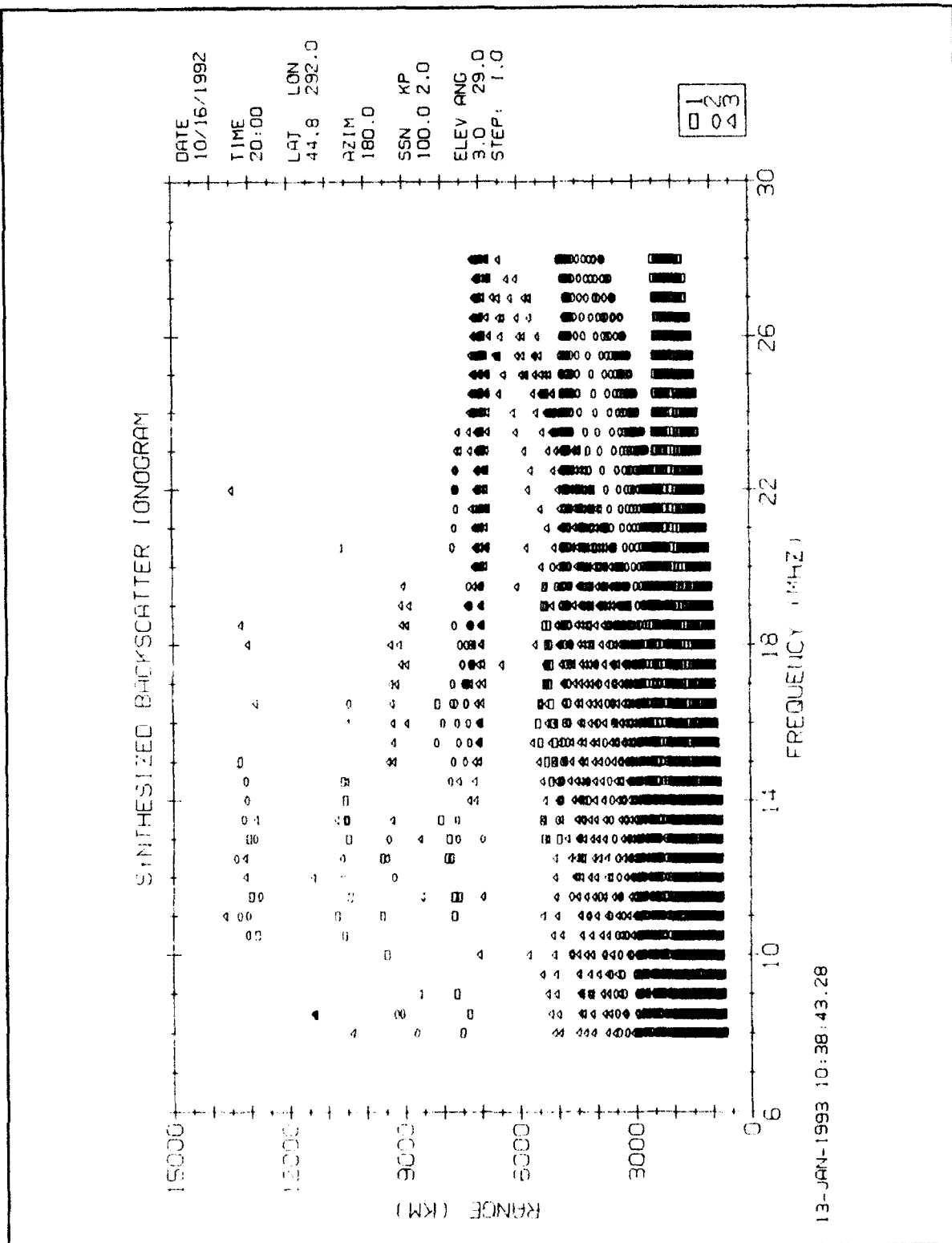


Figure 80. Synthesized backscatter ionogram.

### 3.3 REFERENCES

- Anderson, D. N., and J. M. Forbes, "A Fully Analytic, Low- and Middle-Latitude Ionospheric Model", *J Geophys Res*, Vol 94, No A2, Pp. 1520-1524.
- Basu, Su., S. Basu, R. C. Livingston, H. E. Withney, and E. MacKenzie, "Comparison of Ionospheric Scintillation Statistics From the North Atlantic and Alaskan Sectors of the Auroral Oval Using the Wideband Satellite", AFGL-TR-81-0266, ADA 111871, 1981.
- Basu, Su., S. Basu, R. C. Livingston, E. MacKenzie, and H. E. Withney, "Phase and Amplitude Scintillation Statistics at 244 MHz From Goose Bay Using a Geostationary Satellite", AFGL-TR-82-0222, ADA 124291, 1982.
- BDM Corporation, Data Collection and Analysis Team (DCAT) Data Reduction Product Portfolio: Annex P to the OTH-B ECRS On-site OLDR-I Configuration Report for the Data Collection and Analysis Team (revision 2), Albuquerque, NM, Jan. 25, 1989.
- Bounar, K. H., and S. Basu, *Private Communication*, 1989.
- Buchau, J., B. S. Dandekar, and G. S. Sales, "Long Range Backscatter Soundings of ECRS and WCRS", presented at MITRE Corp., Bedford, MA, August, 1992.
- Croft, T. A., "Sky-Wave Backscatter: A Means for Observing Our Environment at Great Distances", *Reviews of Geophysics and Space Physics*, Vol 10, No 1 (Feb., 1972), Pp. 73-155.
- Fremouw, E. J., and J. M. Lasinger, "Recent High Latitude Improvement in A Computer Based Scintillation Model", *Proc. Ionospheric Effects Symposium*, 3rd, 1981, Alexandria, Va., edited by J. M. Goodman, Naval Research Lab., Washington, D.C., 1982.
- Fremouw, E. J., and C. L. Rino, "A Signal-Statistical and Morphological Model of Ionospheric Scintillation", *Proc. AGARD Conf. Operational Modelling of the Aerospace Propagation Environment*, Ottawa, Canada, 1978.
- Jones, M. R., and J. J. Stephenson, A Versatile Three-Dimensional Ray Tracing Computer Program for Radio Waves in the Ionosphere, U.S. Department of Commerce, Office of Telecommunications, Boulder, CO, October, 1975.
- Jursa, A. S., Scientific Editor, *Handbook of Geophysics and the Space Environment*, Chapter 10, 1985, AFGL-TR-85-0315, ADA167000.
- Providakes, J., "Propagation Issues on OTH Radar Modeling", presented at MITRE Corp., Bedford, MA, August, 1992.
- Sales, G. S., "Scattering From A Three Dimensional, Anisotropic Random Medium", presented at MITRE Corp., Bedford, MA, August, 1992.



Weber E. J., R. T. Tsunoda, J. Buchau, R. E. Sheehan, D. J. Strickland, W. Whiting, and J. G. Moore,  
"Coordinated Measurements of Auroral Zone Plasma Enhancements", *J. Geophys. Res.*, 90,  
6497-6513, 1985.

Whartenby, W. G., "PIM User's Guide, Version 1.0.3", Computational Physics, Inc., Newton, MA;  
draft version, November 16, 1992.

## 4. MAGNETOMETER DATA PROCESSING SYSTEMS

### 4.1 CALIBRATION AND PROCESSING OF THE CRRES FLUXGATE MAGNETOMETER DATA

The calibration and data processing system developed for the analysis of the Fluxgate Magnetometer [Singer, *et al.*, 1992] was the result of several years of analysis, simulation, and software development. The system performed well, allowing the calibration factors for the instrument to be made available virtually from the start of the mission, in spite of a misdeployment of the instrument, that led to pointing directions of the axes that were different from those planned by over  $18^\circ$ . The processing also resulted in a data set that was extremely clear of contamination from spacecraft induced fields and from spin tone. The processing proved to be relatively trouble free, most of it ultimately performed in batch with little human intervention necessary.

The algorithms developed for calibration relied on the spin of the spacecraft and on the changes in magnitude and direction of the background field. Viewed as a comprehensive treatment of the problem of magnetometer calibration, we believe they are somewhat unique. The details of the treatment have been documented elsewhere [McNeil, 1993], and here we briefly highlight the problem and its solution.

#### 4.1.1 The Satellite and Instrument

The CRRES satellite was launched in July of 1991, with an orbital period of about 10 hours, an inclination of around  $18^\circ$ , a perigee of 350 km, and an apogee of 35,000 km altitude. CRRES was a spin stabilized satellite with a spin rate of around 2 rpm. Because of the high eccentricity, the satellite encountered external fields from as high as 35,000 nT down to less than 100 nT, meaning that the magnetometer required a large dynamic range. The rapid traversal of perigee at speeds of more than 10 km/sec gave the changes in field magnitude required for successful calibration. The satellite required the sun to spin axis angle to be between  $5^\circ$  and  $15^\circ$ , a requirement satisfied by periodic attitude adjustment maneuvers. Although these maneuvers gave rise to long term anomalies in the spin that proved problematic for magnetic field processing, they also provided for the calculation of the spin axis magnetic offset.

Originally, the magnetometer x axis was to be directed along the negative x axis of the satellite. The y axis was to be nearly along the negative z axis (spin axis), and the z axis along the negative y axis of the satellite, but with the whole assembly rotated by  $2.5^\circ$  around the x axis. This was to allow for spin tone in the y sensor to aid in on-orbit calibration. After deployment, inspection of the data indicated that the boom had not fully extended. This led to an elevation of the x axis of the magnetometer that was initially more than  $18^\circ$  above the spin plane. This angle changed slowly in time, from orbit to orbit, indicating that the boom may have been restricted by a cable in the last few degrees of its final turn. The boom never did fully deploy, reaching only about  $13^\circ$  at the end of the mission. Fortunately, the calibration algorithms allowed for a fully general alignment of the instrument, and for the direct calculation of arbitrary alignments, so that the data quality did not suffer.

#### 4.1.2 Pre-Launch Activities

Prior to launch of the satellite, a great deal of effort was expended in the simulation of the magnetometer data and in the development of algorithms and software for analysis. The pre-launch package included many features that improved the realism, as well as provided for detailed testing of the software. Satellite

attitude data for the simulation was obtained directly from the Attitude Fit Coefficients generated by the attitude determination routine for simulated CRRES orbits. Simulation and analysis was carried out using the same ephemeris data files that would be used in actual operation of the system. In this way, the structure was present to easily simulate signals for comparison with real data as well.

Additionally, simulations in cooperation with the development of the overall Orbital Data Processing System testing program incorporated realistic magnetometer data into simulated raw telemetry files, and attempted to recover these data from both the magnetometer experiment file and from the more generally available magnetic field file. The combination of these simulations allowed realistic and verifiable data to flow from start to end of the processing. As a result, there was minimal difficulty in performing a full analysis on the first available data set.

In addition to the simulations of nominal behavior, several studies were carried out to examine the effects of errors in required input values, and of spacecraft wobble and nutation. Experience with these simulated anomalies allowed for increased familiarity with the satellite and instrument behavior, as well as providing confidence levels of the calibration results. Finally, just prior to launch, optical alignment data and orthogonality data were analyzed to provide a set of initial estimates to the required quantities.

#### 4.1.3 Calibration

The calibration efforts were designed for two distinct purposes: (1) the generation of calibration factors for the use of other experimenters in the calculation of pitch angle and of the magnetic field; and (2) the creation of a calibrated, inertial data set for the use of the magnetometer experimenter. This treatment was somewhat unique in that the calibration *factors* were provided, along with the raw counts, rather than providing calibrated geophysical measurements. In this way, calibration of the instrument could lag the overall satellite data processing without causing a disruption in the data flow. Since the CRRES mission involved tens of experiments with data going out world-wide, this arrangement was especially practical. A subroutine was provided to experimenters which read the magnetic field file and the calibration data file, and gave calibrated sensor readings in either sensor or spacecraft coordinates. For these calibrations, it proved adequate to provide one set per orbit, averaging over the small perturbations in offsets arising from spacecraft induced fields. For the final inertial data set, on the other hand, these perturbations were removed by calculating offsets on a shorter time scale.

We think of calibration as the calculation of the position of each of the three axes of the magnetometer in spacecraft coordinates, the three axis offsets  $d_i$  and the three gains  $g_i$ . All of these quantities are needed to transform the sensor signals to spacecraft frame magnetic fields. The alignments are completely specified by the elevations  $\theta_i$  and the azimuth angles  $\phi_i$  of the three sensors. We perform calibration in stages. First, the elevations and relative azimuths are found. Next, we calculate the *ratios* of the gains and the absolute offsets. These are performed on an orbit-by-orbit basis. Two other quantities, the offset along the spin axis and the absolute phase of the x sensor, are obtained less frequently by other means.

Our approach to on-orbit calibration is to separate the magnetometer signals from the three sensor axes into spin modulated and constant components. By the manipulation of these values and the ratios between them, we are able to determine eight independent quantities out of the twelve needed for processing. The four remaining quantities were assumed to be known from the outset. In the course of processing, however, each of these was independently calculated by other methods. Table 31 gives the required

quantities, the quantities available from orbit-by-orbit calibration, and the assumed quantities required to complete the calculation.

**TABLE 31. Observables and Assumed Quantities**

What we need	What we can measure	What we must assume
Phase angles $\phi_x, \phi_y, \phi_z$	Phase differences $\phi_{xy}, \phi_{xz}$	X-sensor phase $\phi_x$
Elevations $\theta_x, \theta_y, \theta_z$	Ratios $T_{ij} = \tan\theta_i / \tan\theta_j$	Orthogonality angles $w_{ij}$
Gains $g_x, g_y, g_z$	Gain ratios $g_{ij} = g_i / g_j$	X-sensor gain $g_x$
Offsets $d_x, d_y, d_z$	Spin-plane offsets $\Delta_1, \Delta_2$	Spin axis offset $\Delta_3$

#### 4.1.3.1 The Spin Fit

The basic quantity measured in on-orbit calibration is the modulated and dc portion of the magnetometer sensor. Assuming that the satellite spins at a uniform rate  $\omega$ , the signal from the  $i$ 'th sensor can be written as

$$s_i = g_i \cos\theta_i b_{xy} \cos(\phi_i + \omega t + \phi_h) + g_i b_z \sin\theta_i + d_i \quad (78)$$

where  $b_{xy}$  is the spin plane component of the external field,  $b_z$  is the spin axis component, and  $\phi_h$  is the right ascension of the external field vector in spacecraft coordinates. We fit these signals to functions of the form

$$s_i = \alpha_i \cos\omega t + \beta_i \sin\omega t + \delta_i \quad (79)$$

from which we can identify

$$\gamma_i = \sqrt{(\alpha_i^2 + \beta_i^2)} \quad \tan^{-1} \frac{\beta}{\alpha} = \phi_h - \phi_i \quad (80)$$

From relations between the  $\alpha$  and  $\beta$ , we can calculate those quantities for phase and elevations given in Table 31.

#### 4.1.3.2 Elevations

The calculation of alignments employs an alternative formulation of the sensor pointing directions in which the system is defined so that the  $x$  axis is collinear with the  $x$  axis of the magnetometer, and the  $y$  axis is in the  $xy$  plane. This allows one to define the pointing directions by two variables,  $\kappa$  and  $\mu$  [McNeil, 1993]. This representation is then combined with known sensor orthogonalities. This is matched to the measured values through the simultaneous equations

$$F = \frac{\tan\theta_x(\kappa, \mu) / \tan\theta_y(\kappa, \mu) - T_{xy}}{T_{xy}} \quad G = \frac{\tan\theta_x(\kappa, \mu) / \tan\theta_z(\kappa, \mu) - T_{xz}}{T_{xz}} \quad (81)$$

where the  $T_{ij}$  are the measured values. The result is a self-consistent solution for the  $\theta_i$  and for the relative phases  $\phi_{ij}$  that preserves the measured orthogonality of the sensors.

#### 4.1.3.3 Gain Ratios

The measured coefficients of the spin fits can be used directly to find the ratios of the sensor gains.

$$d_{ij} = \frac{\delta_i}{\delta_j} = \frac{g_i \sin\theta_i}{g_j \sin\theta_j} \quad g_{ij} = \frac{\gamma_i}{\gamma_j} = \frac{g_i \cos\theta_i}{g_j \cos\theta_j} \quad (82)$$

We found that averaging either of these quantities gave good results for the instrument when in high gain (< 900 nT) operation. For the low gain signals, however, a slightly different approach improved the results. Plotting, for example,  $\gamma_{xl}/\cos\theta_x$  against  $\gamma_{yl}/\cos\theta_y$ , gives the desired value  $g_{xy}$  as its slope. Linear regression was used to arrive at the value. We calculated a third set of ratios between the instrument high and low gain operational modes. This calculation used the averaged sensor signals  $s_i$  instead of the spin fit results. The offsets were subtracted and 60-second summations were taken. One was then plotted against the other to arrive at the ratio between gain in high gain and low gain operation for a particular sensor.

#### 4.1.3.4 Offsets

For both gain states, the results of the spin fit were used to calculate two independent spin plane offsets

$$\begin{aligned} \Delta_1 &= \sin\theta_x \delta_y - r_{xy} \sin\theta_y \delta_x \\ \Delta_2 &= \sin\theta_z \delta_y - r_{yz} \sin\theta_y \delta_z \end{aligned} \quad (83)$$

These are independent of the external field as desired. These values were averaged throughout an entire data set. To them, was added the equation for the spin axis offset

$$\Delta_3 = \sin\theta_x d_x + \sin\theta_y d_y + \sin\theta_z d_z \quad (84)$$

where  $\Delta_3$  is the assumed spin axis offset. With Eq. (83), the three sensor offsets can be obtained.

#### 4.1.3.5 Absolute Gains and Phases

With the gain ratios in hand, and assuming knowledge of one of the gains (we chose  $g_{xh}$ ), there are several ways to find the five other gains from the ratios calculated above. We found that the scheme

$$\begin{aligned} g_{yh} &= g_{xh} / g_{xyh} & g_{zh} &= g_{xh} / g_{xzh} & g_{xl} &= g_{xh} / g_{xlh} \\ g_{yl} &= g_{xl} / g_{xyl} & g_{zl} &= g_{xl} / g_{xzl} \end{aligned} \quad (85)$$

worked consistently well. For the phases of the sensors, we assumed that  $\phi_x$  was known. Then the relative phases calculated before could be used to find the absolute phase of the y and z sensor.

#### 4.1.4 Calculation of Assumed Quantities

We have described how the twelve quantities needed for conversion of the sensor measurements to the spacecraft frame magnetic field were calculated from on-orbit measurements along with some assumed quantities. Three of these assumed quantities, the spin axis offset, the absolute phase of the x sensor, and the absolute gain of the x sensor, were calculated in the course of processing, but not on an orbit-by-orbit basis. The fourth set, the orthogonality angles, were known quite precisely from laboratory testing. Here we describe the calculation of the first three of these.

##### 4.1.4.1 Spin Axis Offset

The calculation of the spin axis offset relies on the motion of the spacecraft spin axis relative to the external field. Originally, a precession maneuver was planned especially for calculation of this value. The maneuver was never carried out, however, we found a "natural" motion of the spin axis from which the same result could be calculated. This was data taken from the nutation that followed the frequent attitude adjustments of the satellite spin axis.

The algorithm required two separate calculations, one quite similar to the calculation of the offsets. This was carried out in periods when there was no motion of the spin axis. The second calculation was performed over the two hours or so immediately following the adjustment. The first calculation used previously determined alignments and gain ratios to cast the signals into a reference frame equivalent to the spacecraft frame. Here, the spin plane offsets were measured. Then, this same transformation was applied to the post-precession data, subtracting the spin plane offsets. This led to a signal that was the calibrated external field vector *plus* the spin axis offset. We assumed that the external field magnitude could be represented as a polynomial in time. Thus, the magnitude was given by

$$(s_x^2 + s_y^2 + (s_z - D_z))(t) = (a_0 + a_1 t + \dots)^2 \quad (86)$$

where  $s_i$  are the measured body-frame sensor signals and  $D_z$  is the spin axis offset. We performed the calculation by minimization of the difference between the lhs and the rhs of Eq. (86) as a function of  $D_z$ .

##### 4.1.4.2 Absolute Phase

Throughout the data processing, the magnetometer data was used to check the accuracy of the attitude solution and of the attitude model. The attitude quality control check was carried out after attitude modeling by calculating the angular difference between the inertial magnetic field, as determined from the reduced magnetometer data, and the IGRF85 model. The angular deviation thus represented the total error from calibration, attitude calculation, and inherent model field inaccuracies. Because of the high perigee of the satellite, the deviation over most of the orbit was high, due to contributions from the external field. However, the data in the first hour or so pre- and post-perigee, where the internal field dominates, served as a good indication of overall accuracy.

We noticed quite early on that there appeared at perigee an approximately 3° discrepancy between the model and measured field. We discovered that this discrepancy was, for the most part, perpendicular to the spin axis. We also noticed that the subtraction of about 2.5° from the phase led to far better

agreement. After a search for possible timing errors, either in the magnetic field or the attitude, we concluded that the phase of the magnetometer was probably somewhat in error. This seemed reasonable, since videotape of ground tests of the boom deployment revealed that the magnetometer mounting rocked somewhat prior to becoming locked in place, which of course never happened in space.

In order to determine an optimum value of the absolute phase  $\phi_x$ , we carried out a survey of one hundred orbits. For the first half-hour of each, the angular deviation of the field was minimized as a function of  $\phi_x$  in  $0.1^\circ$  steps. For all orbits in this period, using the average of the result,  $177.4^\circ$ , gave rms errors less than  $1^\circ$ . This value was adopted for further calibration of the data.

#### 4.1.4.3 Absolute Gain

Just as the direction of a model field can be used to obtain the absolute phase of the magnetometer axes, the magnitude can be used to obtain absolute gain. If we subtract the offsets, multiply the y-sensor signal by  $g_{xy}$  and the z by  $g_{xz}$ , then divide by the magnitude of the model field, we obtain  $g_x$  in units of counts/nT. We performed this calculation on several orbits initially, finding that the values obtained fluctuated around the ground measured value by a part-per-thousand or so. Having thus confirmed the ground measurements on-orbit, we opted to use the ground measured value for all orbits.

#### 4.1.5 Despinning

When the twelve quantities needed for calibration have been obtained, we can recover the spacecraft frame magnetic field. Following conversion to spacecraft coordinates, the attitude model [McNeil, 1991] is evaluated at the point in time of each signal. The attitude model gives the right ascension and declination of the spin axis and the spin phase, which is then converted into the inertial pointing directions of the three spacecraft axes. These vectors provide the matrix required to cast the spacecraft frame magnetic field into inertial coordinates.

#### 4.1.6 Data Products

The main product data base produced by the system was a two-second averaged file in Earth Centered Inertial coordinates. This data was packed to give 32-bit positive integer values, so that it could easily be transported between computers. The full high time resolution data, at 16-samples/second, was not processed in every case. Instead, provisions were made for re-processing selected periods of data where interesting high frequency events occurred. These data periods, when selected, were calibrated and despun to produce high time resolution, packed ECI data in integer format.

Three summary plots were also produced by the system for each orbit. A plot was produced in the VDH coordinate system of the field components and of the total field compared to a model field. Figure 81 shows one typical plot exhibiting PC type pulsations perpendicular to the field. Also, an ultra-low frequency spectrogram was produced to characterize electromagnetic waves in the zero to 100 MHz region. An ion cyclotron wave spectrogram, from zero to 8 Hz was also produced for each orbit to characterize high frequency events.

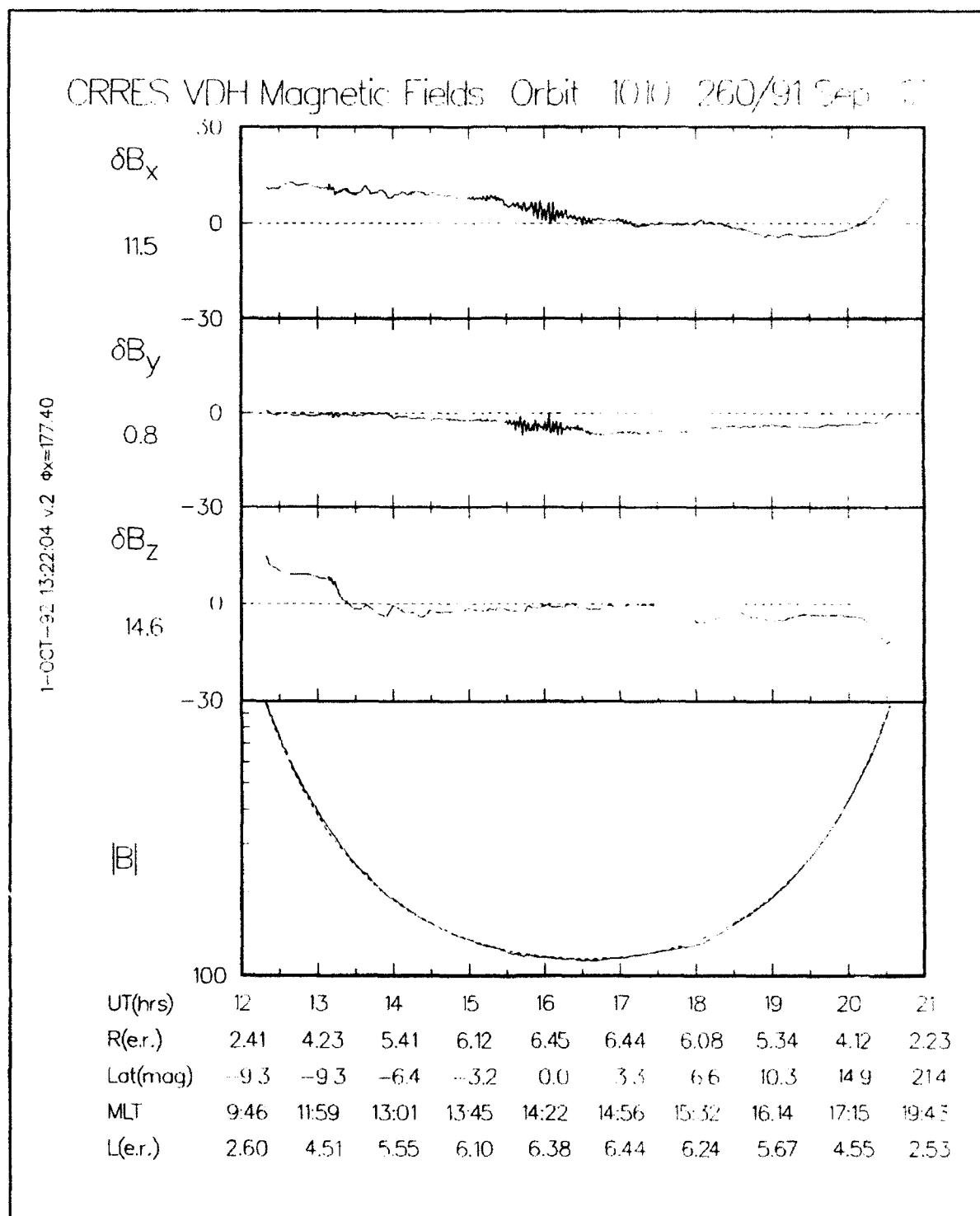


Figure 81. VDH survey plot.



## 4.2 DMSP MAGNETOMETER

One of the instruments aboard the Defense Meteorological Satellite Program (DMSP) satellites is the fluxgate magnetometer (SSM). This instrument measures the magnetic field at an altitude of about 840 km. A software system was developed based on knowledge gained in a previous DMSP F7 mission [Rich, 1984]. This system was written initially on the CYBER and was then ported to the VAX/VMS machine.

The fluxgate magnetometer measures the total magnetic field, which is a superposition of several magnetic fields emanating from several natural and artificial sources. The magnetic fields due to Earth's internal magnetic field and to currents flowing in and out of the ionosphere are of special interest in the understanding of ionospheric phenomena. In addition to these two natural sources of magnetic fields, the SSM instrument picks up magnetic fields originating from other instruments aboard the satellite. These types of magnetic fields may be regarded as noisy signals that must be filtered out. The SSM software system has several filtering routines, which were designed to eliminate the noisy signals. The filtering routines were developed after ground simulation tests were performed, and common interference signals from other instruments were revealed in these tests. The SSM software system was tested on a simulated data set which consists of magnetometer data collected during a previous DMSP mission and the kind of noisy signals revealed by the ground tests [Bounar and Rich, 1989].

#### 4.3 REFERENCES

Bounar, K. H., and F. J. Rich, *Private Communication*, 1989.

McNeil, W. J., "Calculation and Modeling of the Attitude for CRRES", PL-TR-91-2239, 1991, ADA243950.

McNeil, W. J., "Aspects of the Calibration and Processing of the CRRES Fluxgate Magnetometer Data", (in preparation), 1993.

Rich, F. J., "Fluxgate Magnetometer (SSM) for the Defense Meteorological Satellite Program (DMSP) Block 5D-2, Flight 7", AFGL-TR-84-0225, No. 326, 1984, ADA155229.

Singer, H. J., W. P. Sullivan, P. Anderson, F. Mozer, P. Harvey, J. Wygant and W. J. McNeil, "Fluxgate Magnetometer on the CRRES", *J. Space. Res.*, 29, 599, 1992.

## 5. ATMOSPHERIC DENSITY

### 5.1 SEMIANNUAL AND EUV VARIATIONS

#### 5.1.1 Introduction

The neutral thermosphere is an extremely complex system. Nevertheless, accurate and efficient modeling of the thermosphere is important for many applications. Empirical modeling attempts to use simple indices as measures of the energy sources to the thermosphere in the hope that the thermospheric density variations may be simply related to variations in these indices. The extensive PL accelerometer data base (Table 32) provides the opportunity to evaluate and improve these models. In previous contract periods, our work has focused on evaluation of existing empirical models by statistical characterization of the ratios of the measured to model densities. These have generally shown that unmodeled or inaccurately modeled variations produce 5-15% errors in the model densities. During this contract period we have focused on two of these, the semiannual and solar EUV variations.

**TABLE 32. Neutral Atmospheric Density Data Base Characteristics**

SAT	packed/ unpacked	Time/Alt	Julian Date	Season	Alt Range (km)	--AP-- Daily 6.7 Hr	Incl	Mean F10.7	# Files	# Data Recs	# Points
AE-C		Alt	73353 74352	FWSS	135 245		68.4	86.9			62044
S3-1		Alt	74309 75120	FWS	135 245		97	76.3			27315
AE-D		Alt	75281 76029	FW	140 245		90	75.8			29762
AE-E		Alt	75235 76322	FWSS	135 245		20	73.3			35629
AE/S3-1	unpacked	Alt	73353 76322		135 245	Y Y			23	12906	154750
S3-4	unpacked	Time(MIX)	78089 78223	SS	162 285	N Y	96*	145.8	161	4587	54073
SETA-1	unpacked	Time(SEQ)	79079 79100	SPRING	168 250	Y Y	96*	189.8	1	5221	62649
SETA-2	packed	Time(MIX)	82137 82332	SSF	168 297	N N	96*	170.0	114	37034	443805
SETA-3	packed	Time(MIX)	83201 84075	SFWS	163 385	N N	96*	116.0	150	246474	2956869
S85-1	packed	Time(MIX)	84201 84283	SF	179 257	N N	96*	80.6	72	28136	337219

The semiannual variation is that portion of the observed day of year dependence of the density not attributable to seasonal-latitudinal effects. Since the physical mechanism for the semiannual variation is not well understood, no index is used for its representation. Therefore, it is expressed in simple functions of the day number of the year. The term "semiannual" derives from the fact that the principal component is a twice yearly sinusoidal variation. However, there are also observed once yearly variations which are symmetric with respect to the equator (the northern and southern hemispheres are in phase), in contrast to seasonal variations, which are asymmetric (the northern and southern hemispheres are 180° out of phase). For this study, we have thus considered the semiannual variation to be the latitudinally symmetric day-of-year variations.

The principal components of the solar EUV (extreme ultraviolet) variation are the 11 year solar cycle and the 27 day solar rotation period. The source of the 11 year cycle is indexed by the 3-solar-rotation average of the daily 10.7 cm radiometric flux ( $F_{10.7}$ ). This long wavelength flux is used instead of EUV flux since, unlike the latter, it is routinely measured daily at the Earth's surface, and is known to correlate roughly. The source of the 27 day solar rotation is the passage of "active regions" of the sun across the Earth-sun line of sight. These are indexed by the difference between the daily and 3-solar-rotation mean 10.7 cm flux.

The next section details normalization procedures used to remove variations other than the two being studied. The following section summarizes results, including fits of the normalized densities to appropriate functional forms, and comparisons with the MSIS-86 density model.

### 5.1.2 Computational Procedures

For these studies, two normalization techniques have been employed to remove other variations from the data. In the first technique, we compute the normalized density:

$$\rho_N = \rho_{\text{meas}} [\rho_M(P') / \rho_M(P)]$$

where

$\rho_N$  = normalized density

$\rho_{\text{meas}}$  = measured density

$\rho_M$  = MSIS-86 model density

The inputs P in the denominator are the parameters appropriate to the actual time and position of the measurement, *including the 3-hour geomagnetic index values over the preceding 60 hour period*. Thus, the MSIS-86B model was used here. The MSIS models have the property that selected variations in them can be suppressed by turning off appropriate switches. This technique has been applied, as will be detailed below.

The inputs P' in the numerator include the following fixed values of the altitude, local time, and *daily geomagnetic activity index*:

altitude: 180 km for day data, 220 km for night

local time: 1000 hrs for day data, 2200 hrs for night

$A_p$  (daily value): 7 for the  $K_p = 0-3^+$  bin. 56 for the 4-9 bin

Note that the use of fixed daily geomagnetic activity index implies that the A version of the model is used in the numerator, rather than the B version, which would require specifying a fixed value for the 3-hour index over a 60 hour period prior to the time of interest. The more extensive geomagnetic activity calculation in the B model is not justified in the numerator, because of the use of a fixed fictitious value of the index rather than actual values as in the denominator.

In the semiannual study, the solar activity index is fixed in the numerator at 150, and the "seasonal" variation switches are off, so that the resulting density excludes these day-number dependent variations, while retaining the semiannual variation. The seasonal variations are what Hedin refers to as "asymmetrical annual" and "asymmetrical semiannual". They have equal magnitudes and opposite signs at equal northern and southern latitudes. The terms retained are the "symmetrical annual" and "symmetrical semiannual", which are equal in both sign and magnitude at equal latitudes in the northern and southern hemispheres. *Thus, the correct terminology for what we are studying would seem to be "symmetrical day of year" variation, rather than "semiannual" variation.*

In the EUV study, all day of year variations were switched off in the numerator.

In the second technique, we calculate the normalized ratio

$$R_N = \rho_{\text{meas}} / \rho_M (P'')$$

where in the denominator we have used the daily geomagnetic activity index (the use of the 3-hour values might be justified here), and we have turned off the symmetrical annual and symmetrical semiannual variations in the semiannual study, and the solar activity variations in the EUV study.

Daily mean values of the normalized quantities were tabulated in 10° geographic latitude bins for the two  $K_p$  bins for both day and night. For each bin, least squares fits of these results were made to the appropriate functional dependencies of the variable studied (solar activity index or day of year).

The following thoughts indicate that the normalized density is the preferred way to proceed. First, the normalized density can be computed for fixed values of the variables not being studied, for example altitude and local time, which we may call the secondary variables. Thus, the densities can be adjusted to constant values of these variables, for example altitude. Then, we can study the primary variation, in this case either the EUV or semiannual variation, at fixed values of the other variables. The normalized ratio, on the other hand, is always at the data-point values of the secondary variables; it cannot be adjusted to constant values. Secondly, in the normalized density, we can selectively remove coupling between the primary variable and the secondaries, except for altitude, by using the MSIS switches, which allow us to switch off all variations due to a secondary variable, or just the average variation, leaving in the cross-terms carrying the coupling with the primary. Thus, we can choose, for instance, to leave in the seasonal dependence of the EUV variation, or remove it, independently of other variations. In the normalized ratio, all we can do is either remove the coupling between all variables (except altitude) and EUV by leaving the EUV cross-term switch on in  $P''$ , or include all the coupling by turning that switch off; coupling with individual secondary variables cannot be included or removed independently. In short, we prefer using the normalized density because of its apparently greater flexibility in handling coupled variations.

### 5.1.3 Results

#### 5.1.3.1 Semiannual Variation

Figure 82 shows typical results for the semiannual variation. The symbols depict daily averaged normalized density obtained from measurements by accelerometers on-board the indicated satellites. The hatched curve is the least squares fit of the data to the functional form:

$$\begin{aligned} \rho &= A_1 \cos \frac{2\pi t}{365} + A_2 \sin \frac{2\pi t}{365} + A_3 \cos \frac{2\pi t}{182.5} + A_4 \sin \frac{2\pi t}{182.5} + A_5 \\ &= Q_1 \cos \frac{2\pi}{365} (t - \alpha_1) + Q_2 \cos \frac{2\pi}{182.5} (t - \alpha_2) + A_5 \end{aligned} \quad (87)$$

Here, the first line is the form most convenient for linear least squares fitting. The first two terms represent sinusoidal variations of a one year period, while the second two terms represent variations of half-year periods. The second line is the equivalent expression in terms of the amplitudes  $Q_1$ ,  $Q_2$ , and phases  $\alpha_1$ ,  $\alpha_2$  of the yearly (Annual) and half-yearly ("semiannual") sinusoidal variations. The

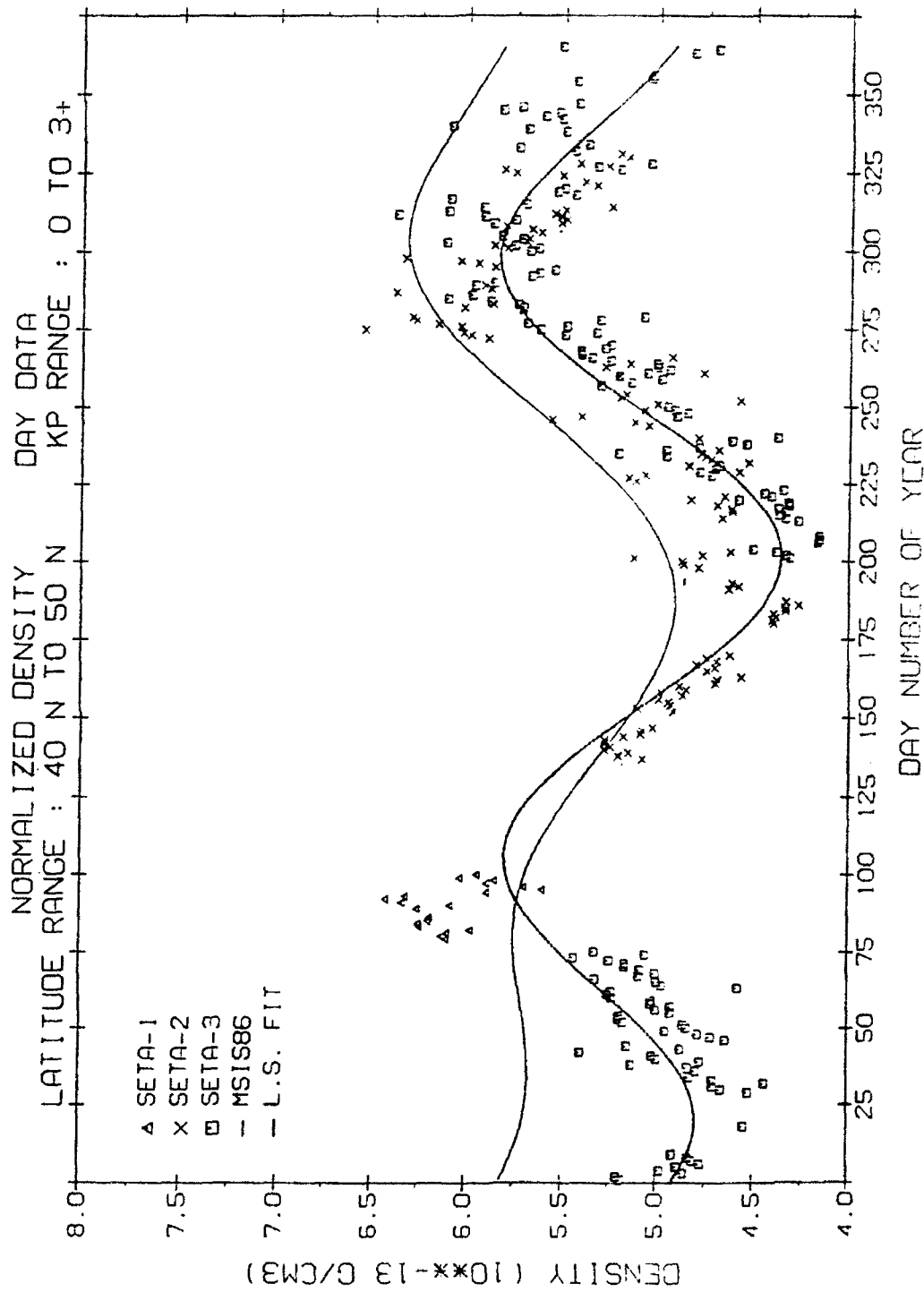


**Figure 82(a).** Semiannual variation of total mass density: measured (symbols), least squares fit (solid curve), and MSIS86 model (light curve).

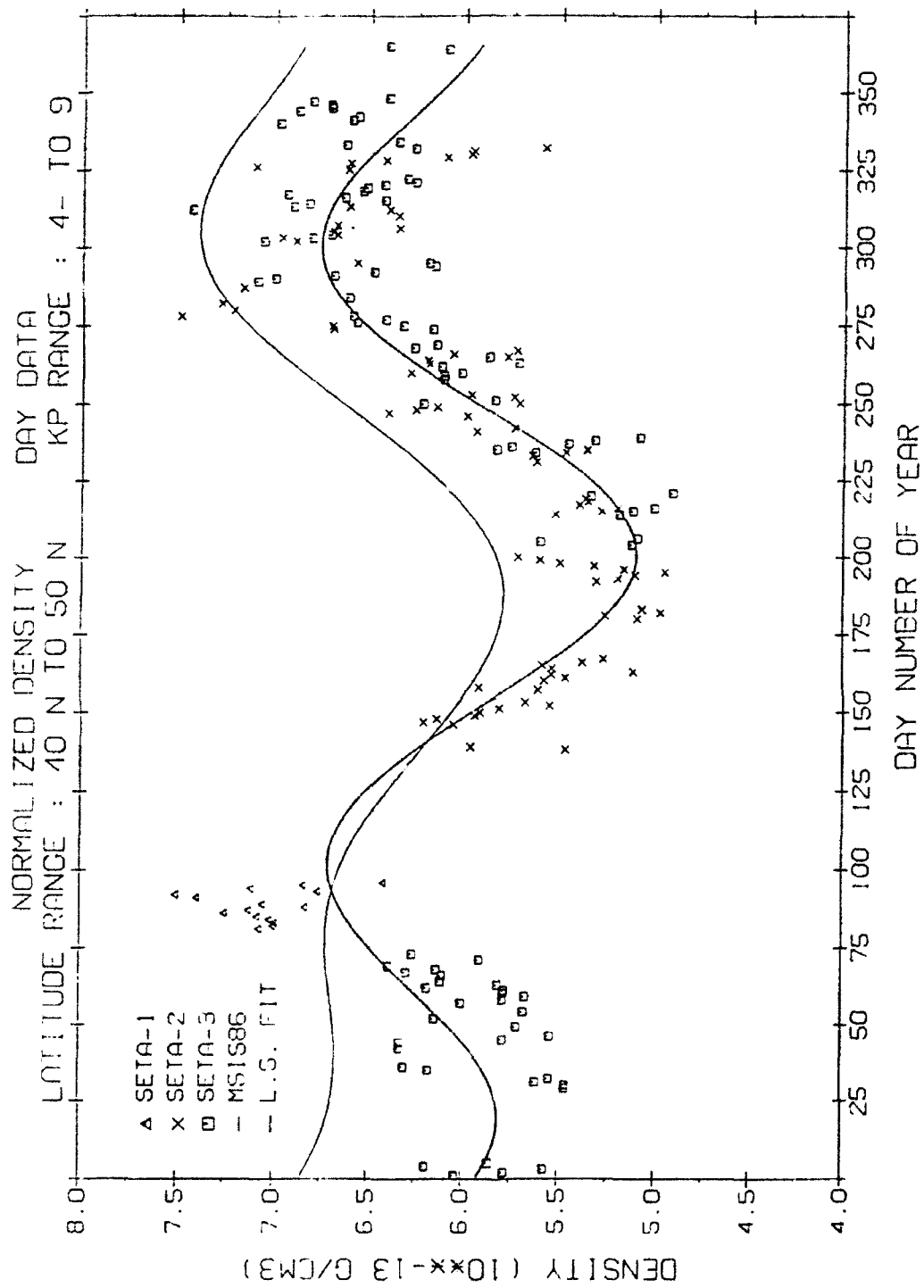


**Figure 82(b).** Semiannual variation of total mass density: measured (symbols), least squares fit (solid curve), and MSIS86 model (light curve).

independent variable  $t$  is the day number in the year. Also shown, as the smooth (unhatched) curve, is the MSIS-86 model density for the center of the latitude bin, with the other variables and switch settings the same as used in the numerator of the data normalization equation. The data and model both exhibit peaks in April and October, but data peaks are nearly equal, while the October peak in the model is larger than its April peak. The individual data points are somewhat scattered about the fit, possibly due to the imperfect removal of other variations, as a result of their not fully accurate representation in MSIS. There is little  $K_p$  dependence evident in the shape of the curves, although there is an average  $K_p$  dependence in the constant ( $A_5$ ) term.

Table 33 details the results for the various latitude/ $K_p$  bins. One notes, for the day data, a strong north-south asymmetry in the annual variation, i.e., the phases  $\alpha_1$  are  $\sim 180$  degrees out of phase at comparable northern and southern latitudes. This indicates that the asymmetrical variation in MSIS is not accurately depicted; otherwise this asymmetry would have been removed in the normalization. The amplitudes of the annual variation are also strongly latitudinally dependent, with significant  $K_p$  dependence at the highest latitudes. The semiannual phases and amplitudes show only slight dependence on latitude and  $K_p$ . Also shown, in the two extreme right-hand columns are the root mean square fit residuals, or standard deviations ("S. D."), and the total number of points (daily averages) used in each fit. The standard deviation is given by

$$SD = \sqrt{\frac{\sum_{i=1}^N (\rho_i - \rho_{fi})^2}{N-1}} \quad (88)$$

where  $N$  is the number of point (last column),  $\rho_i$  is the  $i$ th daily mean normalized density, and  $\rho_{fi}$  is the  $i$ th fitted value.

### 5.1.3.2 EUV Variation

Figure 83 shows the derived EUV variation in the data for equatorial (panel a) and middle (panel b) latitude bins on the day side at low geomagnetic activity. Shown in the figure are the normalized daily averages (symbols), fits (solid curves) to linear and quadratic dependencies of the mean (3 solar rotation) solar flux, and the MSIS-86 model dependence on mean solar flux. The data were fit to the function:

$$\rho = A + B(\overline{F_{10.7}} - 150) + C(\overline{F_{10.7}} - 150)^2 + b(\overline{F_{10.7}} - \overline{F_{10.7}}) + c(\overline{F_{10.7}} - \overline{F_{10.7}})^2 \quad (89)$$

In the solid curves, the last two terms, depending on the difference between daily and smoothed (3-solar-rotation average) solar flux are excluded. The dashed lined curve is the MSIS-86 model density, also with daily variations removed. The MSIS variation is almost strictly linear, in contrast to the nonlinear variation exhibited by the data. Furthermore, the shape of the data variation is dependent on latitude. We should note, that, included in the variations shown here which depend on solar flux, are those which also depend on latitude and local time. Although we are looking at fixed local time, it is likely that local time amplitudes and phases depend on both latitude and solar flux. Then, at fixed local time, the deviation of the density from the local time mean could still depend on latitude and solar flux. An



TABLE 33. Normalized Density, Semiannual Variation Least-Squares Fit Coefficients

LAT BIN	KP BIN	ALT BIN	DAY DATA										S.D.	#PTS
			A1	A2	G1	ALPHA1	A3	A4	Q2	ALPHA2	A5			
60S to 50S	0 to 3+	N/A	-.5697	-.1969	.6028	-.163.17	-.3003	-.6383	.7054	-.58.40	4.954	4.954	.578	254
60S to 50S	4- to 9	N/A	-.6367	-.2159	.6723	-.163.51	-.2164	-.6596	.6942	-.54.83	5.965	5.965	.557	170
50S to 40S	0 to 3+	N/A	-.3576	-.0489	.3609	-.174.60	-.3428	-.5410	.6405	-.62.03	5.030	5.030	.413	254
50S to 40S	4- to 9	N/A	-.2887	-.0807	.2998	-.166.67	-.2485	-.5444	.5984	-.58.06	5.879	5.879	.405	170
40S to 30S	0 to 3+	N/A	-.1120	-.0444	.1205	-.160.60	-.3008	-.4416	.5343	-.62.99	5.104	5.104	.311	254
40S to 30S	4- to 9	N/A	-.0508	-.0423	.0661	-.40.31	-.2474	-.6308	.6967	-.60.77	5.799	5.799	.327	170
30S to 20S	0 to 3+	N/A	-.1184	-.0168	.1194	-.8.19	-.3418	-.3444	.5011	-.67.43	5.202	5.202	.234	254
30S to 20S	4- to 9	N/A	-.2813	-.0087	.2814	1.79	-.2846	-.3552	.4551	-.65.24	5.756	5.756	.268	170
20S to 10S	0 to 3+	N/A	-.1887	-.0356	.1920	10.82	-.3576	-.3705	.5149	-.67.92	5.285	5.285	.248	254
20S to 10S	4- to 9	N/A	-.3295	-.0393	.3319	6.90	-.3603	-.3689	.4715	-.65.15	5.729	5.729	.279	170
10S to 0	0 to 3+	N/A	-.1647	-.0880	.1368	40.60	-.3603	-.3682	.5152	-.68.13	5.343	5.343	.257	252
10S to 0	4- to 9	N/A	-.1967	.0953	.2166	26.21	-.3139	-.3748	.4888	-.65.88	5.713	5.713	.268	170
0 to 10M	0 to 3+	N/A	-.0983	.0277	.1022	166.52	-.3514	-.4502	.5711	-.64.88	5.715	5.715	.297	195
0 to 10M	4- to 9	N/A	-.0432	.0212	.0482	156.01	-.3514	-.4502	.5711	-.64.88	5.715	5.715	.297	195
10M to 20M	0 to 3+	N/A	-.1456	.1116	.1835	144.51	-.4662	-.4248	.6307	-.69.79	5.412	5.412	.274	295
10M to 20M	4- to 9	N/A	-.1395	.1188	.1832	141.53	-.4693	-.4409	.6439	-.69.34	5.875	5.875	.298	195
20M to 30M	0 to 3+	N/A	-.0546	.1195	.1314	116.17	-.5596	-.4033	.6898	-.73.11	5.359	5.359	.264	295
20M to 30M	4- to 9	N/A	-.0534	.1573	.1661	110.25	-.5635	-.4183	.7017	-.72.70	5.947	5.947	.293	195
30M to 40M	0 to 3+	N/A	-.0894	.0674	.1120	37.54	-.5373	-.3941	.6664	-.72.87	5.253	5.253	.235	294
30M to 40M	4- to 9	N/A	-.1670	.1164	.2036	35.37	-.5178	-.4015	.6553	-.72.09	6.001	6.001	.296	194
40M to 50M	0 to 3+	N/A	-.2118	.0532	.2184	14.30	-.4839	-.3791	.6147	-.71.95	5.195	5.195	.282	294
40M to 50M	4- to 9	N/A	-.3441	.0895	.3555	14.78	-.5027	-.3766	.6281	-.72.57	6.084	6.084	.334	192
50M to 60M	0 to 3+	N/A	-.1758	.0549	.1841	17.58	-.5121	-.4015	.6507	-.71.94	5.175	5.175	.303	293
50M to 60M	4- to 9	N/A	-.3489	.0618	.3543	10.18	-.5271	-.4020	.6629	-.72.33	6.219	6.219	.391	194
60M to 70M	0 to 3+	N/A	.0103	.0654	.0662	82.19	-.5427	-.4026	.6757	-.72.71	5.170	5.170	.338	294
60M to 70M	4- to 9	N/A	.2077	.0339	.2104	9.39	-.5765	-.4272	.7175	-.72.72	6.353	6.353	.451	194
70M to 80M	0 to 3+	N/A	-.0704	.0355	.0789	155.37	-.5218	-.4031	.6594	-.72.15	5.075	5.075	.378	295
70M to 80M	4- to 9	N/A	-.1304	.0485	.1390	20.73	-.5593	-.4680	.7292	-.71.01	6.321	6.321	.447	195
80M to 90M	0 to 3+	N/A	-.0358	-.0038	.0360	-6.22	-.5091	-.4009	.6480	-.71.88	4.939	4.939	.387	295
80M to 90M	4- to 9	N/A	-.2990	.0281	.3003	5.44	-.5591	-.4407	.7244	-.71.23	6.096	6.096	.476	195
LAT BIN	KP BIN	ALT BIN	NIGHT DATA										S.D.	#PTS
			A1	A2	G1	ALPHA1	A3	A4	Q2	ALPHA2	A5			
0 to 10M	0 to 3+	N/A	-.0968	-.0258	.1002	-.15.15	-.1023	-.0999	.1430	-.68.78	1.531	1.531	.158	253
0 to 10M	4- to 9	N/A	-.1496	-.0174	.1506	-6.73	-.0940	-.1210	.1532	-.64.82	1.744	1.744	.181	170
10M to 20M	0 to 3+	N/A	.0582	-.0340	.0674	-30.68	-.1204	-.1044	.1594	-.70.49	1.557	1.557	.156	253
10M to 20M	4- to 9	N/A	.1143	-.0136	.1151	-6.88	-.1067	-.1217	.1619	-.66.53	1.790	1.790	.187	170
20M to 30M	0 to 3+	N/A	.0733	-.0170	.0753	-13.25	-.1528	-.0900	.1773	-.75.79	1.567	1.567	.151	253
20M to 30M	4- to 9	N/A	.1236	.0061	.1238	2.85	-.1377	-.1104	.1765	-.71.62	1.832	1.832	.188	170
30M to 40M	0 to 3+	N/A	.1468	.0000	.1468	.02	-.1756	-.0848	.1949	-.78.18	1.569	1.569	.167	253
30M to 40M	4- to 9	N/A	.2002	.0065	.2003	1.88	-.1545	-.1070	.1879	-.73.66	1.862	1.862	.189	170
40M to 50M	0 to 3+	N/A	-.2404	-.0131	.2408	-3.15	-.1436	-.0890	.1843	-.74.78	1.535	1.535	.148	253
40M to 50M	4- to 9	N/A	-.3050	-.0056	.3051	1.06	-.1347	-.1073	.1722	-.71.71	1.859	1.859	.186	170
50M to 60M	0 to 3+	N/A	.2677	.0178	.2683	-3.86	-.1446	-.0845	.1675	-.73.89	1.524	1.524	.142	253
50M to 60M	4- to 9	N/A	.3498	.0142	.3501	-2.35	-.1170	-.1043	.1580	-.69.83	1.851	1.851	.178	170
60M to 70M	0 to 3+	N/A	.2234	-.0114	.2237	-2.96	-.1463	-.0936	.1737	-.74.72	1.492	1.492	.126	253
60M to 70M	4- to 9	N/A	.3456	.0214	.3463	-3.59	-.1469	-.1034	.1561	-.70.22	1.851	1.851	.180	170
70M to 80M	0 to 3+	N/A	.1494	-.0134	.1500	5.19	-.1575	-.1064	.1900	-.74.00	1.461	1.461	.112	253
70M to 80M	4- to 9	N/A	.2752	.0033	.2752	.69	-.1478	-.0967	.1766	-.74.42	1.829	1.829	.165	170
80M to 90M	0 to 3+	N/A	.0630	-.0251	.0667	17.04	-.1753	-.1081	.2061	-.75.21	1.457	1.457	.113	253
80M to 90M	4- to 9	N/A	.2035	.0365	.2067	10.32	-.1733	-.1046	.2025	-.75.47	1.828	1.828	.157	170

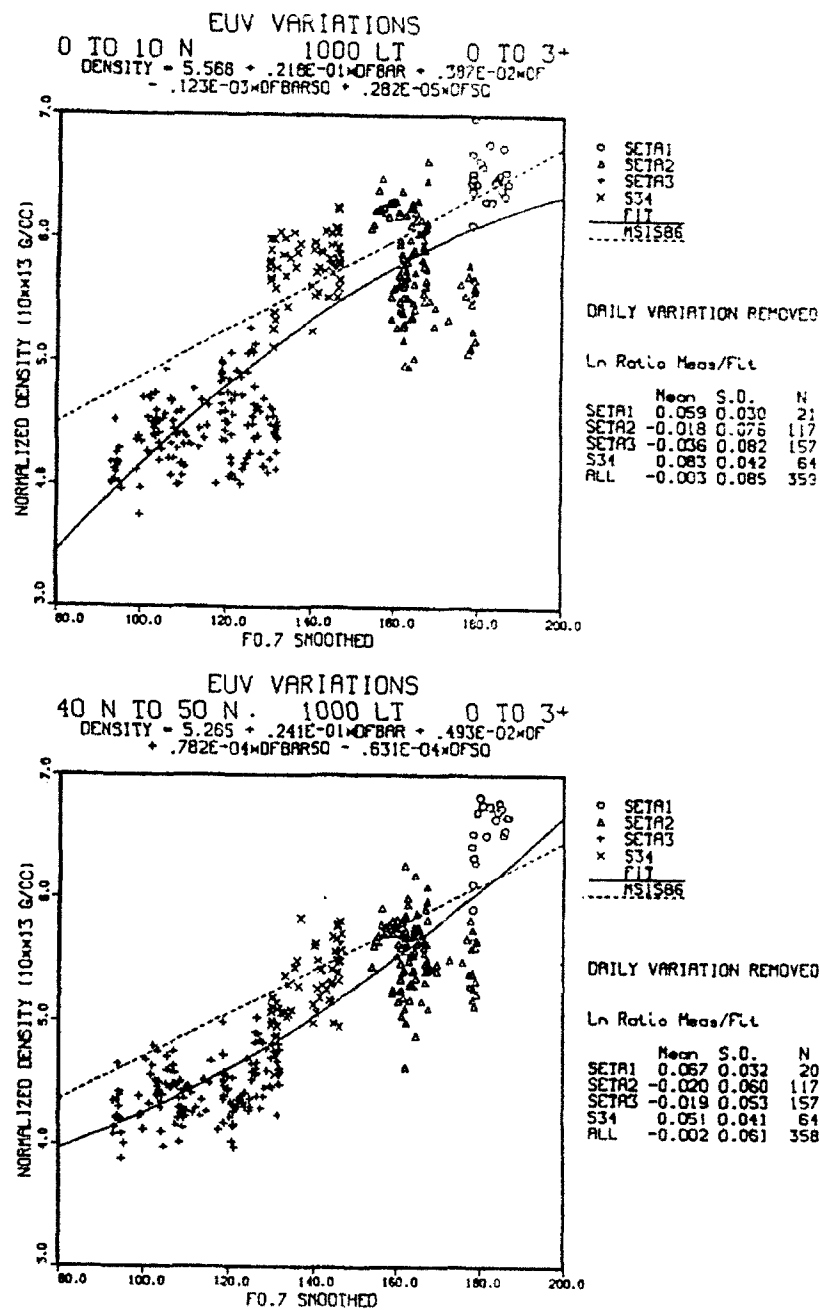


**Figure 83.** Response of total mass density to EUV variations: measured (symbols), least squares fit (solid curve), and MSIS86 model (dashed curve). The curves are with the last two terms of Eq. (89) removed.

examination of the MSIS-86 model indicates that such variations in it are linear. Thus, the data exhibits complex nonlinear variations that are not included in the model. Therefore, we can not use the MSIS-86 model to remove them during the normalization of the data.

## 5.2 ANALYSIS OF VARIATIONS IN LIDAR DENSITY DATA

LIDAR data provides extensive night-time measurements of the neutral mesospheric density in the altitude range 30-90 km. This permits study of local time and other dynamical variations of the density at these altitudes. In a preliminary analysis step, we assisted PL scientists by extracting night-time variations from data obtained at Wright-Patterson AFB. The data were available as 5-minute averaged height profiles for several nights. A significant problem at this early stage, was that the data were available as relative densities, since absolute densities required cross-calibration with balloon data below 40 km. Therefore, the measured density was given as normalized to unity at 40.4 km. Also provided were the experimenter's estimate of the measurement error of the normalized density at each height in the profile. The objective of this effort was to deduce the variations of the density alone from data which contains both measurement and density variations. The results reported here are for a set of 61 5-minute profiles obtained on 7 October, 1990.

We have assumed that the total variation in the LIDAR density data is composed of two parts: the real density variation and the measurement error. The total standard deviation in the data is assumed to be given by:

$$\sigma_{tot}^2 = \sigma_{den}^2 + \sigma_{meas}^2 \quad (90)$$

The LIDAR data has been provided to us as densities, normalized to unity at 40.4 km altitude, and measurement error standard deviations of these normalized densities, at 300 m altitude steps from 30.5 km to 99.2 km. There are 61 profiles in all. We have obtained the mean and total standard deviation of the density data over the 61 profiles. In addition, we obtained the mean squared measurement error by computing the mean of the squares of the measurement error standard deviations over the 61 profiles. Then, using Eq. (90), the estimated mean squared real density variation has been obtained by subtracting the mean squared measurement error from the square of the total standard deviation in the density data. Figures 84-97 display various aspects of these computations in terms of ratios to US76 density model, which was also normalized to unity at 40.4 km.

The estimated mean square of the real density variation was slightly negative at the normalizing altitude, 40.4 km. The negative result at the normalizing altitude is to be expected, since by definition the normalized density, and the ratio to the normalized US76 model, is fixed at unity at this altitude. Therefore, the total standard deviation, as we computed it here, must be identically zero, while the estimated measurement standard deviation given to us is positive. The total standard deviation is generally several times the measurement error standard deviation (Figures 95 and 96). In particular, in the high altitude region, 90-100 km, it is evident that the measurement error has been underestimated, since it is unlikely that the real density has a variation as large as implied by the results shown in Figure 97.

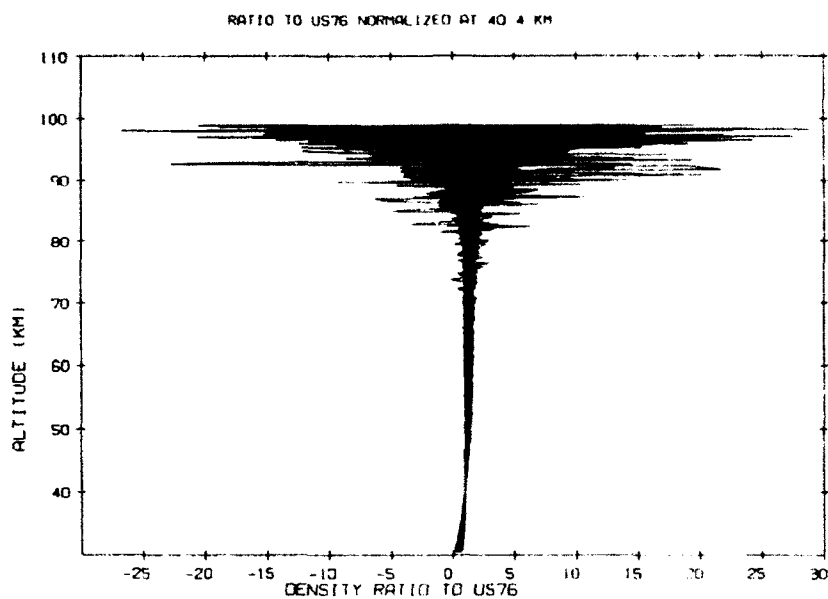


**Figure 84.** The measured density (ratios to US76) for the 61 profiles, overlaid on a single page.

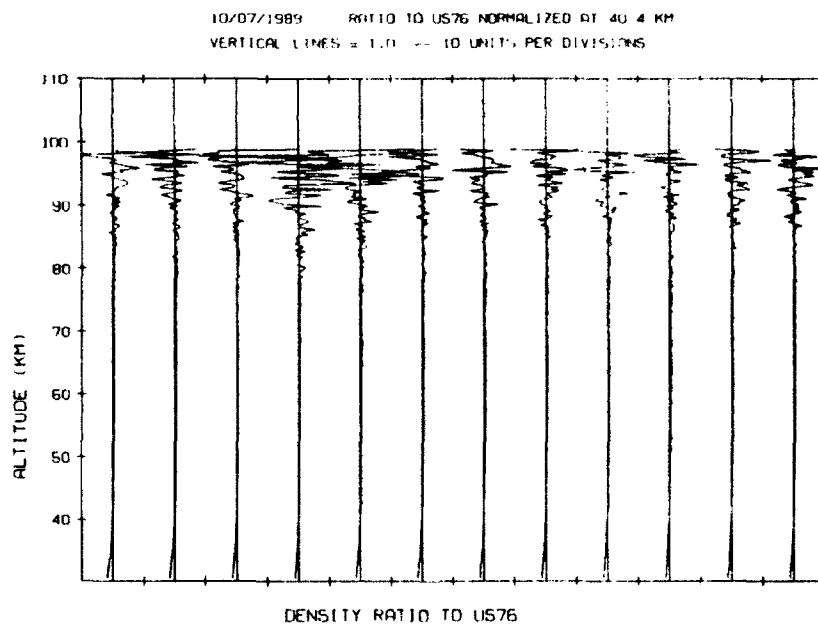


**Figure 85.** (and Figures 86 - 90) The ratios for the individual profiles, seen separately. Each curve is accompanied by a straight vertical line designating unity ratio. The tick mark to the immediately left corresponds to a ratio of -4, and the tick mark to the immediate right designates +6.

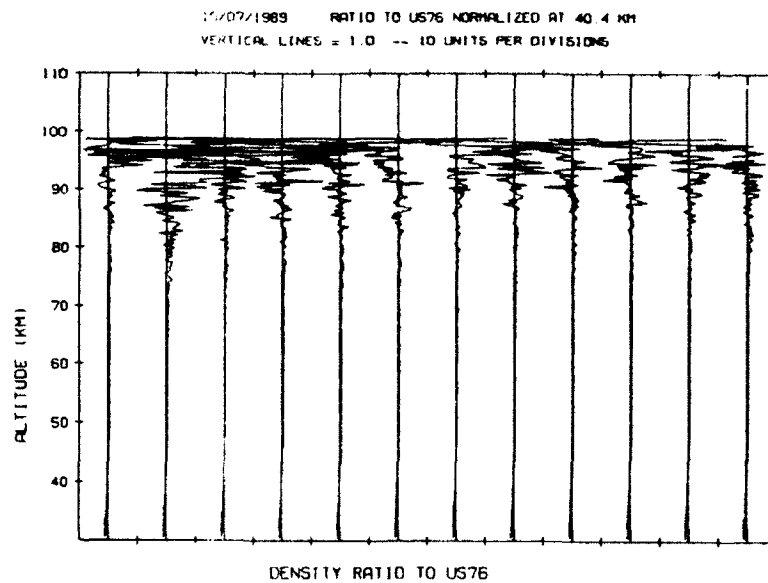


**Figure 86. Ratio for individual profile.**

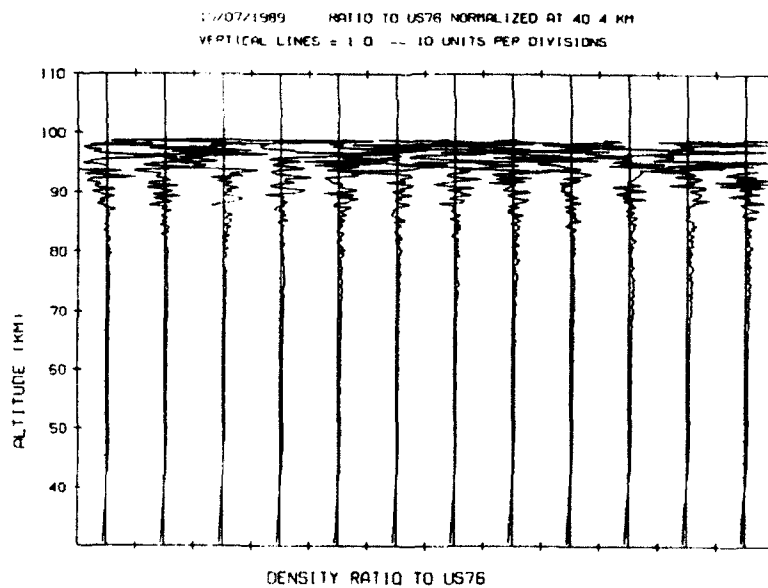


**Figure 87. Ratio for individual profile.**

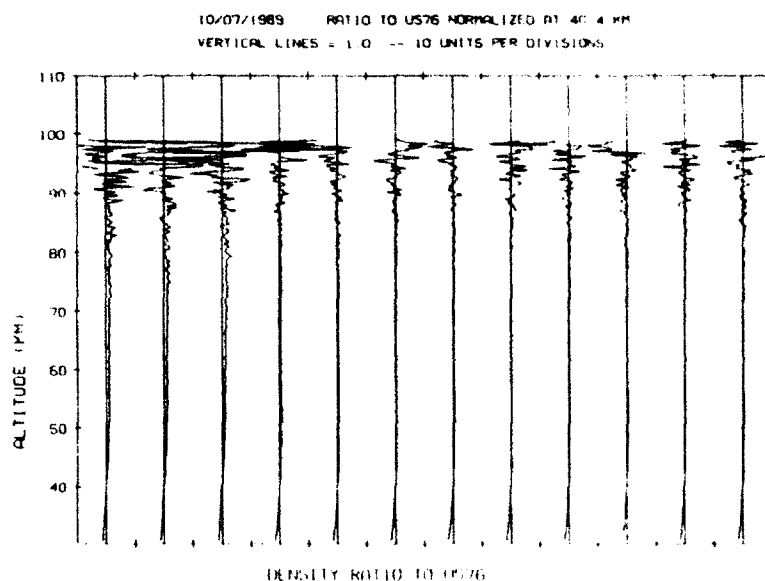


**Figure 88.** Ratio for individual profile.

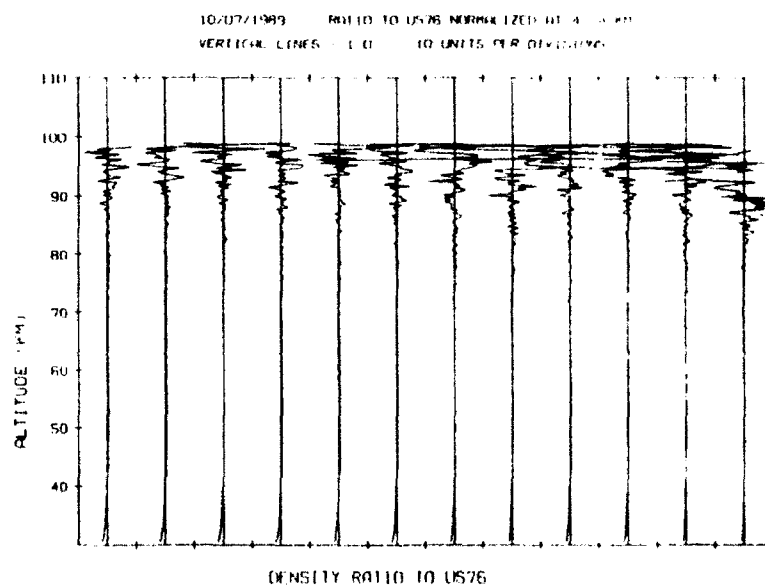


**Figure 89.** Ratio for individual profile.

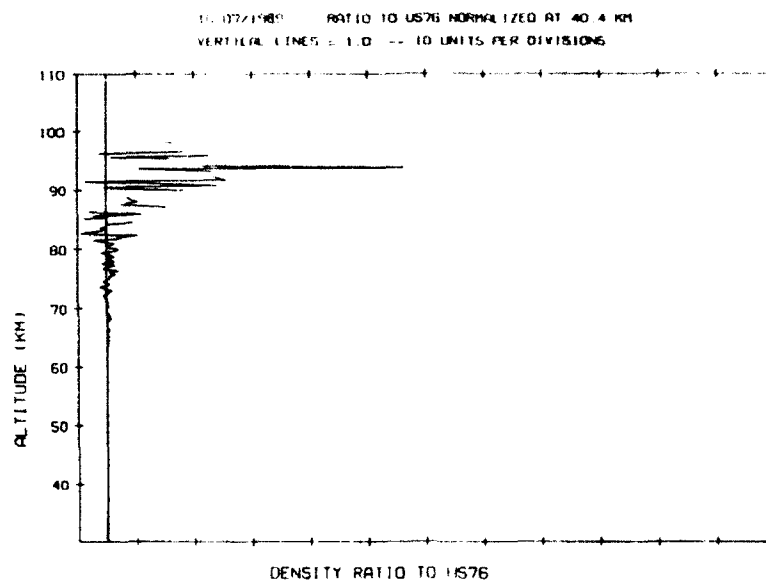


**Figure 90.** Ratio for individual profile.

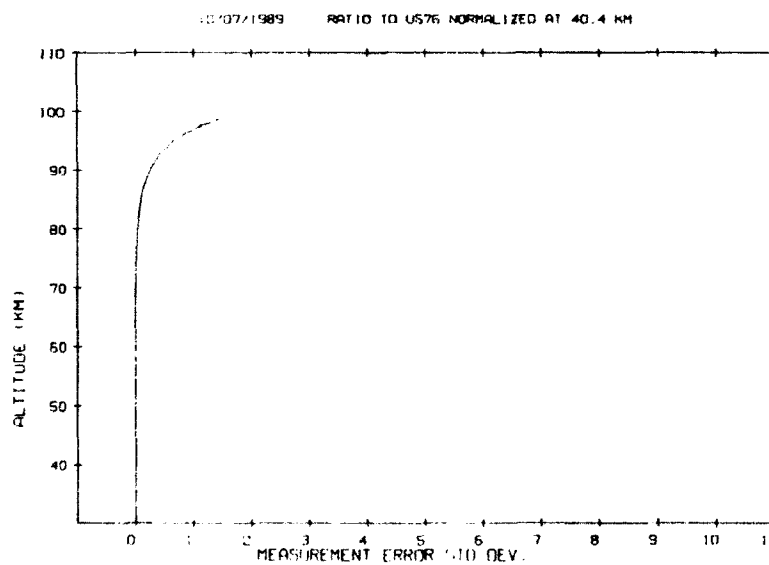


**Figure 91.** The measurement error standard deviation, computed as the square root of the mean of the square of the measurement errors given in the file.

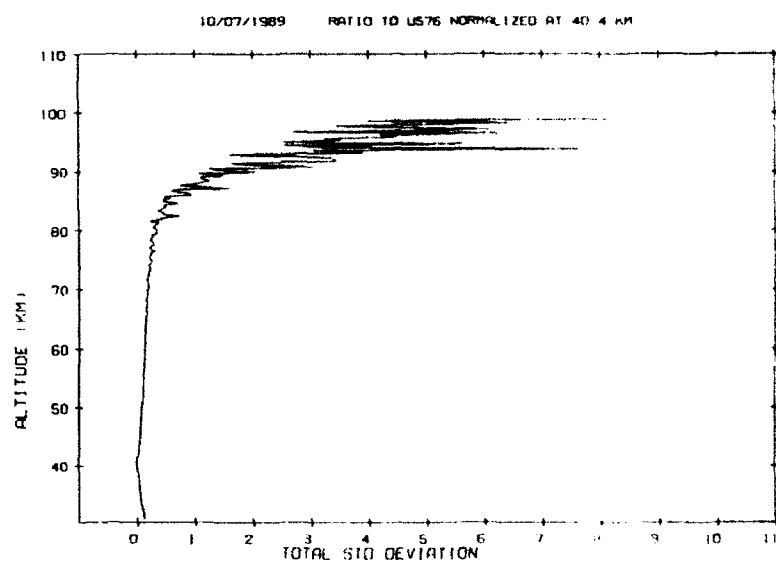


**Figure 92.** The total standard deviation of the density data.

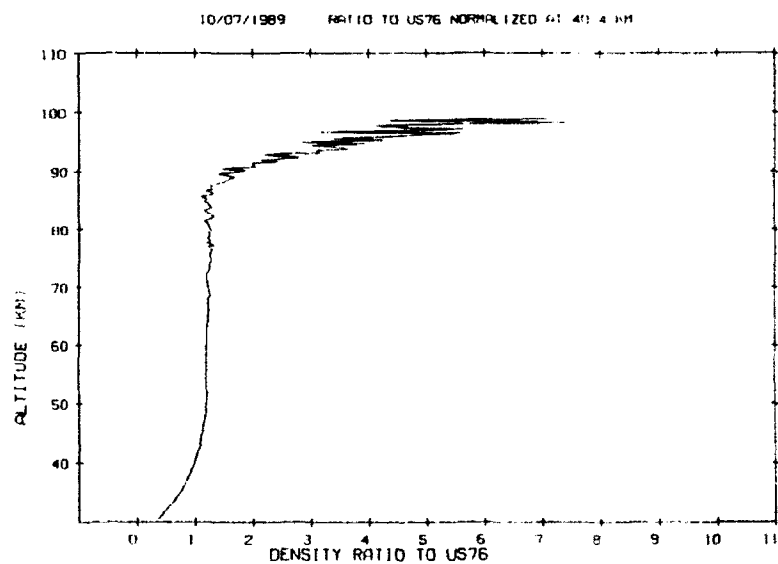


**Figure 93.** The mean density.



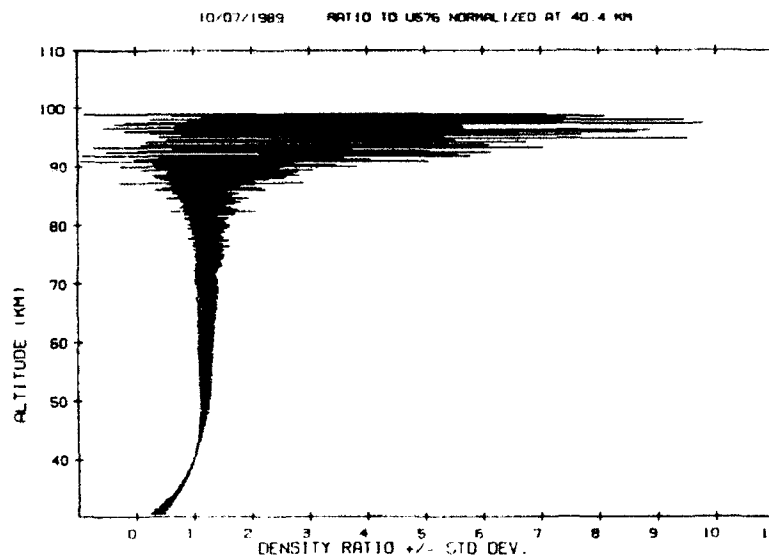


**Figure 94.** The mean density, with horizontal bars running between + and - the estimated real density variation.

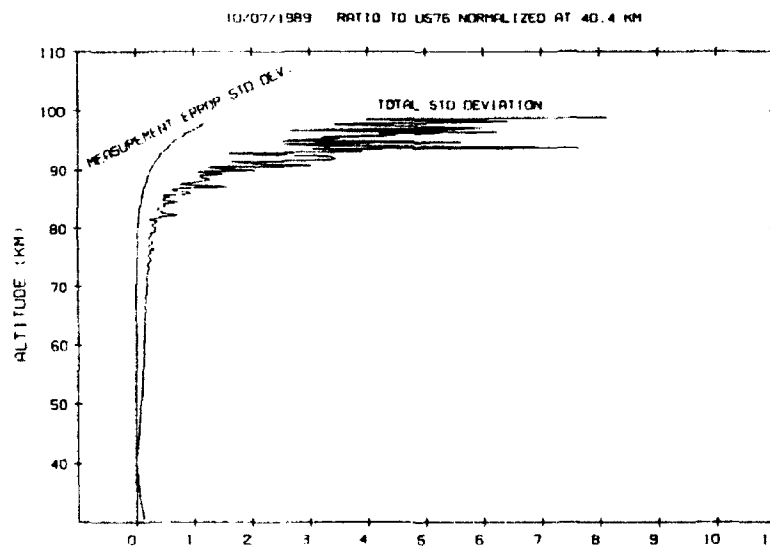


**Figure 95.** The total and measurement error standard deviations.

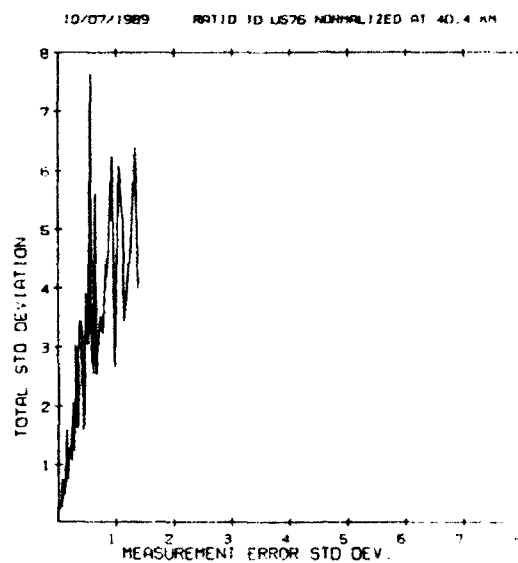


**Figure 96.** The total standard deviation vs. the measurement error standard deviation.

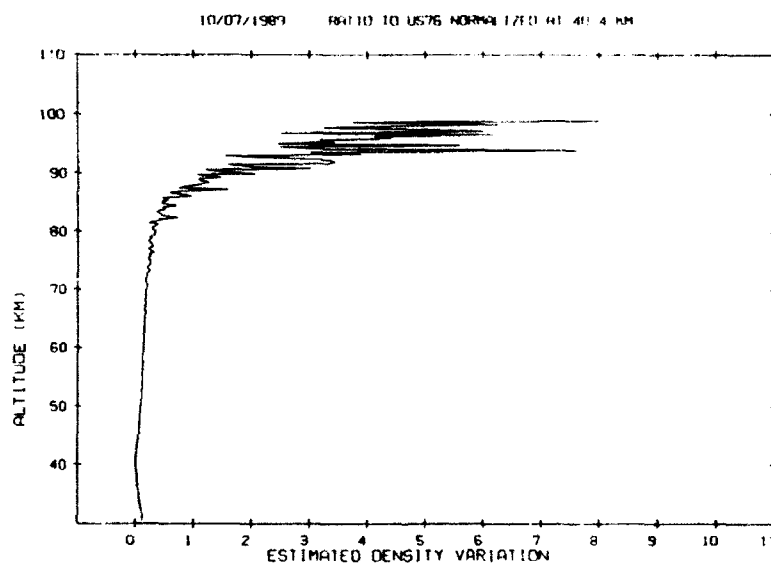


**Figure 97.** The estimated mean square of the real density variation.

### 5.3 EVALUATION OF GRAM88 MODEL

The GRAM88 (Global Reference Atmospheric Model, 1988 version) is a hybrid consisting of three distinct zones and two transition regions. Table 34 summarizes the usage of the Jacchia (1970) and Groves (1971) models, and a 4-D atmospheric model developed for NASA by Allied Research Associates [Justus, *et al.*, 1980].

**TABLE 34. Model Usage**

Altitude (Km)	Model
> 115	Jacchia (1970)
90 - 115	Transition between Jacchia and Groves models
30 - 90	Groves (1971)
25 - 30	Interpolation between 4-D data and Groves model
Surface - 25	4-D Model (NASA)

The GRAM88 model was obtained and implemented at PL, and a number of comparisons were made against other commonly used atmospheric density models. Results from two sample test cases are given in Tables 35 and 36; the parameters used for the comparison runs were the following:

F <sub>10.7</sub>	125.
Mean F <sub>10.7</sub>	125.
Ap	4.
Longitude	0.
Year	1986
Month	3
Day	22
UT	0 <sup>h</sup> 0 <sup>m</sup> 0 <sup>s</sup>

As Figure 98 shows, the GRAM88 model results are nearly identical to those obtained from the Jacchia model above 115 Km, while agreement with other models elsewhere is somewhat irregular.

**TABLE 35. Sample Test Case Results - Latitude = 40°**

Altitude (Km)	Jacchia 70	MSIS83	MSIS86	GROVES	GRAM88
200.	2.546605E-13	2.563069E-13	2.411522E-13	2.562861E-13	2.561504E-13
190.	3.619519E-13	3.585740E-13	3.367099E-13	3.585614E-13	3.633113E-13
180.	5.254318E-13	5.136955E-13	4.814527E-13	5.136490E-13	5.272696E-13
170.	7.860264E-13	7.589445E-13	7.100963E-13	7.587382E-13	7.881724E-13
160.	1.225489E-12	1.168950E-12	1.092330E-12	1.168239E-12	1.227396E-12
150.	2.032394E-12	1.910232E-12	1.785342E-12	1.908065E-12	2.033650E-12
140.	3.734900E-12	3.415725E-12	3.198101E-12	3.409282E-12	3.732551E-12
130.	8.181537E-12	7.109254E-12	6.696236E-12	7.088686E-12	8.160247E-12
120.	2.364258E-11	2.002856E-11	1.917160E-11	2.118722E-11	2.352916E-11
110.	9.722888E-11	9.393836E-11	9.015174E-11	9.993512E-11	9.814222E-11
100.	5.500991E-10	5.579926E-10	5.282176E-10	5.987694E-10	5.714793E-10
90.	3.459394E-09	3.510114E-09	3.274490E-09	3.663433E-09	3.435133E-09
80.	2.058774E-08	I	I	1.908990E-08	1.738695E-08
70.	1.140485E-07	I	I	8.242503E-08	7.621217E-08
60.	5.810569E-07	I	I	3.151513E-07	2.906880E-07
50.	2.665716E-06	I	I	1.060227E-06	9.588800E-07
40.	1.061507E-05	I	I	3.870050E-06	3.600555E-06
30.	3.444234E-05	I	I	1.754574E-05	1.731010E-05
20.	8.174332E-05	I	I	8.854738E-05	8.815356E-05

**TABLE 36. Sample Test Case Results - Latitude = 60°**

Altitude (Km)	Jacchia 70	MSIS83	MSIS86	GROVES	GRAM88
200.	2.643551E-13	2.479298E-13	2.368684E-13	2.480331E-13	2.657522E-13
190.	3.740073E-13	3.464875E-13	3.299836E-13	3.466986E-13	3.750358E-13
180.	5.403354E-13	4.963533E-13	4.709656E-13	4.967144E-13	5.415862E-13
170.	8.045391E-13	7.341366E-13	6.937030E-13	7.346913E-13	8.057387E-13
160.	1.249154E-12	1.133468E-12	1.066331E-12	1.134236E-12	1.249360E-12
150.	2.064769E-12	1.859182E-12	1.742833E-12	1.860079E-12	2.062538E-12
140.	3.787521E-12	3.340220E-12	3.123139E-12	3.340779E-12	3.774258E-12
130.	8.276631E-12	6.980789E-12	6.538142E-12	6.979231E-12	8.224912E-12
120.	2.383027E-11	1.958698E-11	1.861471E-11	2.003885E-11	2.362427E-11
110.	9.774038E-11	8.437828E-11	7.990012E-11	9.057411E-11	9.724310E-11
100.	5.519869E-10	4.867476E-10	4.564555E-10	5.464179E-10	5.178413E-10
90.	3.459394E-09	3.414432E-09	3.169395E-09	3.353009E-09	2.901617E-09
80.	2.038045E-08	I	I	1.681286E-08	1.409854E-08
70.	1.104852E-07	I	I	7.124703E-08	6.200432E-08
60.	5.392480E-07	I	I	2.687806E-07	2.447130E-07
50.	2.280341E-06	I	I	9.028763E-07	8.565250E-07
40.	7.815933E-06	I	I	3.414762E-06	3.428567E-06
30.	1.935973E-05	I	I	1.670284E-05	1.712412E-05
20.	2.848881E-05	I	I	8.663152E-05	8.438627E-05

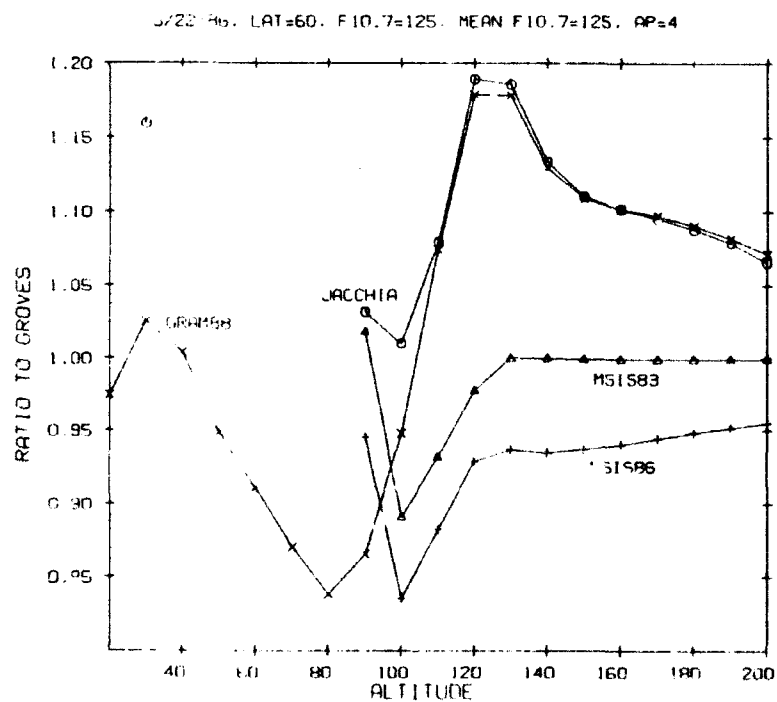
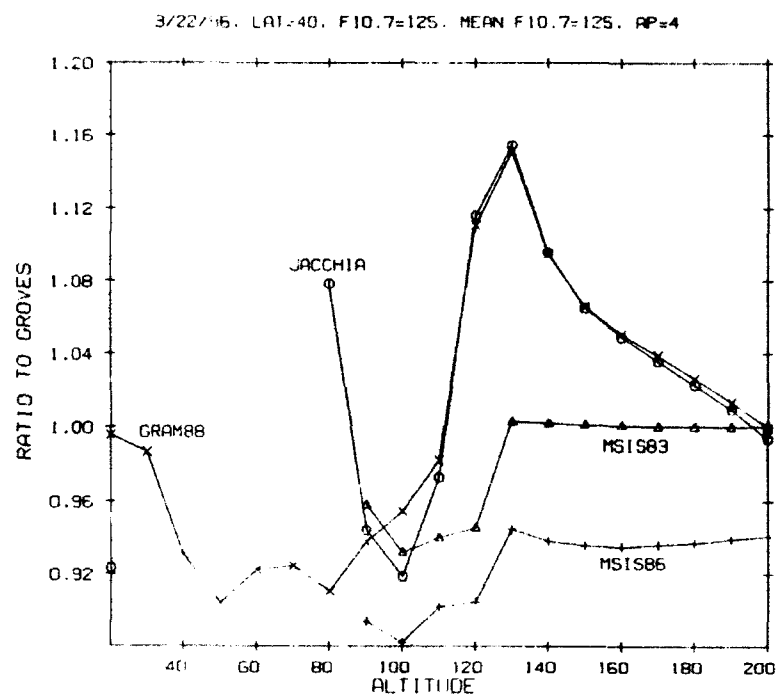


Figure 98. Comparisons of GRAMM88 with other models.

#### 5.4 DETERMINATION OF ATMOSPHERIC DENSITY FROM ORBITAL ELEMENT SETS

The need to accurately reconstruct satellite positional information from observational data has led to the development of a body of analytical theory. Programs which apply this theory have slowly improved in accuracy over a number of years, employing vehicle ephemeris information as input data in the standardized form of mean element sets. The orbital element sets maintained by USSPACECOM contain data which may be used in any one of several computer programs, such as SGP4, SDP4, SGP8, and SDP8, which were designed to apply this theory. These applications differ in the mathematical development of equations which give approximate solutions for the perturbing effects of a non-uniform gravitational field combined with atmospheric drag.

The USSPACECOM orbital elements have these perturbative changes removed in a particular way, and are referred to as "mean" element sets [Brouwer, 1959; Kozai, 1959]. Information concerning the satellite ephemeris can be reconstructed quickly and accurately using the appropriate computer programs to restore the perturbative changes. These changes include the combined effects of a non-uniform gravitational field coupled with atmospheric drag.

The BSTAR term which appears in the element set is an integral part of the theory. It is defined as the satellite drag coefficient, expressed in units of Earth radii, at a reference altitude of 120 km. Density ( $\text{kg/m}^3$ ) at reference altitude is then,

$$\rho_o = 2B^* \frac{m}{C_D A r} \quad (91)$$

where  $r$  is the radius of the Earth in meters. To find the density of a non-rotating atmosphere at the altitude of epoch, one simply applies the equation [Lane, 1965]:

$$\rho_h = \rho_o \left[ \frac{120 - 78}{h - 78} \right]^4 \quad (92)$$

where 120 km is the reference altitude, and  $h$  is the satellite altitude in kilometers at epoch [Hoots, 1981].

As a final step in recovering the density of the rotating atmosphere, we recognize that the SGP model density neglected to account for the relative velocity between the satellite and the atmosphere. As a first order correction, we introduce the  $F$  function of King-Hele,

$$F = \left[ 1 - \frac{i_{p0} w}{v_{p0}} \cos(i_0) \right]^2 \quad (93)$$

which is used to modify the drag expression:

$$D = \frac{1}{2} \rho v^2 F A C_D \quad (94)$$

Properly applied to density expression, we have:

$$\rho_{h,rot} = \rho_h / F \quad (95)$$

Although the F factor changes little with each new element set, it is nonetheless prudent to use the new initial values contained in each set to adjust F accordingly.

Alternatively, one might use the first time derivative of mean motion from the elements directly. There is a method for calculating density from the time derivative of mean motion [King-Hele, 1964] at perigee altitude plus one-half of the scale height.

The most obvious shortcoming of using orbital element sets to determine atmospheric density is that information has been lost in the process of converting observational data into mean element sets. Short term variations in air density experienced by the satellite, such as those resulting from the diurnal bulge, are of too short a frequency to be accounted for properly. Long term variations, such as those related to  $A_p$ , F10.7, and the seasonal dependence on the location of the diurnal bulge, have a combined effect on the elements which is expressed as an average.

It is necessary to identify and resolve these effects if density as derived from the elements is to become a useful tool for model density comparisons. Proper identification of these effects depends on the frequency at which element sets are updated. Historical data bases are available for  $A_p$  and F10.7. The satellite ephemeris can be reconstructed from the elements, thus, the position of the satellite relative to the bulge is also known. It remains to develop a method of quantifying the average position of the satellite with respect to the bulge from the ephemeris. This should be a relatively simple task for orbits with low eccentricity.

A complete set of LDEF orbital elements spanning 2106 days was obtained. These data, which represented 963 element sets, were checked for continuity and consistency. Copies of the SGP4 and SGP8 source code were obtained and analyzed with respect to their treatment of the BSTAR term. The SGP models use a static, spherically symmetric atmosphere with density described by a power function shown in Eq. (92). This presents no difficulty, as long as the interest is in density at epoch. There is a difficulty, however, in that BSTAR is given a "mean" value. This value minimizes the errors in the SGP models when advancing from one element set to the next. If the  $C_D$ ,  $A$ , and  $m$  terms in Eq. (91) are constant, then  $\rho_0$  can be calculated in a straight forward manner. If the orbit is circular, then the variation of the  $h$  term in Eq. (92) is small, and the power law representation of scale height should not introduce significant error. The density at altitude obtained from Eq. (92) is then a measure of the "mean" density encountered by the satellite during the time span of that element set.

Atmospheric densities have been calculated from the LDEF orbital element sets based upon these assumptions. The calculations use the BSTAR term along with the NASA values of mass and surface area. Other constant values were obtained from the SGP4 source code. A copy of the source code was modified to produce a density data base. This data base contains  $\rho_0$  (the density at a reference altitude of 120 km), geodetic altitude at epoch,  $\rho$  (density at epoch altitude), and other parameters required by density models. The BSTAR values tend to show fluctuations due to solar flux and geomagnetic activity, as illustrated in Figure 99. Correlations are complicated, however, because both  $A_p$  and F10.7 have a combined effect on BSTAR, and because the variability of diurnal bulge effects have not been taken into account. Densities at altitude at epoch obtained from these BSTAR values are summarized in Figure 100. MSIS86 density values calculated from the same data base and parameter inputs are shown in Figure 101. The BSTAR derived density values are shown in a semi-logarithmic scale in Figure 102 to better illustrate

12/17/91

ELEMENTS FOR SAT. 14898 FROM 84/098

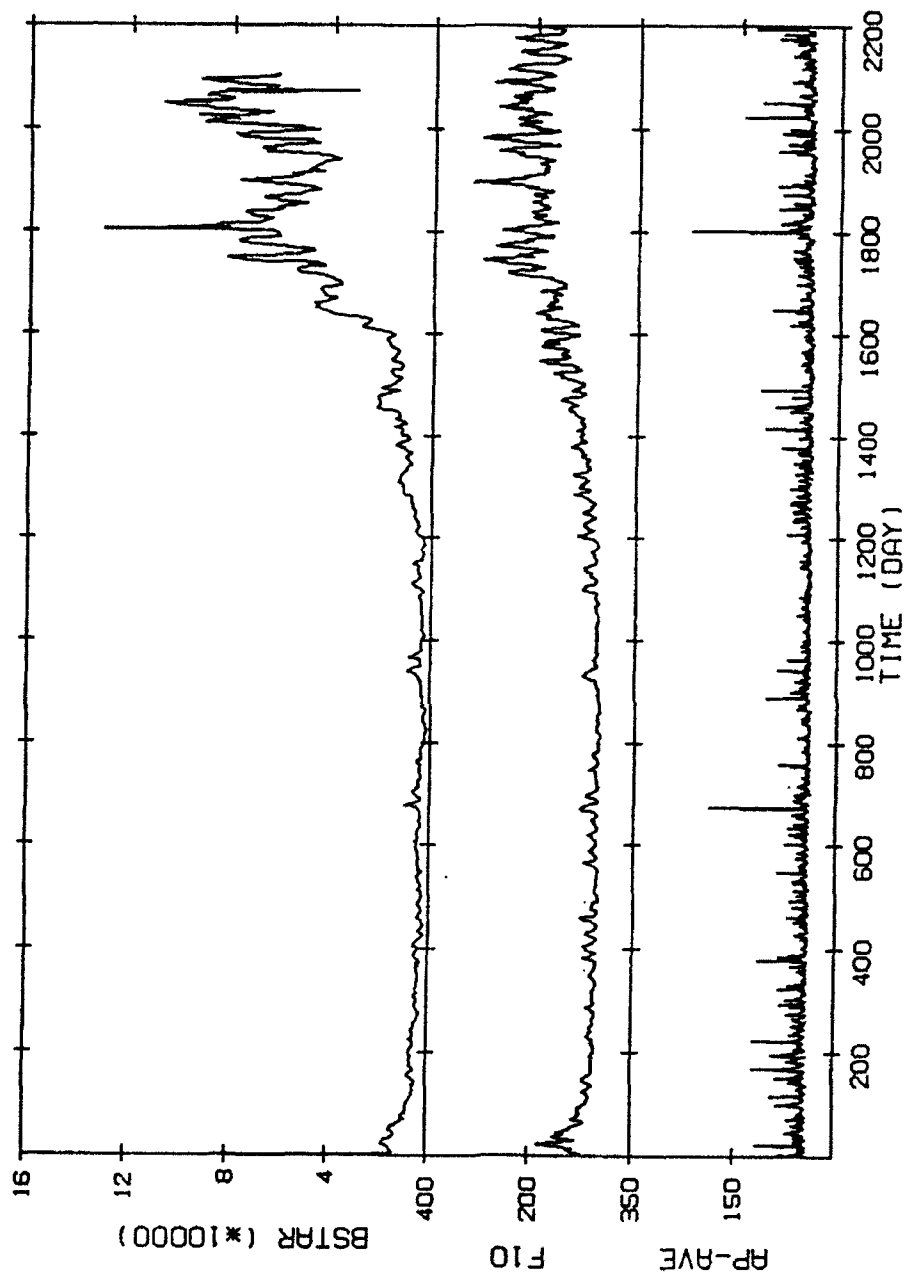
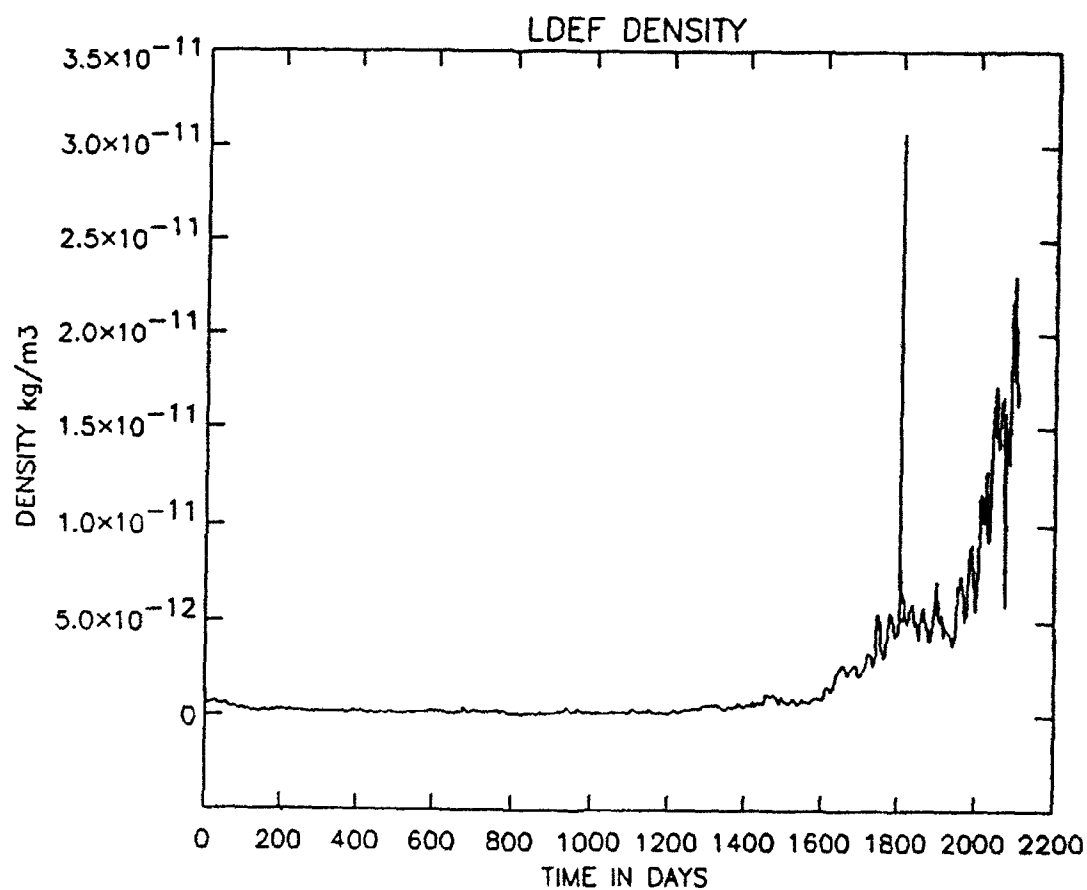


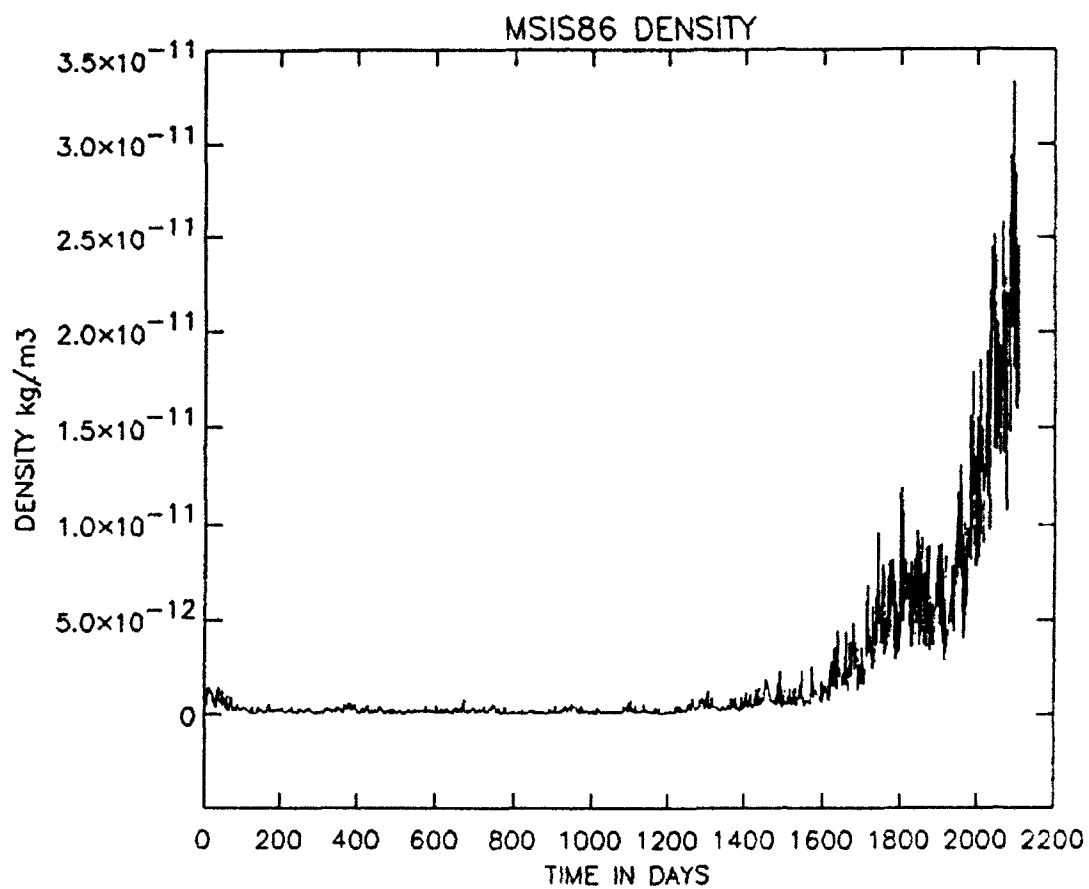
Figure 99. BSTAR values.





START	YYDD.DD	STOP	YYDD.DD	DELTA	DDD.DD
	00000.00		90012.00		000.00

**Figure 100.** Densities at altitude at epoch obtained from BSTAR values.



START	YYDD.DD	STOP	YYDD.DD	DELTA	DDD.DD
	00000.00		90012.00		000.00

**Figure 101.** MSIS86 density values.

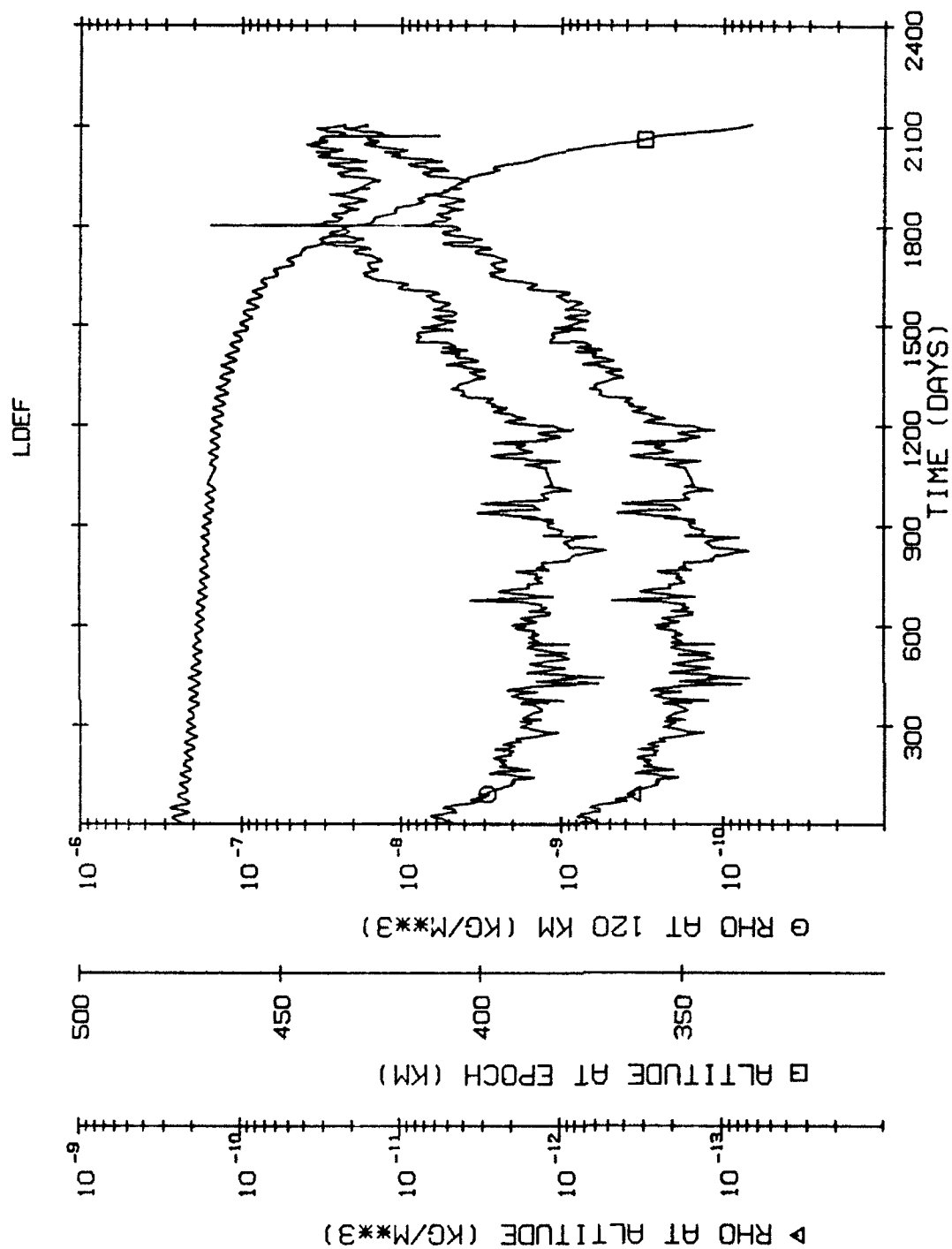


Figure 102. BSTAR derived density values in semi-logarithmic scale.

density variations from 0-1600 days. The large spike at approximately 1800 days is the result of a large geomagnetic storm, which is also seen in the  $A_p$  AVE plot in Figure 99.

## 5.5 ORBITAL DECAY

An effort was initiated to assess orbital decay models for potential application to orbital debris tracking and prediction studies. Several models were examined and compared to recent literature [Chao, *et al.*, 1991], as summarized in Table 37.

It was recognized that the errors resulting from semi-analytic approximations or integration step sizes in the decay models could not easily be separated from errors associated with atmospheric density models. Tools and techniques were developed using the Radex model, EDECAY, to make this distinction and to quantify performance in relative terms. As indicated in Table 37, EDECAY uses numerical integration of King-Hele expressions [King-Hele, 1964]. The differential changes in semi-major axis and eccentricity are calculated for one orbit. The accuracy of this integration is highly dependent on the eccentricity of the orbit. The number of steps necessary to ensure accuracy largely determines the computational efficiency of a numerical approach. The values obtained from this integration are then used to determine orbital changes over larger time steps using Runge-Kutta integration. The variation of the semi-major axis is nearly linear over a time of several days, so the Runge-Kutta method is both accurate and fast when applied to this second integration.

For the first integration, methods were evaluated in terms of both accuracy and computational time. A comparison of results using Simpson's rule, Romberg integration, and Gaussian quadrature was made. Romberg integration is computationally expensive for eccentric orbits, but the relative error may be quantified during each step of the iteration. Thus, Romberg integration was used as a benchmark to assess the accuracy performance of other methods of integration. It was found that the Simpson's rule integration gave acceptable accuracy in a reasonable amount of time for eccentricities of less than 0.1.

A copy of the DECAY code [Mueller, 1978a-e; 1979; 1980; 1981] was obtained from NASA JSC. The principal parts of DECAY are a drag module, a density module, and a solar/lunar perturbation module. The drag module calculates changes in semi-major axis and eccentricity due to atmospheric drag. The King-Hele approach is used, where differential equations are developed and solutions take the form of Bessel functions. The density module consists of a modification of the Jacchia 71 atmosphere model, referred to as the Lineberry Expressions [Mueller, 1982].

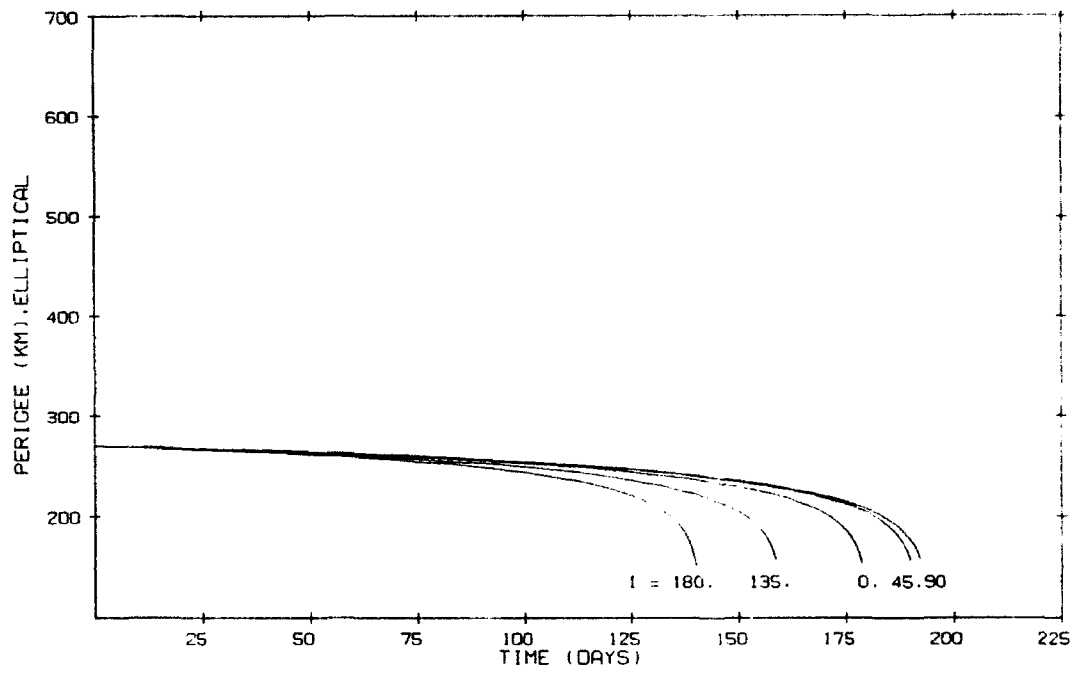
Initial testing was accomplished using data from a recent publication [Chao, *et al.*, 1991], in which the actual decay of a spherical calibration satellite was graphed. The orbital data from Chao's report was first used in our program EDECAY, both to ensure that the results could be reproduced and to establish the validity of using EDECAY for other benchmarking. It was found that the relative velocity between the satellite and the rotating atmosphere needed to be taken into account. This was done through the F function (King-Hele Equation 2.13), which gives a first order approximation using the inclination of the orbit. The effect of inclination on orbit life is shown in Figure 103. A second modification was done to EDECAY, such that the position of the diurnal bulge, caused by heating of the atmosphere in the vicinity of the sub-solar point, was varied through the use of a random number generator. EDECAY test results using these modifications compare favorably to the actual satellite decay data, as illustrated in Figure 104.

TABLE 37. Orbital Decay Models Summary

MODEL	MUELLER	CHAO	ROPP	EDECAY
BASED ON	KING-HELE	LIU	KING-HELE	KING-HELE
EQUATIONS	4.41, 4.44, 4.47, 4.48, 4.50, 4.67, 4.74, 4.77, 4.80, 4.87, 4.125, 4.130	INDEPENDENTLY DEVELOPED [Chao et al., 1991]	INDEPENDENTLY DEVELOPED [Wexler, 1968]	4.10, 4.11
ATMOSPHERE	JACCHIA 71 via LINEBERRY EXPRESSIONS (others possible)	JACCHIA 64 OR JACCHIA 71	JACCHIA 64 (others possible)	JACCHIA 64 (others possible)
CONSIDERATIONS	INTEGRATION USING BESSEL FUNCTIONS	NUMERIC INTEGRATION USING GAUSSIAN QUADRATURE	EIGHTH ORDER ADAMS MOULTON INTEGRATION	NUMERIC INTEGRATION USING RUNGE-KUTTA AND SIMPSON'S RULE
	EXPONENTIAL DENSITY VARIATION BASED ON GEODETIC SCALE HEIGHT FOR EACH TIME INCREMENT	MODEL DENSITY CALCULATED FOR EACH INTEGRATION INTERVAL	EXPONENTIAL DENSITY VARIATION BASED ON GEOCENTRIC SCALE HEIGHT WITH DIURNAL BULGE CORRECTION FOR EACH TIME INCREMENT	MODEL DENSITY CALCULATED FOR EACH INTEGRATION INTERVAL
	a, e, i ARE REQUIRED	ALL ELEMENTS ARE REQUIRED	ALL ELEMENTS ARE REQUIRED	a, e, i ARE REQUIRED
	AVERAGE EARTH RADIUS BASED ON INCLINATION	GEODETIC EARTH RADIUS BASED ON i, f, $\omega$	RADIUS OF OBLATE SPHEROID BASED ON LATITUDE	AVERAGE EARTH RADIUS BASED ON INCLINATION
	POSSIBLE TO ADD FIRST ORDER ATMOSPHERIC ROTATION CORRECTION BASED ON i	ATMOSPHERIC ROTATION CORRECTION BASED ON ELEMENTS	CONTAINS FIRST ORDER ATMOSPHERIC ROTATION CORRECTION BASED ON i	CONTAINS FIRST ORDER ATMOSPHERIC ROTATION CORRECTION BASED ON i
	SOLAR/LUNAR, J2 PERTURBATIONS POSSIBLE IF ALL ELEMENTS KNOWN and APOGEE > 14,000km	J2 and J3 TAKEN INTO ACCOUNT	SOLAR/LUNAR PERTURBATIONS and J TERMS ARE USER SPECIFIED	RANDOM NUMBER GENERATION FOR DIURNAL BULGE LOCATION RELATIVE TO SATELLITE
EXECUTION TIME	2 SEC	> 100 SEC		> 100 SEC

03/15/93

ORBITAL DECAY FOR JACCHIA 1964.  $F10 = .001$   $AP = 20$   
 $A/M = .0036 \text{ M}^2/\text{KG}$   $ECC = 3.E-02$



**Figure 103.** The effect of inclination on orbit life.

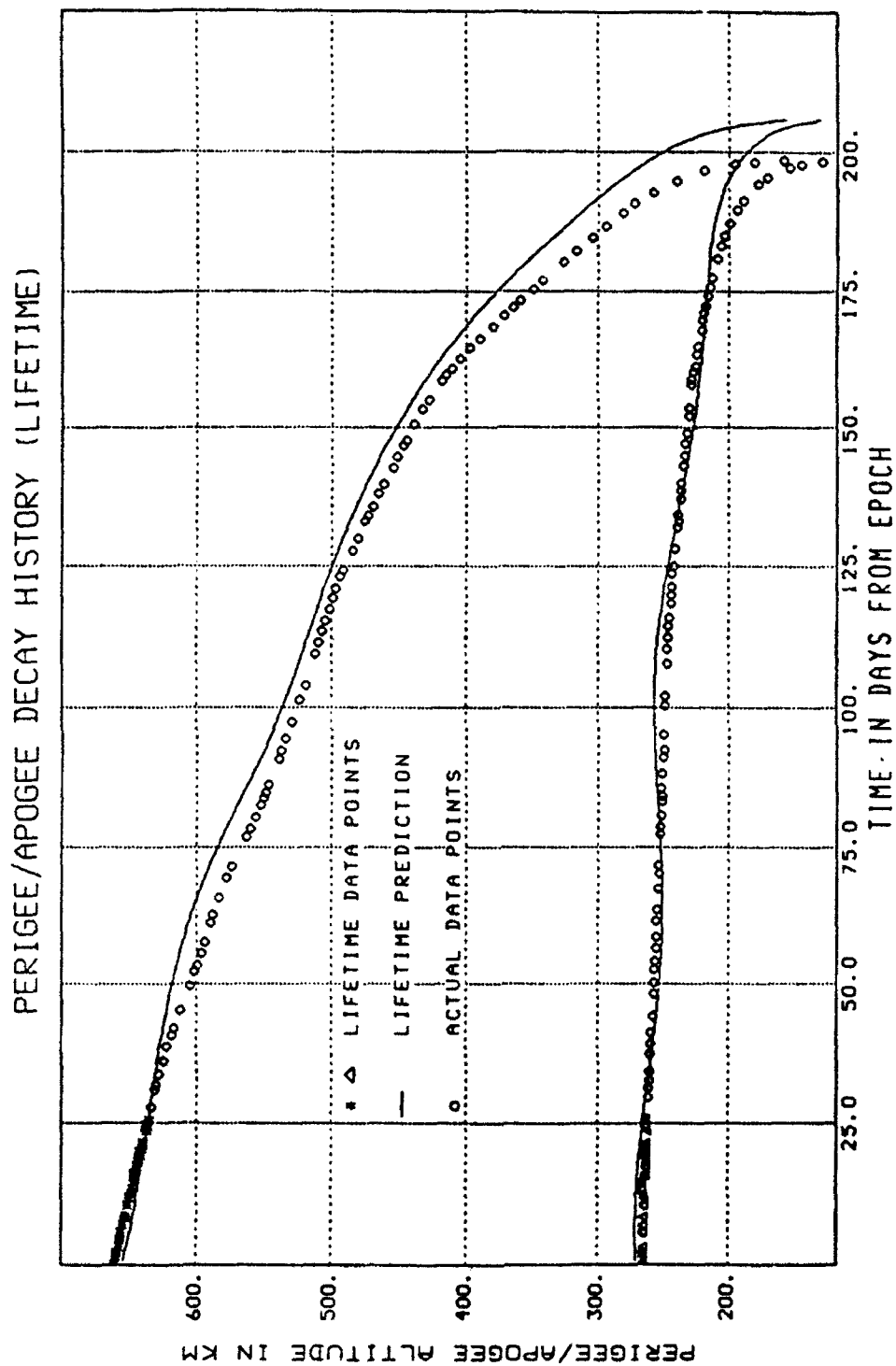


Figure 104. Perigee and apogee decay histories of a slightly elliptical orbit (Case 2).

The first problem encountered in the testing of Mueller's DECAY was that it required the average exospheric temperature as an input parameter. Since a module for this calculation was not included with the code, it was decided to use available code from the Jacchia 64 model to expedite testing. Test results showed DECAY to be in fairly good agreement with Chao and EDECAY. The advantage of using DECAY lies in computing time. Typical execution time for DECAY was 2 seconds, whereas the time required for EDECAY (and also Chao's modeling software) was in excess of 100 seconds. DECAY was also tested using the Jacchia 64 model atmosphere.

Although the internal comments provided sufficient information for running the software, few references were given for the expressions developed in the algorithms. A library search revealed that Mueller published a series of NASA reports shortly after the software was released. These references have been added to the code comments. Additional comments referencing the specific King-Hele equations have been added to the code as well.

During the testing, it was noted that DECAY sometimes calculated abrupt changes in the satellite orbit. In a study of the effect of time increment size on lifetime accuracy, a case was isolated in which this occurred over many consecutive calculations. These results are shown in Figure 105. Curiously, the curve with the most erratic behavior was the one with the smallest time increment. A detailed analysis of the problem found that the coefficient of one of the Bessel functions was incorrect. After correcting this coefficient, the problem no longer occurs, as indicated in Figure 106. Additional Bessel function terms were added to the code where it was appropriate.

King-Hele's F function was added to the Mueller DECAY code, since it also failed to account for atmospheric rotation. King-Hele's treatment includes the F factor in the delta (modified drag) term, which is assumed to be a constant, because it changes very little during satellite lifetime. Delta appears outside of the King-Hele integrals, thus, Mueller's algorithms for integration are unaffected by the addition of the F factor. Testing was accomplished by generating a curve from King-Hele's Figure 2.5, which is reproduced here in Figure 107. The F function is not used by Mueller's DECAY code directly. To apply this correction, the driver program which calls DECAY must modify the drag term with the value returned by the F function. In this way, the rotating atmosphere correction is kept as an option, which may be exercised by the user.

After obtaining and reviewing Mueller's publications, the T infinity expression used by Mueller was found and added to the DECAY code. The Lineberry expressions used in the density calculation were then tested by comparing their results to the benchmark case results of Chao and EDECAY. It was found that the Mueller code results, shown in Figure 108, compared favorably to the benchmark cases. However, Mueller's model is much faster.

An updated copy of the Mueller DECAY code has been released and made available to NASA JSC. This new release contains the corrected Bessel coefficients, King-Hele's F function, comments which indicate the particular King-Hele equation used, and a more complete list of references. It also includes Mueller's T infinity expression and the option to include a first order correction to account for the effects of a rotating atmosphere, as described.



03/15/93

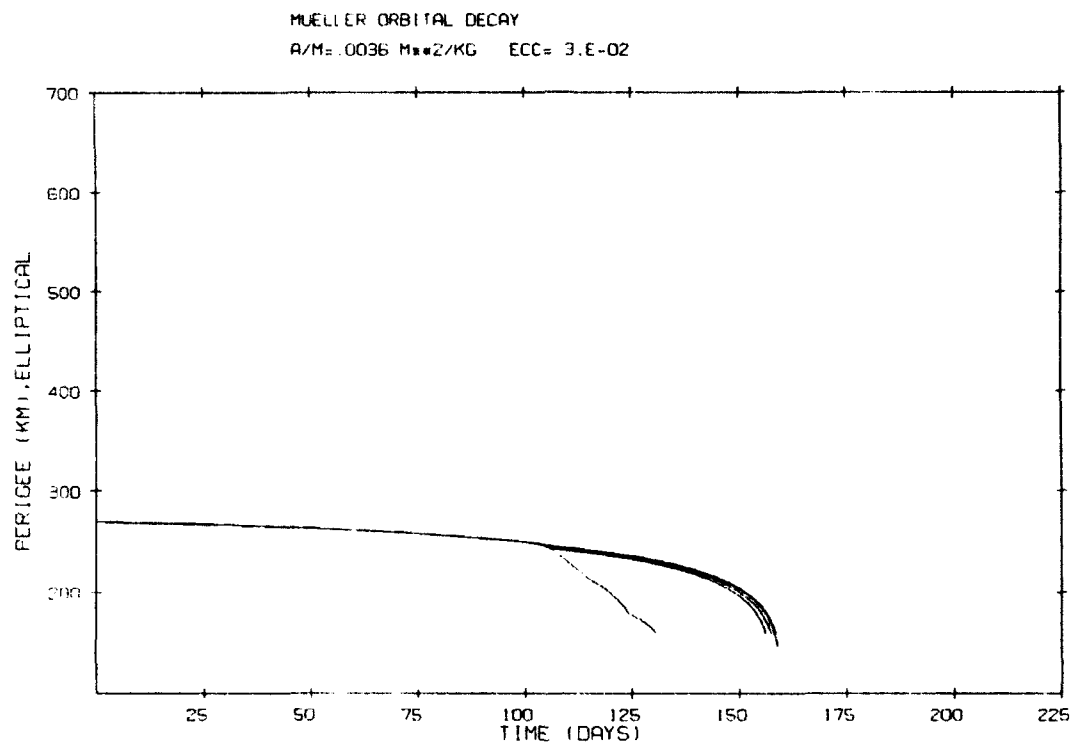


**Figure 105.** Abrupt changes in satellite orbit as calculated by DECAY.

03/15/93

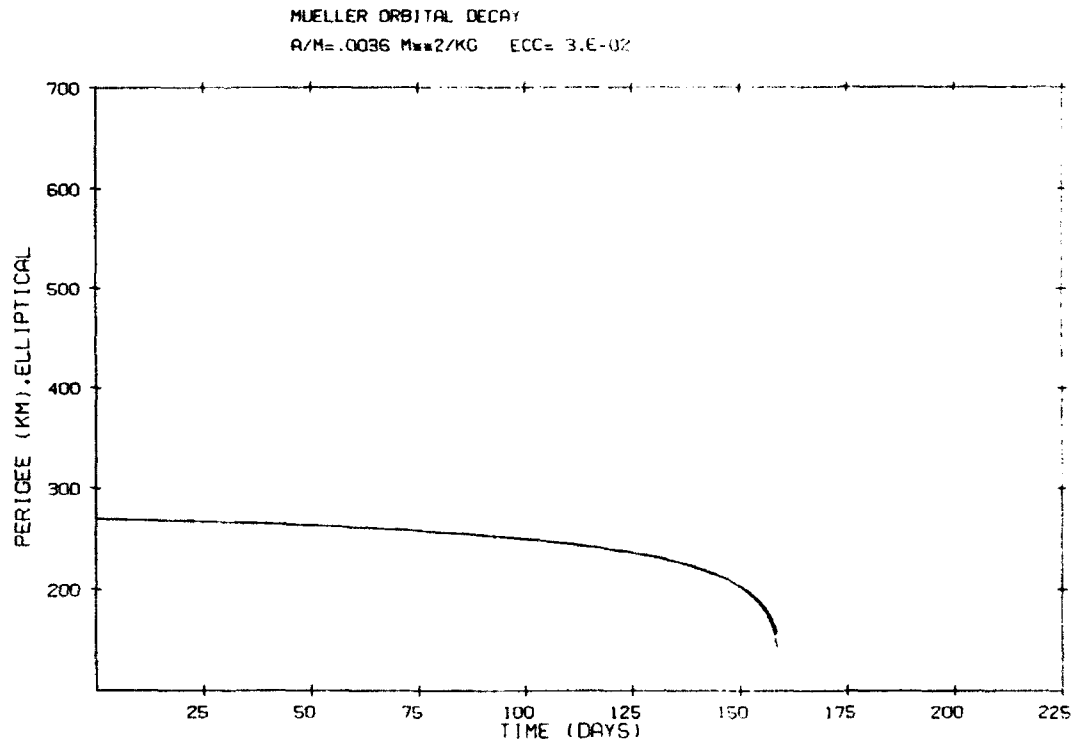


**Figure 106.** DECAY calculations after correction of Bessel function coefficient.

03/15/93

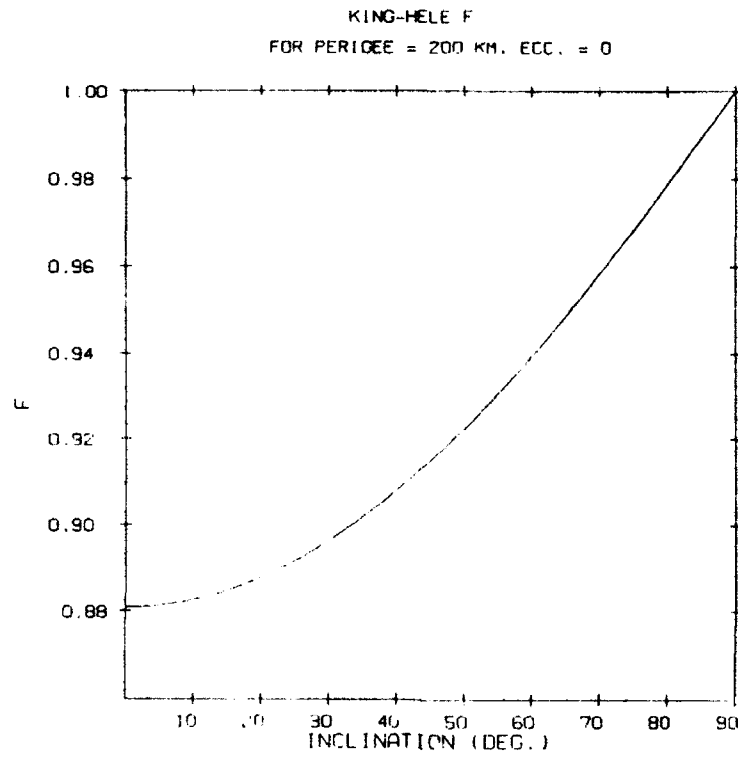


Figure 107. Reproduction of King-Hele's Figure 2.5.

03/15/93

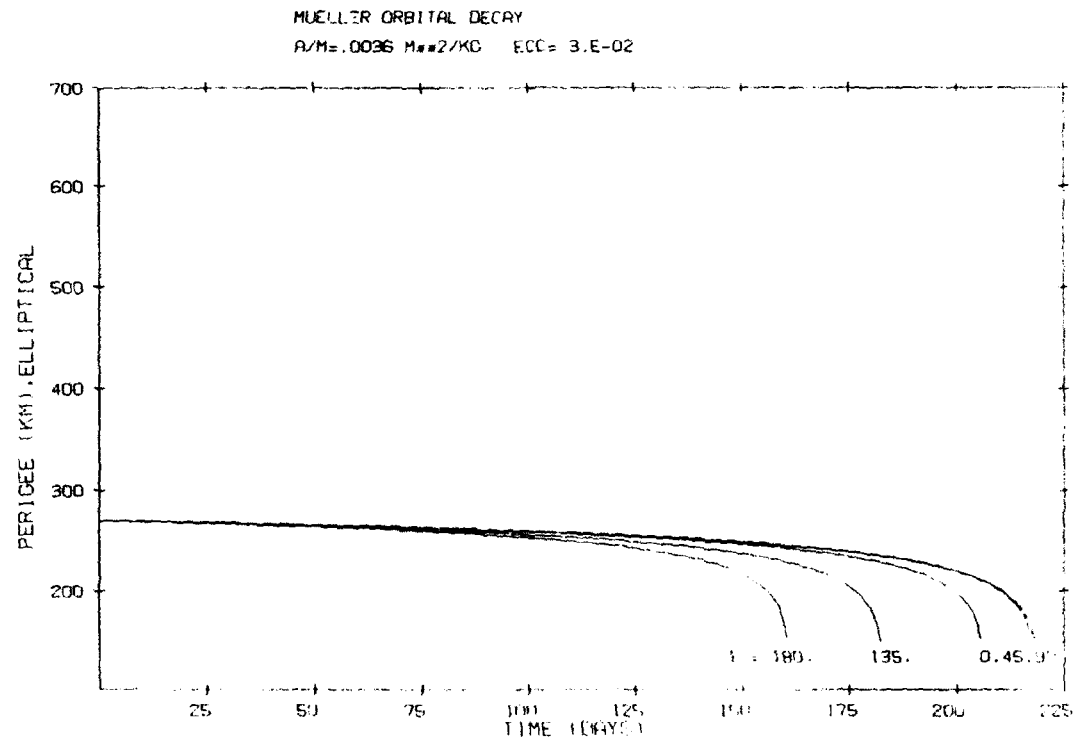


Figure 108. Mueller code results.

## 5.6 REFERENCES

- Brouwer, D., "Solution of the Problem of Artificial Satellite Theory Without Drag", *The Astronomical Journal*, 64, 378, November 1959.
- Chao, C. C. and M. H. Platt, "An Accurate and Efficient Tool for Orbit Lifetime Predictions", AAS Paper 91-134, 1991.
- Hoots, F. R., "A Short, Efficient Analytical Satellite Theory", AIAA Paper 80-1659, 1980.
- Hoots, F. R., "Theory of the Motion of an Artificial Earth Satellite", *Celestial Mechanics*, 23, 307, 1981.
- Jacchia, L. G., "A Variable Atmospheric-Density Model from Satellite Accelerations", *Journal of Geophysical Research*, 65, 2775, September 1960.
- Justus, C. G., G. R. Fletcher, F. E. Gramlink, and W. B. Pace, The NASA/MSFC Global Reference Atmospheric Model - MOD 3 (With Spherical Harmonic Wind Model), NASA Contractor Report 3256, March, 1980.
- King-Hele, D. G., Theory of Satellite Orbits in an Atmosphere, Butterworths, London, 1964.
- Kozai, Y., "The Motion of a Close Earth Satellite", *The Astronomical Journal*, 64, 367, November 1959.
- Lane, M. H., "The Development of an Artificial Satellite Theory Using a Power-Law Atmospheric Density Representation", AIAA Paper 65-35, 1965.
- Lane, M. H. and K. H. Cranford, "An Improved Analytical Drag Theory for the Artificial Satellite Problem", AIAA Paper 69-925, 1969.
- Mueller, A. C., "A Singularity Free Analytical Solution of Artificial Satellite Motion with Drag", NASA-CR-151601, 1978.
- Mueller, A. C., "An Analytical State Transition Matrix for Orbits Perturbed by an Oblate Spheroid", NASA-CR-151602, 1978.
- Mueller, A. C., "Atmospheric Density Models", NASA-CR-151604, 1978.
- Mueller, A. C., "An Atmospheric Density Model for Application in Analytical Satellite Theories", NASA-CR-151605, 1978.
- Mueller, A. C., "The Method of Averages Applied to the KS Differential Equations", NASA-CR-151607, 1978.
- Mueller, A., G. Scheifele, and S. Starke, "An Analytical Orbit Predictor for Near-Earth Satellites", AIAA Paper 79-0122, 1979.

Mueller, A. C., "Decay Model for use in Space Object Collision Studies", Memorandum No. 250 ,  
Analytical and Computational Mathematics, Inc., Houston, Texas, 31 July 1980.

Mueller, A. C., "The Decay of the Low Earth Satellite", Lockheed Engineering and Management  
Services Company Publication # LEMSCO - 17520, 1981.

Mueller, A. C., "Jacchia-Lineberry Upper Atmosphere Density Model", NASA-CR-167824, 1982.

Wexler, D. M., "Rapid Orbit Prediction Program", TRW Systems, 1968.

## 6.0 AURORAL PARTICLE PRECIPITATION

### 6.1 ELECTRON PRECIPITATION

#### 6.1.1 Introduction

Determination of the global pattern of auroral particle precipitation is important, both for the understanding of the physical processes producing and maintaining the auroral oval, and for the prediction of the effects of auroral particle precipitation on operational Air Force systems. For this reason, an extensive set of studies has been conducted to quantify the global pattern using measurements from the SSJ/3 and SSJ/4 particle spectrometers flown on the spacecrafts of the Defense Meteorological Satellite Program (DMSP) [Hardy, *et al.*, 1985; McNeil, *et al.*, 1984; McNeil, *et al.*, 1985; Hardy, *et al.*, 1987; Hardy, *et al.*, 1989; Hardy, *et al.*, 1991; Brautigam, *et al.*, 1991, Bounar and Hardy, 1992]. These studies have been of two types: 1) studies where the behavior of the average electron and ion spectrum is determined as a function of either the level of geomagnetic activity or the value of solar wind parameters; and 2) studies where the probability of occurrence of different levels of auroral precipitation is determined as a function of the level of geomagnetic activity.

The DMSP data set is well suited for such studies because of its size. The SSJ/3 and SSJ/4 detectors are operated continuously on the DMSP satellites, recording complete electron and ion spectra once per second. Approximately fifteen years of the data is available, consisting of approximately 150 million spectra. Such a large data set allows determination of the averages and probability distribution to a high precision. In addition, DMSP satellites are in circular polar orbits with either a dawn-dusk meridian or a 1030-2230 meridian, and their combined measurements cover nearly all of the high-latitude regions.

#### 6.1.2 Electron Precipitation Data Base

All of the available auroral electron precipitation data from three DMSP satellites, F7, F8 and F9, were unpacked and processed. This is approximately 15 years worth of data, which is about a total of 159,734,933 particle flux measurements (at a rate of one measurement per second). The total number of semi-monthly packed magnetic tapes is 87 files for the F7 satellite, for a total of 52,319,044 flux spectra. The number of total seconds processed for the F8 satellite is 58,405,729 flux spectra from 105 semi-monthly packed files. The number of total seconds processed for the F9 satellite is 49,010,160 flux spectra from 90 semi-monthly packed files.

The electron one-second measurements have been binned individually into an array of 600 by 676 by 8, containing the event occurrences per second. This array is divided into 600 spatial bins, where the magnetic local time (MLT) has been divided into 24 hourly bins and the corrected geomagnetic latitude ranging from 40° to 90° has been divided into 25 2° bins. The array is also divided into 26 integral energy flux bins and 26 integral number flux bins. The integral number (energy) flux range is from  $10^5$  to  $10^{11}$  e/(cm<sup>2</sup>-sr-sec) (Kev/(cm<sup>2</sup>-sr-sec)), with four bins per decade, log-uniformly spaced (*i.e.* each bin covers  $10^{1/4}$  Kev/(cm<sup>2</sup>-sr-sec)). The array is further divided into 8 Kp bins. The Kp bins are: 0<sub>o</sub> to 1-, 1<sub>o</sub> to 1+, 2- to 2<sub>o</sub>, 2+ to 3-, 3<sub>o</sub> to 3+, 4- to 4+, 5- to 6-, and 6<sub>o</sub> to 9<sub>o</sub>.

There are three individually binned matrices corresponding to different DMSP satellites, and all three arrays have been merged into a single matrix. The binned data base is available in ASCII format.

### 6.1.3 Electron Precipitation Models

Auroral models can be used very efficiently by means of compression techniques. Empirical models can be fitted and represented by look-up tables, or a set of equations and coefficients. This makes it easy to use such a parameterized model, instead of using the actual measurements. Characteristic auroral values can then be obtained for a particular spatial position within a given time, without relying on the global picture. We had previously developed a set of analytical expressions using DMSP data to model the patterns of ionospheric conductivity, as well as the auroral energy and number flux [Hardy, *et al.*, 1987]. The Epstein-Fourier function was used to describe the pattern of fluxes in the auroral oval. The Epstein coefficients were derived from fits to the latitudinal variation, and the Fourier coefficients from fits to the local time dependence of the Epstein coefficients. A study was also undertaken to parameterize the auroral flux occurrence distribution in terms of two lognormal probability functions, whose coefficients depend on spatial geomagnetic location and geomagnetic activity level.

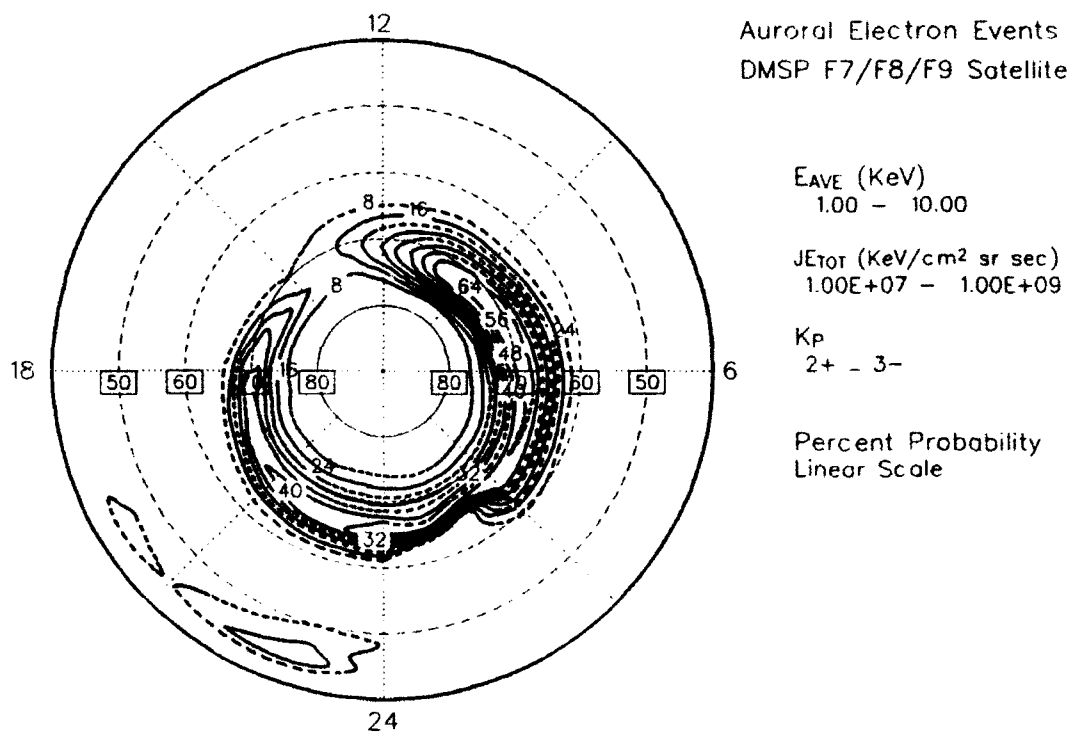
Data processing and analysis software was developed to better analyze the electron precipitation data. Two of the software systems, called EPROM and FLXDIS, were developed to analyze the frequency of electron event occurrences in the auroral oval and the two-dimensional probability distributions of these types of events in the high latitude regions, respectively. A sample plot from EPROM is shown in Figure 109. It shows a contour polar plot of the frequency of occurrence of events in the average energy range from 1.0 to 10.0 KeV and integral energy flux range from  $10^7$  to  $10^9$  KeV/(cm<sup>2</sup>-sec-ster). The geomagnetic activity is for a  $K_p$  range of 2+ to 3- corresponding to a moderate geomagnetic activity. The probability contour levels are equally-spaced at increments of 8%. In Figure 109, the maximum probability of occurrence of about 79% is at MLT = 0900 hrs and CGL = 70°.

Figure 110 was generated by the FLXDIS program. It is the contour plot of the probability distribution of the electron average energy vs. integral energy flux. The figure is for a MLT from 2200 to 2300 hrs, and a CGL range of 68° to 70°. This is the spatial location with the greatest likelihood of observing the auroral arcs. The geomagnetic activity, defined by  $K_p$ , is in the range of 2+ to 3-, which is a moderate geomagnetic activity. Figure 110 shows that one maximum percent probability of about  $10^{0.4}$  is located at approximately  $\text{Log}(E_{ave})=0.25$  and  $\text{Log}(JE_{tot})=8.25$ , and another maximum (about  $10^{0.1}$ ) occurs at  $\text{Log}(E_{ave}) \approx -0.75$  and  $\text{Log}(JE_{tot}) \approx 5.75$ .

### 6.1.4 Integral Probability of Electron Flux Events

The averaged auroral models for the determination of characteristic parameters of the auroral particle precipitations are valuable tools in determining the background auroral emission. They, however, do not provide an insight on the duration, spatial extent, or correlations of the high intensity emissions. In order to answer one of these concerns, we conducted a study using the 1990 flux measurements from the F9 satellite taken in the 1030-2230 meridian [Bounar and Hardy, 1992]. The purpose of such a study was to determine not only the probability of locating an event at a given spatial grid location, but also the integral probability of locating this same event over several latitude zones starting from a particular spatial grid location. Only the first part of these issues was addressed in earlier studies of DMSP data from satellites F2 and F4 [McNeil and Hardy, 1985]. The results of such a study allow the determination of the integral probability of occurrence for auroral precipitation events above any specified level in integral energy flux and average energy for any line of sight through the auroral region. This is an important tool for determining background and interference signals for any system operating in the auroral region. Satellite flight mission planners can use the results from such a study to determine the pointing of onboard systems to maximize the probability of observing specific levels and types of auroral phenomena. More





**Figure 109.** Polar contour plot of the percent probability of the electron event occurrence in corrected geomagnetic coordinate system. The geomagnetic activity level (given  $K_p$ ), and the characteristics of the event (given by  $E_{ave}$  and  $JE_{10t}$ ) are shown on the right. The percent probability values are given in linear scale.

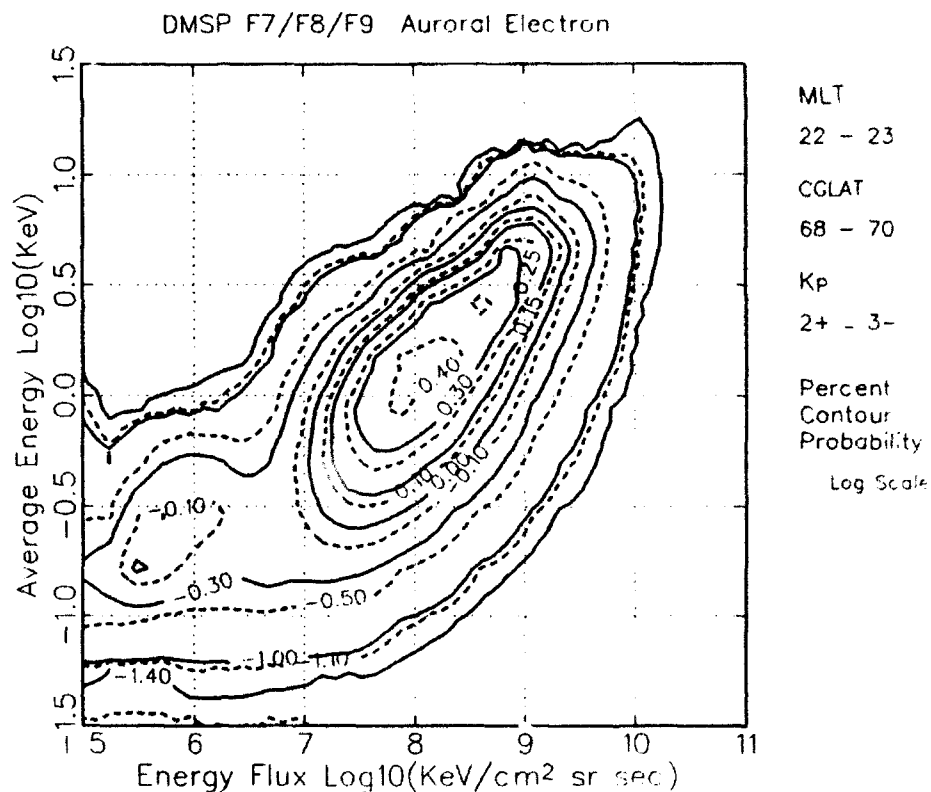


**Figure 110.** Contour plot of the probability distribution of the average energy versus the energy flux in geomagnetic coordinate system. The geomagnetic location (given by MLT and CGL), and the geomagnetic activity level (given by  $K_p$ ) are shown on the right. The percent probability values are given in logarithmic scale.

importantly, the results provide the capability to determine, for operational Air Force systems, the probability that auroral precipitation at a specific level is producing background to surveillance systems operating through the oval or ionospheric perturbations for C<sup>3</sup>I operating in and through the auroral oval.

As an example of the results of this study, we found that for auroral electrons with energies exceeding 7 KeV in the premidnight sector and for a moderate geomagnetic activity, the likelihood of their occurrence drops from about 9% (see Figure 111) for energy fluxes exceeding  $\frac{1}{2}$  kR to less than 1% for energy fluxes exceeding 160 kR (see Figure 112). Note that these figures show the integral probability of occurrence of auroral events defined by the parameters shown on the right-hand side. The probability is given as a function of the corrected geomagnetic latitude (CGL) and the differential latitude ( $\Delta$ CGL), which is positive poleward ( $\Delta$ CGL > 0) of the reference latitude and negative ( $\Delta$ CGL < 0) otherwise. The integral probabilities can increase whenever more than one latitude zone is traversed. In this instance, looking poleward from about 66° latitude will increase the chances of observing this event by a factor of 2 for low energy flux thresholds, as shown in Figure 111, and by a factor of 9 for high energy flux thresholds, as shown in Figure 112. When we fixed the energy flux thresholds of the electron events to 5 kR and varied the geomagnetic activity, we found that the probability maximum occurred near 67° for low Kp (see Figure 113), and moved equatorward to about 61° for high Kp values (see Figure 114). This is a well known phenomena of the equatorward expansion of the aurora with an increase in geomagnetic activity. Figure 115 shows that the integral probability for such an event integrated over 6° latitude poleward of the 67° latitude for Kp=2- to 3+, increases to about 13% from 8%.

The main deficiency in this study arises from the availability of only one year of DMSP F9 SSJ/4 data. The use of only the SSJ/4 data from the F9 satellite limits the magnetic local time coverage of the study, and the use of only one year limits the statistical accuracy of the results. These problems can be eliminated through the use of data from the SSJ/4 detectors on the F7, F8, F10, and F11 satellites. In combination, these instruments have recorded many years of data and provide nearly complete MLT coverage of the oval.

#### 6.1.5 Persistence of Auroral Electron Flux Events

Another study consisted of estimating the persistence of auroral electron activity and correlating this activity to the geomagnetic activity, which is measured by the Kp index [Bounar and McNeil, 1992]. Using known values of Kp, this study determines the average number of occurrences of auroral events of varying intensity. These auroral events are defined by an electron energy flux ( $JE_{\text{tot}}$ ) that exceeds specified threshold values.

To study the relationship between the auroral DMSP electron precipitation events and the geomagnetic Kp index, the superposed epoch analysis technique was implemented. This approach was used by Nagai in determining the relationship between several geomagnetic indices [Nagai, *et al.*, 1988]. The epoch is defined as the time at which Kp values persisted above a specified threshold value for a specified duration. The epochs are located in the available data, and the Kp series are superposed over a time window ranging from one day before the epoch to three days after. The superposed Kp series are then averaged over all epochs. The same procedure is used to obtain the corresponding time series of electron auroral events for comparison with the Kp index.

To measure the correlation between Kp and the number of events, the normalized correlation coefficient is computed for Kp above the specified threshold value. The correlation coefficient is defined as the ratio of the expected value of the product of Kp and the number of events, to the product of their standard

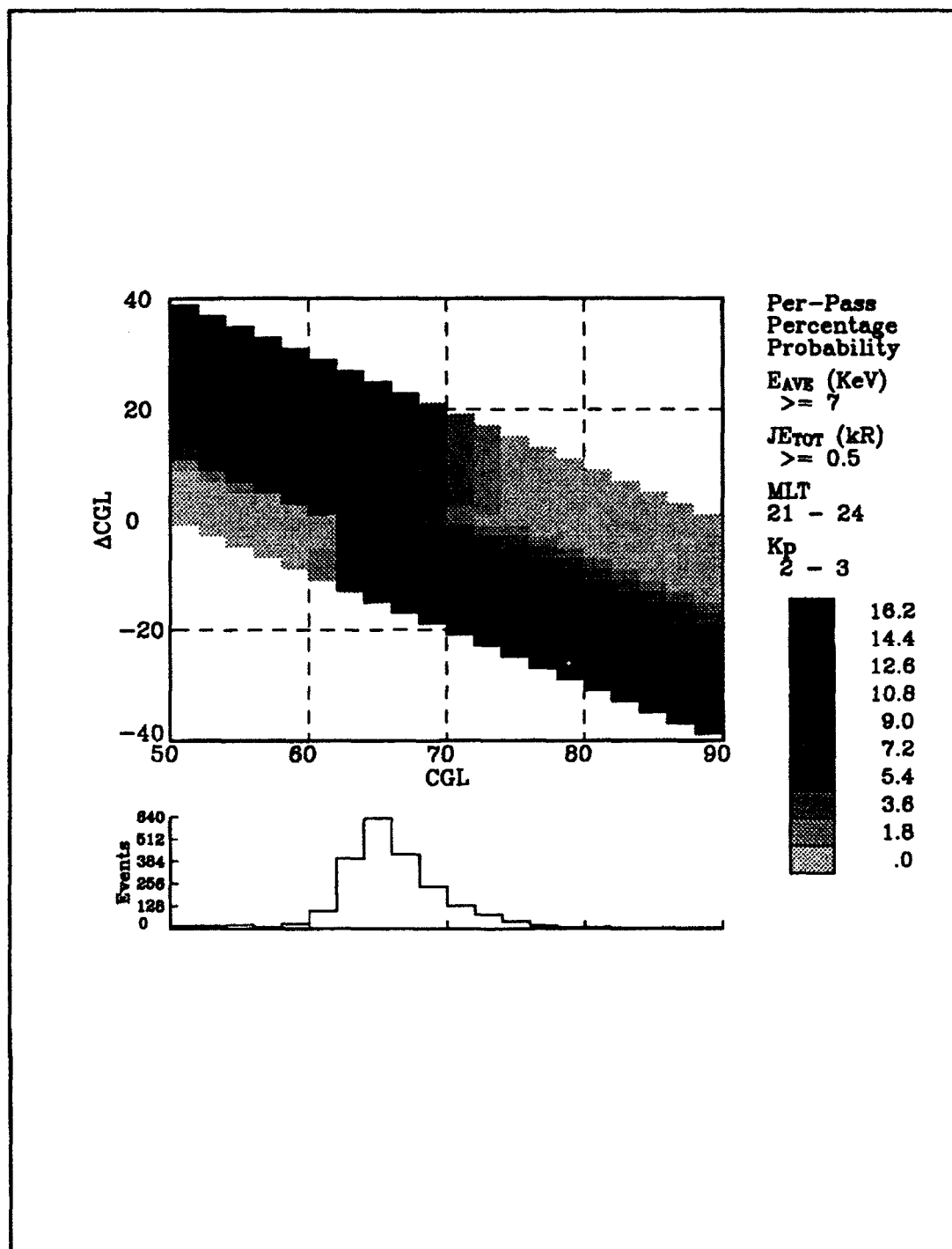


**Figure 111.** Integral probability of occurrence of auroral electron events defined by the parameters ranges shown on the right. The probability is given as a function of the reference latitude (CGL) and the differential latitude ( $\Delta CGL$ ) which takes positive values poleward of CGL and negative values otherwise. The bottom panel shows the total count for this event as a function of geomagnetic location. The maximum probability for  $JE_{tot} \geq 0.5$  kR is 9% and occurs at  $65^\circ$  CGL. By varying  $\Delta CGL$ , an integral probability as high as 16.2% can be achieved.

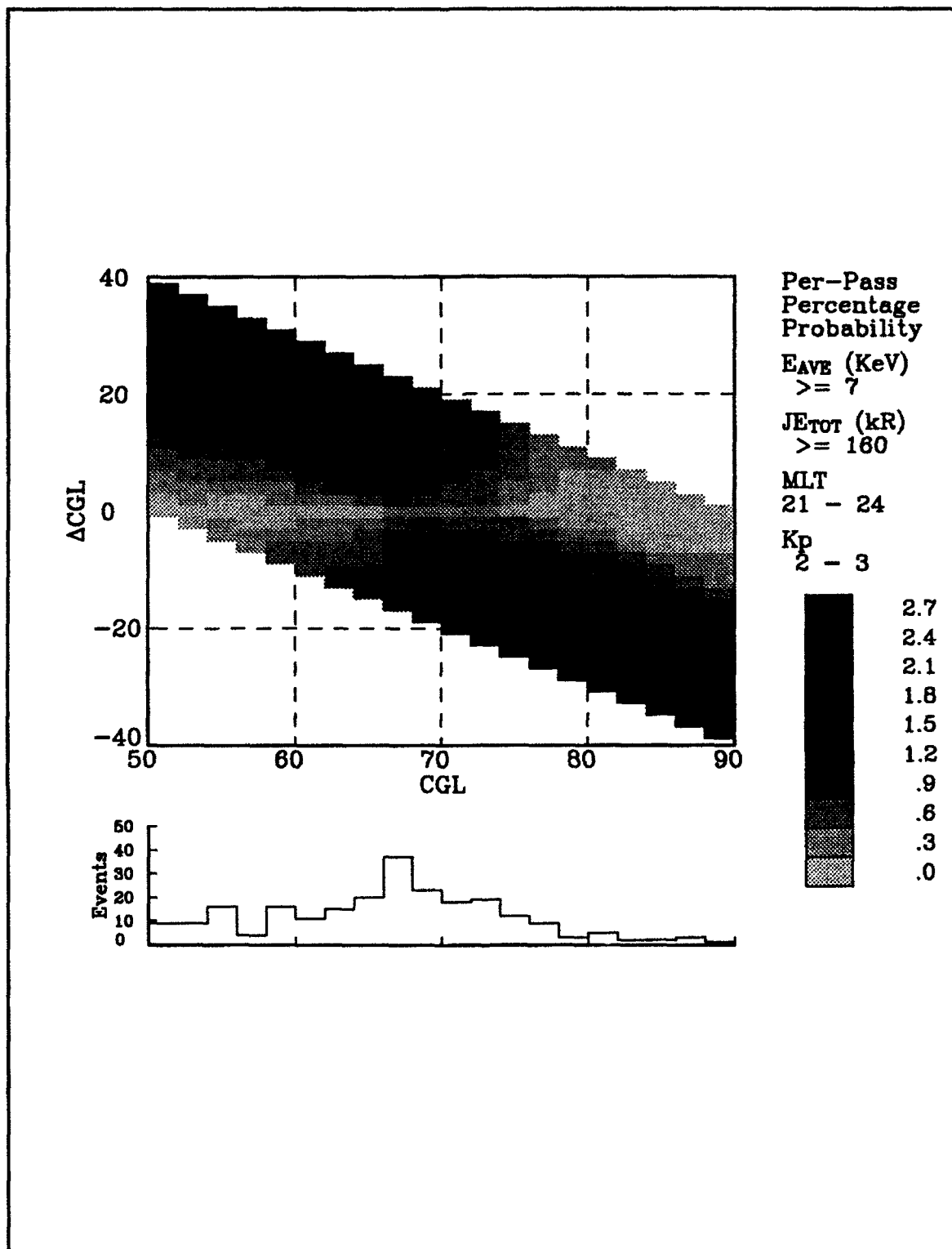


**Figure 112.** Integral probability of occurrence of same auroral electron events as in Figure 111 except that  $JE_{tot} \geq 160$  kR. The maximum probability drops to about 0.3% and occurs at  $67^\circ$  CGL. By varying  $\Delta CGL$ , an integral probability of about 2.7% can be achieved.

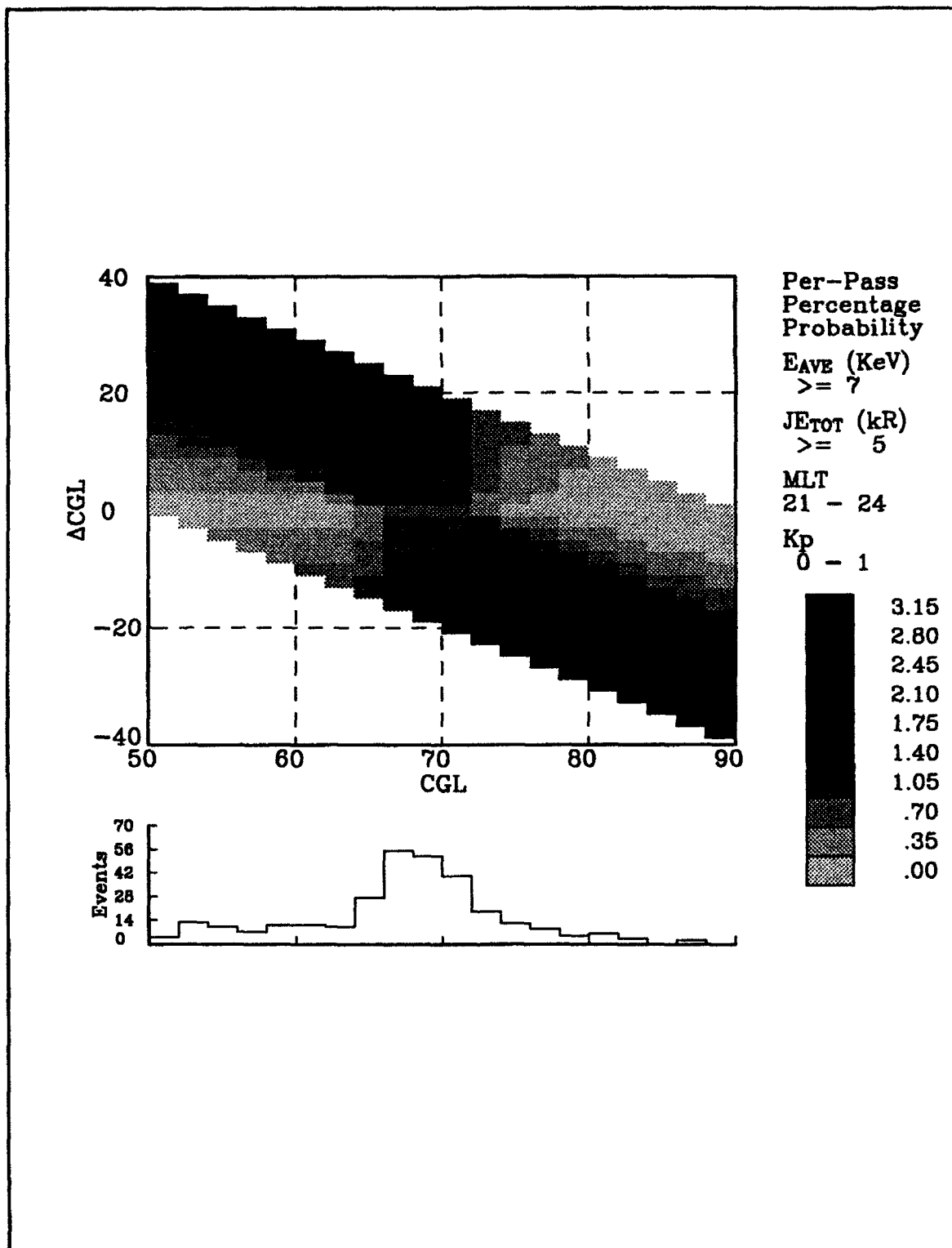


**Figure 113.** Integral probability of occurrence of auroral electron events defined by the parameter ranges shown on the right of the plot. The maximum probability for a low  $K_p$  ( $0_0$  to  $1_+$ ) of 0.7% occurs at  $67^\circ$  CGL and by varying  $\Delta CGL$  the maximum probability can be as much as 3.15%.

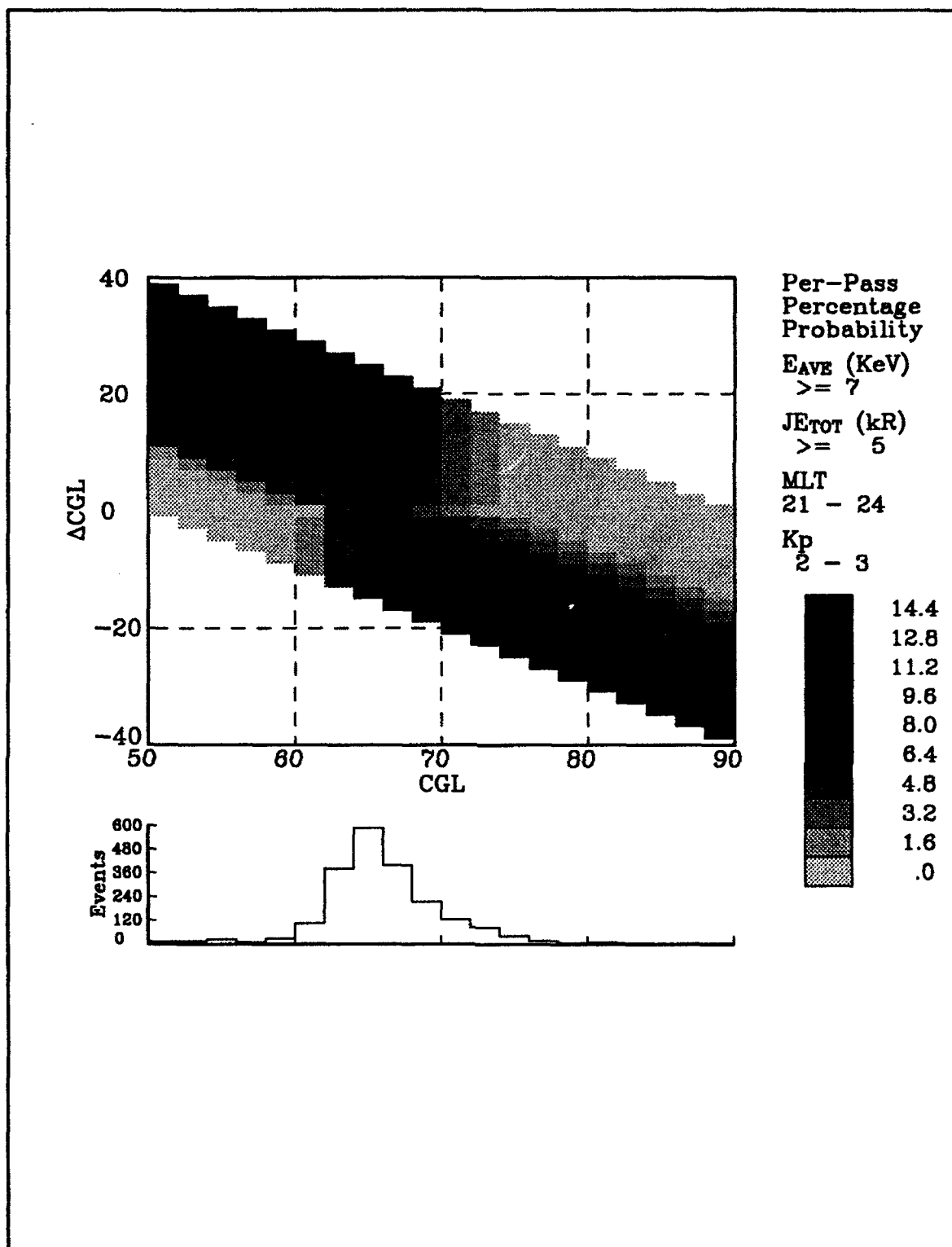


**Figure 114.** Integral probability of occurrence of auroral electron events as defined in Figure 113 for a moderate  $K_p$  level (2- to 3+). The maximum probability of 8% occurs at 65° CGL and by varying  $\Delta CGL$  the maximum probability can be as much as 14.4%.

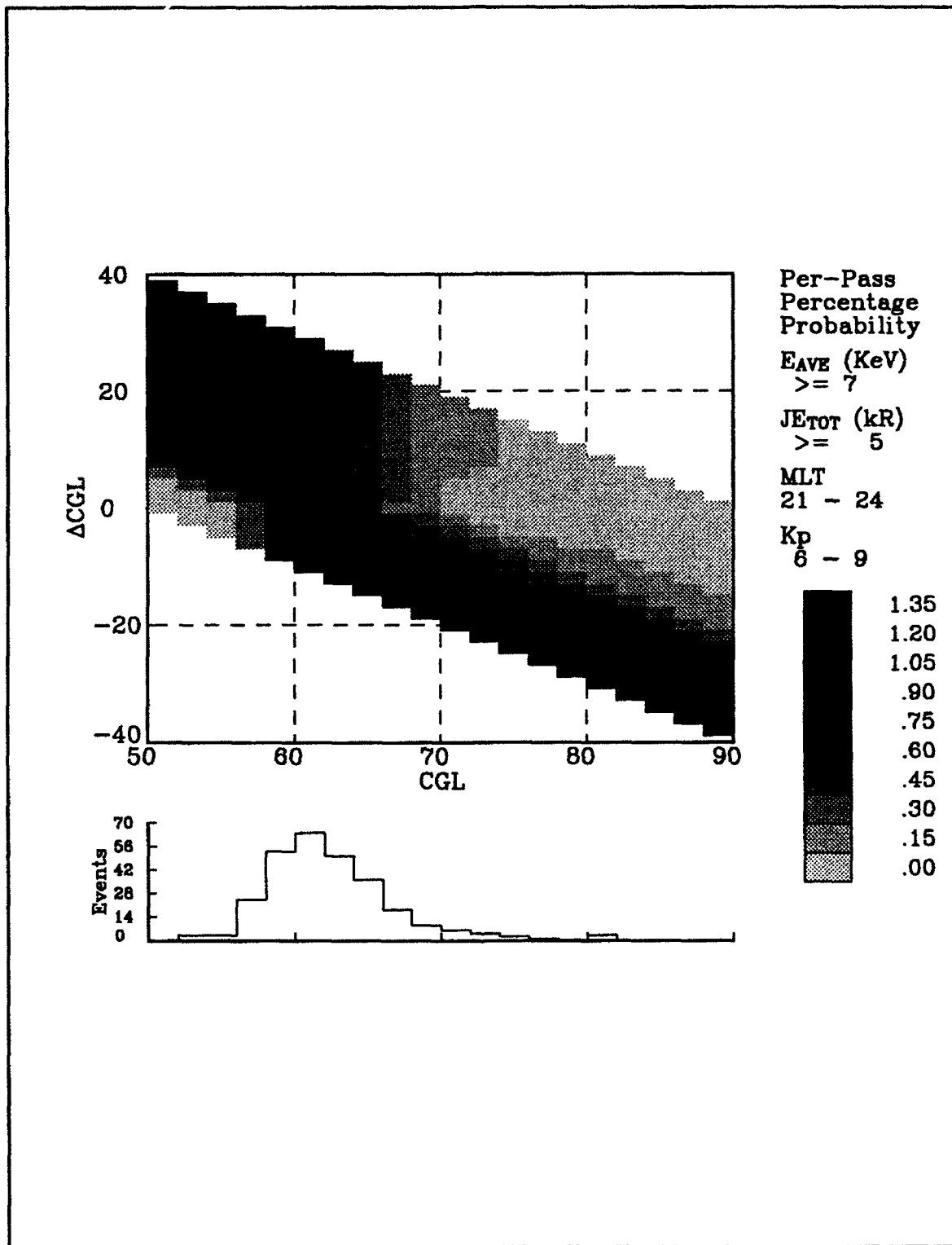


**Figure 115.** Integral probability of occurrence of auroral electron events as defined in Figure 113 but for a disturbed  $K_p$  level (6- to 9<sub>o</sub>). The maximum probability drops to 0.75% at 61° CGL and by varying  $\Delta CGL$  a maximum probability of 1.5% can be achieved.



deviations. Assuming stationarity in Kp and the auroral events, the time average is used, instead of ensemble average, in estimating these quantities.

The correlation coefficient is about 0.97 for events with  $JE_{tot}$  greater than or equal to 2 kR (Figure 116) and 6 kR, and drops to about 0.89 for  $JE_{tot} \geq 20$  kR. A correlation coefficient of 0.7 to 1.0 shows that the two time series are highly dependent. Hence, we can assert that the geomagnetic activity, as represented by the Kp index, and the auroral activity, as measured by the precipitating electron events, are highly correlated indeed.

The observation of enhanced Kp is generally indicative of an increased number of bright arcs. The increase in the auroral activity of precipitating electrons is significant for only a limited time period. During this time period, a high correlation between enhanced Kp and the number of bright arcs can be achieved. The waiting time to increase the chance of observing bright auroral arcs after enhanced Kp values are observed should be between 3 to 6 hours. Figure 120 shows a sample plot where the persistence of  $K_p$  values exceeding 4.0 lasted for at least 3 hours. It also shows an increase in the number of events from about the mean value of 63 to 97 in approximately 15 hours. At the same time,  $K_p$  has increased by 2.0. In general, the substantial increase in the number of observations of intense events as a result of enhanced Kp lingers a maximum of 36 to 48 hours. After this time period, this number drops to the average number of random observations. In conclusion, the nearer the observation can be made to the time of elevated Kp, the better the chances for observing arcs.

This study also shows that increasing the persistence time of high Kp values above a certain threshold does not improve the likelihood of occurrence of intense auroral events. That is, the persistence or lingering of the enhanced geomagnetic activity (as seen in Kp values) does not mean that the probability of observing bright arcs is increased.

Future studies that can provide additional understanding of the auroral activity events can be readily accomplished using the existing data base. Two studies can be implemented using the present data base, which would certainly reveal important features in the electron auroral events that the present study did not cover.

One study would be a superposed epoch analysis on the number of electron events, as a function of specified thresholds of the number of events, and how long they persist above the threshold values. This differs from the present study, in which the epochs are obtained based on the Kp threshold values and their persistence duration above these thresholds.

Another study would be a superposed epoch analysis on the probability of occurrence of electron events as a function of specified thresholds of the number of events and how long they persist above the threshold values. For each hemispheric pass, the occurrence of an event will be indicated by 1, and no occurrence by 0. This study would then yield an averaged probability distribution of occurrence of events around the zero epoch. A probability distribution of the auroral electron activity as a function of time can be a valuable tool in estimating the persistence of auroral events.

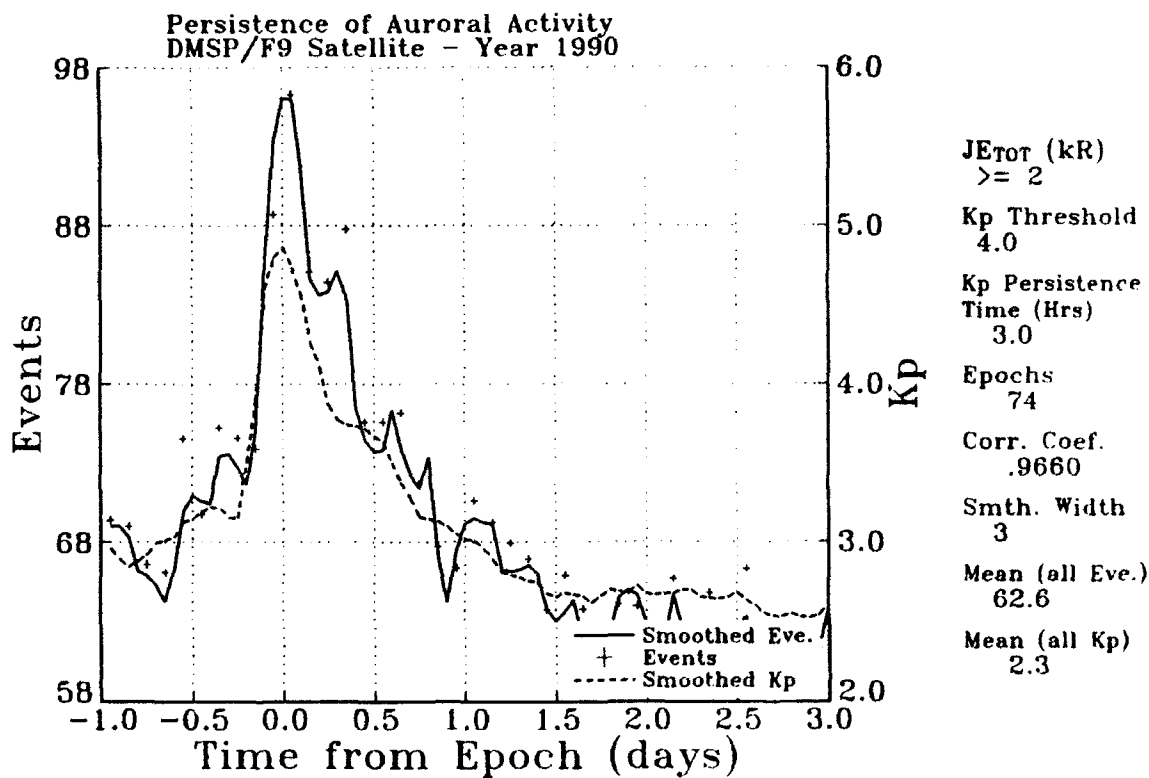


**Figure 116.** Superposed epochs of 4-day Kp (dashed line) and auroral events per hemispheric pass (solid line) sampled at 1.2 hours. The auroral events are given by an energy flux greater than 2 kR. The solid curve is a 3-point smoothing of the electron events shown in plus signs (+). There were 74 cases where the Kp threshold of 4.0 is satisfied for at least 3.0 hours.

## 6.2 FUNCTIONAL REPRESENTATION OF PATTERNS OF AVERAGE AURORAL ION PRECIPITATION

### 6.2.1 Introduction

Studies of the average pattern of high-latitude electron and ion precipitation as a function of geomagnetic activity have used DMSP data to generate maps of average energy and number flux. These maps provide important information on auroral precipitation, but they are somewhat inconvenient for use in modeling, since each map contains some 1440 discrete values at each activity level. It is cumbersome to include such large arrays of values in numerical models. In the past, to aid in the application of the results, we have fit the maps of electron precipitation to simple functional forms [Hardy, *et al.*, 1987]. In the present work [Hardy, *et al.*, 1991], these models are extended to include ion number and energy flux.

### 6.2.2 The Statistical Model

The statistical data base that was the basis for these fits was created from SSJ/4 particle spectrometers flown on the DMSP F6 and F7 satellites. These determined electron and ion spectra once per second, over 20 channels from 30 eV to 30 keV. The data base divided the high-latitude region into a series of spatial bins in corrected geomagnetic latitude and magnetic local time with 48 half-hour divisions in MLT, and 30 divisions between 50° and 90° latitude, each 2° wide. The integral number flux and integral energy flux were averaged in each spatial element by integrating over the average spectrum in this particular element.

Typical meridional cuts of the integral energy and number flux show that the latitudinal variation is smooth and regular, and that it is slowly varying in MLT with a drop-off for values at latitude above and below the peak. The slopes above and below the peak are different, making these good candidates for fitting to the Epstein transition functions.

### 6.2.3 Fitting Procedures

The original electron model employed a single Epstein function spanning the latitude range. For the ions, the single function approach proved to be less well suited, and good results were obtained by using a modified function with two break points. These had the form

$$e(h) = r_0 + S_0[h - h_0] + [S_1 S_0] \ln\{[1 + e^{h-h_0}]/2\} \\ + [S_2 - S_1] \ln\{[1 + e^{h-h_0}]/[1 + e^{h-h_1}]\} \quad (96)$$

where

$r_0$	is the value at breakpoint 1;
$h_0$	is the latitude at breakpoint 1;
$h_1$	is the latitude at breakpoint 2;
$S_0$	is the slope for $h < h_0$ ;
$S_1$	is the slope for $h_0 < h < h_1$ ; and
$S_2$	is the slope for $h > h_1$ .

Using this definition, the model is specified at each MLT by the six parameters above. It is more convenient for calculations, however, to specify a value  $r_1$ , representing the value of the function at  $h_1$ . This is used to replace  $S_1$  in the formulation through

$$S_1 = [r_1 - r_0 - S_0(h_1 - h_0) + S_0 b_1 - s_2 b_2] / (b_1 - b_2) \quad (97)$$

$$b_1 = \ln\{[1 + e^{h_1 - h_0}]/2\} \quad (98)$$

$$b_2 = \ln\{2/[1 + e^{h_0 - h_1}]\} \quad (99)$$

Using the functional forms, the altitude and MLT dependence of the fluxes at each  $K_p$  division were determined as follows. First, for each MLT sector, two breakpoint latitudes  $h_0$  and  $h_1$  were selected, often referring to the preceding MLT sector results to ensure continuity in the MLT variation of the coefficients. The values of  $r_0$  and  $r_1$  were obtained from the data, and least squares fits were used to calculate  $S_0$  and  $S_2$ . The slopes were determined only for those points on either side of the maximum that appeared to be above the background level. This background level was also incorporated into the model. The breakpoint latitudes were adjusted at each MLT to obtain the best possible fits to the peak values of the fluxes. When this had been done for all 48 MLT divisions of a given  $K_p$  level, the 48 values of each of the six coefficients were fit to the function

$$a(T) = C_0^a + \sum_{n=1,5} C_n^a \cos \frac{n\pi T}{12} + S_n^a \sin \frac{n\pi T}{12} \quad (100)$$

where  $a(T)$  is one of the six parameters, and  $T$  is the magnetic local time in hours.

Following this, the coefficients regenerated from Eq. (99) were examined again. In several cases, it was necessary to revise these regenerated coefficients and redo the Fourier fit in order to preserve the quality of the fits at individual MLT values in the regenerated model. This iterative technique was necessitated, in part, by the fact that the latitudinal profiles were fit quite adequately at some MLT by a single breakpoint, leaving some ambiguity as to the choice of the second breakpoint.

#### 6.2.4 Results

These procedures resulted in a continuous model of good quality which provided for smoothing of the original data as well. Figure 117 compares contours of constant flux in the raw data and the regenerated model for number flux at  $K_p$  of 3. Results for other values are comparable to these. In all cases, the functional fit closely reproduced the original statistical model, tending to smooth the model yet reproducing the major features in detail. The quality of the fit was uniform over latitude except for a slight tendency for the fit to deviate from the data at latitudes well above and below the peak. To quantify the quality of the fit, we calculated the distribution of differences between the fit and the original data for each  $K_p$  map. The fits were approximately Gaussian, with the FWHM being  $0.24 (\pm 12\%)$ .

In order to provide a model cutoff at low and high latitudes, the data was examined in a different way. To determine the limiting values, the data well poleward and equatorward of the central precipitation region were examined separately. For each  $K_p$  separation for each of these regions, the residual rms

ION NUMBER FLUX  $K_p=3$

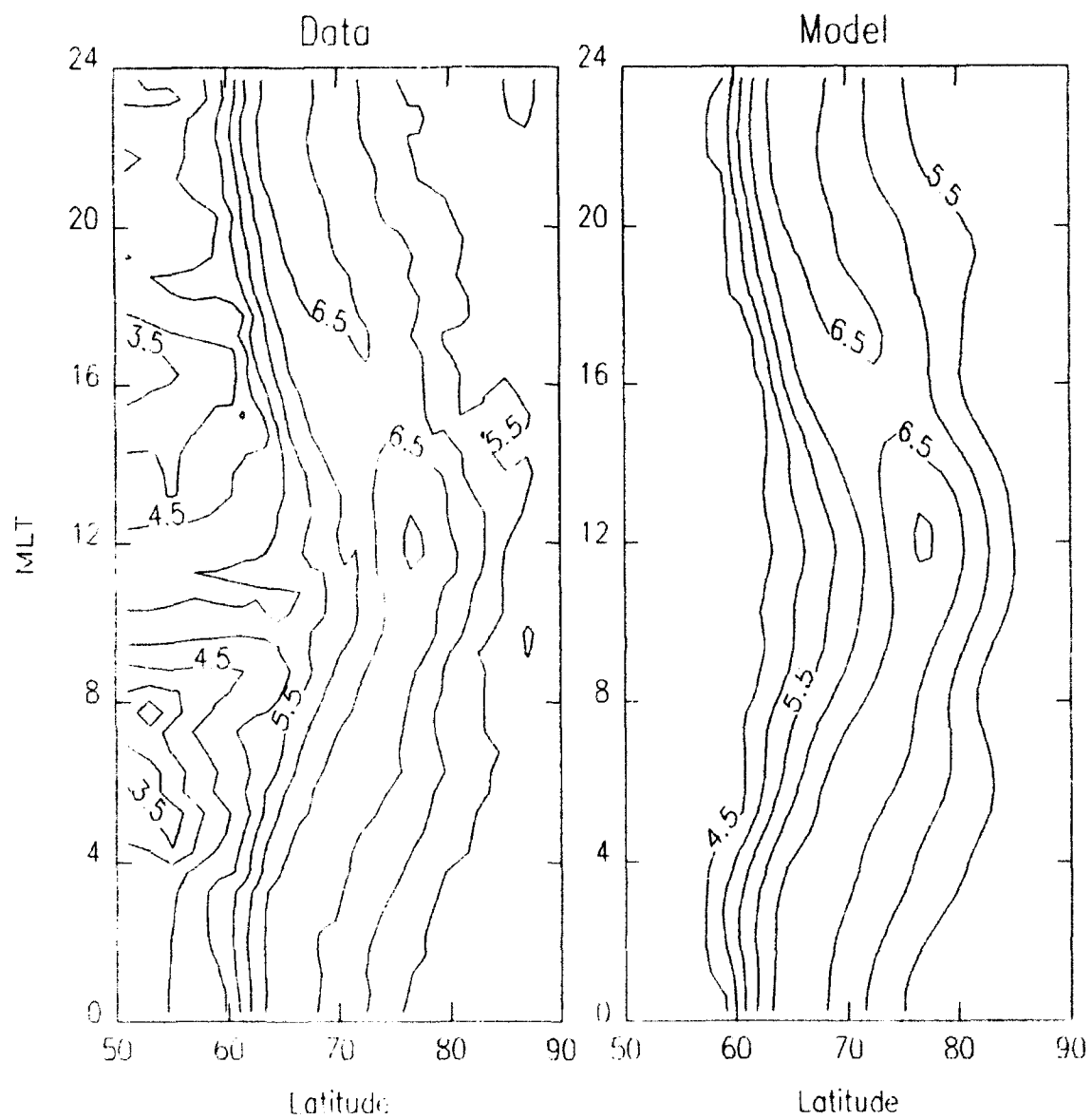


**Figure 117.** Sample contour plot of raw ion data (left) and model (right) for  $K_p=3$ .

deviation was calculated between the data of the statistical model and a specified constant level. This variation in the residual rms value was then determined as a function of the cutoff level. For both integral number and energy flux, and for all levels of  $K_p$ , the variation in the residual rms value with cutoff displayed a clear minimum. This minimum was chosen as the best cutoff for each  $K_p$ . The poleward limiting values,  $L_p$ , displayed no significant variation with  $K_p$  for either flux. They were thus chosen by averaging, giving 1.41(5) keV/cm<sup>2</sup>-s-sr for energy flux, and 6.31(5) ions/cm<sup>2</sup>-s-sr for number flux. The equatorward limiting values were well represented by

$$\begin{aligned} I_e(\text{number flux}) &= 8.32 \times 10^3 \times 10^{0.157 K_p} \\ I_e(\text{energy flux}) &= 4.17 \times 10^2 \times 10^{0.126 K_p} \end{aligned} \quad (101)$$

In using the model, the Epstein function value is used if it is greater than these limits.

The model provides a representation of the statistical auroral ion precipitation and offers a simple means for reconstructing the hemispheric precipitation pattern, without storing the large data matrices of the original data. A software subroutine that does the reconstruction was also written and provided for distribution.

### 6.3 NEURAL NETWORKS

Neural networks are multi-layered networks, where a layer consists of a set of inputs and a set of outputs. In addition, the inputs and outputs are connected by a set of weights, which are summed and then fed through an activation or transfer function before reaching the outputs.

The type of network commonly used is the layered feed-forward neural network, which is trained by error back-propagation [Muller and Reinhardt, 1990]. The back-propagation neural networks have been applied to a number of time series predictions of solar-terrestrial effects and energetic particle flux [Lundstedt, 1991; Koons and Gorney, 1990]. During the training stage of a back-propagation network, the weights in all the connections in both layers are adjusted by applying the delta rule. Activation functions introduce the nonlinearity in the input-output relationship. The selection of the transfer function can then be critical in the performance of a neural network. The transfer function that has commonly been used for most science applications is either the sigmoid (Fermi function) or the hyperbolic tangent (TanH) function. One of these functions can be better suited than the other in a given application.

In designing a neural network, the choice of the number of processing elements (PEs) in the hidden layer can be very critical. Generally, a rule of thumb is that the number of PEs is essentially half the total number of inputs and outputs. Another rule of thumb to keep in mind when deciding on the number of hidden PEs, is that the noisier the data (that is, data with very small-scale variations), the more PEs may be required. We must caution that the number of cases used to train the network is also critical. The more cases that are used to train the network, the better the network will be able to generalize.

To complete the training stage, a network must satisfy the convergence criterion. The root mean square (RMS) of the sum of the errors between the target and the estimated value is calculated after a certain number of cycles of records is presented to the network. One cycle represents all of the available records in the training file. The number of cycles used in the computation of the RMS value is called the epoch,

and is measured in cycles. It is believed that the larger the epoch, the better the network generalizes. The convergence is achieved when the RMS value is less than or equal to a minimum specified value.

The neural network techniques were employed in the prediction and estimation of geomagnetic indices [Bounar, *et al.*, 1991, Rubin, *et al.*, 1992]. We built a neural network to predict the midnight equatorward boundary (MEB) of the auroral oval. We found that the one-hour ahead MEB prediction of the neural network was substantially better than the commonly used persistence estimate or a linear predictor. In a linear network, this problem is essentially an autoregressive time series based on previous samples. Traditionally, time series forecasting has been done using the Box-Jenkins methodology. Some recent studies compared this method against neural networks [Tang, *et al.*, 1991] and found that, for a time series with long memory, both methods produced comparable results, but for series with short memory, neural networks outperformed the Box-Jenkins model. Moreover, neural networks are robust, provide good long-term forecasting, and are parsimonious in their data requirements. Neural networks represent a promising alternative to conventional methods of forecasting.

The one-hour ahead neural network to predict MEB is a feedforward network consisting of four PEs in the input layer, four PEs in the hidden layer, and one PE in the output layer. The inputs are the previous hourly MEB samples. The back-propagation method is employed in the training stage on MEB hourly data for the year 1983. One-hour MEB neural network predictions are compared to results obtained using a linear prediction estimate, as well as a persistence estimate. The MEB data for the training and testing must satisfy a threshold value of the boundary location. The neural network prediction outperforms both the persistence estimate and the linear predictor. The estimate performance was gauged using the prediction efficiency, which is defined as one minus the ratio of the error variance to the MEB variance. The error variance is the sample variance of the error between actual MEB samples and their estimates. We found that the prediction estimate was about 40% for the neural network, 26% for the persistence estimate, and 19% for the linear predictor.

## 6.4 REFERENCES

- Bounar, K. H., and D. A. Hardy, "Integral Probability of Auroral Electron Flux Events from SSJ/4 DMSP F9 Electron Measurements", PL-TR-92-2091, May 1992.
- Bounar, K. H., and W. J. McNeil, "Persistence of Auroral Electron Flux Events from DMSP/F9 Electron Measurements", PL-TR-92-2019, 31 Jan 1992, ADA251241.
- Bounar, K. H., A. G. Rubin and D. A. Hardy, "Neural Network Prediction of the Midnight Equatorward Auroral Boundary", *AGU Spring Meeting*, May 1991.
- Brautigam, D. H., M. S. Gussenhoven, and D. A. Hardy, "A Statistical Study on the Effects of IMF  $B_z$  and Solar Wind Speed on Auroral Ion and Electron Precipitation", *J. Geophys. Res.*, 96, 5525, 1991.
- Hardy, D. A., W. J. McNeil, M. S. Gussenhoven and D. Brautigam, "A Statistical Model of Auroral Ion Precipitation 2. Functional Representation of the Average Patterns", *J. Geophys. Res.*, 96, 5539, 1991.
- Hardy, D. A., M. S. Gussenhoven, and D. Brautigam, "A Statistical Model of Auroral Ion Precipitation", *J. Geophys. Res.*, 94, 370, 1989.
- Hardy, D. A., M. S. Gussenhoven, R. Raistrick and W. J. McNeil, "Statistical and Functional Representations of the Pattern of Auroral Energy Flux, Number Flux and Conductivity", *J. Geophys. Res.*, 92, 12,275, 1987.
- Hardy, D. A., M. S. Gussenhoven, and E. Holeman, "A Statistical Model of Auroral Electron Precipitation", *J. Geophys. Res.*, 90, 4229, 1985.
- Koons, H. C., and D. J. Gorney, "A Neural Network Model of the Relativistic Electron Flux at Geosynchronous Orbit", *J. Geophys. Res.* 86, 9961, 1991.
- Lundstedt, H., "Neural Networks and Predictions of Solar-terrestrial Effects", *Planet. Space Sci.* 40, 457, 1992.
- McNeil, W. J., D. A. Hardy, and R. R. O'Neil, *Private Communication*, September 1984.
- McNeil, W. J., and D. A. Hardy, *Private Communication*, October 1985.
- Muller, B., and J. Reinhardt, *Neural Networks, An Introduction*, Springer Verlag, 1990.
- Nagai, T., "Space Weather Forecast: Prediction of Relativistic Electron Intensity at Synchronous Orbit, *Geophys. Res. Lett.* 15, 425, 1988.



Rubin, A. G., D. A. Hardy, and K. H. Bounar, "Neural Network Prediction of the Midnight Equatorward Auroral Oval Boundary", *Solar-Terrestrial Prediction Workshop*, Ottawa, Canada, 18-22 May 1992.

Tang, Z., C. S. De Almeida, P. A. Fishwick, "Time Series Forecasting Using Neural Networks vs. Box-Jenkins Methodology", *Simulation* 57:5, 303, 1991.

## 7. EPHEMERIS

### 7.1 LOKANGL

#### 7.1.1 STS53 Mission Support with Ephemeris and Graphics Software

As part of the detailed satellite tracking information provided by LOKANGL output tables, the solar elevation angles can be used to extract reports on when and where the portions of shuttle mission will be spent in darkness. Defining solar depression angles to be the same as the negative-valued solar elevation angles, a set of specialized tables and accompanying plots can be used to provide darkness transition reports as functions of orbital number. Two kinds of plots are given to depict the periods of darkness for a given mission.

One type is the orbital track projection overlaid on a pair of solar depression terminators. These particular plots portray a selected range of stepped orbits where the sun elevation angle is less than 2 degrees. The indicated orbits are usually chosen to represent the range of a week-long mission; typically, the range steps from orbit number 1 to 141 by 10. Superimposed upon those plots for visual clarification is the shaded region depicting the sun depression angle spread of [0,-10] degrees.

The second kind of plot is the orbital darkness-duration time chart. These charts illustrate the darkness transit time in minutes for each individual orbit. The code has interpolated in time the cross-over points at zero-degree solar depression angle to determine a more precise duration period.

The ephemeris tables were derived from the LOKANGL output files, and the post-processing graphics of the same files was accomplished using a read-data program with built-in HPGL laserprinter driver and Microsoft FORTRAN 5.1 DOS screen graphics interface.

A sample set of plots is given in Figure 118. These plots are based upon a study requested by the Glow Experiment at PL. The group, from the summer of 1992 until the actual launch of space shuttle STS53, have requested for and received ephemeris output tables and accompanying plots corresponding to different launch delay cases. The sample plots have provided the predicted darkness-duration information based upon the actual shuttle launch on December 2, 1992, at 13:24 UT.

#### 7.1.2 Viewing Diagrams for Low Earth Satellites (Hussey Charts)

LOKANGL output provides detailed satellite tracking information over an extended period at regular time intervals, such as one minute steps. A convenient means of viewing the data in compact format is implemented in routine VIEWSAT (Figure 119) which was translated from Basic to Fortran, adapted to employ a Fortran interface to Scientific Endeavors package GraphiC, and also modified to improve presentation.

All opportunities for viewing a low Earth satellite during a calendar month or an arbitrary 30 day interval are presented on a single sheet plot. The day of the month and the day number for the year are displayed on the left and right sides of the plot, respectively. Time of the day (UT) is displayed on the top and bottom of the plot. Each viewable pass is displayed as a circle, centered in time at the maximum elevation. The time in minutes at which maximum elevation occurs is printed within the circle. Dots or crosses within the circle depict the predicted azimuth and elevation on a uniform time step basis, such as every minute on each pass. Elevations less than a user specified value are dispensed with.

STS53 LAUNCH AT 12/02/92 13:24 UT -- ORBITS 91 TO 141  
WITH 0-10 DEG. SOLAR DEPRESSION TERMINATORS

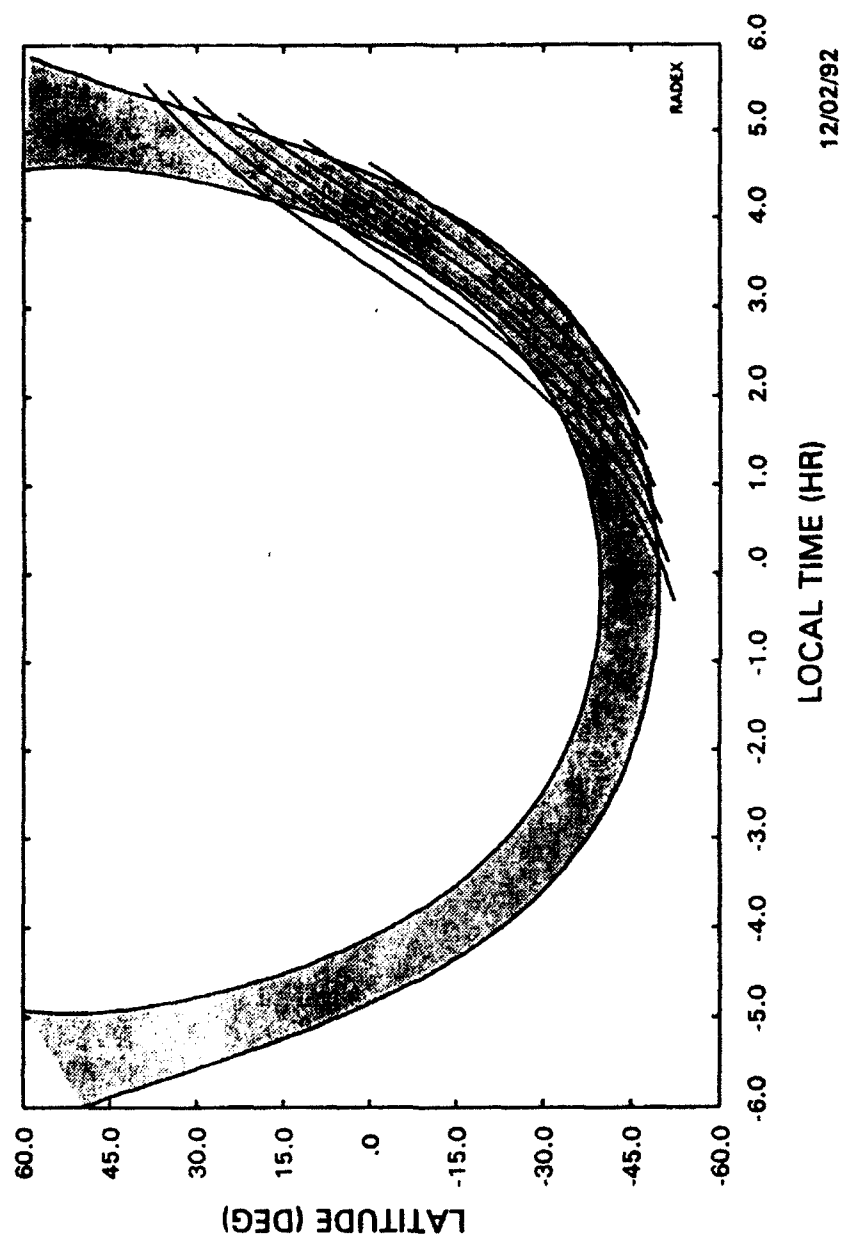


Figure 118. Sample set of plots.

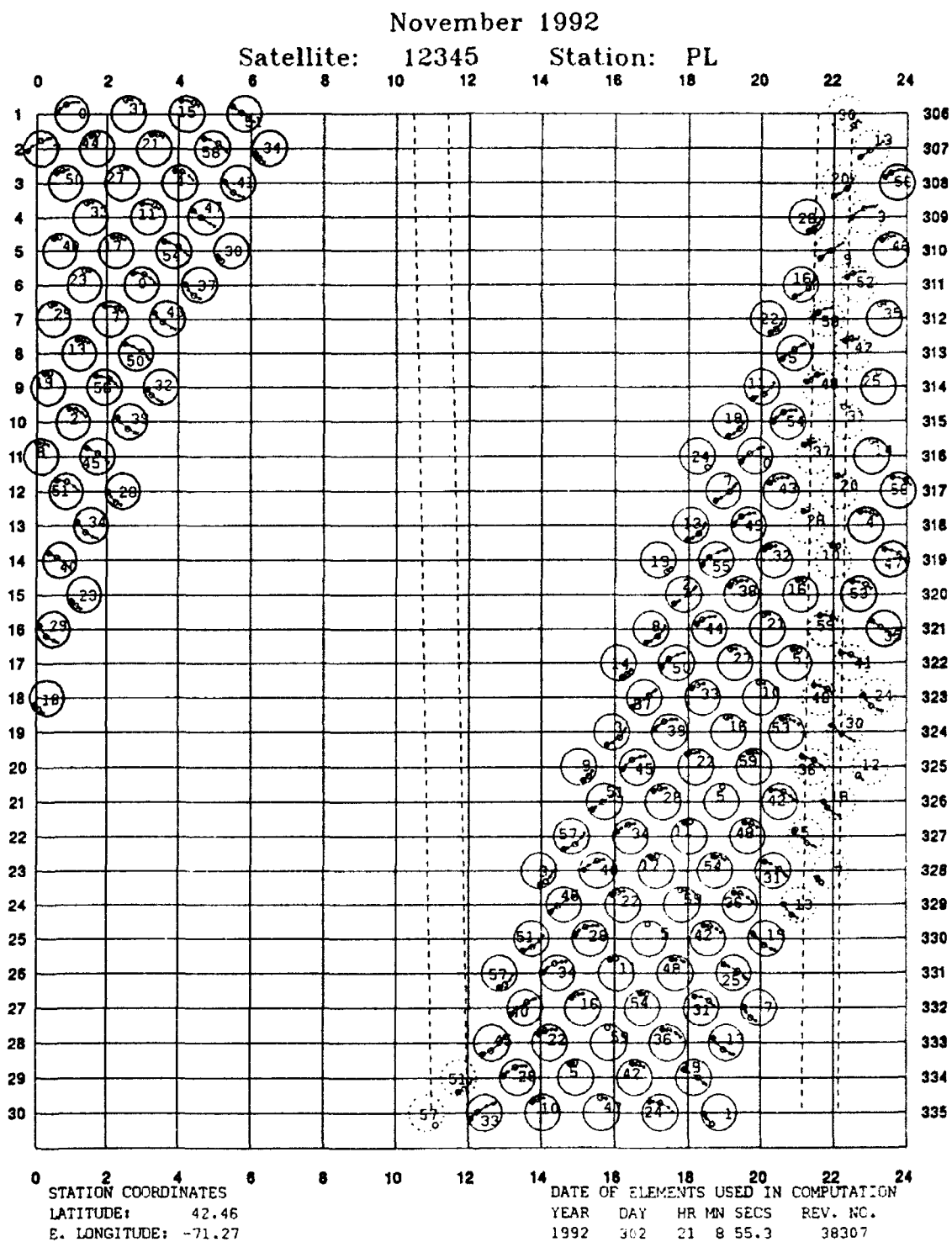


Figure 119. Satellite viewing (Hussey) charts.

The observer is considered to be at the center of the circle, with the circumference at the horizon ( $0^\circ$  elevation). Elevations from zero to directly overhead can be deduced. Azimuth is also implicit, with North at the top and East to the right. A large dot near the horizon shows where the observations would commence, and therefore also indicates the direction of motion. The position of maximum elevation is indicated by a large open dot.

Solar conditions on the ground and on the satellite appear as follows:

Two pairs of dashed lines show the daily ground sunrise and sunset times at the horizon and at an elevation of  $-10^\circ$ .

Dark circles show the cases when the satellite is in darkness at maximum elevation.

Light circles show when the observer and the satellite are in sunlight at maximum elevation.

Dashed circles show when the observer is in darkness and the satellite is illuminated by the sun at maximum elevation. These are the best conditions for visual sighting of the satellite. If the satellite is in Earth's shadow during part of the pass, the corresponding points are marked with an "X".

## 7.2 COORDINATE SYSTEMS AND TRANSFORMATIONS

### 7.2.1 Coordinate Systems for Space and Geophysical Applications

Many different coordinate systems are used in the analysis, processing, and display of data acquired in aerospace experiments, because physical processes may be better understood if the experimental data are more ordered, or if calculations are more easily performed, in one particular coordinate system.

An extensive repertoire of coordinate systems, particularly astronomical, geomagnetic, and spacecraft ephemeris/attitude related systems, are pertinent to the research activities involved in this report. A report was written [Bhavnani and Vancour, 1991] which considerably edited a previous report [Cottrell and McInerney, 1985]. The latter described many of the coordinate systems which had been or could have been used. In the report [Bhavnani and Vancour, 1991], the descriptions, glossary, and bibliography were extended. The basic categorization method was used to eliminate extraneous coordinate systems; the diagram presentations were improved; coordinate transformations were defined more consistent with mathematical notation, and, epochs and coefficients were brought up to date 1990.0. Terms and symbols that are prevalent and subsequently used were defined.

Some of the individual coordinate systems have several names associated with them. In the above-mentioned report, each named system is described separately and cross-referenced to other systems that have the same characteristics. Comparisons of the various rectangular coordinate systems are shown in the report and are described as either Earth-fixed, inertial, quasi-inertial, magnetic, or in a category of "other". There are four major fields that categorizes them, viz, astronomical, orbital, geomagnetic, and local observation. Most, although not all, of the coordinate systems have both rectangular and spherical representations. Some of the systems have adjunctive representations in addition to rectangular and spherical. Each system is described in terms of its origin, orientation, characteristics, and applications. Unless otherwise indicated, coordinate systems are true-of-date. Due to a secular variation of Earth's internal magnetic field, the geomagnetic dipole and, therefore, a primary reference axis for

the geomagnetic coordinate systems, changes with time when referred to an Earth-fixed system. The geographic latitude and longitude of the magnetic poles have been updated to Epoch 1990.0 by propagation of the IGRF85 model.

The report [Bhavnani and Vancour, 1991] describes coordinate system transformations, particularly those from the Earth Centered Inertial system, which is frequently used as the fundamental system associated with raw experimental data, to several of the coordinate systems described. It is shown that other coordinate transformations can always be accomplished through intermediate transformations into ECI coordinates. Subsequently, some angular rotation transformations that are pertinent to attitude determination are discussed.

Reference material is given in the report which discusses the basis of the Geomagnetic Dipole models. The centered dipole model is readily derived from the first order representation of Earth's magnetic field. For space particles up to geosynchronous altitude, the eccentric dipole may provide a superior magnetic reference frame. The dip pole model, of interest only near Earth's surface, is presented for completeness.

#### 7.2.2 Reference Frames - FK4/FK5/J2000

The foundation of the M50 system is set in FK4 stellar catalog. By the early 1970's, it was recognized that a systematic, time dependent error existed in the FK4 (and thus M50) reference frame [Lieske, 1979; Lieske, et al., 1979]. Since this error was embedded in the proper motions of the cataloged stars, a decision was made to assemble a new catalog. The FK5 catalog incorporates a revised set of fundamental constants, including a new value for the precession rate of the earth, and a new model for nutation. A standard epoch based on the FK5 catalog, the mean equator, and the Julian century was adopted for the year 2000 and designated as the J2000 reference frame. These changes were implemented by the Naval Observatory starting in 1984 with the publishing of that year's Astronomical Almanac.

The J2000 system is based on the new standard epoch J2000.0 (JD 2451545.0), and is a significantly more accurate model of a true ECI reference frame than M50. In time, conversion from the old system to the new will result in more accurate ephemerides. Perhaps the greatest source of confusion lies in the fact that true-of-date (TOD) position, as derived from M50 information and the 1960 Supplement to the Astronomical Almanac [Wilkins, 1961], is not the same as TOD position as derived from J2000 information and the 1984 Supplement [Seidelmann, et al., 1984]. As described above, the dynamical equinox for each system depends on stellar proper motions tabularized in each catalog. The systematic errors in the FK4 catalog result in systematic errors in TOD positions calculated from the M50 reference frame of approximately 0.085 seconds in right ascension per Julian century.

Concurrent with the development of these more accurate inertial reference frames, the Defense Mapping Agency [DMA, 1987] embarked on a program to establish an updated Earth Centered Fixed (ECF) reference frame. This work required adopting a set of constants related to geodetic and geopotential parameters, and resulted in a highly accurate geographic mapping system called the World Geodetic System 1984 (WGS84). Of particular importance is the value used for the equatorial radius of the Earth, 6378.137 km. This system has been validated by satellite sounding measurements to an accuracy of  $\pm 2$  m. Because the WGS84 system uses the same models for precession, nutation, and sidereal time as the J2000 and FK5 systems, it is possible to convert satellite ephemeris and line of sight vectors into a geographic reference frame with similar accuracy.

While conversion from the M50 to J2000 systems should entail simple multiplication by the appropriate rotation matrix [Smith, *et al.*, 1989; Yallop, *et al.*, 1989; Kaplan, *et al.*, 1989], several different rotation matrices have appeared in print since 1976. It is not clear why these values do not agree, since each of these rotation matrices are presented in an authoritative manner. The potential impact on satellite ephemerides could be on the order of tens of meters for LEO, depending on which matrix values are used. The Julian date of epoch M50 associated with each matrix is slightly different; NASA Johnson uses JED 2433282.423357, JPL uses JED 2433282.42345905, and The Astronomical Almanac uses JED 2433282.423. Tables and equations published in the Almanac are probably designed to use this truncated form.

Reconciliation of the various reference frames is much more difficult for astronomers than for orbital analysts. An example for converting FK4 stellar position and proper motion to FK5 equivalents was first provided on pages B42-B43 of the 1987 Astronomical Almanac. Unfortunately, this method is not of practical use to the analyst.

The M50 software developed to provide TOD conversion of parameters given in the M50 system has been described in a previous report [Pratt, *et al.*, 1988]. It is based on the models for precession and nutation described in the Supplement to the 1961 Astronomical Almanac. The subroutine PRECESS constructs a rotation matrix from the precession model and the subroutine NUTATE constructs a second rotation matrix from the nutation model.

The most important change affecting J2000 conversion is the new value for the precession rate of Earth. While the new constant together with an updated model for precession are expected to give better accuracy over longer periods of time, it greatly complicates conversions between the M50 and J2000 systems. The nutation constant and model have been changed as well. The nutation changes, however, serve primarily to increase the accuracy of the calculations by including more significant figures and a greater number of terms.

The J2000 models for precession and nutation are described in the Supplement to the 1984 Astronomical Almanac, which is found as a separate section at the end of the 1984 Almanac. Since the form of this model is similar to that of the M50 model, the J2000 update has been coded as subroutines NUTAT2 and PRECS2. The arguments to the subroutines have changed to be consistent with the J2000 system. Tests of the new routines indicate that they are able to duplicate the rotation matrix values listed in the Almanac down to the least significant digit (eight significant figures.)

This work originated from an attempt to verify the values given for an M50 to J2000 rotation matrix given in a COPS document. Differences in the sixth significant figure were found during comparisons to Almanac values. Similar differences were found when the Almanac values on p. S37 of the 1984 Supplement were used. Such differences would amount to errors in position vector components on the order of tens of meters for LEO.

Several attempts were made to discover an improved M50 to J2000 conversion matrix. The first was to use TOD rotation matrix values given in the Almanac for each system on overlapping dates. The 1983 Almanac contains an M50 to TOD rotation matrix for JD 2445700.5. The 1984 Almanac contains a J2000 to TOD rotation matrix for the same JD. The product of the first and the transpose of the second results in the desired M50 to J2000 matrix, shown in Table 38.

Using the transpose of these values together with the M50 to TOD software allows one to calculate J2000 to TOD rotation matrices. A test case for a selected date in 1990 gave differences in the seventh significant figure compared to Almanac values. This was a substantial improvement relative to the results using COPS or Almanac values as described in the preceding paragraph.

A second attempt at improvement was made using the PRECESS subroutine to construct a precession rotation matrix for epoch J2000.0. This resulted in a rotation matrix accurate to seven significant figures, but judged to be of slightly poorer quality than that just given. A third attempt, using PRECS2 for epoch B1950.0, gave errors in the fifth significant figure.

Such differences become important only where high accuracy is needed; that is, in situations where six or more significant figures are required. In such cases, the systems and values employed by the original software which processed the raw data should be used. If they are not known, the M50 to J2000 rotation matrix published by Lieske, reproduced in Table 39, is recommended.

The question of why the conversion from one system to the other is so difficult remains to be answered. One would think that there is one rotation matrix which will always accomplish such a transformation with high accuracy. Using the M50 and J2000 software in combination allows one to construct rotation matrices for arbitrary overlapping dates. This, in turn, allows one to study the M50 to J2000 rotation matrix over time. These studies, shown in Table 40, indicate that the values of the elements change with time. To further address this problem, a study of the papers cited in the 1984 Supplement was done.

In converting state vectors to the desired reference frame, we can ignore the fact that the M50 system is not truly inertial. The rotational effect is only 0.085 seconds in right ascension per Julian century. This greatly simplifies the conversion process, because position and velocity vectors may be separated and converted to the desired reference frame using 3x3 rotation matrices. The routines PRECESS and NUTATE are used to convert M50 to FK4 TOD coordinates. Routines PRECS2 and NUTAT2 are used to convert J2000 to FK5 TOD coordinates. These routines have tested and accurately reproduce the rotation matrix elements published in the Astronomical Almanac.

Conversion between the FK4 and FK5 TOD systems is accomplished by determining the right ascension of FK4 relative to FK5 according to the formula S17 in the 1984 Supplement:

$$E = 0.035 + 0.085(y-1950)/100 \quad (102)$$

where E is the position of the equinox in seconds of time. A rotation matrix for converting from FK4 to FK5 is calculated by a yaw maneuver by the negative angle E.

This method was tested using CSTC state vectors supplied in M50, J2000, and TOD coordinates for the same satellite at the same epoch. Results are listed in tables on following pages. Original CSTC supplied state vectors are shown in Table 41.

There was excellent agreement between the CSTC TOD values and the CSTC J2000 values converted to TOD (FK5), as shown in Table 42. The maximum difference in position vector components was 0.04 meters. The maximum difference in velocity vector components was  $2 \times 10^{-5}$  m/s.



**TABLE 38. M50 to J2000 Rotation Matrix Calculated from the Astronomical Almanac**

0.999925727	-0.011177002	-0.004858186
0.011176998	0.999937537	-0.000027273
0.004858191	-0.000027028	0.999988200

**TABLE 39. Leiske's M50 to J2000 Rotation Matrix**

0.9999257079523629	-0.0111789381377700	-0.0048590038153592
0.0111789381264276	0.9999375133499888	-0.0000271625947142
0.0048590038414544	-0.0000271579262585	0.9999881946023742

[Lieske, 1979a]

**TABLE 40. Studies of M50 to J2000 Rotation Matrix Over Time**

IYEAR, IMONTH, IDAY, GMT (SEC): 2000,1,1,0.					
R(1,1) =	.999925744	R(1,2) =	-.011176204	R(1,3) =	-.004857854
R(2,1) =	.011176204	R(2,2) =	.999937544	R(2,3) =	-.000027185
R(3,1) =	.004857854	R(3,2) =	-.000027109	R(3,3) =	.999988200
IYEAR, IMONTH, IDAY, GMT (SEC): 1990,1,1,0.					
R(1,1) =	.999925735	R(1,2) =	-.011176882	R(1,3) =	-.004858140
R(2,1) =	.011176881	R(2,2) =	.999937536	R(2,3) =	-.000027229
R(3,1) =	.004858141	R(3,2) =	-.000027072	R(3,3) =	.999988199
IYEAR, IMONTH, IDAY, GMT (SEC): 1980,1,1,0.					
R(1,1) =	.999925730	R(1,2) =	-.011177253	R(1,3) =	-.004858293
R(2,1) =	.011177252	R(2,2) =	.999937532	R(2,3) =	-.000027229
R(3,1) =	.004858294	R(3,2) =	-.000027075	R(3,3) =	.999988198
IYEAR, IMONTH, IDAY, GMT (SEC): 1970,1,1,0.					
R(1,1) =	.999925721	R(1,2) =	-.011177982	R(1,3) =	-.004858603
R(2,1) =	.011177982	R(2,2) =	.999937524	R(2,3) =	-.000027219
R(3,1) =	.004858603	R(3,2) =	-.000027093	R(3,3) =	.999988197
IYEAR, IMONTH, IDAY, GMT (SEC): 1960,1,1,0.					
R(1,1) =	.999925717	R(1,2) =	-.011178246	R(1,3) =	-.004858710
R(2,1) =	.011178246	R(2,2) =	.999937521	R(2,3) =	-.000027203
R(3,1) =	.004858711	R(3,2) =	-.000027111	R(3,3) =	.999988196
IYEAR, IMONTH, IDAY, GMT (SEC): 1950,1,1,0.					
R(1,1) =	.999925708	R(1,2) =	-.011178933	R(1,3) =	-.004859000
R(2,1) =	.011178932	R(2,2) =	.999937513	R(2,3) =	-.000027295
R(3,1) =	.004859001	R(3,2) =	-.000027025	R(3,3) =	.999988195

Our conversion of CSTC M50 values to TOD FK4, listed in Table 43, gave differences of approximately 24 meters compared to the CSTC supplied TOD FK5 values. Proportional differences in velocity vector components exist as well. As expected, these differences are seen in the X and Y components, but not the Z.

When Equation 102 was applied to convert TOD FK4 to TOD FK5 at epoch, differences in position vector components on the order of 2.6 meters still existed. These values are shown in Table 44. Differences could be reduced to smaller values if the conversion was done for epoch 1 January 1984 at 0h, as shown in Table 45. This epoch gave maximum differences in the position vector components of 0.4 meters and  $6 \times 10^{-4}$  m/s the velocity vector components.

At this point, there are two questions which should be answered when PL attempts to work with CSTC state vectors in the J2000 and TOD FK5 systems. One question concerns the number of significant figures which CSTC routinely supplies in its state vectors. The CSTC TOD vectors appear to be zero filled after the seventh significant figure. The second question concerns conversion from FK4 to FK5 on 1 January 1984. That epoch is appropriate when converting proper motions of stars from one catalog to the other, but it is clearly in error when trying to quantify the relationship between the M50 and J2000 equinoxes at some other arbitrary epoch.

Even when orbital elements are supplied as TOD, care must be taken to make the distinction between FK4 and FK5 TOD. These reference frames contain differences identical to those which distinguish the M50 and J2000 systems; although these differences are small, truly accurate ephemerides are not possible unless this information is known. The conversion process is not easy to understand, and there is a danger that it is not applied consistently by different space agencies. Presumably, CSTC works in FK5 TOD, while NASA works in FK4. Although the differences are small, truly accurate ephemerides are not possible unless this information is known. The above discussion highlights the pitfalls inherent in converting between coordinate systems, which have plagued the astronomers as well as the orbital analysts, and our calculations suggest that some conversions may not have been addressed accurately enough by the space agencies. Published inter-agency standards would be welcome.

In conclusion, the user is cautioned not to look for simple answers. Conversion from M50 to TOD is possible with the routines described above, as is conversion from J2000 to TOD. The Almanac cautions against mixing systems, and this advice seems to apply to the TOD systems as well. TOD values calculated from the M50 system should continue to use M50 constants and algorithms. TOD values calculated from the J2000 system should continue to use only those constants and algorithms defined for that system. Failure to work within these constraints will result in continued degradation of data. In cases where high accuracy is not required, the matrix given above will work well. In cases where high accuracy is required and conversion is mandatory, rotation matrices for the epoch of interest should be constructed for each system, then combined as described above. If data must then be converted back to the original system, the inverse transformation for the same epoch can easily be constructed. Such an approach will ensure that data is not inadvertently degraded and that high accuracy is maintained.

**TABLE 41. CSTC Supplied State Vectors, Epoch 22 March 1993 at 14:15:29.13**

M50	POSITION	-.5187013361E+04	-.5086961210E+04	.2180325085E+02
M50	VELOCITY	-.8568459460E+00	.8423424201E+00	-.7315939998E+01
J2000	POSITION	-.5129853430E+04	-.5144642893E+04	-.3256987906E+01
J2000	VELOCITY	-.8306595991E+00	.8329064792E+00	-.7320039286E+01
TOD	POSITION	-.5137261000E+04	-.5137247000E+04	-.6399999722E-02
TOD	VELOCITY	-.8340420000E+00	.8340540000E+00	-.7319524000E+01

**TABLE 42. Rotation Matrix, J2000 to TOD FK5 Using PRECS2 and NUTAT2**

		.999998766	.001440702	.000626146
		-.001440706	.999998962	.000006605
		-.000626136	-.000007507	.999999804
CSTC J2000 state vectors converted to TOD FK5				
FK5	POSITION	-.5137261037E+04	-.5137246963E+04	-.6380346385E-02
FK5	VELOCITY	-.8340420166E+00	.8340540006E+00	-.7319523998E+01

**TABLE 43. Rotation Matrix, M50 to TOD FK4 Using PRECESS and NUTATE**

		.999943646	-.009736295	-.004232047
		.009736326	.999952601	-.000013390
		.004231976	-.000027815	.999991045
CSTC M50 state vectors converted to TOD FK4				
FK4	POSITION	-.5137285167E+04	-.5137222834E+04	-.6767821493E-02
FK4	VELOCITY	-.8340375540E+00	.8340579243E+00	-.7319524064E+01

**TABLE 44. Rotation Matrix, FK4 to FK5 at 14:15:29.13 on 22 MAR 93 Using Equation 102**

		1.000000000	-.000005217	.000000000
		.000005217	1.000000000	.000000000
		.000000000	.000000000	1.000000000
Table 6 state vectors converted to TOD FK5				
FK5	POSITION	-.5137258367E+04	-.5137249635E+04	-.6767821544E-02
FK5	VELOCITY	-.8340419053E+00	.8340535731E+00	-.7319524064E+01

**TABLE 45. Rotation Matrix, FK4 to FK5 at 0h on 1 JAN 84 Using Equation 102**

		1.000000000	-.000004647	.000000000
		.000004647	1.000000000	.000000000
		.000000000	.000000000	1.000000000
Table 6 state vectors converted to TOD FK5				
FK5	POSITION	-.5137261295E+04	-.5137246707E+04	-.6767821493E-02
FK5	VELOCITY	-.8340414298E+00	.8340540485E+00	-.7319524064E+01

### 7.2.3 Quaternions

The Coordinate Systems Conversion Software (CSCS) is a collection of general purpose subroutines and functions which may be used to transform parameters from one coordinate system to another. It is intended for use by persons with a good working knowledge of the coordinate systems and parameters of interest. The routines are low level in the sense that a single call is only a single step in the conversion process. By combining several steps, however, the user will find the CSCS to be a powerful, general purpose tool which is capable of solving a wide variety of problems [*Kendra and Bonito, 1990.*]

The CSCS collection contains routines which fall into five categories: quaternion conversion, rotation matrix construction, attitude manipulation, M50 to Aries true-of-date conversion, and vector manipulation. Some routines may fall entirely within a single category. Others span multiple categories, thus forming a bridge between them. By using such bridges, the user may, for example, convert a quaternion into a rotation matrix, which is then used to manipulate a vector. The following sections describe the routines in the collection and give several example programs to demonstrate their application.

Attitude sequences, quaternions, and rotation matrices are used by the space community to store and transmit coordinate system conversion information. Each method has its own distinct advantages and disadvantages, and the adoption of one method in preference to another takes such considerations into account. In theory, attitude sequences contain all of the conversion information in the form of three rotation angles. They are easy to understand in human terms and translate easily into motions such as turning one's body, looking up, and tilting the head. If the sequence of rotations is not known, however, their meaning is lost. In addition, they must be converted using trigonometric functions before they may be used for vector analysis. Quaternions store the conversion information as four unambiguous numbers. They may be converted to a form suitable for vector analysis somewhat more easily than attitude sequences, since the conversion of a quaternion to a rotation matrix does not require the use of trigonometric functions. Thus, they are favored in situations where speed and machine storage considerations dominate. They are not easy to understand in human terms and cannot be used directly in vector analysis. Rotation matrices consist of a 3x3 array of nine numbers. They can be used directly in vector multiplication, and thus are preferred for data analysis using computing machines. The CSCS is capable of working with data in any of these forms and converting it to any of the other forms to meet the needs of the user.

In selecting a reference ECI coordinate system, the space community has commonly employed two different systems, the M50 and the Aries true-of-date. A particular mission will generally maintain orbital and ephemeris information in one reference system but not the other. The CSCS provides the ability to convert data to the other ECI system for any date and time selected by the user.

Finally, the CSCS contains vector manipulation routines. One routine allows the user to convert vectors from one coordinate system to another. A different routine gives the user the ability to reverse the process, that is, to align an axis with a vector and obtain the associated rotation matrix. With this capability, the CSCS becomes a powerful tool which lets the user construct coordinate systems of interest together with their related inter-conversion.

The Coordinate System Conversion Software described in this document was developed for IBM PC compatible systems using Microsoft FORTRAN. All floating point variables and calculations are double precision to ensure high accuracy. Constants, such as  $\pi$  are defined by the operating environment

whenever possible. ANSI FORTRAN-77 standards were adhered to so that the code may be transported to other environments with a minimum of conversion effort.

Two references were used in the development of the CSCS software. The NASA PATH documentation [Cooper, *et al.*, 1985] was referred to for all routines which use quaternions. Wertz [1986] was referred to for routines which involve attitude conversions and coordinate system rotations. The Appendices of Wertz were especially helpful in this respect. Wertz also discusses quaternions in great detail and relates them to these other areas. NASA and Wertz have defined the order of operations differently, however, and the unwary can quickly fall victim to this unfortunate choice. The NASA definition,  $V' = q V q^*$ , works just as well as that of Wertz,  $V' = q^* V q$ , as long as one does not mix conventions.

In the development of the CSCS quaternion routines, the NASA convention was followed. Much of the material discussed by Wertz is still relevant, but the derivations look quite different in the end. If a Wertz convention quaternion is encountered, it is recommended that the user convert it to its conjugate before proceeding. This may be done with the QTPOSE routine, which will return a quaternion consistent with the NASA convention.

### 7.3 REFERENCES

- Alfano, S., D. Negron, and J. L. Moore, "Rapid Determination of Satellite Visibility Periods", *The Journal of the Astronomical Sciences*, 40, 2, 281-296, 1992.
- Cooper, D. H., K. C. Parker, and J. G. Torian, OPS On-Orbit Postflight Attitude and Trajectory History (PATH) Product Description, JSC-18645, 1985.
- DMA, Supplement of Department of Defense World Geodetic System 1984 Technical Report Part I - Methods, Techniques, and Data Used in WGS 84 Development, Defense Mapping Agency, Washington, 1987.
- Hamilton, W. R., Elements of Quaternions (3<sup>rd</sup> Ed.), Chelsea Publishing, New York, 1969.
- Kaplan, G. H., J. A. Hughes, P. K. Seidelmann, C. A. Smith, and B. D. Yallop, "Mean and Apparent Place Computations in the New IAU System. III. Apparent, Topocentric, and Astronomic Places of Planets and Stars", *The Astronomical Journal*, 97, 4, 1197-1210, 1989.
- Kendra, M. J. and N. A. Bonito, "Coordinate System Conversion Software User's Guide for Attitude, Quaternion, M50 and Related Applications", GL-TR-90-0327, 1990, ADA234455.
- Lieske, J. H., "Precession Matrix Based on IAU (1976) System of Astronomical Constants", *Astronomy and Astrophysics* 73, 282-284, 1979.
- Lieske, J. H., T. Lederle, W. Fricke, and B. Morando, "Expressions for the Precession Quantities Based on IAU (1976) System of Astronomical Constants", *Astronomy and Astrophysics* 58, 1-16, 1979.
- Pratt, M. M., N. A. Bonito, and E. C. Robinson, *Private Communication*, November 1988.
- Seidelmann, P. K. and G. A. Wilkins, (Eds.), The Astronomical Almanac, Washington D.C., 1984.
- Seidelmann, P. K. and G. A. Wilkins, (Eds.), The Astronomical Almanac, Washington D.C., 1987.
- Smith, C. A., G. H. Kaplan, J. A. Hughes, P. K. Seidelmann, B. D. Yallop, and C. Y. Hohenkerk, "Mean and Apparent Place Computations in the New IAU System. I. The Transformation of Astronomic Catalog Systems to the Equinox J2000.0", *The Astronomical Journal*, 97, 1, 265-273, 1989.
- Wertz, J. R., Spacecraft Attitude Determination and Control, Reidel Publishing, Boston, 1986.

Wilkins, G. A. (Ed.), Explanatory Supplement to the Ephemeris, London, 1961.

Yallop, B. D., C. Y. Hohenkerk, C. A. Smith, G. H. Kaplan, J. A. Hughes, and P. K. Seidelmann,  
"Mean and Apparent Place Computations in the New IAU System. II. Transformation of Mean  
Stellar Places from FK4 B1950.0 to FK5 J2000.0 Using Matrices in 6-Space", *The Astronomical  
Journal*, 97, 1, 274-279, 1989.

## 8. SOFTWARE SYSTEMS

### 8.1 AITS AND IBSS SUNRISE AND SUNSET

During in-house testing of AITS and IBSS, it was noted that the sunrise and sunset times differed from those given by both NASA Supertape and PATH tapes. These differences were small, generally on the order of 2-6 seconds. Considerable time and effort was expended in an attempt to identify the causes of these differences. Our solar ephemeris software was checked against the Astronomical Almanac, and was found to be in closer agreement than the PATH tape values were. We also adopted the revised value for the Astronomical Unit, which further increased the solar ephemeris accuracy. The derivations for calculating tangent height above an oblate spheroid were then independently verified, and their conversion to Fortran code checked line by line. Flattening coefficients were checked and updated where appropriate.

Although this process led to improvements in our products, the differences in question were essentially unaffected. The available NASA documentation did not contain sufficient detail for further analysis. In addition, neither the PATH tape nor the Supertape list solar elevation angle. It was decided that since atmospheric effects would alter the effective sunrise and sunset times by over 20 seconds, expending greater effort to resolve a 4 second (typical) difference was not warranted.

Testing of AITS with the Aerospace Corporation Flight Design System brought these differences into question once again. We decided to reproduce the differences reported by Aerospace, and then attempt to identify their causes. The reproduction was accomplished by comparing IBSS output to STS39 Supertape values. Extensive testing of AITS and IBSS has shown their outputs to be virtually identical, thus using the IBSS results is a valid approach to the problem.

The first modification to IBSS was to account for the diameter of the solar disk in establishing sunrise and sunset times. Our solar ephemeris gives the location of the center of the sun, whereas the Supertape defines sunrise and sunset in terms of the upper limb of the sun being at Earth's horizon relative to the observer. A constant value of 0.25 degrees was added to the IBSS solar elevation angle to account for the solar radius. This change was expected to result in sunrise 4 seconds earlier and sunset 4 seconds later than previously calculated. Typical results, summarized in Table 46 below, indicated that the differences reported by Aerospace had been duplicated.

TABLE 46. Results of First Modification

Rise/Set	Supertape	IBSS (unmodified)	IBSS (limb corrected)
S	09:18:36.4	09:17:41	09:17:46
R	09:53:22.6	09:53:21	09:53:17

There was a possibility that propagation errors, combined with omission of higher order geopotential terms, could result in errors in the position vector sufficiently large to explain these differences. The angle between the IBSS and Supertape position vectors at 09:18:00 was determined to be  $2.047 \times 10^{-3}$  degrees, however, far too small to explain the difference at 09:17:36.4 reported above.



Since the differences are consistent with a larger Earth, IBSS was further modified to calculate solar elevation angle based on a spherical Earth of radius 6378.140 Km. The results, summarized in Table 47 below, show much smaller differences, which become larger in time. These differences were found to be consistent with propagation errors in the position vector.

**TABLE 47. Results of Second Modification**

Rise/Set	Supertape	IBSS (limb corrected, spherical Earth)
R	08:23:41.5	08:23:42
S	09:17:36.4	09:17:36
R	12:52:44.1	12:52:46
S	13:46:34.1	13:46:36
S	16:45:51.8	16:45:55
R	17:21:45.0	17:21:49

As a final check, the propagation errors were removed by supplying IBSS with additional vectors. These results, in Table 48, show that IBSS is capable of duplicating Supertape sunrise/sunset times if the solar limb correction is applied, and a spherical Earth is used for tangent point calculations.

**TABLE 48. Results with Propagation Errors Removed**

Rise/Set	Supertape	IBSS (limb corrected, spherical Earth)
R	08:23:41.5	08:23:42
S	09:17:36.4	09:17:36
R	12:52:44.1	12:52:45
S	13:46:34.1	13:46:34
S	16:45:51.8	16:45:52
R	17:21:45.0	17:21:46

In conclusion, our calculation of the solar elevation angle above an oblate spheroid offers a significant improvement to what is commonly used. The differences in question were a result of our efforts to satisfy the performance requirements of the project and, if required, our products can be modified to duplicate the results of NASA and Aerospace.

## 8.2 SUATEK ENHANCEMENTS

The SUATEK program, originally formulated by GPD to support PL researchers [Ziemba and McInerney, 1979], has evolved over many years of use on PL mainframes. In recent years, the program has been migrated to other platforms, including IBM PC's [Bhavnnani and Reynolds, 1990]. Recently, a menu-driven version, SUAMENU, has been developed to aid occasional or beginning SUATEK users. Advanced users may find the menu interface beneficial, due to the continuously updated display of plot options. SUAMENU retains all features of the SUATEK program, dividing the available options into three categories on five display screens, which may be accessed from a central menu.

Plot parameters and functions are controlled by entering values within fields. Each page contains a number of fields marked with descriptive labels. The user may cycle through the fields with any combination of <ENTER> and the cursor keys. Illegal or out-of-range input is sensed immediately, and must be corrected before leaving the violated field. Parameters for special functions that are normally given in response to prompts in the SUATEK program (for example, the number of points to use for a cubic fit) are also controlled within the menu structure. These parameter fields are activated when the particular feature is selected.

Typical SUAMENU usage is illustrated by the following two examples.

### 8.2.1 SUAMENU Example I

This example illustrates the development of the plot in Figure 120. The program is initiated by typing SUAMENU. As with SUATEK, the user is prompted for the data file name unless it is included on the command line (i.e., SUAMENU SAMPLE.DAT). SUAMENU determines the input file format (ASCII or binary) and performs conversion to binary if necessary. SUAMENU then displays an audit of the data file:

SUATEK APPLICATION TO A DATA BASE				
Variable Number	Minimum Value	Maximum Value	Variable Name	
1	0.000	360.000	TIME	
2	84.869	512.000	RAW DATA	
3	75.457	163.516	GEO INDEX	
4	164.000	196.000	SOURCE	

Total Variables: 4  
Number of Records: 361

F5 = Next Ten Variables  
F6 = Previous Ten Variables

Variable Number	Axis Length	Begin Value	End Value	
X-Axis: 1	8.000	0.000	400.000	TIME
Y-Axis 1: 2	8.000	-100.000	700.000	RAW DATA

Do You Wish Multiple Y-Axes? (Y or N): Y

After a response of Y the user is prompted with:

Enter Number of Y-Axes To Be Used (2, 3, or 4): 3

The displayed options may now be changed by positioning the cursor with either <ENTER> or the arrow keys, and editing the appropriate fields on the lower portion of the screen. If the file contains more than ten variables, the F5 and F6 keys allow scrolling through the audit display on the top portion of the screen.

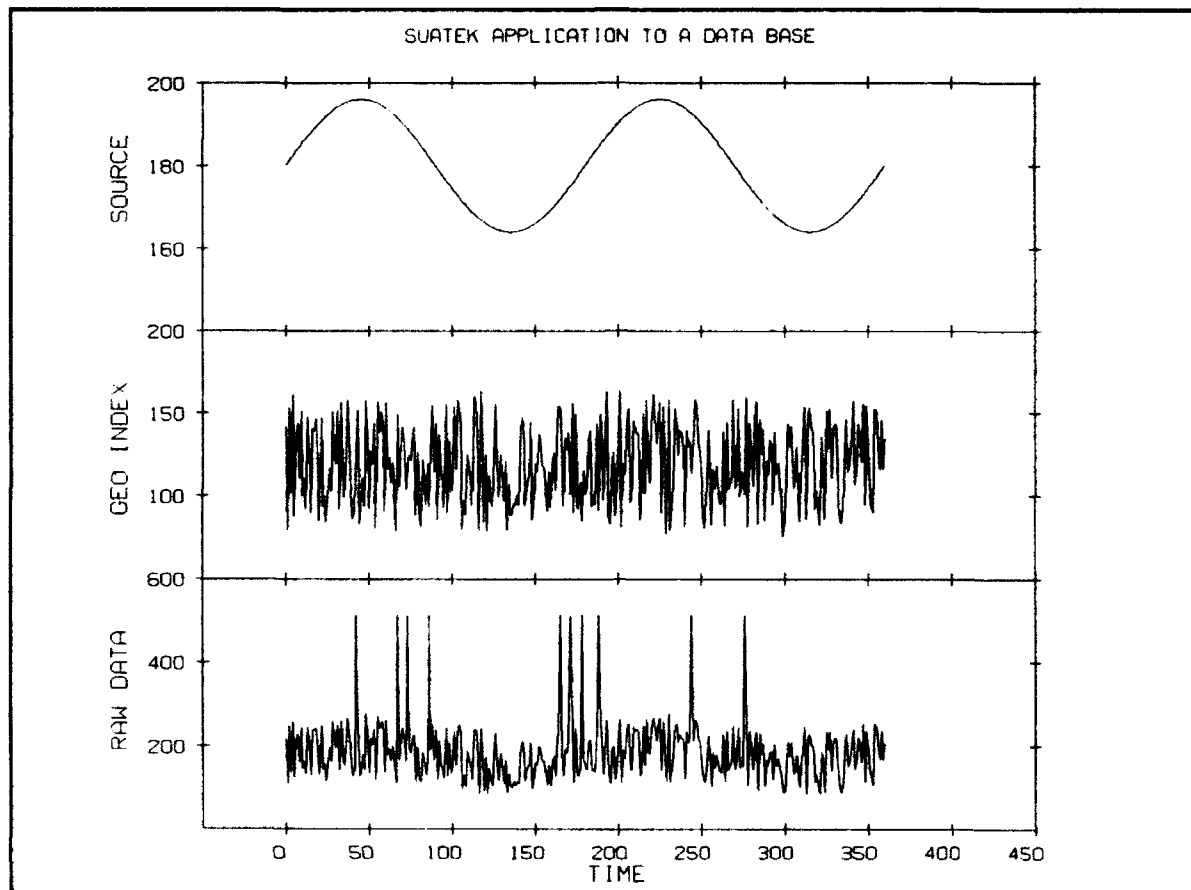


Figure 120. Typical SUAMENU plot.

SUATEK APPLICATION TO A DATA BASE				Variable Name
Variable Number	Minimum Value	Maximum Value		
1	0.000	360.000		TIME
2	84.869	512.000		RAW DATA
3	75.457	163.516		GEO INDEX
4	164.000	196.000		SOURCE

Total Variables: 4  
Number of Records: 361

F5 = Next Ten Variables  
F6 = Previous Ten Variables

Variable Number	Axis Length	Begin Value	End Value	
X-Axis: 1	8.000	0.000	400.000	TIME
Y-Axis 1: 2	3.000	0.000	600.000	RAW DATA
Y-Axis 2: 3	3.000	50.000	200.000	GEO INDEX
Y-Axis 3: 4	3.000	140.000	200.000	SOURCE

Press F7 To View Second Page    Press F8 To Continue

Axis offset variables appear on the second page, which may be accessed by pressing F7. This page also provides options to save or restore a "SUSPEC" file.

<b>F5 Save Plot Specifications</b>		<b>F6 Restore Plot Specifications</b>	
	<b>Subdivisions</b>	<b>Decimal Places</b>	
X Axis	0	0	
Y Axes	0	0	
<b>Change Axis Offsets:</b>			
<b>Variable</b>	<b>Axis Offset</b>		
X Axis:	0.000		
Y Axis 1:	0.000		
Y Axis 2:	3.000		
Y Axis 3:	6.000		
Press <b>F7</b> To View First Page		Press <b>F8</b> To Continue	

The user may continue to make modifications while switching between the two pages with F7, proceeding to the main menu with **F8** when completed:

### S U A T E K

From Here You May:

1. Change or Select Variable Specifications by Pressing Key **F5**.
2. Choose Special Graphing Options by Pressing Key **F6**.
3. Choose Special Functions by Pressing Key **F7**.
4. Plot the Graph by Pressing Key **F8**.

Do You Wish to Exit? (Y or N):

Note that this screen provides the option of terminating the program (by entering **Y**). Pressing **F8** again initiates plotting; before the plot is actually created, the user is presented with a two page display plot summary:

<b>THESE ARE THE PARAMETERS YOU ARE USING TO PLOT YOUR GRAPH</b>					<b>1 of 2</b>
<b>Variable Number</b>	<b>Axis Length</b>	<b>Begin Value</b>	<b>End Value</b>		
X-Axis: 1	10.000	-50.000	450.000		TIME
Y-Axis 1: 2	3.000	0.000	600.000	RAW DATA	
Y-Axis 2: 3	3.000	50.000	200.000	GEO INDEX	
Y-Axis 3: 4	3.000	140.000	200.000	SOURCE	
X-Axis Scale	Linear	0			
Y1-Axis Scale	Linear	2	Produces Line Through Data Points		
Y2-Axis Scale	Linear	2	Produces Line Through Data Points		
Y3-Axis Scale	Linear	2	Produces Line Through Data Points		
Start Reading From Record Number 1		Stop Reading After Record Number 361			
Repeat Factor For Reading Records, Skipping 1					
Press <b>F6</b> For Command Screen					
Press <b>F7</b> To View Second Page		Press <b>F8</b> To Continue			

The layout of the second page is presented in the second example. The plot is generated by again selecting **F8**.

#### 8.2.2 SUAMENU Example II

This example performs a "Linear Combination" of two variables, in order to eliminate noise from a measurement and recover a signal pattern.

On the first screen, a response of **N** was given to the "Do You Wish Multiple Y Axes?" prompt. Begin and end values for the Y axis were set to 0 and 400. Selecting **F7** from the main menu activates the special functions menu. The various options are activated by entering **Y** in the appropriate fields. Many

of these functions require parameters, which may be entered once the option has been activated. A typical display appears below, showing selection of the linear combination and cubic fit options:

```

Select Any Special Graphing Functions:

    Use a Running Average of Data Points:  N
    Make Polynomial to Fit Data in Range:  N
Find First or Second Derivative of Polynomial:  N
    Find Correlation Coefficient:          N
    Linear Combination up to 4 Variables:  Y  Number of Variables:  3
    Exponential Product up to 4 Variables: N
    Keep Running Cubic Fit for Data Points: Y  How Many Data Points: 15
Delete, Replace, Interpolate, or Smooth Data:  N
    Annotate The Plot:                    N
    Suppress The Date Display:            N
    Linear Combination
        Variable Number: 0  Constant: 200.00
        Variable Number: 3  Constant: -2.00
        Variable Number: 2  Constant:  1.00

```

Press **F8** To Continue

Returning to the main menu and selecting **F6** (Special Graphing Options) introduces a two page system. The first page allows selection of linear or log axis scales, and provides control over the range and frequency of data points that are read:

1 of 2

```

Choose Any of These Special Graphing Options:

    Linear(0) Log(1)

X-Axis Scale  Linear  0

    Linear(0,2,4) Log(1,3,5) Bi-Polar(-1,-3,-5)
    -1,0,1 Symbols at Data Points
    -3,2,3 Line Through Data Points
    -5,4,5 Connected Symbols

Y1-Axis Scale  Linear  2  Produces Line Through Data Points

Start Reading From Record Number 1  Stop Reading After Record Number 361
Repeat Factor For Reading Records, Skipping 1

Press F7 To View Second Page  Press F8 to Continue

```

Selecting **F7** displays the second page, which allows modification of axis labels (note the revised Y axis label):

2 of 2

```

Choose Any of These Special Graphing Options:

    Axis Labels and Headings May Be Changed

1.) Title of Graph:          SUATEK APPLICATION TO A DATA BASE  <
2.) X-Axis Label:           TIME  <
3.) Y1-Axis Label:  RAW DATA - 2 * GEO INDEX + 200  <

Enter Line Number of Label You Wish To Change  3

Press F7 To View First Page  Press F8 To Continue

```

The second plot preview page will now summarize the special functions and special graphing options:

THESE ARE THE PARAMETERS YOU ARE USING TO PLOT YOUR GRAPH

2 of 2

- 1.) Title of Graph: SUATEK APPLICATION TO A DATA BASE <
- 2.) X-Axis Label: TIME <
- 3.) Y1-Axis Label: RAW DATA - 2 \* GEO INDEX + 200 <

Keep Running Cubic Fit for Data Points: Number of Data Points: 15

Linear Combination  
Variable Number: 0 Constant: 200.00  
Variable Number: 3 Constant: -2.00  
Variable Number: 2 Constant: 1.00

Press F6 For Command Screen  
Press F2 To View First Page Press F8 To Continue

Figure 121 shows the plot resulting from this example.

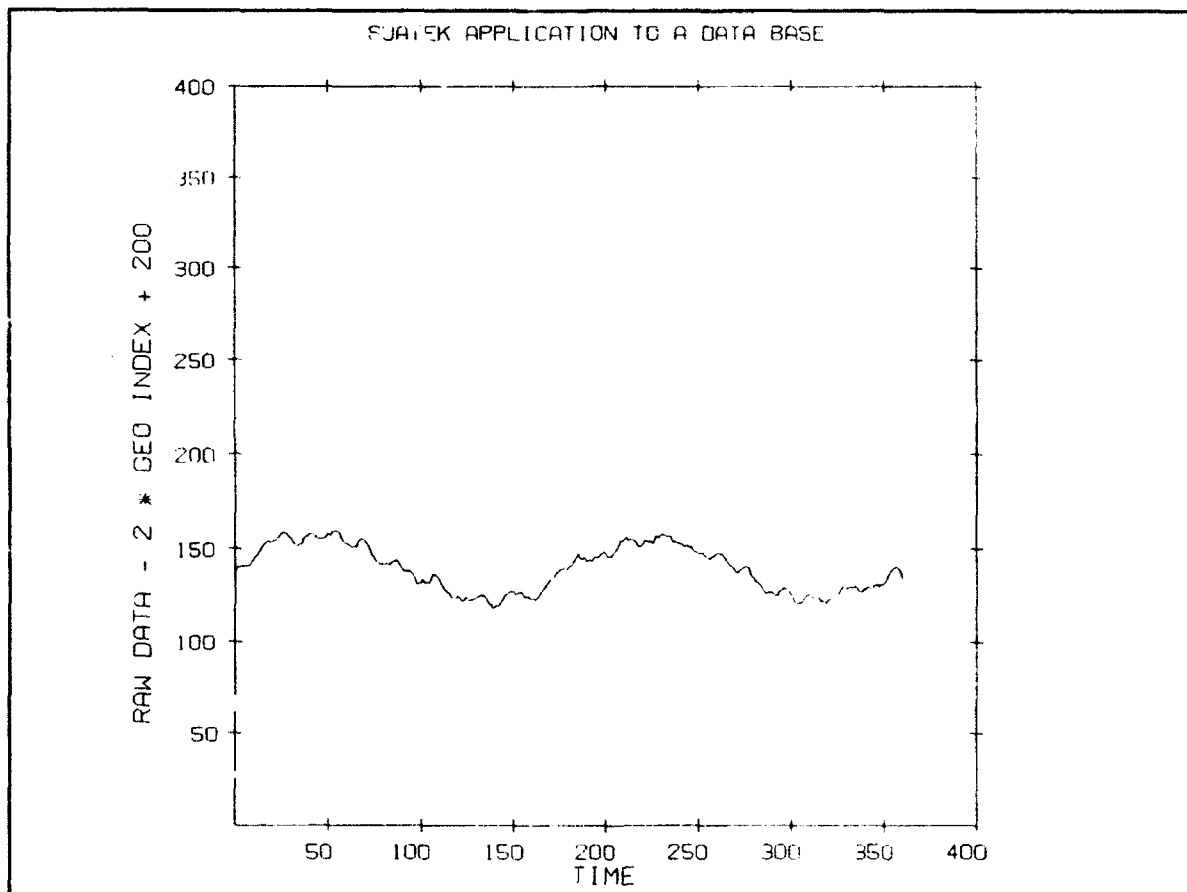


Figure 121. Linear Combination example.

### 8.3 ROCKET TRAJECTORY

The PL Rocket Trajectory Software System provides optimum trajectory solutions for a variety of rocket models with one-stage or multiple-stage flights. This system consists of four main programs: DRIVEA, DRIVEB, DRIVEC, and REGEN [Bhavnani and Robinson, 1979]. DRIVEA uses the raw radar data obtained at the rocket range to generate an intermediate edited file of rocket trajectory parameters. The output from DRIVEA can then be used as an input to DRIVEB. DRIVEB provides a filtered best-estimate trajectory in one of several optional filtering modes. In the event that multi-radar tracking data is available, a statistically weighted final trajectory is developed in DRIVEC. The outputs from DRIVEB and DRIVEC have identical formats, and summary files can be used to recreate listings and plots of results using REGEN.

The program DRIVEB was revised to better handle the generation of the thrust model for each module in a rocket flight. In the past, the thrust profile per rocket module was kept in DATA program statements in the THRUST routine, but this approach became unwieldy as more rocket models were flown. The THRUST routine was upgraded, so that the thrust parameters for each rocket module can be stored in a separate thrust table. THRUST then generates a thrust model based on the thrust and mass losses as a function of time elapsed since the rocket launch. The thrust look-up table contains these two parameters and other pertinent information needed to model the thrust effects. It is a multi-file, where individual files are separated by a end-of-file marker. The look-up table includes both single-stage and multiple-stage flights. Each rocket module has a unique identification number, and THRUST scans the look-up table to find the appropriate rocket module selected by the user.

With these revisions, DRIVEB can provide the filtered best-estimate trajectory for each of the separating modules in a rocket flight. The upgraded Rocket Trajectory Software System was used to provide the optimum trajectory on a number of multiple-stage rocket flights (e.g. ECHO 7, and EXCEDE III). Some of the results are described in Bounar and Robinson [1990].

### 8.4 PC TEKSIM

To meet evolving PL hardware support requirements, the TEKSIM graphics library has been ported to the PC environment [Reynolds, et al., 1992]. Originally, this effort was undertaken to facilitate development of a PC version of the SUATEK graphics package [Bhavnani, et al., 1990]. Subsequently, a number of original PC programs have utilized TEKSIM, including PHIZYX [Bhavnani, et al., 1991]. While the PC version of TEKSIM is not yet a full implementation of the mainframe versions, most of the documented subroutines are available. Augmentation of the library has been on-going, in response to specific customer requests.

Support of the wide variety of graphics boards and printers available in the PC environment is accomplished by utilizing the package *GraphiC* (written in C), from Scientific Endeavors Corp. [1991] of Kingston, TN. A site license has been obtained for use of *GraphiC* at PL, and equivalents to the low-level TEKSIM routines have been developed using calls to *GraphiC* subroutines. A number of enhancements have also been possible through the resources of *GraphiC*, such as improved fonts and an annotation capability.

The following list indicates the subroutines and functions presently available in the PC TEKSIM library. Subroutines followed by "\*" are primarily intended for internal TEKSIM use, while "+" indicates a PC TEKSIM extension. Note also that several functions have been added to provide VAX capabilities not available in the Microsoft FORTRAN library.

ANMODE	GETLST*	NEWPEN	SETPAT
ANOTAT+	GLOBAL+	NOTIN*	SHELL+
APAGE+	GNUMBER+	NOTOUT*	SIND
AXFONT+	GOSVER*	NOTSAV*	STRTSEG
AXIS	GRCROSS	NUMBER	SWPAGE+
AXISL	GRMODE+	PANFIL*	SYMBOL
AXLOG	GSTRWID+	PICKFNT+	TAND
BELL	GSYMBOL+	PLOT	TEKGO
CHREAD+	HDCOPY	PLOT2*	TEXT+
CHWRITE+	HOME	PLTID1*	TEXT1*
CLRSCR+	IDATE	PLTID3	TEXTM+
CNEWPAG*	JSHIFT	RADLOG*	TKFSWP*
CNEWPEN*	KILLSEG	RDCHAR+	TXTCLR+
COSD	LCASE+	RDINT+	UCASE+
CREPLAY*	LDFONT+	RDREAL+	UPDATE*
ENDPLT	LINE	REPLAY+	VPAGE+
ENDSEG	LOCATE+	RPLOT	WHERE
EXASCI	NEWNAM+	SELFNT+	WIPELN+
FRAME	NEWORG*	SETBOR+	WRTFNT*
FSTRWID*	NEWPAG	SETCOL	

## 8.5 PHIZYX

### 8.5.1 Introduction

An important aspect of the evaluation of experimental and analytical geophysical data is the depiction and manipulation of extensive data sets. Although various plotting packages are now available on desktop computers for displaying data in Cartesian plots, and a user friendly interactive package, SUATEK [Bhavnani, *et al.*, 1990], has been developed which incorporates editing capabilities, three-dimensional and/or color plotting packages for manipulating scientific data interactively are unavailable. The PL Interactive color/three-dimensional plotting package, PHIZYX, provides an implementation based on specifications which have evolved from our experience on various applications appropriate to this approach.

Incorporation of color display technology into color graphics terminals provides a significant opportunity to enhance the visualization of data bases. The PHIZYX package evolved as requirements of an assortment of applications were satisfied, and the operational features and the standard data format reflect many inherent technical and usage considerations. Servicing of varied applications and data bases is an on-going activity. Valuable extensions such as multi-file handling, contouring, and even dynamic displays are some of the capabilities that may be integrated into the package, so that this development continues to be evolutionary.



### 8.5.2 Development

PHIZYX is based on the TEKSIM graphics library, which originated on PL mainframes and has been migrated to the PC environment [Reynolds, *et al.*, 1992]. The PC TEKSIM development was based on *GraphiC*, a product of Scientific Endeavors Corporation [1991] of Kingston, TN. *GraphiC* includes drivers for a wide variety of graphics boards and printers, so the PC TEKSIM package can support many output devices in their high resolution modes.

Emphasis for SUATEK and PHIZYX has been on development of user friendly packages for use in the IBM PC environment. SUATEK incorporates data editing and smoothing capabilities, and uses the Tektronix file concept extensively, together with the facilities of *GraphiC*, to produce high resolution hard copy on any of a wide variety of laser and dot matrix printers. SUATEK and PHIZYX source codes are written in FORTRAN, and an implementation guideline has been to retain compatibility with TEKSIM, so that the programs may be readily portable to PL/GD mainframes.

PHIZYX has been written as a separate package for various reasons. The PHIZYX data format is compatible with the standard SUATEK format, but a separate package has alleviated development constraints. Interactive editing and smoothing may be achieved by employing SUATEK, but preferred capabilities for color and/or 3-D presentation and manipulation may differ from SUATEK, and these features have yet to be specified and implemented.

### 8.5.3 Features

PHIZYX provides a means for interactive contour type color presentation of data, consisting of X-Y-Z plots, where each X-Y block is given a Z-dependent colorization level. The user is not required to do any programming, although the data must be made available in a specified standard format. In order to enable interactive editing and conventional plotting capabilities, the data format is designed to be nearly identical to the SUATEK ASCII file format.

The following is a brief summary of the most important PHIZYX capabilities:

- The data file can have any number of variables up to 99, and an arbitrary number of records.
- Gray scaling may be obtained on *PostScript* printers.
- A fixed color bar with 14 levels is used, and the Z levels for color transition can be entered interactively, saved on an auxiliary specification file, and be read or modified during the current or a subsequent session. An option is available to scan the data for the Z range prior to specifying the color transition levels.
- A dependency parameter option is available for up to four parameters, similar to SUATEK. When dependency parameters are invoked, a temporary internal file is created to avoid processing all the data again, and the Z scan is initiated automatically.
- Tick marks at block boundaries or centers are possible, and should be specified within the file format, since information pertinent to this choice is implicit with the data sets. Tick mark positioning is also available, and allows plot placement control.

#### 8.5.4 Concepts

Familiar 3-D black-and-white presentations are contour plots which interpolate X and Y values to trace and label fixed Z-values, and the truly three-dimensional "hidden-line" plots, both of which suffer in visualization. Figures 122 and 123 show typical plots that PHIZYX will generate. The presentation provides a concurrent view of three parameters from a data base, and may be considered to constitute a three-dimensional equivalent of the basic X-Y Cartesian plot. Two parameters provide the X and Y axes of the plot, and the third parameter provides the Z or color scale. The X and Y scales may be selected by the user, may cover all or part of the actual X and Y data ranges, and may be subject to optional dependency constraints on other parameters in the data base. The Z scale must cover the range of Z data values encountered in the given X-Y range. The color bar at the right defines the Z scale. Although any variety of colors is possible for the presentation, a fixed color bar was established once and for all, and the user must assign numerical values at the color boundaries. For this, the user may initiate PHIZYX to pre-scan the data in the specified X and Y range, before determining the numerical values at each color boundary.

Although the Z value determines the block color, two types of X-Y presentations must be considered. When data is accumulated more or less randomly, arbitrary X and Y values will occur. In this case, Z values may be collected and averaged into bins defined by specific X and Y ranges, which in turn determine specific plotted blocks. In Figure 122, tick marks identify the specific X and Y range values. If known models need to be portrayed instead, Z values are determined at reasonable intervals at specific X and Y values. In this case, tick marks centered on each colored block are appropriate for specifying each X and Y value. Figure 123 shows such an example.

Due to the limited effective area for the color plot itself, efficient placement of the X- and Y-axis scales is always desirable. The initial tick marks on the X and Y axes can be positioned for this purpose, and Figure 122 shows this capability being employed beneficially.

#### 8.5.5 PHIZYX Data Format

Display of X-Y-Z data by block coloring, places requirements on some of the values themselves. In order to produce a regular plot, variables that are employed to define the X and Y axes should be spaced at equal increments. This PHIZYX data format can be specified to be nearly identical to the "flat file" format of SUATEK data files, including the first few records which provide content, control, and label information. Only one SUATEK format definition parameter, which is very infrequently used, has been assigned a special meaning for use by PHIZYX and, although other non-conflicting assignments have also been suggested, the SUATEK program would eventually be modified only if these usages prove satisfactory.

Group #1	NOV, -	Number of Variables
(1 record)	MN, -	Flag (presently unused)
	LAE, -	0 to 2 alphanumeric 'MLBL' labels follow
	IBC -	= 0, mark ticks at block boundaries;
		= 1, mark ticks at block centers.
		(see description that follows)

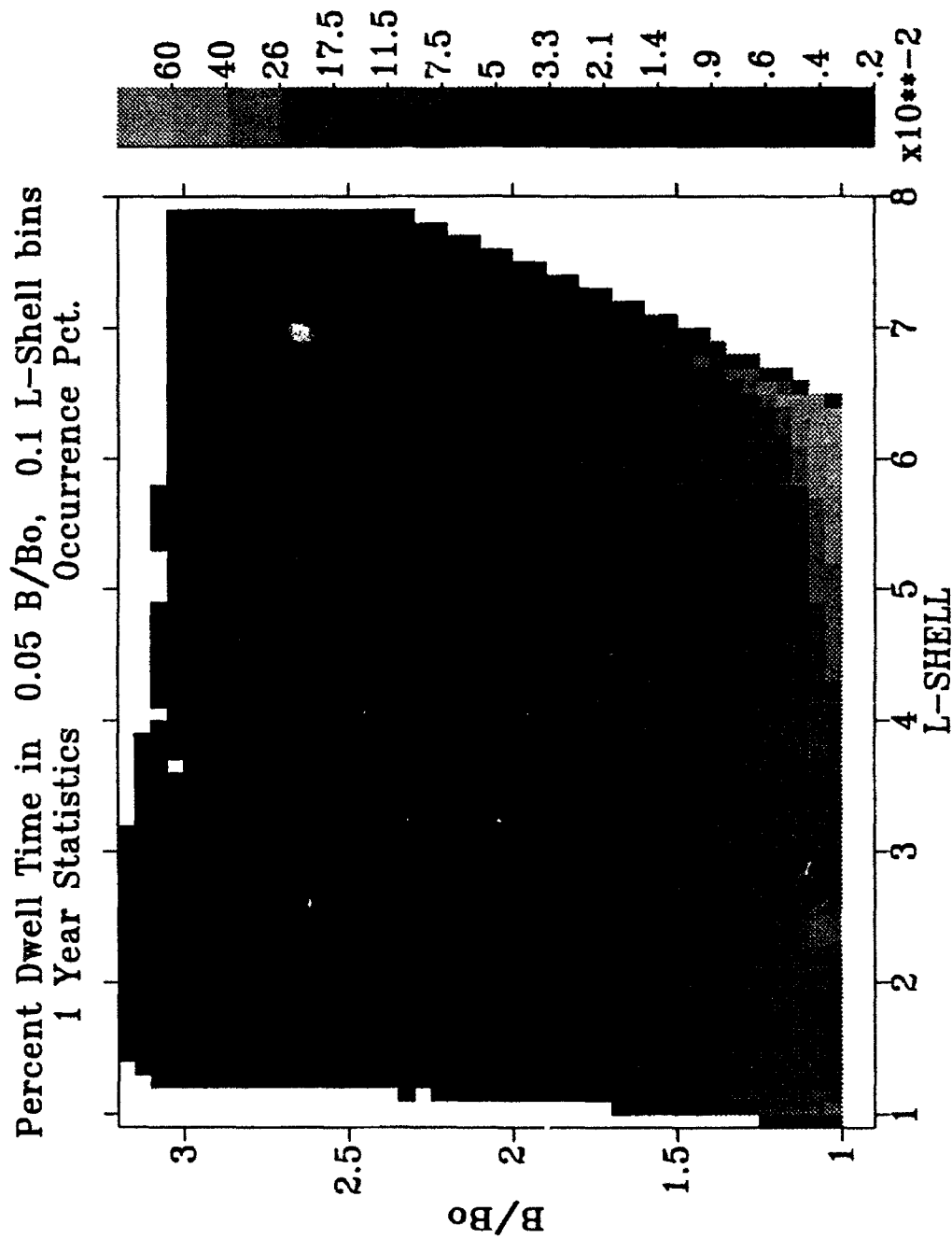


Figure 122. Typical PHIZYX plot, where Z values were collected and averaged into bins defined by specific X and Y ranges.

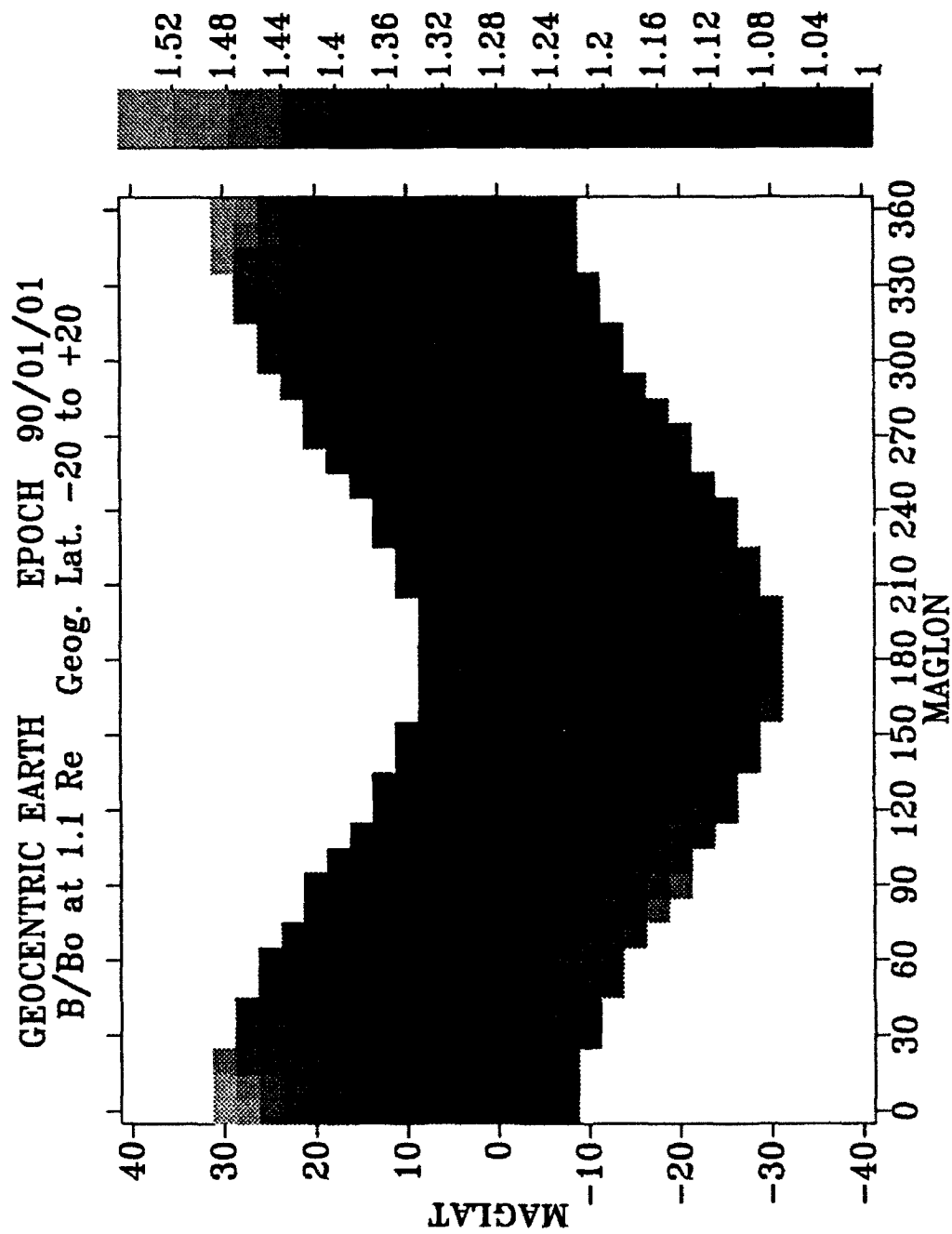


Figure 123. Typical PHIZYX plot, where Z values were determined at reasonable intervals at specific X and Y values.

Group #2 (NOV records)	LBL -	One alphanumeric label per variable (up to 32 characters)
	DMN,DMX,	followed by min, max and increment for that variable
	DVAL	(see description that follows)

Group #3 (LAE records)	MLBL -	LAE (0 to 2) title labels (up to 52 characters)
---------------------------	--------	---

Subsequent records consist of 'NOV' real numbers, one each per variable.

Note: -9.0E35 denotes a deliberately deleted value,  
 -9.9E35 denotes that value should be ignored.  
 (these meanings are consistent with SUATEK)

The above variables have generally been defined previously for SUATEK, and the following additional parameters apply to PHIZYX files:

'IBC' indicates whether the data:

- 1) should be considered to be accumulated into bins, in which case tick marks are appropriate at the block boundaries, OR
- 2) is assigned to specific equally spaced X and Y values, in which case the tick marks are appropriate at block centers.

'DMN', 'DMX', 'DVAL' are required data minimum, maximum and increment values, although only the DVAL increment for each variable that could be assigned to the X- or Y-plot axis is actually needed, since a data scan cannot determine this increment if data is missing. DMN and DMX are used to dispense with the data scan altogether.

## 8.6 MODELING OF THE CRRES ATTITUDE

The Combined Release and Radiation Effects Satellite (CRRES) scientific payload contained several experiments for which accurate and dependable attitude information was required. Among these, were the fluxgate magnetometer instrument and the ion and neutral mass spectrometers. The post-flight attitude determination program was developed by Space Applications Inc., based upon a nominal satellite. However, the actual behavior of the satellite was sufficiently different so that the original processing routines and attitude model would have led to intolerable attitude errors. We undertook the development of improved models and processing techniques which resulted in a high quality data set, satisfying all mission requirements [McNeil, 1991].

### 8.6.1 The CRRES Attitude Problem

The CRRES satellite is spin stabilized at a spin rate of around 2 rpm, with the spin axis directed within a few degrees of the sun. The attitude hardware consists of a one-axis sun sensor, a three-axis low resolution magnetometer, and a horizon sensor which, because of the eccentricity of the orbit, has Earth in view only for a relatively small fraction of the time. The methods for attitude solution consist of the deterministic calculation of inertial pointing direction of the spin axis and of spin phase from each complete set of measurements taken during about one spin period. This arrangement leads to an attitude solution about every 30 seconds. However, each solution is not of comparable accuracy.

Nominal vehicle operation, for which the CRRES Attitude Determination Program (CADP) was designed, presented two major limitations during actual flight. First, the low resolution of the magnetometer, coupled with natural deviations of the field model from the actual field in the magnetosphere, made attitude based on magnetometer data virtually useless, except for the data taken near perigee. Second, the interaction of the wire booms led to a substantially non-constant spin rate, especially during and immediately after eclipses. The use of the original attitude model under these conditions produced intolerable errors in the attitude. Figure 124 shows the deviation of the measured magnetic field (from the high resolution fluxgate magnetometer) from the model field over the course of an orbit. One can see errors of several tens of degrees and large discontinuities, especially away from perigee. The task, then, was to use the measured data to produce an attitude model without these problems.

### 8.6.2 The Model

Anticipating some potential problems with the attitude model, especially for the processing of the fluxgate magnetometer data for which accuracy is essential, we had previously designed an interactive attitude modeling package. We had intended to use this as an alternative to the attitude model produced from the CADP, should the need arise in all or in specific cases where increased control of the model became necessary. As it turned out, the interactive modeling system was needed for all processing.

#### 8.6.2.1 Spin Axis Vector

The only reliable spin axis data comes from periods when both the sun and Earth limb are in view. Fortunately, aside from a small steady precession of the spin axis of about  $0.05^\circ$  per orbit, the spin axis pointing direction is actually constant in inertial space. Since one requirement was to process each orbit independently, the incorporation of this small change would be impossible, due to the fact that attitude resolution is only about  $0.5^\circ$  in the sun sensor anyway.

A typical orbit has two to three periods of Earth horizon data, the number, duration, and position depending on the orientation of perigee with respect to the sun. These periods were used solely for a global fit to the spin axis direction for each orbit. However, for orbits containing one of the frequent attitude adjustments, in which the spin axis is re-oriented toward the sun, two global fits were done, one prior to the attitude adjustment and one after it.

#### 8.6.2.2 Spin Rate

The direct result of the attitude computation is an instantaneous spin phase. This is incorporated into the attitude model as a reference phase and a spin rate, both of which were intended to be constant. In order to allow for some deviation, the approximately ten hour orbit was divided into segments, during which independent attitude models were produced. Although this proved adequate in test data, for which nominal operations were assumed in the simulations, the natural changes in spin rate found in practice were too large to be treated in this manner.

The first step taken in modeling the spin phase was to use the global averaged spin axis position to calculate a set of phase zero times. Then, these zero times were used to create a set of time zero. Essentially, this allows for a zero phase  $\phi_0(t)$ , to which is added a phase obtained assuming a constant spin rate, for model generation. We took the zero phase up to order 3 in time leading to an expression for the phase of

## CRRES Attitude Quality Control Plot 313 335/90 Dec 1

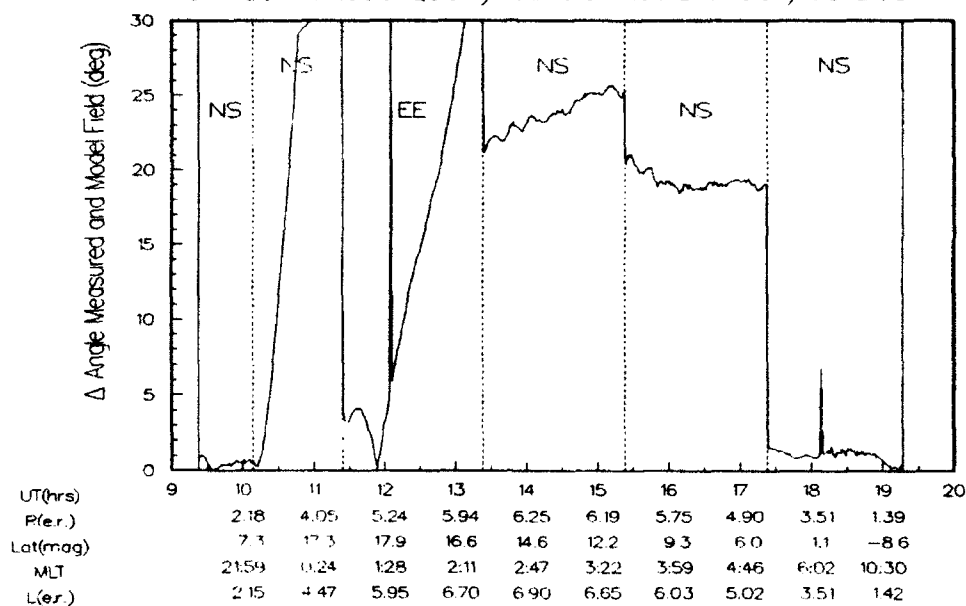


**Figure 124.** The angle between a model magnetic field and the field as measured by the fluxgate magnetometer. Attitude is modeled by the original CADP routine.

## CRRES Attitude Quality Control Plot 313 335/90 Dec 1

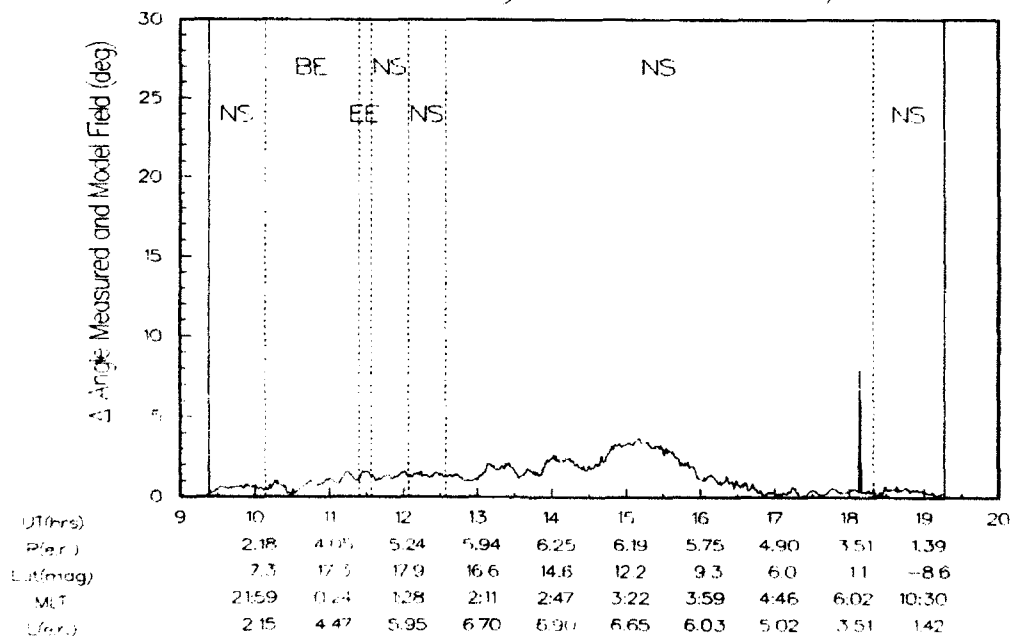


**Figure 125.** Same as Figure 124, but with the attitude model generated by the current attitude modeling software.

$$\Phi(X) = \omega_A t \pi_0 + \pi_1 X + \pi_2 [2X^2 - 1] + \pi_3 [4X^3 - 3X] \quad (103)$$

where  $X$  is the Chebyshev variable for the time within the segment. This addition allowed for good representation of the spin phase throughout reasonably large segments. Also, in routine processing, small corrections were made to terms in each segment to create continuous segment boundaries. This feature is important for producing continuous processed magnetic field data.

#### 8.6.2.3 Eclipses

During the eclipse, the only information of practical use is the spin rate measured by the time between zero crossings of the magnetic field. To model the spin rate increase during eclipse, we performed a fit to the calculated spin rate. The characteristics of this fit were then used to model the spin phase during the eclipse. Specifically, we required that the phase at the beginning of the eclipse match the end of the pre-eclipse phase. Further, we chose the first derivative of the spin rate during eclipse so that the phase at the end matched the beginning of the first post-eclipse segment. Then, the measured first and second derivatives of the spin rate were used for the model of the change in phase during eclipse.

#### 8.6.3 Results

Figure 125 shows the same data as Figure 124, but with the improved attitude model. As can be seen, the measured and model fields agree to within one degree at perigee. The boundaries between segments (delineated by dotted vertical lines) can be seen to be continuous. In all, the incorporation of these changes into the attitude model resulted in a fully adequate representation of the attitude for the processing of scientific data.

### 8.7 APEX ATTITUDE & EPHEMERIS

The Advanced Photovoltaic and Electronic Experiment (APEX) satellite (P90-1) supports three experiments; the Photovoltaic Array Space Power Plus Diagnostics (PASP-Plus) experiment, the Cosmic Ray Upset Experiment/Cosmic Ray Environment and Dosimeter Experiment (CRUX/CREDO), and the Ferroelectric Memory Experiment (FERRO). Although the attitude and ephemeris requirements for the APEX mission are somewhat different from that of CRRES, the CRRES ephemeris and attitude processing system algorithms proved to be a valuable starting point for the design of an equivalent system for APEX.

#### 8.7.1 Ephemeris

Ephemeris parameters are generated from position/velocity vectors obtained from the Consolidated Space Test Center (CSTC) at intervals of about one per day. The vectors are quality checked for transmission errors and entered into a sequential state vector data base. Vectors for specific APEX periods are then converted to mean elements averaged over  $J_2$  and  $J_3$  geopotential terms, and interpolated to uniform times. These are then converted back to position/velocity vectors. From the satellite position, a variety of properties are computed that are necessary for attitude determination and for scientific analysis of the experimental data. Solar ephemeris in the common Earth Centered Inertial (ECI) coordinate frame and the International Geomagnetic Reference Field model is used to provide a model magnetic field and to trace field lines to determine the magnetic equator, the conjugate point, and L-shell at each 60 second



interval. Position is generated in several common coordinate systems and eclipse times are calculated for inclusion in file headers. Reference vectors, such as the dipole direction and offset and satellite velocity, are included in the ECI coordinate system, making the task of conversion to additional coordinate systems easier and less prone to discrepancy from one application to another.

Some important modifications were made to the CRRES ephemeris software, both to increase the convenience of use and to incorporate specific features more appropriate to the APEX mission. The orbit segmentation algorithms were abandoned, since the APEX periods will be segmented by day instead of by perigee crossing, as was the case for CRRES. Also, the relatively complex eclipse calculator was replaced by a simple quadratic interpolation routine that works on previously generated position and solar information. This proved to be more than adequate for the calculation of eclipse times. The external field model was abandoned, since APEX is a low-Earth satellite. We believe the end result will be a system more trouble free than was that for CRRES.

#### 8.7.2 Attitude

The attitude determination instruments aboard the satellite consist of a two-axis sun sensor, which measured the sun normal vector directly, and a magnetometer, which can be used to calculate the roll angle during sunlit operation and the three-axis attitude in eclipse. The attitude control requirements are strictest during sunlit operation, when the sun must be normal to the solar arrays to within one-half degree. This requires the spacecraft x axis to be collinear with the sun direction to this precision. A less precise requirement is that the dosimeter (spacecraft y axis) lie in the ecliptic plane to within 5°. There are no set requirements for attitude knowledge, however, knowledge must be sufficient to assess the level of control. For the APEX satellite, assessment of the degree of attitude control is the primary purpose of post-flight attitude computation.

We have undertaken a detailed modeling program [McNeil, 1992] in order to: (1) verify that post-flight attitude computation can satisfy the attitude knowledge requirements; and (2) design and test algorithms for attitude determination. The simulation program incorporated a realistic APEX orbit, with drag and gravity gradient perturbations to the attitude. The attitude itself was modeled with realistic representations of the control imparted by the momentum wheel and torque rods in response to the environmental torques. Figure 126 shows typical results for the attitude arising from the simulated system. Details are given in McNeil [1992].

##### 8.7.2.1 Magnetometer Calibration

Since the attitude instruments consist of only sun sensor and magnetometer, the calibration of the magnetometer becomes an important determinant of the overall accuracy. We have developed a calibration scheme with which an averaged gain and the three-axis offsets of the magnetometer can be calculated on-orbit from the minimization of the difference in magnitude between the measured field and the model. This has proven to function well on simulated data.

##### 8.7.2.2 Sunlit Attitude

In sunlight, the two axis sun sensor is used to determine the rotation cone of the satellite x axis around the sun line. Then, the magnetometer measurement is used to find three-axis attitude. These are fairly standard techniques [Wertz, 1978]. The chosen algorithm is deterministic, producing one attitude for each combined sun sensor and magnetic field measurement. It retains the full accuracy inherent in the sun

APEX Attitude Simulation  
 Case 1  $T_c=0.80$   $T_s=0.20$   
 $Bi=1$   $Br=120$   $P=600$  s

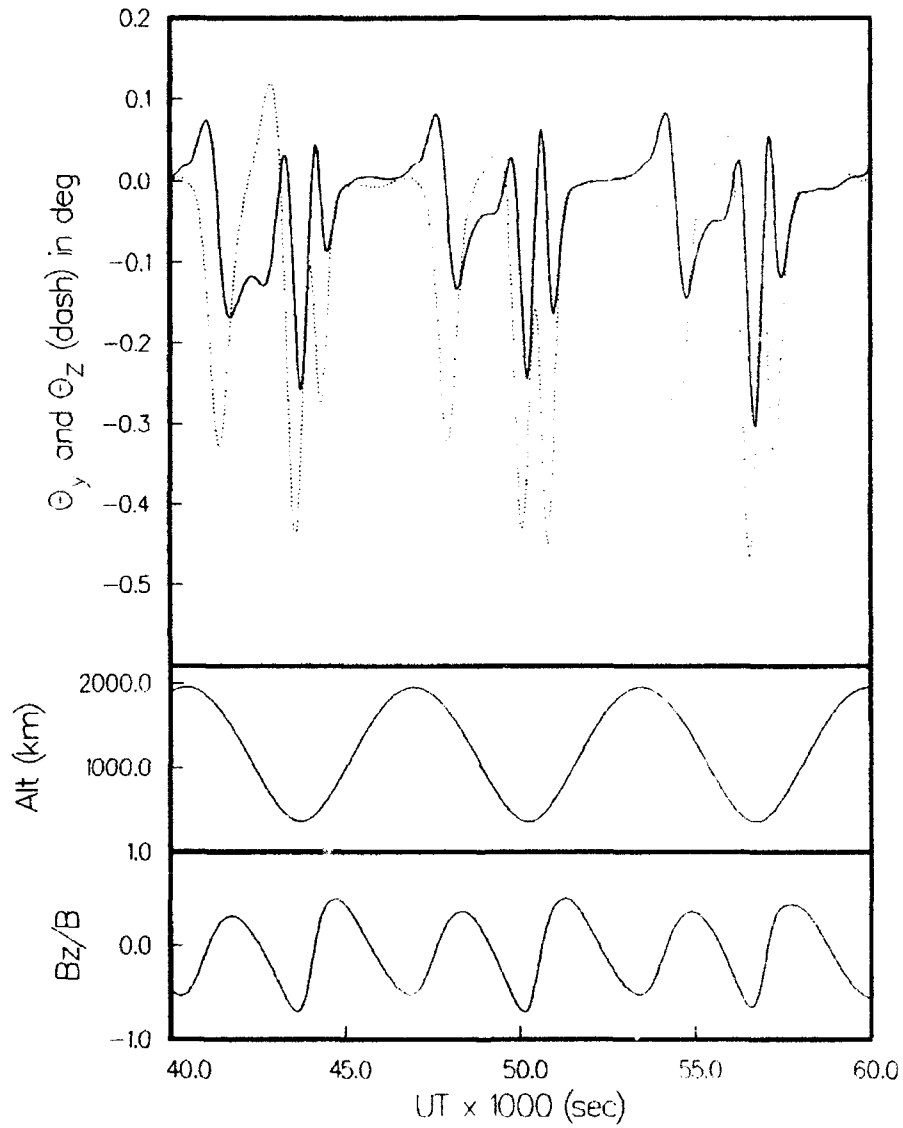


**Figure 126.** Typical pitch and yaw (sun directed) angles during sunlit operation.

sensor measurement, so that the resulting values of sun angle (pitch and yaw) are precisely the results of the sun sensor, while any error in the roll axis is that due to the magnetic field measurements.

#### 8.7.2.3 Eclipse Attitude

An important aspect of the attitude solution during eclipse is that the only reference vector available is the measured magnetic field. One reference vector is not enough to uniquely specify the attitude at any moment. Therefore, a series of measurements must be combined to yield an attitude estimate. We have opted for a least-squares approach to the problem. One reason for this choice is the necessity to process the data in selected periods, where other filtering techniques requiring a historical approach are not appropriate. A second reason is to provide as fully an independent attitude as possible from that computed on-board, where a Kalman filter will be used for eclipse attitude.

In our basic approach, the attitude is represented as a constant over an interval of a few minutes. The attitude is cast in terms of three variables, the position of the  $x$  axis and the rotation  $\phi$  around this axis. The best set of values for the three attitude variables in this parameterization are then calculated by minimization of the difference between a series of magnetic field measurements from a model and from the magnetometer. This method is quite accurate when the motion of the satellite is reasonably small, compared to the motion of the magnetic field in satellite coordinates. We have found that it is adequate for verification of the degree of attitude control in the satellite, which is the desired result.

## 8.8 REFERENCES

- Bhavnani, K. H. and D. S. Reynolds, "PHIZYX: Phillips Laboratory Interactive 3-Dimensional Color Plotting Package", Radex, Inc., Bedford, MA, October, 1991.
- Bhavnani, K. H. and D. S. Reynolds, "SUATEK Interactive Graphics PC User's Guide", Radex, Inc., Bedford, MA, July, 1990.
- Bhavnani, K. H. and E. C. Robinson, "Functional and Operational Advances in the AFGL Rocket Trajectory System - I", AFGL-TR-79-0183, July 1979, ADA081447.
- Bounar, K. H. and E. C. Robinson, *Private Communication*, 1990.
- McNeil, W. J., Simulation and Calculation of the APEX Attitude, PL-TR-92-2209, 1992, ADA258716.
- McNeil, W. J., Calculation and Modeling of the Attitude for the Combined Release and Radiation Effects Satellite, PL-TR-91-2239, 1991, ADA243950.
- Reynolds, D. S. and R. J. Raistrick, "PC TEKSIM User's Guide", Radex, Inc., Bedford, MA, November, 1992.
- Scientific Endeavors Corporation, GraphiC<sup>TM</sup> 6.0 Publication Quality Scientific Graphics, May, 1991, Kingston, TN.
- Wertz, J. R. ed., "Spacecraft Attitude Determination and Control", D. Riedel Publishing Company, Boston, 1986.
- Ziemba, E. J. and R. E. McNerney, *Private Communication*, August 1979.

END